

Science

1 November 2013 | \$10

The Heavily Connected **Brain**

 AAAS

SPECIAL SECTION

The Heavily Connected Brain

INTRODUCTION

577 Connection, Connection, Connection ...

REVIEWS

578 Cortical High-Density Counterstream Architectures

N. T. Markov et al.

Review Summary; for full text:

<http://dx.doi.org/10.1126/science.1238406>

579 Structural and Functional Brain Networks: From Connections to Cognition

H.-J. Park and K. Friston

Review Summary; for full text:

<http://dx.doi.org/10.1126/science.1238411>

580 Functional Interactions as Big Data in the Human Brain

N. B. Turk-Browne

585 Predispositions and Plasticity in Music and Speech Learning: Neural Correlates and Implications

R. J. Zatorre

>> Science Podcast

>> Editorial p. 533; News story p. 548; Reports pp. 632 and 637; and Science Express Report by G. M. Sia et al.

EDITORIAL

533 Seize the Neuroscience Moment

Alan I. Leshner

>> The Heavily Connected Brain section p. 577

NEWS OF THE WEEK

540 A roundup of the week's top stories

NEWS & ANALYSIS

542 New Experiment Torpedoes Lightweight Dark Matter Particles

543 RNA Helps Resurrect Ancient DNA

544 Industry Lobbying Derails Trawling Ban in Europe

545 French Mathematician Tapped to Head Key Funding Agency

546 Structural Biology Triumph Offers Hope Against a Childhood Killer

HIV Surface Proteins Finally Caught Going Au Naturel

>> Research Article p. 592

NEWS FOCUS

548 Short-Circuiting Depression

>> The Heavily Connected Brain section p. 577; Science Podcast

552 Dark Matter's Dark Horse

LETTERS

558 Health and Obesity: A New Normal?

M. E. Deutsch

Health and Obesity: Not Just Skin Deep

E. Arner and P. Arner

Emerging Arsenic Threat in Canada

V. D. Martinez et al.

559 Life in Science: Zombiology

559 CORRECTIONS AND CLARIFICATIONS

BOOKS ET AL.

560 The Sports Gene

D. Epstein, reviewed by D. Greenbaum et al.

561 When People Come First

J. Biehl and A. Petryna, Eds.,

reviewed by N. S. Berry

POLICY FORUM

562 Doctoral Students and U.S. Immigration Policy

K. E. Maskus et al.

PERSPECTIVES

564 Our Fallen Genomes

E. Z. Macosko and S. A. McCarroll

>> Report p. 632

565 Dust Unto Dust

M. C. Scholes and R. J. Scholes

>> Report p. 621



page 552

566 A Pathway to Flowering—Why Staying Cool Matters

O. Nilsson

>> Report p. 628

568 Storing Quantum Information in Schrödinger's Cats

P. J. Leek

>> Report p. 607

569 Quantized Electronic Heat Flow

B. Sothmann and C. Flindt

>> Report p. 601

570 Rhythmic Respiration

G. Rey and A. B. Reddy

>> Research Article p. 591

572 Retrospective: David H. Hubel (1926–2013)

R. H. Wurtz

CONTENTS continued >>

ON THE WEB THIS WEEK

>> Science Podcast

Listen to stories on neural correlates for music and speech learning, understanding the role of scars in spinal cord injury, deep-brain stimulation for depression, and more.

>> Find More Online

Check out Science Express, our podcast, videos, daily news, our research journals, and Science Careers at www.sciencemag.org.



COVER

Fiber pathways of a female human brain mapped noninvasively with diffusion magnetic resonance imaging. The image shows an axial view from above (front is at top). Major pathways of the human frontal lobes, and their organization as orthogonal grids, are shown here (cerebral association pathways, vertical; transverse pathways, horizontal). For a description of cortical networks, see the special section beginning on page 577.

Image: Van J. Wedeen, Aapo Nummenmaa, Ruopeng Wang, and Lawrence L. Wald/Athinoula A. Martinos Center for Biomedical Imaging, Massachusetts General Hospital, with support of NIH Human Connectome Project and NSF

DEPARTMENTS

- 531 This Week in Science
- 535 Editors' Choice
- 538 Science Staff
- 641 New Products
- 642 Science Careers

SCIENCE PRIZE ESSAY

- 573 **Space Bats: Multidimensional Spatial Representation in the Bat**
M. M. Yartsev

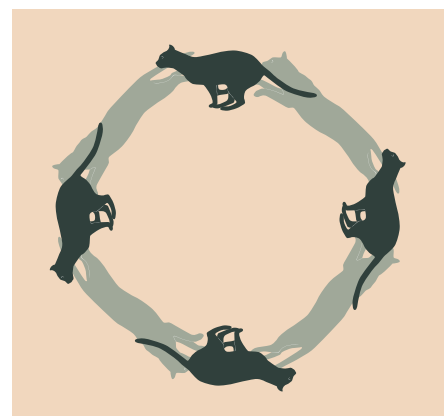
RESEARCH ARTICLES

- 590 **On and Off Retinal Circuit Assembly by Divergent Molecular Mechanisms**
L. O. Sun et al.
Work in mice reveals how motion-detection circuitry is established during visual system development.
Research Article Summary; for full text: <http://dx.doi.org/10.1126/science.1241974>
- 591 **Circadian Clock NAD⁺ Cycle Drives Mitochondrial Oxidative Metabolism in Mice**
C. B. Peek et al.
The coenzyme nicotinamide adenine dinucleotide mechanistically links the circadian clock to control of energy production by mitochondria.
Research Article Summary; for full text: <http://dx.doi.org/10.1126/science.1243417>
>> *Perspective p. 570*
- 592 **Structure-Based Design of a Fusion Glycoprotein Vaccine for Respiratory Syncytial Virus**
J. S. McLellan et al.
Molecular engineering of a childhood virus surface protein significantly improves protective responses in mice and macaques.
>> *News story p. 546*

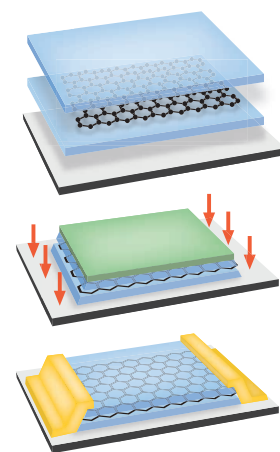
REPORTS

- 598 **Evolution of the Magnetic Field Structure of the Crab Pulsar**
A. Lyne et al.
Long-term measurements show the systematic evolution of the radiation pattern of one of the youngest neutron stars known.
>> *Perspective p. 569*
- 601 **Quantum Limit of Heat Flow Across a Single Electronic Channel**
S. Jezouin et al.
The unit of heat carried by electrons is measured using noise thermometry and found to be consistent with predictions.
>> *Perspective p. 569*
- 604 **Parameter Space Compression Underlies Emergent Theories and Predictive Models**
B. B. Machta et al.
An information-theoretical approach is used to distinguish the important parameters in two archetypical physics models.
- 607 **Deterministically Encoding Quantum Information Using 100-Photon Schrödinger Cat States**
B. Vlastakis et al.
A scheme is demonstrated for coherently mapping the state of a single superconducting qubit onto a large number of photons.
>> *Perspective p. 568*

- 611 **Real-Space Identification of Intermolecular Bonding with Atomic Force Microscopy**
J. Zhang et al.
An atomic force microscope tip bearing a single carbon monoxide molecule was used to resolve hydrogen bonding contacts between molecules.
- 614 **One-Dimensional Electrical Contact to a Two-Dimensional Material**
L. Wang et al.
Metal contacts to graphene along its edge improve bonding and, in turn, electronic performance.
- 617 **Pacific Ocean Heat Content During the Past 10,000 Years**
Y. Rosenthal et al.
Marine records show how ocean heat content has varied in step with climate over the past 10,000 years.
- 621 **Reconstructing the Microbial Diversity and Function of Pre-Agricultural Tallgrass Prairie Soils in the United States**
N. Fierer et al.
Analysis of microbiota in prairie soil relicts offers insights into the ecological function of a near-extinct biome.
>> *Perspective p. 565*
- 624 **Structural Basis for flg22-Induced Activation of the *Arabidopsis* FLS2-BAK1 Immune Complex**
Y. Sun et al.
The molecular basis for how a plant heterodimeric receptor responds to bacterial infection signals is elucidated.
- 628 **Regulation of Temperature-Responsive Flowering by MADS-Box Transcription Factor Repressors**
J. H. Lee et al.
A warm spring favors early flowering by invoking less transcriptional repression by a floral repressor complex.
>> *Perspective p. 566*
- 632 **Mosaic Copy Number Variation in Human Neurons**
M. J. McConnell et al.
Single-cell genomics reveals that individual adult human neurons acquire diverse individual genomes.
>> *Perspective p. 564; The Heavily Connected Brain section p. 577*
- 637 **Resident Neural Stem Cells Restrict Tissue Damage and Neuronal Loss After Spinal Cord Injury in Mice**
H. Sabelström et al.
Glial scarring helps to maintain the integrity of the injured spinal cord in mice.
>> *The Heavily Connected Brain section p. 577; Science Podcast*



pages 568 & 607



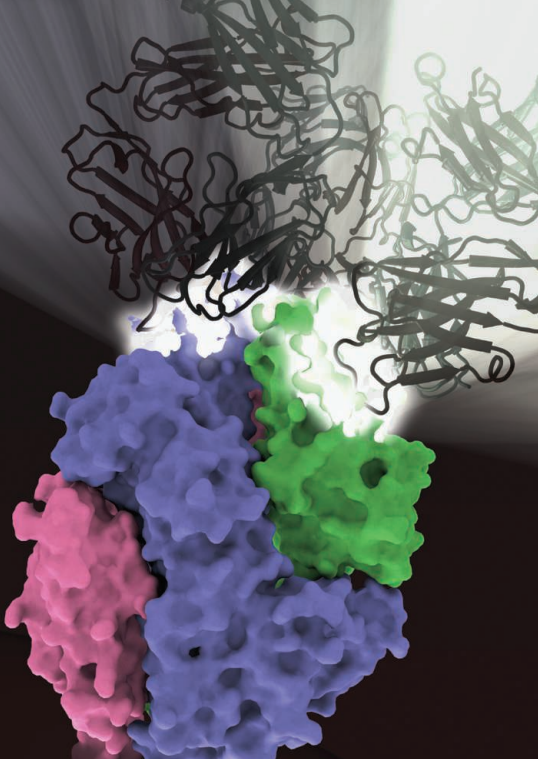
page 614



pages 565 & 621

SCIENCE (ISSN 0036-8075) is published weekly on Friday, except the last week in December, by the American Association for the Advancement of Science, 1200 New York Avenue, NW, Washington, DC 20005. Periodicals Mail postage (publication No. 484460) paid at Washington, DC, and additional mailing offices. Copyright © 2013 by the American Association for the Advancement of Science. The title SCIENCE is a registered trademark of the AAAS. Domestic individual membership and subscription (51 issues): \$149 (\$74 allocated to subscription). Domestic institutional subscription (51 issues): \$990; Foreign postage extra: Mexico, Caribbean (surface mail) \$55; other countries (air assist delivery) \$85. First class, airmail, student, and emeritus rates on request. Canadian rates with GST available upon request, GST #1254 88122. Publications Mail Agreement Number 1069624. Printed in the U.S.A.

Change of address: Allow 4 weeks, giving old and new addresses and 8-digit account number. Postmaster: Send change of address to AAAS, P.O. Box 96178, Washington, DC 20090-6178. Single-copy sales: \$10.00 current issue, \$15.00 back issue prepaid includes surface postage; bulk rates on request. Authorization to photocopy material for internal or personal use under circumstances not falling within the fair use provisions of the Copyright Act is granted by AAAS to libraries and other users registered with the Copyright Clearance Center (CCC) Transactional Reporting Service, provided that \$30.00 per article is paid directly to CCC, 222 Rosewood Drive, Danvers, MA 01923. The identification code for Science is 0036-8075. Science is indexed in the Reader's Guide to Periodical Literature and in several specialized indexes.



Designer Vaccine

Respiratory syncytial virus (RSV) is one of the last remaining childhood diseases without an approved vaccine. Using a structure-based approach, **McLellan *et al.*** (p. 592) designed over 150 fusion glycoprotein variants, assessed their antibody reactivity, determined crystal structures of stabilized variants, and measured their ability to elicit protective responses. This approach yielded an immunogen that elicits higher protective responses than the postfusion form of the fusion glycoprotein, which is one of the current leading RSV vaccine candidates entering clinical trials. Importantly, highly protective responses were elicited in both mice and macaques.

Magnetic Crab

Since pulsars—highly magnetized rotating neutron stars—were discovered 45 years ago, the evolution of their magnetic field structure has been subject to much theoretical conjecture. However, observational evidence has been sparse. Now **Lyne *et al.*** (p. 598) report high-precision measurements, spanning more than two decades, that reveal the systematic evolution of the radiation pattern of the pulsar in the Crab Nebula, one of the youngest neutron stars known.

Deep Heating

Global warming is popularly viewed only as an atmospheric process, when, as shown by marine temperature records covering the last several decades, most heat uptake occurs in the ocean.

How did subsurface ocean temperatures vary during past warm and cold intervals? **Rosenthal *et al.*** (p. 617) present a temperature record of western equatorial Pacific subsurface and intermediate water masses over the past 10,000 years that shows that heat content varied in step with both northern and southern high-latitude oceans. The findings support the view that the Holocene Thermal Maximum, the Medieval Warm Period, and the Little Ice Age were global events, and they provide a long-term perspective for evaluating the role of ocean heat content in various warming scenarios for the future.

Quantum Heating

Mesoscopic wires exhibit peculiar properties at low temperatures. Their electric conductance can show plateaus at evenly spaced values, which reflects the sequential opening of “quantum transport channels,” each of which can only carry a finite amount of charge or heat.

Whereas the step size for the electric conductance depends on the type of the particle carrying the charge, for heat conduction this “quantum” is universal. **Jezouin *et al.*** (p. 601, published online 3 October; see the Perspective by **Sothmann and Flindt**) measured the quantum of heat conduction through a single electronic channel by comparing the amount of heat needed to heat a small metal plate to a constant temperature, while varying the number of electronic channels through which the heat was dissipated from the plate. Encouragingly, the measurement was in agreement with the theoretical prediction.

Not All Neurons Are Alike

As life proceeds, many cells acquire individualized mutations. In the immune system, genome rearrangements generate useful antibody diversity. **McConnell *et al.*** (p. 632; see the Perspective by **Macosko and McCarroll**) now show that human neurons also diversify. Neurons taken from postmortem human frontal cortex tissue and neurons derived from induced pluripotent stem cell differentiation in vitro showed surprising diversity in individual cell genomes. Up to 41% of the frontal cortex neurons had copy number variations—no two alike—with deletions more common than duplications.

Better Contact Along the Edge

Electrical contact to graphene is normally done with metal contacts on its flat face, where there are few strong bonding sites for the metal.

Wang *et al.* (p. 614) encapsulated graphene with hexagonal boron nitride sheets and made metal contacts along its edge, where bonding orbitals are exposed. The resulting heterostructures had high electronic performance, with room-temperature carrier mobilities near the theoretical phonon-scattering limit.

Prairie Redux

Tallgrass prairie is extinct across much of its former range in the midwestern United States, but relics preserved in cemeteries and nature reserves allow functional comparison of former grassland soils with modern agricultural soils.

Fierer *et al.* (p. 621; see the Perspective by **Scholes and Scholes**) took matched soil samples from sites representing the gamut of climate conditions and modeled the combination of genomic analysis and environmental data to resurrect the historical prairie soil communities, identifying the nutrient-scavenging *Verrucomicrobia* as keystone bacteria in functioning prairie.

First Defense

In defense against bacterial infection, plants carry a cell-surface receptor, known as FLS2, that can bind to a fragment of bacterial flagellin and trigger defense responses. **Y. Sun *et al.*** (p. 624, published online 10 October) investigated the structural details that govern the binding between FLS2, its co-receptor BAK1, and the flagellin fragment flg22. The assembled complex initiates signals to activate the plant's innate immune response.

The Good Scar

We tend to think of scars as bad and, in the central nervous system, as counterproductive to recovery. Studying mice, **Sabelström *et al.*** (p. 637) prevented resident stem cells from proliferating after spinal cord injury. Without the astrocytes generated by the neural stem cells, recovery from spinal cord lesions was poorer than normal. Thus, somewhat counterintuitively, glial scarring appears to limit spinal cord damage and support the remaining cells.

Additional summaries

Wiring the Retina

Starburst amacrine cells in the retina detect motion by responding to light going on or off. **L. O. Sun *et al.*** (p. 590) analyzed how the cellular circuits develop in the mouse retina to form the basis of motion detection. Expression patterns of semaphorin 6A and its receptor plexin A2 defined the shape and reactivity of the starburst amacrine cells. Semaphorin 6A expression was restricted to particular cells, generating two classes of starburst amacrine cells with distinct morphologies and opposing functions.

Dinner Time!

Biological clocks allow organisms to anticipate cycles of feeding, activity, and rest so that metabolic enzymes in mitochondria are ready when needed. **Peek *et al.*** (p. 591, published online 19 September; see the Perspective by **Rey and Reddy**) describe a mechanism by which the biochemical elements of the circadian clock are linked to such control of mitochondrial metabolism. The clock controls rhythmic transcription of the gene encoding the rate-limiting enzyme required for synthesis of nicotinamide adenine dinucleotide (NAD⁺). The concentration of NAD⁺ in mitochondria determines the activity of the deacetylase SIRT3, which then controls acetylation and activity of key metabolic enzymes. NAD⁺ also influences clock function, and thus appears to be a versatile point at which regulation of oxidative metabolism is coordinated with the daily cycles of energy consumption.

Information Physics

Multiparameter models, which can emerge in biology and other disciplines, are often sensitive to only a small number of parameters and robust to changes in the rest; approaches from information theory can be used to distinguish between the two parameter groups. In physics, on the other hand, one does not need to know the details at smaller length and time scales in order to understand the behavior on large scales. This hierarchy has

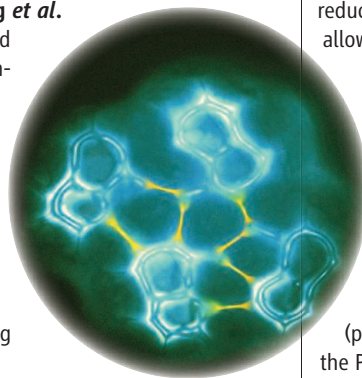
been recognized for a long time and formalized within the renormalization group (RG) approach. **Machta *et al.*** (p. 604) explored the connection between two scales by using an information-theoretical approach based on the Fisher Information Matrix to analyze two commonly used physics models—diffusion in one dimension and the Ising model of magnetism—as the time and length scales, respectively, were progressively coarsened. The expected “stiff” parameters emerged, in agreement with RG intuition.

Imaging Hydrogen Bonds

The decoration of atomic force microscope tips with terminal CO molecules has afforded much higher resolution of the bonding of adsorbed molecules. **Zhang *et al.***

(p. 611, published online 26 September)

show that this method, in combination with density function theory calculations, can image and characterize hydrogen-bonding contacts formed between 8-hydroxyquinoline molecules adsorbed on the (111) surface of copper under cryogenic conditions. At room temperature, a different bonding configuration was revealed that was the result of the molecules dehydrogenating on the copper surface and coordinating with surface copper atoms.



Chilly Repression Stalls Flowering

In a cool spring, flowering might be delayed compared to a warm spring, even though the change in day length marches on regardless of temperature. **Lee *et al.*** (p. 628, published

online 12 September; see the Perspective by **Nilsson**) now show that this delay in flowering is a regulated process, not simply a consequence of sluggish metabolism. In the model plant *Arabidopsis*, transcription of the gene encoding the regulator SHORT VEGETATIVE PHASE (SVP) is unaffected by temperature, but the stability of the SVP protein is decreased at higher temperatures. Its regulatory partner, *FLOWERING LOCUS M* (*FLM*)- β , is the product of alternative splicing of transcripts from the gene encoding *FLM* that favors the β form at lower temperatures. SVP and *FLM*- β form a complex that represses flowering. At lower temperatures, more of the repressive complex is present and flowering is delayed. At higher temperatures, SVP tends to degrade and *FLM*- β tends not to be produced, yielding reduced levels of the repressive complex, which allows flowering to proceed.

Coherently Controlling Large Cats

The control and manipulation of quantum information based on superconducting circuits is an attractive route because of the possibility of scale-up. **Vlastakis *et al.*** (p. 607, published online 26 September; see the Perspective by **Leek**) were able to generate and control quantum entanglement between a superconducting qubit and hundreds of photons stored in a cavity resonator by using deterministic methods for on-demand generation of large Schrödinger cat states in a microwave cavity with arbitrary size and phase. The ability to map the state of a qubit to large Schrödinger cat states should provide a robust quantum resource in future quantum-based technologies.



Alan I. Leshner is the chief executive officer of AAAS and executive publisher of *Science*.

Seize the Neuroscience Moment

THERE SEEMS TO BE AN ABUNDANCE OF NEUROSCIENCE INITIATIVES RIGHT NOW. THIS YEAR, THE European Commission launched a Human Brain Project, and the U.S. government announced its Brain Research through Advancing Innovative Neurotechnologies (BRAIN) project. They join other recent neuroscience efforts across the world aimed at advancing our understanding of the brain. Exploiting these diverse initiatives to yield scientific, clinical, and economic benefits, however, will require not only political and policy-maker support but also endorsement and extensive involvement by the neuroscience community, which already saw a “Decade of the Brain” come and go about 20 years ago, with little direct result. What’s different now?

In 1990, U.S. President George H. W. Bush declared the 1990s the Decade of the Brain; a European Decade of Brain Research was announced shortly thereafter. Yet relatively little special funding was ever allocated to them. These projects did spur private support for U.S. and European versions of the Dana Alliance for Brain Initiatives, which have done much to educate the public about the importance and excitement of brain research. But in the absence of substantial dedicated funding, little scientific coordination, and no real champions of the efforts in the policy-making community, neither brain project ever really gained momentum or generated unified advocacy among scientists or anyone else.

Circumstances are different now. With or without special efforts, neuroscience research has progressed at an explosive rate over the past three decades. Never before has the often-quoted adage of having learned more about the brain in the past decade than in all of recorded history been more apt. Some of this progress has resulted from advances in the technologies that allow neuroscientists to ask wholly new kinds of questions; some from the collaboration among multiple fields that characterizes so much of modern science. An increasing focus on translational research is yielding new treatment approaches in neurology and psychiatry and greater hope for practitioners and patients.

And there now are policy-maker champions for neuroscience. In the United States, the BRAIN project is being coordinated by the White House Office of Science and Technology Policy, directly involves the leaders of many U.S. science funding agencies, involves major private philanthropies, and is taking shape under the guidance of a superb group of scientific advisors. There is an active Neuroscience Caucus in the Congress, and influential members, such as Representative Chaka Fattah (D-PA), have been touting BRAIN wherever they can. Some money has already been set aside for it in federal agency budgets, and if the project gains momentum, one can imagine the commitment of additional financial support. The European Human Brain Project and other national brain projects similarly have high-level policy-maker advocates and dedicated funding.

The neuroscience community should fully exploit these opportunities, even if it requires some behavior change among scientists. In many ways, these initiatives resemble “big science,” like the Human Genome Project, requiring extensive coordination among many scientists and subfields. On the other hand, in spite of increasing interdisciplinary collaboration, neuroscience still remains more typically a “small science” field, characterized by individual investigators working with a small group of students and postdoctoral fellows. Moreover, neuroscientists have never really rallied in a unified way behind a large-scale effort that could probably benefit the entire field; neuroscience advocacy typically has focused on the needs and opportunities in individual investigators’ own areas of interest. Large-scale projects require a different, more unified style of advocacy, whether or not the benefits to individual scientists are immediately evident. Many other fields, such as physics and astronomy, have successfully come together to participate in and support large projects that subsequently garnered substantial public and policy-maker support and funding. The new brain initiatives have great potential to accelerate progress in all of neuroscience. They should be fully embraced.

— Alan I. Leshner

10.1126/science.1247343





ECOLOGY

Caribbean Coral

Coral reefs occupy a vanishingly small proportion of the oceans yet are home to 25% of marine diversity, nurture important fisheries, provide vital coastal protection, and offer a variety of economic benefits from tourism and associated activities. Predictions of how well and how rapidly reefs can recover from damage due to extreme weather events or disease are often highly uncertain, largely because of the lack of long-term, systematically collected data. Manfrino *et al.* established transects and quadrats around Little Cayman Island in the Caribbean, a region that is notorious for the generally degraded state of its reef systems. Half of the coastline of this small island is marine protected area, which includes zones of no-take fisheries. Between 1999 and 2004, thermal stress led to coral bleaching and infectious disease that reduced coral cover by more than 40%, yet 7 years later, the coral cover, the density of juvenile colonies, and the overall size structure of the coral assemblages all had returned to the pre-1999 state. The ability of this reef to recover was attributed to limited human disturbance, its relative isolation, and the recruitment of juvenile herbivorous fish, which help to keep competing seaweeds at bay. — CA

PLOS ONE 8, e75432 (2013).

MICROBIOLOGY

From Drowning to Dried Up

Anthropogenic methane emitted into the atmosphere is a concern because of its behavior as a greenhouse gas. However, naturally abundant anaerobic microorganisms in soils and sediments also produce methane. In lake sediments, this occurs at depths in the sediment column where oxygen is no longer present and when the sediments are constantly submerged in water. To understand how methanogenic microbial communities respond to periods of desiccation and exposure to oxygen, Conrad *et al.* compared

lakes become more common as a result of climate change, the balance of microbial methane production relative to consumption this may become unbalanced, and may have unknown consequences for the carbon cycle. — NW

Environ. Microbiol. 10.1111/1462-2920.12267 (2013).

GENETICS

Double Dealing

Many plants are polyploid, that is, they carry an n -fold excess, often two, of entire sets of chromosomes relative to their ancestors. Some species exhibit variation in chromosome number within populations. One such plant is *Arabidopsis arenosa*, a close relative of the model system plant *A. thaliana*; however, it is not known how these plants can avoid missegregation after chromosome doubling. Yant *et al.* examined meiotic chromosomes in natural tetraploid (resulting from a single doubling of chromosome number) and diploid *A. arenosa* and observed that the number of chiasmata (a measure of recombination) was reduced in the polyploid

individuals. Induced polyploids, however, showed cytological abnormalities and significantly reduced fertility, suggesting that diploid *A. arenosa* are not adapted for the polyploid condition and that polyploids are subject to selection that acts to maintain proper meiosis and gamete formation. Genome-wide scans identified regions of the genome enriched in eight meiosis-related genes, suggesting that the

transition to polyploidy resulted in selection for genes that function in ways that mitigate the potentially deleterious consequences. — LMZ

Curr. Biol. 23, 10.1016/j.cub.2013.08.059 (2013).

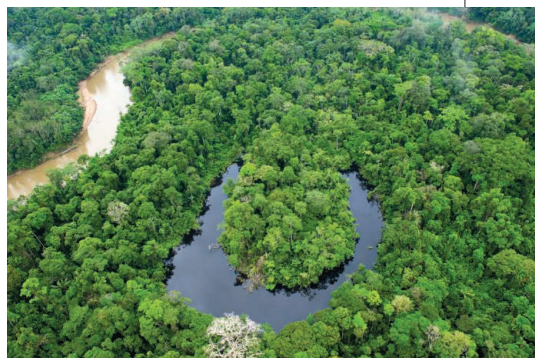
NEUROSCIENCE

Better Together

G protein (heterotrimeric guanine nucleotide-binding protein)-coupled receptors (GPCRs) are one of the most abundant and most important families of integral membrane proteins, and evidence continues to accumulate showing that they can function as heterodimers. These have been especially promising findings because GPCRs are common drug targets, and heteromers could offer an additional means of tuning drug specificity. Baba *et al.* show that in mice, type 1 and type 2 melatonin receptors function together in the retina to produce physiological increases in the sensitivity of photoreceptors to light during the night. Tagged receptors were localized in complexes in the retina, and the loss of one receptor subtype or the other prevented melatonin's effects in the retina. Furthermore, the heteromeric receptors coupled to a signaling pathway distinct from that activated by the monomeric receptors, increasing the efficacy and potency of the receptor complex in the activation of phospholipase C and protein kinase C. An ability to replenish such melatonin signaling could be useful in limiting age-related loss of retinal function, as can occur in macular degeneration. — LBR

Sci. Signal. 6, ra89 (2013).

Continued on page 537



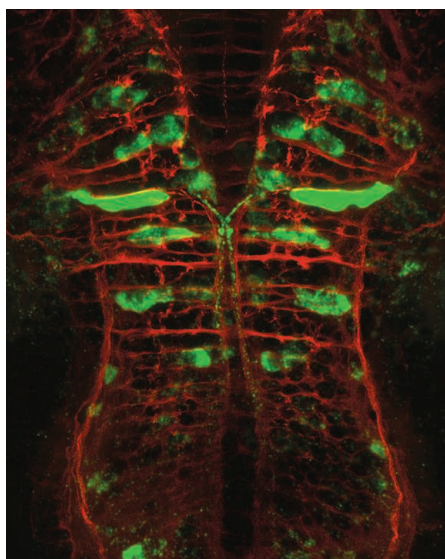
the rates of methanogenesis, gene abundance, and microbial community structure of anoxic sediments from nine oxbow lakes in the Brazilian Amazon region, before and after a cycle of drying and rewetting. In lakes where water was clear or contained a high concentration of organic matter, archaeal and bacterial diversity decreased, but methane production rates increased. If extreme drying events in oxbow

Continued from page 535

NEUROSCIENCE

Selective Delivery

In an extremely elongated nerve cell, the nucleus is a considerable distance from the growing tip of the axon. Baraban *et al.* have used zebrafish embryos to show that some messenger RNAs (mRNAs) manage to find their way to the axon tip and that the machinery that transports them



there is selective. The authors focused on zebrafish mRNAs that are orthologous to mRNAs that had previously been identified in axons of neurons cultured from rat, mouse, and frog. Of the three mRNAs studied, the one encoding a tubulin variant was the mRNA most effectively delivered into axons of the optic, cranial, and posterior lateral-line nerves in the developing zebrafish embryo. Transport into axons depended on an intact microtubule system and was discriminatory; some mRNA types were transported with more variability, whereas others were not transported at all. Using a reporter system with a membrane-bound fluorescent protein, the authors narrowed down the element required for transport of the tubulin mRNA to a 37-nucleotide portion of the 3' untranslated region. This selective delivery of mRNA molecules to the axon could facilitate axon guidance in response to changing developmental conditions. — PJH

J. Neurosci. **33**, 15726 (2013).

PHYSICS

Periodic Ions

Cold gases of both charged and neutral atoms have been used to simulate more complex quantum systems. Whereas neutral atoms are relatively easy to trap in optical lattices (which

mimic the periodic potentials found in solids), ions present a bigger challenge because stray electric fields may cause them to escape the trap. Thus, the typical trapping time of an ion in an optical lattice has been on the order of 10 to 100 μ s. Karpa *et al.* trapped an ion in a combined electrostatic and one-dimensional optical lattice potential and cooled it by manipulating its energy levels with an external magnetic field and by using optical pumping. The ion was cooled to the lowest vibrational level of the lattice potential; similar results were obtained with a three-ion system. By periodically driving an ion and measuring its position, the authors found that it remained localized to a single lattice site for up to 10 ms: four orders of magnitude longer than the vibrational period. With an increase in the number of trapped ions, it is expected that the technique will enable the quantum simulation of many-body systems with long-range interactions. — JS

Phys. Rev. Lett. **111**, 163002 (2013).

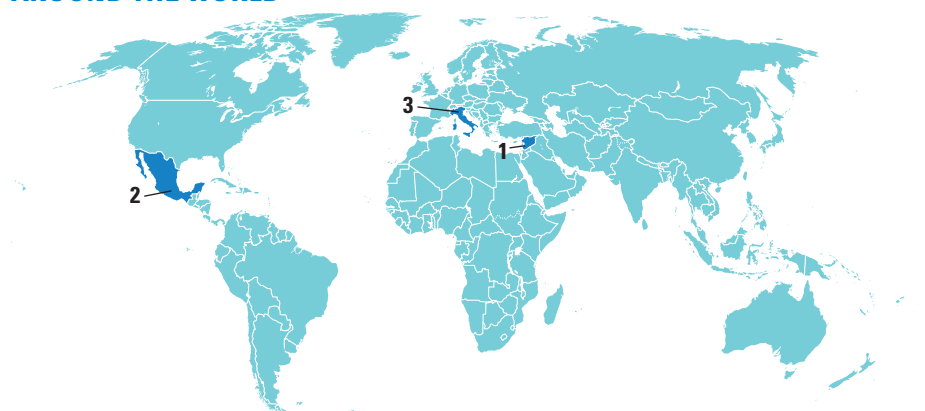
CHEMISTRY

Bacterial Pockets

Just like their sometimes human hosts, bacteria need to eat, migrate, communicate, reproduce, and interact with their neighbors. Thus, to study bacterial behavior, it is necessary to create a three-dimensional host environment that allows for these processes to occur—and ideally in a way where one can position different bacteria at will. Connell *et al.* tackle these challenges using a microscopic three-dimensional printing strategy. Bacteria of interest are trapped by mixing them with a warm solution of gelatin that is then allowed to cool. By including a photoexcitable molecule in the solution, the gel can be selectively cross-linked to form pockets of bacteria that form free-floating, adjacent, or nested communities. Removal of the unreacted gel creates a set of porous channels that can be used for the transportation of food, waste, or signaling molecules. The mechanical properties of the gel can be tuned through the addition of bovine serum albumin, which cross-links with the gelatin. The authors fabricated a range of gels with mixtures of *Staphylococcus aureus* and *Pseudomonas aeruginosa*, which often form coinfections in human patients, to determine how bacterial concentration and location affected each of the populations. When a dense shell of *P. aeruginosa* was fabricated around a core of *S. aureus*, the former enhanced the survival of the latter when exposed to the antibiotic β -lactam. — MSL

Proc. Natl. Acad. Sci. U.S.A. **110**, 10.1073/pnas.1309729110 (2013).

AROUND THE WORLD



Damascus 1

Hunting Syria's Chemical Weapons Stockpile

Syria's military is thought to hold about 1000 tons of chemicals, mostly precursors for sarin and mustard gas, said Paul Walker, a chemical weapons expert at Green Cross International, at a forum held on 23 October at AAAS, the publisher of *Science*. The Organisation for the Prohibition of Chemical Weapons (OPCW), whose inspectors are overseeing the demolition of equipment and facilities used to produce these chemical weapons, expects this work to be completed by 1 November.

That date is part of an agreement imposed on Syria in September, after the United States threatened a military strike in response to a chemical weapons attack in

OPCW faces stiff challenges, including the hostile environment, the possibility that Syria might try to hide part of its chemical weapons arsenal, and possibly incomplete record-keeping of stockpile locations. If the operation succeeds, three countries not party to the 1997 Chemical Weapons Convention would still be presumed to hold chemical weapons: Egypt, Israel, and North Korea. <http://scim.ag/syriachem>

Mexico City 2

University Lifts Sanctions In Misconduct Case

The National Autonomous University of Mexico (UNAM) has lifted sanctions imposed on microbiologists Mario Soberón and Alejandra Bravo after a misconduct investigation. The husband-and-wife team at the university's Institute of Biotechnology (IBt) was found to have manipulated images in 11 published papers on *Bacillus thuringiensis* toxins, used in engineered crops to target insect pests.

After IBt launched an internal investigation, Bravo and Soberón acknowledged modifying the images; in the fall of 2012, an external committee convened by IBt concluded that some of the modifications were "inappropriate and categorically reprehensible" but did not constitute scientific fraud because they did not affect the papers' conclusions. The panel recommended sanctions, including asking Soberón to resign as head of UNAM's molecular microbiology department and demoting Bravo from "academic leader" to "associate researcher."

But UNAM's ombudsman Jorge

Carmona lifted the sanctions on 23 October, citing irregularities in IBt's investigation. The same day, IBt called for UNAM—widely viewed as Mexico's most important university—to establish guidelines for handling misconduct allegations in the future. <http://scim.ag/Mexmisconduct>

Parma, Italy 3

Report: Industry Influence Persists At E.U. Food Watchdog

In 2012, the European Food Safety Authority (EFSA) adopted a new independence policy to improve its management of conflicts of interest. But a report released on 23 October by Corporate Europe Observatory (CEO),

a group seeking to expose private sector lobbying, says industry's influence over the body is still "dismaying," noting

that experts with conflicts of interest dominate all EFSA panels but one.

CEO defines "conflict of interest" more broadly than EFSA does; according to CEO, conflicts arise when a scientist with ties to any industry under EFSA's remit sits on any EFSA panel, not just the panel for that particular industry.

Unlike the much larger U.S. Food and Drug Administration, EFSA relies on unpaid outside experts rather than in-house experts. But many European countries encourage researchers to work with the private sector, making it difficult to find experts with no conflicts of interest. The CEO report advocates for a 5-year, rather than the current 2-year, "cooling-off period" before anyone leaving a job in the commercial sector can

BY THE NUMBERS

\$70 million Amount that the Defense Advanced Research Projects Agency promised on 24 October to support the next generation of brain implants, part of President Barack Obama's BRAIN Initiative.

0 Number of female scientists invited to BBC's inaugural "100 Women" conference on 25 October, meant to open a discussion on the challenges facing modern women.



Searching. A U.N. team investigating chemical weapons use in Syria collects ground samples in August.

Damascus that killed hundreds of civilians in August. Syria must grant OPCW inspectors "unfettered access" to sites and individuals associated with its chemical weapons program, and its entire arsenal must be eliminated by 1 July 2014.



PARTICLE PHYSICS

New Experiment Torpedoes Lightweight Dark Matter

It's not the result physicists were hoping for, but data from a new experiment may put an end to a contentious subplot in the search for dark matter, the mysterious stuff whose gravity binds the galaxies. This week, researchers working with the Large Underground Xenon (LUX) detector at the Sanford Underground Research Facility in Lead, South Dakota, announced that they see no

in physicists' prevailing model and suggests that WIMPs should be a few hundred times as heavy as a proton. As a result, physicists tend to favor WIMPs over a rival dark matter candidate, called axions (see p. 552).

In recent years, however, a few groups have reported signs of unexpectedly light WIMPs weighing less than 10 times as much as a proton. In 2010, physicists working with

their results refute the CDMS signal and the other hints of light WIMPs. Lurking 1480 meters underground, LUX cost \$10 million and started taking data in April. It contains 370 kilograms of liquid xenon, making it more sensitive than either XENON or CDMS. Had CDMS detected WIMPs and not extraneous background radiation, LUX researchers should have seen roughly 1600 events by now, Gaitskell says. They saw none.

So will the LUX results settle the debate over light WIMPs? The key is how well LUX researchers have calibrated their detector and whether they can show that it's truly sensitive to low-mass WIMPs, says Juan Collar, a physicist at the University of Chicago in Illinois and leader of the CoGeNT team. "It will all depend on what [energy] threshold they achieve and how cautious they have been" in their analysis, Collar says.

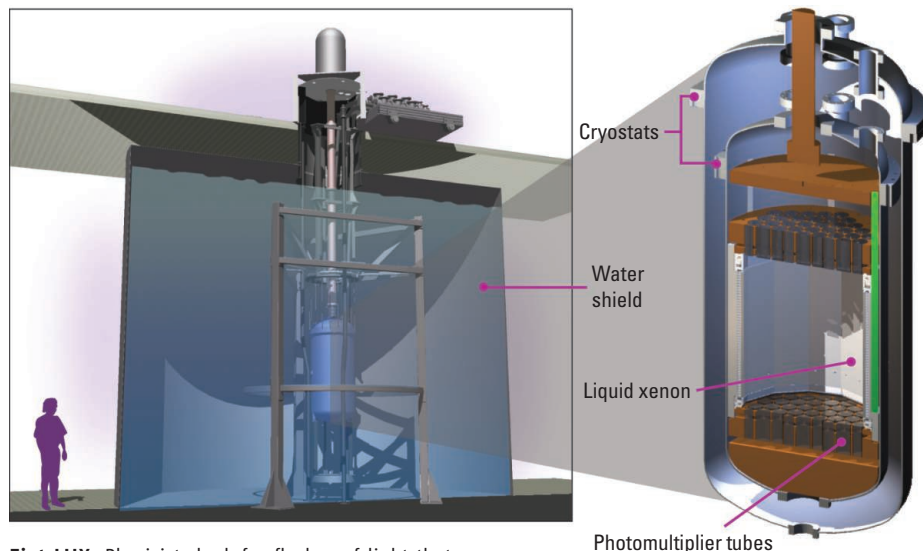
Of course, the real goal is to detect WIMPs, light or heavy. LUX researchers will take data for another 2 years. They then propose to build a 7-tonne detector called LZ. Meanwhile, XENON researchers plan to start up a 1-tonne version of their experiment next year, and CDMS researchers are upgrading their detector—to SuperCDMS—and are planning to move it to the deeper SNOLAB in Sudbury, Canada.

Practically, the most immediate repercussion from the LUX result could be political. The U.S. Department of Energy (DOE)—which funds LUX and, in part, CDMS—has begun a review of the next rounds of its dark-matter experiments. Late last year, it whittled a list of 13 proposals for "second generation" experiments down to five finalists, including LZ and CDMS. DOE officials will select just two or three of those ideas to move forward with construction. Final proposals are due this month, and a decision could come as early as January, researchers say.

However, DOE has also allotted just \$38 million for the new experiments, and some researchers say that won't be enough to afford both LZ and CDMS, the two most expensive efforts. "With the money as it is, it's just impossible to do both," Collar predicts.

LUX researchers say they wanted to get their first results out before that decision to show that their detector is working as promised. And Collar says that the team has "positioned itself very well" for that review. Rumor has it that CDMS will weigh in with another result shortly, he says. For dark matter researchers in the United States, now is no time to hide your light under a bushel.

—ADRIAN CHO



Fiat LUX. Physicists look for flashes of light that would signal a WIMP striking a xenon nucleus.

signs of the lightweight dark matter particles hinted at by other experiments. "It's a significant miss," says Richard Gaitskell, a LUX team member from Brown University. "We should have seen hundreds or thousands of events and we simply don't see any."

LUX stalks weakly interacting massive particles (WIMPs), physicists' best guess at what makes up dark matter. WIMPs would interact with other matter and each other only through gravity and the weak nuclear force. Theory suggests that if the early universe swarmed with particles capable of interacting only through the weak force, then just enough of them would remain to supply the dark matter, so long as they weighed between one and 1000 times as much as a proton. WIMPs also typically emerge from a concept called supersymmetry, which posits a more massive partner for every particle

the Coherent Germanium Neutrino Technology (CoGeNT) experiment reported possible signs of lightweight WIMPs striking their 440-gram detector in the Soudan mine in northern Minnesota (*Science*, 4 March 2011, p. 1132). However, physicists with the ongoing XENON experiment in Italy's subterranean Gran Sasso National Laboratory argued that their data ruled out light WIMPs. A squabble then ensued over whether XENON researchers had properly calibrated their detector, which was filled with 100 kilograms of frigid liquid xenon (*Science*, 3 June 2011, p. 1144).

By most accounts, the most credible hint of light WIMPs came in April. Physicists working with the Cryogenic Dark Matter Search (CDMS) in Soudan reported three clean events that were consistent with light WIMPs crashing into the ultracold disks of silicon in their detector (*Science*, 26 April, p. 418).

Now, however, LUX researchers say

GENETICS

RNA Helps Resurrect Ancient DNA

BOSTON—With the genomes of Ötzi, the 5300-year-old iceman, and even Neanderthals pouring out of DNA sequencing labs lately, you might think that it's now a piece of cake to glean the entire genetic code of an ancient human. But it turns out that such studies used exceptionally pure samples of DNA taken from human bone, tooth, or hair typically preserved in frozen soil, ice, or a chilly cave. More often, human remains found by scientists have long sat in soil warm enough to harbor bacteria, whose genes swamp out the human DNA and make it too costly to analyze. A clever new method for purifying ancient human DNA samples, reported here last week at the annual meeting of the American Society of Human Genetics, could change that, however.

The average ancient DNA sample taken from, say, a human tooth or bone is often less than 1% human DNA and that material is typically short, degraded sequence; the rest is bacterial DNA. Although scientists could sequence this *gemisch*, they would have to run the samples through their sequencing machines many times to zoom in on the human DNA portion, and that remains too costly in most instances. Instead, researchers often prepare stretches of modern human DNA that roughly match the genes or sequences they're interested in and use these so-called probes to filter the sample. (Modern and ancient human DNA are similar enough that the modern probes will stick to the ancient DNA.) But this is still expensive, and those DNA probes reveal the sequence of only a subset of the genome.

A team at Stanford University in Palo Alto, California, has now come up with a better idea. Postdoctoral researcher Meredith Carpenter and others in the lab of Carlos Bustamante found a new way of synthesizing stretches of RNA matching the human genome, making it "super cheap," Bustamante says, to cover a whole human genome with these RNA probes. (Existing techniques for making the probes would have been much more expensive—Bustamante's group estimates that their test, which costs \$50 per sample, avoids at least \$300,000 in startup costs to make probes covering the entire genome using one standard method.) The RNA probes have a chemical group that sticks to special beads, so when the researchers mix the probes with an ancient DNA

sample, they can wash away the nonhuman DNA. The final step is to use an RNA-chewing enzyme to get rid of the probes, leaving only pure ancient human DNA that can then be fed into a genome sequencing machine.

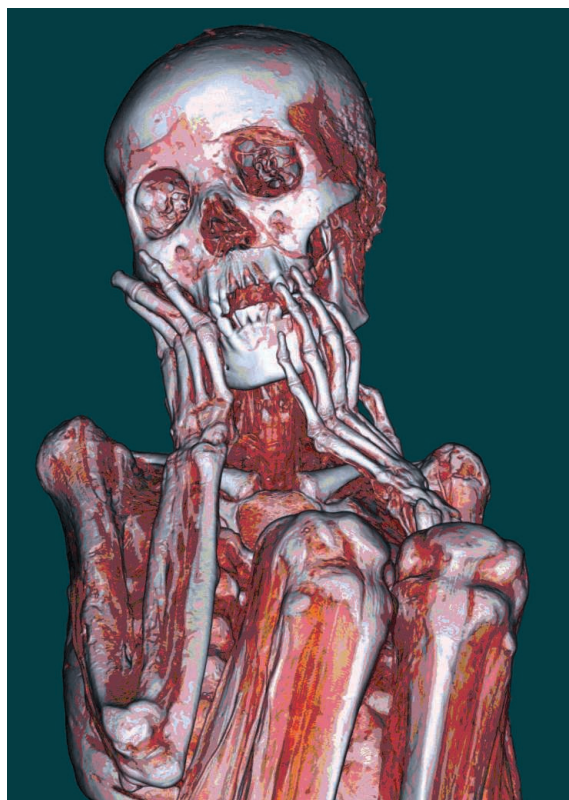
When the researchers tested this filtering method on a dozen ancient DNA samples from bone, teeth, and hair between 500 and 3500 years old, they gleaned twofold to 13-fold more human genetic sequence from the samples than they could have by simply sequencing the mixture the same number of times. This higher resolution yielded new information about the samples. For instance, while previously they could only say that a more than 2500-year-old Bronze Age tooth from Bulgaria was European, the more detailed DNA sequence they could read could now narrow its ethnic origin down to central or southern European. The team was also able to determine that a Peruvian mummy dating from more than 500 years ago did not have European ancestry, as Spanish explorers claimed.

This new method will "substantially increase the number of samples amenable to whole genome sequencing," said Bustamante in a talk at the conference. (The study also appeared online last week in *The American Journal of Human Genetics*.) He and his colleagues are now trying it on ancient dog DNA to elucidate the domestication of dogs. They also think the approach might come in handy for modern-day forensic scientists dealing with bacteria-tainted human DNA samples, as well as for microbial genomics researchers who need to remove contaminant human DNA from a sample.

Adds ancient DNA researcher Eske Willerslev of the Natural History Museum of Denmark in Copenhagen, a co-author on the paper: "A lot of other enrichment methods we have tried do not work well on degraded DNA. It's not a miraculous cure, but if you have very little endogenous DNA that in reality will make any attempts to even get a low coverage genome hugely expensive, this

approach may help make it feasible."

The method is "super exciting and very interesting," says geneticist David Reich of Harvard University, who studies the Neanderthal genomes. He notes that there are Neanderthal samples that have enough DNA to sequence, but it's not worth the expense because they're too contaminated by bacteria. "I think it remains to be seen whether the approach will become a prac-



Mummy code. A new technique could make it cheaper to decipher DNA from ancient humans such as this Peruvian mummy.

tical method for whole genome sequencing of these difficult but important ancient DNA samples, but I think it is exciting that this is even conceivable."

Evolutionary geneticist Hendrik Poinar of McMaster University in Hamilton, Canada, is working on a similar method for enriching DNA of extinct animals. He says there are still questions to be addressed, such as how sensitive the technique will be and how it will work for animals with no closely related modern relative. But the method could be a game-changer by making it possible to study groups of ancient people and animals, not just a few rare specimens. "It is good stuff and an exciting way forward for ancient DNA to move towards population level genomics," Poinar says.

—JOCELYN KAISER

MARINE BIOLOGY

Industry Lobbying Derails Trawling Ban in Europe

BRUSSELS—Les Watling, a marine biologist at the University of Hawaii, Manoa, loves visiting seamounts and studying the ecosystems of these underwater peaks. But these days he is spending time in a different setting, equally important to marine ecosystems: the European Parliament in Brussels. Watling is one of several scientists who have campaigned alongside environmental groups to influence two important votes

October, when the Parliament voted to commit part of a €6.5 billion, 7-year aid package for Europe's fisheries industry to curbing overfishing and slowing the growth of the fishing fleet. But sources close to the negotiations on the trawling ban say that the environmentalists should expect to be disappointed by the upcoming vote. The sources say that opposition from the fishing industry and some members of the European Parliament (MEPs) has led to a watered-down regulation that would restrict bottom trawling practices but not end them.

Both battles show that the European Union is getting more serious about reforming its fisheries. According to the European Commission, 80% of Mediterranean stocks and 47% of Europe's Atlantic stocks are overfished, compared with only 21% for U.S. stocks. In 2011, the European Commission proposed an ambitious reform of its Common Fisheries Policy to curb overexploitation and make the industry more sustainable (*Science*, 22 July 2011, p. 396); it was approved by the European Parliament in February of this year.

The new aid package, the European Maritime and Fisheries Fund (EMFF), puts some of those goals into practice. A group of 14 marine scientists had sent MEPs an open letter—signed by 186 other researchers online—urging them to cut down on aid that encourages overfishing, including

fuel subsidies and funds to build or modernize boats. "Instead public money should be ... focussed on control of compliance with management rules, data collection, scientific research and stock assessments," they wrote. The Parliament largely agreed. At least €716 million should be spent on data collection and €690 million on control and enforcement, the Parliament decided, increases of 100% and 45% respectively compared with the commission's 2011 proposal. This would be offset by a decrease to the remaining budget for the development of fisheries. The Parliament must now negotiate the package with member states and the European Commission.

Meanwhile, there has been more vocal opposition to the commission's proposed ban on deep-sea trawling, which involves dragging heavy nets and gear along the sea floor, and bottom-set gillnets, which are placed on the seabed and retrieved after a while. These types of fisheries, mostly based in France and Spain, represent only about 1% of all fish landings in the Northeast Atlantic, but some scientists say they cause a disproportionate amount of ecological havoc to fish populations and deep-water corals.

The methods are not selective; 20% to 40% of the catch consists of unwanted fish. And deep-sea species often have slow reproduction rates, so collapsed populations need a long time to recover. About 300 marine scientists have signed a petition in favor of the ban, released in June by a French marine conservation nongovernmental organization called Bloom. Watling says the science accumulated in the past decades is clear about the benefits of a ban. "This should be a no-brainer regulation," he says.

But the fishing industry says that trawling can be made sustainable through management measures, such as setting catch limits or "freezing the footprint" of existing fisheries—that is, closing off deep-sea areas that are not yet fished to future bottom trawling.

And some scientists have been hesitant to support a ban as well. In a note published on its website in June, Ifremer, a government-funded fisheries research institute that operates 26 sites in France, said that current fisheries management has already "put an end to most overexploitation for deep fish." The institute added that a ban on deep-sea trawling "does not appear necessary" because the practices have reached "at least partly sustainable levels." The International Council for the Exploration of the Sea (ICES), an organization funded by 20 member countries to provide science-based advice, has not supported a full ban either.

In the end, the industry's arguments appear to have carried the day within the Fisheries Committee, where 13 of the 25 members from across the political spectrum have fiercely opposed a ban—enough to derail the commission's proposal. On 4 November, after multiple delays, the committee is finally slated to adopt a watered-down report: Instead of an actual ban, the committee is expected to agree that deep-sea areas harboring vulnerable ecosystems should be mapped and closed to trawling,



Sea battle. A French campaign poster calls deep-sea trawling a "weapon of mass destruction."

with the potential to curb destructive fishing practices in Europe—and set precedents for the global fishing industry.

He and his colleagues are focused on a 4 November vote in the Parliament's Fisheries Committee on whether to curb deep-sea trawling and bottom gillnetting, practices that they say cause devastating damage to marine ecosystems. In July last year, the European Commission, the European Union's executive arm, proposed phasing them out in the Northeast Atlantic, a landmark decision that would influence fishing debates worldwide.

The scientists and environmentalists were heartened by an earlier victory, on 23

existing fisheries should be better monitored, and detailed fishing plans and impact assessments should be required before any new areas can be opened to exploitation. The amended report would then move on to a vote in the plenary parliament, which cannot reinstate the ban, and is likely to confirm the committee's vote. Bloom Director Claire Nouvian says that, although better than nothing, the outcome would be disappointing.

Even that modest victory is not secure. Member countries' fisheries ministers need to sign off on the plan, and they haven't even started discussing the issue. "It is no secret that France, and to a lesser extent Spain, have blocked the discussion," says a source close to the Council of Ministers. Nouvian fears the reform may slip into oblivion if it doesn't move forward before the European Union's Parliament and

commission are renewed in 2014.

The E.U. vote is not the final verdict on bottom trawling. Calls for a global moratorium on the practice are growing, and 2 years from now, the general assembly of the United Nations will review its 2011 resolution on oceans and sustainable fisheries. Watling may have to start visiting other capitals. "There really should be no trawling in the deep sea," he says.

—TANIA RABESANDRATANA

EUROPE

French Mathematician Tapped to Head Key Funding Agency

In a video called *A Beautiful Formula*, posted on the Internet in 2012, French mathematician Jean-Pierre Bourguignon spends 8 minutes lecturing while scribbling on a blackboard, ending in a declaration of love for a short equation known as Euler's identity, $e^{i\pi} + 1 = 0$, which is very difficult to prove, unless it is approached through geometry. The moral of the story, Bourguignon explained: "A change in point of view turns out to be an extremely powerful tool in mathematics."

Now, Bourguignon's own point of view is about to shift dramatically, giving him greater power over the course of European science. After 19 years at the helm of the Institute of Advanced Scientific Studies (IHÉS), a private institute in the southern suburbs of Paris, he will move to Brussels to become the new president of the European Research Council (ERC), Europe's funding agency for basic research.

Bourguignon, 66, will succeed Austrian sociologist Helga Nowotny on 1 January. (The European Commission has yet to announce the appointment and declined to comment, but sources close to the commission confirmed that Bourguignon is its choice.) He will take the helm at a young agency that has become popular among European scientists for its prestige and relatively easy procedures, with a budget that will balloon from just over €7 billion in its first 7 years to €13 billion for the period 2014 to 2020.

His main challenges, European science policy followers say, will be to jealously

guard ERC's independence and to resist pressure from countries in southern and eastern Europe that want a bigger slice of ERC's pie, which is part of Europe's long-debated, gargantuan Horizon 2020 package. Researchers from those countries have often fared poorly with the ERC, which awards funding solely based on excellence. "Everything that we have achieved needs to be safeguarded," Nowotny says.

Bourguignon, who has also been a fellow at France's National Center for Scientific Research for the past 45 years, is "an un-French Frenchman. ... He is very direct and very international in his outlook; he makes

contacts very easily," says Peter Tindemans, the secretary-general of EuroScience, an organization that Bourguignon co-founded in the 1990s as a counterpart to AAAS, *Science's* publisher.

Colleagues say that Bourguignon gave IHÉS, conceived in 1958 as a European version of the famed Institute for Advanced Study in Princeton, a solid financial footing by raising money around the world. "He is extremely dynamic, efficient and reliable," says Daniel Barlet, a mathematician at the University of Lorraine and, like Bourguignon, a former president of the French Mathematical Society. In France,

Bourguignon is also known for his efforts—including last year's video—to share his fascination for math and its applications with a broad audience.

Tindemans says that Bourguignon, who declined an interview request, will have to maintain his distance from the European Commission. Nowotny worked from an office in Vienna; Bourguignon will be the first president based at the Executive Agency, a Brussels-based body that does the ERC's day-to-day work. (The position of ERC secretary-general, filled by Canadian-German geophysicist Donald Dingwell through the end of the year, will disappear.) "That means the new president is drawn more tightly into the commission's net than is good for the ERC," Tindemans says. "I trust Bourguignon will be able to handle that—but it won't be easy."

—MARTIN ENSERINK



Doing the math. The European Research Council's budget is set to grow sharply after Jean-Pierre Bourguignon takes over on 1 January.

VACCINES

Structural Biology Triumph Offers Hope Against a Childhood Killer

Overcrowding at an HIV lab has had a serendipitous effect. A postdoc who agreed to work in a space two floors below became intrigued by the work of a senior scientist who studied a different virus. The result was a collaboration that has made dazzling progress toward a badly needed vaccine against respiratory syncytial virus (RSV), a major killer of infants.

In one of the first examples of its kind, postdoc Jason McLellan, Barney Graham, and colleagues from the Vaccine Research Center (VRC) at the U.S. National Institute of Allergy and Infectious Diseases in Bethesda, Maryland, used structural biology to successfully engineer an immunogen—the working heart of a vaccine. In mice at least, the carefully engineered RSV protein triggers a remarkably potent antibody response, 40 times higher than what's needed to thwart the virus.

The result, reported in this week's issue of *Science* (p. 592), is a striking departure from the usual trial-and-error approach to vaccinemaking. It also shakes up the crowded field searching for a vaccine against RSV, which causes pneumonia and other lower respiratory tract diseases, hospitalizing an estimated 3 million-plus chil-

dren worldwide each year, killing 160,000. Virologist José Melero, whose RSV studies at the Instituto de Salud Carlos III in Madrid helped lay the groundwork for the VRC success, calls the work “a very important achievement.”

The work began 5 years ago by happenstance. Peter Kwong, a structural biologist at VRC, had no place in his overstuffed fourth-floor HIV lab for McLellan, a new postdoctoral student. So McLellan (now at Dartmouth College) set up shop on the second floor, near the lab bench of Graham, an infectious disease researcher who has worked on RSV for 30 years. The two began to work together on a modest RSV project that grew into an attempt to solve a formidable challenge. Researchers had isolated potent neutralizing antibodies to RSV from infected people, but had failed to develop an immunogen that could stimulate their production. Could structural biology guide the way?

RSV has a protein on its surface, known as F, that orchestrates its fusion with cells during the infection process. The flexible F protein has two distinct shapes, adopting one before fusion begins and one after it's completed. In 2011, the team published

the structure of postfusion F protein bound to neutralizing antibodies, hoping these data might help vaccine design. Around the same time, Melero and co-workers found evidence that the postfusion protein was not the target for most of the protective antibodies. When they eliminated antibodies that bound to postfusion F from the serum of people infected with RSV, the leftover antibodies continued to neutralize the virus. “That was puzzling, but created a great opportunity,” Kwong says. “That told us there was another type of response that could be much better than the one to postfusion F.”

This spring, the VRC group reported in *Science* (31 May, p. 1113) that it had crystallized a potent antibody bound to the prefusion F structure, spotlighting a site on the virus that was especially vulnerable to neutralization. But the prefusion protein was unstable, making it impossible to formulate as an immunogen. So the team set out to effectively freeze the prefusion F structure, forcing it to continuously display that vulnerable site.

The team stabilized the F protein into the specific shape it wanted by introducing new chemical bonds and swapping out naturally occurring amino acids for substitutes that would fill cavities in its structure. They constructed more than 100 variants of the prefusion protein, then selected a favorite that was relatively easy to produce, stable, and triggered the desired antibodies. “This

HIV Surface Proteins Finally Caught Going Au Naturel

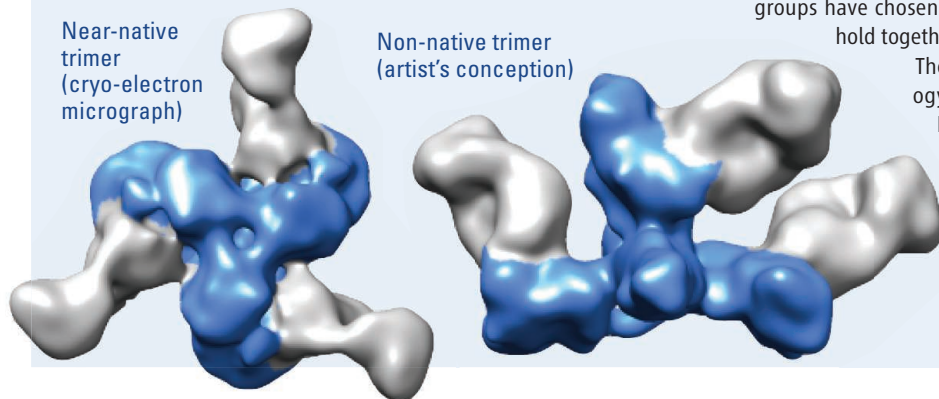
After nearly 2 decades of effort, researchers have artificially produced and structurally analyzed proteins that they say closely mimic those naturally appearing on the surface of HIV. Many investigators have high hopes that these “near native” versions of the proteins will usher in a new era of AIDS vaccine design, just as new insights into protein structure have invigorated the quest to develop a vaccine for respiratory syncytial virus (RSV) (see main story). In the shorter term, the three new studies—two published

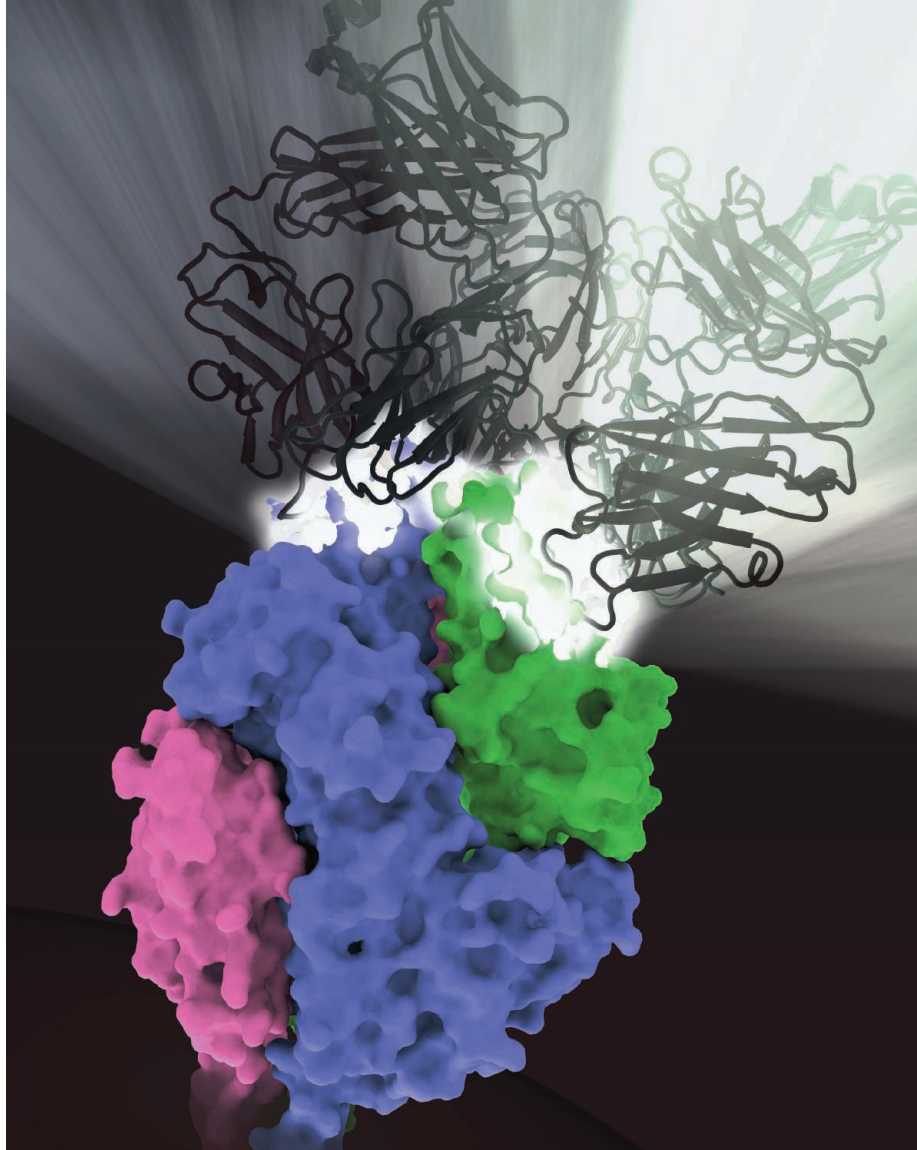
online this week in *Science*—will stoke long-standing debates about the precise shape of these proteins, which cluster into what resemble mushrooms sprouting from the viral surface, and how they stimulate an immune response to HIV.

HIV infects cells via two attached surface proteins that bud through the viral membrane in groups of three, called trimers (the mushrooms). For technical reasons, membrane-bound trimers are difficult to produce in large enough quantities for fine-grained structural analysis. When researchers manufacture these proteins without the membrane anchoring them, the fragile trimers fall apart, making them impossible to study. Many groups have chosen to make specific amino acid changes so the trimers hold together, but these are far from the native form.

The two *Science* papers describe how a structural biology team led by Ian Wilson of the Scripps Research Institute in San Diego, California, finally got high-resolution portraits of the near-native trimers. Key to their success were stable, lab-made versions of the proteins, designed by immunologist John

Mimicking nature. “Near-native” HIV trimers have a consistent shape (antibodies attached in gray), but non-native trimers always differ.





Hot spot. An antibody (black) can cripple RSV by binding to a vulnerable site (white) on its F protein.

is the first time anyone has gone from antibody to vaccine and proved that it's not just a pipe dream," Kwong says.

James Crowe, a pediatrician at Vanderbilt University Medical Center in Nashville who studies B cell responses to RSV and other viruses, says it's impressive that they've effectively tamed an "ill-behaved" protein. "This is a seminal paper in terms of stabilizing a dynamic structure to increase immunogenicity," Crowe says. He cautions, however, that safety concerns will complicate tests of this protein in infants.

In a clinical trial in the mid-1960s, an RSV vaccine made from a killed version of the virus *enhanced* disease in children between 2 and 7 months of age, increasing hospitalization rates and leading to two deaths. The highly refined VRC protein may sidestep these problems, but Graham says they have no intention of testing it in infants. Instead, he suggests that trials should vaccinate pregnant women to test whether they produce antibodies that are then transferred to their babies, protecting them for their first few months, when they're most vulnerable to RSV. He expects they will have a "clinical grade protein," made by either VRC or an industrial partner, ready for human tests within 2 years. Says Graham: "There are a lot of motivated people and companies."

—JON COHEN

Moore of the Weill Medical College of Cornell University in New York City and his co-workers. "This has been on the Top 10 Most Wanted list for structural biologists," says Peter Kwong, who does structural analyses of both HIV and RSV at the Vaccine Research Center (VRC) of the National Institute of Allergy and Infectious Diseases in Bethesda, Maryland.

The new findings promise to guide attempts to devise immunogens—vaccine components—that can trigger production of so-called broadly neutralizing antibodies (bNAbs), which many immunologists believe a successful HIV vaccine needs to elicit. (Isolated from infected people, bNAbs offer them little help because they take years to appear and are made in tiny amounts.) Unlike ordinary antibodies, which the virus easily evades by mutating or which don't have neutralizing power to begin with, bNAbs can thwart many variants of the virus (*Science*, 13 September, p. 1168). "It's elegant, beautiful work," says VRC Director John Mascola. "I think we'll see a whole new wave of immunogen design that will come out of this."

Moore and colleagues spent 15 years attempting to create stable versions of the native trimer outside of a membrane, adding chemical bonds and removing parts of the proteins to enable them to maintain their native configuration. The result could help settle contentious debates about the trimer's structure (*Science*, 2 August, p. 443). Kwong and others say the new structures are especially convincing because two different techniques—x-ray crystallography and cryo-electron microscopy—

independently arrived at the same images. A group at the U.S. National Cancer Institute that analyzed earlier versions of the trimers used in the *Science* studies confirms the new structures in a 23 October online report in *Nature Structural & Molecular Biology*.

Wilson says the sharper picture of the near-native trimers may give vaccine designers new ideas about the infection process and how to thwart it. Moore suggests that because native trimers trigger bNAbs naturally, they might work better as immunogens than the non-native trimers other researchers have been studying. Test-tube studies also show that bNAbs bind better to native trimers. "I'm not saying every bNAb ever induced must have been derived from a native trimer, but I think it's reasonable that many of them will have been," Moore says.

Moore's lab-made trimers have not been tested in animals, although those studies are under way. Several groups making immunogens with non-native structures caution that just because a bNAb binds to a trimer, it doesn't mean that trimer can teach an immune system to make the same antibody. "These two papers provide some exquisite structural biology that is very appealing, however beauty is in the eye of the beholder, and, in this respect, it's the immune system that is the final arbiter," says Robin Shattock, an immunologist at Imperial College London. "So in the race to induce broadly neutralizing antibodies, only time will tell whether these structures are a game changer or an incremental step."

—J. C.

CREDIT: JONATHAN STUCKEY/VACCINE RESEARCH CENTER/NIH/NIH



Short-Circuiting Depression

Experimental deep brain stimulation surgeries for depression are giving old theories about the disorder a jolt

BY THE TIME SHE CALLED HELEN MAYBERG'S lab at Emory University in Atlanta to ask the neurologist to stick metal electrodes into her brain, former high school principal Linda Patterson was at the end of a long, dark road. She had grappled with depression for 40 years, trying a battery of treatments with no relief. One night, she saw a CNN show about Mayberg's clinical trial of deep brain stimulation (DBS) surgery for the treatment of severe depression. The next day, she called to enroll.

The 4-hour-long surgery involves drilling two nickel-sized holes in the skull and snaking long metal electrodes into tiny nodules of tissue in a deep brain region called area 25. Once the electrodes are in place,

the operating team flips a switch on an external generator and high-frequency bursts of electricity begin to stimulate the tissue. The device remains in the brain indefinitely, with a battery implanted below the clavicle supplying continuous electrical stimulation like a pacemaker.

Patients remain semiconscious through part of the surgery so that Mayberg and her team can probe their mental and emotional states when the current starts to flow. Patterson recalls feeling as though she was being lifted out of a deep ocean vortex and returned to dry land. After the surgery, "I felt the best I've felt in my entire life—joy, exhilaration, contentedness," she says. "My cognitive abilities were sharper. I was living

in a different world."

More than 6 months later, Patterson has shown no signs of relapse. Carol, her partner of 11 years, also sees a profound difference in Patterson's well-being. "She has the ability to feel joy again, to set goals and say things she wants to do."

Mayberg first tried DBS of area 25 on a depressed person a decade ago. She and other groups, some targeting different brain regions, have subsequently used DBS to treat depression in more than 200 others. Between 40% and 60% of these patients demonstrated significant improvements, she says. The prospect that this experimental procedure can bring recovery for people who had given up hope has "reinvigorated

Last resort. Neurologist Helen Mayberg (in scrubs) oversees while a neurosurgeon performs deep brain stimulation surgery on a person with severe depression, a procedure she has been refining for more than a decade.

the field” of depression treatment, says Hussein Manji, former director of the National Institute of Mental Health’s Mood and Anxiety Disorders Program and head of therapeutic neuroscience at Janssen Pharmaceuticals. And it has given researchers a powerful way to pursue an old but largely untested hypothesis: that much depression results not from an imbalance in the soup of neurochemicals that bathes the brain, but from disrupted neural “circuits.”

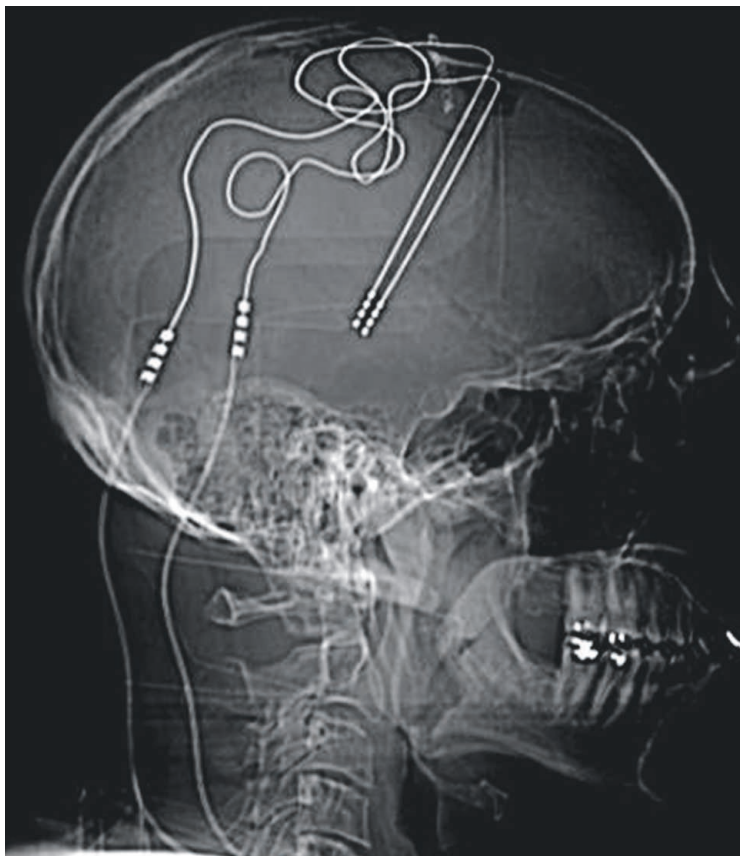
The tools to properly test hypotheses about the neural circuitry underlying mood weren’t available until quite recently, notes Scott Russo, a neuroscientist at Mount Sinai Hospital in New York City. That changed as DBS was shown to be effective in brain disorders such as Parkinson’s disease and obsessive-compulsive disorder, demonstrating that it is possible to precisely alter the activity of key neural circuits in the brain, while leaving others intact. And in “just the past 5 years or so,” Russo says, new techniques such as optogenetics, in which brain cells are made light-sensitive, have allowed scientists to begin tracing and manipulating neural networks in animal models of depression. “It’s a great time to be doing this research,” says psychiatrist Ronald Duman of the Yale University School of Medicine.

And research it remains, Mayberg cautions. Patterson’s recovery has been an “extraordinary success,” she says, but not all depressed people who receive DBS experience such immediate or lasting benefits. Hoping to move beyond anecdotal success stories, Mayberg and several other groups are now running DBS clinical trials, targeting area 25 and other brain regions. To rule out a placebo effect, which can be powerful in surgical procedures, the researchers compare subjects who receive DBS with those who undergo the same surgery but receive

no electrical stimulation during the trial, or parts of it. All eyes in the field are on these “sham” studies, says Wayne Drevets, a neuroscientist at Janssen: “There’s a sense of people holding their breath to make sure this is really going to work.”

Tuning the circuit

The concept of manipulating neural circuits with electricity to influence mood is



Going deep. Thin metal wires conduct electricity nonstop from a battery pack implanted below the clavicle to a brain region called area 25, acting like a pacemaker.

hardly new, notes Joseph Price, a neuroanatomist at Washington University in St. Louis. Physicians began using electric shocks to treat hysteria as early as the 17th century, and 19th century neuroscientist Paul Broca discovered that making lesions in or stimulating specific brain areas could produce strange emotional behaviors in monkeys, causing them to become remarkably tame or hypersexual, for example.

More recently, depression researchers have returned to the concept. One motivation is a growing frustration with available medicines, which aim to restore “imbalanced” brain chemistry. Although drugs such as fluoxetine (Prozac), which boosts the neurotransmitter serotonin, appear to help some people, they don’t work for

everyone and often cause side effects.

Neuroimaging studies revealing abnormal patterns of brain activity correlated with depression, as well as studies showing loss of brain volume in key areas involved with processing emotion, suggest that the chemical brain imbalance model of depression is “simplistic,” Duman says. At the same time, the success of nondrug treatments—particularly those that use electricity to alter

neuronal activity, such as electroconvulsive therapy—has hinted that clinicians may be able to “reset” aberrant brain activity, like rebooting a computer, says Kafui Dzirasa, a psychiatrist at Duke University in Durham, North Carolina.

If the depressed brain indeed has a reset button, Mayberg thinks area 25 may be it. Labeled in 1909 by the neuroanatomist Korbinian Brodmann, area 25 abuts the corpus callosum, a band of nerve fibers that connects the brain’s right and left hemispheres. At a July meeting at Cold Spring Harbor Laboratory in New York, Mayberg zoomed through a tour of this region and its web of connections, emphasizing every preposition. “It speaks *to* the nucleus accumbens—goes *to* the shell, not the core—connects *up* the cingulum bundle to the dorsal anterior and mid-cingulate, *out* to the medial frontal cortex, and deep *into* the amygdala via both branches of the uncinate

fasciculus, then *down* to the dorsal raphe and periaqueductal gray matter as well as to the nucleus reuniens of the thalamus. Basically, area 25 dysfunction or problems with its connections can wreak potential havoc on every functional circuit ever implicated in patients with major depression.”

Mayberg and other groups first identified area 25 as a subject of interest by examining brain scans of people with depression who were being treated with Prozac. In those who responded well to the drug, she noticed that the region’s metabolic activity was dampened. In patients who did not respond to the drug, area 25 did not change. Later studies showed that the region lights up when someone recalls a sad event—seeing their grandmother on a hospital respirator, or tak-

ing care of a friend who was dying of AIDS, for example. But in healthy people, it calms down when the memory passes.

Imaging studies of area 25 indicate that its activity is yoked to many other regions affected by depression, Mayberg says. Some are involved in cognitive skills such as attention, while others have to do with emotional regulation, self-awareness, and rumination. Still more are involved in more visceral sensations of unease. When area 25 is hyperactive, these linked regions also alter their activity, as though they're different instruments in the same orchestra, Mayberg notes. "All roads seemed to lead to area 25, so I said, 'Why don't we tune it there?'"

Since 2003, Mayberg and others have used DBS in area 25 to treat depression in

patients now being treated at Emory University. Tractography, a technology that maps how water diffuses along neuronal connections in the brain, has allowed the team to image white matter tracts in individuals and better guide where to insert electrodes into them. Comparing the tracts to a complicated highway system, Mayberg notes that the road map differs in every individual. "In some people maybe three roadways will branch at the exact same place, and in other people the off-ramp is another few meters down," she says. A difference of a millimeter in the placement of the four electrode contacts, she explains, can end up stimulating very different connections throughout the brain. By comparing patients' responses to different contacts, she says, the team is able to ask,

in a study sponsored by the medical device company Medtronic, there was no difference in the level of depression after 16 weeks when people were having "sham" stimulation versus real electrical pulses.

One possible reason the trial failed, Rezaei suggests, is that 16 weeks may simply not be enough time to detect a benefit. Although some patients, like Patterson, experience immediate effects after DBS, most people do not recover immediately, he says. Instead, they may see the first benefits after a few weeks, then progress gradually over the long term, he says.

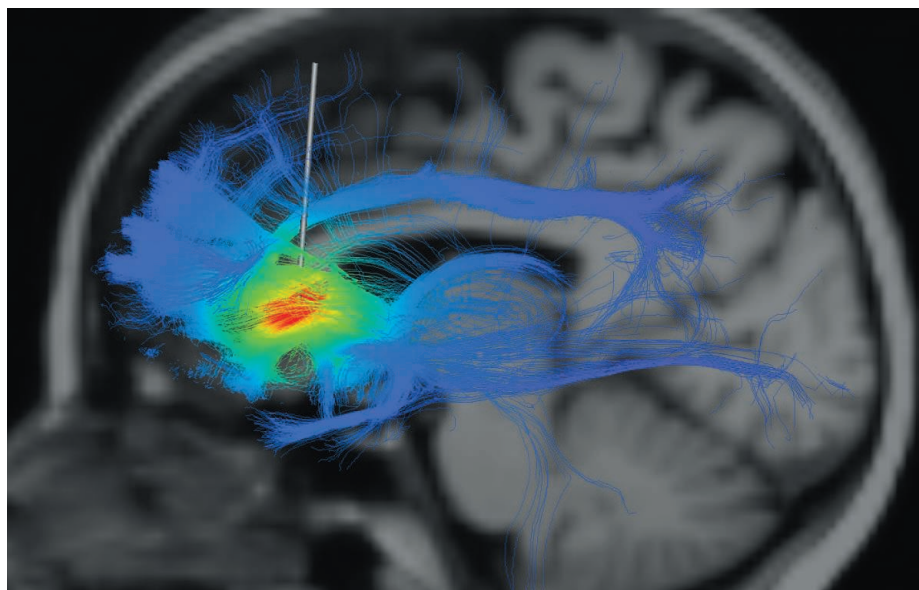
Or the researchers may have chosen the wrong brain area to target. They implanted the DBS electrodes not in area 25 but in a brain region called the ventral striatum, which they chose because the Food and Drug Administration has approved it as a DBS target for obsessive-compulsive disorder and because Rezaei and others had noticed mood alterations when the area was stimulated.

The ventral striatum is just one of many brain regions that depression researchers are targeting (see diagram, p. 551). They include the nucleus accumbens, a brain region involved with pleasure and reward; the inferior thalamic peduncle, implicated in depression and obsessive-compulsive disorder; and the lateral habenula, a brain region that shows higher-than-average activity in people with depression.

The range of brain circuitry at which researchers are aiming their electrodes reflects fundamental differences in how they view depression. For Mayberg, its core is an unrelenting mental pain. "Patients say, over and over, 'There's something in my way,' and 'Take away this pain,'" she says. "If you're so turned inward that nothing else matters, then by definition you are disconnected from the outside world." With stimulation of area 25, she says that burden appears to lift and patients are free to enjoy their lives again.

Researchers who focus on stimulating brain areas associated with reward, in contrast, tend to think of depression's most important symptom as anhedonia—the inability to anticipate or experience pleasure. "The reward system is there all day; it guides us," says Volker Coenen, a neurologist at the University of Bonn in Germany. "You think, 'I will have a shower. I will have a coffee. I will shave and put on a nicely washed shirt.'" This ability to look forward to coming pleasures has been extinguished in his most depressed patients, Coenen says.

Consequently, he focuses on the medial forebrain bundle, which connects reward-



Sweet spot. This tracing of area 25 and its extensive nerve connections, overlaid on a brain image, reveals the node just outside the area that Helen Mayberg now targets with electrodes to treat depression.

more than 100 patients. Between 30% and 40% of patients do "extremely well"—getting married, going back to work, and reclaiming their lives, says Sidney Kennedy, a psychiatrist at Toronto General Hospital in Canada who is now running a DBS study sponsored by the medical device company St. Jude Medical. Another 30% show modest improvement but still experience residual depression. Between 20% and 25% do not experience any benefit, he says. People contemplating brain surgery might want better odds, but patients with extreme, relentless depression often feel they have little to lose. "For me, it was a last resort," Patterson says.

By making minute adjustments in the positions of the electrodes, Mayberg says, her team has gradually raised its long-term response rates to 75% to 80% in 24

"which tracts does everybody need hit?"

Now, Mayberg has found what she believes is the precise place to stimulate near area 25 to lift depression's dark cloud. The sweet spot is a tiny bundle of nerve fibers, tucked under the corpus callosum right at the place where they intersect with two other tracts. When the surgeon hits that mark, Mayberg says, "we are getting people consistently well."

Trial and error

Still, the first publicly announced results from a DBS trial using sham stimulation as a control are "disappointing," acknowledges Ali Rezaei, a neurosurgeon at Ohio State University, Columbus. He and principal investigators Don Malone of the Cleveland Clinic and Darin Dougherty from Harvard University have reported at several recent meetings that

related brain areas to the prefrontal cortex. In a recently published study, he reported that in six of seven people with depression, stimulating the medial forebrain bundle through DBS surgery caused that *joie de vivre* to return.

In the most severely depressed patients, Mayberg suspects that more than just one neural circuit involved in depression is dysfunctional. For those patients, a recommendation to “think of all the good things” or go for a run will not help, because it “assumes the machinery still has that adaptive capacity,” she says. In those cases, the electrodes implanted in DBS surgery have to take over before recovery begins, Mayberg suggests.

Scalpels versus sledgehammers

It’s an appealing picture, but some researchers think that before DBS should be used on a large scale, Mayberg and other researchers need a much better map of the brain’s pathways. “The problem is that the highways all converge,” says Kay Tye at the Massachusetts Institute of Technology in Cambridge. “We have no idea which projection that is in this white matter bundle is actually the critical one.”

It’s also unclear what the electrical stimulation in DBS actually does to networks of brain cells, says Eric Nestler, a neuroscientist at Mount Sinai Hospital who studies animal models of depression. Neural circuits are made of many different types of neurons linked together. Depending on their structure and chemical makeup, some cells make their neighbors more excitable and ready to fire, while others put a brake on neural signaling. This complexity raises an important question, Nestler says: “When you lower an electrode into the brain and crank it up really high, what are you doing that might make a person feel better?”

One tool helping scientists dissect how DBS affects depression circuits at the cellular level desired by Tye and others is optogenetics, which allows researchers to manipulate specific cells and nerve circuits with light. Nestler and his colleagues, for example, have used the technique to study the antidepressant effects of DBS in mice. No mouse is truly “depressed” in a human sense, Nestler emphasizes. Features of depression such as suicidal tendencies, guilt, and sadness are, so far as we know,

uniquely human. However, mice do show symptoms that resemble depression under certain kinds of stress—when threatened by bigger, meaner mice, for example, the rodents lose interest in food, withdraw from other mice, and don’t struggle as hard to escape from threats.

In 2010, Nestler, Herbert Covington and Ming-Hu Han, also at Mount Sinai, joined forces with Karl Deisseroth at Stanford University to try a DBS-like treatment on mice that had become depressed after prolonged bullying. Rather than inserting electrodes into the animals’ brains, the team used light to stimulate the rodents’ medial prefrontal cortex (mPFC)—an area that some neuroanatomists consider homologous to a human brain region called the anterior cingulate cortex, which contains area 25. When the researchers shone high-frequency bursts of light on this region, the gloomy rodents instantly rebounded, taking new-found interest in companions and sweets, Nestler says.

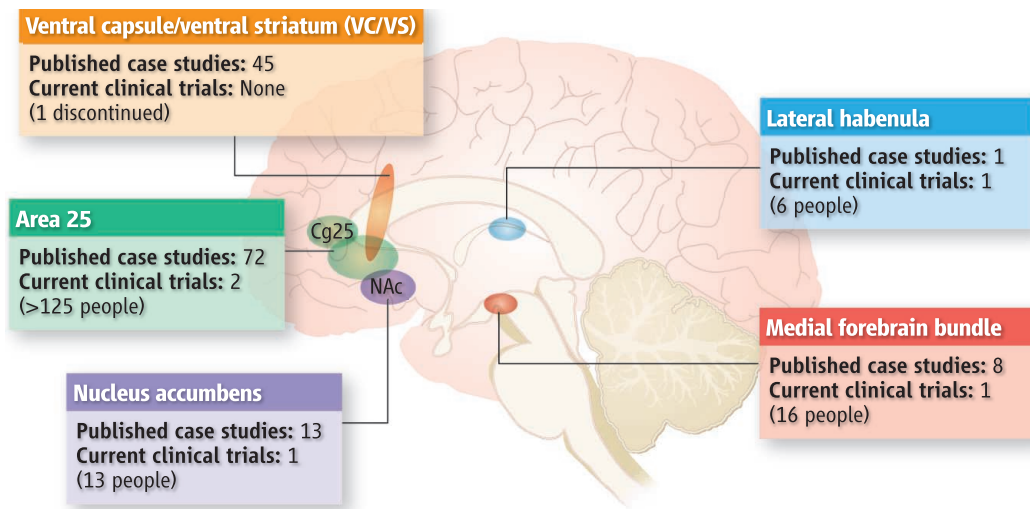
Along with Russo’s lab at Mount Sinai, Nestler and his team have since further used optogenetics to pinpoint which neurons in the mPFC are key to the antidepressant effect, and what brain regions they influence. According to Russo, neurons within the mouse mPFC that use the chemical glutamate to transmit signals may be central. Some of these nerve cells extend out of the mPFC to the nucleus accumbens, a brain region that assigns positive or negative meanings to our experiences. When the researchers stimulated activity of the mPFC neurons at the place where they attach to the nucleus accumbens, the mice

perked up. Inhibiting the same neurons with toxins caused the mice to become depressed again, Russo says.

It’s too early to know whether the same mechanism helps explain how DBS works in humans, Russo emphasizes. For one thing, “there’s a real question” about whether the region that the team stimulated in mice is indeed a homolog of a DBS target in humans, he says. However, neurons of the same subtype atrophy and die in people with depression, suggesting that the researchers are on the right track, he says. The group is preparing their results for publication and plans to present them at the Society for Neuroscience conference this month.

The fact that changing the firing rates of a few neurons can transform a mouse’s mood shows just how sensitive and complex neural circuitry is, Tye says. To her, it suggests that DBS researchers should proceed cautiously. “If you actually get a bigger behavioral change using a scalpel than a sledgehammer, that really tells you something about how the brain works,” she says. Eventually, she hopes that treatments for depression will be able to target not just brain regions, but specific neurons.

Mayberg shares Tye’s dreams of greater precision, and hopes that combining results from animals and humans will lead to treatments that don’t involve surgery. Eventually, she says, it might be possible to target cells in area 25 with a drug, or tweak the circuit noninvasively with current applied precisely to the skull. Yet she, and people like Patterson, aren’t willing to wait until then. “Even with our noisy ways and cattle prods in the brain, we have to take care of sick people, now,” Mayberg says. —EMILY UNDERWOOD



Branching out. Although area 25 is the best studied target, researchers are exploring deep brain stimulation of several other brain regions to determine if there’s a better place to treat depression.

Online

sciencemag.org

Podcast interview with author Emily Underwood (http://scim.ag/pod_6158).



Gearing up. Gray Rybka (*front*) and Leslie Rosenberg with ADMX.

whose gravity holds the galaxies together. As a dark-matter candidate, axions have long been eclipsed by so-called weakly interacting massive particles, or WIMPs. But despite decades of searching, no one has definitively detected WIMPs, and the odds may be shifting in axions' favor. "I think there's a lot more focus on axions now because WIMPs haven't been found," says Pierre Sikivie, a theorist at the University of Florida in Gainesville and a member of the ADMX team.

ADMX isn't new. The collaboration started in 1996 at Lawrence Livermore National Laboratory in California and has made successive improvements to the experiment. The current iteration commenced in 2010, when Leslie Rosenberg, the leader of the effort, moved from Livermore to Washington, carting the experiment with him. Now ADMX researchers are about to take a crucial step. In the next few years they should achieve the sensitivity to provide a rare thing in dark-matter searches: a clear-cut yes-or-no answer.

Theory constrains the properties of axions so tightly that if ADMX researchers don't see them, then axions must *not* constitute the universe's dark matter, Rosenberg says. In contrast, a null result in a WIMP search generally sets a limit on how detectable WIMPs are but can't harpoon the basic concept. ADMX "is the only dark matter experiment I know of that can either see a candidate at a high confidence level or exclude it at a high confidence level," Rosenberg says.

Strong suspicions

Theorists didn't invent the axion to explain dark matter. Rather, they cooked it up to solve a puzzle involving the strong nuclear force, which is conveyed by particles called gluons and binds particles called quarks in trios to form the protons and neutrons in atomic nuclei. The problem is that the interplay of

Dark Matter's Dark Horse

A rare yes/no effort promises to prove either that hypothetical particles called axions are the universe's elusive dark matter—or that they can't be

SEATTLE, WASHINGTON—In the age of the 27-kilometer-long atom smasher and the 50,000-tonne underground particle detector, the Axion Dark Matter Experiment (ADMX) hardly looks grand enough to make a major discovery. A modest 4-meter-long metal cylinder, it dangles from a wall here at the University of Washington's Center for Experimental Nuclear Physics and Astrophysics, as shiny and inscrutable as a tuna hung up for display. A handful of physicists tinker with

the device, which they are preparing to lower into a silolike hole in the floor. The lab itself, halfway down a bluff on the edge of campus, is far from the bustle of the university. Yet ADMX researchers will soon perform one of the more important and promising experiments in particle physics.

Starting late this year, ADMX will search for elusive, superlight particles called axions. Predicted by nuclear theory, axions could provide the mysterious dark matter

quarks and gluons has a kind of symmetry not predicted by physicists' well-tested theory of the strong force.

Imagine a gaggle of quarks, antiquarks, and gluons. Swap all the particles and antiparticles and invert each particle's position and momentum. The system looks and behaves exactly as it did before—a sameness called charge-parity (CP) symmetry.

If CP symmetry didn't hold in strong interactions, the neutron would have more positive charge toward one of its magnetic poles and more negative charge toward the other. That distribution, known as an electric dipole moment, would flip with all the swapping and inverting. But experimenters have shown that, to very high precision, the neutron has no electric dipole moment. So the symmetry reigns.

That's a puzzle because according to the theory of the strong force, certain interactions among gluons ought to knock CP symmetry out of kilter. This "strong CP problem" leaves physicists with two alternatives. The parameter that sets the strength of those gluon interactions, an abstract angle called Θ , could happen to be miraculously close to zero—less than 0.0000000001. But that's the kind of "fine-tuning" physicists loathe. Or some unknown mechanism could force the offending interactions to vanish.

The axion is part of such a mechanism, which was invented in 1977 by the American theorists Roberto Peccei and Helen Quinn. They assumed that the vacuum contains a quantum field a bit like an electric field, which interacts with gluons in a way that cancels out the CP-violating interactions. In this scheme, Θ can be thought of as a marble in a circular track more or less created by the field. If the track is level, the marble can sit anywhere. But tilt the track and the marble rolls to the lowest point. The gluons and the quantum field interact in a way that always tilts the track in the direction of zero. Axions are the quantum particles associated with that field.

The scheme may sound contrived, but it resembles another famous bit of particle physics. Quarks, electrons, and other fundamental particles get their mass by interacting with a different field in the vacuum, one made up of a type of particle called the Higgs boson, which to great fanfare was discovered in 2012. Theorists have no other solution to the strong CP problem as elegant as the Peccei-Quinn mechanism, says Washington's Ann Nelson: "I'm one of the authors of the other potential solution to that problem, and I would say that the axion is more likely."

Dark matter comes as a bonus. After the big bang, different regions of the universe had different values of Θ . As the cosmos cooled, Θ in each region rolled to zero and then jiggled about that value. Such oscillations correspond to the generation of axions, in various amounts depending on how far Θ started from zero. The axions would linger today in vast numbers, making up the dark matter.

Cosmological and astrophysical observations set limits on the properties of the axion.

a fixed frequency emanating from a strong magnetic field. "In the end, it's very much like a superfancy, very high-end AM radio, and you're just trying to find your station," says Gray Rybka, a research professor and ADMX team member at Washington.

In practice, the experiment requires a herculean effort. The chances that an axion will turn into a photon are tiny, so to have a shot at producing a signal, researchers must use a huge magnet. ADMX employs a 6-tonne

	Axions	WIMPs
Year invented	1977	1985
Original purpose	Solve technical problem in theory of strong nuclear force	Explain dark matter
Detectable because they	Turn into photons in strong magnetic fields	Bounce off atomic nuclei
Pros	Solve more than one problem; allow for decisive test	Flow naturally from supersymmetry; provide many models and multiple avenues of detection
Cons	Provide few models and one means of detection	Resist decisive testing; haven't shown up in decades of looking

It must have a mass of at least 1 millionth of an electron volt (1 μeV)—2 trillionths the mass of an electron. Otherwise, the infant universe would have produced so many axions that their gravity would have warped the geometry of the cosmos. Conversely, it can't be heavier than 1000 μeV , or axions would interfere with nuclear reactions and distort stellar explosions known as supernovae.

The case for the axion isn't as strong as that for the Higgs was, but some physicists says it's still so compelling that it almost has to be true. "The aesthetic arguments are very strong," says Frank Wilczek, a theorist at the Massachusetts Institute of Technology in Cambridge. "It would be a pity if it didn't exist."

Tuning into the signal

The challenge is to detect it. In principle, the task is simple. As well as feeling the strong force, axions should also interact with the electromagnetic force responsible for light and other radiation. When an axion passes through a magnetic field, it should sometimes reveal itself by turning into a photon. Given the axion's tiny mass, the photons should be low-energy radio waves. So to hunt for axions, ADMX physicists search for radio signals of

superconducting coil a meter long and half a meter wide that produces a field 152,000 times as strong as Earth's field. To further enhance the signal, researchers slide inside the magnet a cylindrical "resonant cavity," in which radio waves of a specific frequency will resonate just as sound of a specific pitch resonates in an organ pipe. The cavity should amplify the production of photons 100,000-fold, and its resonant frequency can be changed by moving metal or insulating rods within it.

Boosting the volume isn't enough; as much as possible, researchers also have to silence everything else. The experimental equipment itself generates random radio waves at a rate proportional to its temperature. To tamp down such "thermal noise," researchers must cool the equipment to near absolute zero. The latest incarnation of ADMX will be equipped with a liquid-helium refrigerator capable of cooling the experiment to 0.3 kelvin. Next year, researchers will go a step further and add a refrigerator that will reach 0.1 kelvin.

Temperature control is not the only problem. The amplifiers that beef up the signals generate their own ineluctable heat and noise as electrons ricochet through them. In principle, researchers could sift a signal from such noise by collecting enough data. But conven-

tional amplifiers would require enormous “integration times.”

To speed things up, Rosenberg and colleagues sought help from John Clarke, a condensed matter physicist at the University of California (UC), Berkeley. Clarke is an expert on so-called superconducting quantum interference devices, or SQUIDs, tiny rings of superconducting metal that can be used, among other things, as extremely low-noise amplifiers. A SQUID’s noise is set not by its temperature but by unavoidable quantum uncertainty, making it, in a sense, the quietest amplifier possible.

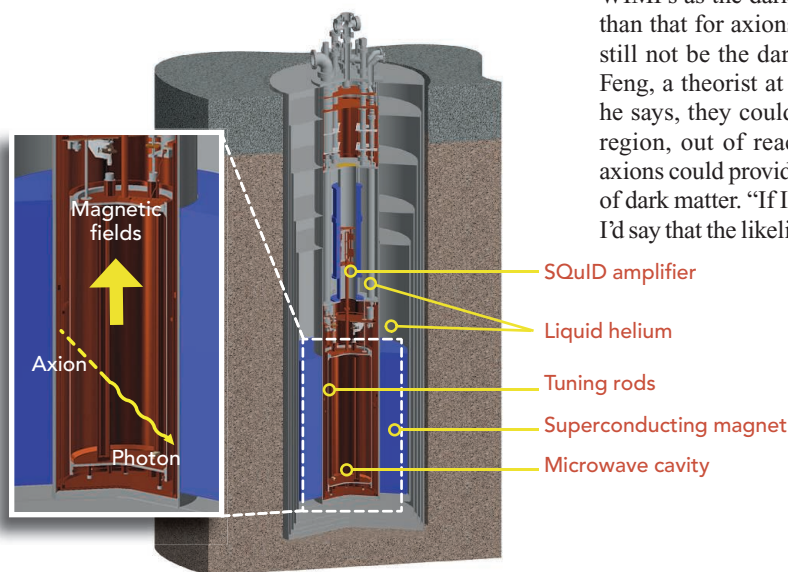
In 2010, the ADMX team showed that the specially designed amplifiers worked as hoped. They should make the experiment go thousands of times faster, Clarke says, “so instead of taking centuries it takes roughly 100 days.” With the SQUID in place, ADMX is the most sensitive radio receiver on Earth, capable of detecting a signal with a strength of a few billionths of a billionth of a watt, says Dmitry Lyapustin, a graduate student at Washington. “It’s so powerful that if you were on Mars and you had our receiver hooked to your cell phone, you’d still get four bars,” he says.

Axions may not call as soon as the physicists start taking data, which will happen by the end of the year. Over the next 3 years, they aim to work through much of the axion’s potential mass range. They’ll cover the low end, from 1 to 10 μeV , fairly quickly, Rosenberg predicts. The middle range, from 10 to 100 μeV , may take longer, as a heavier axion would produce higher frequency radio waves that require smaller resonant cavities. The high range, from 100 to 1000 μeV , lies out of reach of the current technology. But if nothing shows up by then, Rosenberg says, ADMX would have bagged a major result already: If the axion is that heavy, it would be too scarce to account for most of the dark matter.

Axions versus WIMPs

For a high-profile particle physics experiment, the ADMX collaboration is unusually small. It numbers about 30 researchers from seven institutions. Rosenberg says he has invited in only experts, such as Clarke, who possess essential skills. “We’re very, very small because we don’t need to be any bigger,” he says. At the same time, much of

the experiment is being built by students. For example, Lisa McBride, a graduate student at Washington, started on ADMX as an undergraduate, when she designed the gear boxes that move the cavity’s tuning rods in 200-nanometer steps. Such an assignment “shows a lot of trust,” she says.



Hi-fi. When an axion passes through a magnetic field, it can turn into a radio-frequency photon. ADMX aims to tune in to that radio signal, which may be a few quadrillionths of a nanowatt.

ADMX researchers are vastly outnumbered by the many teams stalking WIMPs. These particles—no more certain than axions—interact only through the weak nuclear force, which triggers a certain type of nuclear decay. In the 1980s, theorists realized that if the infant universe spawned such particles, then just enough of them should remain to supply the dark matter, provided they weigh between one and 1000 times as much as a proton. That tantalizing coincidence is called the “WIMP miracle.” Interest in WIMPs surged when theorists realized that a concept called supersymmetry, which posits for every particle known now a more massive partner, generally predicts the existence of WIMPs.

Which are more likely, axions or WIMPs? Opinions vary. As the solution to a precise technical problem, the axion is “better motivated” than the WIMP, Washington’s Nelson says. Moreover, experimenters have searched for signs of WIMPs pinging off atomic nuclei with ever larger, more-sensitive detectors deep underground. Those have yet to come up with unequivocal signals, and they have gradually ruled out some of the many combinations of mass and other properties—the so-called parameter space—allowed in supersymmetric models. (As *Science* went to print, the team working with the LUX exper-

iment at the Sanford Underground Research Facility in Lead, South Dakota, was preparing to release the results of the most sensitive WIMP search yet; see p. 542.) So the WIMP miracle “is looking a little frayed these days,” Wilczek says.

Still, some theorists find the case for WIMPs as the dark matter more compelling than that for axions. Axions could exist and still not be the dark matter, notes Jonathan Feng, a theorist at UC Irvine. For example, he says, they could fall in that higher mass region, out of reach for ADMX, in which axions could provide no more than a smidgen of dark matter. “If I had to put a number on it, I’d say that the likelihood that the axion solves

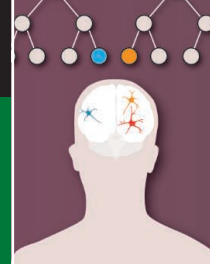
the strong CP problem is 90%, but the chances that the axion is the dark matter is 10%,” Feng says. He argues that roughly half the parameter space for WIMPs remains viable.

Whatever ADMX sees, it will tell physicists something important. A null result would skewer the axion as a dark-matter candidate, Rosenberg says. Some theorists, however, expect the death rattle to come slowly. Die-hards would just concoct more contrived models to explain why the axion wasn’t seen, says Marc Kamionkowski, a theorist at Johns Hopkins University in Baltimore, Maryland. “A theory is only dead when everybody agrees it’s dead,” he says.

For example, Nelson says, theorists already know one way to dodge the lower limit on the axion’s mass without producing more dark matter than astrophysicists observe. Cosmologists think that in the first instants after the big bang, the universe underwent a growth spurt called inflation, in which space expanded at greater than light speed. Axions emerged after inflation, theorists assume. But if axions emerged before inflation, all of the universe we can see could have started out as a tiny patch in which the density of axions happened to be very low. That just-so story would allow axions to be abundant on a cosmic scale and light enough to elude ADMX.

Or ADMX might just hear the faint radio whisper of passing axions. Rosenberg says he’d be surprised if the particles didn’t show up. “We’re true believers,” he says. To build such an intricate, sensitive experiment, he says, “I think you have to be.”

—ADRIAN CHO



LETTERS

edited by Jennifer Sills

Health and Obesity: A New Normal?

IN THEIR PERSPECTIVE “THE HEALTH RISK OF OBESITY—BETTER METRICS imperative” (23 August, p. 856), R. S. Ahima and M. A. Lazar ask how a normal body mass index (BMI) could be deleterious to health. A better question might be: Why should a value of BMI be arbitrarily defined as “normal” and used as a benchmark in discussing health risks, when it is possible to define an optimal value of BMI by reference to unequivocal data points such as BMI versus age at death?

Ahima and Lazar cite Flegal *et al.* (1), who found that “overweight was associated with significantly lower...mortality.” That is, subjects in Flegal *et al.*’s “overweight” group (BMI

25 to 30) had a lower mortality rate than subjects in her “normal” group. These data suggest that the optimal BMI is higher than the “normal” BMI. Other studies, which use the unequivocal end point of death to define optimality, confirm this implication. For instance, Durazo-Arvizu *et al.* found that minimal mortality was associated with BMI ranging from 23 to 30 (2). Another study showed that adults with BMIs of 18.5 to 24.9 at the onset of diabetes had higher mortality than those with BMIs of 25 or higher (3). Others have demonstrated that optimal BMI increases with increasing age (4). In a review of 40 studies, Hamer and Stamatakis could not find a confounding factor that could explain the better outcomes in overweight and mildly obese groups (5).

MARSHALL E. DEUTSCH

Sudbury, MA 01776–2328, USA. E-mail: med41@aol.com

References

1. K. M. Flegal *et al.*, *JAMA* **309**, 71 (2013).
2. R. A. Durazo-Arvizu *et al.*, *Am. J. Epidemiol.* **147**, 739 (1998).
3. M. R. Carnethon *et al.*, *JAMA* **308**, 581 (2012).
4. R. Andres, E. L. Bierman, W. R. Hazzard, *Principles of Geriatric Medicine* (McGraw-Hill, New York, 1985).
5. M. Hamer, E. Stamatakis, *Prev. Med.* **57**, 12 (2013).

Health and Obesity:
Not Just Skin Deep

IN THEIR PERSPECTIVE “THE HEALTH RISK OF obesity—better metrics imperative” (23 August, p. 856), R. S. Ahima and M. A. Lazar discuss findings that suggest positive effects of obesity on mortality and call for better body shape and fat distribution measurements. Other adipose factors may also be important.

It has long been known that the size of

fat cells is important in metabolic obesity complications (1). Recent evidence suggests additional connections to fat cell number and turnover. At any level of body fat, human adipose tissue can have either hypertrophy (a small number of large cells) or hyperplasia (a large number of small cells). Human fat cells turn over at a high rate (2), but turnover is markedly lower in subjects with adipose hypertrophy (3). Hypertrophy is linked to a disadvantageous metabolic profile in all body types: healthy lean, overweight, obese (3), and morbidly obese subjects (4). Genetic predisposition for type 2 diabetes is also associated with adipose hypertrophy (5). In other words, it is possible to look lean and healthy on the outside but have obesity/diabetes-prone adipose tissue on the inside.

Taking early and recent findings together, it is possible that in hypertrophy, adipocyte production rate is low, requiring existing fat cells to accumulate more lipids than in hyperplasia. Supporting this notion is the strong

connection between fat cell lipid turnover, lipid metabolism, and insulin sensitivity (6). Fat cell turnover and morphology may also be linked to insulin resistance through adipose inflammation (7).

Ahima and Lazar point out that weight loss alone may not reduce cardiovascular disease (8). Similarly, a hallmark study found no improvement of metabolic profile after removing large amounts of adipose tissue from the abdominal wall of obese patients (9), further implying that the quality rather than the amount of adipose tissue is important. Perhaps an improvement of metabolic profile is partly dependent on remodeling of adipose tissue from hypertrophy to hyperplasia rather than weight loss alone. Targeted studies of potential effects of weight loss on fat cell morphology and turnover may reveal further links between adipose tissue composition and metabolic risk factors.

ERIK ARNER^{1,2*} AND PETER ARNER¹¹Department of Medicine, Karolinska Institutet at Karolinska

Letters to the Editor

Letters (~300 words) discuss material published in *Science* in the past 3 months or matters of general interest. Letters are not acknowledged upon receipt. Whether published in full or in part, Letters are subject to editing for clarity and space. Letters submitted, published, or posted elsewhere, in print or online, will be disqualified. To submit a Letter, go to www.submit2science.org.



Sensing temperature
for flowering

566

University Hospital, Huddinge, SE-141 86 Huddinge, Sweden. *RIKEN Center for Life Science Technologies, Division of Genomic Technologies, Yokohama, Kanagawa, 230-0045 Japan.

*Corresponding author. E-mail: arner@gsc.riken.jp

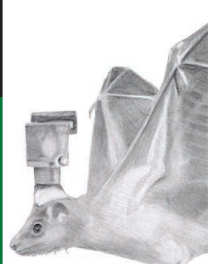
References

1. L. B. Salans, J. L. Knittle, J. Hirsch, *J. Clin. Invest.* **47**, 153 (1968).
2. K. L. Spalding *et al.*, *Nature* **453**, 783 (2008).
3. E. Arner *et al.*, *Diabetes* **59**, 105 (2010).
4. J. Hoffstedt *et al.*, *Diabetologia* **53**, 2496 (2010).
5. P. Arner, E. Arner, A. Hammarstedt, U. Smith, *PLOS ONE* **6**, e18284 (2011).
6. P. Arner *et al.*, *Nature* **478**, 110 (2011).
7. E. Arner, M. Rydén, P. Arner, *N. Engl. J. Med.* **362**, 1151 (2010).
8. Look AHEAD Research Group *et al.*, *N. Engl. J. Med.* **369**, 145 (2013).
9. S. Klein *et al.*, *N. Engl. J. Med.* **350**, 2549 (2004).

Emerging Arsenic Threat in Canada

L. RODRÍGUEZ-LADO *ET AL.*'S GEOSTATISTICAL model ("Groundwater arsenic contamination throughout China," Reports, 23 August, p. 866) has revealed the hidden risk of arsenic exposure in drinking water, particularly in China. The accompanying Perspective by H. A. Michael ("An arsenic forecast for China," p. 852) highlighted the global burden of arsenic-contaminated drinking water and the potential utility of Rodríguez-Lado's model to identify populations exposed to arsenic before the development of symptoms.

In Canada, arsenic is not currently a primary public health concern. However, we would like to point out the urgency of this emerging threat. More than a quarter of a million tons of arsenic generated over 50 years during the operation of the Giant Mine in Yellowknife (Northern Canada) reside underground and in piles aboveground. Because cleanup is deemed too great a health risk, the arsenic will be frozen in the ground, at a cost of nearly one billion Canadian dollars (1). In almost every province, arsenic-contaminated drinking water is a growing health concern in Canada. From Nova Scotia to British Columbia, arsenic levels frequently exceed those deemed safe by the World Health Organization (WHO) (2). Tools such as those described by Rodríguez-Lado *et al.* will not only help identify areas to prioritize for immedi-



Neurobiology
Prize Essay

573

ate action in Canada and around the world, but also encourage public health agencies to monitor those already chronically exposed.

VICTOR D. MARTINEZ,* EMILY A. VUCIC,
STEPHEN LAM, WAN L. LAM

British Columbia Cancer Agency, Vancouver, BC V5Z1L3, Canada.

*Corresponding author. E-mail: vmartinez@bccrc.ca

References

1. B. Weber, "Giant Mine's high cleanup bill shakes up policy on toxic sites," *The Globe and Mail* (1 April 2013).
2. C. F. McGuigan, C. L. A. Hamula, S. Huang, S. Gabos, X. C. Le, *Environ. Rev.* **18**, 291 (2010).

LIFE IN SCIENCE

Zombiology

I step behind the podium and announce, "Today is zombie biology."

The students look up.

"First things first: What would cause a person to turn into a zombie?"

A few hands rise. "Radioactivity," a student says. "A disease," offers another.

"Excellent. And how would this disease be transmitted?"

Question after question, more and more students join in. Facing a zombie outbreak, how should institutions react?

How would survivors organize? Would they be able to carry on as before, or do careers and mortgages become secondary concerns when a horde of walking dead approaches? Would governments still manage to protect individuals, or should everyone take their safety into their own hands?

Finally, one last question: "When you get home," I say, "think about whether this class was really about zombies. See you next week!"

My "zombie biology" lecture is fictional, but zombie classes have begun to emerge (1, 2). The course descriptions are reassuring enough: Learn how to build a shelter, what kind of food to keep at the ready, and how to lead a group of survivors. Zombie apocalypse prevention may prove useful. Perhaps those who know how to survive a zombie outbreak won't panic when word spreads of a bad strain of the flu or a radioactive leak.

Even so, we need to tread carefully. We don't want students leaving the class convinced that zombies are real. Inviting zombies into a class may be a risky initiative—but if the students survive it, the results could be scarily effective.

MATTHIEU J. GUITTON* AND CÉCILE CRISTOFARI

Faculty of Medicine, Laval University, Quebec City, Canada.

*Corresponding author. E-mail: matthieu.guitton@fmed.ulaval.ca

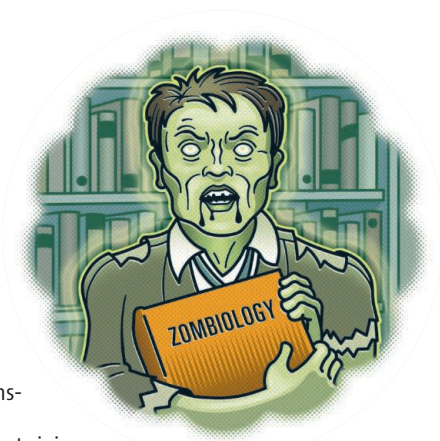
References

1. "Preparedness 101: Zombie Apocalypse," Centers for Disease Control and Prevention 2011 (<http://blogs.cdc.gov/publichealthmatters/2011/05/preparedness-101-zombie-apocalypse/>).
2. "Society, science, survival: Lessons from AMC's The Walking Dead" (www.canvas.net/courses/the-walking-dead).

CORRECTIONS AND CLARIFICATIONS

Reports: "Representation of three-dimensional space in the hippocampus of flying bats," by M. M. Yartsev and N. Ulanovsky (19 April, p. 367). In Fig. 1, some graphic elements were misaligned. The HTML and PDF versions online have been corrected.

Reports: "Declining coral calcification on the Great Barrier Reef" by G. De'ath *et al.* (2 January 2009, p. 116). The Report cited a 14.2% decline in coral calcification from 1990 to 2005 based on analyses of 328 *Porites* colonies from the Great Barrier Reef (GBR). The authors now note that some of outermost annual growth bands were incomplete, and thus their estimate of the magnitude of the calcification decline was too high. They have adjusted for the incomplete outermost bands, and the decline in calcification for the period 1990–2005 drops to between 11.4 and 9.0%, depending on the method used. The most efficient adjusted estimate shows a decline of 11.4% [95% CI = (10.4, 12.4)]. The revised estimate of 11.4% still suggests a bleak future for corals of the GBR due to climate change.



GENETICS

Deep Inside Champions, Just Genes?

Dov Greenbaum, Jieming Chen, Mark Gerstein

In *The Sports Gene*, David Epstein provides a well-researched collection of interesting anecdotal cases related to the long-standing nature-versus-nurture debate. These lean heavily toward track and field. In addition to Epstein's personal experiences as a former collegiate runner, track potentially provides a more direct connection between genetics and basic physical phenotypes (such as strength, speed, and endurance) than other sports in which confounding factors such as team play may make for a more complex relationship.

The book sets out to present a balanced account of the debate. Epstein (a science writer at *Sports Illustrated*) argues that genetic influences are not necessarily uniform across a sport. Rather, different influences come into play at different points over an athlete's career. Gender differences provide an example of his nuanced treatment. Notwithstanding seemingly hardwired differences (due to, among other influences, variation in testosterone levels), some had predicted, given historical trajectories, that women's athletic abilities would eventually converge on men's (1, 2). Epstein counters that—because current data suggest that female athletic abilities are plateauing below those of men—earlier trends might have been confounded by doping during the Cold War. Epstein also discusses a group of female athletes who have naturally higher levels of testosterone (possibly enhancing their performances): those who are genetically XY. However, the devil is in the biological details: some XY females are insensitive to the effects of increased testosterone, and, Epstein argues, these athletes are sometimes unfairly disqualified from competing against XX-female colleagues.

As evidenced throughout the book, athletes make excellent research subjects. Their physical traits are carefully measured and recorded. Moreover, society treats the pri-

vacy of their personal data as less sacrosanct than legally protected medical records. This enables researchers to more readily link substantial amounts of quantifiable physiological measurements, physical abilities inherent from genetics, and the underlying mechanistic biology.

Also, with the near-universal pop-cultural qualities of sport, discussing genetics in athletics provides an optimal vehicle for teaching basic biological concepts to a broad audience. It's much more palatable to learn about Usain Bolt's genes than about the depressing phenotype of a rare genetic disorder.



Why so fast? Usain Bolt on his way to a world's record in the 100-m finals at the 2008 Olympics in Beijing.

In addition, sports, like genetics, is concerned fundamentally with outliers. Rare mutations with strong effects are nature's gift to genetics in that they can sometimes illuminate the underlying biochemical mechanisms. In a similar vein, the never-ending search for exceptional talent that will lead to victory in highly competitive sports effectively picks out individuals in the upper end of the athletic bell curve (with those rare mutations that genetics seeks).

Epstein provides many instances of identifiable outliers (even within the rarified context of world-class performers) and describes their connections to genetics. For example, we learn about a Finnish skier whose rare mutation in the erythropoietin receptor gave him hemoglobin levels so high that he was suspected of doping. Else-

where, Epstein explains what supermuscular babies, beefy cows, and incredibly fast whippets have taught us about the function of the myostatin gene. He also describes loss-of-function variants in the *ACTN3* gene and how these are related to the contrast between top-notch endurance runners (particularly those from East Africa) and exceptionally fast sprinters (from West Africa).

The erythropoietin receptor, myostatin, and *ACTN3* provide classic single-gene stories. Despite the obvious constraints on books written for a broad audience, we would have appreciated more on how sports relates to current efforts in genome-wide studies. In particular, personal genomics provides a new way for athletes to fully grapple with the totality of their underlying nature. One can imagine athletes devising customized training regimens using these increasingly affordable

The Sports Gene
Inside the Science of
Extraordinary Athletic
Performance/
What Makes the
Perfect Athlete

by David Epstein
Current, New York, 2013.
352 pp. \$26.95. ISBN
9781591845119. Yellow
Jersey, London. £16.99.
ISBN 978-0224091619.

and available data. These data may prove especially useful for avoiding athletic injuries. Epstein, for instance, discusses a number of specific genes that can provide some light on injuries, including the *ApoE* gene (where the $\epsilon 4$ allele worsens the prognosis after a concussion) and the genes associated with hypertrophic cardiomyopathy.

Akin to personal genomics in its emphasis on building databases of personal information, the quantified-self movement focuses on taking real-time measurements of individuals' physiology using smart sensors. Sports training will be revolutionized by these measurements, which offer a much more precise view of an athlete's dynamic physiology throughout the day and over the course of training. The merger of personal genomics and quantified-self measurement

The reviewers are at the Program in Computational Biology and Bioinformatics and the Department of Molecular Biophysics and Biochemistry, Yale University, New Haven, CT 06520, USA. E-mail: dov.greenbaum@yale.edu; mark@gersteinlab.org

could culminate in real-time “personal functional genomics” in which large-scale biochemical assays, such as RNA sequencing, help athletes prepare for competition. The Personal Genomes Project has already taken steps to make shareable collections of such data sets possible (3), and one researcher has already integrated his genome with his transcript, protein, and metabolite measurements to chart his physiological states over time (4).

Through Epstein’s easily accessible presentation, supported by comprehensive and copious notes, *The Sports Gene* provides a wonderful background to a future in which emerging technologies will bring the nature-versus-nurture debate into even sharper focus. Perhaps in this future, the author will write an equally compelling sequel: “Sports Genomics.”

References

1. B. J. Whipp, S. A. Ward, *Nature* **355**, 25 (1992).
2. A. J. Tatem, C. A. Guerra, P. M. Atkinson, S. I. Hay, *Nature* **431**, 525 (2004).
3. www.personalgenomes.org.
4. R. Chen et al., *Cell* **148**, 1293 (2012).

10.1126/science.1245795

PUBLIC HEALTH

An Ethnographic Check-Up

Nicole S. Berry

The field of global health has undergone a profound transformation over the past 15 years. The amount of money earmarked as “global assistance for health” has increased fourfold from 1990 levels (1). The majority of this money previously streamed from government treasuries to international organizations (e.g., the World Health Organization or the World Bank). Yet, the past decade has brought substantial increases in funding from private philanthropists (e.g., the Bill and Melinda Gates Foundation); a redirection of state monies toward new players, such as public-private partnerships (e.g., The Global Fund); and a superfluity of nongovernmental organizations. What was a relatively staid field at the end of the Cold War has now been reworked into a fresh field with new players, emphases, and modes of engagement (2).

Given these recent transformations, *When People Come First: Critical Studies in Global Health* is a welcome examination of “the actual impacts of [global health] initiatives on care, health systems, and governance.” For the authors, considering people first articulates with a theoretical commitment to analyze the lived experiences and knowledges of those whom the enterprise of global health seeks to help. Indeed, the authors argue that to meet our obligations to people, within this domain such knowledges are as crucial as “gold standard” evidence. On an applied level, the authors align themselves with recent work by economist Michael Porter (3), anthropologist (and World Bank president) Jim Yong Kim, and physician-anthropologist Paul Farmer (4) to emphasize that putting people first means shifting from a focus on program success (e.g., access, patient compliance, or deliverables) to “results obtained by the patients (measured in survival rates and in the degree and sustainability of recovery).”

The editors—anthropologists João Biehl (Princeton University) and Adriana Petryna (University of Pennsylvania)—showcase work by scholars who waded into the new territory of global health concerned that the programs, paradigms, and interventions that dot the world’s landscape frequently do little to alleviate the profound suffering and ill health of marginalized and vulnerable communities they are meant to help. The volume draws on ethnography-based case studies that intentionally pull in social, economic, and political context to push the reader to think critically about the assumptions that underlie practices that epitomize contemporary global health. These include evidence-based public health (Vincanne Adams), reliance on nongovernmental organizations to distribute money (James Pfeiffer), public-private mixes (Stefan Ecks and Ian Harper), and attention to compliance (Ian Whitmarsh).

The volume is divided into three main thematic sections. The essays about “evidence” point to a current propensity to seek improved health outcomes by streamlining approaches—e.g., only admitting certain types of evidence, searching for magic bullets, and favoring technological fixes. The authors argue that aspects that get bracketed out of these approaches—such as public health histories (Marcos Cueto) and the complexities of “clients’” experiences (Adams)—are central to actually trans-

forming health outcomes. The second section offers a more fine-grained attention to global health interventions. Following the impetus of the volume’s title, these chapters explore the complex lives of people and consider how global health interventions designed to help intersect these lives only in limited ways. These essays demonstrate the partiality of what we seek to achieve as well as what we have achieved. The last section,

“markets,” contextualizes people’s experiences at the intersection of the increasing importance of the private sector in global health, greater divides in wealth, and states’ commitments to provide health for their citizens. The authors consider the effects of new modes of organizing access to health [e.g., public-private partnerships (Ecks and Harper)] and approaches predicated on a right to treatment (chapters by Clara Han and by Biehl and Petryna). Although these have been championed as better for the disenfranchised, they have instead resulted in complicated and less than ideal forms of care.

The authors’ empirical accounts of the complexities of the global health landscape expose a litany of assumptions that drive global health and demonstrate why we must be suspicious of these. One such assumption is that many of the interests that underwrite contemporary global health activity (such as increasing private competition, creating a “science of global health,” and demonstrating programmatic achievements) are proxies for global health success. The authors argue that these competing interests not only subvert the moral necessity of putting people first, they frequently hinder the goal of improving people’s health. Another assumption is that medical technologies themselves save lives. These technologies must be put to work in a complex global environment marked not only by ethnic, linguistic, cultural, and political heterogeneity but also by increasing inequity and inequality. *When People Come First* shows that the issue of how people get access to the treatments they need—be those pain killers, tuberculosis drugs, or cutting-edge DNA therapies—is very much alive.

References

1. N. Ravishankar, *Lancet* **373**, 2113 (2009).
2. J. Cohen, *Science* **311**, 162 (2006).
3. M. E. Porter, *N. Engl. J. Med.* **361**, 109 (2009).
4. J. Y. Kim, P. Farmer, M. E. Porter, *Lancet* **382**, 1060 (2013).

10.1126/science.1243510

The reviewer is in the Faculty of Health Sciences, Simon Fraser University, 8888 University Drive, Burnaby, BC V5A 1S6, Canada. E-mail: nicole_berry@sfu.ca

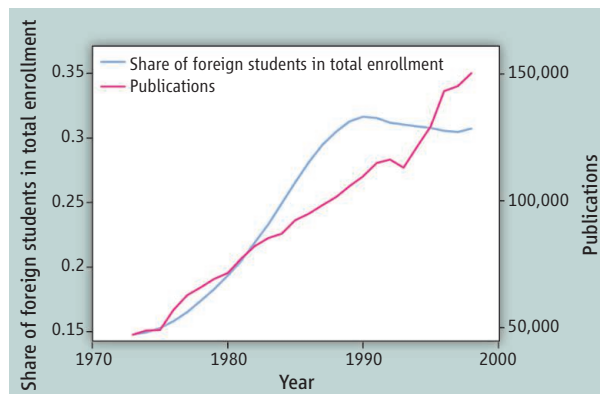
Doctoral Students and U.S. Immigration Policy

Keith E. Maskus,¹ A. Mushfiq Mobarak,^{2*} Eric T. Stuenkel³

Whether the United States should make it easier for foreign graduates of U.S. universities to acquire visas and permanent residency is an important question raised by current immigration reform proposals (1). Such policies should be informed by rigorous analyses of whether international doctoral students are important for research and support technological innovation. We discuss the evidence on this point, its implications, and some new policy ideas.

There are three rationales commonly cited to ease foreign student entry. First, academic scientists argue that their ability to perform research and generate new knowledge is impaired when universities are unable to recruit the best doctoral students, domestic or foreign (2, 3). Second, the perceived difficulty of getting and sustaining a visa for graduate work in science and engineering (S&E), combined with rapidly improving training around the world, may be diminishing the willingness of international doctoral students to come to U.S. universities (4, 5). Finally, U.S. immigration policies raise barriers that must be surmounted by foreign students wishing to launch careers in the United States after graduation. Many believe this dampens competitiveness by pushing innovative people abroad (6). This policy is increasingly out of touch with more welcoming standards in Canada, Australia, and Europe (7).

In recent decades, the numbers and percentages of foreign doctoral students in S&E programs have grown tremendously. Over the same period, there has been a major increase in research output from those laboratories (see the figure). Yet these trends may simply reflect incidental correlation, both having risen for other reasons, e.g., expanded federal research funding, or increased commercial demand for technical applications of basic science. Without a clear demonstration that enrolling more international students is an instrumental source of more and better



U.S. S&E publications and the share of S&E doctoral students at U.S. universities who are foreign-born, have both increased over time. This is illustrative, but not indicative, of a causal relationship. Enrollment data derived from the NSF Survey of Earned Doctorates. Publications data from Web of Science. Details in (11).

science, the claims made above lose much of their force. Any innovation benefits have to be weighed against downsides to immigrant entry discussed in the literature: Foreign students are expensive to train; they drive out domestic counterparts; they reduce salaries of native-born postdoctoral students and scientists and engineers (8, 9). The theoretical basis for adverse effects on native employment and wages is that immigrants and domestic workers are substitutes within skill classes. Recent theoretical and empirical work shows that substitutability may be imperfect, which limits adverse effects of immigrants on salaries (10). Influx of immigrants with certain skills may even raise demand for workers with complementary skill sets (10).

Productivity and Quality

Our analysis of contributions of foreign and domestic doctoral students to creation of knowledge at 100 research-intensive U.S. universities across 23 S&E fields (11) found that both international and U.S. graduate students are essential and causal inputs into scientific discovery. Our research exploits fluctuations in supplies of foreign students due to macro or policy shocks in source countries to identify casual effects on innovation. For example, changes in study-abroad restrictions in China led to variation in the number of Chinese students in the U.S. that was unre-

Policies should promote skilled non-U.S. students to study, and stay, in the United States.

lated to conditions in U.S. academia. Each additional international Ph.D. student led to 0.92 to 0.97 publications and 33 citations per year or about 2.3% of the average university-field knowledge production. Each additional domestic Ph.D. student supported 0.84 to 1.05 publications and 45 citations. These contributions of international and domestic students were statistically indistinguishable, which suggests that the two groups are comparable at the margin.

We also studied gains in knowledge production from bringing in students of particularly high aptitude for research. Using two different types of foreign-student supply fluctuations (those correlated with the ability to pay for graduate study and others that had nothing to do with their economic situations), we find suggestive evidence that publication contributions of international students admitted based on aptitude were about twice as high as for students admitted because of ability to pay. The logic is that, when incomes rise unexpectedly abroad, universities expand admission offers to less-qualified, but fee-paying, students. There may be long-term costs to restricting entry of high-quality foreign students, as departments may not be able to replace such students as easily.

These effects buttress the case for sustaining and increasing access to the best graduate students regardless of nationality. The results have implications for immigration policy regarding the highly skilled. The student quality results call into question the focus in U.S. entry requirements on students' access to sufficient financial resources at home to complete their programs of study, as well as incentives and ability to return home upon graduation. Other countervailing policies, such as the National Science Foundation Graduate Fellowship Program, aim to induce universities to admit more high-quality students, even at the expense

¹University of Colorado at Boulder, Boulder, CO 80309, USA. ²Yale University, School of Management, New Haven, CT 06520, USA. ³University of Idaho, Moscow, ID 83844, USA.

*Corresponding author. E-mail: ahmed.mobarak@yale.edu

of fee-paying students, but these fellowships only apply to natives, not to foreign students.

U.S. policy also requires foreign nationals who complete their doctoral studies to leave the country unless they find employers that are willing to sponsor their stay using short-term training visas or longer-term employment visas that may or may not lead to permanent residency status. In 2009, about 62% of foreign doctoral students remained in the United States on temporary visas 5 years after graduation, down from 67% in 2005 (12). Ph.D. earners from major study-abroad countries, such as India and China, are sometimes caught between binding caps for H-1B temporary employment visas and per-country limits for green cards (13).

Although our research is limited to effects of immigrants on academic knowledge output in the short run (while still enrolled as students), others (14–16) have examined impacts of high-skilled immigrants more broadly on innovation (patents) produced by private industry, wages, employment, and total-factor productivity in U.S. cities and states. These studies support the proposition that high-skilled immigrants contribute to innovation and higher productivity.

Spillover Effects, Field Specifics

The evidence and underlying theories are not conclusive, however. Echoing earlier concerns (8, 9), a recent study found no net productivity gains from the influx of Soviet mathematicians at the end of the Cold War (17). This was due to the displacement of publications that otherwise would have been created by U.S. mathematicians. This highlights the possibility that net benefits of immigration may vary greatly by context and field. Field-specific effects have not been carefully explored in the literature and are an important topic for further research. Other papers study all STEM fields (Science, Technology, Engineering, and Mathematics) in aggregate, and either do not find similar displacement effects (11, 15), or find positive spillover effects on native skilled wages (16).

The benefits from skilled immigration, net of displacement, may depend on whether the field of research requires close interaction between members of scientific teams. Our study found limited evidence that increased diversity is one channel through which increased foreign student presence benefits innovation. Other studies indicate that teamwork has become increasingly important for research (18, 19). The talent of coauthors and Ph.D. mentors has been found to have effects on research productiv-

ity (20, 21); colocation has been shown not to impact productivity (22).

In line with the belief that foreign-born doctoral recipients in S&E who quickly gain residency status might contribute to U.S. innovation and economic growth (23), there are proposals to emulate Germany and other nations by offering permanent residency to doctoral graduates in accredited STEM programs (24, 25). The U.S. Senate bill (25), passed in June, would exempt foreign applicants with advanced STEM degrees from caps on green cards and the per-country limits. It would also issue additional H-1B visas for international students who recently received an M.A. or higher degree in STEM fields from U.S. universities.

Policy discussions and academic literature (8, 9) have pointed to potential adverse effects on U.S. citizens who may find it more difficult to find high-technology jobs or whose wages may be undermined by immigration. There are more than 2 million S&E research and development (R&D) workers in the U.S. private sector (26), and roughly 10,000 STEM doctorates are awarded each year in the United States to temporary visa holders. A policy of facilitating permanent residency for doctoral graduates who wish to stay is unlikely to have significant wage and employment effects on most U.S. R&D workers. However, there may be noticeable effects on certain disciplines.

Another option, given concerns about threats to U.S. citizens' job access and wages, would be to provide an entrepreneurship-based path to immigration. S&E graduates who have ideas for marketable products based on their research should be encouraged to launch entrepreneurial ventures in the United States, to support job creation, rather than risk job displacement.

At present, there are well-established paths to permanent residency through sponsorship by an employer or a family member and for investors with capital, but no large-scale program to attract entrepreneurs. This should be fixed, with safeguards to prevent abuse. Entrepreneurship visas could be based on verifiable signals of the market value and practical relevance of the new ideas, including patents that have achieved some commercialization milestones or products that have received venture capital financing. Canada recently designed a "Start-up Visa Program" to fast-track permanent residency for immigrant entrepreneurs, with a goal of attracting STEM graduates from leading U.S. universities (27). The U.S. Senate bill would establish such entrepreneurship-based visas (25).

Based on our reading of existing evidence, we think that a combination of immigration

reforms to encourage more talented foreign students to study at U.S. universities, as well as for science and engineering Ph.D. graduates to remain in the United States to work or to start entrepreneurial ventures, would help revitalize innovation and economic growth. This also appears to be the consensus view among an expert panel of economists (28), who often disagree on policy issues otherwise.

References and Notes

1. C. Grimes, E. Alden, *Financial Times*, 16 May 2004.
2. G. Brumfiel, *Nature* **431**, 231 (2004).
3. National Academies of Science, *Policy Implications of International Graduate Students and Postdoctoral Scholars in the United States* (National Academy Press, Washington, DC, 2005).
4. K. Fischer, *Chronicle of Higher Education*, 8 April 2013.
5. Task Force on the Future of American Innovation, "The knowledge economy: Is the United States losing its competitive edge?" 16 February 2005; www.ipadvocate.org/mision/pdfs/Knowledge%20Economy.pdf.
6. "Germany eases post-study work and immigration legislation for foreign students," *ICEF Monitor*, 7 May 2012; <http://monitor.icef.com/2012/05/germany-eases-post-study-work-and-immigration-legislation-for-foreign-students>.
7. L. A. Nelson, *Inside Higher Ed*, 30 January 2013; www.insidehighered.com/news/2013/01/30/obamas-immigration-plan-would-expand-stem-visas-fund-science-education-offer-path.
8. G. Borjas, in *Science and the University*, P. Stephan and G. Ehrenberg, Eds. (Univ. of Wisconsin Press, Madison, WI, 2007), pp. 134–149.
9. G. Borjas, in *Science and Engineering Careers in the United States*, R. Freeman and D. Goroff, Eds. (Univ. of Chicago Press, Chicago, 2009), pp. 131–161.
10. G. Ottaviano, G. Peri, *J. Eur. Econ. Assoc.* **10**, 152 (2012).
11. E. Stuenkel, *Econ. J.* **122**, 1143 (2012).
12. M. Finn, Oak Ridge Institute for Science and Education Programs, 2012; <http://orise.orau.gov/files/sep/stay-rates-foreign-doctorate-recipients-2009.pdf>
13. H. Shen, *Nature* **499**, 17 (2013).
14. J. Hunt, M. Gauthier-Loiselle, *Am. Econ. J.: Macroecon.* **2**, 31 (2010).
15. W. Kerr, W. Lincoln, *J. Labor Econ.* **28**, 473 (2010).
16. G. Peri, K. Shih, C. Sparber, "STEM workers, H1B visas and productivity in U.S. cities" (Norface Discussion paper 2013009, University College London, 2013).
17. G. Borjas, K. Doran, *Q. J. Econ.* **127**, 1143 (2012).
18. S. Wuchty et al., *Science* **316**, 1036 (2007).
19. J. Adams, G. Black, J. Clemmons, P. Stephan, *Res. Policy* **34**, 259 (2005).
20. P. Azoulay et al., *Q. J. Econ.* **125**, 549 (2010).
21. F. Waldinger, *J. Polit. Econ.* **118**, 787 (2010).
22. F. Waldinger, *Rev. Econ. Stud.* **79**, 838 (2012).
23. G. Peri, *Wall Street Journal*, 12 February 2013.
24. U.S. House of Representatives, Judicial Committee, Fact Sheet: the STEM Jobs Act (H.R. 6429), 2012.
25. U.S. Senate, Border Security, Economic Opportunity, and Immigration Modernization Act (S. 744), 2013.
26. National Science Foundation/National Center for Science and Engineering Statistics, Scientists and Engineers Statistical Data System (SESTAT) 2008; www.nsf.gov/statistics/sestat/.
27. B. Bouw, *The Globe and Mail*, 1 April 2013.
28. I. G. M. Chicago Booth, Forum, High-Skilled Immigrants; www.igmchicago.org/igm-economic-experts-panel/poll-results?SurveyID=SV_0JtSLKwzqN5fRAf

Acknowledgments: This research was supported by NSF SciStP Grant SBE 0738036.

10.1126/science.1239572

GENETICS

Our Fallen Genomes

Evan Z. Macosko^{1,2} and Steven A. McCarroll^{1,2}

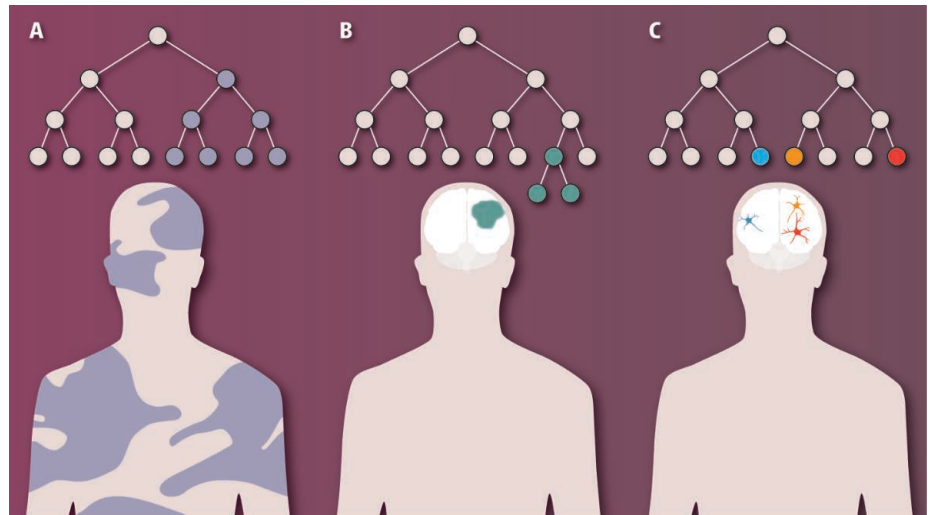
Few human conceits are as relentlessly undermined by science as humans' naïve assumptions about our own perfection. Charles Darwin abolished one such set of assumptions by showing that "inferior creations" are man's evolutionary cousins. However, Darwin's theory of evolution ultimately abetted a modern conceit—that the genomes in our cells are highly optimized end products of evolution. Genome sequencing is now challenging this view on many levels. On page 632 of this issue, McConnell *et al.* show that somatic mutations are abundant in neurons in the human brain (1).

It is often assumed that genome sequencing will explain disease cases by revealing the causative genetic blemish—the mutation that stands out on a background of otherwise flawless molecular function. But whole-genome analysis shows that dysfunction abounds. Rare and common structural variants, including deletions of long genomic segments, pervade every genome (2). Each human genome also harbors an average of 120 gene-inactivating variants, with about 20 of these genes being inactivated in both copies (3). Far from pinpointing single mutations on a background of perfect function, genome sequencing has instead generated its own needle-in-a-haystack problem: distinguishing the variants that truly matter to an illness from the far-larger number of functional variants that are present in every genome. It is now clear that, beyond simple, monogenic disorders, understanding complex disease will require sequencing thousands of genomes and ascertaining the patterns shared among the genomes of many affected individuals (4).

Many studies are now also finding that genomes are themselves transmitted to individual cells with large apparent mistakes—somatically acquired deletions, duplications, and other mutations. These results have been most clear for disorders involving cellular proliferation, which allows clonal expansion of a mutated genome. The blood of many individuals becomes increasingly clonal with age, and these expanded clones often contain large deletions and duplications; this clonality is a risk factor for developing cancer later

¹Department of Genetics, Harvard Medical School, Boston, MA 02115, USA. ²Stanley Center for Psychiatric Research, Broad Institute of MIT and Harvard, Cambridge, MA 02141, USA. E-mail: mccarroll@genetics.med.harvard.edu (S.A.M.)

A human brain can cope with many genomic variations scattered among its neurons.



Transmitting genomes. Deletions, duplications, and other mutations may arise at different places in a developmental lineage. (A) Mutations that arise early in development may cause large-scale somatic mosaicism in the body. (B) Mutations that cause cells to proliferate may lead to detectable somatic mosaicism, even if they arise later in development. (C) Mutations that arise late in development may be unique events in individual cells.

in life (5, 6). Disorders involving hypertrophy and proliferation can also arise from somatic mutations that activate cell-growth pathways (7–9) (see the figure), such as a brain overgrowth syndrome arising from somatic gain-of-function mutations in the *AKT3* gene.

What about apparently normal cells in healthy adults? Such cells may be more likely to harbor large, somatically acquired copy-number variations (CNVs) than is generally thought. For example, 30% of skin fibroblast cells may have somatic CNVs in their genomes (10). In brain, in situ experiments have suggested that large-scale copy-number changes exist in individual cells (11, 12).

McConnell *et al.* have used single-cell genomic analyses to deal another blow to humans' tendency to draw idealized models about how our biology works. The authors first explored genomic variations in individual neurons derived from human induced pluripotent stem cells (hiPSCs). The amplified genomes of individual cells were hybridized to single-nucleotide polymorphism arrays, revealing several CNVs. All 17 of the genomic changes observed were "singletons"—none were present in multiple neurons from the same hiPSC line.

McConnell *et al.* then looked at postmortem brain tissue from the frontal cortex, a

region that has been examined for aneuploidy and other forms of somatic genetic variation (11, 12). They sequenced the genomes of 110 individual neurons from three different brains, revealing somatic CNVs in almost half of the neurons. These deletions and duplications ranged from about 3 Mb to an entire chromosome in size. A small subset of the neurons—approximately 15%—accounted for 73% of the identified CNVs.

As with the CNVs observed in reprogrammed neurons, the CNVs observed in brain-resident neurons were singletons—none appeared to represent an early developmental event. It is possible that in other individuals, such mutations arise earlier in the developmental lineage and become present in a substantial fraction of cells. Such mutations could be part of the genetic architecture underlying intellectual disability, developmental delay, and the more severe, syndromic forms of autism—although somatic mutations seem less likely to explain substantial fractions of highly heritable disorders such as schizophrenia and bipolar disorder.

The observations of McConnell *et al.* may relate to other recent discoveries about how mitotic cells replicate their genomes. Cells replicate the transcriptionally active parts of their genomes in careful, structured,

CREDIT: C. BICKEL/SCIENCE

deliberate ways, then hurry through the replication of transcriptionally silent chromatin (13). Replication errors, including both point mutations and larger CNVs, tend to be concentrated in this late-replicating DNA (14). One implication is that cells are most careless about replicating the parts of their genomes that they are not using. An important direction will therefore be to ascertain the extent to which somatic CNVs affect genes that neurons use, and how these mutations influence the cells' physiological properties.

The brain may be an organ particularly able to cope with scattered genomic eccentricities at the single-cell level. Developmental processes in the brain generate an overabundance of connections, then prune syn-

apses that do not contribute to functional circuitry. Dysfunctional neurons may be given minimized roles in mature circuitry; it is even conceivable that eccentric neurons are creatively incorporated. Although the somatic mutations observed in individual neurons may undermine our sense that neurons should be the most flawless of human cells, we should remember that the great accomplishments of human cognition are in the emergent properties of billions of cells working and rewiring in dynamic ways.

We are often advised “not to let the perfect be the enemy of the good”—to accept a flawed product, in the name of finishing and getting on to the next task. It seems that this is a practice that nature adopted long ago.

References

1. M. J. McConnell *et al.*, *Science* **342**, 632 (2013).
2. R. E. Handsaker, J. M. Korn, J. Nemes, S. A. McCarroll, *Nat. Genet.* **43**, 269 (2011).
3. D. G. MacArthur *et al.*, *Science* **335**, 823 (2012).
4. A. Kiezun *et al.*, *Nat. Genet.* **44**, 623 (2012).
5. C. C. Laurie *et al.*, *Nat. Genet.* **44**, 642 (2012).
6. K. B. Jacobs *et al.*, *Nat. Genet.* **44**, 651 (2012).
7. J. G. Gleeson *et al.*, *Am. J. Hum. Genet.* **67**, 574 (2000).
8. K. C. Kurek *et al.*, *Am. J. Hum. Genet.* **90**, 1108 (2012).
9. A. Poduri *et al.*, *Neuron* **74**, 41 (2012).
10. A. Abyzov *et al.*, *Nature* **492**, 438 (2012).
11. Y. B. Yurov *et al.*, *PLOS ONE* **2**, e558 (2007).
12. S. K. Rehen *et al.*, *J. Neurosci.* **25**, 2176 (2005).
13. A. Koren, S. A. McCarroll, *Genome Res.* 10.1101/gr.161828.113 (2013).
14. A. Koren *et al.*, *Am. J. Hum. Genet.* **91**, 1033 (2012).

10.1126/science.1246942

ECOLOGY

Dust Unto Dust

Mary C. Scholes¹ and Robert J. Scholes²

In the past, great civilizations have fallen because they failed to prevent the degradation of the soils on which they were founded (1). The modern world could suffer the same fate at a global scale. The inherent productivity of many lands has been dramatically reduced as a result of soil erosion, accumulation of salinity, and nutrient depletion. In Africa, where much of the future growth in agriculture must take place, erosion has reduced yields by 8% at continental scale (2), and nutrient depletion is widespread (3). Although improved technology—including the unsustainably high use of fertilizers, irrigation, and plowing—provides a false sense of security, about 1% of global land area is degraded every year (4). As Fierer *et al.* show on page 621 of this issue, the diversity of soil biota in the prairie soils of the American Midwest has changed substantially since cultivation (5). We have forgotten the lesson of the Dust Bowl: Even in advanced economies, human well-being depends on looking after the soil (6). An intact, self-restoring soil ecosystem is essential, especially in times of climate stress.

Soil fertility—the capacity to sustain abundant plant production—was a mystery to the ancients. Traditional farmers speak of soils becoming tired, sick, or cold; the solution

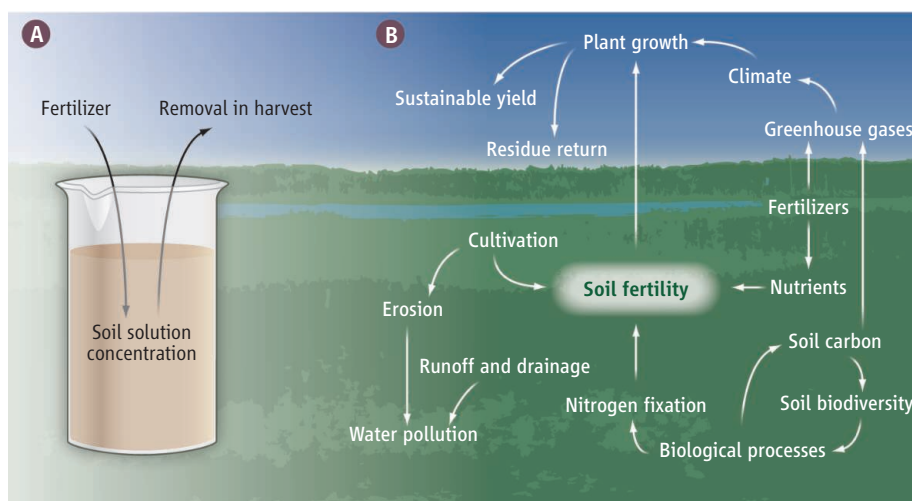
was typically to move on until they recovered. Enlightenment science brought the insight that plant growth combined carbon dioxide from the air with water and nutrients from the soil. By the mid-20th century, soils and plants could be routinely tested to diagnose deficiencies, and a global agrochemical industry set out to fix them (7). Soil came to be viewed as little more than an inert supportive matrix, to be flooded with a soup of nutrients.

This narrow approach led to an unprecedented increase in food production, but also contributed to global warming and pollution of aquifers, rivers, lakes, and coastal ecosystems. Activities associated with agriculture

Modern agriculture diminishes the diversity of soil biota, thereby reducing long-term soil fertility.

are currently responsible for just under one-third of greenhouse gas emissions; more than half of these originate from the soil (8). The eroded sediments and excess nutrients drain into rivers. Diminishing freshwater quality is a constraint on human development in many places, and freshwater biodiversity is the most threatened on the planet (9). Replacing the fertility-sustaining processes in the soil with a dependence on external inputs has made the soil ecosystem, and humans, vulnerable to interruptions in the supply of those inputs, for instance due to price shocks.

The key to understanding the behavior of life-supporting elements such as car-



Soil complexity. Soil fertility management still largely follows a simplistic chemical model (A). Sustainable agriculture requires a more complex view that includes soil biodiversity (B), as shown by Fierer *et al.*

¹School of Animal, Plant & Environmental Science, University of the Witwatersrand, Johannesburg 2000, South Africa. ²Council for Scientific and Industrial Research, Pretoria 0001, South Africa. E-mail: mary.scholes@wits.ac.za (M.C.S.); bscholes@csir.co.za (R.J.S.)

bon, nitrogen, and phosphorus lies not in the absolute amounts present, but in the fluxes between their various forms in the environment, modulated by biology. Microbiological and genetic analysis has shown that there is more genetic variability in a healthy soil than in all of the plants and animals it supports. The variety of ways in which soil constituents can be processed and transformed by a diverse soil microbial community provides an energy-efficient, nonleaky, self-regulating system that can adapt to changing environments (10).

Fierer *et al.* provide an example of this more ecological approach to understanding the functioning of soils. They find that soil microbial taxonomic diversity is strongly correlated with independently measured functional diversity, which suggests that high diversity is useful rather than redundant. In particular, the Verrucomicrobia, bacteria specialized for low-nutrient conditions, are lost from the cultivated soils, making the soils less able to supply nutrients other than those provided as fertilizer.

Including biology in the concept of soil fertility has been an important advance, but a further conceptual broadening is needed to manage soils in a sustainable way. In the modern world, no soil is unaffected by human actions, and the arable soils on which we depend for food are dominated by them.

The fertility attributes of a soil cannot be separated from the purpose for which the land is used, nor from the unintended consequences of this usage. Thus, soil fertility is an emergent property of the soil-plant-human system, replete with the interactions, limits, and surprises that characterize complex systems (see the figure).

The challenge is to build and sustain high soil fertility in a world with rising direct and environmental costs of fossil energy and declining external supplies of critical nutrients, such as phosphates (11). Restoring soil biological processes is the key to achieving lasting food and environmental security. Ensuring that the biological system is resilient under an uncertain future requires that soil biological diversity be restored as well. Rebuilding soil organic matter is both an indicator of success in this endeavor and a way to reduce the carbon load in the atmosphere (12). However, it is not possible to feed the current and future world population with a dogmatically “organic” approach to global agriculture (13), nor would such an approach avert climate change, spare biodiversity, or purify the rivers, given the large additional area it would require. An agricultural soil ecosystem that more closely approximates the close and efficient cycling in natural ecosystems, and that also benefits from the yield increases made possible

by biotechnology and inorganic fertilizers, is needed to increase agricultural production to the levels that will be required while minimizing its adverse effects. Integration of the insights, innovation, and best practice from agronomy, ecology, soil biology, chemistry, physics, plant breeding, and natural resource governance is the only viable route to both feeding the world and keeping it habitable.

References

1. J. M. Diamond, *Collapse: How Societies Choose to Fail or Succeed* (Penguin, New York, 2005).
2. R. Lal, *Soil Sci. Soc. Am. J.* **59**, 661 (1995).
3. P. A. Sanchez, *Science* **295**, 2019 (2002).
4. Food and Agriculture Organization of the United Nations, *The State of Food and Agriculture 2010–11*; www.fao.org/publications/sofa.
5. N. Fierer *et al.*, *Science* **342**, 621 (2013).
6. T. Egan, *The Worst Hard Time: The Untold Story of Those Who Survived the Great American Dust Bowl* (Mariner, New York, 2006).
7. V. Smil, *Enriching the Earth: Fritz Haber, Carl Bosch, and the Transformation of World Food Production* (MIT Press, Cambridge, MA, 2004).
8. P. Smith *et al.*, *Global Change Biol.* **19**, 2285 (2013).
9. E. Bennett, S. Carpenter, N. F. Caraco, *Bioscience* **51**, 227 (2001).
10. K. E. Giller, M. H. Beare, P. Lavelle, A. Izac, M. J. Swift, *Appl. Soil Ecol.* **6**, 3 (1997).
11. P. Déry, B. Anderson, *Energy Bull.* (13 August 2007); www.energybulletin.net/node/33164.
12. M. W. I. Schmidt *et al.*, *Nature* **478**, 49 (2011).
13. D. J. Connor, *Field Crops Res.* **106**, 187 (2008).

10.1126/science.1244579

PLANT SCIENCE

A Pathway to Flowering—Why Staying Cool Matters

Ove Nilsson

Temperature is one of the most important cues that plants use to flower at the right time of the year—a process crucial for adaptation and reproductive success. We live in a world where climate change is already affecting our everyday lives and where, in the not too distant future, we will likely face huge challenges associated with increasing global temperatures (1). One of these challenges is to understand how flowering and growth of agricultural crops and trees will be affected by changing temperatures. The report by Lee *et al.* on

page 628 of this issue (2), together with a recently published paper by Posé *et al.* (3), provide insight into the basic mechanisms controlling temperature regulation of plant growth and development.

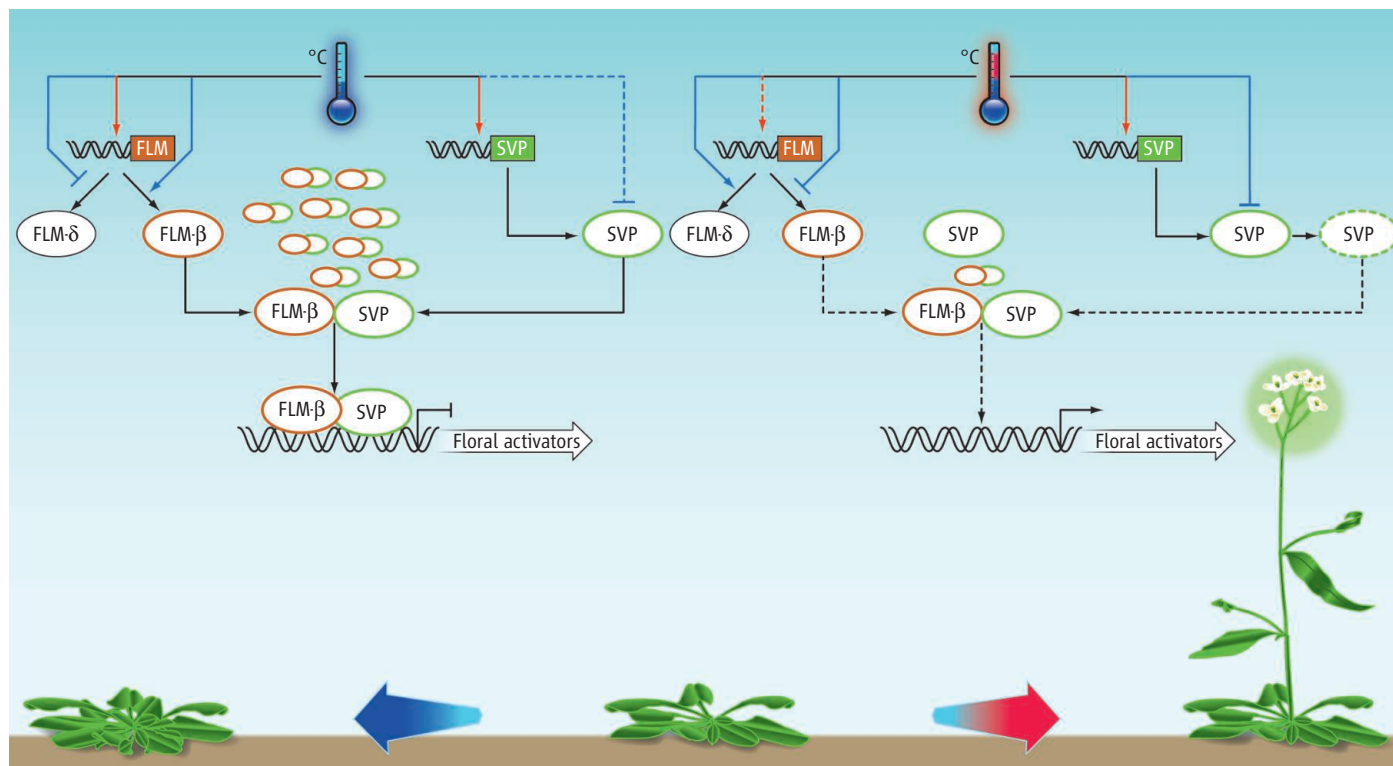
In terms of regulation of flowering, plants can respond to temperature in two different ways. Many plants, including several important crop species, require an extended period of cold during winter before they can respond to the increasing temperatures and day lengths during spring that will trigger flowering. This process, called vernalization, is a way for the plant to tell during which part of the year it is growing, and ensures that the plant does not flower prematurely. The molecular genetics underlying this reg-

Plants time flowering through temperature-sensing mechanisms involving differential RNA abundance, alternative splicing, and protein stability.

ulation has been studied extensively in the model plant *Arabidopsis thaliana*, which has natural variants (accessions) that do or do not show vernalization. Through such variants, we have acquired a detailed knowledge about how this process is controlled (4).

Summer annual *Arabidopsis* accessions that flower rapidly without the need of vernalization can, if grown at 27°C, flower a couple of weeks after germination. But if the same plants are instead grown in cooler conditions (16°C), flowering occurs significantly later (5). This is not simply an effect of slower growth rates or lowered metabolic activity because several genes have been identified that, when mutated, make the plants less temperature-responsive, resulting in the mutants

Umeå Plant Science Centre, Swedish University of Agricultural Sciences, Umeå 90183, Sweden. E-mail: ove.nilsson@slu.se



Arabidopsis flowering time and ambient temperature. Under colder conditions (left), SVP–FLM-β accumulates and represses transcription of floral activators. In warmer conditions (right), the concentration of SVP–FLM-β decreases, floral activators are induced and flowering occurs. Arrows and black lines denote activation and repression, respectively. Red lines depict regulation of transcriptional activity. Light blue lines depict posttranscriptional regulation of splicing (*FLM*) and protein stability (*SVP*).

flowering as early or earlier at 16°C as the wild-type plants at 27°C (5). The behavior of these mutants suggests that an active repression of flowering is taking place at lower temperatures. Two of the genes involved, *FLOWERING LOCUS M* (*FLM*) and *SHORT VEGETATIVE PHASE* (*SVP*), are central to repression of flowering in the cold (5, 6). Both genes encode transcription factors (7–9), and natural variations in both genes have been associated with different flowering times of different *Arabidopsis* accessions (10, 11). However, the exact mechanism for how the regulation of these genes can be coupled to temperature regulation of flowering has remained something of a mystery until now.

The two new studies show that the *FLM* and *SVP* proteins act in the same complex to repress flowering, providing an explanation for their genetic interaction. The research also confirms that the *FLM*–*SVP* complex can bind to the promoters of floral activator genes to repress their transcription (2,

3). They also reveal how temperature regulation is achieved. Both studies show that although overall transcription of *FLM* is reduced at higher temperatures, the most dramatic down-regulation occurs for the highly abundant splice variant encoding the active form of the repressor, *FLM*-β (2, 3), consistent with results showing that splicing of the *FLM* transcript is differentially regulated by temperature (6).

Although genetic data have also implicated *SVP* in the temperature regulation of flowering (5), the floral repressor counter-intuitively shows higher levels of transcription at warmer temperatures, when flowering occurs (2, 3, 5). Lee *et al.* provide a resolution to this apparent conundrum by showing that the stability of the *SVP* protein decreases at warmer temperatures (2). Together, these two mechanisms lead to decreased levels of *SVP*–*FLM* repressor complexes at higher temperatures, and therefore to earlier flowering.

Posé *et al.* suggest that there may be yet another layer of thermoregulation in flowering. They show that the other major translated splice variant of *FLM*, called *FLM*-δ, can also bind to *SVP*. However, this *SVP*–*FLM*-δ complex is inactive, as it cannot bind DNA; *FLM*-δ acts as a dominant negative form of the protein (3). Because warmer temperatures lead to higher levels of the *FLM*-δ splice variant, it might contribute to earlier flowering through a further reduction in active *SVP*–*FLM*-β repressor complexes (3).

It will be critical to determine how the regulation of these genes occurs under natural field conditions and to understand how relevant this pathway is for other (more commercially important) species of plants: Perhaps these genes also affect other plant developmental processes that are controlled by temperature. Understanding how plants respond to temperature will enable improved modeling of the effects of climate change on plant growth and development and will also provide new tools for a targeted breeding of new crop and tree varieties better adapted to these changes in temperature.

References

1. Intergovernmental Panel on Climate Change, Working Group 1. Contribution to the IPCC Fifth Assessment Report (WG1 AR5) (2013).
2. J. H. Lee *et al.*, *Science* **342**, 628 (2013); 10.1126/science.1241097.
3. D. Posé *et al.*, *Nature* 10.1038/nature12633 (2013).
4. J. Song, A. Angel, M. Howard, C. Dean, *J. Cell Sci.* **125**, 3723 (2012).
5. J. H. Lee *et al.*, *Genes Dev.* **21**, 397 (2007).
6. S. Balasubramanian, S. Sureshkumar, J. Lempe, D. Weigel, *PLOS Genet.* **2**, e106 (2006).
7. K. C. Scortecci, S. D. Michaels, R. M. Amasino, *Plant J.* **26**, 229 (2001).
8. O. J. Ratcliffe, G. C. Nadzan, T. L. Reuber, J. L. Riechmann, *Plant Physiol.* **126**, 122 (2001).
9. U. Hartmann *et al.*, *Plant J.* **21**, 351 (2000).
10. J. D. Werner *et al.*, *Proc. Natl. Acad. Sci. U.S.A.* **102**, 2460 (2005).
11. B. Méndez-Vigo, J. M. Martínez-Zapater, C. Alonso-Blanco, *PLOS Genet.* **9**, e1003289 (2013).

10.1126/science.1245861

APPLIED PHYSICS

Storing Quantum Information in Schrödinger's Cats

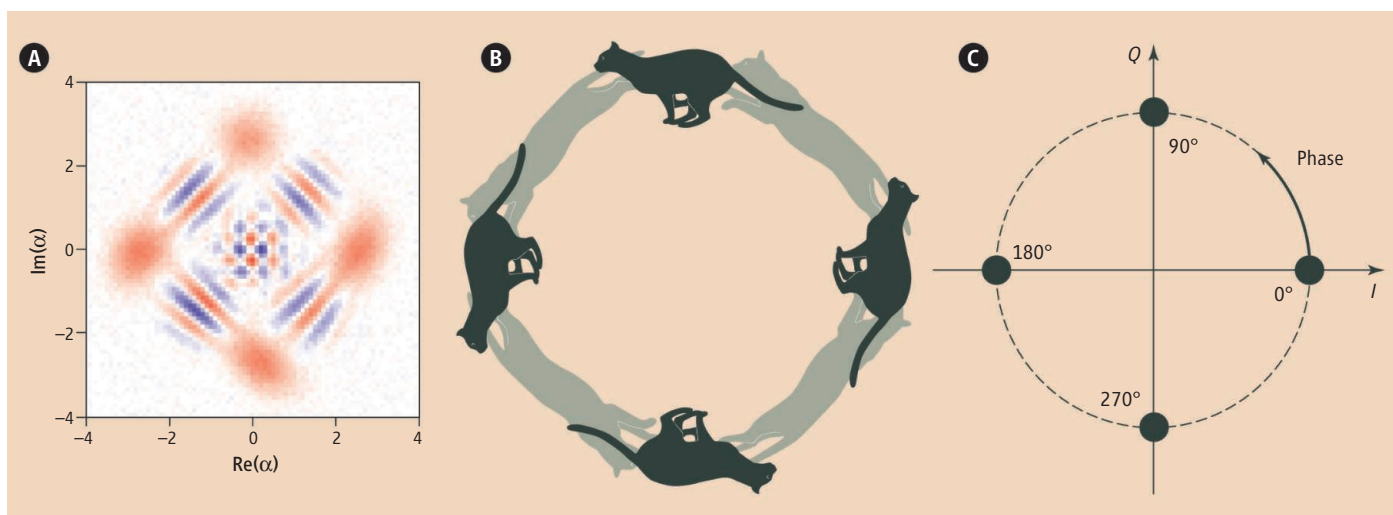
Peter J. Leek

When Schrödinger came up with his thought experiment connecting the fate of a cat in a box to the quantum-mechanical process of radioactive decay (1), he probably did not consider that the idea might one day be used in technology. However, the transfer of the state of a superconducting quantum bit (qubit) to a 100-photon light state to map and store the

we experience is something that has been a puzzle ever since the early days of quantum theory. Researchers are increasingly able to create and control quantum states of larger, more complex objects than individual atoms and bridge this quantum-to-classical gap step by step, at the same time bringing new technologies like quantum computing ever closer (3).

Superposition states created with more than 100 photons enable the storage of multiple bits of quantum information.

can then live undisturbed for milliseconds or more (7, 8). Recent work by Paik *et al.* has showed that it is possible to realize record lifetime superconducting qubits strongly coupled to microwave photons in a surprisingly simple device in which the qubits are housed inside a three-dimensional (3D) superconducting cavity (6). The setup bears some resemblance to that used in the recent



Four-state Schrödinger cats. (A) A superposition of four coherent light states, measured by Vlastakis *et al.* displays rich features in its Wigner function (plotted as a function of the real and imaginary parts of the superposition state α). The four coherent states appear as red smudges, and the sign of the quantum character of the superposition state is seen in the red-blue interference fringes in

between. This state is related to a superposition of cats at four different positions on a circle (B) and is also closely related to a communications protocol called quadrature phase-shift keying (C), which combines together four signals that differ from each other by a 90° phase shift, shown here as points on the complex plane, where I is the in-phase component and Q is the quadrature component.

contained quantum information, as reported by Vlastakis *et al.* on page 607 of this issue (2), is analogous to this iconic thought experiment. In contrast with the original version, however, the researchers are in complete control of the process and envision its use to store multiple bits of quantum information in a future quantum processor.

Quantum mechanics is typically associated with very small things, like atoms, rather than large everyday objects (like cats), and the contrast between the strange quantum world of superpositions and entanglement and the familiar classical world that

Creating large, complex quantum objects is a substantial challenge, because the fragile states easily lose their coherence (their quantum nature) through interaction with the surrounding environment, unless that environment is exquisitely well controlled. In solid-state systems like superconducting circuits (4), overcoming environmental decoherence has always been a major research challenge. Superconducting qubits are macroscopic in size, and particularly strongly coupled to their electromagnetic environment. Decisive steps forward in the field have been made by “hiding” qubits from the outside world by embedding them inside high-quality resonant cavities (5, 6), in which electromagnetic fields (or photons) can only reside if they have very specific resonant frequencies, and

pioneering experiments with Rydberg atom and microwave photon cavity quantum electrodynamics by Haroche and co-workers (7).

The strong coupling and coherence possible in this new architecture, along with a new protocol for efficiently transferring qubit states to coherent light states (9), have now enabled Vlastakis *et al.* to create Schrödinger cats of an impressive size, consisting of up to 111 microwave photons trapped inside the 3D cavity. Controlled generation of modest-sized cat states has been demonstrated before, using trapped ions (10) and photons (11, 12), and also in superconducting circuits (13), but key to this new work is the efficiency and flexibility of the implemented protocol. It does not grow in complexity with the size of the generated

Department of Physics, Clarendon Laboratory, University of Oxford, Parks Road, Oxford, OX1 3PU, UK. E-mail: peter.leek@physics.ox.ac.uk

cat states and allows generation of states with any chosen amplitude and phase.

The telltale sign of the quantum nature of the created states is seen by measuring a kind of phase diagram for the light, called the Wigner function (see the figure, panel A), which visualizes interference fringes between the superposed states, much like those observed in the classic double-slit experiment. Whereas Schrödinger's original concept involved superpositions of two classical states (a dead and living cat), Vlastakis *et al.* demonstrate cats with up to four different states in superposition (see the figure, panel B). Extended further, this approach could be very useful in a quantum computer; with a coherent enough cavity, superpositions of many more than four states could be stored in it, making it an excellent candidate for a quantum memory.

Interestingly, Vlastakis *et al.* point out that the methods they use are similar to those already in use in communications technol-

ogy, in a scheme known as phase-shift keying (PSK). Here, multiple bits of information on communications channels are stored by the same frequency carrier wave, but at different phases (two or four are typically used; see the figure, panel C) to increase data rates. In much the same way, quantum PSK could be useful in future quantum technology for efficient storage and communication of quantum data.

The Schrödinger cat states may be useful not only in quantum memories but also in quantum metrology because of the interference patterns present in the phase space representation of the states (2, 14). Imagine measuring a point near the center of the diagram of the cat state shown in panel A of the figure. Just a small shift or rotation of the picture would give a large change in the measurement at that point (for example, a shift from a red to a blue spot). Such sensitive measurements are impossible with a classical state, in which these interference fringes

are simply not present. This example illustrates a key point of much of quantum information research, that coherent quantum systems often display behavior that has no classical counterpart and that may be exploited to realize transformative new technologies.

References

1. E. Schrödinger, *Naturwissenschaften* **23**, 807 (1935).
2. B. Vlastakis *et al.*, *Science* **342**, 607 (2013); 10.1126/science.1243289
3. Special Issue on Quantum Information Processing, *Science* **339**, 1163 (2013).
4. M. H. Devoret, R. J. Schoelkopf, *Science* **339**, 1169 (2013).
5. A. Wallraff *et al.*, *Nature* **431**, 162 (2004).
6. H. Paik *et al.*, *Phys. Rev. Lett.* **107**, 240501 (2011).
7. S. Gleyzes *et al.*, *Nature* **446**, 297 (2007).
8. M. Reagor *et al.*, *Appl. Phys. Lett.* **102**, 192604 (2013).
9. Z. Leghtas *et al.*, *Phys. Rev. A* **87**, 042315 (2013).
10. D. Leibfried *et al.*, *Nature* **438**, 639 (2005).
11. A. Ourjoumtsev, H. Jeong, R. Tualle-Broui, P. Grangier, *Nature* **448**, 784 (2007).
12. S. Deléglise *et al.*, *Nature* **455**, 510 (2008).
13. M. Hofheinz *et al.*, *Nature* **459**, 546 (2009).
14. W. H. Zurek, *Nature* **412**, 712 (2001).

10.1126/science.1245510

PHYSICS

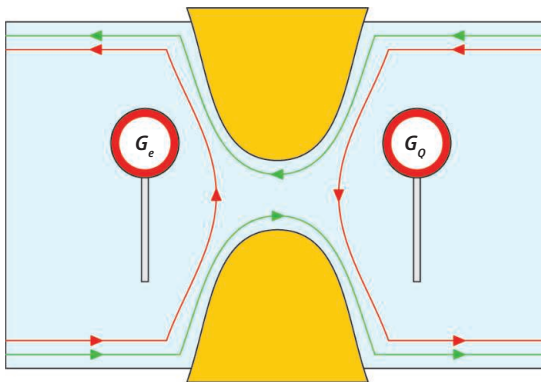
Quantized Electronic Heat Flow

Björn Sothmann and Christian Flindt

Traffic laws impose strict limits on the maximum speed of cars on a highway. In nanoscale electronics, the laws of quantum physics similarly set an upper limit to the electrical conductance of a conductor. This was first demonstrated three decades ago (1, 2) on a quantum point contact—a narrow constriction connecting two electronic reservoirs. A similar prediction has been made for the maximal heat conductance of an electronic conductor (3, 4), but an experimental verification has so far been missing. On page 601 of this issue, Jezouin *et al.* (5) measure the quantum-limited electronic heat flow in a quantum point contact, paving the way for novel heat-control technologies at the nanoscale.

In quantum electronics, electrons behave as waves. They may be spread out over a spatial region, and they may interfere with themselves, as well as with other electrons. Quantum electronics is typically implemented in two-dimensional electron gases captured at the interface between semiconducting materials. With a magnetic field

applied, the electrons in the gas move along the boundaries of the sample in directional edge states, which function as electronic



Speed limits on the highway. Quantum physics predicts an upper limit to the electrical conductance (G_e), as well as the heat conductance (G_0) of a single quantum channel. For electrons, the quantum-limited electrical conductance was measured nearly 30 years ago (1, 2). Now, Jezouin *et al.* have measured the quantum-limited heat conductance in a quantum point contact—the narrow constriction connecting two electronic reservoirs. Edge states running along the boundaries of the sample function as the lanes on an electronic highway. The number of edge states going through the quantum point contact can be controlled. Here, only the edge states in green pass through the quantum point contact, allowing Jezouin *et al.* to measure the maximal heat conduction of a single electronic conduction channel.

A measurement of the quantum-limited heat flow in an electronic conductor opens a pathway to the nanoscale control of heat currents.

highways (6). The number of one-way lanes (or edge states) on the highway can be controlled with an external gate voltage. Each edge state is a conduction channel that can guide a stream of electrons toward a quantum point contact. The width of the quantum point contact can be adjusted to control the number of channels passing through it. Quantum point contacts constitute one of the fundamental building blocks in quantum electronics.

A hallmark prediction in the field of mesoscopic physics is the quantization of the electrical conductance of a quantum point contact. The conductance quantifies the current that runs in a conductor in response to a small voltage applied across it. Each fully open conduction channel in a quantum point contact contributes to the total conductance with one conduction quantum whose value is determined by fundamental constants only (7). Specifically, the electronic conduction quantum is simply the square of the electronic

Département de Physique Théorique, Université de Genève, 24 quai Ernest Ansermet, CH-1211 Genève 4, Switzerland. E-mail: bjorn.sothmann@unige.ch (B.S.)

charge e divided by Planck's constant h , or $G_e = e^2/h$. This effect was demonstrated experimentally nearly 30 years ago (1, 2).

The electrons in a quantum channel do not only carry electrical charge, but may also transport energy, or heat, along it. Similarly to the electrical conductance, one may ask how a quantum point contact reacts to a temperature difference across it. The heat conductance quantifies the heat current that runs in a conductor in response to a small temperature gradient. It has been predicted that each conduction channel should contribute to the total heat conductance with one quantum of heat conduction $G_Q = \pi^2 k_B^2 T / (3h)$, where T is the temperature and k_B is the Boltzmann constant (3, 4). This prediction is expected to hold for any kind of particles. For the one class of particles called bosons, the prediction has been experimentally verified both for photons (particles of light) (8, 9) and phonons (quantized lattice vibrations) (10, 11). In contrast, for the class of particles known as fermions (e.g., electrons), this fundamental limit on the heat conductance had so far not been confirmed experimentally.

Jezouin *et al.* assembled a setup consisting of a micrometer-sized metallic plate connected to two external electrodes by quantum point contacts, enabling exchange of heat between the metal plate and the electrodes (5). To observe the quantum-limited heat flow, the temperature must be as low as possible to suppress other heat transport

mechanisms. They cooled their sample to 20 mK, and detected the noise of the outgoing electrical current, which provides an accurate measure of the plate temperature (12, 13).

The experiment by Jezouin *et al.* is based on a balance of heat flows. A controlled amount of heat (Joule power) is injected into the metal plate through one of the quantum point contacts. Once the metal plate has reached a steady temperature, the amount of injected heat must equal the output heat leaving the plate, including the heat that escapes via the quantum point contacts. Importantly, the number of channels in each quantum point contact that carry heat away from the metal plate can be controlled. In particular, when adding just a single outgoing channel, the increased Joule power needed to keep the temperature of the metal plate constant can be monitored. This increase corresponds to the additional heat that is conducted by the extra channel, allowing the heat conducted by a single electronic channel to be inferred and, thus, enabling the value of the heat conduction quantum G_Q to be determined.

With the experiment by Jezouin *et al.*, the quantum limit of heat flow in a conduction channel is now firmly established, for bosons and fermions. To complete the picture, we are left only with the exotic class of particles called anyons, which arise, for instance, in the fractional quantum Hall effect. Apart from these principle questions of quantized heat conduction, the work of Jezouin *et al.*

has important implications for future quantum technologies. The quantum limit of heat flow will be an essential design parameter in the construction of nanoelectronic circuits that need to be refrigerated for optimal performance (14). Additionally, the improved understanding of the quantum physics of heat flow will facilitate further progress in nanoscale energy harvesting based on tiny thermal engines that convert heat to work to power other devices (15). Finally, the intimate connections between heat, entropy and information (3) suggest that a number of other fundamental restrictions on the flows in quantum channels might exist.

References

1. B. van Wees *et al.*, *Phys. Rev. Lett.* **60**, 848 (1988).
2. D. A. Wharam *et al.*, *J. Phys. Chem.* **21**, L209 (1988).
3. J. B. Pendry, *J. Phys. Math. Gen.* **16**, 2161 (1983).
4. L. G. C. Rego, G. Kirczenow, *Phys. Rev. Lett.* **81**, 232 (1998).
5. S. Jezouin *et al.*, *Science* **342**, 601 (2013); 10.1126/science.1241912.
6. M. Büttiker, *Phys. Rev. B* **38**, 9375 (1988).
7. M. Büttiker, *Phys. Rev. B* **41**, 7906 (1990).
8. M. Meschke, W. Guichard, J. P. Pekola, *Nature* **444**, 187 (2006).
9. A. V. Timofeev, M. Helle, M. Meschke, M. Möttönen, J. P. Pekola, *Phys. Rev. Lett.* **102**, 200801 (2009).
10. K. Schwab, E. A. Henriksen, J. M. Worlock, M. L. Roukes, *Nature* **404**, 974 (2000).
11. C. S. Yung, D. R. Schmidt, A. N. Cleland, *Appl. Phys. Lett.* **81**, 31 (2002).
12. M. Büttiker, *Phys. Rev. Lett.* **65**, 2901 (1990).
13. Y. M. Blanter, M. Büttiker, *Phys. Rep.* **336**, 1 (2000).
14. J. R. Prance *et al.*, *Phys. Rev. Lett.* **102**, 146602 (2009).
15. A. N. Jordan, B. Sothmann, R. Sánchez, M. Büttiker, *Phys. Rev. B* **87**, 075312 (2013).

10.1126/science.1246105

PHYSIOLOGY

Rhythmic Respiration

Guillaume Rey and Akhilesh B. Reddy

Mitochondria provide an adequate supply of energy for the myriad processes that keep a cell functioning. These organelles are often thought of as machines that continuously supply energy to the cell in the form of adenosine triphosphate (ATP). However, cellular physiology is not static; rather, the internal milieu of a cell changes according to a ~24-hour (circadian) rhythm that is regulated by a molecular clock. On page 591 of this issue, Peek *et al.* show that circadian rhythms in the

availability of nicotinamide adenine dinucleotide (NAD⁺), a coenzyme crucial for energy conversion in the cell, control oscillations in oxidative metabolism in mammalian mitochondria (1).

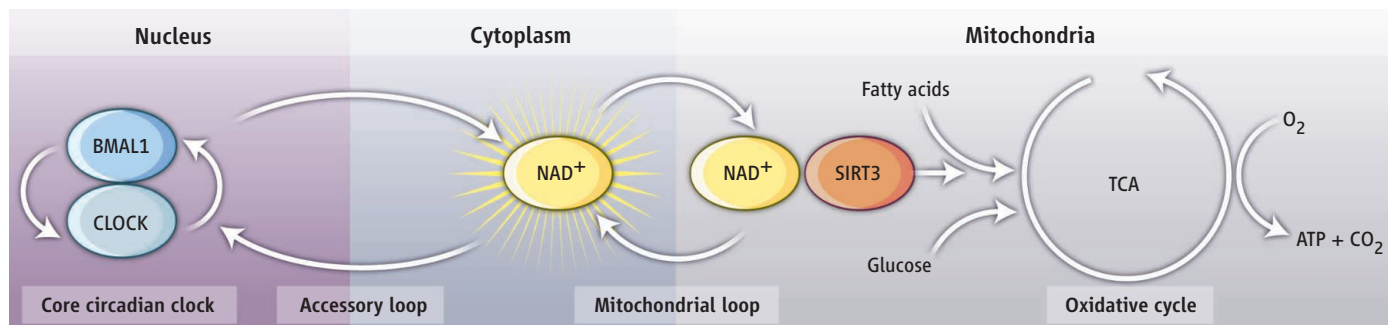
Organisms as diverse as bacteria and humans use circadian clocks to temporally organize their physiology and behavior around the 24-hour day. Such cellular timing mechanisms ensure that activity and feeding cycles resonate with geophysical time and, in this way, guarantee efficient energy homeostasis by appropriately timed energy storage and utilization through the day and night. Disrupting these rhythms is associated with long-term adverse health consequences including metabolic and mental

Cellular respiration is under circadian control.

disorders (2). In mammals, many metabolic processes are under circadian control, but whether oxidative metabolism is similarly regulated has been unclear, even though circadian reduction-oxidation (redox) oscillations are likely to be present in all oxygen-consuming organisms (3). Given the links between oxidative stress and age-related diseases (4), defining the temporal landscape of oxidative metabolism in health and disease is of emerging importance.

The current view of the clockwork is modeled by interlocked transcriptional and translational feedback loops that generate daily rhythms at the genomic scale, extensively using posttranscriptional and posttranslational modifications. In mam-

Department of Clinical Neurosciences, University of Cambridge Metabolic Research Laboratories, NIHR Biomedical Research Centre, Wellcome-MRC Institute of Metabolic Science, University of Cambridge, Addenbrooke's Hospital, Cambridge CB2 0QQ, UK. E-mail: areddy@cantab.net (A.B.R.)



mals, such cell-autonomous oscillators also encompass a cytosolic component consisting of accessory feedback loops that couple the nuclear oscillator to cellular physiology (5). In particular, a cytosolic NAD^+ loop includes the circadian transcriptional factors BMAL1 and CLOCK, which control the expression of nicotinamide phosphoribosyltransferase, the rate-limiting enzyme in NAD^+ synthesis (6, 7). NAD^+ concentrations feed back onto the clockwork through the NAD^+ -dependent deacetylase sirtuin 1 (SIRT1), which regulates several core clock proteins including PER2 and CLOCK (8, 9). Moreover, the NAD^+ /NADH ratio, which reflects the balance in intracellular redox potential (“redox poise”), might also control BMAL1 and CLOCK affinity to DNA (10).

Using fasted mice (to remove the confounding effects of feeding rhythms on metabolism), Peek *et al.* measured the rate of oxidation of fatty acids (one of the mitochondrion’s fuel sources) and NAD^+ concentrations in the liver and found that both reached their maximum levels at the end of the rest phase—“daytime” for the ordinarily nocturnal mouse. This makes physiological sense: There is an anticipatory rise in NAD^+ before the majority of activity and feeding commences. In the absence of *Bmal1*, circadian mutant mice had a substantial decrease in NAD^+ , suggesting that BMAL1 and CLOCK are necessary to maintain sufficient amounts of NAD^+ for fatty acid oxidation to proceed.

Peek *et al.* further found that mitochondria isolated from circadian mutant mice had reduced flux through the tricarboxylic acid (TCA) cycle, the metabolic pathway providing electrons required for ATP production. This was measured with fatty acids and pyruvate (the end-product of glucose breakdown by glycolysis) as input sources for the respiratory reactions of the TCA cycle. The results are consistent with the requirements of both fatty acid β -oxidation and pyruvate decarboxylation for sufficient amounts of NAD^+ to produce ATP. Bypassing the NAD^+ “bottleneck” with intermediary metabo-

lites of the TCA cycle as alternative inputs restored normal oxygen consumption. This was validated in *Bmal1*-deficient mice using nicotinamide mononucleotide, the precursor of NAD^+ , to replenish the NAD^+ pool.

Circadian rhythms in NAD^+ synthesis could conceivably drive redox rhythms by modulating the NAD^+ /NADH ratio and thereby affect metabolic activity in mitochondria. However, Peek *et al.* show that the NAD^+ /NADH poise is not disturbed by the absence of *Bmal1* in cells, and therefore a mechanism for sensing absolute NAD^+ concentrations is more likely to convey information from transcriptional cycles of the core clock to mitochondrial oxidative metabolism. SIRT3, a NAD^+ -dependent deacetylase, seemed a reasonable candidate to relay this signal, given that it regulates mitochondrial fatty acid oxidation through reversible acetylation. Indeed, Peek *et al.* observed an increase in mitochondrial protein acetylation in liver from *Bmal1*-deficient animals relative to the wild type, indicating circadian acetylation of mitochondrial enzymes (11).

The crucial role of NAD^+ in controlling mitochondrial metabolism indicates that so-called “accessory loops” in the cytoplasm might be fundamental parts of the circadian oscillator and also suggests the existence of “mitochondrial loops”—a possible new layer in the architecture of the mammalian circadian oscillator—given the growing evidence that reactive oxygen species and redox balance impinge on the circadian clockwork (12) (see the figure). The striking attenuation of NAD^+ concentrations in the absence of *Bmal1* indicates that BMAL1 and CLOCK not only modulate NAD^+ synthesis in a circadian fashion, but are essential to maintain cellular NAD^+ availability. Such a critical role of circadian transcription factors in basal cytosolic processes points to potential noncircadian functions for BMAL1 and CLOCK in the cell.

How is energy homeostasis maintained throughout the circadian cycle if mitochondrial respiration—and thus most ATP production—is segregated to a specific epoch?

Cell’s got rhythm. Oscillations in the concentration of cytosolic NAD^+ control mitochondrial oxidative metabolism in a circadian fashion. NAD^+ -dependent SIRT3 regulates fatty acid oxidation rate in response to daily variations in NAD^+ and, in this way, generates rhythmic respiration in mammalian cells.

Arranging peak energy consumption around these respiratory rhythms, as occurs in the yeast metabolic oscillator (13), but having enough ATP available at other times, may be the most efficient temporal setup. More generally, the results of Peek *et al.* raise questions about the circadian organization of metabolism and the influence of the circadian clock on mammalian metabolic cycles; the latter are likely to be regulated at the cellular level and not, as previously thought, to be solely a consequence of whole-animal physiology. Understanding how these clock-driven metabolic cycles relate to nontranscriptional circadian redox oscillations (3, 14, 15) will help to delineate the origin and function of metabolic circadian rhythms. An intriguing possibility is that mitochondrial respiratory rhythms, and possibly cycles observed in plastids, could be an ancient mechanism inherited from the endosymbiotic integration of bacterial oscillators into primitive eukaryotic cells.

References

1. C. B. Peek *et al.*, *Science* **342**, 1243417 (2013).
2. A. B. Reddy, J. S. O’Neill, *Trends Cell Biol.* **20**, 36 (2010).
3. R. S. Edgar *et al.*, *Nature* **485**, 459 (2012).
4. M. T. Lin, M. F. Beal, *Nature* **443**, 787 (2006).
5. G. Rey, A. B. Reddy, *Trends Cell Biol.* **23**, 234 (2013).
6. K. M. Ramsey *et al.*, *Science* **324**, 651 (2009).
7. Y. Nakahata, S. Sahar, G. Astarita, M. Kaluzova, P. Sassone-Corsi, *Science* **324**, 654 (2009).
8. G. Asher *et al.*, *Cell* **134**, 317 (2008).
9. Y. Nakahata *et al.*, *Cell* **134**, 329 (2008).
10. J. Rutter, M. Reick, L. C. Wu, S. L. McKnight, *Science* **293**, 510 (2001).
11. S. Masri *et al.*, *Proc. Natl. Acad. Sci. U.S.A.* **10**, 10731/ pnas.1217632110 (2013).
12. A. Stangherlin, A. B. Reddy, *J. Biol. Chem.* **288**, 26505 (2013).
13. B. P. Tu, A. Kudlicki, M. Rowicka, S. L. McKnight, *Science* **310**, 1152 (2005).
14. J. S. O’Neill, A. B. Reddy, *Nature* **469**, 498 (2011).
15. J. S. O’Neill *et al.*, *Nature* **469**, 554 (2011).

10.1126/science.1246658

RETROSPECTIVE

David H. Hubel (1926–2013)

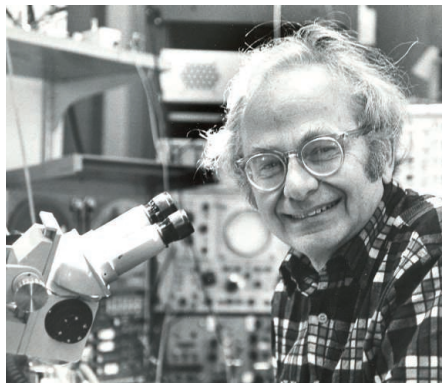
Robert H. Wurtz

On 22 September, David Hunter Hubel died at his home in Lincoln, Massachusetts. He was 87. We have lost one of the great neuroscientists of the 20th century, whose work revealed the beautifully ordered activity of single neurons in the visual cortex and how these neurons might be assembled to ultimately produce vision. We have also lost the most innovative, enthusiastic, and witty person you could ever meet.

Vision begins when an image falls on the retina of the eye. Individual receptors break this image into hundreds of thousands of fragments, which are transmitted to the primary visual area of the cerebral cortex. The task of the cerebral cortex is to reconstruct these fragments so that the brain can “see” the image. In the 1950s, there was little idea of how this reconstruction occurs and if we could not understand how visual input leads to vision, how could we possibly learn how the brain produces such higher functions as attention, learning, and emotion? Beginning in 1958, the landmark experiments of David H. Hubel and Torsten N. Wiesel provided the first insight into how the cerebral cortex converts signals from the eye into visual perception. For this and subsequent experiments, they were awarded the Nobel Prize for Physiology or Medicine in 1981.

When the collaboration with Torsten Wiesel began, they knew basic information about the output of the retina from the work of their mentor and friend, Steve Kuffler. The retinal neurons responded not to full-field illumination but to light or dark spots in one tiny part of the visual field, the neuron’s receptive field. The next question seemed simple: What changes in the receptive fields would they find in cerebral cortex?

When they recorded the electrical activity of neurons in visual cortex of anesthetized cats, they found that only a few neuronal spikes were evoked by spots, and no amount of manipulation improved the response. But the neurons produced a burst of activity as they inserted a slide into the instrument projecting the spots toward the cat’s eye. It was the line produced by the slide edge that excited the neuron. Changing the line’s orientation



changed the neuron’s activity. Different neurons preferred different orientations, and in a sample of neurons, all orientations were represented. The discovery demonstrates what we tend to forget: Tenacity frequently precedes rather than follows serendipity.

Hubel and Wiesel published these results in 1959. With further experiments came their first magnum opus in 1962. Here, they differentiated between classes of visual neurons (simple and complex); found them organized into columns extending through cortex (as established for the somatosensory cortex by Vernon Mountcastle); showed that within a column, neurons preferred similar orientations; and proposed how neurons might be connected to form a progression of steps that could eventually lead to visual perception. They subsequently made a long series of discoveries, including that columns of visual cortex neurons are dominated by either one eye or the other, that the dominance showed plasticity as demonstrated by occlusion of one eye, and that this plasticity peaks at a specific time during development—the critical period. Many of these experiments have opened entirely new fields, a number of which are led by their former students. The work also laid the foundation for exploring higher visual and higher brain functions at the level of single neurons. The collaboration between Hubel and Wiesel flourished for 25 years, and is summarized in their 2005 book, *Brain and Visual Perception*.

David Hunter Hubel was born in 1926 in Windsor, Ontario, and grew up in Montreal, Quebec. As an undergraduate at McGill University, he majored in the honors program in mathematics and physics, in part, he said, because he preferred solving problems

A neuroscientist and Nobel laureate transformed our understanding of how input to the brain produces vision and provided new insights into brain development.

to learning facts. He was accepted both for graduate work in physics and medical school. He chose medical school (apparently overcoming his aversion to facts) and did both an internship and a year of neurology residency, all at McGill. During those years, he worked in Herbert Jasper’s laboratory at the Montreal Neurological Institute, one of the leading brain research institutes in the world. He read electroencephalograms for Jasper, vowed never to read one again when he left, but regarded Jasper as a major mentor in his life. He did a second year of neurology residency at Johns Hopkins Hospital, which also exposed him to the doctor’s draft (his parents were American), which he fulfilled at Walter Reed Army Institute of Research. He then joined Torsten at Johns Hopkins, and they both moved with Steve Kuffler to Harvard Medical School in 1959, where David remained for the rest of his career.

David did his first experiments at Walter Reed. Using a microdrive and a tungsten electrode, both of which he had developed, he recorded the activity of individual neurons from the visual cortex of awake cats. He found neurons that responded to his waving hand but was unable to study their organization. He should have been first to report single-neuron activity in awake animals, but he had helped Jasper’s lab with his electrodes, and Jasper published first. I asked him many years later why he and Torsten had not returned to the awake animal; his reply, “too much else to do.”

David particularly enjoyed interactions with students. I directly experienced this enthusiasm after being riveted by his talk as a graduate student at Woods Hole, Massachusetts, in 1961. Detecting my more than casual interest, he invited me to visit their laboratory, put me up overnight, and let me watch the day’s experiments (involving long microelectrode penetrations through cortex). It changed my life, as interactions with David changed the lives of so many others. He enjoyed teaching Harvard junior fellows even after he became professor emeritus at Harvard. David must have believed in the Greek aphorism that a society grows great when old men plant trees in whose shade they shall never sit. There are many neuroscientists sitting in the shade of David’s trees.

10.1126/science.1247113

Laboratory of Sensorimotor Research, National Eye Institute, National Institutes of Health, 49 Convent Drive, Bethesda, MD 20892 USA. E-mail: bob@lsr.nei.nih.gov

CREDIT: COURTESY OF HARVARD MEDICAL SCHOOL

EPENDORF

Space Bats: Multidimensional Spatial Representation in the Bat

Michael M. Yartsev

It is estimated that more than 8 million different species reside on our planet, many of which live a very different life-style (1). But whether on the ground, in the ocean depths, or in the sky, all animals must have knowledge of their whereabouts to survive. The possible mechanisms subserving this core function and how these are implemented in the brain have been long-standing questions in neuroscience.

Scientists began studying the neural basis of spatial representation with the report of neurons in the rat dorsal hippocampus that fired when the animal entered a specific location (2). These neurons were called “place cells.” More recently, scientists discovered “grid-cells” in the rat medial entorhinal cortex (MEC), which activate in multiple locations, all arranged on the vertexes of a hexagonal grid (3, 4). Place cells and grid cells are widely considered key elements of the mammalian spatial representation system (5), yet their detailed properties have been studied almost exclusively in rodents. This convergence in choice of an animal model has occluded the understanding of which neuronal mechanisms involved in spatial representation generalize across species and whether different solutions have been reached by different brains. To explore this question and to study the functional properties of these cell types, we used a novel mammalian animal model, the bat. The findings in the bat helped revise our understanding of this important circuitry and show how divergence can powerfully complement convergence in the choice of animal models in neuroscience.

We first asked whether the bat can provide insight into the neural mechanisms giving rise

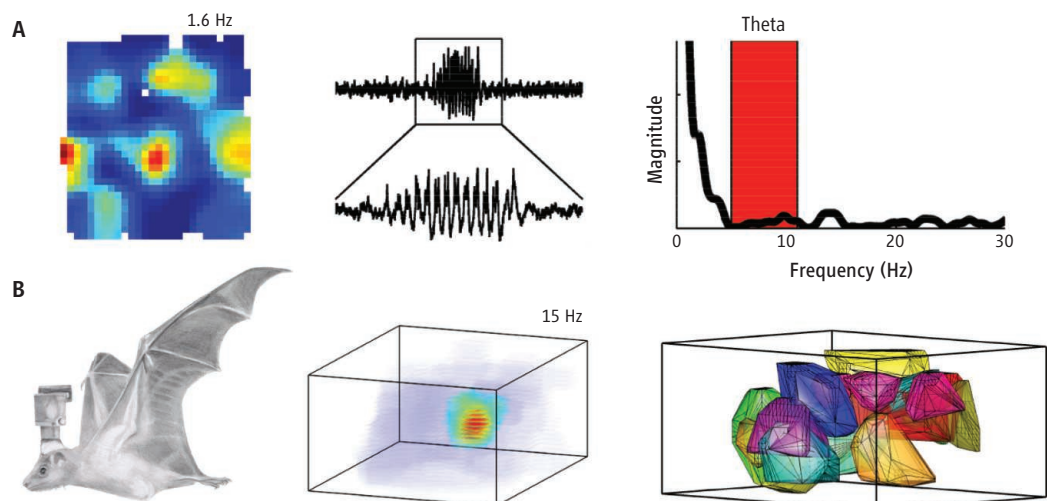


Eppendorf and *Science* are pleased to present the prize-winning essay by Michael M. Yartsev, the 2013 winner of the Eppendorf and *Science* Prize for Neurobiology.

to the grid formation. Two major classes of computational models were proposed to account for this phenomena (6): Attractor-based network models and single-neuron, “oscillatory-interference” models relying on theta-band (5 to 11 Hz) oscillations. The latter class of models received much experimental attention in rodent studies, but all evidences were of a correlative nature (6). We reasoned that, because place cells in bat hippocampus exist in the absence of con-

A novel animal model, the bat, is used to elucidate place-cell and grid-cell phenomena.

tinuous theta oscillations (7, 8), perhaps grid cells might also exist in their absence. This would causally argue against the validity of the oscillatory-interference class of models or, at least, against their generality across mammals. We recorded the activity of single MEC neurons in bats crawling inside a large arena (8) and found many of them to be grid cells [see the figure (A), left] with properties strikingly similar to those previously described in rats. We further found in the bat MEC all the other spatial cell types previously described in the rat MEC, such as neurons that encode the animal’s head orientation (9) and the borders of its current environment (10). We even found many of the same neural oscillations previously reported in the rat, such as high-frequency “ripple” oscillations (11) and fast and slow gamma oscillations (12). However, as we had hypothesized, theta oscillations in the bat were very different from those in rats. Theta oscillations in the bat were not



Properties of spatial cell types in crawling and flying bats. (A) (Left) Color-coded two-dimensional firing-rate map, with peak rate indicated, of a single grid cell recorded from the MEC of a crawling bat. (Middle) Raw local field potential trace recorded from the MEC of a crawling bat showing a single intermittent theta-bout (top: 20-s trace; bottom: 7-s zoom-in). (Right) Power-spectrum of a single grid-cell spike-train autocorrelogram showing no power in the theta frequency range (5 to 11 Hz, highlighted in red). (B) (Left) Illustration of a bat flying with the custom-made telemetry system, drawn to scale [Illustration: S. Kaufman]. (Middle) Color-coded three-dimensional firing-rate map, with peak rate indicated, of a single 3D place cell recorded from the hippocampus of a freely flying bat. (Right) All place fields (individual colored convex hulls) recorded from the hippocampus of a single bat. Figures in (A) and (B) are adopted from (8) and (14), respectively.

Princeton Neuroscience Institute, Princeton University, Princeton, NJ 08540, USA.
E-mail: myartsev@gmail.com

continuous [see the figure (A), middle], and the firing patterns of bat grid cells were not theta-modulated [see the figure (A), right], which put them in striking contrast to prerequisites of the oscillatory-interference models. Thus, our study in bats (8) allowed for causal examination of a major class of models that were based solely on data from rats.

After establishing the existence of place cells and grid cells in a two-dimensional (2D) environment, we wanted to go one step further and ask: How is the complete 3D volumetric space represented in the mammalian hippocampal formation? This question is pivotal because many animals on our planet, whether in air, in water, or on land, move in 3D environments. However, all studies conducted to date were in either 1D or 2D environments (13), which left this question unresolved. The bat's flight capability provided us with a unique opportunity to address this question. We focused on the hippocampus and developed the technology to record the activity of single place cells in freely flying bats (14) [see the figure (B), left]. We found that individual place cells provided a stable and nearly isotropic representation of the animal's position in 3D space. Each place cell fired mainly in a single restricted region of the 3D environment, and all axes were represented with similar resolution [see the figure (B), middle]. Furthermore, each place cell activated in a different location, and the combined activity of multiple place cells represented the 3D environment uniformly [see the figure (B), right]. We further found that the firing patterns of 3D place cells were not theta-rhythmic during flight, which supported our previous findings from the crawling bats and strongly argued against the cross-mammalian generality of oscillatory-based temporal codes for spatial representation (14).

The importance of our findings is four-fold. First, they support the generality of the place-cell and grid-cell phenomena across mammals. Second, they argue in favor of a rate-coding mechanism underlying the formation of spatial firing patterns in these cell types and, by this, constrain the possible computations responsible for their generation. Third, they reveal a coding mechanism for 3D space in the mammalian brain. Finally, they demonstrate that the use of novel animal models in neuroscience can complement existing knowledge and provide insights into the inner workings of the brain.

2013 Grand Prize Winner



The author of the prize-winning essay, **Michael Yartsev**, received his undergraduate and master's degrees in biomedical engineering from Ben-Gurion University in 2007. For his Ph.D., he joined the lab of Dr. Nachum Ulanovsky at the Weizmann Institute of Science. There, he recorded the activity of single neurons from the hippocampal formation of freely behaving and flying bats to study the underlying neural mechanisms of spatial memory and navigation in the mammalian brain. Since 2012, Dr. Yartsev is a C. V. Starr Fellow at the Princeton Neuroscience Institute at Princeton University where he is conducting postdoctoral work in the lab of Prof. Carlos Brody studying the neural basis of decision-making.

Finalists

Daniel Bendor for his essay, "Play it again, brain." Dr. Bendor is a lecturer in the Department of Cognitive, Perceptual, and Brain Sciences and the Institute of Behavioral Neuroscience at University College London. Dr. Bendor received his Ph.D. from Johns Hopkins University under the mentorship of Dr. Xiaoqin Wang, studying temporal processing in auditory cortex and the neural correlate of pitch and flutter perception. For his postdoctoral research, he investigated the role of the hippocampus in memory encoding and consolidation, while working with Dr. Matthew Wilson at the Massachusetts Institute of Technology. He has recently started his own lab at University College London, where his research focuses on how neural ensembles encode perceptual and memory-related information. http://scim.ag/_Bendor



Sophie Caron for her essay, "Brains don't play dice—or do they?" Dr. Caron is currently a postdoctoral fellow in the Department of Neuroscience at Columbia University. Sophie grew up in St-Blaise-sur-Richelieu in Canada and earned a B.Sc. in Biochemistry at the Université de Montréal. She moved to New York City to study the developmental mechanisms behind the diversification of sensory neurons in the laboratory of Dr. Alexander Schier at New York University and, later, Harvard. Having completed her Ph.D., Sophie joined the laboratory of Dr. Richard Axel at Columbia University, where she studies how the information gathered through the senses is represented in higher brain centers; in particular, those involved in memory. http://scim.ag/_Caron



For the full text of finalist essays and for information about applying for next year's awards, see *Science Online* at <http://scim.ag/eppendorf>.

References

1. C. Mora, D. P. Tittensor, S. Adl, A. G. B. Simpson, B. Worm, *PLoS Biol.* **9**, e1001127 (2011).
2. J. O'Keefe, J. Dostrovsky, *Brain Res.* **34**, 171 (1971).
3. M. Fyhn, S. Molden, M. P. Witter, E. I. Moser, M.-B. Moser, *Science* **305**, 1258 (2004).
4. T. Hafting, M. Fyhn, S. Molden, M. B. Moser, E. I. Moser, *Nature* **436**, 801 (2005).
5. E. I. Moser, E. Kropff, M.-B. Moser, *Annu. Rev. Neurosci.* **31**, 69 (2008).
6. L. M. Giocomo *et al.*, *Neuron* **71**, 589 (2011).
7. N. Ulanovsky, C. F. Moss, *Nat. Neurosci.* **10**, 224 (2007).
8. M. M. Yartsev, M. P. Witter, N. Ulanovsky, *Nature* **479**, 103 (2011).
9. F. Sargolini *et al.*, *Science* **312**, 758 (2006).
10. T. Solstad, C. N. Boccara, E. Kropff, M.-B. Moser, E. I. Moser, *Science* **322**, 1865 (2008).
11. G. Buzsáki, F. L. D. Silva, *Prog. Neurobiol.* **98**, 241 (2012).
12. G. Buzsáki, X.-J. Wang, *Annu. Rev. Neurosci.* **35**, 203 (2012).
13. P. Andersen, R. Morris, D. G. Amaral, T. Bliss, J. O'Keefe, *The Hippocampus Book* (Oxford Univ. Press, New York, 2007).
14. M. M. Yartsev, N. Ulanovsky, *Science* **340**, 367 (2013).

10.1126/science.1245809

EPENDORF

Brains Don't Play Dice—or Do They?

Sophie J. C. Caron

Life is often unpredictable. The brain thus needs to draw on past experience to prepare for future events. It does so by associating sensory stimuli, such as an odor, with desirable or undesirable outcomes. The smell of burning wood, for example, can evoke the soothing recollection of a cozy campfire or the traumatic memory of a burning house. It is through such associations that sensory stimuli that are a priori neutral become endowed with meaning. But life is full of possibilities. So how are associative brain centers able to account for an infinite number of possible associations?

Using the olfactory system of the fruit fly *Drosophila melanogaster*, I tackled this question in the laboratory of Richard Axel at Columbia University (1). The *Drosophila* olfactory circuit is similar to that of vertebrates in terms of its design logic, but consists of far fewer neurons. Fruit flies can learn to associate an odor with an electric shock or a sugar reward. On the basis of these associations, they will adjust their behavior when encountering that odor again. Such olfactory associative memories are formed in the mushroom body, a brain center comprising about 2000 neurons (known as Kenyon cells) and receiving mainly olfactory input (2, 3).

Fruit flies detect odors by means of olfactory sensory neurons located on their antennae and maxillary palps. Most of these neurons express only one of about 50 odorant receptor proteins (4–7). The olfactory sensory neurons project to the antennal lobe, where they are sorted such that neurons expressing the same receptor converge onto one of the 51 glomeruli (6, 7). This wiring



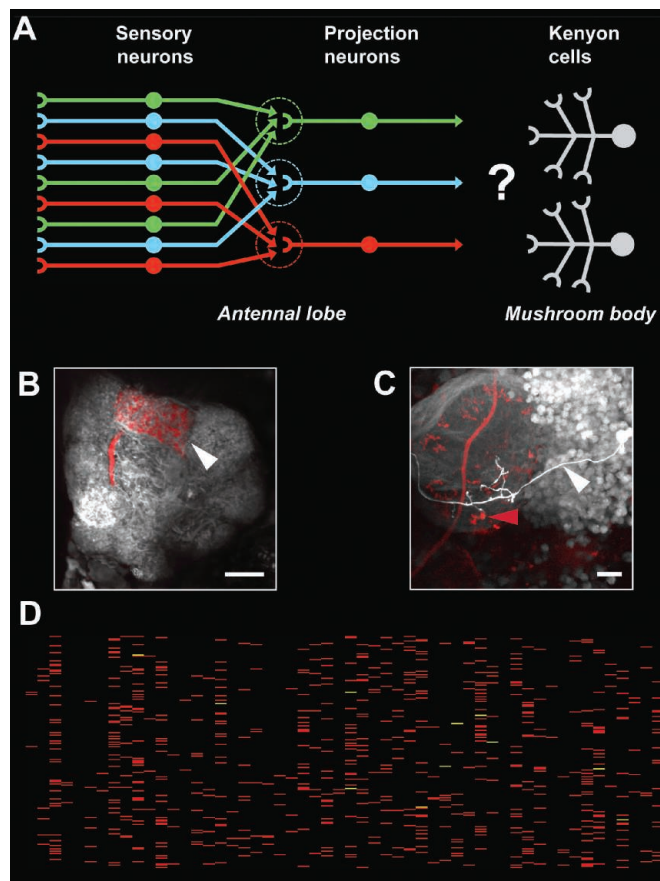
Eppendorf and *Science* are pleased to present the essay by Sophie Caron, a 2013 finalist for the Eppendorf and *Science* Prize for Neurobiology.

ing diagram (see the figure), in which each odorant receptor is mapped onto one glomerulus, prefigures how odors are represented in the antennal lobe. When an odorant molecule binds to its cognate receptors, the sensory neurons expressing these receptors fire, and an odor-specific pattern of glomerular activity emerges, a so-called “odor-evoked map” (8). Projection neurons dedicated to each glomerulus then relay olfactory information to two higher brain centers: the lateral

Associative brain centers are able to account for an infinite amount of possible associations through randomized sensory input.

horn, which mediates innate behaviors, and the mushroom body, where associative olfactory memories are formed (9, 10).

How does the mushroom body represent odors such that olfactory associations can emerge? We reasoned that, much like in the antennal lobe, the wiring diagram might hold the key. Together with my colleagues at Columbia University, I developed a technique to identify the input of individual Kenyon cells. Kenyon cells were labeled in order to visualize their synaptic endings, revealing that each Kenyon cell is connected to, on average, seven projection neurons. Subsequently, between two to seven of the connected projection neurons were marked with a neural tracer such that their cognate glomeruli could be identified. We charted 654 connections of 200 Kenyon cells and assigned them to the 51 antennal lobe glomeruli (11). Some glomeruli are represented more often than others, but this skewed frequency is simply a conse-



Mapping mushroom body connections.

(A) Schematic of the *D. melanogaster* olfactory circuit. All olfactory sensory neurons expressing the same odorant receptor (like colors) converge in one of the 51 antennal lobe glomeruli (dotted circles). One or more projection neurons connect each glomerulus to the lateral horn (not shown) and the mushroom body, where associative memories are formed. How projection neurons are wired to Kenyon cells was unknown. (B and C) Mapping Kenyon cell inputs (Scale bars, 10 μ m). (C) Starting with a single photolabeled Kenyon cell (white arrowhead), a projection neuron (red) connected to one of the dendritic endings of that Kenyon cell (red arrowhead) was filled with dye. (B) The innervation pattern of the red-labeled projection neuron in the antennal lobe allows for the identification of the corresponding glomerulus (arrowhead). (D) Matrix of 654 connections between 51 glomeruli and 200 Kenyon cells. Each row corresponds to the glomerular inputs of a single Kenyon cell, and each column represents one of the antennal lobe glomeruli. Red bars indicate a connection between a Kenyon cell and a glomerulus. Yellow bars indicate two connections to the same glomerulus. Differences in the number of connections per glomerulus are a function of the number of synaptic endings of their projection neurons. Statistical analyses revealed a random pattern of connectivity.

Department of Neuroscience, New York University, 701 West 168th Street, New York, NY 10032, USA. E-mail: sc2992@columbia.edu

quence of the number of presynaptic endings specific to the different projection neurons.

Within this set of connections, we then searched for any discernible pattern that might predict how glomeruli connect to the Kenyon cells. We first tested whether there are certain pairs of glomeruli that preferentially converge on a Kenyon cell, but could not find any preferred pairings. Likewise, there are no Kenyon cells dedicated to a specific glomerulus. Next, we searched for any biological criteria, such as glomerulus position, odor-response profile, or developmental origin, by which one input on a Kenyon cell would predict its other inputs. We statistically tested more than 10 different criteria but could not detect any such predictive pattern. Instead, the connections appeared to be completely random (11).

To confirm this notion, we created a data set in which the relative frequency of glomerular connections remained the same, but the Kenyon cells that they connect to were randomly shuffled. This shuffled data set behaved the same as our observational data set in all statistical tests. The lack of any discernible pattern in the connections between glomeruli and Kenyon cells means that each Kenyon cell receives its input from an essentially random set of glomeruli (11), which is in line with the odor responses of an individual Kenyon cell varying between individual flies (12).

This result might seem puzzling: Why would the ordered, odor-evoked map established in the antennal lobe be randomized in the mushroom body? The answer may lie in the way odors are represented there: Any given odor activates only about 5% of the Kenyon cells, regardless of the number of active glomeruli (13). To understand how random connectivity affects the formation of these sparse representations, we devised a computational model of the fly olfactory circuit in collaboration with Larry Abbott. The model reveals that randomization of Kenyon cell input allows the mushroom body to generate activity patterns that

Finalist

Sophie Caron is currently a postdoctoral fellow in the Department of Neuroscience at Columbia University. Sophie grew up in St-Blaise-sur-Richelieu in Canada and earned a B.Sc. in Biochemistry at the Université de Montréal. She moved to New York City to study the developmental mechanisms behind the diversification of sensory neurons in the laboratory of Dr. Alexander Schier at New York University and, later, Harvard. Having completed her Ph.D., Sophie joined the laboratory of Dr. Richard Axel at Columbia University, where she studies how the information gathered through the senses is represented in higher brain centers, in particular those involved in memory.



For the full text of finalist essays and for information about applying for next year's awards, see *Science Online* at <http://scim.ag/eppendorf>.

overlap minimally between different odors. In fact, as soon as any order is imposed on the connections between projection neurons and Kenyon cells, the resulting activity patterns begin to overlap and render the system less able to form odor-specific associations. Counterintuitive as it may seem, randomization appears to be an advantageous strategy for forming associations, because it minimizes the similarity between different sensory representations.

The randomization of inputs we discovered in the *Drosophila* mushroom body may be a general principle of neural circuit architecture in associative brain centers. In the vertebrate cerebellum, which processes sensorimotor information, granule cells, like Kenyon cells, also receive a limited number of inputs. David Marr and James Albus postulated that, owing to their limited inputs, the granule cells encode different motor patterns as sparse representations; and to accommodate more representations in the coding space defined by granule cells, they proposed that granule cell input would have to be randomly organized (14).

Our characterization of Kenyon cell connections in *Drosophila* provides the first anatomical evidence for randomized sensory

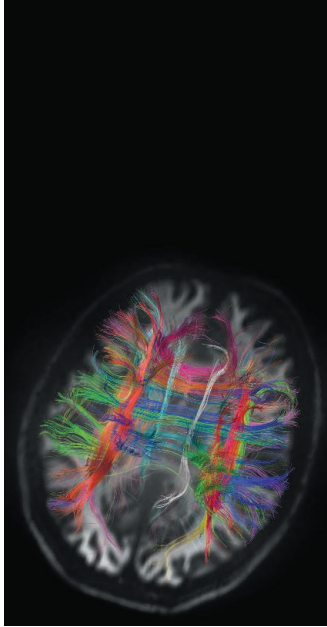
input in an associative brain center. Randomization may be a fundamental strategy to represent the vast number of possible associations with a limited number of neurons, it might be the very embodiment of the unpredictability of life.

References and Notes

1. L. B. Vosshall, R. F. Stocker, *Annu. Rev. Neurosci.* **30**, 505 (2007).
2. M. Heisenberg, *Nat. Rev. Neurosci.* **4**, 266 (2003).
3. Y. Aso et al., *J. Neurogenet.* **23**, 156 (2009).
4. P. J. Clyne et al., *Neuron* **22**, 327 (1999).
5. L. B. Vosshall, H. Amrein, P. S. Morozov, A. Rzhetsky, R. Axel, *Cell* **96**, 725 (1999).
6. A. Couto, M. Alenius, B. J. Dickson, *Curr. Biol.* **15**, 1535 (2005).
7. E. Fishilevich, L. B. Vosshall, *Curr. Biol.* **15**, 1548 (2005).
8. J. W. Wang, A. M. Wong, J. Flores, L. B. Vosshall, R. Axel, *Cell* **112**, 271 (2003).
9. A. M. Wong, J. W. Wang, R. Axel, *Cell* **109**, 229 (2002).
10. E. C. Marin, G. S. Jefferis, T. Komiyama, H. Zhu, L. Luo, *Cell* **109**, 243 (2002).
11. S. J. Caron, V. Ruta, L. F. Abbott, R. Axel, *Nature* **497**, 113 (2013).
12. M. Murthy, I. Fiete, G. Laurent, *Neuron* **59**, 1009 (2008).
13. K. S. Honegger, R. A. Campbell, G. C. Turner, *J. Neurosci.* **31**, 11772 (2011).
14. D. Marr, *J. Physiol.* **202**, 437 (1969).

Acknowledgments: I thank V. Ruta, L. F. Abbott, and R. Axel for our collaboration.

10.1126/science.1245982



INTRODUCTION

Connection, Connection, Connection...

THERE ARE APPROXIMATELY 86 BILLION NEURONS IN THE HUMAN BRAIN. OVER THE past decades, we have made enormous progress in understanding their molecular, genetic, and structural makeup as well as their function. However, the real power of the central nervous system lies in the smooth coordination of large numbers of neurons. Neurons are thus organized on many different scales, from small microcircuits and assemblies all the way to regional brain networks. To interact effectively on all these levels, neurons, nuclei, cortical columns, and larger areas need to be connected. The study of neuronal connectivity has expanded rapidly in past years. Large research groups have recently joined forces and formed consortia to tackle the difficult problems of how to experimentally investigate connections in the brain and how to analyze and make sense of the enormous amount of data that arises in the process.

This year's neuroscience special issue is devoted to general and also several more specific aspects of research on connectivity in the brain. We invited researchers to review the most recent progress in their fields and to provide us with an outlook on what the future may hold in store.

To make sense of larger structures, we first have to understand the composition of their basic building blocks. Markov *et al.* (p. 578) describe how interareal connectivity at the single-cell level, revealed by quantitative anatomical tract tracing, is relevant to our understanding of large-scale cortical networks and their hierarchical organization.

A different but also rapidly growing research direction deals with the use of connectivity measures to link brain structure and cognition. From the perspective of network theory, Park and Friston (p. 579) review our current understanding of structure-function relationships in large-scale brain networks and their underlying mechanisms.

One of the biggest breakthroughs in understanding the heavily connected brain has been the development of noninvasive brain-scanning methods, especially functional magnetic resonance imaging (fMRI). Turk-Browne (p. 580) provides an overview of recent exciting developments in large-scale fMRI data analysis, with a focus on unbiased approaches for examining whole-brain functional connectivity during cognitive tasks. Increased computational power now allows investigation of the whole-brain correlation matrix, the temporal correlation of every voxel with every other voxel throughout the brain, and the application of multivariate pattern analysis to these correlational data.

A sophisticated system that depends on the astonishingly precise interaction of a large number of cortical areas is the human ability to produce and understand language and music. Zatorre (p. 585) discusses how brain plasticity in the music and speech domains can be affected by predisposing factors that relate to brain structure and function.

— PETER STERN

The Heavily Connected Brain

CONTENTS

Reviews

- 578 Cortical High-Density Counterstream Architectures
N. T. Markov et al.
- 579 Structural and Functional Brain Networks: From Connections to Cognition
H.-J. Park and K. Friston
- 580 Functional Interactions as Big Data in the Human Brain
N. B. Turk-Browne
- 585 Predispositions and Plasticity in Music and Speech Learning: Neural Correlates and Implications
R. J. Zatorre

See also Editorial p. 533; News story 548; and Podcast


Science

Cortical High-Density Counterstream Architectures

Nikola T. Markov, Mária Ercsey-Ravasz, David C. Van Essen, Kenneth Knoblauch, Zoltán Toroczkai,* Henry Kennedy*

READ THE FULL ARTICLE ONLINE

<http://dx.doi.org/10.1126/science.1238406>

 Cite this article as N. T. Markov *et al.*, *Science* **342**, 1238406 (2013). DOI: 10.1126/science.1238406

Background: The cerebral cortex is divisible into many individual areas, each exhibiting distinct connectivity profiles, architecture, and physiological characteristics. Interactions among cortical areas underlie higher sensory, motor, and cognitive functions. Graph theory provides an important framework for understanding network properties of the interareal weighted and directed connectivity matrix reported in recent studies.

Advances: We derive an exponential distance rule that predicts many binary and weighted features of the cortical network, including efficiency of information transfer, the high specificity of long-distance compared to short-distance connections, wire length minimization, and the existence of a highly interconnected cortical core. We propose a bow-tie representation of the cortex, which combines these features with hierarchical processing.

Outlook: The exponential distance rule has important implications for understanding scaling properties of the cortex and developing future large-scale dynamic models of the cortex.

ARTICLE OUTLINE

Density and Small-World Architectures

Binary Specificity in the High-Density Cortical Graph

Hierarchical Organization

Rich-Club and Bow-Tie Structure

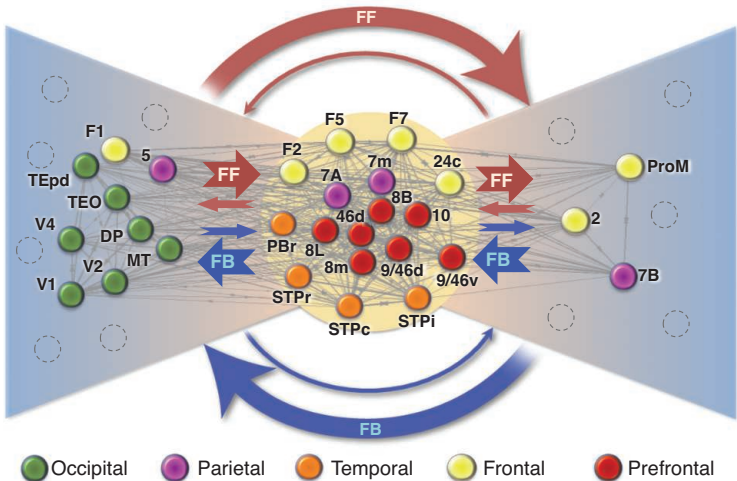
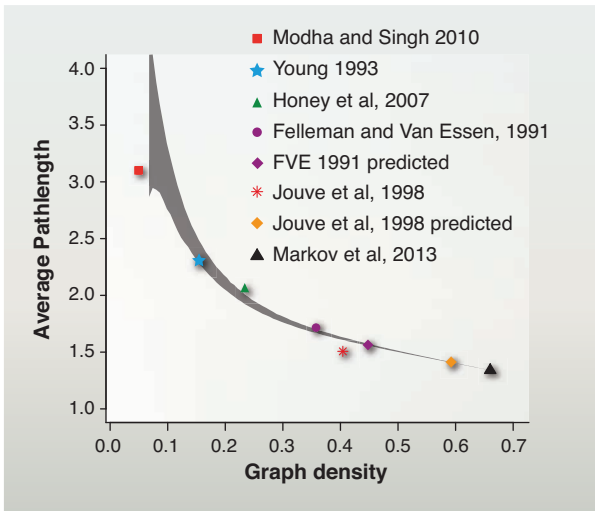
A Cortical Distance Rule as Cost-of-Wiring Principle: The EDR Model

Efficiency of Information Transfer

Optimal Placement

Concluding Remarks

Future Perspectives



Density and topology of the cortical graph. (Left) The 66% density of the cortical matrix (black triangle) is considerably greater than in previous reports (colored points) and is inconsistent with a small-world network. (Right) A bow-tie representation of the high-density cortical matrix. The high-efficiency cortical core has defined relations with the cortical periphery in the two fans.

The list of author affiliations is available in the full article online.
*Corresponding author. E-mail henry.kennedy@inserm.fr (H.K.); toro@nd.edu (Z.T.)

REVIEW

Cortical High-Density Counterstream Architectures

Nikola T. Markov,^{1,2,3} Mária Ercsey-Ravasz,⁴ David C. Van Essen,⁵ Kenneth Knoblauch,^{1,2,*} Zoltán Toroczkai,^{6,7,*†} Henry Kennedy^{1,2,*†}

Small-world networks provide an appealing description of cortical architecture owing to their capacity for integration and segregation combined with an economy of connectivity. Previous reports of low-density interareal graphs and apparent small-world properties are challenged by data that reveal high-density cortical graphs in which economy of connections is achieved by weight heterogeneity and distance-weight correlations. These properties define a model that predicts many binary and weighted features of the cortical network including a core-periphery, a typical feature of self-organizing information processing systems. Feedback and feedforward pathways between areas exhibit a dual counterstream organization, and their integration into local circuits constrains cortical computation. Here, we propose a bow-tie representation of interareal architecture derived from the hierarchical laminar weights of pathways between the high-efficiency dense core and periphery.

Because the concepts of localization of function and parcellation into cortical areas are closely intertwined, elucidating the global pattern of areal interactions is central to understanding higher brain functions (1–5). Cerebral cortex in the macaque monkey is subdivided into a mosaic of ~100 cortical areas, each displaying characteristic features, including cytoarchitecture (6). Each area has a characteristic connectivity profile thought to contribute to determining its functional properties (1, 7, 8). Here, we review how interareal connectivity at the single-cell level (9), revealed by quantitative anatomical tract tracing, is relevant to our understanding of large-scale cortical networks and their hierarchical organization (8, 10–13).

The circuitry of cerebral cortex is dominated by local (within-area) connections, and interareal connections constitute only about 20% of total cortical connectivity. Hence, the dozens of long-distance projections to areas beyond the immediate neighboring areas account for ~5% (10). Local networks conform in many ways to a canonical microcircuit that spans all cortical layers (14, 15) and includes recurrent excitation presumed to shape and amplify the sparse

input from subcortical and distant cortical sources (16).

Felleman and Van Essen (FVE) showed that interareal connectivity obeys hierarchical constraints rooted in the strong anatomical regularities of feedforward and feedback pathways (17). In this way, multiple distributed cortical hierarchies form a large-scale model of the cortex (17) that reflects the laminar integration of interareal connectivity into local circuits (18) and is relevant to sensory (17, 19, 20), motor (21, 22), and cognitive (23–27) systems. The structural features of interareal interactions may provide important insights into the observed dynamics of large-scale interareal networks controlling information flow through the cortex (1, 28, 29).

Density and Small-World Architectures

Graph theory provides a powerful framework for investigating complex networks such as those found in the brain. Many insights into the functional processes supported by such networks have been gleaned from analysis at the binary level (i.e., connections present or absent; see Glossary for definitions) (30). One important class of models that has received much attention is that of small-world (SW) networks, distinguished by high clustering coupled with a short average path length (also called characteristic path length) across the graph (31). The relevance of the SW property to understanding the cortex comes from its proposed capacity to optimize essential cortical features, including functional integration and segregation (32, 33).

Several studies based on collations of published anatomical tract tracing data (34–38) concluded that the cortical interareal network conforms to the SW network model of Watts and Strogatz (31). According to this hypothesis, efficient signal propagation through cortical circuits benefits

from a modest number of shortcuts connecting different communities across the cortical graph.

The SW hypothesis for interareal connectivity has been challenged by recent studies that used a consistent and optimized methodology to establish a quantitative data-base of macaque interareal connectivity (8, 11). We segmented the cortical sheet into 91 cortical areas and quantitatively analyzed the incoming connections to a subset of 29 areas chosen to represent five major regions of the cortex. By using similar procedures and identical area definitions across brains, this effort set out to overcome the limitations inherent in collated datasets that combine results across many anatomical studies (39). These limitations arise from the diversity of procedures used among different anatomical studies, including cross-study differences in parcellation schemes, extent of cortex examined, tracer sensitivity, criteria for accepting the presence or absence of a connection, and the spatial resolution of the analysis.

Injections of retrograde tracers in the 29 areas revealed 36% more connections than previously reported (8, 10). These so-called new-found projections (NFPs) were presumably missed by earlier studies for several reasons, including that they link widely separated areas (long-distance connections) and tend to be sparse, therefore requiring high resolution obtained by optimized sampling frequency for their detection (40, 41). Notably, repeat injections in selected areas and statistical modeling of the variability of projection magnitude demonstrated well-defined weighted connectivity profiles for each area and indicated high consistency for pathways of sufficient strength (8, 10). Inclusion of the NFPs considerably increases the cortical network density (i.e., the number of binary connections that exist relative to the total number of connections possible) (42). The density of the full interareal network (FIN), represented by the graph (or matrix) $G_{91 \times 91}$, remains unknown. However, a dominating set analysis of the currently known interareal network represented as the $G_{29 \times 91}$ subgraph of the FIN predicts that the FIN is itself a densely connected network (8).

The $G_{29 \times 29}$ interareal subgraph, formed among the injected (target) nodes, is edge-complete (see Glossary), and it has a link density of 66% (i.e., two-thirds of connections that can exist do exist) (8). The $G_{29 \times 29}$ is denser than any subgraph used in previous studies of the cortical network. Figure 1A displays the differences in density and average path length of various published subgraphs that have been used to investigate the large-scale properties of the cortex. FVE analyzed several hundred publications and reported on 32 visual areas and 305 pathways, for a graph density of 32% (17). In their meta-analysis, many pathways were identified as untested (i.e., the subgraph was edge-incomplete); they predicted a density of 45% if the unknown connections were to be tested. Three subsequent studies added collated data to the FVE data set, thus generating subgraphs of 47

¹Stem cell and Brain Research Institute, INSERM U846, 18 Avenue Doyen Lépine, 69500 Bron, France. ²Université de Lyon, Université Lyon I, 69003 Lyon, France. ³Yale University, Department of Neurobiology, New Haven, CT 06520, USA. ⁴Faculty of Physics, Babeş-Bolyai University, Cluj-Napoca, 400084 Romania. ⁵Department of Anatomy and Neurobiology, Washington University School of Medicine, St. Louis, MO 63110–1093, USA. ⁶Department of Physics and Interdisciplinary Center for Network Science and Applications, University of Notre Dame, Notre Dame, IN 46556, USA. ⁷Max Planck Institute for the Physics of Complex Systems, 01187 Dresden, Germany.

*These authors contributed equally to this work.

†Corresponding author. E-mail: henry.kennedy@inserm.fr (H.K.); toro@nd.edu (Z.T.)

The Heavily Connected Brain

areas $G_{47 \times 47}$ (34), 71 areas $G_{71 \times 71}$ (43), and 179 areas $G_{179 \times 179}$ (44), respectively. The resulting subgraphs were also edge-incomplete, but untested connections were assigned a “nonconnection” status, leading to low density estimates ranging from 5 to 25%. Jouve *et al.* updated the FVE data set with additional connections reported during the 7-year interval between the two studies, yielding an observed density of 37% (45). They used an inference algorithm based on second-order connection regularities and arrived at a density prediction of 58% for visual cortex.

The aggregate evidence suggesting high density of the FIN of the macaque neocortex led us to explore the implications for putative SW properties of the dense cortical graph. In contrast with d -dimensional regular lattices, where the characteristic path length L grows as a power-law $L \propto n^{1/d}$ with the number of nodes n , in a SW network path length growth is logarithmic with the number of nodes and hence much slower, i.e., as $L \propto \frac{\ln n}{\ln k}$, where k is the average degree in the network (31, 46). Figure 1B examines the effect of density on a hypothetical 1000-node ring lattice network on the interval over which the SW phenomenon of high clustering and short path length exists. The reduction in average path length and

increase in clustering of a lattice by random rewiring of connections is density dependent. At densities below about 42%, even limited rewiring substantially decreases average path length while maintaining high clustering, thereby providing shortcuts characteristic of a SW architecture. By contrast, at high densities rewiring barely affects path length, because density alone determines this feature, independently of the more detailed structure of the network. Figure 1C shows the SW coefficient as a function of rewiring probability for regular networks (lattices) with increasing density [defined as in (31)]. These results indicate that the density predicted by FVE (45%) and that reported by Markov *et al.* (8) would reject the hypothesis of the large-scale interareal cortical network being a Watts-Strogatz-type SW network.

The $G_{29 \times 29}$ matrix discussed here has a density of 66% and includes pathways with few labeled neurons. As we have argued elsewhere, weak pathways could fulfill diverse roles (8, 10, 11, 13, 39), and given that injections involve only a fraction of a target area, we do not capture the full complement of neurons for each weak pathway. Thresholding would reduce the range of weights that we report. For example, eliminating pathways with, on average, fewer than 10 neurons per tracer in-

jection would reduce the graph density from 66 to 53%, and the range of connection weights (8) from five to four orders of magnitude. At 53%, our conclusions concerning the SW would not change. However, 37% of the pathways that would be eliminated by this thresholding have been reported in earlier publications. Further, these conservative steps would ignore the possibility that much larger injections coupled with higher sampling could potentially reveal larger cell numbers, thereby increasing the range of connection weights, numbers of areas connected, and the graph density with respect to the values reported here.

At graph densities approaching 100%, the point when all pairs of nodes are interconnected, the variability within the graph’s structure approaches zero. Hence, at the high density found in the $G_{29 \times 29}$ matrix, little binary specificity might be expected. However, because the probability of connections drops steeply with distance, the subset of long-distance connections can show binary specificity, as we demonstrate in the next section.

Binary Specificity in the High-Density Cortical Graph

Figure 2A shows the $G_{29 \times 29}$ matrix with the NFPs indicated in red and organized so that target areas

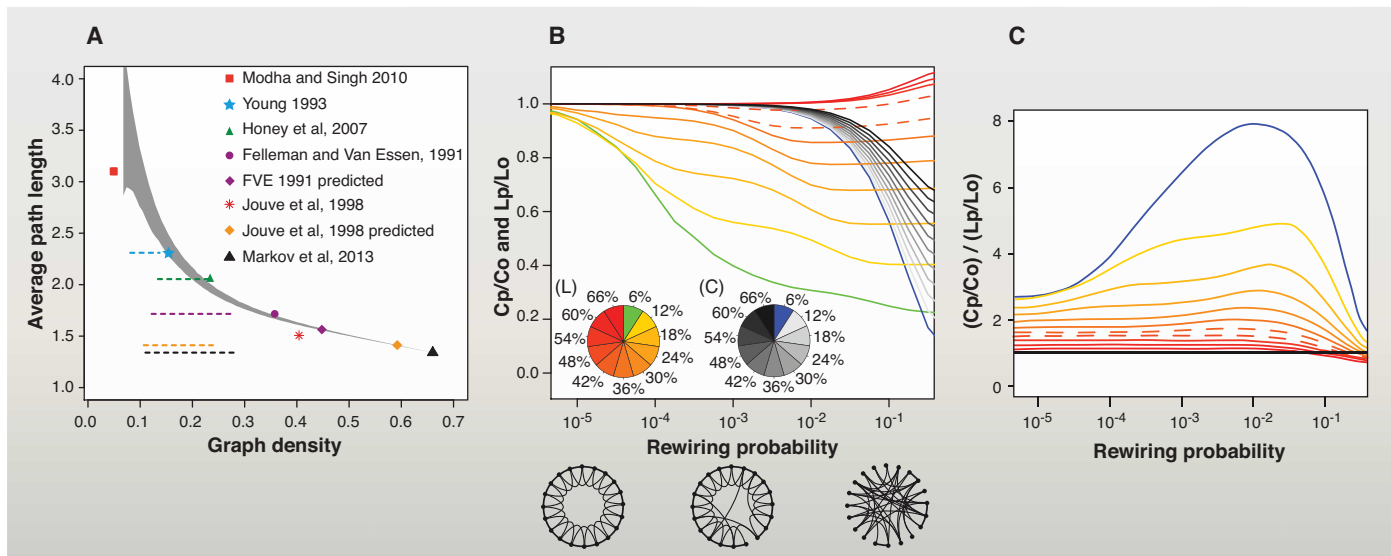


Fig. 1. High density of the cortical graph excludes sparse small-world architecture. (A) Comparison of the average shortest path length and density of the $G_{29 \times 29}$ subgraph with the graphs of previous studies. Sequential removal of weak connections causes an increase in the characteristic path-length. Black triangle: $G_{29 \times 29}$; gray area: 95% confidence interval following random removal of connections from $G_{29 \times 29}$. Dotted horizontal lines indicate the 5 to 95% interval with at least one unreachable node (after repeated and graded, random edge removal). The three least dense graphs are near their 5% unreachability levels. Data incompleteness meant that some of the initial networks have unreachable nodes (the latter are removed and not considered here); 14 unreachable nodes are from Modha and Singh (44); 1 unreachable node is from Young (43); and 2 unreachable nodes are from Felleman and Van Essen (17). Modha and Singh 2010: (44); Young 1993: (43); Honey *et al.*, 2007: (34); Felleman and Van Essen 1991: (17); Jouve *et al.*, 1998: (45); Markov *et al.*, 2012: (8). “Jouve *et al.*, 1998 predicted” indicates values of the graph inferred using the published algorithm

(45). (B) Effect of density on Watts and Strogatz’s formalization of the small world. Clustering and average path-length variations generated by edge rewiring with probability range indicated on the x axis applied to regular lattices [of 1000 nodes in a 1D ring as in (31)] of increasingly higher densities. The pie charts show graph density encoded via colors for path length (L) and clustering (C). On the y axis, we indicate the average path length ratio (Lp/Lo) and clustering ratio (Cp/Co) of the randomly rewired network, where Lo and Co are the path length (Lo) and clustering (Co) of the regular lattice, respectively. Lp and Cp are the same quantities measured for the network rewired with probability (p). Hence, for each density value indicated in the L and C pie charts, the corresponding Lp/Lo and Cp/Co curves can be identified. Three diagrams below the x axis indicate the lattice (left), sparsely rewired (middle), and the randomized (right) networks. (C) The small-world coefficient $\frac{Cp/Co}{Lp/Lo}$ (33, 136) corresponding to each lattice rewiring. Color code is the same as in (B). Dashed lines in (B) and (C) indicate 42% and 48% density levels. For electronic data files, see www.core-nets.org.

are associated with one of the five regions of the cortex (occipital, temporal, parietal, frontal, and prefrontal; see Fig. 2D). Earlier anatomical studies suggested that cortical areas are preferentially connected to physically nearby areas in the region in which they are located, whereas the additional NFPs mainly interconnect area pairs located in different regions (8). Because regionally related areas tend to have similar connectivity patterns, this raises the question of whether the NFPs are perhaps important because they connect areas having dissimilar connectivity patterns. Using a similarity index (see Fig. 2B), we measured the degree to which two areas receive (or avoid receiving) input from common sources (in-link similarity) (11). This confirmed that within-region similarity was high; between-region similarity was lower and, notably, declined with increasing distance between regions (Fig. 2B). The observation that NFPs tend to interconnect distant areas with low similarity provides one indication of their specificity.

Additional evidence for the NFP-related specificity comes from a dominating set analysis, a graph theoretical method that quantifies the ex-

tent to which connections are gathered (“dominated”) by a small set of nodes (8, 11). In the case of directed networks, in-link and out-link domination are specified separately. Because with retrograde tracers all the in-links are revealed for an injected target area (but not the out-links), we focused on in-link domination (8, 11). A subset of nodes is said to be fully in-link dominating if all nodes of the graph each project to at least one edge into this subset. There can be several fully dominating sets of nodes (areas); a minimum fully dominating set (MDS) is the smallest such set. The smaller the MDS, the more concentrated the input, indicating the increased role that this set plays in the network. A more refined measure is given by encoding the percentage of all nodes that project into a group of given target areas (8, 11) (thus 100% corresponds to full domination). The histogram of this fraction over all possible groups of a given size (e.g., all combinations of two or more targets) gives an overall picture of domination; see fig. S3, A and B, in (11) for the $G_{29 \times 91}$ network. In this case, the low value of 2 for the MDS along with the high domination percentage of many small groups of target

areas indicates that the FIN must also be a dense network [see (8) for more details]. Comparing these histograms with and without the NFPs included shows that the NFPs play a key role in the statistics of the inputs to area groups, as their removal appreciably reduces domination for all sets, and the MDS size jumps from 2 to 5 (11).

Besides suggesting a key role for the NFPs, the dominating set analysis confirms the high density of the cortical graph (11). However, this density is not homogeneously distributed. The percentage of areas projecting to a target area is 99% for areas within 10 mm, 85% between 10 and 20 mm, 50 to 60% between 20 and 40 mm, and below 40% at 40 mm or greater. Examination of the cortical areas projecting to a target region shows that a modest number of areas outside that region project to all of the injected areas included in the target region (11) (Fig. 2D). Thus each target region has a set of common input areas, which constitute a connectivity signature of the target region (1, 7, 11). The number of common input areas to a region is substantially larger when NFPs are included (red versus blue in Fig. 2D). Comparisons with randomly permuted networks indicate

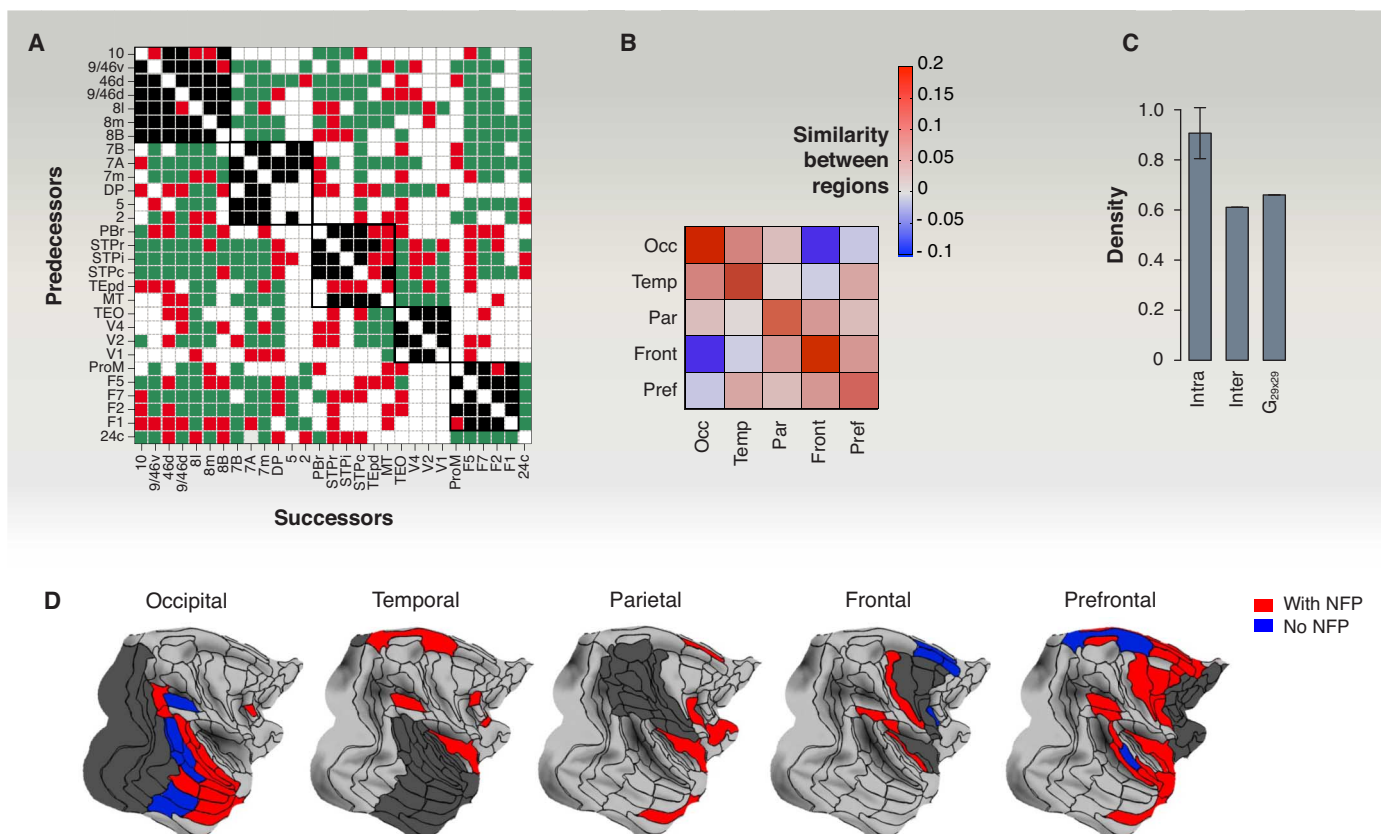


Fig. 2. Binary specificity in the dense network. (A) The $G_{29 \times 29}$ subgraph adjacency matrix organized so as to illustrate the connectivity within (black squares) and between regions (in green). In red, new-found projections (NFPs). (B) Regional in-link similarity of binary connections; positive values indicate positive correlation and negative values indicate anticorrelation between area pairs, within and between regions. The diagonal corresponds to average

intraregion similarity; everywhere else is interregion similarity. Occ, occipital region; Temp, temporal region; Par, parietal region; Front, frontal region; Pref, prefrontal. (C) Densities of the interregion, intraregion, and $G_{29 \times 29}$ edge-complete subgraphs. (D) Interregion common inputs to one of the five regions (dark gray), including the NFP, increases the number of common inputs. [Panels (B) to (D) adapted from (11)]

The Heavily Connected Brain

that the increase in the number of common inputs after inclusion of NFPs significantly exceeds that which would occur from an increase in density by the addition of an equivalent number of random connections (11). Further, the specificity of the long-distance connections and hence of the NFP is indicated by the fact that the density of the interregional edge-complete graphs is considerably lower than for those formed by intraregional connections (Fig. 2C). Note, that the specificity of the NFP connectivity is the same as for all long-distance connections, including those already known (11).

The impact of the interareal pathways on the physiology of the target areas is constrained by the laminar origins of the parent neurons of the pathway and the cortical layers targeted by their

synaptic terminals. These laminar constraints on interareal pathways contribute to determining cortical hierarchies (17), which we address in the next section.

Hierarchical Organization

More than 70% of all the projections to a given locus on the cortical sheet arise from within 1.5 to 2.5 mm, so that cortical connectivity is dominated by short-distance (10), local connections that conform to a canonical microcircuit optimized to amplify and shape weaker long-distance cortical inputs (Fig. 3A) (16). Therefore, when considering long-distance interareal pathways, it is important to consider not only the strength and the specificity of the connections, but also their pronounced

laminar asymmetry determined by the direction of the connection. Hence, feedforward (FF) pathways (mostly directed rostrally) originate principally from supragranular layers and terminate in layer 4 in higher areas (47–49), whereas feedback (FB) pathways (mostly directed caudally) originate mainly from infragranular layers in higher areas and avoid layer 4 in lower areas (47, 49–51). Pairwise comparison of the connections has been used to reveal cortical hierarchies (17, 52). While the FVE model is indeterminate (53), it can be partially resolved by using a continuous scale such as hierarchical distance based on the fraction of supragranular layer neurons (SLNs) (Fig. 3B) (54–56). The SLN index quantifies an order relation between areas as defined by their laminar

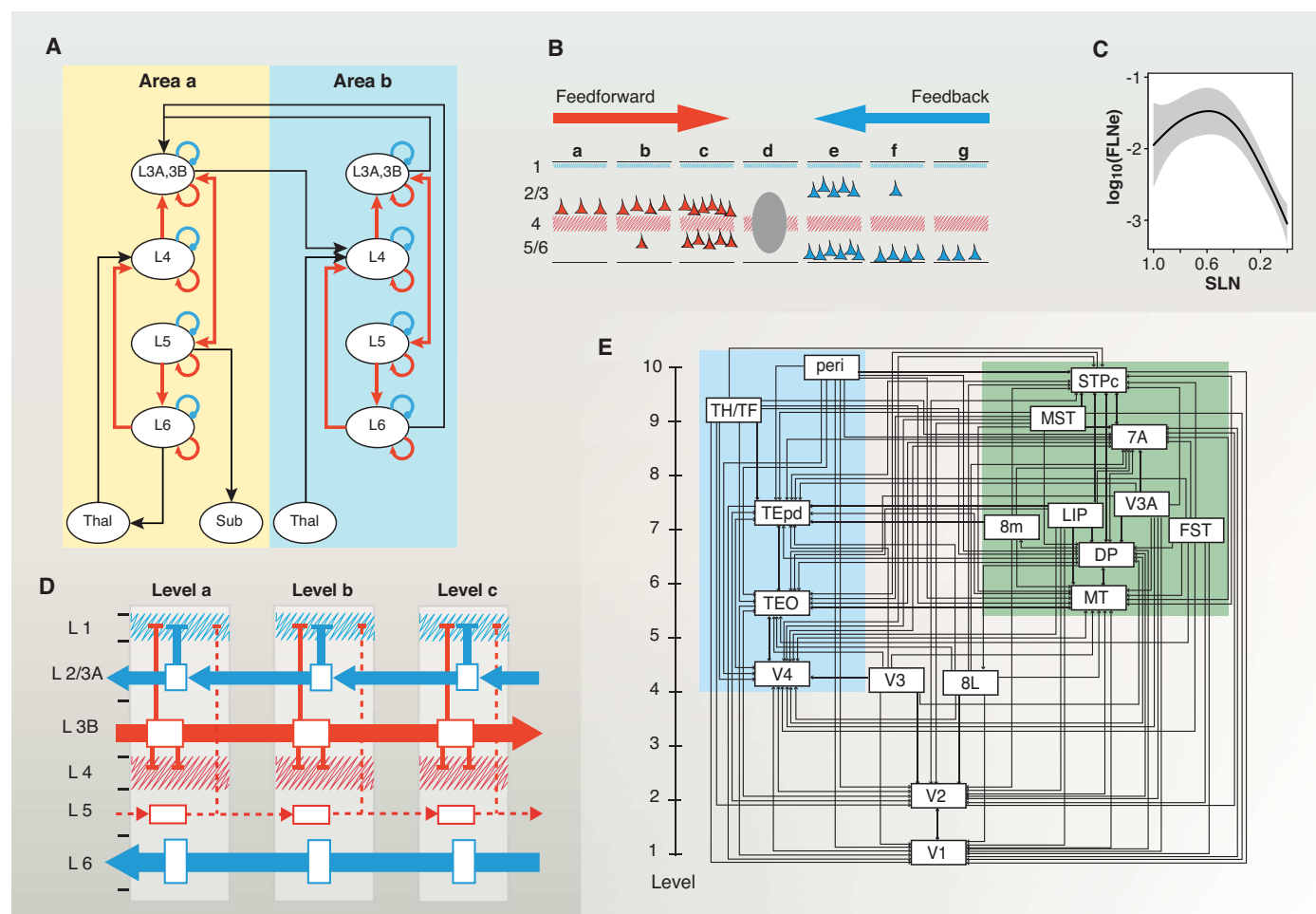


Fig. 3. Cortical hierarchy. (A) Canonical microcircuit [adapted with permission (131)]. (B) Cartoon of the laminar distribution of projections to a cortical mid-level area. (C) Relationship of SLN and FLN. The strongest pathways are the short-distance lateral connections with an SLN of ~0.5; long-distance FF and particularly FB are substantially weaker. (D) Cortical counterstreams. FB and FF are organized in a dual counterstream system localized in supra- and infragranular compartments. In the supragranular compartment, the layer 3B pyramidal cells have long-distance FF axons targeting layer 4 of higher-order areas, while the pyramidal neurons of layer 3A have short-range FB axons targeting the supragranular layers of lower-order areas. In the infragranular compartment, layer 6 has long-distance FB axons that avoid layer 4 and

largely target layer 1, whereas layer 5 has short-distance FF axons. Layers 3A and B are the major supragranular output layers and layer 4 is the major input layer for FF projections, and layer 1 the major input layer for FB projections. Apical dendrites of pyramidal cells of layers 3A and 3B and, to a lesser extent, layer 5 reach layer 1, where they can receive FB influences, while some of the basal dendrites of FF layer 3B neurons are located in layer 4. (E) A hierarchical organization of the visual cortical areas using SLN as a hierarchical distance measure (12). The projection of area 8L (frontal eye field) to area V4, and from area V4 to area 8L, are both defined by their SLN as FF and therefore form a strong loop (12). (D and E) Color coding: red, FF; blue, FB. [Panel (D) from (12)]. For electronic data files, see www.core-nets.org.

profiles of connectivity and thereby allows estimation of the hierarchical distance separating them (57). Further analysis shows that connections between neighboring areas have the highest weight, defined as the fraction of labeled neurons (FLN) (10, 58), whereas long-distance FF and FB connections have lower weights (Fig. 3, B and C).

Interest in the hierarchical organization of the cortex is fueled by evidence that FF and FB processes are distinct physiologically. A useful, albeit oversimplified characterization is that FF connections are “driving” and FB connections are “modulatory” (59–63). Further, FF and FB pathways engage different glutamate receptor subtypes (64). If the two polarities indeed have relatively distinct roles, one might predict that any given neuron would contribute to only one type of pathway, rather than supplying axons to both. This has been tested by injecting two distinguishable retrograde tracers in higher and lower cortical areas and examining the intermediate areas for double-labeled neurons (i.e., neurons with a bifurcating axon directed at both pathways). The results showed that the FF and FB neurons in the intermediate areas were virtually all single-labeled, which is striking given the commonality of axonal bifurcation (57, 65). Not only do FF and FB constitute distinct populations, but they also form two segregated streams, consistent with earlier observations (47, 66, 67). The supra- and the infragranular layers each have a counterstream organization, most pronounced in the supragranular layers (Fig. 3D) (12, 68). Further, the supragranular counterstream showed a point-to-point (i.e., topographical) precise connectivity in both FF and FB directions, whereas the infragranular counterstream has a more diffuse topography showing high divergence and convergence in both directions (12). Hence, contrary to previous assertions, topographic precision distinguishes supragranular layer from infragranular connections and not FB versus FF pathways (12).

The integration of interareal connections into the canonical microcircuit of a target area presumably determines how top-down and bottom-up streams affect processing within the target area (18). The concept of hierarchical processing has influenced theories of cortical computation, predictive coding, and emerging concepts of inference in cortical function (18, 69, 70). Recent progress in elucidating interareal communication includes the demonstration of gamma-band phase coherence in the supragranular and beta-band coherence in the infragranular layers (71, 72). These differences in coherence reflect differences in interareal synchronization (73–76), which are thought to facilitate effective communication (74, 77). Recently beta-gamma asymmetries have been shown to correlate with the aforementioned SLN fraction, suggesting a match between anatomically and functionally defined hierarchies (18). The SLN analysis revealed infrequent, but potentially important, departures from the reciprocity

of FF and FB projections. For instance, instead of FF being invariably reciprocated by FB, a few FF pathways are reciprocated by a FF, thereby forming a strong loop (54, 78, 79), which is illustrated in Fig. 3E, where the FF projection of V4 to the frontal eye field (area 8L) is reciprocated by a FF and not a FB connection (12, 54). Given the evidence for different physiological roles of FF and FB pathways, such anti-hierarchical pathways may allow circulation of information up and down the cortical hierarchy entirely via FF pathways. The functional importance of these rare so-called strong loops (79) remains to be determined.

Rich-Club and Bow-Tie Structure

Previous studies based on sparse cortical networks have suggested an important structural heterogeneity in the cortex, where hub areas are statistically more interconnected than expected, forming a so-called rich club (80–82) or central core (44). Using methods adapted to high-density graphs (83), we have shown that the $G_{29 \times 29}$ subgraph harbors 13 cliques (complete subgraphs in which all possible connections are present) of size 10. This results in a very high, 92% density core formed of 17 nodes in the edge-complete $G_{29 \times 29}$ (13), a periphery of 12 nodes with a density of 49%, and a 54% density of connectivity between the periphery and core. Because additional in-

jections cannot change the structure of the $G_{29 \times 29}$ subgraph, this implies that the FIN also has a dense core (to which the core of $G_{29 \times 29}$ must belong, being 92% dense), possibly larger than that of $G_{29 \times 29}$. The core-periphery distinction is also supported by the average strength of connections, as the fraction of labeled neurons (FLN, see Glossary) between the core and periphery is on average weaker than within either the core or periphery (13).

Next, we present a method (see captions of Table 1 and Fig. 4) that uses both the FLN weights and the SLN fractions to reveal correlations among core and periphery links (Fig. 4A), thereby providing further information on the large-scale organization of the cortical network. In Fig. 4B, peripheral nodes are split into two groups (Table 1). In the left fan, the preponderant pathways are FF going from the periphery to the core reciprocated by FB from the core to the periphery. In the right fan, the preponderant pathways are FB going from the periphery to the core reciprocated by FF pathways from the core to the periphery (Fig. 4B). The preponderant pathways being FF from left to right and FB in the inverse direction also holds for the small number of direct links between the two fans (see Fig. 4B). The core includes areas in the frontal, prefrontal, and parietal regions [see Fig. 2D for region locations and (8) for area members of each region].

Table 1. Properties of connections between periphery nodes and the core. All the individual links of an area from P (column A) have been classified into one of four classes. If a link had an SLN > 0.5, it was designated as FF, otherwise as FB. The index “o” indicates connections from the node to the core, and the index “i” indicates connections from the core into that node. Columns B to E give the number of links of a given type for an area. Columns F to I provide the cumulative effective SLN values (see below) for the four types of connection groups (streams) after subtracting 0.5 from the values. The closer the value to 0.5 (–0.5), the stronger the effective FF (FB) nature of the group of links is. The cumulative effective SLN values were obtained as follows. Let $L_j(x)$ denote the set of nodes in the C that a node x in the P connects with via a link of type j (one of the four types). The effective SLN measure $S_j(x)$ for node x for its connectivity with C, within every link class, weighted by the strength (FLN) of the connections is given by $S_j(x) = (\sum_{y \in L_j(x)} s_{xy} f_{xy}) / \sum_{y \in L_j(x)} f_{xy}$. Here f_{xy} is the FLN and s_{xy} is the SLN; $s_{xy} f_{xy}$ is thus proportional to the number of supra neurons in that individual (x-y) projection, which is then summed over all connections within that class that node x has with C, normalized by the total strength of the connections within that class. Exploiting the correlations between the streams shown in Fig 4, A to C, we generated in columns J and K two counterstream indices by adding the absolute values of the paired columns. If the outstreams into the C were strong FF (correlated with strong FB from the core), we designated them as L (left wing of the bow tie), otherwise as R (right wing). According to these criteria, TEpd is an outlier; see legend of Fig. 4.

A	B	C	D	E	F	G	H	I	J	K	L
Area	#FF _o	#FB _o	#FF _i	#FB _i	FF _o –0.5	FB _o –0.5	FF _i –0.5	FB _i –0.5	F+ I	G +H	L/C/R
2	4	6	3	2	0.136	–0.205	0.063	–0.035	0.171	0.268	R
5	5	6	2	5	0.225	–0.083	0.157	–0.205	0.430	0.240	L
7B	8	3	7	4	0.154	–0.328	0.069	–0.233	0.388	0.397	R-C
DP	10	1	2	11	0.203	–0.268	0.018	–0.158	0.361	0.287	L
F1	6	8	0	8	0.187	–0.253	N/A	–0.073	0.260	0.253	L-C
MT	6	4	4	7	0.384	–0.015	0.174	–0.377	0.760	0.189	L
ProM	2	7	4	2	0.104	–0.199	0.255	–0.145	0.249	0.453	R
TEO	3	4	6	8	0.211	–0.029	0.247	–0.434	0.645	0.276	L
TEpd	3	8	2	8	0.065	–0.336	0.157	–0.104	0.168	0.493	R
V1	3	1	0	4	0.318	–0.500	N/A	–0.442	0.760	0.0	L
V2	8	4	0	5	0.277	–0.260	N/A	–0.394	0.671	0.260	L
V4	8	1	1	6	0.395	–0.500	0.074	–0.463	0.858	0.074	L

The Heavily Connected Brain

The predominant FF inputs from the left wing to the core areas may serve as feeders for the central core processing (consistent with the inclusion of primary sensory and motor areas in this left wing; see Fig. 4B), whereas the FB pathway predominance from the right wing could correspond to a monitoring or coordinating role for the members of this group.

A Cortical Distance Rule as Cost-of-Wiring Principle: The EDR Model

The above observations suggest a general picture of the interareal network: It is a dense network,

but with high binary specificity ensured by long-distance connections and characterized by the existence of a core-periphery structure organized into a bow tie via FF/FB pathways. The specificity of connections increases with projection distance and with decreasing connection weights. Is there a fundamental, biophysical principle-based model that can capture most of these properties with a minimal number of fitting parameters? The answer is yes, as discussed below.

A clue to the importance of weight-distance relations for understanding the properties of the cortical network comes from the observation that

the FLN weights are highly heterogeneous, following a log-normal distribution varying over five orders of magnitude (8, 10) (Fig. 5A). The log-normal distribution may directly reflect the interplay between metabolic costs associated with projection lengths and a geometrical or spatial property of areal locations (13). Axonal projections out to a distance d through the white matter come at an energy (metabolic) cost, irrespective of the areas involved. This is suggested by the exponential decay of the number of labeled neurons as a function of projection distance d : $p(d) = c \exp(-\lambda d)$, corresponding to an exponential

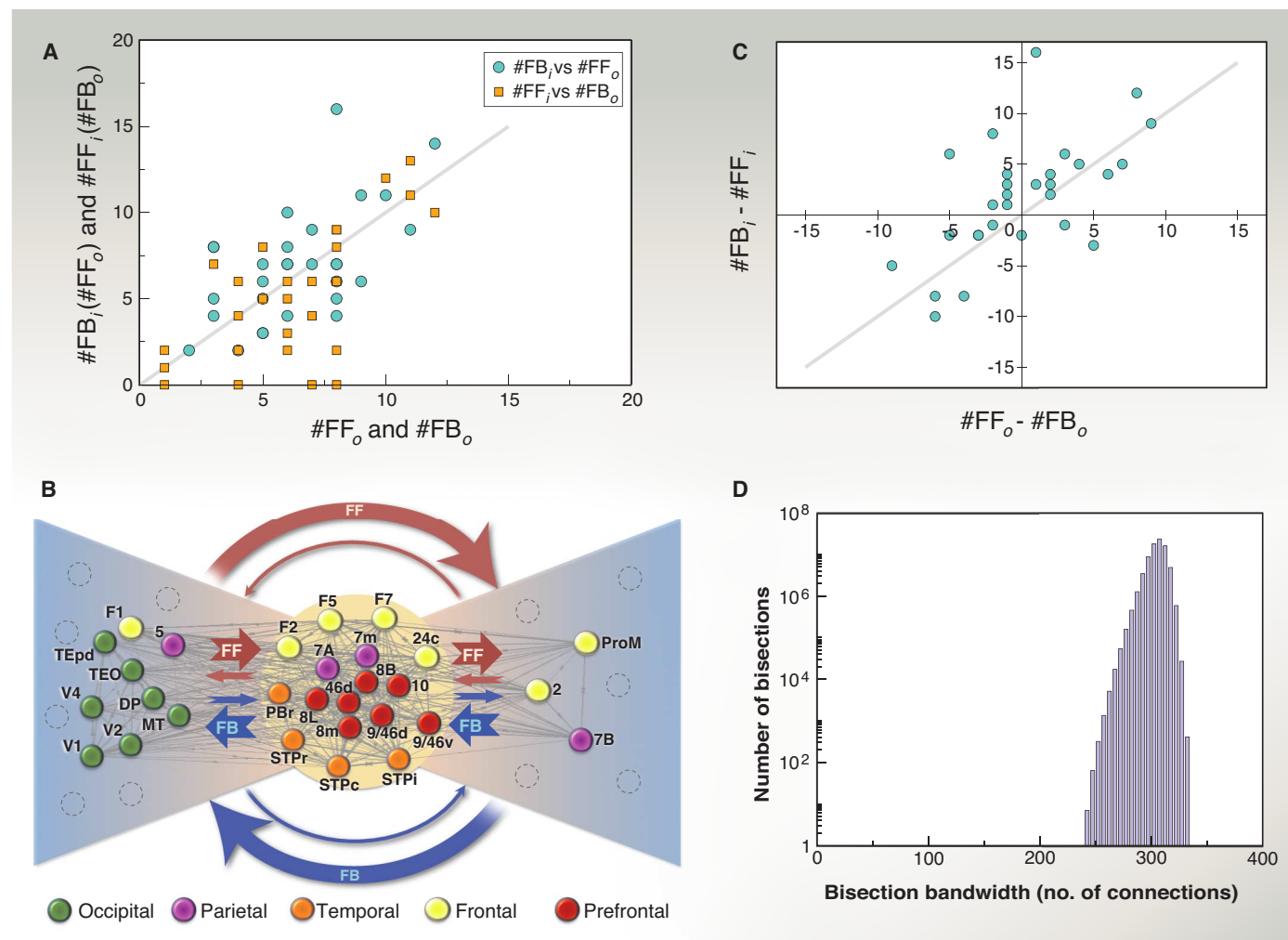


Fig. 4. Bow-tie representation. Links are classified according to their SLN value being below 0.5 (that is, infra dominated, also called FB) or above 0.5 (that is, supra dominated, also called FF) and according to whether they are oriented toward the core ("out" or "o") or from the core ("in" or "i"). This generates a total of four possibilities for link types (y is an area from the core, x is noncore): (1) x projecting to y ($x \rightarrow y$) as FF (denoted FF_o), (2) $x \rightarrow y$ as FB (denoted FB_o), (3) y projecting into x ($x \leftarrow y$) as FF (or FF_i), and (4) $x \leftarrow y$ as FB (or FB_i). (A) The numbers of link types are correlated over the set of all nodes (both from periphery, P, and core, C); the number of FF links into the core ($\#FF_i$) correlates on average with the number of FB links from the core ($\#FB_o$) and $\#FF_i$ correlates with $\#FB_o$. (B) A bow-tie representation of the $G_{29 \times 29}$. The dense core (92%) is shown in the middle. The left and right wings of the tie were obtained based on the FF/FB counterstreams into and from the core and their

cumulative effective SLN values; see Table 1 legend for details. The cumulative effective SLN is an average SLN to or from the C for the given connection type, weighted by link strengths. In this way, for every area in the P, we obtain four numbers all between 0 and 1, shown in Table 1, columns F to I. A strong FF into C pairs with a strong FB from C, and vice versa, the connections forming FF/FB counterstreams. Computing two indices of effective SLN strengths in absolute value for the two pairs $|FF_o - 0.5| + |FB_i - 0.5|$ and $|FF_i - 0.5| + |FB_o - 0.5|$ (columns J and K of Table 1), we classify the nodes into one of two groups (L or R) depending on which value is larger. (C) The imbalance between the number of FF and FB links from a node to C is mirrored on average by imbalance between the FF and FB connections from C to the same node. (D) The edge-complete $G_{29 \times 29}$ has a very high bisection bandwidth of 242 links, out of 536 total (see Glossary). For electronic data files, see www.core-nets.org.

distance rule (EDR) (Fig. 5B). The spatial decay constant $\lambda = 0.188 \text{ mm}^{-1}$ expresses the growth rate of the metabolic cost with distance. We therefore expect that the FLN between two areas separated by a distance d is determined to a first approximation by this cost, independently of areal identity. A relevant spatial property is expressed by the inset in Fig. 5B, showing that the fraction of area pairs separated by a distance d is well approximated by a truncated Gaussian. Hence, combining the EDR with the Gaussian distribution of interareal distances, one finds that the distribution of area pairs with a given FLN indeed obeys a log-normal distribution (13).

These observations suggest that the EDR, which is a global distance rule, acts as a principle for resource allocation via the probability factor determined by the space constant λ . To what extent is the cortical network determined by this principle? To address this question, we defined two random network models [see (13) for details], one based on the EDR and the other on a constant distance rule (CDR, where projection length bears uniform cost). We then compared the statistical properties of these two sets of networks to those of the observed $G_{29 \times 29}$ subgraph. Only the EDR model captures the binary statistical graph properties of $G_{29 \times 29}$ on all scales (from local to

global), including motif distributions (84) and graph spectral properties. Most notably, the EDR but not the CDR generates graphs with a pronounced core-periphery structure, closely tracking the distribution of cliques in the $G_{29 \times 29}$ (Fig. 5C). This figure also demonstrates that the CDR model fails to produce cliques of size 8 and larger. This finding suggests that the existence of the dense core in the cortex reflects the cost-of-wiring principle expressed in the EDR.

Efficiency of Information Transfer

A simple measure of bandwidth for information transfer in complex networks can be defined via the average conductance between all source-target pairs in the network (85), called global efficiency, or (E_g). Conductance here is interpreted as in physics, by the inverse resistance of the directed path of minimal total path resistance through the network from the source node to the target node (see Box 1 for definitions of the quantities in terms of FLNs). The path resistance can be interpreted as the negative logarithm of the probability that activity in the source node will generate activity in the target node. Here, we equate bandwidth with axon number as reflected by FLN. Thus, a sequence of edges having large FLN values (or “high bandwidth” edges) directed from source to target would form a path of low resistance (high conductance), providing a high-bandwidth pathway for information transmission. To obtain a graded measure of global efficiency within the structure of $G_{29 \times 29}$ and to understand the role of weak projections, we computed E_g on the remaining network after the sequential removal of the weakest link (smallest FLN) and plotted it as function of the network density. Figure 5D shows that the global efficiency of the network does not change before 76% of the weakest links are removed, indicating the existence of a high global efficiency (high bandwidth) backbone formed by short-range paths (see Fig. 5, E and F). Indeed, the average length of the remaining edges at 24% remaining density is 16 mm compared to the 27-mm average length of the removed edges. This suggests that the cortical network is organized in such a manner as to be independent of the activity along the weak projections for high-bandwidth information transfer. We speculate that these long-range pathways, which we have shown to have a high binary specificity, may contribute to interareal synchronization between cooperating areas.

A more local notion of information transfer can be similarly defined (86), via the average conductance between all the pairs of nodes that are neighbors of a given node i , after the removal of node i , then averaging this quantity over all nodes i (see Box 1), called local efficiency, E_l . One can think of E_l as a measure of accessibility between the satellites of a town via routes that avoid the town. Figure 5D shows this quantity as a function of density (following the same weakest-

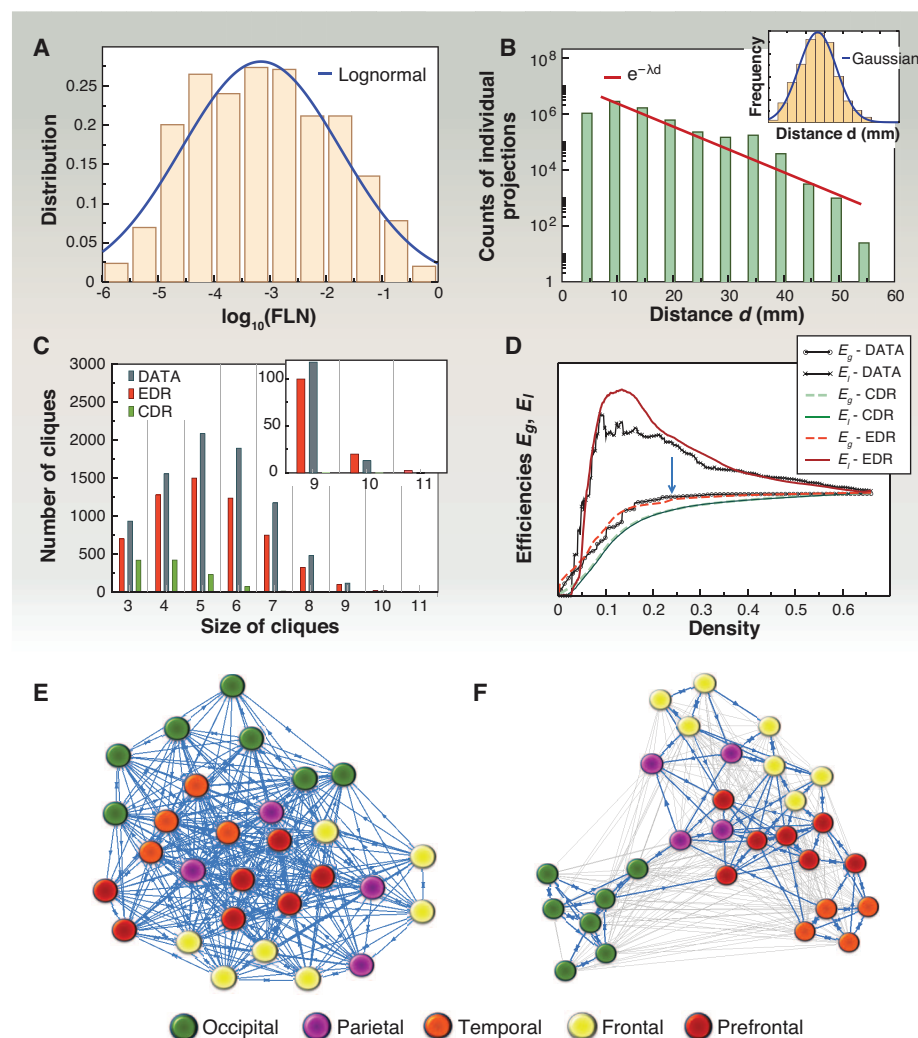


Fig. 5. A spatial network model of the cortex. (A) Distribution of FLN weights and its approximation by a log-normal. (B) The number of projections as function of projection distance d . (Inset) The distribution of interareal distances through the white matter is well approximated by a Gaussian. (C) The distribution of cliques in the $G_{29 \times 29}$ data network is well captured by the EDR model [see main text and (13)]. (D) Global (E_g) and local (E_l) efficiencies (see Box 1) as a function of network density during sequential removal of the weakest link. The EDR model (red) captures both data curves (black) much better than the CDR (green). (E) The $G_{29 \times 29}$ subgraph using a Kamada-Kawai force-based layout algorithm with all links considered with unit weight. (F) Same as (E) but considering the 24% strongest links only [blue arrow in (D)], with FLN weights. In this case, the areas are clustered into functional regions (13). Color code in (E) and (F) refers to regions (see key). For electronic data files, see www.core-nets.org.

The Heavily Connected Brain

link removal procedure as above). Intriguingly, local efficiency increases sharply with weak-link removal (or inactivity), compared to the global efficiency. The weak-link removal increases locality because the weak links are long-range. This tends to prune the interregional shortcuts and physiologically would be predicted to decrease interactions between diverse functional modalities, leading to a more localized structure of the remaining network. It eliminates those neighbors of a node to which it connects via weak links, thus disconnecting regions and modalities but preserving dense within-region connections. Accordingly, the paths linking the remaining neighbors of the node (avoiding that node) are all strong, having small path resistance (large conductance), and hence the measure of local ef-

iciency becomes large. The redundancy of local strong paths [the complete triangle is the most abundant three-motif, formed by strong links as shown in figure 3B of (13)] guarantees that the number of edges on a path between two nodes is small, which further decreases the path resistance between the nodes and hence further increases the local efficiency.

These changes in local efficiency indicate flexibility of network modularity and long-distance functional interactions—for example, in response to changes in cognitive load (13, 87). This suggests that in the cortical network, local information processing is voluminous, and because of the redundancy of local high-conductance paths, it is much more efficient than global information processing, whose efficiency acts at a constant base

line (Box 1). Notably, the organization of the cortical network around a high-efficiency backbone with constant global efficiency and optimal local efficiency behavior is also captured well by the EDR (Fig. 5D). These efficiencies are not binary graph measures, but are based on weights (FLNs). By contrast, the CDR fails completely, especially for the local efficiency measure (Fig. 5D).

Optimal Placement

The ability of the weight-distance relations of the $G_{29 \times 29}$ to predict numerous features of the cortical network underlines the importance of the embedded nature of real-world networks where nodes are located in three-dimensional (3D) Euclidean space and are linked by weighted and directed edges (88). An important aspect of the embedded cortical network is the spatial layout of cortical areas. Numerous studies have presented evidence that the spatial layout is optimized to minimize total wire length (89–91). A recent study used collated data for 95 areas of the macaque and claimed that optimized component rearrangements based on a simulated annealing algorithm could substantially reduce total wire (92). However, the database used by that study was edge-incomplete and the network density derived from it had a low density. In addition, weights were only classified as being on one of four levels. We adapted evolutionary optimization algorithms and applied them to our database to search for areal placements that minimize total wire length; we found alternative organizations that shorten the binary network by 5%. For the weighted network, the maximum reduction was less than 1% and involved a small number of switches between adjacent areas (Fig. 6) (13). Figure 6A shows a 3D representation of the $G_{29 \times 29}$ network with areas color coded to indicate regional identity. Figure 6B is an example of shuffled areal positions leading to increased wire length and loss of adjacency of areas originally from the same region. An optimization procedure applied to the randomized network leads to regional clustering similar to that observed in the cortex (Fig. 6C). Further, random networks based on the EDR had significantly shorter wire lengths than CDR-generated networks. These results therefore confirm that wire minimization is a constitutive organizational principle of the cortical network (89–91, 93–99) and suggest that this design constraint is at least partially implemented by the operation of the EDR generating the weight distributions of interareal projections (13).

Concluding Remarks

In summary, the interareal network achieves economy of connectivity and communication efficiency by means of a distribution of weights, spatial organization and a core-periphery structure in the form of a bow tie with a dense core. Interareal connections integrate across the local circuits via dual counter-streams located in the supra- and

Box 1. Efficiency measures for information transfer in networks.

In the simplest approximation, we may interpret the FLN weight f_{ij} of the projection from source area i to target area j as the probability $p_{i \rightarrow j}$ that activity in i will induce activity in j . Assuming that these are independent events, the probability of activity in area k induced along the path $i \rightarrow j \rightarrow k$ will be given by the product of the FLNs: $p_{i \rightarrow j \rightarrow k} = f_{ij} \cdot f_{jk}$ or $\ln(p_{i \rightarrow j \rightarrow k}) = \ln(p_{i \rightarrow j}) + \ln(p_{j \rightarrow k})$. Then, the positive quantity $w_{ij} = -\ln(f_{ij})$ can be interpreted as a measure of resistance for information transfer along the $i \rightarrow j$ link, as small FLN (weak links) induce a large resistance and vice versa. Additionally, based on our assumption above, the link resistance is additive along network paths. We define the resistance r_{xy} from an arbitrary node x to an arbitrary node y as the smallest sum of link resistances among all directed paths ω_{xy} from x to y , that is,

$r_{xy} = \min_{\omega_{xy}} \sum_{(i,j) \in \omega_{xy}} w_{ij}$. The highest transmission probability path will be the one, ω_{xy}^* , that achieves this minimum (see figure). The global efficiency measure E_g is defined as the average conductance (inverse resistance) between all the possible $N(N-1)$ node pairs, where N is the number of nodes in the network as shown in (A).

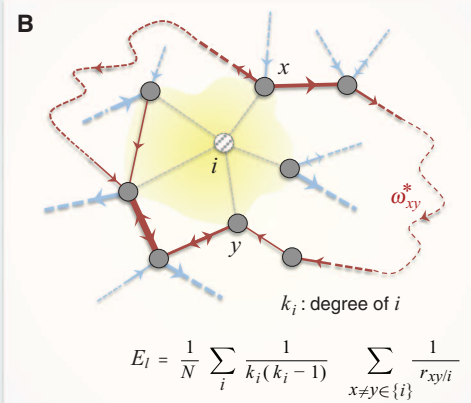
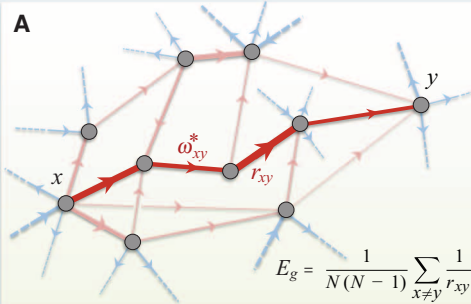
A local efficiency measure E_l is defined in (B): We remove a node i with all its links and then we compute the average of the resistances between all pairs of its neighbors as measured through the rest of the network, and finally, we average these quantities over all nodes i . Thus, E_l quantifies the degree to which the satellites of a typical city can communicate via paths that avoid the city (B).

A local efficiency measure E_l is defined in (B): We remove a node i with all its links and then we compute the average of the resistances between all pairs of its neighbors as measured through the rest of the network, and finally, we average these quantities over all nodes i . Thus, E_l quantifies the degree to which the satellites of a typical city can communicate via paths that avoid the city (B).

Schematics for efficiency measures.

(A) Global efficiency and (B) local efficiency. The dashed curves are schematic paths through the rest of the network (not shown). Here $\{i\}$ denotes the set of network neighbors of node i .

$p_{i \rightarrow j} = f_{ij}$, $p_{i \rightarrow j \rightarrow k} = f_{ij} f_{jk}$ or $\ln p_{i \rightarrow j \rightarrow k} = \ln f_{ij} + \ln f_{jk}$
link resistance: $w_{ij} = -\ln f_{ij} \implies w_{ik} = w_{ij} + w_{jk}$ - additive
 $i \rightarrow j$ Large FLN f_{ij} , small link resistance $w_{ij} = -\ln f_{ij}$
 $i \rightarrow j$ Small FLN f_{ij} , large link resistance $w_{ij} = -\ln f_{ij}$



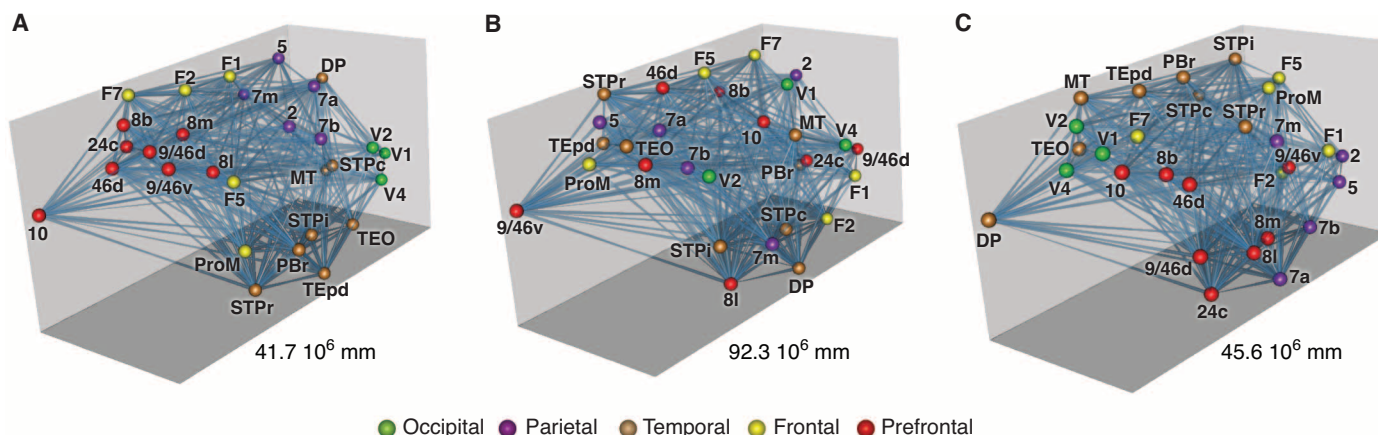


Fig. 6. Spatial positioning of areas and overall wire-length minimization. (A) A 3D representation of $G_{29 \times 29}$, nodes positioned at the barycenters of the corresponding areas identified on brain surface reconstructions (not shown). Edges are visualized as straight lines, but the wire-length calculations for pairs of areas use the axonal trajectory generated as the shortest possible path restricted to the white matter. Color coded for regions (see key). Wire length is the product of the number of neurons involved in

the pathway with the estimated pathway length. (B) Random repositioning of areas with connectivity preservation leads to wire-length increase. (C) An adapted harmony search algorithm reduces the wire length of the starting network in (B). Wire reduction is accompanied by restoration of areal adjacencies. Solutions that fail to reconstruct the initial network exhibit increased wire length with respect to (A). Number in each panel refers to wire lengths.

infragranular layers, which have distinct physiological properties. Further explorations of the impact of the cortical core on the local circuit should improve our understanding of their dynamic interaction.

The broadband connections involving large number of cells that form the global efficiency backbone and that are expected to shape receptive fields in target areas are short range and strongly cluster areas of a given modality. The considerably more numerous long-distance connections are sparse and exhibit high binary specificity; we speculate that these connections serve to promote cortical communication by controlling oscillatory coherence (77) possibly via contraction dynamics (100). During primate evolution the increase in numbers of areas and their spatially restricted broadband connections raises the possibility that increases in brain size would lead to increased isolation of clustered communities (101, 102). We hypothesize that weak long-distance connections appeared during recent evolution and may facilitate cooperation between distant areas. Assuming that a high-density connectivity is a characteristic feature of the interareal cortical graph, long-distance weak links may allow preservation of the connectedness of the cortical network following cortical expansion. Further, long-distance connections allow accommodation of novel information processing, thereby building over evolutionary time upon the existing repertoire of dynamic functions. There are a number of advantages to be gained (see below) by developing a high efficiency central core that we along with others have observed. Long-distance connections particularly for the higher association areas play a special role in forming the cortical core. The high incidence of long-distance projections involving prefrontal areas (11) suggests a

particular importance of this cortical region in core-periphery integration, indicating the cortical core as an important component of higher order interareal architectures (103, 104).

Self-organization in cortical development is well established (105). The findings summarized above suggest interesting parallels with other, highly functional, self-organizing information-processing networks. The high density, yet highly specific nature, of $G_{29 \times 29}$ suggests a heterogeneous, expandable, and cost-efficient information-processing network subject to evolutionary constraints. In particular, we find (i) high connectivity, (ii) high global accessibility, and (iii) large path diversity. Additional evidence supports several further constraints: (iv) a high bisection bandwidth (Fig. 4D); (v) resilience to connectivity failures (global conductance measurements in Fig. 5D show that during sequential removal of the weakest links, a substantial decline in the network's global efficiency is not reached until a density of 24%); and (vi) incremental expandability that allows addition of new areas to the network during evolution, without a substantial wiring overhaul to maintain or improve performance, also supported by optimal placement studies. The global efficiency and the optimal layout of the $G_{29 \times 29}$ are supportive of (vi). As seen in Fig. 5D, global efficiency stays constant with weak-link removal. Weak links are long-range and might be more prevalent in large brains. Conversely, adding long-range links (during cortical expansion) seems not to affect the global efficiency, much less worsen it (as would be expected in a complete overhaul). In terms of optimal layout, the total wiring in $G_{29 \times 29}$ [see (13)] is minimal as a consequence of the EDR. It remains minimal following the addition of new areas with strong links to their neighbors and progressively weaker links to distant areas.

This corresponds to an optimal spatial arrangement, consistent with incremental expandability. In an interesting parallel, a recent study on efficient, massive data-processing networks shows that for their purposes, random structures with a pronounced core-periphery organization allow incremental growth without sacrificing their high bisection bandwidth and throughput capability (106).

Although primate neocortex shares a number of common features with human-made, large-scale information-processing networks, there are also crucial differences, and so the analogies should not be overextended. One important difference is that in current technological information networks, information (including a destination address) is encoded within the units (packets) that are sent along the edges of the network (packet-switching networks), whereas this does not appear to be the case for the brain. Our results show that spatial location does influence the wiring properties of the brain. Further, in the brain, the location and timing of activity (in the context of other firing activities) represent the message (neural coding), thus linking network activity to the structural properties of the cortical network. In the Internet or World Wide Web, however, it does not matter where the routers are physically in space, because the packets are routed on the basis of network addresses encoded into the packet. This key difference suggests that spatio-temporal network models should hold more promise for brain science than generic, purely graph theoretical models such as the SW model.

Future Perspectives

While the high density of the binary interareal graph is not consistent with a SW architecture at the computational level of a cortical area, the SW

The Heavily Connected Brain

concept may nonetheless be relevant at finer spatial scales. For example, the high clustering and short path lengths indicative of SW architecture are suggested by diffusion magnetic resonance imaging (MRI) analysis at a node scale of a few millimeters (about the size of the voxels) (107). Here, the importance of the SW parameters revealed by this approach must be considered with respect to the methodological thresholding imposed by the whole-brain imaging technique. The

nonrandom connectivity at the single-cell level raises the issue of SW architecture at this scale (108, 109). The rich variety of cell identities posits a conceptual challenge for the potential of SW network at the single-cell level. Large-scale circuit mapping at the single-cell level is not currently feasible, although innovative approaches might conceivably provide the appropriate data in mice (110). At the interareal level, our results indicate that the spatially embedded nature of the

cortical network determines many of its properties, such as structural and weighted graph characteristics. Could similar weight-distance relations operate for single neurons, thereby suggesting a similar operational logic over different scales? Like interareal connectivity, local connectivity shows an exponential density decay (10), reflecting the decrease in the likelihood of synaptic contact with distance (111). Also, log-normal distributions like that of interareal weights have been observed for the distribution of synaptic strengths of single neurons (109).

The EDR that we describe shows that the spatial constant of interareal density decay accounts for many of the binary and weighted features of the cortical graph, as well as the important design feature of wire minimization. Given the high scalability of mammalian neocortex, accommodating five orders of magnitude range of brain weight (112), we examined the spatial location of cortical areas in the $G_{29 \times 29}$ subgraph and found that when magnitude of connections is taken into account, it shows an optimal placement of area positions indicating minimization of metabolic expenditure on total wire length, also well predicted by the EDR. Given these results it will be instructive to explore the weight-distance relations in different species to determine how the decay parameter λ changes with brain size. This may provide insights into a common rule governing scaling properties of the brain and also allow improved extrapolation of our understanding of the connectivity of the macaque brain obtained using invasive techniques to the larger and less directly accessible human brain.

A core-periphery structure has been observed in other self-organized information-processing architectures, both human-made such as the World Wide Web (113) and the Internet (114, 115), and in biological networks, such as in metabolism (116, 117), the immune system (118), and cell signaling (119–121). The resulting bow tie is an evolutionarily favored structure for a wide variety of complex networks (122, 123), expressing the fact that functional or living systems have an input interface, a processing unit, and an output interface. This is because these systems are not in thermodynamic equilibrium and are required to maintain energy and matter flow through the system. While the overall bow-tie structure is common, we have seen that for the brain it emerges through a counterstream organization of the directed links between core and periphery, showing its specific nature when compared to other bow ties in biology or technical networks. However, the full details of this structural organization will only become evident when additional tracer-based anatomical data are incorporated.

Although the interareal connectivity data explored here has revealed interesting features of the cortical network, many additional analyses remain to be done. It will be important to complement the quantification of connectivity by func-

Box 2. Glossary of technical terms.

1. Area: A region of the cortex with specific cytoarchitecture and associated with a function. **Target area:** An area that received a retrograde tracer injection. **Source area:** An area containing labeled neurons projecting to a target area.

2. Average path length: Average value of shortest path lengths between all node pairs in the graph. Length here is measured in hop-counts along directed edges.

3. Binary specificity: The degree to which a network or a graph differs in its binary graph theoretical properties from a random graph.

4. Bisection bandwidth: The minimum of the number of connections between two, equal-size partitions of the nodes of a graph, taken over all such partitions.

5. Clustering: The average of the fraction of connected neighbors of a node (fraction of triangles).

6. Counterstream: Refers to the organization principle by which there are streams ascending (supragranular layer) and descending (infragranular layer) the cortical hierarchy (135). Recently, this has been extended to include a dual counterstream organization where an ascending and descending stream is identified in each of the two compartments (12).

7. Dominating set: A set of nodes in a graph such that all nodes of the graph have at least one edge with one of their end-nodes in this set.

8. Edge: A link or connection between two nodes directed from one to the other, here interareal pathway. There can be at most two directed links, oppositely oriented between any two nodes.

9. Edge-complete subgraph: A subgraph that has exactly the same connections between its nodes as the connections between the same nodes in the larger graph that this subgraph is part of.

10. FLN: Fraction of labeled neurons: For a given injection (target area i) and source area j , the FLN is the ratio f_{ji} between the number of labeled neurons in area j and the total number of extrinsic (not in i) labeled neurons for that injection. We use FLN as a measure of weight (10, 58).

11. $G_{n \times m}$ (sub)graph or matrix: For every one of the n targets (injected areas), it specifies which of the m sources project into that target (0 if no projection, 1 if there is a projection). Here, $G_{91 \times 91}$ denotes the full graph of interareal connections, $G_{29 \times 91}$ represents the currently known projections from all areas into the injected 29 areas, and $G_{29 \times 29}$ denotes the subgraph formed by the connections among the target areas only. The latter is edge-complete, i.e., the status of connectivity is fully known within this set of nodes.

12. Nodes: Discrete entities represented as points or vertices in graph theory for the purpose of studying the patterns of interactions among them (represented as links or edges). In this case, a node represents a cortical area.

13. SLN: The fraction of supragranular labeled neurons is defined for each source area projecting to an injected target area. SLN corresponds to the number of retrogradely labeled neurons located in the supragranular layer divided by the total number of neurons (in infra- and supragranular layers). SLN distinguishes FF and FB pathways and can be used to calculate hierarchical distance (12, 54, 55).

tional and improved molecular characterization of cortical areas and also of the parent neurons (124–126). A necessary and complementary development will be to use anterograde tracers to examine the laminar integration of interareal connectivity, combining quantification and morphological characterization at the synaptic level (127, 128). Finally, our use of the term “canonical microcircuit” in the sense of a stereotyped circuit constituting a fundamental cortical building block should be tempered by the evidence for large regional differences in cell densities and dendritic arbor sizes (129, 130). While it is generally accepted that the local circuit exhibits cell-specific connectivity across the cortex (thereby conforming to a canonical circuit) and likewise that there are consistent input-output patterns across the different areas (131), there is nevertheless only a single quantitative interlaminar connectivity map, namely, for cat area 17 (132). The concept of the canonical microcircuit provides a coherent framework for thinking about neocortical function, and evidence of variations of local connectivity point to the need to establish additional quantitative interlaminar maps. Dynamic models built on existing quantitative interlaminar maps (132, 133) give realistic dynamics (134). Extending this type of modeling to include interareal relations becomes a reasonable next step.

References and Notes

- S. L. Bressler, V. Menon, Large-scale brain networks in cognition: Emerging methods and principles. *Trends Cogn. Sci.* **14**, 277–290 (2010). doi: [10.1016/j.tics.2010.04.004](#); pmid: [20493761](#)
- V. B. Mountcastle, The columnar organization of the neocortex. *Brain* **120**, 701–722 (1997). doi: [10.1093/brain/120.4.701](#); pmid: [9153131](#)
- M. G. Rosa, R. Tweedale, Brain maps, great and small: Lessons from comparative studies of primate visual cortical organization. *Philos. Trans. R. Soc. Lond. B Biol. Sci.* **360**, 665–691 (2005). doi: [10.1098/rstb.2005.1626](#); pmid: [15937007](#)
- S. Zeki, The Ferrier Lecture, The Ferrier Lecture 1995 behind the seen: The functional specialization of the brain in space and time. *Philos. Trans. R. Soc. Lond. B Biol. Sci.* **360**, 1145–1183 (2005). doi: [10.1098/rstb.2005.1666](#); pmid: [16147515](#)
- A. Schüz, M. Miller, *Cortical Areas: Unity and Diversity* (Taylor and Francis, London, 2002).
- D. C. Van Essen, M. F. Glasser, D. L. Dierker, J. Harwell, Cortical parcellations of the macaque monkey analyzed on surface-based atlases. *Cereb. Cortex* **22**, 2227–2240 (2012). doi: [10.1093/cercor/bhr290](#); pmid: [22052704](#)
- S. L. Bressler, Inferential constraint sets in the organization of visual expectation. *Neuroinformatics* **2**, 227–238 (2004). doi: [10.1385/Nl:2:2:227](#); pmid: [15319518](#)
- N. T. Markov *et al.*, A weighted and directed interareal connectivity matrix for macaque cerebral cortex. *Cereb. Cortex* (2012). doi: [10.1093/cercor/bhs270](#); pmid: [23010748](#)
- J. L. Lanciego, F. G. Wouterlood, A half century of experimental neuroanatomical tracing. *J. Chem. Neuroanat.* **42**, 157–183 (2011). doi: [10.1016/j.jchemneu.2011.07.001](#); pmid: [21782932](#)
- N. T. Markov *et al.*, Weight consistency specifies regularities of macaque cortical networks. *Cereb. Cortex* **21**, 1254–1272 (2011). doi: [10.1093/cercor/bhq201](#); pmid: [21045004](#)
- N. T. Markov *et al.*, The role of long-range connections on the specificity of the macaque interareal cortical network. *Proc. Natl. Acad. Sci. U.S.A.* **110**, 5187–5192 (2013). doi: [10.1073/pnas.1218972110](#); pmid: [23479610](#)
- N. T. Markov *et al.*, The anatomy of hierarchy: Feedforward and feedback pathways in macaque visual cortex. *J. Comp. Neurol.* n/a (2013). doi: [10.1002/cne.23458](#); pmid: [23983048](#)
- M. Ercsey-Ravasz *et al.*, A predictive network model of cerebral cortical connectivity based on a distance rule. *Neuron* **80**, 184–197 (2013). doi: [10.1016/j.neuron.2013.07.036](#); pmid: [24094111](#)
- C. D. Gilbert, T. N. Wiesel, Morphology and intracortical projections of functionally characterised neurones in the cat visual cortex. *Nature* **280**, 120–125 (1979). doi: [10.1038/280120a0](#); pmid: [552600](#)
- R. J. Douglas, K. A. C. Martin, D. Whitteridge, A canonical microcircuit for neocortex. *Neural Comput.* **1**, 480–488 (1989). doi: [10.1162/neco.1989.1.4.480](#)
- R. J. Douglas, C. Koch, M. Mahowald, K. A. Martin, H. H. Suarez, Recurrent excitation in neocortical circuits. *Science* **269**, 981–985 (1995). doi: [10.1126/science.7638624](#); pmid: [7638624](#)
- D. J. Felleman, D. C. Van Essen, Distributed hierarchical processing in the primate cerebral cortex. *Cereb. Cortex* **1**, 1–47 (1991). doi: [10.1093/cercor/1.1.1](#); pmid: [1822724](#)
- A. M. Bastos *et al.*, Canonical microcircuits for predictive coding. *Neuron* **76**, 695–711 (2012). doi: [10.1016/j.neuron.2012.10.038](#); pmid: [23177956](#)
- J. H. Kaas, T. A. Hackett, M. J. Tramo, Auditory processing in primate cerebral cortex. *Curr. Opin. Neurobiol.* **9**, 164–170 (1999) [published erratum appears in *Curr. Opin. Neurobiol.* **9**, 500 (1999)]. doi: [10.1016/S0959-4388\(99\)80022-1](#); pmid: [10322185](#)
- D. Bousaoud, L. G. Ungerleider, R. Desimone, Pathways for motion analysis: Cortical connections of the medial superior temporal and fundus of the superior temporal visual areas in the macaque. *J. Comp. Neurol.* **296**, 462–495 (1990). doi: [10.1002/cne.902960311](#); pmid: [2358548](#)
- S. Shipp, The importance of being agranular: A comparative account of visual and motor cortex. *Philos. Trans. R. Soc. Lond. B Biol. Sci.* **360**, 797–814 (2005). doi: [10.1098/rstb.2005.1630](#); pmid: [15937013](#)
- R. A. Adams, S. Shipp, K. J. Friston, Predictions not commands: Active inference in the motor system. *Brain Struct. Funct.* **218**, 611–643 (2013). doi: [10.1007/s00429-012-0475-5](#); pmid: [23129312](#)
- H. Barbas, Pattern in the laminar origin of corticocortical connections. *J. Comp. Neurol.* **252**, 415–422 (1986). doi: [10.1002/cne.902520310](#); pmid: [3793985](#)
- H. Barbas, N. Rempel-Clower, Cortical structure predicts the pattern of corticocortical connections. *Cereb. Cortex* **7**, 635–646 (1997). doi: [10.1093/cercor/7.7.635](#); pmid: [9373019](#)
- E. Koehlin, C. Ody, F. Kouneither, The architecture of cognitive control in the human prefrontal cortex. *Science* **302**, 1181–1185 (2003). doi: [10.1126/science.1088545](#); pmid: [14615530](#)
- R. C. O'Reilly, S. A. Herd, W. M. Pauli, Computational models of cognitive control. *Curr. Opin. Neurobiol.* **20**, 257–261 (2010). doi: [10.1016/j.conb.2010.01.008](#); pmid: [20185294](#)
- M. M. Botvinick, Hierarchical models of behavior and prefrontal function. *Trends Cogn. Sci.* **12**, 201–208 (2008). doi: [10.1016/j.tics.2008.02.009](#); pmid: [18420448](#)
- E. Bullmore, O. Sporns, The economy of brain network organization. *Nat. Rev. Neurosci.* **13**, 336–349 (2012). pmid: [22498897](#)
- M. E. Raichle, Two views of brain function. *Trends Cogn. Sci.* **14**, 180–190 (2010). doi: [10.1016/j.tics.2010.01.008](#); pmid: [20206576](#)
- M. E. J. Newman, The structure and function of complex networks. *SIAM Rev.* **45**, 167–256 (2003). doi: [10.1137/S0036144503042480](#)
- D. J. Watts, S. H. Strogatz, Collective dynamics of ‘small-world’ networks. *Nature* **393**, 440–442 (1998). doi: [10.1038/30918](#); pmid: [9623998](#)
- G. Tononi, O. Sporns, G. M. Edelman, A measure for brain complexity: Relating functional segregation and integration in the nervous system. *Proc. Natl. Acad. Sci. U.S.A.* **91**, 5033–5037 (1994). doi: [10.1073/pnas.91.11.5033](#); pmid: [8197179](#)
- O. Sporns, C. J. Honey, Small worlds inside big brains. *Proc. Natl. Acad. Sci. U.S.A.* **103**, 19219–19220 (2006). doi: [10.1073/pnas.0609523103](#); pmid: [17159140](#)
- C. J. Honey, R. Köster, M. Breakspear, O. Sporns, Network structure of cerebral cortex shapes functional connectivity on multiple time scales. *Proc. Natl. Acad. Sci. U.S.A.* **104**, 10240–10245 (2007). doi: [10.1073/pnas.0701519104](#); pmid: [17548818](#)
- O. Sporns, G. Tononi, G. M. Edelman, Theoretical neuroanatomy: Relating anatomical and functional connectivity in graphs and cortical connection matrices. *Cereb. Cortex* **10**, 127–141 (2000). doi: [10.1093/cercor/10.2.127](#); pmid: [10667981](#)
- C. C. Hilgetag, G. A. Burns, M. A. O'Neill, J. W. Scannell, M. P. Young, Anatomical connectivity defines the organization of clusters of cortical areas in the macaque monkey and the cat. *Philos. Trans. R. Soc. Lond. B Biol. Sci.* **355**, 91–110 (2000). doi: [10.1098/rstb.2000.0551](#); pmid: [10703046](#)
- K. E. Stephan *et al.*, Computational analysis of functional connectivity between areas of primate cerebral cortex. *Philos. Trans. R. Soc. Lond. B Biol. Sci.* **355**, 111–126 (2000). doi: [10.1098/rstb.2000.0552](#); pmid: [10703047](#)
- O. Sporns, J. D. Zwi, The small world of the cerebral cortex. *Neuroinformatics* **2**, 145–162 (2004). doi: [10.1385/Nl:2:2:145](#); pmid: [15319512](#)
- H. Kennedy, K. Knoblauch, Z. Toroczkai, Why data coherence and quality is critical for understanding interareal cortical networks. *Neuroimage* **80**, 37–45 (2013). doi: [10.1016/j.neuroimage.2013.04.031](#); pmid: [23603347](#)
- J. Vezoli *et al.*, Quantitative analysis of connectivity in the visual cortex: Extracting function from structure. *Neuroscientist* **10**, 476–482 (2004). doi: [10.1177/1073858404268478](#); pmid: [15359013](#)
- For criteria for inclusion of injection sites, see Markov *et al.* (8); for discussion of the sensitivity and location of uptake zones of the tracers used, see supplementary information in Markov *et al.* (10); for sampling frequency and detection of weak connections see Vezoli *et al.* (40); for atlases and electronic data files, see [www.core-nets.org](#).
- M. E. J. Newman, *Networks: An Introduction* (Oxford Univ. Press, Oxford, 2010).
- M. P. Young, The organization of neural systems in the primate cerebral cortex. *Proc. R. Soc. Lond. B Biol. Sci.* **252**, 13–18 (1993). doi: [10.1098/rspb.1993.0040](#); pmid: [8389046](#)
- D. S. Modha, R. Singh, Network architecture of the long-distance pathways in the macaque brain. *Proc. Natl. Acad. Sci. U.S.A.* **107**, 13485–13490 (2010). doi: [10.1073/pnas.1008054107](#); pmid: [20628011](#)
- B. Jouve, P. Rosenstiel, M. Imbert, A mathematical approach to the connectivity between the cortical visual areas of the macaque monkey. *Cereb. Cortex* **8**, 28–39 (1998). doi: [10.1093/cercor/8.1.28](#); pmid: [9510383](#)
- M. Barthélemy, Spatial networks. *Phys. Rep.* **499**, 1–101 (2011). doi: [10.1016/j.physrep.2010.11.002](#)
- K. S. Rockland, D. N. Pandya, Laminar origins and terminations of cortical connections of the occipital lobe in the rhesus monkey. *Brain Res.* **179**, 3–20 (1979). doi: [10.1016/0006-8993\(79\)90485-2](#); pmid: [116716](#)
- D. C. Van Essen, S. M. Zeki, The topographic organization of rhesus monkey prestriate cortex. *J. Physiol.* **277**, 193–226 (1978). pmid: [418173](#)
- M. Wong-Riley, Reciprocal connections between striate and prestriate cortex in squirrel monkey as demonstrated by combined peroxidase histochemistry and autoradiography. *Brain Res.* **147**, 159–164 (1978). doi: [10.1016/0006-8993\(78\)90781-3](#); pmid: [77701](#)
- J. H. Kaas, C. S. Lin, Cortical projections of area 18 in owl monkeys. *Vision Res.* **17**, 739–741 (1977). doi: [10.1016/S0042-6989\(77\)80013-8](#); pmid: [414440](#)
- J. Tigges, W. B. Spatz, M. Tigges, Reciprocal point-to-point connections between parastriate and striate cortex

The Heavily Connected Brain

- in the squirrel monkey (Saimiri). *J. Comp. Neurol.* **148**, 481–489 (1973). doi: [10.1002/cne.901480406](#); pmid: [4350354](#)
52. J. H. R. Maunsell, D. C. van Essen, The connections of the middle temporal visual area (MT) and their relationship to a cortical hierarchy in the macaque monkey. *J. Neurosci.* **3**, 2563–2586 (1983). pmid: [6655500](#)
53. C. C. Hilgetag, M. A. O'Neill, M. P. Young, Indeterminate organization of the visual system. *Science* **271**, 776–777 (1996). doi: [10.1126/science.271.5250.776](#); pmid: [8628990](#)
54. P. Barone, A. Batardiere, K. Knoblauch, H. Kennedy, Laminar distribution of neurons in extrastriate areas projecting to visual areas V1 and V4 correlates with the hierarchical rank and indicates the operation of a distance rule. *J. Neurosci.* **20**, 3263–3281 (2000). pmid: [1077791](#)
55. A. T. Reid, A. Krumnack, E. Wanke, R. Kötter, Optimization of cortical hierarchies with continuous scales and ranges. *Neuroimage* **47**, 611–617 (2009). doi: [10.1016/j.neuroimage.2009.04.061](#); pmid: [19398021](#)
56. A. Krumnack, A. T. Reid, E. Wanke, G. Bezgin, R. Kötter, Criteria for optimizing cortical hierarchies with continuous ranges. *Front. Neuroinform.* **4**, 7 (2010). pmid: [20407634](#)
57. N. T. Markov, H. Kennedy, The importance of being hierarchical. *Curr. Opin. Neurobiol.* **23**, 187–194 (2013). doi: [10.1016/j.conb.2012.12.008](#); pmid: [23339864](#)
58. S. Clavagnier, A. Falchier, H. Kennedy, Long-distance feedback projections to area V1: Implications for multisensory integration, spatial awareness, and visual consciousness. *Cogn. Affect. Behav. Neurosci.* **4**, 117–126 (2004). doi: [10.3758/CABN.4.2.117](#); pmid: [15460918](#)
59. H. Supér, V. A. Lamme, Strength of figure-ground activity in monkey primary visual cortex predicts saccadic reaction time in a delayed detection task. *Cereb. Cortex* **17**, 1468–1475 (2007). doi: [10.1093/cercor/bhl058](#); pmid: [16920884](#)
60. J. F. Jehee, P. R. Roelfsema, G. Deco, J. M. Murre, V. A. Lamme, Interactions between higher and lower visual areas improve shape selectivity of higher level neurons—explaining crowding phenomena. *Brain Res.* **1157**, 167–176 (2007). doi: [10.1016/j.brainres.2007.03.090](#); pmid: [17540349](#)
61. H. S. Scholte, J. Jolij, J. J. Fahrenfort, V. A. Lamme, Feedforward and recurrent processing in scene segmentation: Electroencephalography and functional magnetic resonance imaging. *J. Cogn. Neurosci.* **20**, 2097–2109 (2008). doi: [10.1162/jocn.2008.20142](#); pmid: [18416684](#)
62. C. M. Chen *et al.*, Functional anatomy and interaction of fast and slow visual pathways in macaque monkeys. *Cereb. Cortex* **17**, 1561–1569 (2007). doi: [10.1093/cercor/bhl067](#); pmid: [16950866](#)
63. L. B. Ekstrom, P. R. Roelfsema, J. T. Arsenault, G. Bonmassar, W. Vanduffel, Bottom-up dependent gating of frontal signals in early visual cortex. *Science* **321**, 414–417 (2008). doi: [10.1126/science.1153276](#); pmid: [18635806](#)
64. M. W. Self, R. N. Kooijmans, H. Supér, V. A. Lamme, P. R. Roelfsema, Different glutamate receptors convey feedforward and recurrent processing in macaque V1. *Proc. Natl. Acad. Sci. U.S.A.* **109**, 11031–11036 (2012). doi: [10.1073/pnas.1119527109](#); pmid: [22615394](#)
65. H. Kennedy, J. Bullier, A double-labeling investigation of the afferent connectivity to cortical areas V1 and V2 of the macaque monkey. *J. Neurosci.* **5**, 2815–2830 (1985). pmid: [3840201](#)
66. K. S. Rockland, in *Extrastriate Cortex in Primates*, K. S. Rockland, J. H. Kaas, A. Peters, Eds. (Plenum Press, New York, 1997), vol. 12, pp. 243–293.
67. J. Tigges *et al.*, Areal and laminar distribution of neurons interconnecting the central visual cortical areas 17, 18, 19, and MT in squirrel monkey (Saimiri). *J. Comp. Neurol.* **192**, 539–560 (1981). doi: [10.1002/cne.902020407](#); pmid: [7298914](#)
68. J. Bullier, in *23 Problems in Systems Neuroscience*, J. L. van Hemmen, T. J. Sejnowski, Eds. (Oxford University Press USA, 2006), pp. 103–132.
69. T. S. Lee, D. Mumford, Hierarchical Bayesian inference in the visual cortex. *J. Opt. Soc. Am. A Opt. Image Sci. Vis.* **20**, 1434–1448 (2003). doi: [10.1364/JOSAA.20.001434](#); pmid: [12868647](#)
70. K. Friston, The free-energy principle: A unified brain theory? *Nat. Rev. Neurosci.* **11**, 127–138 (2010). doi: [10.1038/nrn2787](#); pmid: [20068583](#)
71. E. A. Buffalo, P. Fries, R. Landman, T. J. Buschman, R. Desimone, Laminar differences in gamma and alpha coherence in the ventral stream. *Proc. Natl. Acad. Sci. U.S.A.* **108**, 11262–11267 (2011). doi: [10.1073/pnas.1011284108](#); pmid: [21690410](#)
72. D. Xing, C. I. Yeh, S. Burns, R. M. Shapley, Laminar analysis of visually evoked activity in the primary visual cortex. *Proc. Natl. Acad. Sci. U.S.A.* **109**, 13871–13876 (2012). doi: [10.1073/pnas.1201478109](#); pmid: [22872866](#)
73. G. G. Gregoriou, S. J. Gotts, H. Zhou, R. Desimone, High-frequency, long-range coupling between prefrontal and visual cortex during attention. *Science* **324**, 1207–1210 (2009). doi: [10.1126/science.1171402](#); pmid: [19478185](#)
74. C. A. Bosman *et al.*, Attentional stimulus selection through selective synchronization between monkey visual areas. *Neuron* **75**, 875–888 (2012). doi: [10.1016/j.neuron.2012.06.037](#); pmid: [22958827](#)
75. R. F. Salazar, N. M. Dotson, S. L. Bressler, C. M. Gray, Content-specific fronto-parietal synchronization during visual working memory. *Science* **338**, 1097–1100 (2012). doi: [10.1126/science.1224000](#); pmid: [23118014](#)
76. X. J. Wang, Neurophysiological and computational principles of cortical rhythms in cognition. *Physiol. Rev.* **90**, 1195–1268 (2010). doi: [10.1152/physrev.00035.2008](#); pmid: [20664082](#)
77. P. Fries, A mechanism for cognitive dynamics: Neuronal communication through neuronal coherence. *Trends Cogn. Sci.* **9**, 474–480 (2005). doi: [10.1016/j.tics.2005.08.011](#); pmid: [16150631](#)
78. J. C. Anderson, H. Kennedy, K. A. Martin, Pathways of attention: Synaptic relationships of frontal eye field to V4, lateral intraparietal cortex, and area 46 in macaque monkey. *J. Neurosci.* **31**, 10872–10881 (2011). doi: [10.1523/JNEUROSCI.0622-11.2011](#); pmid: [21795539](#)
79. F. Crick, C. Koch, Constraints on cortical and thalamic projections: The no-strong-loops hypothesis. *Nature* **391**, 245–250 (1998). doi: [10.1038/34584](#); pmid: [9440687](#)
80. L. Harriger, M. P. van den Heuvel, O. Sporns, Rich club organization of macaque cerebral cortex and its role in network communication. *PLOS ONE* **7**, e46497 (2012). doi: [10.1371/journal.pone.0046497](#); pmid: [23029538](#)
81. M. A. de Reus, M. P. van den Heuvel, Rich club organization and intermodule communication in the cat connectome. *J. Neurosci.* **33**, 12929–12939 (2013). doi: [10.1523/JNEUROSCI.1448-13.2013](#); pmid: [23926249](#)
82. M. P. van den Heuvel, R. S. Kahn, J. Goñi, O. Sporns, High-cost, high-capacity backbone for global brain communication. *Proc. Natl. Acad. Sci. U.S.A.* **109**, 11372–11377 (2012). doi: [10.1073/pnas.1203593109](#); pmid: [22711833](#)
83. C. Bron, J. Kerbosch, Algorithm 457: Finding all cliques of an undirected graph. *Commun. ACM* **16**, 575–577 (1973). doi: [10.1145/362342.362367](#)
84. R. Milo *et al.*, Superfamilies of evolved and designed networks. *Science* **303**, 1538–1542 (2004). doi: [10.1126/science.1089167](#); pmid: [15001784](#)
85. V. Latora, M. Marchiori, Economic small-world behavior in weighted networks. *Eur. Phys. J. B* **32**, 249–263 (2003). doi: [10.1140/epjbe/e2003-00095-5](#)
86. I. Vragović, E. Louis, A. Díaz-Guilera, Efficiency of informational transfer in regular and complex networks. *Phys. Rev. E Stat. Nonlin. Soft Matter Phys.* **71** (3 Pt. 2A), 036122 (2005). doi: [10.1103/PhysRevE.71.036122](#); pmid: [15903508](#)
87. M. G. Kitzbichler, R. N. Henson, M. L. Smith, P. J. Nathan, E. T. Bullmore, Cognitive effort drives workspace configuration of human brain functional networks. *J. Neurosci.* **31**, 8259–8270 (2011). doi: [10.1523/JNEUROSCI.0440-11.2011](#); pmid: [21632947](#)
88. S. Boccaletti, V. Latora, Y. Moreno, M. Chavez, D. U. Hwang, Complex networks: Structure and dynamics. *Phys. Rep.* **424**, 175–308 (2006). doi: [10.1016/j.physrep.2005.10.009](#)
89. C. Cheriak, Z. Mokhtarzada, R. Rodriguez-Esteban, K. Changizi, Global optimization of cerebral cortex layout. *Proc. Natl. Acad. Sci. U.S.A.* **101**, 1081–1086 (2004). doi: [10.1073/pnas.0305212101](#); pmid: [14722353](#)
90. V. A. Klyachko, C. F. Stevens, Connectivity optimization and the positioning of cortical areas. *Proc. Natl. Acad. Sci. U.S.A.* **100**, 7937–7941 (2003). doi: [10.1073/pnas.0932745100](#); pmid: [12796510](#)
91. A. Raj, Y. H. Chen, The wiring economy principle: Connectivity determines anatomy in the human brain. *PLOS ONE* **6**, e14832 (2011). doi: [10.1371/journal.pone.0014832](#); pmid: [21915250](#)
92. M. Kaiser, C. C. Hilgetag, Nonoptimal component placement, but short processing paths, due to long-distance projections in neural systems. *PLOS Comput. Biol.* **2**, e95 (2006). doi: [10.1371/journal.pcbi.0020095](#); pmid: [16848638](#)
93. C. Cheriak, Component placement optimization in the brain. *J. Neurosci.* **14**, 2418–2427 (1994). pmid: [8158278](#)
94. C. Cheriak, Neural wiring optimization. *Prog. Brain Res.* **195**, 361–371 (2012). doi: [10.1016/B978-0-444-53860-4.00017-9](#); pmid: [22230636](#)
95. C. Cheriak, M. Changizi, D. Kang, Large-scale optimization of neuron arbors. *Phys. Rev. E Stat. Phys. Plasmas Fluids Relat. Interdiscip. Topics* **59** (5 Pt. B), 6001–6009 (1999). doi: [10.1103/PhysRevE.59.6001](#); pmid: [11969583](#)
96. D. B. Chklovskii, Optimal sizes of dendritic and axonal arbors in a topographic projection. *J. Neurophysiol.* **83**, 2113–2119 (2000). pmid: [10758121](#)
97. D. B. Chklovskii, T. Schikorski, C. F. Stevens, Wiring optimization in cortical circuits. *Neuron* **34**, 341–347 (2002). doi: [10.1016/S0896-6273\(02\)00679-7](#); pmid: [11988166](#)
98. A. A. Koulikov, D. B. Chklovskii, Orientation preference patterns in mammalian visual cortex: A wire length minimization approach. *Neuron* **29**, 519–527 (2001). doi: [10.1016/S0896-6273\(01\)00223-9](#); pmid: [11239440](#)
99. M. Rivera-Alba *et al.*, Wiring economy and volume exclusion determine neuronal placement in the *Drosophila* brain. *Curr. Biol.* **21**, 2000–2005 (2011). doi: [10.1016/j.cub.2011.10.022](#); pmid: [22119527](#)
100. W. Wang, J. J. Slotine, On partial contraction analysis for coupled nonlinear oscillators. *Biol. Cybern.* **92**, 38–53 (2005). doi: [10.1007/s00422-004-0527-x](#); pmid: [15650898](#)
101. S. Herculano-Houzel, B. Mota, P. Wong, J. H. Kaas, Connectivity-driven white matter scaling and folding in primate cerebral cortex. *Proc. Natl. Acad. Sci. U.S.A.* **107**, 19008–19013 (2010). doi: [10.1073/pnas.1012590107](#); pmid: [20956290](#)
102. R. J. Douglas, K. A. Martin, Behavioral architecture of the cortical sheet. *Curr. Biol.* **22**, R1033–R1038 (2012). doi: [10.1016/j.cub.2012.11.017](#); pmid: [23257185](#)
103. K. Man, J. Kaplan, H. Damasio, A. Damasio, Neural convergence and divergence in the mammalian cerebral cortex: From experimental neuroanatomy to functional neuroimaging. *J. Comp. Neurol.* **10.1002/cne.23408** (2013). doi: [10.1002/cne.23408](#); pmid: [23840023](#)
104. S. Dehaene, J. P. Changeux, Experimental and theoretical approaches to conscious processing. *Neuron* **70**, 200–227 (2011). doi: [10.1016/j.neuron.2011.03.018](#); pmid: [21521609](#)
105. H. Kennedy, C. Dehay, Self-organization and interareal networks in the primate cortex. *Prog. Brain Res.* **195**, 341–360 (2012). doi: [10.1016/B978-0-444-53860-4.00016-7](#); pmid: [22230635](#)
106. A. Singla, C.-Y. Hong, L. Popa, P. Brighten Godfrey, in *3rd USENIX Workshop on hot topics in cloud computing (HotCloud)* (2011).
107. P. Hagmann *et al.*, Mapping human whole-brain structural networks with diffusion MRI. *PLOS ONE* **2**, e597 (2007). doi: [10.1371/journal.pone.0000597](#); pmid: [17611629](#)
108. Y. Yoshimura, J. L. Dantzer, E. M. Callaway, Excitatory cortical neurons form fine-scale functional networks.

- Nature* **433**, 868–873 (2005). doi: [10.1038/nature03252](#); pmid: [15729343](#)
109. S. Song, P. J. Sjöström, M. Reigl, S. Nelson, D. B. Chklovskii, Highly nonrandom features of synaptic connectivity in local cortical circuits. *PLOS Biol.* **3**, e68 (2005). doi: [10.1371/journal.pbio.0030068](#); pmid: [15737062](#)
 110. A. M. Zador *et al.*, Sequencing the connectome. *PLOS Biol.* **10**, e1001411 (2012). doi: [10.1371/journal.pbio.1001411](#); pmid: [23109909](#)
 111. V. Braitenberg, A. Schüz, *Cortex: Statistics and Geometry of Neuronal Connectivity* (Springer-Verlag, Berlin Heidelberg New York, ed. 2, 1998).
 112. G. F. Striedter, *Principles of Brain Evolution* (Sinauer Associates, Sunderland, MA, 2005).
 113. A. Broder *et al.*, Graph structure in the Web. *Comput. Netw.* **33**, 309–320 (2000). doi: [10.1016/S1389-1286\(00\)00083-9](#)
 114. S. L. Tauro, C. Palmer, G. Siganos, M. Faloutsos, in *Global Telecommunications Conference, 2001. GLOBECOM'01. IEEE* (IEEE, San Antonio, TX, 2001), vol. 3, pp. 1667–1671.
 115. G. Siganos, S. L. Tauro, M. Faloutsos, Jellyfish: A conceptual model for the as internet topology. *J. Commun. Networks* **8**, 339–350 (2006). doi: [10.1109/JCN.2006.6182774](#)
 116. H. Ma *et al.*, The Edinburgh human metabolic network reconstruction and its functional analysis. *Mol. Syst. Biol.* **3**, 135 (2007). doi: [10.1038/msb4100177](#); pmid: [17882155](#)
 117. H. Ma, A. P. Zeng, Reconstruction of metabolic networks from genome data and analysis of their global structure for various organisms. *Bioinformatics* **19**, 270–277 (2003). doi: [10.1093/bioinformatics/19.2.270](#); pmid: [12538249](#)
 118. M. Natarajan, K. M. Lin, R. C. Hsueh, P. C. Sternweis, R. Ranganathan, A global analysis of cross-talk in a mammalian cellular signalling network. *Nat. Cell Biol.* **8**, 571–580 (2006). doi: [10.1038/ncb1418](#); pmid: [16699502](#)
 119. K. Oda, H. Kitano, A comprehensive map of the toll-like receptor signaling network. *Mol. Syst. Biol.* **2**, 2006 0015 (2006).
 120. K. Oda, Y. Matsuoka, A. Funahashi, H. Kitano, A comprehensive pathway map of epidermal growth factor receptor signaling. *Mol. Syst. Biol.* **1**, 2005 0010 (2005).
 121. N. Polouliaxh, R. Nock, F. Nielsen, H. Kitano, G-protein coupled receptor signaling architecture of mammalian immune cells. *PLOS ONE* **4**, e4189 (2009). doi: [10.1371/journal.pone.0004189](#); pmid: [19142232](#)
 122. M. Csete, J. Doyle, Bow ties, metabolism and disease. *Trends Biotechnol.* **22**, 446–450 (2004). doi: [10.1016/j.tibtech.2004.07.007](#); pmid: [15331224](#)
 123. J. C. Doyle, M. Csete, Architecture, constraints, and behavior. *Proc. Natl. Acad. Sci. U.S.A.* **108** (suppl. 3), 15624–15630 (2011). doi: [10.1073/pnas.1103557108](#); pmid: [21788505](#)
 124. T. Yamamori, Selective gene expression in regions of primate neocortex: Implications for cortical specialization. *Prog. Neurobiol.* **94**, 201–222 (2011). doi: [10.1016/j.pneurobio.2011.04.008](#); pmid: [21621585](#)
 125. P. R. Hof, J. H. Morrison, Neurofilament protein defines regional patterns of cortical organization in the macaque monkey visual system: A quantitative immunohistochemical analysis. *J. Comp. Neurol.* **352**, 161–186 (1995). doi: [10.1002/cne.903520202](#); pmid: [7721988](#)
 126. A. Bernard *et al.*, Transcriptional architecture of the primate neocortex. *Neuron* **73**, 1083–1099 (2012). doi: [10.1016/j.neuron.2012.03.002](#); pmid: [22445337](#)
 127. Q. Wang, O. Sporns, A. Burkhalter, Network analysis of corticocortical connections reveals ventral and dorsal processing streams in mouse visual cortex. *J. Neurosci.* **32**, 4386–4399 (2012). doi: [10.1523/JNEUROSCI.6063-11.2012](#); pmid: [22457489](#)
 128. J. C. Anderson, T. Binzegger, K. A. Martin, K. S. Rockland, The connection from cortical area V1 to V5: A light and electron microscopic study. *J. Neurosci.* **18**, 10525–10540 (1998). pmid: [9852590](#)
 129. C. E. Collins, Variability in neuron densities across the cortical sheet in primates. *Brain Behav. Evol.* **78**, 37–50 (2011). doi: [10.1159/000327319](#); pmid: [21691046](#)
 130. Q. Wen, A. Stepanyants, G. N. Elston, A. Y. Grosberg, D. B. Chklovskii, Maximization of the connectivity repertoire as a statistical principle governing the shapes of dendritic arbors. *Proc. Natl. Acad. Sci. U.S.A.* **106**, 12536–12541 (2009). doi: [10.1073/pnas.0901530106](#); pmid: [19622738](#)
 131. R. J. Douglas, K. A. Martin, Neuronal circuits of the neocortex. *Annu. Rev. Neurosci.* **27**, 419–451 (2004). doi: [10.1146/annurev.neuro.27.070203.144152](#); pmid: [15217339](#)
 132. T. Binzegger, R. J. Douglas, K. A. Martin, A quantitative map of the circuit of cat primary visual cortex. *J. Neurosci.* **24**, 8441–8453 (2004). doi: [10.1523/JNEUROSCI.1400-04.2004](#); pmid: [15456817](#)
 133. A. M. Thomson, D. C. West, Y. Wang, A. P. Bannister, Synaptic connections and small circuits involving excitatory and inhibitory neurons in layers 2-5 of adult rat and cat neocortex: Triple intracellular recordings and biocytin labelling in vitro. *Cereb. Cortex* **12**, 936–953 (2002). doi: [10.1093/cercor/12.9.936](#); pmid: [12183393](#)
 134. T. C. Potjans, M. Diesmann, The cell-type specific cortical microcircuit: Relating structure and activity in a full-scale spiking network model. *Cereb. Cortex* (2012). doi: [10.1093/cercor/bhs358](#); pmid: [23203991](#)
 135. S. Ullman, in *High-Level Vision* (Bradford/MIT Press, Cambridge, MA, 2000).
 136. M. D. Humphries, K. Gurney, T. J. Prescott, The brainstem reticular formation is a small-world, not scale-free, network. *Proc. Biol. Sci.* **273**, 503–511 (2006). doi: [10.1098/rspb.2005.3354](#); pmid: [16615219](#)

Acknowledgements: We acknowledge C. Lamy and P. Misery for histology and M. A. Gariel for data analysis. This work was supported by FP6-2005 IST-1583 (H.K.); FP7-2007 ICT-216593 (H.K.); ANR-11-BSV4-501 (H.K.); LabEx CORTEX (ANR-11-LABX-0042) (H.K.); PN-II-RU-TE-2011-3-0121, FP7-PEOPLE-2011-IF-299915 (M.E.-R.); National Institute of Mental Health grant R01 MH60974 (D.C.V.E.); Notre Dame's Interdisciplinary Center for Network Science and Applications (iCeNSA) funds; and, in part, by grant FA9550-12-1-0405 from the U.S. Air Force Office of Scientific Research and Defense Advanced Research Projects Agency (Z.T.).

10.1126/science.1238406

REVIEW SUMMARY

Structural and Functional Brain Networks: From Connections to Cognition

Hae-Jeong Park^{1*} and Karl Friston²

Background: The human brain presents a puzzling and challenging paradox: Despite a fixed anatomy, characterized by its connectivity, its functional repertoire is vast, enabling action, perception, and cognition. This contrasts with organs like the heart that have a dynamic anatomy but just one function. The resolution of this paradox may reside in the brain's network architecture, which organizes local interactions to cope with diverse environmental demands—ensuring adaptability, robustness, resilience to damage, efficient message passing, and diverse functionality from a fixed structure. This review asks how recent advances in understanding brain networks elucidate the brain's many-to-one (degenerate) function-structure relationships. In other words, how does diverse function arise from an apparently static neuronal architecture? We conclude that the emergence of dynamic functional connectivity, from static structural connections, calls for formal (computational) approaches to neuronal information processing that may resolve the dialectic between structure and function.

Advances: Much of our understanding of brain connectivity rests on the way that it is measured and modeled. We consider two complementary approaches: the first has its basis in graph theory that aims to describe the network topology of (undirected) connections of the sort measured by noninvasive brain imaging of anatomical connections and functional connectivity (correlations) between remote sites. This is compared with model-based definitions of context-sensitive (directed) effective connectivity that are grounded in the biophysics of neuronal interactions.

Recent topological network analyses of brain circuits suggest that modular and hierarchical structural networks are particularly suited for the functional integration of local (functionally specialized) neuronal operations that underlie cognition. Measurements of spontaneous activity reveal functional connectivity patterns that are similar to structural connectivity, suggesting that structural networks constrain functional networks. However, task-related responses that require context-sensitive integration disclose a divergence between function and structure that appears to rest mainly on long-range connections. In contrast to methods that describe network topology phenomenologically, model-based theoretical and computational approaches focus on the mechanisms of neuronal interactions that accommodate the dynamic reconfiguration of effective connectivity.

We highlight the consilience between hierarchical topologies (based on structural and functional connectivity) and the effective connectivity that would be required for hierarchical message passing of the sort suggested by computational neuroscience.

Outlook: In summary, neuronal interactions represent dynamics on a fixed structural connectivity that underlie cognition and behavior. Such divergence of function from structure is, perhaps, the most intriguing property of the brain and invites intensive future research. By studying the dynamics and self-organization of functional networks, we may gain insight into the true nature of the brain as the embodiment of the mind. The repertoire of functional networks rests upon the (hidden) structural architecture of connections that enables efficient hierarchical functional integration. Understanding these networks will require theoretical models of neuronal processing that underlies cognition.

Schematic of the multiscale hierarchical organization of brain networks. Brain function or cognition can be described as the global integration of local (segregated) neuronal operations that underlies hierarchical message passing among cortical areas, and which is facilitated by hierarchical modular network architectures.

READ THE FULL ARTICLE ONLINE

<http://dx.doi.org/10.1126/science.1238411>

Cite this article as H.-J. Park and K. Friston, *Science* 342, 1238411 (2013).
DOI: 10.1126/science.1238411

ARTICLE OUTLINE

Integration of Integration

Nodes and Edges and How They Are Measured

Structural Organization

Structure Function Convergence

Structure Function Divergence

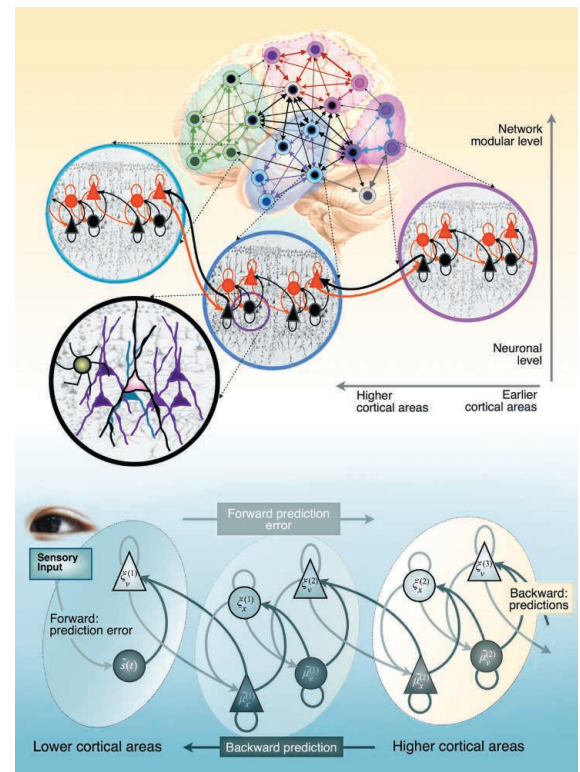
From Phenomena to Mechanisms

Return to Reality: Modeling Links Gaps

Getting Closer to Brain Network

RELATED ITEMS IN SCIENCE

See the special section beginning on page 580.



¹Department of Nuclear Medicine, Psychiatry, Severance Biomedical Science Institute, BK21 Project for Medical Science, Yonsei University College of Medicine, Seoul, Republic of Korea. ²The Wellcome Trust Centre for Neuroimaging, University College London, Queen Square, London WC1N 3BG, UK.

*Corresponding author. E-mail: parkhj@yuhs.ac

REVIEW

Structural and Functional Brain Networks: From Connections to Cognition

Hae-Jeong Park^{1*} and Karl Friston²

How rich functionality emerges from the invariant structural architecture of the brain remains a major mystery in neuroscience. Recent applications of network theory and theoretical neuroscience to large-scale brain networks have started to dissolve this mystery. Network analyses suggest that hierarchical modular brain networks are particularly suited to facilitate local (segregated) neuronal operations and the global integration of segregated functions. Although functional networks are constrained by structural connections, context-sensitive integration during cognition tasks necessarily entails a divergence between structural and functional networks. This degenerate (many-to-one) function-structure mapping is crucial for understanding the nature of brain networks. The emergence of dynamic functional networks from static structural connections calls for a formal (computational) approach to neuronal information processing that may resolve this dialectic between structure and function.

One of the major challenges in neuroscience is to understand functional anatomy on the basis of its structural substrates, namely, neuronal circuits and connections. This challenge is not trivial, especially in higher brain systems, whose complexity increases exponentially with the number of neuronal elements. To explain the rich functionality that arises from a relatively fixed structure, neuroscientists have recently focused on the topology of brain networks by using analyses that have proven successful in sociology and systems biology (1).

Integration of Integration

To date, network analyses suggest that the organization of the brain's structural connections enable the efficient processing of information and thus supports complex brain functions. This structural organization is both modular and hierarchical; a module (subnetwork of the whole brain network) comprises multiple submodules (Fig. 1A).

In this structural hierarchy, the function of a module is to integrate and contextualize the more specialized functions of its submodules. For example, visual perception in the primary visual cortex V1 assimilates the diverse orientations detected by a multitude of ocular columns, which themselves integrate more basic neuronal operations, within each macrocolumn.

In this respect, brain function or cognition can be described as global integration of local integrators. To highlight this hierarchical aspect of neuronal architectures, we will use local integration instead of functional segregation or specialization (2). Local integration entails specialized

functional processing mediated by short-range connections, intrinsic to a module at any scale, whereas global integration subserves higher cognition, facilitated by long-range connections, such as extrinsic corticocortical connections.

In both local and global integration, the integration within and between submodules depends on (hidden or unobserved) coupling parameters, such as connection strengths and timing. Therefore, understanding the true nature of neuronal interactions that underlie specific brain functions requires a formal theory of hierarchical integration based on neurally plausible models with coupling parameters and a well-defined computational objective.

This brief review considers recent characterizations of large-scale brain networks and our current understanding of structure-function relationships from the perspective of network theory. We begin by introducing the concepts of nodes and edges in networks, explaining three types of connections (or edges) between nodes and describing *in vivo* neuroimaging methods for estimating brain connectivity. After reviewing the topology of structural brain networks, we then consider the convergence and divergence (context sensitivity) of structure-function mappings. Formally, this divergence complements cognitive degeneracy (3, 4), in that the same structural connectivity can support many functions. To understand this flexible and pleiotropic organization, we then turn to the nature of message passing in these networks, in terms of information coding and computational modeling of integration. Last, we conclude with a brief outline of future directions.

Nodes and Edges and How They Are Measured

Network analysis for both structure and function in the brain starts with the identification of nodes as interacting units and their interconnections, called edges. Node identification usually

involves parcellation of a spatially continuous cortical manifold into homogeneous and unique regions. Because homogeneity and uniqueness are generally defined with respect to function, identifying nodes is a key challenge for establishing structure-function mappings. In the past, node identification focused on cytoarchitectonics and macrostructures, but more recent schemes exploit the similarity of long-range structural or functional connectivity patterns [for details, see (5)].

In large-scale networks from *in vivo* neuroimaging, an edge can be defined by three types of connectivity: structural connectivity, for anatomical links; functional connectivity, for undirected statistical dependencies; and effective connectivity, for directed causal relationships among distributed responses (6) (Fig. 1B). This three-way categorization is not restricted to large-scale networks but also applies at mesoscopic and microscopic scales, although the precise definitions depend on the measurements and the models available at any particular scale.

Structural connectivity measured by using *in vivo* neuroimaging usually reflects large-range fiber bundles inferred from diffusion (or diffusion tensor) magnetic resonance imaging (MRI) (7). One can derive a structural brain network in terms of fiber bundles according to the regions they interconnect [e.g., (8, 9)] (Fig. 2A). Structural connectivity based on diffusion MRI is however undirected and cannot differentiate between excitatory or inhibitory connections. This contrasts with structural connectivity based on tracing studies that can have different strengths or densities in either direction and in some instances be associated with excitatory or inhibitory postsynaptic effects.

Functional connectivity is generally inferred by the correlation between nodal activities on the basis of blood oxygenation level-dependent (BOLD) functional MRI (fMRI) or coherence in electro- or magnetoencephalogram (EEG/MEG) signals acquired during task performance or the resting state. In particular, resting-state fMRI has become an important basis for functional network analysis, after the discovery of spatially organized endogenous low-frequency fluctuations of BOLD signals (10).

Effective connectivity is defined as the influence one node (neuronal population) exerts over another, under a particular network model of causal dynamics. Effective connectivity is then inferred by using a model of neuronal integration. This usually involves estimating the model parameters (effective connectivity) that best explain observed BOLD or EEG/MEG signals. Although the neuronal model is generally constrained by structural connectivity, structural connectivity does not fully determine effective connectivity, which is dynamic (state-dependent) and changes with experimental context. Furthermore, in some models, effective connectivity can be polysynaptic and does not necessarily entail direct axonal connections. Effective connectivity is becoming increas-

¹Department of Nuclear Medicine, Psychiatry, Severance Biomedical Science Institute, BK21 Project for Medical Science, Yonsei University College of Medicine, Seoul, Republic of Korea.

²The Wellcome Trust Centre for Neuroimaging, University College London, Queen Square, London WC1N 3BG, UK.

*Corresponding author. E-mail: parkhj@yuhs.ac

The Heavily Connected Brain

ingly important in the analysis of functional integration because the underlying model defines the mechanisms of neuronal coupling. We will return to this in a later section.

Recent studies of large-scale human brain networks have mostly had their bases in structural and functional connectivity, using in vivo neuroimaging. However, structural connectivity based on diffusion MRI cannot resolve intracortical or intrinsic connections. It is also potentially blind to weak long-range axonal connections, which may serve as weak ties for global integration (11, 12). Conversely, functional connectivity (statistical dependencies) may exist between anatomically unconnected nodes, for example, synchronous activity in two (anatomically unconnected) nodes that is driven by common sources, polysynaptic connections, or other configurations of bidirectional circuits (13). Neither structural nor functional connectivity in large-scale networks specify the direction or sign (inhibitory or excitatory) of underlying directed (effective) connectivity.

Despite its many challenges, our current connectivity mapping ability is analogous to cartography in the Age of Exploration. The gross atlas, even if not comparable to Google Earth, delineated the boundary of the world, directed new explorations, and changed the world from an unfathomable entity into a tangible object, amenable to further charting and exploration. Likewise, technical advances in neuroimaging have led researchers to regard the human brain as a system that can be explored as a whole, leaving the details for the fullness of time.

Structural Organization

The analysis of network topology in the brain (14) highlights the principles underlying its organizational properties—such as efficient information passing, robustness, adaptability, resilience—and, more importantly, the divergent functionalities within a fixed structure. Many characterizations suggest that the structural architecture of the brain may reflect a compromise between wiring costs and the computational imperatives above (15). Structural brain networks exhibit small-worldness (14) and modularity (15). Small-worldness indicates a short average path length between all node pairs, with high local clustering, whereas modularity denotes dense intrinsic connectivity within a module but sparse, weak extrinsic connections between modules.

More recently, the rich-club phenomenon may offer a more cogent description of networks that facilitate dynamic and diverse brain functions (Fig. 1C), in which rich-club hubs (heavily connected nodes) are highly interconnected to promote global communication among modules (16). Rich-club organization is seen in a wide range of neuronal systems from the neuronal systems of *Caenorhabditis elegans* (17) and the macaque cerebral cortex (18) to the human brain (16). In humans, rich-clubs have been found to include

the precuneus, superior frontal and superior parietal cortex, hippocampus, putamen, and thalamus (16) (Fig. 2B).

Several organizational properties of structural brain networks have been studied; for example, a computational modeling study showed a relatively

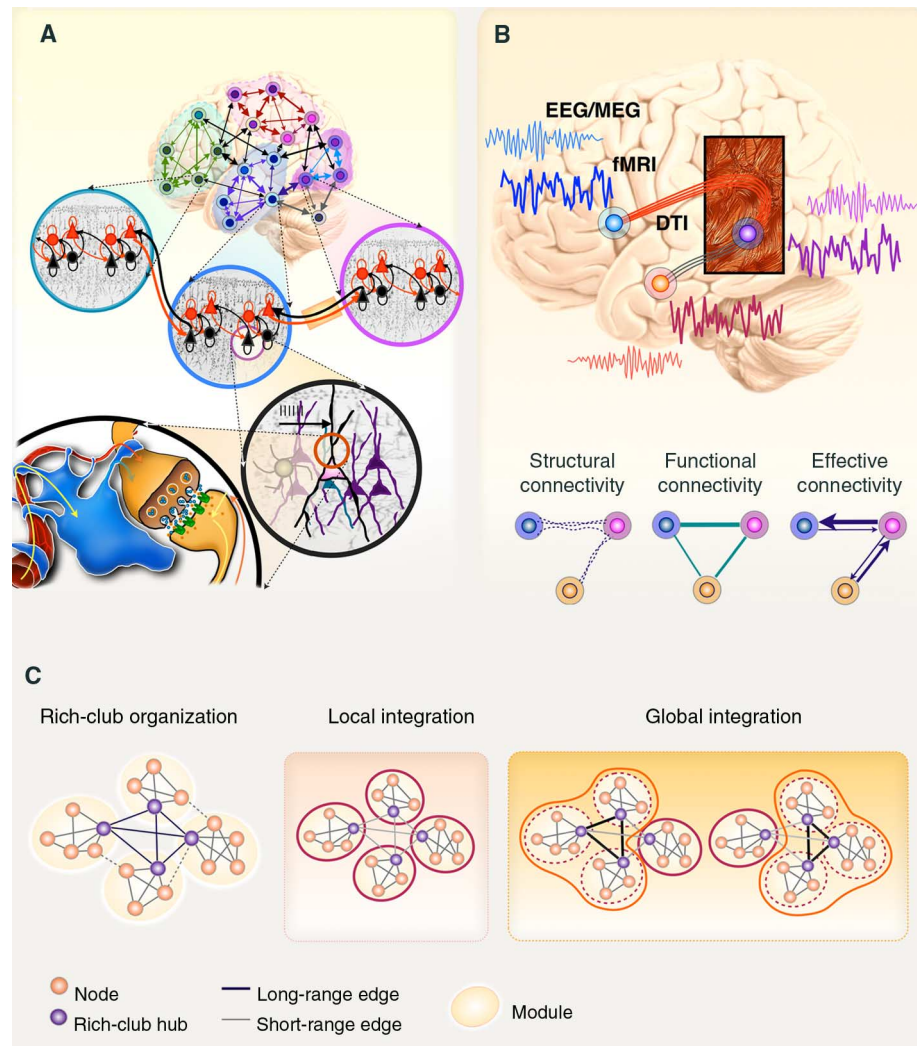


Fig. 1. Node, edge, and organization in the brain network. (A) Schematic of the multiscale hierarchical organization of brain networks: from neurons and macrocolumns to macroscopic brain areas. A network is composed of nodes and their links, called edges. A node, defined as an interacting unit of a network, is itself a network composed of smaller nodes interacting at a lower hierarchical level. (B) Depictions of “edges” in a brain network, as defined by three types of connectivity: structural, functional, and effective. Structural connectivity refers to anatomical connections and (macroscopically) is usually estimated by fiber tractography from diffusion tensor MRI (DTI). These connections are illustrated with broken lines in the bottom images. Functional and effective connectivity are generally inferred from the activity of remote nodes as measured by using BOLD-fMRI or EEG/MEG signals. Functional connectivity, defined by the correlation or coherence between nodes, does not provide directionality or causality and is therefore depicted without arrows. Because effective connectivity is estimated by using a model of neuronal interactions, it can evaluate directionality. This is illustrated by the one-sided arrows. Adjacency (or connectivity) matrices subserve graph theoretical analyses of brain systems and encode structural and functional connectivity between pairs of nodes. (C) Rich-club organization describes many aspects of the hierarchical (modular) brain. As shown in this (simplified) schematic, the brain is highly modular, with nodes integrated locally through strong short-range edges (thin gray lines). Rich-club hubs are densely interconnected among themselves (mainly through long-range edges in thick black lines). These hubs facilitate intermodular communication or global integration that may be contextualized via weaker long-range connections (dotted lines). Brain functions can be characterized by local integration within segregated modules for specialized functions and global integration of modules for perception, cognition, and action. Context-dependent global integration recruits a subset of modules with different configurations that nuances the collaboration between different modules. See also (2).

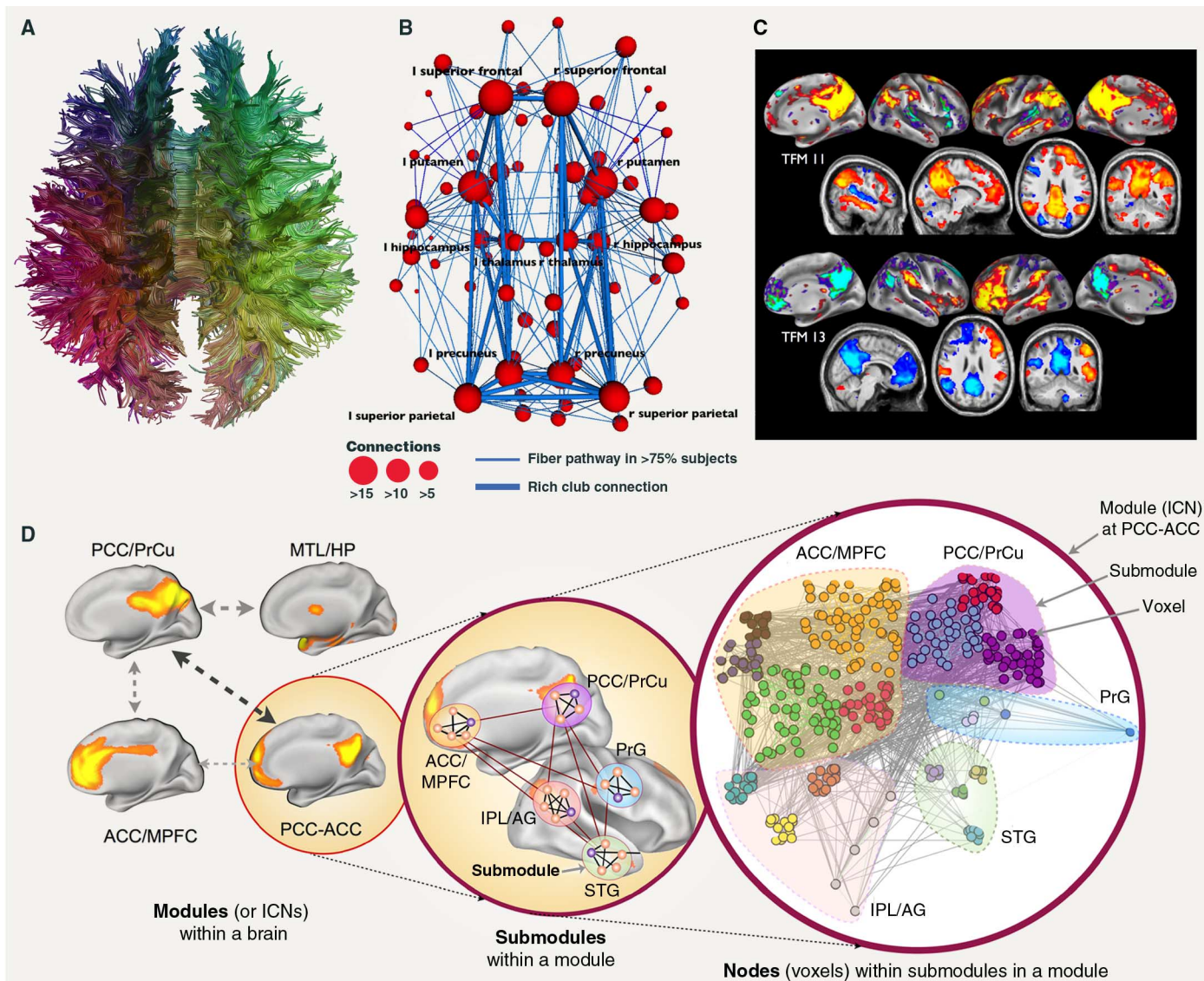


Fig. 2. Convergence: structural and functional brain network organization. (A) Whole-brain fiber bundles reconstructed from diffusion tensor MRI are colored according to their connection similarity (8). A structural brain network can be constructed by parcellating fibers according to the cortical or subcortical regions they interconnect. (B) The human brain's structural network constructed from diffusion tensor MRI (16) has rich-club hubs in the precuneus, superior frontal and superior parietal cortex, the subcortical hippocampus, putamen, and thalamus. Dark (thick) blue and light (thin) blue lines represent connections between rich clubs and connections from rich clubs to others, respectively. The sizes of the nodes reflect the number of their connections. (C) Repertoires of spatial modules have emerged from the analysis of spontaneous BOLD fluctuations in the brain at rest, i.e., ICNs that comprise clusters of nodes fluctuating synchronously. This figure shows two examples of temporal functional modes (TFMs, more detailed ICNs) derived from temporal independent component analysis of fast resting-state fMRI (25). TFMs often correspond to task-related neurocognitive modules. As an example, TFMs 11 and 13 are similar to the task-activated semantic network and the lateralized language network, respectively. (D) Hierarchical (modular) resting-state functional network. Changes in dynamic global coupling occur between the four ICNs (modules) associated with the default mode network (26). However, relatively stable coupling exists among the

submodules (red lines within the second circle) within a given ICN, and highly stable local coupling is maintained among nodes within individual submodules (black solid lines within submodules in the second circle). The stability of connectivity estimated over a relatively long time period suggests that, at the level of the submodule, functional connectivity is closely related to the underlying structural connectivity, especially intracortical connectivity (which diffusion MRI cannot resolve). Note that ICNs show a hierarchical modularity: Submodules within ICNs are composed of hierarchically clustered voxels. This hierarchical modularity is neurally plausible, considering the multiscale nature of neuronal circuits from micro- to macroscopic brain networks. See also (21). The ICNs displayed in this figure are networks located mainly in the posterior cingulate cortex and precuneus (PCC/PrCu), the anterior cingulate cortex and medial prefrontal cortex (ACC/MPFC), the posterior cingulate cortex and anterior cingulate cortex (PCC-ACC), and the medial temporal lobe and hippocampal formation (MTL/HP). Submodules within the PCC-ACC ICN in the second and the third circles are ACC/MPFC (node size, 6 mm by 6 mm by 6 mm, $n = 188$ nodes), PCC/PrCu ($n = 104$), inferior parietal lobe and angular gyrus (IPL/AG) ($n = 52$), precentral gyrus (PrG) ($n = 7$), and superior temporal gyrus (STG) ($n = 25$). Modified from (8) for (A) and from (26) for (D), and permitted to reproduce from (16) for (B) and from (25) for (C).

The Heavily Connected Brain

high resilience to random node removal (attack) (19). However, there appears to be a greater vulnerability and topological reorganization after damage to central hubs or rich clubs (16, 19). In a study of schizophrenia, the connection density among rich-club hubs was significantly reduced (20), suggesting a disruption of global communication in this disease.

Although the rich-club phenomenon is consistent with hierarchical brain architectures (21), it largely has its basis in “strong” structural connectivity, measured with neuroimaging. In contrast to noninvasive human studies, recent tracing studies in the macaque brain suggest a denser connectivity matrix, with many “weak” long-range connections (11). These weak long-range connections may play an important role in hierarchically organized functional modules (12).

Despite differences in detail, the overall concept of modules (defined by dense short-range

connections) that are integrated by relatively sparse long-range connections remains valid. We use the term rich-club phenomenon in this context, not as a mathematical definition. Notably, the modular, hierarchical, and rich-club-like brain organization may furnish the structural constraints under which functional connectivity emerges.

Structure Function Convergence

Like the Lake Isle of Innisfree, the resting brain was originally thought to be calm and peaceful. This view, however, ignores turbulent interactions beneath the surface. Although fMRI measures the “resting-state” brain, what is measured is restless (22). When endogenous fluctuations in resting-state BOLD signals are decomposed (by using independent component analysis), they reveal repertoires of spatial modules, that is, clusters of nodes fluctuating synchronously, called

intrinsic connectivity networks (ICNs). Considerable correspondence can be found between ICNs and task-related neurocognitive modules (23, 24). Some representative ICNs are the default mode network; dorsal attention network; executive control network; salience network; and sensorimotor, visual, and auditory systems (22). Analyses of faster resting-state fMRI further have revealed temporally independent functional modes (extended ICNs) (Fig. 2C), which map more precisely to task-evoked modules than conventional ICNs, some of which contain submodules overlapping with other modes (25).

Setting aside the many interesting questions about ICNs (e.g., why are ICNs not at rest when they are not needed?), we note that most ICNs incorporate two or more segregated submodules within and between hemispheres. A submodule (subnetwork) within an ICN comprises synchronously active

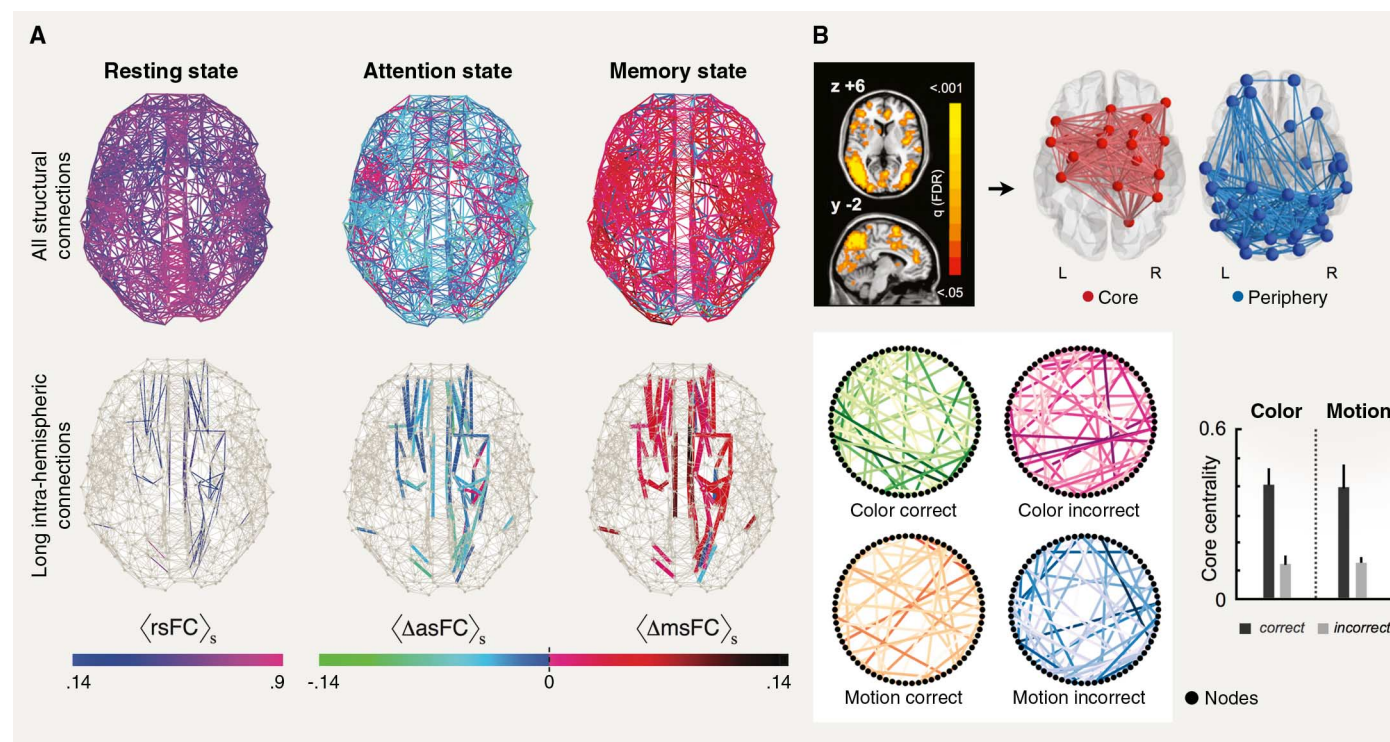


Fig. 3. Context-sensitive divergence. (A) Task-dependent reconfiguration of functional connectivity was found predominantly in long-range intrahemispheric connections (31). All structural connections (top row), especially long-range intrahemispheric connections (bottom row), are colored according to the functional connectivity during rest ($rsFC$, left column) and task-dependent deviations in functional connectivity from rest during attention ($\Delta asFC$, middle column) and memory ($\Delta msFC$, right column). In the maps of intrahemispheric connections (bottom row), thicker lines in the resting state indicate stronger $rsFC$; thicker lines during attention indicate larger decreases in FC, and thicker lines during memory indicate larger increases in FC relative to rest, averaged across participants. An overall decrease in functional connectivity was observed during the attentional task, whereas a memory task elicited an overall increase of functional connectivity. Furthermore, the functional connectivity of long-range intrahemispheric pathways decreased to a greater degree during attentional demands and increased during the memory task, compared with the other subgroups of connections during task performance. This suggests that global

integration by modulating long-range connectivity is crucial for task-dependent functions. (B) Functional MRI activations during the preparatory phase of a visual discrimination task for color and motion (32) were used as nodes for graph analysis (top left). FDR, false discovery rate. These nodes were decomposed into either core nodes (red in top middle) or peripheral nodes (blue in top right) according to their connection densities. Visual areas V4 (color processing) and V5/hMT (motion processing) were categorized as peripheral nodes. Functional networks during the preparatory period before either correct or incorrect responses for color and motion stimuli are shown in the bottom left (black dots in circle maps indicate nodes and colored lines for task-dependent functional connectivity). During both color and motion discrimination tasks, erroneous preparation trials had significantly lower core centrality, a global measure of the core's ability to integrate and control information flow (bottom right). This finding indicates that aberrant core-periphery interactions may be responsible for the incorrect responses in this study. Redrawn from (31) for (A) (courtesy of A. M. Hermundstad) and modified with permission from (32) for (B).

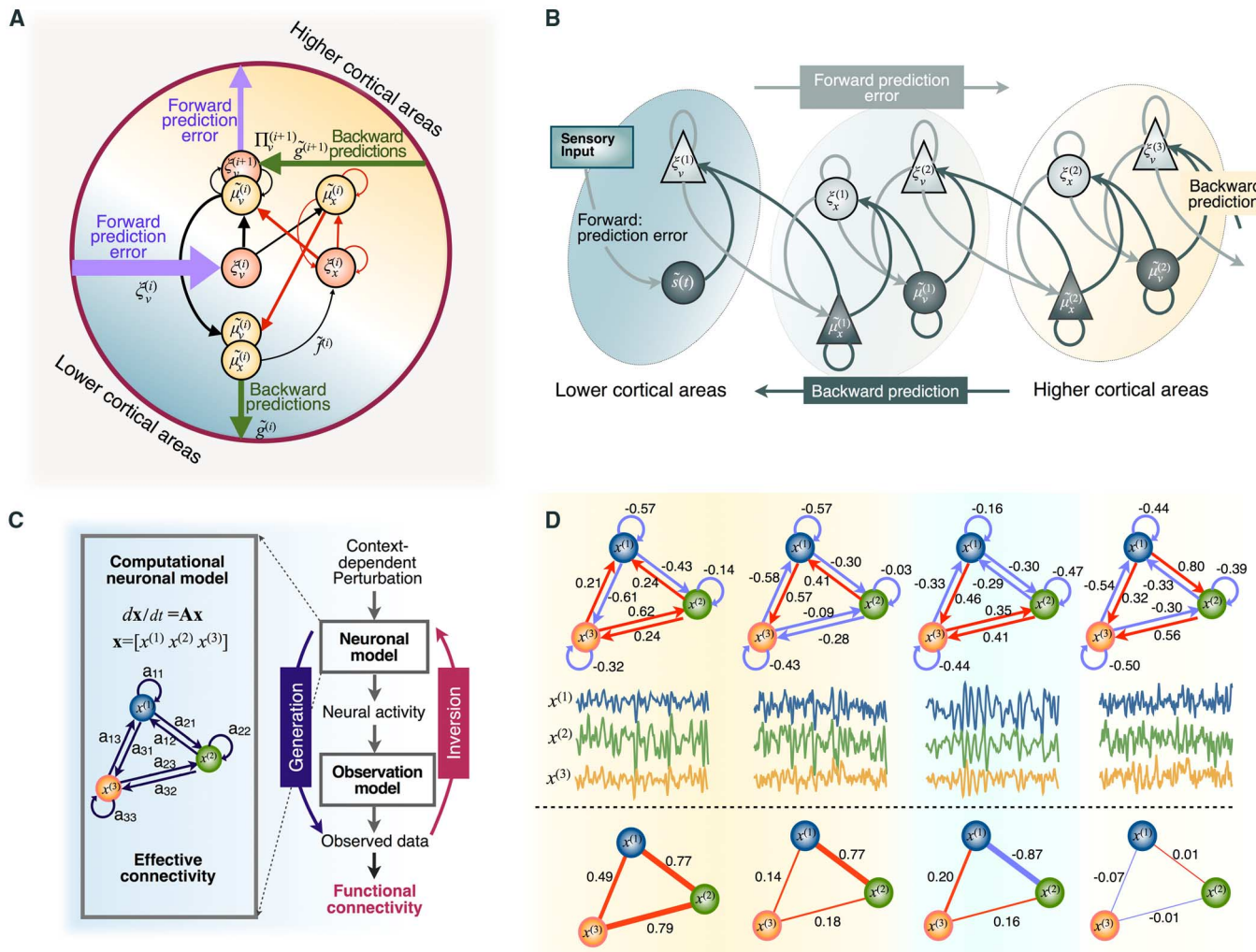


Fig. 4. Mechanisms and simulations of functional networks. (A) An example of a canonical microcircuit. A simplified canonical microcircuit (36) includes intrinsic connectivity (inhibitory and excitatory) and extrinsic forward and backward connectivity. Inhibitory connections are colored in red, and excitatory connections are in black. Unlike the simple role edges play in most current network analyses, a canonical microcircuit node is equipped with intrinsic connections and states. (B) A theory of predictive coding in the hierarchical brain network may explain what information is broadcast within the network and how edge strengths are adjusted (39). According to this theory, the brain entails a hierarchical generative model that is used to predict sensory or lower level input. The predictions of the generative model are adjusted at each hierarchical level until the prediction errors between sensory inputs and predictions are minimized. This prediction error minimization process is mediated by forward driving connections, delivering prediction errors (light arrows) from an earlier area to a higher area, and (modulatory) backward connections (dark arrows) that build context-sensitive predictions. Prediction errors for hidden causes and hidden states, at the i th level, $[\xi_v^{(i)}, \xi_x^{(i)}]$ are the weighted [by precisions, $\Pi_v^{(i)}, \Pi_x^{(i)}$] difference between conditional expectations about hidden causes and states $[\mu_v^{(i)}, \mu_x^{(i)}]$ and their predicted values. The ellipses correspond to nodes in a network. See (39) for details. (C) The neuronal mechanism, i.e., causal influences among nodes underlying observed data, is inferred via computational modeling, where

parameters of a dynamic network model (e.g., effective connectivity) are estimated by using model inversion. During model inversion, the effective connectivity in the model is optimized to minimize errors between predicted signals and observed data, in a manner similar to the predictive coding theory for the brain in (B). In fMRI, the observation model represents the hemodynamic response to underlying neural activity. Functional connectivity of the observed data describes the undirected statistical dependencies among nodes. (D) Four simulations using a model with a linear differential equation for three nodes and four different sets of effective connectivity [top, based on the computational model in (C)], generating four sets of signals at each node (middle). The functional connectivity among nodes was evaluated by using correlation coefficients (bottom). Notably, effective connectivity with different signs and weights generated diverse functional connectivity patterns from an identical structural wiring; for example, different mechanisms but almost identical functional connectivity between nodes 1 and 2 emerged in the first and second simulations, whereas negative functional connectivity under the same structural connectivity resulted from the third simulation. As shown in the fourth simulation, the third node plays an important role in shaping the dynamics of nodes 1 and 2 as a modulator or a neuronal context, suppressing functional connectivity. These simulations address the importance of computational modeling for a mechanistic understanding of the brain network. Modified from (36) for (A) and from (39) for (B).

The Heavily Connected Brain

voxels, with a stable coupling that persists over time, although the coupling between different ICNs may be more dynamic and context-sensitive than the strong coupling among the nodes that comprise any given ICN (26, 27) (Fig. 2D).

This enduring and tight synchrony can be attributed to local integration by short-range, strong-tied dense connectivity within the submodule. High-density local projections in the macaque brain characterized by using retrograde tracers support this notion [e.g., (17)].

Meanwhile, the coupling between submodules of an ICN is plausibly mediated by strong long-range structural connections, such as commissural fibers for bilateral submodules and longitudinal fibers within a hemisphere. For example, submodules of the default mode network appear to be interconnected through long-range fibers characterized with diffusion tensor MRI (28).

Clearly, functional connectivity depends on how it is measured, and correlations measured over shorter periods of time may themselves fluctuate. However, it is likely that functional connectivity over long time periods (5 to 10 min.) reflects underlying structural connectivity because functional connectivity measures the average statistical dependencies between two nodes over the measured period. In other words, functional connectivity is highly constrained by structural connectivity.

Simulation studies of the human brain network show that structural connectivity can predict resting-state functional connectivity (29). A study based on macaque brain connectivity also demonstrated that anatomical connectivity derived from axonal tract tracing provided a good explanation for resting-state functional connectivity (30). Inferring structural connectivity from resting-state functional connectivity may also be possible within subgroups of structural connections (31).

In this respect, resting-state functional connectivity may be more informative about short-range intracortical connectivity, which diffusion tensor MRI cannot resolve easily. Resting-state functional network analysis reveals a hierarchical modularity in brain networks (Fig. 2D) that is consistent with the multiscale nature of brain anatomy from the microscopic to the macroscopic (21). However, if structural connectivity determines functional connectivity, why is functional connectivity so context and state-dependent?

Structure Function Divergence

Comparisons of functional connectivity statistics during the performance of attention and memory tasks demonstrate that functional connectivity changes according to task, with an overall reduction for attention and an overall increase for memory (31). Moreover, long-range intrahemispheric connections show a larger decrease in functional connectivity during visual attention and a greater increase during memory task, com-

pared with short-range connections (Fig. 3A). These results indicate that changes in global integration via long-range connections facilitate diverse cognitive functions and disclose its context sensitivity.

The importance of global integration for successful task performance was also documented in a study by using a color-or-motion judgment task. When perceptual areas were recruited for their specialized functions (for example, V4 for color perception), they were tightly integrated into the large-scale network topology (32). Crucially, aberrant interactions between nodes in the network's core and periphery predicted performance errors. This implies a strong link between behavioral performance and anticipatory reconfiguration of the topology of the network core (e.g., rich clubs) (Fig. 3B).

These studies suggest that the divergence between invariant structural connectivity and context-sensitive functional connectivity may be expressed more at the level of global integration of segregated modules than local integration within a module. In this respect, the rich-club architecture supports functional diversity by providing long-range interconnections among modules. These long-range connections are clearly flexible and facilitate diverse integration for various functional demands (31, 32). Modulating synaptic gains or nonlinear synchronous interactions, or both, may underpin this versatility.

How global network architectures self-organize or reconfigure for specific tasks remains an open question. More investigations of task-specific functional topologies are required to answer this question. However, even with our current capabilities, it is clear that, for any one structural connectivity pattern, there are many possible patterns of functional connectivity. This should be of no surprise because one-to-many and many-to-one structure-function mappings are ubiquitous in systems biology, from molecular to the macroscopic level (3). In short, recent coarse-grained topological characterizations of structural and functional networks may not be sufficient to illuminate the dynamical mechanisms of functional integration.

From Phenomena to Mechanisms

What neuronal architectures support integration within and between submodules? What information is conveyed from one submodule to another during functional integration? Under what principle do submodules distribute incoming information within themselves, and how do their nodes remain integrated while doing so? At this point, these questions remain open; however, our current understanding of canonical neuronal circuits and their putative roles within the principles of brain functioning may shed some light on these questions.

Numerous attempts have been made to assimilate diverse anatomical and physiological findings into a canonical microcircuit, a model architecture

of cortical processing at the millimeter scale (33–35). Recent formulations have considered extrinsic and intrinsic connections among excitatory and inhibitory populations specific to granular, supra-, and infragranular cortical layers (36) (Fig. 4A). In a hierarchical setting, extrinsic connections can be forward, backward, or lateral. Forward and backward connections emphasize driving and modulatory properties, respectively.

Canonical circuits of intrinsic connections are easily concatenated into a hierarchical network. In these architectures, a canonical microcircuit node does not function as a simple convergence of edges, as in most current network analyses, but is equipped with intrinsic connections and states. The intrinsic neuronal state, self-organized by intrinsic connections, is crucial for processing unexpectedly weak extrinsic input. For example, in the macaque monkey, the extrinsic lateral geniculate nucleus (LGN) input to V1, which is small (~1%) compared with the intrinsic inputs in V1 (~85%) (11), can drive V1 very efficiently because of state-dependent dynamics of V1 microcircuitry. In other words, recurrent connections within V1 may amplify feedforward input from LGN (37).

In the brain, like the Internet, information coding is as crucial as structural topology in reducing information transfer costs. In the Internet, coding is usually conducted offline before transmission (e.g., MPEG video compression). Neural information, however, is manipulated online, while traveling within and between subnetworks. For example, a visual impression in the primary visual cortex is transferred to the frontal cortex in a compact and abstract form that is comprehensible to the frontal cortex. This online coding may be conducted through dynamic integration of distributed nodes by adjusting edge strengths (i.e., connectivity) within the network.

What information is distributed within the network, and under what principle is it integrated by state-dependent (adjustable) edge strengths? One of the most appealing theories is predictive coding, which is supported by a growing body of evidence in neuroscience and theoretical neurobiology (38, 39). In predictive coding, neuronal networks constitute a probabilistic generative model of incoming sensory input: Brain networks make top-down predictions about ascending input and then refine these predictions by minimizing prediction errors. Prediction tuning (or learning) is a process of adjusting the model parameters (e.g., edge strength) by changing synaptic efficacy. In a hierarchical setting (36), backward connections deliver predictions to lower levels, whereas forward connections convey prediction errors to upper levels (39) (Fig. 4B). Intrinsic states and edge strengths are recursively updated to produce better predictions at each level of the hierarchy. Under models like predictive coding, the directed edge strength corresponds to the effective connectivity of the network en-

gaged during a specific task. This sort of computationally informed modeling of neuronal message passing may provide an appealing and plausible explanation for the functional integration among hierarchical subnetworks.

Return to Reality: Modeling Links Gaps

In reality, no in vivo imaging to date can measure effective connectivity directly. Furthermore, effective connectivity can only be defined within an experimental or neuronal context (40), as realized many years ago in electrophysiology (41): “in particular, ‘effective connectivity’ may be only a subset of the actual structural connectivity since it deals only with connections and relations that are active during the time of measurement.” This context sensitivity makes direct measurement of effective connectivity unattainable without a very carefully controlled neuronal context and an explicit model of neuronal interactions.

As in early electrophysiology studies [e.g., (41)], effective connectivity is quantified by estimating the parameters of biophysical or computational models from measured time series (Fig. 4, C and D). Several methods now exist to estimate directed connectivity on the basis of either phenomenological time series models, such as Granger causality, or realistic neuronal models, such as dynamic causal modeling (DCM). The pros and cons of these methods have been discussed elsewhere (42, 43). DCM is a Bayesian identification scheme based on a model of neuronal interactions and an observation model (e.g., the hemodynamic model for fMRI) (44). This model-based approach is gradually being validated by animal and human studies, using EEG/MEG or fMRI, and is being used increasingly widely (42).

Because models are judged by their predictive validity, models of effective connectivity must be updated in light of new structural connectivity findings and empirical evaluations. Recent advances in microscopic techniques—such as microscopic tracing and imaging [e.g., (45)], a structural and molecular interrogation technique called CLARITY (46), and precise optogenetic stimulation—may allow us to refine our models for macroscopic functional imaging data. Crucially, because effective connectivity rests on structurally constrained network models to explain functional activity, computational modeling can serve as an interface between structure and function.

Getting Closer to Brain Network

This review has suggested that (i) the relationship between structure and function is an integration problem, (ii) the organization of structural networks supports local and global integration, (iii) the inherent context sensitivity of functional integration mandates a divergence of functional connectivity from structural connectivity, and (iv)

understanding the dynamic configuration of connectivity will benefit from theoretically informed and realistic neuronal models.

However, our understanding of structure-function mapping at the network level is still in its infancy. We have only looked at a few aspects of brain networks with rather crude measurements. Some examples of the many topics reserved for future research include dynamic and transient-state functional networks (47), coordination of task-specific brain networks, reconfiguration of effective networks because of extrasynaptic neuromodulators (48), long-term modification of structural network for functional demands, and individual variations, particularly in neurological and neuropsychiatric disease. Toward these ends, effort should be devoted to constructing finer maps of structural connectivity, especially directed and weighted connectivity, by combining research from microscopic and macroscopic scales. Last, effective connectivity needs to be quantified by using more realistic computational modeling for both resting and task-induced states.

Function may deviate from structure to exhibit dynamic and contextualized behavior. Such divergence of function from structure is perhaps the most intriguing property of the brain and invites intensive future research. By studying the dynamics and self-organization of functional networks thereby enabled, we may gain insight into the true nature of the brain as the embodiment of the mind. The repertoire of functional networks will most likely emerge from the (hidden) structural architecture that enables the efficient global integration of local integrations.

References and Notes

- D. J. Watts, S. H. Strogatz, Collective dynamics of ‘small-world’ networks. *Nature* **393**, 440–442 (1998). doi: [10.1038/30918](#); pmid: [9623998](#)
- O. Sporns, Network attributes for segregation and integration in the human brain. *Curr. Opin. Neurobiol.* **23**, 162–171 (2013). doi: [10.1016/j.conb.2012.11.015](#); pmid: [23294553](#)
- G. M. Edelman, J. A. Gally, Degeneracy and complexity in biological systems. *Proc. Natl. Acad. Sci. U.S.A.* **98**, 13763–13768 (2001). doi: [10.1073/pnas.231499798](#); pmid: [11698650](#)
- C. J. Price, K. J. Friston, Degeneracy and cognitive anatomy. *Trends Cogn. Sci.* **6**, 416–421 (2002). doi: [10.1016/S1364-6613\(02\)00197-9](#); pmid: [12413574](#)
- G. S. Wig, B. L. Schlaggar, S. E. Petersen, Concepts and principles in the analysis of brain networks. *Ann. N. Y. Acad. Sci.* **1224**, 126–146 (2011). doi: [10.1111/j.1749-6632.2010.05947.x](#); pmid: [21486299](#)
- K. J. Friston, Functional and effective connectivity in neuroimaging: A synthesis. *Hum. Brain Mapp.* **2**, 56–78 (1994). doi: [10.1002/hbm.460020107](#)
- P. J. Basser, J. Mattiello, D. LeBihan, MR diffusion tensor spectroscopy and imaging. *Biophys. J.* **66**, 259–267 (1994). doi: [10.1016/S0006-3495\(94\)80775-1](#); pmid: [8130344](#)
- H. J. Park et al., Method for combining information from white matter fiber tracking and gray matter parcellation. *AJNR Am. J. Neuroradiol.* **25**, 1318–1324 (2004). pmid: [15466325](#)
- P. Hagmann et al., Mapping human whole-brain structural networks with diffusion MRI. *PLoS ONE* **2**, e597 (2007). doi: [10.1371/journal.pone.0000597](#); pmid: [17611629](#)
- B. Biswal, Z. F. Yetkin, V. M. Haughton, J. S. Hyde, Functional connectivity in the motor cortex of resting human brain using echo-planar MRI. *Magn. Reson. Med.* **34**, 537–541 (1995). doi: [10.1002/mrm.1910340409](#); pmid: [8524021](#)
- N. T. Markov et al., Weight consistency specifies regularities of macaque cortical networks. *Cereb. Cortex* **21**, 1254–1272 (2011). doi: [10.1093/cercor/bhq201](#); pmid: [21045004](#)
- L. K. Gallos, H. A. Makse, M. Sigman, A small world of weak ties provides optimal global integration of self-similar modules in functional brain networks. *Proc. Natl. Acad. Sci. U.S.A.* **109**, 2825–2830 (2012). doi: [10.1073/pnas.1106612109](#); pmid: [22308319](#)
- Y. Adachi et al., Functional connectivity between anatomically unconnected areas is shaped by collective network-level effects in the macaque cortex. *Cereb. Cortex* **22**, 1586–1592 (2012). doi: [10.1093/cercor/bhr234](#); pmid: [21893683](#)
- O. Sporns, J. D. Zwi, The small world of the cerebral cortex. *Neuroinformatics* **2**, 145–162 (2004). doi: [10.1385/NI:2:2:145](#); pmid: [15319512](#)
- E. Bullmore, O. Sporns, The economy of brain network organization. *Nat. Rev. Neurosci.* **13**, 336–349 (2012). pmid: [22498897](#)
- M. P. van den Heuvel, O. Sporns, Rich-club organization of the human connectome. *J. Neurosci.* **31**, 15775–15786 (2011). doi: [10.1523/JNEUROSCI.3539-11.2011](#); pmid: [22049421](#)
- E. K. Towson, P. E. Vértés, S. E. Ahnert, W. R. Schafer, E. T. Bullmore, The rich club of the C. elegans neuronal connectome. *J. Neurosci.* **33**, 6380–6387 (2013). doi: [10.1523/JNEUROSCI.3784-12.2013](#); pmid: [23575836](#)
- L. Harriger, M. P. van den Heuvel, O. Sporns, Rich club organization of macaque cerebral cortex and its role in network communication. *PLOS ONE* **7**, e46497 (2012). doi: [10.1371/journal.pone.0046497](#); pmid: [23029538](#)
- J. Alstott, M. Breakspear, P. Hagmann, L. Cammoun, O. Sporns, Modeling the impact of lesions in the human brain. *PLoS Comput. Biol.* **5**, e1000408 (2009). doi: [10.1371/journal.pcbi.1000408](#); pmid: [19521503](#)
- M. P. van den Heuvel et al., Abnormal rich club organization and functional brain dynamics in schizophrenia. *JAMA Psychiatr.* **70**, 783–792 (2013). doi: [10.1001/jamapsychiatry.2013.1328](#); pmid: [23739835](#)
- D. Meunier, R. Lambiotte, A. Fornito, K. D. Ersche, E. T. Bullmore, Hierarchical modularity in human brain functional networks. *Front. Neuroinform.* **3**, 37 (2009). doi: [10.3389/fninf.11.037.2009](#); pmid: [19949480](#)
- M. E. Raichle, The restless brain. *Brain Connect.* **1**, 3–12 (2011). doi: [10.1089/brain.2011.0019](#); pmid: [22432951](#)
- S. M. Smith et al., Correspondence of the brain’s functional architecture during activation and rest. *Proc. Natl. Acad. Sci. U.S.A.* **106**, 13040–13045 (2009). doi: [10.1073/pnas.0905267106](#); pmid: [19620724](#)
- A. R. Laird et al., Networks of task co-activations. *Neuroimage* **80**, 505–514 (2013). doi: [10.1016/j.neuroimage.2013.04.073](#); pmid: [23631994](#)
- S. M. Smith et al., Temporally-independent functional modes of spontaneous brain activity. *Proc. Natl. Acad. Sci. U.S.A.* **109**, 3131–3136 (2012). doi: [10.1073/pnas.1121329109](#); pmid: [22323591](#)
- B. Park et al., Are brain networks stable during a 24-hour period? *Neuroimage* **59**, 456–466 (2012). doi: [10.1016/j.neuroimage.2011.07.049](#); pmid: [21807101](#)
- E. A. Allen et al., Tracking whole-brain connectivity dynamics in the resting state. *Cereb. Cortex* (2012). doi: [10.1093/cercor/bhs352](#); pmid: [23146964](#)
- M. D. Greicius, K. Supekar, V. Menon, R. F. Dougherty, Resting-state functional connectivity reflects structural connectivity in the default mode network. *Cereb. Cortex* **19**, 72–78 (2009). doi: [10.1093/cercor/bhn059](#); pmid: [18403396](#)
- C. J. Honey et al., Predicting human resting-state functional connectivity from structural connectivity. *Proc. Natl. Acad. Sci. U.S.A.* **106**, 2035–2040 (2009). doi: [10.1073/pnas.0811168106](#); pmid: [19188601](#)

The Heavily Connected Brain

30. K. Shen *et al.*, Information processing architecture of functionally defined clusters in the macaque cortex. *J. Neurosci.* **32**, 17465–17476 (2012). doi: [10.1523/JNEUROSCI.2709-12.2012](https://doi.org/10.1523/JNEUROSCI.2709-12.2012); pmid: [23197737](https://pubmed.ncbi.nlm.nih.gov/23197737/)
31. A. M. Hermundstad *et al.*, Structural foundations of resting-state and task-based functional connectivity in the human brain. *Proc. Natl. Acad. Sci. U.S.A.* **110**, 6169–6174 (2013). doi: [10.1073/pnas.1219562110](https://doi.org/10.1073/pnas.1219562110); pmid: [23530246](https://pubmed.ncbi.nlm.nih.gov/23530246/)
32. M. Ekman, J. Derrfuss, M. Tittgemeyer, C. J. Fiebach, Predicting errors from reconfiguration patterns in human brain networks. *Proc. Natl. Acad. Sci. U.S.A.* **109**, 16714–16719 (2012). doi: [10.1073/pnas.1207523109](https://doi.org/10.1073/pnas.1207523109); pmid: [23012417](https://pubmed.ncbi.nlm.nih.gov/23012417/)
33. S. Zeki, S. Shipp, The functional logic of cortical connections. *Nature* **335**, 311–317 (1988). doi: [10.1038/335311a0](https://doi.org/10.1038/335311a0); pmid: [3047584](https://pubmed.ncbi.nlm.nih.gov/3047584/)
34. D. Mumford, On the computational architecture of the neocortex. II. The role of cortico-cortical loops. *Biol. Cybern.* **66**, 241–251 (1992). doi: [10.1007/BF00198477](https://doi.org/10.1007/BF00198477); pmid: [1540675](https://pubmed.ncbi.nlm.nih.gov/1540675/)
35. V. B. Mountcastle, The columnar organization of the neocortex. *Brain* **120**, 701–722 (1997). doi: [10.1093/brain/120.4.701](https://doi.org/10.1093/brain/120.4.701); pmid: [9153131](https://pubmed.ncbi.nlm.nih.gov/9153131/)
36. A. M. Bastos *et al.*, Canonical microcircuits for predictive coding. *Neuron* **76**, 695–711 (2012). doi: [10.1016/j.neuron.2012.10.038](https://doi.org/10.1016/j.neuron.2012.10.038); pmid: [23177956](https://pubmed.ncbi.nlm.nih.gov/23177956/)
37. R. J. Douglas, C. Koch, M. Mahowald, K. A. Martin, H. H. Suarez, Recurrent excitation in neocortical circuits. *Science* **269**, 981–985 (1995). doi: [10.1126/science.7638624](https://doi.org/10.1126/science.7638624); pmid: [7638624](https://pubmed.ncbi.nlm.nih.gov/7638624/)
38. A. Clark, Whatever next? Predictive brains, situated agents, and the future of cognitive science. *Behav. Brain Sci.* **36**, 181–204 (2013). doi: [10.1017/S0140525X12000477](https://doi.org/10.1017/S0140525X12000477); pmid: [23663408](https://pubmed.ncbi.nlm.nih.gov/23663408/)
39. K. Friston, The free-energy principle: A unified brain theory? *Nat. Rev. Neurosci.* **11**, 127–138 (2010). doi: [10.1038/nrn2787](https://doi.org/10.1038/nrn2787); pmid: [20068583](https://pubmed.ncbi.nlm.nih.gov/20068583/)
40. S. L. Bressler, A. R. McIntosh, in *Handbook of Brain Connectivity*, V. Jirsa, A. R. McIntosh, Eds. (Springer-Verlag, New York, 2007), pp. 403–419.
41. G. L. Gerstein, P. Bedenbaugh, M. H. Aertsen, Neuronal assemblies. *IEEE Trans. Biomed. Eng.* **36**, 4–14 (1989). doi: [10.1109/10.16444](https://doi.org/10.1109/10.16444); pmid: [2646211](https://pubmed.ncbi.nlm.nih.gov/2646211/)
42. K. Friston, R. Moran, A. K. Seth, Analysing connectivity with Granger causality and dynamic causal modelling. *Curr. Opin. Neurobiol.* **23**, 172–178 (2013). doi: [10.1016/j.conb.2012.11.010](https://doi.org/10.1016/j.conb.2012.11.010); pmid: [23265964](https://pubmed.ncbi.nlm.nih.gov/23265964/)
43. S. M. Smith *et al.*, Network modelling methods for FMRI. *Neuroimage* **54**, 875–891 (2011). doi: [10.1016/j.neuroimage.2010.08.063](https://doi.org/10.1016/j.neuroimage.2010.08.063); pmid: [20817103](https://pubmed.ncbi.nlm.nih.gov/20817103/)
44. K. J. Friston, B. Li, J. Daunizeau, K. E. Stephan, Network discovery with DCM. *Neuroimage* **56**, 1202–1221 (2011). doi: [10.1016/j.neuroimage.2010.12.039](https://doi.org/10.1016/j.neuroimage.2010.12.039); pmid: [21182971](https://pubmed.ncbi.nlm.nih.gov/21182971/)
45. J. W. Lichtman, W. Denk, The big and the small: Challenges of imaging the brain's circuits. *Science* **334**, 618–623 (2011). doi: [10.1126/science.1209168](https://doi.org/10.1126/science.1209168); pmid: [22053041](https://pubmed.ncbi.nlm.nih.gov/22053041/)
46. K. Chung *et al.*, Structural and molecular interrogation of intact biological systems. *Nature* **497**, 332–337 (2013). doi: [10.1038/nature12107](https://doi.org/10.1038/nature12107); pmid: [23575631](https://pubmed.ncbi.nlm.nih.gov/23575631/)
47. D. S. Bassett *et al.*, Dynamic reconfiguration of human brain networks during learning. *Proc. Natl. Acad. Sci. U.S.A.* **108**, 7641–7646 (2011). doi: [10.1073/pnas.1018985108](https://doi.org/10.1073/pnas.1018985108); pmid: [21502525](https://pubmed.ncbi.nlm.nih.gov/21502525/)
48. E. Marder, Neuromodulation of neuronal circuits: Back to the future. *Neuron* **76**, 1–11 (2012). doi: [10.1016/j.neuron.2012.09.010](https://doi.org/10.1016/j.neuron.2012.09.010); pmid: [23040802](https://pubmed.ncbi.nlm.nih.gov/23040802/)

Acknowledgments: This research was supported by the Brain Research Program through the National Research Foundation of Korea funded by the Ministry of Science, ICT, and Future Planning (20100018839 for H.J.P.). K.F. is supported by the Wellcome trust. The authors thank L. Quattrocki Knight, D.-J. Kim, B. Park, and two anonymous reviewers for helpful discussions and suggestions; especially B. Park for preparing the material for this review.

10.1126/science.1238411

Functional Interactions as Big Data in the Human Brain

Nicholas B. Turk-Browne*

Noninvasive studies of human brain function hold great potential to unlock mysteries of the human mind. The complexity of data generated by such studies, however, has prompted various simplifying assumptions during analysis. Although this has enabled considerable progress, our current understanding is partly contingent upon these assumptions. An emerging approach embraces the complexity, accounting for the fact that neural representations are widely distributed, neural processes involve interactions between regions, interactions vary by cognitive state, and the space of interactions is massive. Because what you see depends on how you look, such unbiased approaches provide the greatest flexibility for discovery.

Why does the brain, and not the pancreas or any other human organ, arouse such popular interest? The key reason is that the brain implements the mind. Understanding how the brain works could help uncover the fundamental principles of cognition and behavior.

The development of magnetic resonance imaging (MRI) began a new era in cognitive neuroscience. Exploiting differences in magnetic susceptibility between oxygenated and deoxygenated blood [blood oxygenation level-dependent (BOLD) contrast], functional MRI (fMRI) detects metabolic activity, and by inference, neuronal activity, noninvasively throughout the brain. This technique generates complex data sets: ~100,000 locations, measured simultaneously hundreds of times, resulting in billions of pairwise relations, collected in multiple experimental conditions, and from dozens of participants per study. With this powerful technology in widespread use, data analysis has become the bottleneck for progress. What is the best way to find the mind in brain data?

This review is organized around four desiderata for examining the mind with fMRI, each embracing a different aspect of the nature and complexity of human brain function: (i) neural representations are widely distributed within and across brain regions, (ii) neural processes depend on dynamic interactions between regions, (iii) these interactions vary systematically by cognitive state, and (iv) the space of possible interactions has high dimensionality. All four complexities can be accounted for by harnessing recent advances in large-scale computing. Such unbiased approaches are beginning to reveal how disparate parts of the brain work in concert to orchestrate the mind.

Distributed Representations

The most basic approach for finding the mind in the brain is to test for homologies between mental functions and brain regions. The expectation that

functions should align to discrete regions emerged from studies of patients with focal brain damage, an emphasis in systems neuroscience on brain “areas,” and theoretical views about modular brain organization. This approach identified several specialized brain regions, including areas for perception, action, language, emotion, and memory.

In fMRI, brain activity is not measured at the level of regions but rather in terms of volumetric pixels (voxels). The average amplitude of BOLD activity evoked by trials relative to baseline (“activation”) identifies voxels that are responsive to the function engaged by that trial type (Fig. 1). A classic discovery is that discrete clusters of voxels in visual cortex are selective for particular object categories (*1*). This univariate approach remains dominant and productive; for example, it was used recently to show that category selectivity may, in fact, be organized as a continuous gradient, with each voxel reflecting a point in semantic space (*2*).

There is nothing intrinsically flawed about measuring activation in a voxel or region in isolation from the rest of the brain. Limitations can arise, however, from the use and interpretation of this approach, especially when voxels or regions are assumed to be independent. Although fMRI discretizes the brain into images, the underlying areas of tissue are not necessarily discrete. Because the goal is to understand the brain—not the content of these images per se—methods sensitive to dependence between voxels are necessary.

Multivariate pattern analysis (MVPA) was developed in response (*3*). This technique relies on tools from machine learning to decode patterns of activation across voxels. One of the first discoveries enabled by MVPA was that information about a category is present throughout visual cortex, beyond voxels with the strongest activation to that category (*4*). This was a watershed moment: Seemingly atomic mental functions could be reflected in distributed and overlapping patterns in the brain.

The value of MVPA is especially clear when the overall activation in a region is weak or similar across conditions, but the pattern over voxels is

informative. For instance, it has long been known that expectations influence perception—but how? There are two potential mechanisms: Either neurons coding for expected stimuli in sensory cortex are suppressed to minimize the redundancy of information in the brain, or neurons coding for unexpected stimuli are suppressed to sharpen population responses around expected stimuli. Neuronal activity in visual areas, such as V1, should decrease on average in both cases, which leads to attenuated but indistinguishable activation. However, MVPA revealed more information about expected versus unexpected stimuli in V1, consistent only with sharpening (*5*).

As another example, how can we hold vivid images in our mind’s eye? Frontal and parietal regions that help maintain information in working memory lack detailed visual selectivity, and visual areas with the needed selectivity show little delay-period activation in working memory tasks. Despite this weak activation, however, MVPA of visual cortex can successfully decode what information is being held in mind (*6, 7*)—revealing that sensory machinery is recruited for working memory.

Interactive Processes

The advent of MVPA eliminated a bias to interpret brain regions as having homogeneous and discrete functions. This approach helped capture another core aspect of brain function: Regions do not work in isolation, with computation depending on local and long-range interactions. This can be reflected in fMRI coactivation: Voxels containing interacting neurons are more likely to activate together, which could produce distributed patterns visible to MVPA.

However, a limitation of most uses of MVPA is that they focus on (patterns of) activation and are thus blind to certain kinds of interactions. Voxels need not vary in activation to have selectivity: Neuronal populations may generally be active, with their function defined on the basis of which specific neurons are communicating with each other (*8*). (This is not a flaw of MVPA itself, which, as discussed later, can work with any kind of pattern.)

Examining temporal correlations in BOLD activity between voxels—functional connectivity (*9*)—helped address this issue. Even if a voxel has stable activation across experimental conditions, its functional connectivity with other voxels may vary. This technique has limitations, including that BOLD correlations do not indicate neuronal communication, say little about directionality, and must be interpreted cautiously (two voxels may interact with a common third voxel or a global factor, such as head motion, rather than each other). Nonetheless, some initial concerns have been allayed: Correlation is generally an appropriate metric, candidate neuronal substrates exist (*10*), and functional connectivity is anatomically constrained (*11*).

The most common application of functional connectivity is examining intrinsic correlations while participants rest, typically by modeling whole-brain BOLD activity with the time course from a seed

Department of Psychology and Princeton Neuroscience Institute, Princeton University, Princeton, NJ, 08540, USA.

*E-mail: ntb@princeton.edu

region. This approach has helped characterize the functional architecture of the brain, namely, how regions group together into broader systems. One such system is the “default network,” a set of regions that are robustly correlated at rest. However, this finding did not fully realize the promise of functional connectivity for new discovery, as the same network had previously been identified in terms of baseline activation (12).

The added value of this approach is more apparent in a study that examined the default network with higher temporal resolution (13). Accelerated multiband fMRI sequences revealed that the default network may not be a stable network: Over time, its constituents interact differently with each other and with the rest of the brain. The existence of these temporally distinct “modes” is consistent with the neuronal populations above—the function of a region in the default network may only be definable with respect to its functional connectivity at that moment. Such investigations may also enhance our understanding of disorders like Alzheimer’s disease, which targets the default network, as reflected in amyloid plaque deposits and disrupted function (12).

Active Tasks

The proliferation of functional connectivity eliminated a bias toward using activation as the basic unit of study, placing emphasis on pairwise relationships instead. However, as noted above, most functional connectivity studies are conducted at rest. There are advantages to this, including that data sets can be

collected and compared across research sites and clinical populations (14). But, if the goal is to understand the mind, resting connectivity is only partly the answer—cognition is neither manipulated nor measured. Indeed, functional connectivity can be similar over rest and task states, but this is not guaranteed (15). For instance, resting connectivity itself is influenced by recent tasks (16, 17).

Studying connectivity during tasks is a more direct way to understand how cognitive processes are realized in the brain. There are many flavors of task-based functional connectivity, each with strengths and weaknesses (9). To highlight one approach, “background connectivity” retains the simplicity of resting connectivity but accounts for different cognitive states (18). The logic is that BOLD activity contains two task-related sources of variance: evoked activity related to stimuli and responses and endogenous activity related to establishing and maintaining the current cognitive state (19). After accounting for nuisance variables, precise models of the evoked activity leave the endogenous activity in the residuals, which can be correlated across voxels to estimate background connectivity in different cognitive states.

As a case study, consider selective attention—our ability to prioritize sensory input that is important for achieving one’s current goals (20). In humans, this has typically been examined with activation. For example, when shown a blended image of a face and a scene, attending to the face activates face-selective visual cortex and attending to the scene activates scene-selective visual cortex (21). Attended information gets prioritized be-

cause these strengthened representations compete better against those of unattended information.

A different mechanism is suggested by models of cognitive control, which emphasize the guidance of activity along neural pathways (22), and by neurophysiological studies, which link attention to long-range synchrony (23). Attention may act as if switching train tracks: Goals represented in frontal and parietal cortex establish connections between visual areas to route sensory information along relevant pathways. We recently found evidence consistent with this mechanism (Fig. 2): In the task above, attending to faces increased background connectivity between brain area V4 and face-selective cortex, and attending to scenes increased connectivity between V4 and scene-selective cortex (24). This modulation of connectivity predicted behavior, was unrelated to activation, and persisted without stimulation. These findings in the human brain join with recent findings in nonhuman primates (25, 26) to form a coherent story about how functional connectivity within the visual system supports attention.

Task-based connectivity is especially useful for understanding how brain systems influence each other. For example, we frequently make decisions between options with which we have no direct experience, such as new restaurants or books—how is this possible? Interactions between the striatum and hippocampus may help: When a stimulus is rewarded, the value created in the striatum not only attaches to the rewarded stimulus, but also, via functional connectivity, to other associated stimuli reactivated in the hippocampus—creating preferences

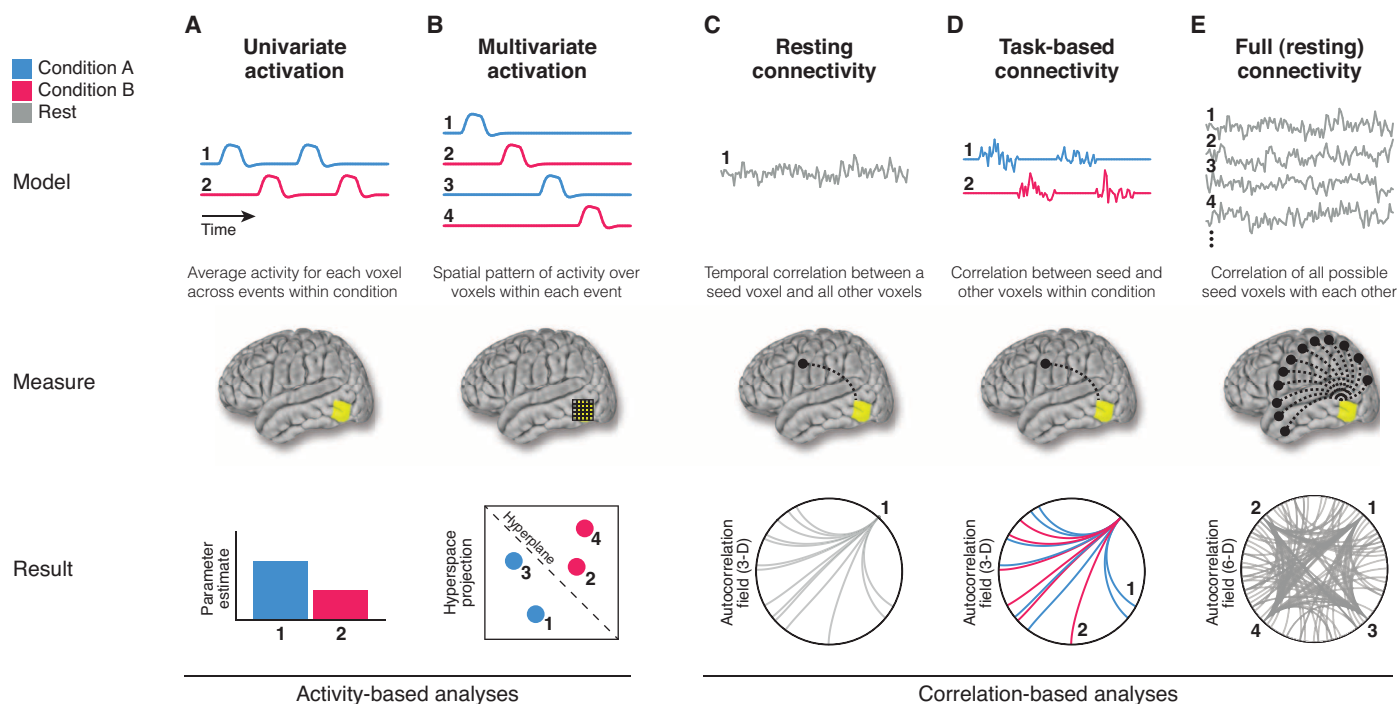


Fig. 1. Standard types of fMRI analysis. (A) Univariate activation refers to the average amplitude of BOLD activity evoked by events of an experimental condition. (B) Multivariate classifiers are trained on patterns of activation across voxels to decode distributed representations for specific events. (C)

Resting connectivity is the temporal correlation of one or more seed regions with the remainder of the brain during rest. (D) Task-based connectivity examines how these correlations differ by cognitive state. (E) Full connectivity considers all pairwise correlations in the brain, most commonly at rest.

The Heavily Connected Brain

by association (27). This technique can even be used to study how entire brains influence each other: during communication, the brains of speakers and listeners become coupled, and the extent of coupling predicts comprehension (28).

Full Correlation

Relating brain dynamics to tasks eliminated a bias to assume that functional connectivity is stationary. Nevertheless, this approach is not fully unbiased, as seed regions typically need to be chosen. This is problematic for two reasons. First, it resurrects the issue that inspired functional connectivity in the first place: Seeds are often defined on the basis of activation in different tasks, which leads to an assumption that regions with robust activation (or activation differences) are most interactive or that their interactions are most informative. Second, seeds restrict analysis to a tiny

subset of possible interactions. A brain with $N = 50,000$ voxels contains $N(N-1)/2 = 1,249,975,000$ unique voxel pairs, but only $N - 1 = 49,999$ of these are considered for any given seed. Placing such limits on analysis can hamper progress when the effects of interest in a field are unknown (29).

Why then does functional connectivity analysis use seeds at all, rather than the full voxelwise correlation matrix? One reason is to avoid the statistical challenges associated with big data and to allow more specific models to be tested with greater power. A second reason is that calculating such matrices is computationally demanding, and seeds shorten and simplify analysis. With the increased availability of high-performance computing, however, such compromises are becoming unnecessary.

The full correlation matrix can be represented as a six-dimensional (6-D) autocorrelation field: For each voxel in the 3-D brain, there is a 3-D brain of

functional connectivity with every other voxel. Computing all pairwise correlations was prohibitively slow in the past—up to hours or days (30). Matrix multiplication can be used for drastically improved computational speed: If each voxel's time course is mean-centered and the result is divided by its root sum of squares, the Pearson correlation of any two voxels is reduced to the sum of pointwise products over time (the dot product), and the full matrix of coefficients is obtained by the product of a voxels-by-time matrix and its transpose (31). Technological advances can reduce such large matrix multiplication operations to less than 1 s.

Analysis of the full correlation matrix during rest has started yielding insights into the topology and dynamics of human brain networks. If each voxel is treated as a node, and all correlations between that and other nodes above some threshold are treated as edges, then the resulting binary matrix

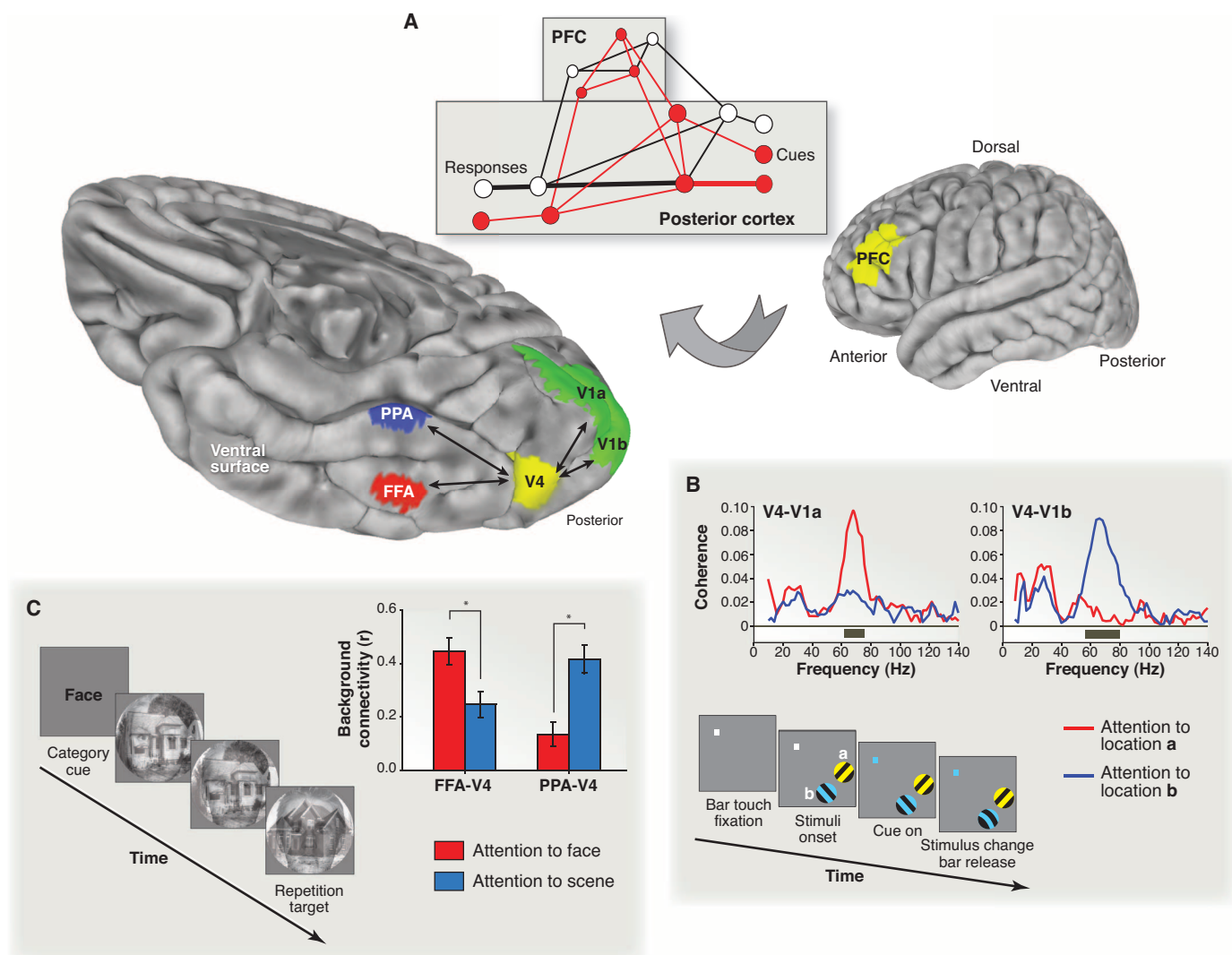


Fig. 2. Attentional modulation of functional connectivity. (A) The guided activation theory of cognitive control posits that prefrontal cortex (PFC) sends feedback to posterior cortex to switch connectivity between areas and establish task-relevant pathways (22). (B) Such pathways exist in the visual cortex of nonhuman primates: V4 shows enhanced coherence with the

area of V1 containing receptive fields for the attended target (25). (C) This mechanism also supports category-based selection in human visual cortex: V4 shows stronger background connectivity with the fusiform face area (FFA) when faces are attended and with the parahippocampal place area (PPA) when scenes are attended (24). Figures adapted with permission.

generates a graph (32). These voxelwise graphs can be characterized quantitatively with network measures (33), including degree, number of edges for a node; modularity, density of edges within versus between node clusters; path length, minimum number of edges between nodes; and centrality, proportion of shortest paths passing through a node.

In this lexicon, functional brain networks exhibit high modularity and short path lengths (32, 34). High modularity reflects strong connections between nodes that contribute to the same function, such as in visual cortex, whereas short path lengths reflect connections between these node communities via “hub” nodes that have high centrality and tend to be connected to each other, such as in frontal cortex (35). These two properties fit the definition of a “small-world” network, an organizational scheme found in many biological and nonbiological complex systems that enables efficient information processing, both locally within modules and globally across the network (33).

Thinking of brain function as a small-world network has enabled progress on several fronts. For example, it was recently discovered that although voxelwise graphs from infants’ brains also have small-world properties, their cortical hubs are located in different places than adults—unexpectedly, in primary sensorimotor cortex (36). There is variation in network properties even among adults: Some brains have shorter path lengths, and these individuals score higher on an intelligence test (37). These studies suggest that investigating how information is integrated across the brain holds particular promise for understanding the origins and limits of cognition.

Outlook

Taking stock, we have considered four desiderata: fMRI analysis should account for the fact that neural representations are widely distributed, that neural processes depend on interactions, that these interactions differ by cognitive state, and that the space of interactions is massive. Developing approaches that incorporate all of these complexities holds tremendous potential. Although the full correlation studies described above come close, they have largely only examined the resting state, missing an opportunity to relate the brain’s large-scale structure and dynamics directly to ongoing cognition.

The full combined approach (or full correlation matrix analysis, FCMA) could involve several steps (Fig. 3). During an fMRI experiment with different experimental conditions, whole-brain BOLD activity might be divided into separate time windows for each instance of a condition. The full correlation matrix would be computed for each window. This restructures the data from 4-D (3-D brain over time) to 7-D (6-D autocorrelation field over windows). The resulting matrices might then be mined using MVPA, with voxel pairs defining the dimensions of a large hyperspace, and the correlation coefficient for each pair providing the value in that dimension. Several outcome measures are possible, including the classifier’s cross-validation accuracy, which indicates

the extent to which task-related interactions were present. In addition, the weights of the classifier or the output from a feature selection step could be used to identify which specific pairwise relationships discriminated best between conditions. A software toolbox that we developed to implement this analysis pipeline on a compute cluster shows that it is computationally tractable (www.princeton.edu/fcma).

There are several challenges for the large-scale multivariate analysis of task-based functional connectivity, including consideration of statistical correction, spatial and temporal resolution, spectral frequency,

causality, intersubject alignment, and visualization. Indeed, although there are likely bigger “big data” in neuroscience, such as cellular-level structural connectivity and gene expression assays, FCMA presents unique opportunities related to studying the dynamics of human brain function in vivo and noninvasively. The greater resolution enabled by multiband fMRI (13)—coupled with consideration of multiple time windows, window lengths, and phase offsets, as well as a large number of psychological variables and the rich repertoire of human behavior—increases the computational load by several orders of magnitude.

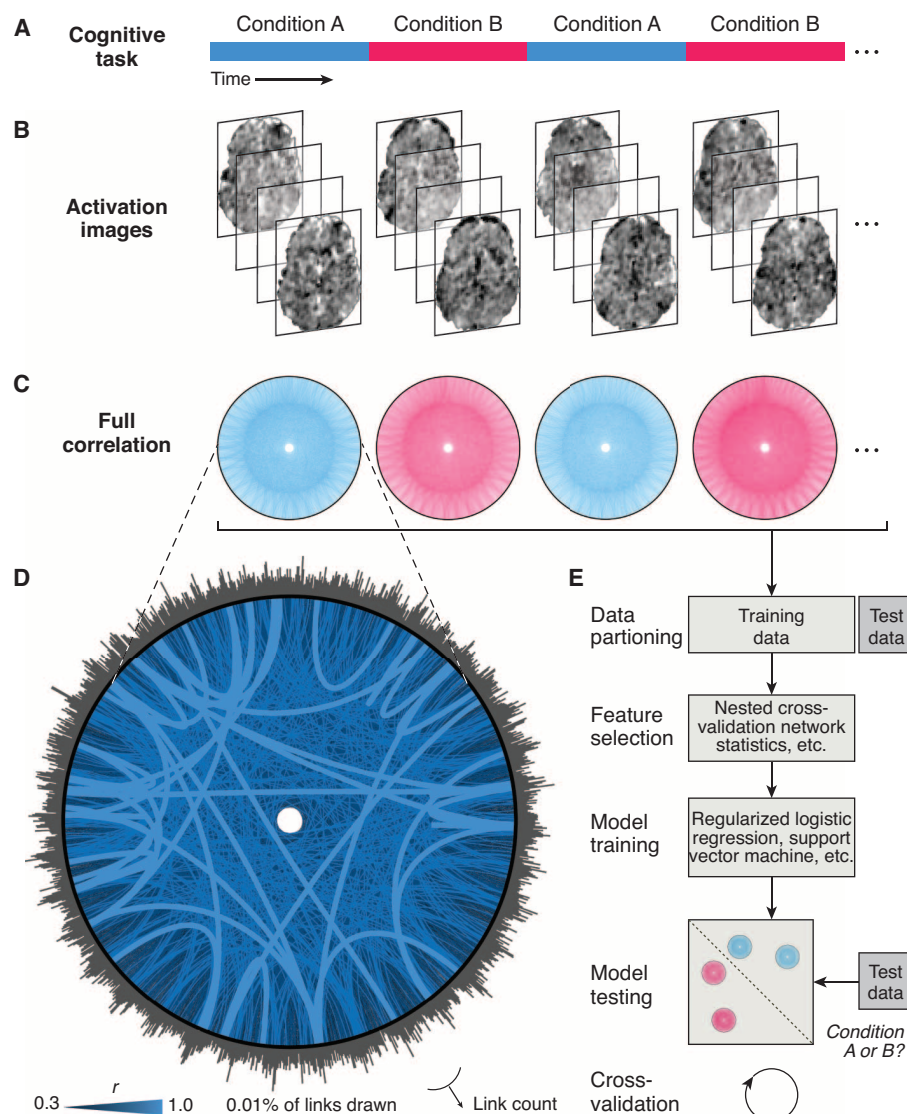


Fig. 3. Full correlation matrix analysis pipeline. (A) An fMRI data set is divided into time windows, which are labeled with an experimental condition. (B) Each window contains multiple time points, and each time point corresponds to a 3-D brain image. (C) The time course of BOLD activity in every voxel is correlated with every other voxel to produce a full correlation matrix for each window. (D) An example matrix from a 36-s block of fMRI data is depicted with 39,038 voxels arranged in a circle and 0.01% of correlations of >0.3 plotted as links (visualization created with Circos, www.circos.ca). The luminance and thickness of links reflects the absolute correlation in four graded steps. The surrounding histogram is a count of the number of above-threshold links per voxel. (E) These matrices can be submitted as examples to MVPA, with each voxel pair as an input dimension. Data-driven feature selection helps discover meaningful relationships for classification. For more information: www.princeton.edu/fcma.

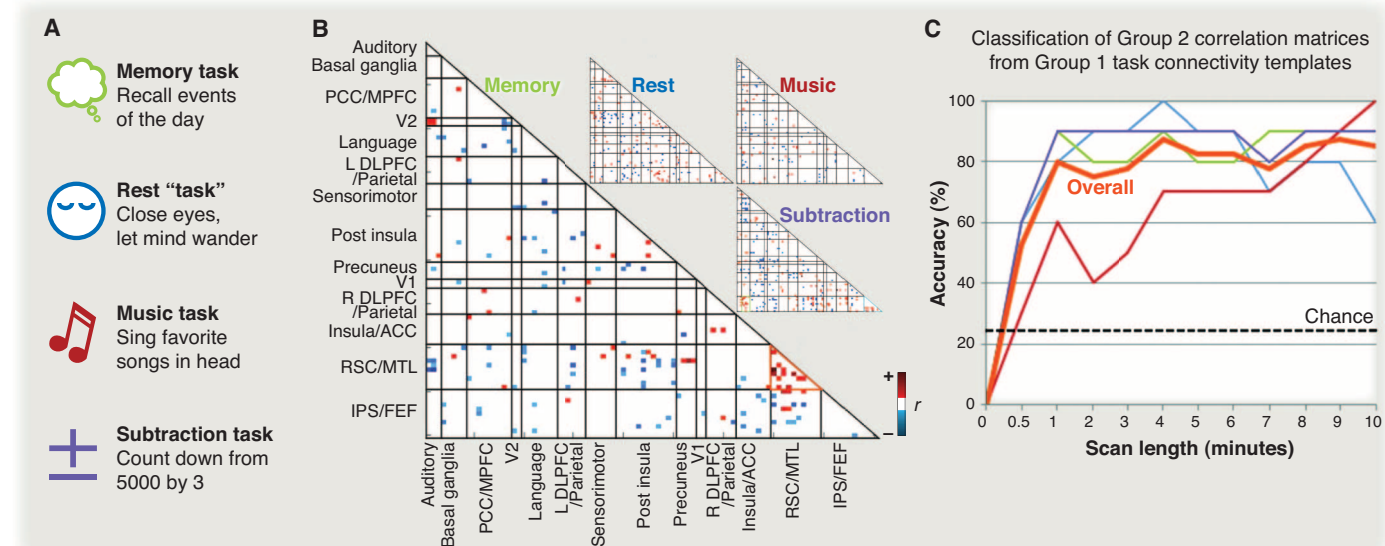


Fig. 4. Pattern analysis of correlations. (A) fMRI data were collected during four cognitive states. (B) The correlation matrix of 90 functional regions during each state. Each cell reflects the correlation between two regions, thresholded on the basis of the reliability of the correlation across participants. Pairs that were reliable in more than one state were excluded,

generating a task-specific template. Grid lines demarcate anatomical regions, each containing a variable number of functional regions. (C) Using these templates, correlation matrices from a second group of participants could be decoded into cognitive states with high accuracy. Figures adapted with permission from (42).

Nevertheless, elements of FCMA can be found in the literature. Some studies have computed large correlation matrices during different cognitive states but did not use MVPA. Instead, they focused on relating network measures to cognitive states. For example, path length is shorter when awake compared to when in stage-1 sleep (38) and also in successful versus unsuccessful auditory learners (39). Other studies have used MVPA to classify cognitive states but only over smaller regional or subregional correlation matrices (40, 41).

One study of the latter type engaged participants in four tasks: remembering the day's events, resting with eyes closed, silently singing lyrics, or counting backward (42). The correlation matrix from 90 functional regions of interest was computed for each task in one group of participants, and the cells in the matrix (region pairs) selective for each task were used to construct "connectivity templates" (Fig. 4). Correlation matrices were computed for the same tasks in a separate group of participants. The task from which these matrices were obtained could be classified with high accuracy on the basis of their similarity to the other group's templates.

Conclusions

Interactions between variables may hold the key to understanding complex biological and social systems (43). There is precedence for this in neuroscience, where physiological recordings of single neurons are giving way to large multiunit arrays and multiple recording sites (44). Immensely rich data are generated by fMRI, of which only a fraction is typically analyzed. An unbiased approach, combining advances in computer science (from large-scale computing, machine learning, and graph

theory) with clever experiments in psychology and cutting-edge tools from neuroscience, provides a fruitful platform for new discovery about the human brain—and about the mind that it implements.

References and Notes

- N. Kanwisher, *Proc. Natl. Acad. Sci. U.S.A.* **107**, 11163–11170 (2010).
- A. G. Huth, S. Nishimoto, A. T. Vu, J. L. Gallant, *Neuron* **76**, 1210–1224 (2012).
- K. A. Norman, S. M. Polyn, G. J. Detre, J. V. Haxby, *Trends Cogn. Sci.* **10**, 424–430 (2006).
- J. V. Haxby et al., *Science* **293**, 2425–2430 (2001).
- P. Kok, J. F. M. Jehee, F. P. de Lange, *Neuron* **75**, 265–270 (2012).
- S. A. Harrison, F. Tong, *Nature* **458**, 632–635 (2009).
- J. T. Serences, E. F. Ester, E. K. Vogel, E. Awh, *Psychol. Sci.* **20**, 207–214 (2009).
- E. Vaadia et al., *Nature* **373**, 515–518 (1995).
- S. M. Smith, *Neuroimage* **62**, 1257–1266 (2012).
- L. Wang, Y. B. Saalmann, M. A. Pinsk, M. J. Arcaro, S. Kastner, *Neuron* **76**, 1010–1020 (2012).
- C. J. Honey et al., *Proc. Natl. Acad. Sci. U.S.A.* **106**, 2035–2040 (2009).
- R. L. Buckner, *Neuroimage* **62**, 1137–1145 (2012).
- S. M. Smith et al., *Proc. Natl. Acad. Sci. U.S.A.* **109**, 3131–3136 (2012).
- B. B. Biswal et al., *Proc. Natl. Acad. Sci. U.S.A.* **107**, 4734–4739 (2010).
- R. M. Hutchison et al., *Neuroimage* **80**, 360–378 (2013).
- W. D. Stevens, R. L. Buckner, D. L. Schacter, *Cereb. Cortex* **20**, 1997–2006 (2010).
- A. Tambini, N. Ketz, L. Davachi, *Neuron* **65**, 280–290 (2010).
- S. V. Norman-Haignere, G. McCarthy, M. M. Chun, N. B. Turk-Browne, *Cereb. Cortex* **22**, 391–402 (2012).
- C. Summerfield et al., *PLOS Biol.* **4**, e128 (2006).
- M. M. Chun, J. D. Golomb, N. B. Turk-Browne, *Annu. Rev. Psychol.* **62**, 73–101 (2011).
- K. M. O'Craven, P. E. Downing, N. Kanwisher, *Nature* **401**, 584–587 (1999).
- E. K. Miller, J. D. Cohen, *Annu. Rev. Neurosci.* **24**, 167–202 (2001).
- B. Noudoost, M. H. Chang, N. A. Steinmetz, T. Moore, *Curr. Opin. Neurobiol.* **20**, 183–190 (2010).
- N. Al-Aidroos, C. P. Said, N. B. Turk-Browne, *Proc. Natl. Acad. Sci. U.S.A.* **109**, 14675–14680 (2012).

- C. A. Bosman et al., *Neuron* **75**, 875–888 (2012).
- Y. B. Saalmann, M. A. Pinsk, L. Wang, X. Li, S. Kastner, *Science* **337**, 753–756 (2012).
- G. E. Wimmer, D. Shohamy, *Science* **338**, 270–273 (2012).
- G. J. Stephens, L. J. Silbert, U. Hasson, *Proc. Natl. Acad. Sci. U.S.A.* **107**, 14425–14430 (2010).
- C. F. Beckmann, M. DeLuca, J. T. Devlin, S. M. Smith, *Philos. Trans. R. Soc. London B Biol. Sci.* **360**, 1001–1013 (2005).
- D. Tomasi, N. D. Volkow, *Proc. Natl. Acad. Sci. U.S.A.* **107**, 9885–9890 (2010).
- K. J. Worsley, J.-I. Chen, J. Lerch, A. C. Evans, *Philos. Trans. R. Soc. London B Biol. Sci.* **360**, 913–920 (2005).
- V. M. Eguíluz, D. R. Chialvo, G. A. Cecchi, M. Baliki, A. V. Apkarian, *Phys. Rev. Lett.* **94**, 018102 (2005).
- E. Bullmore, O. Sporns, *Nat. Rev. Neurosci.* **13**, 336–349 (2012).
- J. A. Mumford et al., *Neuroimage* **52**, 1465–1476 (2010).
- J. D. Power, B. L. Schlaggar, C. N. Lessov-Schlaggar, S. E. Petersen, *Neuron* **79**, 798–813 (2013).
- P. Fransson, U. Åden, M. Blennow, H. Lagercrantz, *Cereb. Cortex* **21**, 145–154 (2011).
- M. P. van den Heuvel, C. J. Stam, R. S. Kahn, H. E. Hulshoff Pol, *J. Neurosci.* **29**, 7619–7624 (2009).
- T. Uehara et al., *Cereb. Cortex* (2013).
- J. P. Sheppard, J.-P. Wang, P. C. M. Wong, *J. Cogn. Neurosci.* **24**, 1087–1103 (2012).
- F. Mokhtari, G.-A. Hossein-Zadeh, *J. Neurosci. Methods* **212**, 259–268 (2013).
- S. P. Pantazatos, A. Talati, P. Pavlidis, J. Hirsch, *PLOS Comput. Biol.* **8**, e1002441 (2012).
- W. R. Shirer, S. Ryali, E. Rykhlevskaia, V. Menon, M. D. Greicius, *Cereb. Cortex* **22**, 158–165 (2012).
- D. N. Reshef et al., *Science* **334**, 1518–1524 (2011).
- M. A. L. Nicolelis, A. A. Ghazanfar, B. M. Faggin, S. Votaw, L. M. O. Oliveira, *Neuron* **18**, 529–537 (1997).

Acknowledgments: The author thanks N. Hindy, V. Jackson-Hanen, and Y. Wang for help with manuscript preparation; J. Cohen, K. Li, and Y. Wang for formative discussions; and A. Ghazanfar, U. Hasson, C. Honey, and K. Norman for insightful comments on an earlier draft. This work was supported by the Pyne fund from Princeton University, the John Templeton Foundation, NSF grant MRI BCS1229597, and NIH grant R01 EY021755. The opinions expressed in this paper are those of the author and do not necessarily reflect the official views of these funding sources.

10.1126/science.1238409

REVIEW

Predispositions and Plasticity in Music and Speech Learning: Neural Correlates and Implications

Robert J. Zatorre*

Speech and music are remarkable aspects of human cognition and sensory-motor processing. Cognitive neuroscience has focused on them to understand how brain function and structure are modified by learning. Recent evidence indicates that individual differences in anatomical and functional properties of the neural architecture also affect learning and performance in these domains. Here, neuroimaging findings are reviewed that reiterate evidence of experience-dependent brain plasticity, but also point to the predictive validity of such data in relation to new learning in speech and music domains. Indices of neural sensitivity to certain stimulus features have been shown to predict individual rates of learning; individual network properties of brain activity are especially relevant in this regard, as they may reflect anatomical connectivity. Similarly, numerous studies have shown that anatomical features of auditory cortex and other structures, and their anatomical connectivity, are predictive of new sensory-motor learning ability. Implications of this growing body of literature are discussed.

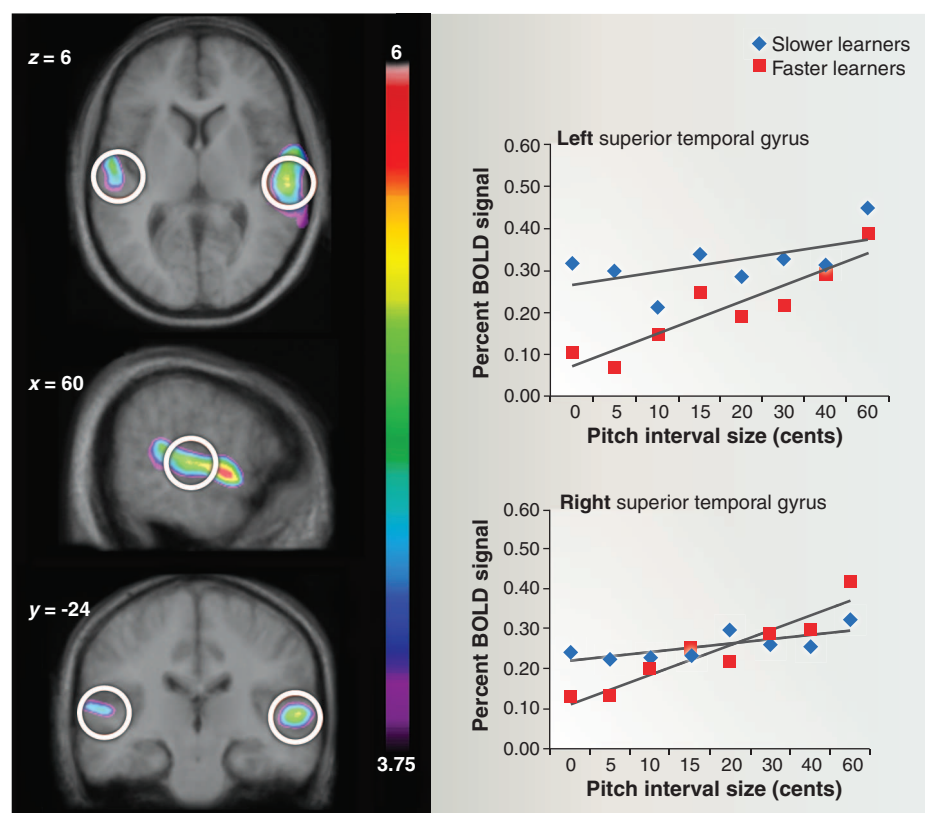
The nervous system's remarkable capacity to learn has been a central concern of neuroscience since its origins. Manifestations of change, plasticity, or adaptation to environ-

mental signals can be discerned at every level of analysis, from molecular to synaptic, to systems, to cognitive. What makes the problem intriguing is that changes in the nervous system must occur for an organism to optimize its behavior in relation to its environment; but the initial state of the nervous system when it is exposed to the learning situation is not identical for all individuals.

Montreal Neurological Institute, McGill University, 3801 University Street, Montreal, QC H3A 2B4 Canada.

*Corresponding author. E-mail: robert.zatorre@mcgill.ca

Fig. 1. Relationship between speed of learning in a microtonal pitch discrimination task and fMRI activity before start of training. The figure demonstrates that those who learned more quickly showed better initial encoding of pitch differences. (**Left panel**) fMRI data showing blood oxygen level-dependent (BOLD) activity increases as a function of increasing pitch-interval size in left and right auditory cortices. (**Right panels**) Function relating BOLD signal to increasing pitch-interval size, divided according to two subgroups of faster and slower learners; fMRI data were extracted from symmetrical left and right auditory cortical sites (white circles in left panel) on the basis of the pre-training data alone, independently of later group classification. Those individuals who subsequently showed more rapid pitch discrimination learning (red squares) had significantly higher slopes of this function than those who subsequently learned more slowly (blue diamonds), indicating an enhancement of pitch encoding in auditory cortex of faster compared to slower learners. [Adapted with permission from (26)]



Here, I consider this problem in the context of cognitive neuroscience of auditory-motor learning. Speech and music constitute the two most complex and characteristically human auditory-motor functions. These domains are interesting to compare (1) because they share some important similarities, while differing in critical ways as well. Recent advances in cognitive neuroscience have resulted in several related models of the interactions between auditory and motor systems that underlie performance and learning in both speech (2–4) and music (5–7). Furthermore, there are interesting individual differences in people's music and speech learning skills, whose neural correlates have recently begun to be investigated more. It is by now quite well established that various kinds of auditory-motor learning situations will engender changes in brain activity and also anatomical configuration; but the premise that I will defend is that there may also be important predisposing factors that influence the outcome of learning in both music and speech domains and that these factors can be discerned in terms of brain function and structure with neuroimaging techniques.

Functional Brain Activation Patterns Relevant to Learning: Effects and Causes

The pattern of changes in hemodynamic brain activity associated with learning is quite complex and includes both activity increases and decreases in various sensory and associative cortical

The Heavily Connected Brain

regions, depending on the nature of the learning (8, 9). Cross-sectional studies of musical training have shown that electrical and magnetic responses from auditory cortex are enhanced as a function of appropriate training (10–12). Electrical measures of brainstem responses have also shown enhanced fidelity of frequency encoding in musically trained individuals (13–15). A persistent question in these studies is whether such effects can be causally attributed to the training. In other words, because musical training is to some extent self-selected, it may be that those who seek out the training have some propensity. One argument in favor of experience-dependent effects is that the magnitude of the change is typically corre-

lated with the age of commencement (10, 13), suggesting a causal relationship. Stronger evidence for causality comes from longitudinal studies, which have demonstrated that after training, both in children (16) and in adults (17), there are clear changes in auditory cortical evoked responses and in the brainstem (18); however, these findings do not logically exclude the possibility that predispositions may also exist and interact with training.

The interpretation of an enhanced response originating in auditory cortex among musicians seems straightforward because musicians' training in an auditory domain presumably leads to more robust or higher-quality neural representations, which in turn are reflected in the evoked

responses. Functional magnetic resonance imaging (fMRI) studies, however, show that in response to various musical task manipulations, musical training can also manifest itself in a variety of ways in extra-auditory regions, especially frontal and parietal areas (19–23). This heterogeneity may be related to many factors, especially as musical training itself is not unitary and the tasks used in the various studies probe many distinct cognitive abilities. But the outcome of training could also differ if individuals have different profiles before they begin learning. A few fMRI studies on auditory learning of tonal patterns using a longitudinal design have in fact noted the presence of subgroups who learn well or rapidly, versus those who learn poorly or slowly (24, 25), but the origin of these differences is unknown.

These individual differences raise the question of how preexisting brain activity patterns might be relevant to explain the heterogeneous outcome of learning-related brain activity changes. We examined this factor using a task in which listeners had to learn, over a 2-week period, to distinguish tonal patterns using microtonal pitch intervals (i.e., much smaller than commonly used in musical scales) (26). Auditory cortices respond parametrically to increasing pitch-interval size (27), allowing the slope of the function relating activity to pitch change to serve as an index of cortical sensitivity to pitch processing. Learning was globally associated with a decrease in the magnitude of this function, which is consistent with a number of observations in other sensory domains (8) and can be understood in terms of fewer neural units being required for sensory encoding (28). But of greater relevance is that some individuals demonstrated very rapid learning, within the first day of training, whereas others showed much more gradual learning. When we examined the pitch-activation functions collected before the start of training, we discovered that those who subsequently went on to learn quickly initially had significantly steeper functions than those whose later learning was slower (Fig. 1). Thus, the faster learners could be thought of as having a finer-grained encoding of pitch information in auditory cortex, which in turn allowed them to learn more quickly.

These findings in the music domain are mirrored to some extent in the speech domain. Behaviorally, it is well known that certain speech contrasts are difficult to learn in adulthood if they are not part of one's native phonetic repertoire; however, certain people are better able to learn these features than others (29, 30). Explicit training with novel speech contrasts of this sort has been shown to enhance evoked electrical or magnetic responses from auditory cortices (31, 32). fMRI studies involving learning of these speech sounds also show effects comparable to those using musical training, to the extent that they show changes to auditory cortical responses as a function of learning, while others also implicate

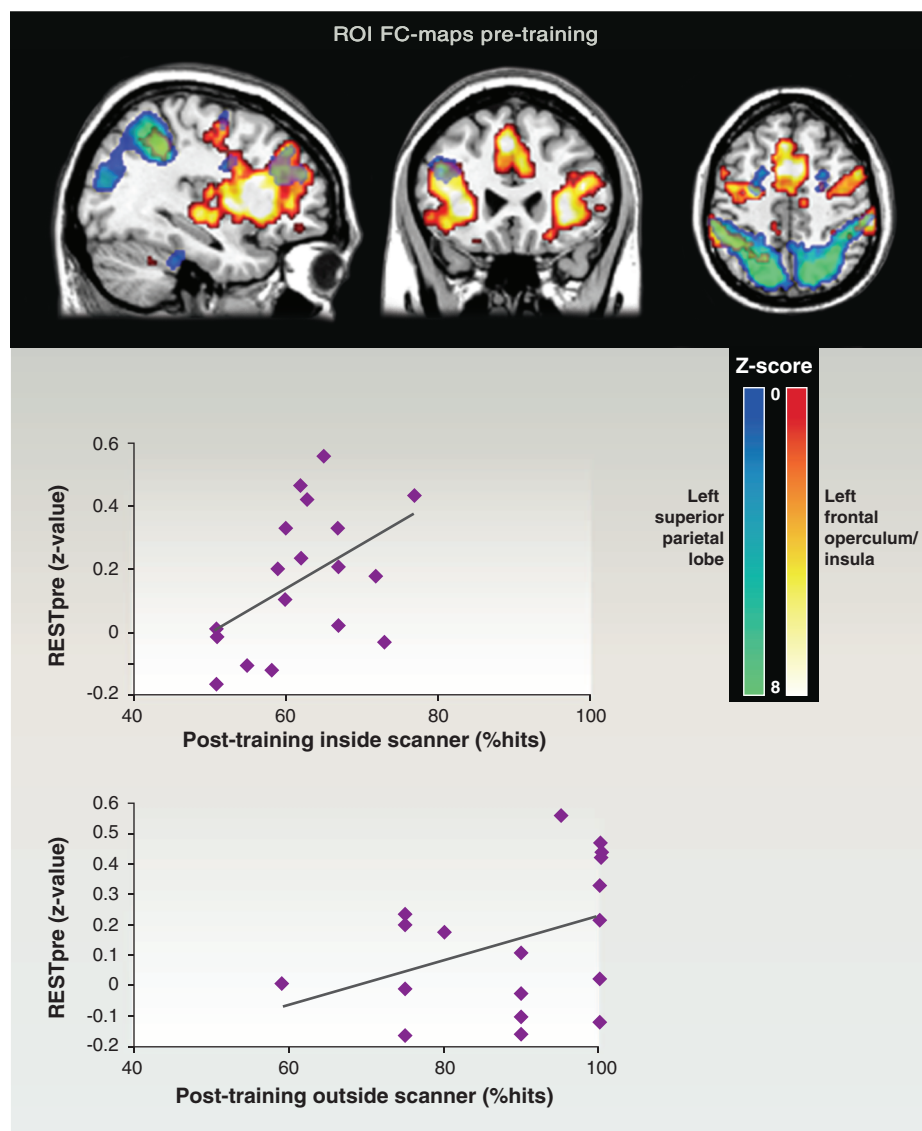


Fig. 2. Networks of resting-state fMRI activity and their relation to speech learning success. (Top) Temporal correlations in BOLD signal determine functional connectivity (FC) maps based on seed areas in the left frontal operculum/insula (red–orange bar) and the left superior parietal lobe (blue–green bar) before training. ROI, region of interest. (Bottom) Pretraining resting-state functional connectivity between the frontal and parietal regions was significantly correlated with subsequent speech-task identification performance for each individual, measured both inside and outside the scanner. [Adapted with permission from (37)]

nonsensory cortical areas, including especially classical language zones such as inferior frontal cortex and supramarginal gyrus (33–35).

Some intriguing predictive factors have recently been detected in functional properties of these neural systems. Paralleling some of the music-related findings, people who subsequently learn a linguistic pitch contour more quickly have a higher auditory cortical response at the outset than those who go on to learn less well (36). Resting-state connectivity networks may also serve as indicators of subsequent speech learning success (37). This fMRI measure has received much attention because it captures spontaneous fluctuations in brain activity that characterize the natural interactions across cortical regions, and that in turn form cognitively relevant networks (38). Those individuals who were better able to learn a nonnative speech contrast showed higher levels of functional connectivity between key components of a language-relevant network, especially inferior frontal and parietal nodes, compared to those who subsequently demonstrated poorer learning (Fig. 2). This effect was seen both in shorter- and longer-term training (37). This and other similar studies—for example, in the visual

domain (39)—provide interesting information in terms of putative mechanisms underlying individual differences in learning potential. Specifically, one interpretation of the findings is that the spontaneous fluctuations between these regions might reflect variability in anatomical connectivity, a topic to which we now turn.

Anatomical Features Relevant to Learning: Effects and Causes

The development of whole-brain MRI-based anatomical measurement techniques, such as voxel-based morphometry, cortical thickness, and diffusion imaging, has spurred research showing that brain anatomy can change noticeably as a function of learning. The microstructural features that underlie effects visible to MRI are multifaceted, and so far largely unconfirmed, but likely include alterations in vascularization, synaptogenesis, and glial cells, as well as myelination and axonal sprouting, among others (40). Cross-sectional studies of musicians consistently show changes in auditory and motor cortical regions in gray-matter volume (12), concentration (41), and cortical thickness (42), and in the organization of related white-matter pathways (43, 44), implying that musical training

can effect changes at the anatomical level. Network analysis of cortical thickness correlation patterns also suggests a more focused organization between auditory cortical and inferior frontal cortex (42), a critical network for many aspects of auditory processing, particularly working memory.

The observation that certain anatomical features differ across groups of people who differ in their training or other background is useful but insufficient by itself to demonstrate that the feature is relevant to the training or that it is caused by the training. To address the first issue, it is necessary to show a relationship to a relevant behavior, which several studies have done. Gray-matter features in auditory cortex are predictive of task performance on certain pitch tasks (12, 45), such that better performance is associated with greater gray-matter concentration or thickness in a pitch-sensitive region of auditory cortex. To address the second issue, some studies have shown that degree of anatomical change is related to amount of training (43, 45) or to age of commencement (44), implying that experience is the cause of the change. However, this may not be the only factor at play because the relationship between anatomical features and behavior persists even after accounting for amount of training (45) and also exists in groups of people without training (12), suggesting that some individual differences are due to other factors, including perhaps predispositions.

Convincing evidence in favor of experience-dependent plasticity comes from longitudinal studies, which have shown changes in cortical morphology in both auditory and motor regions among children who received musical training (46); these anatomical effects were directly linked to improved performance because the degree of change correlated with behavioral measures. Similarly, in the speech domain there have been demonstrations that brain morphology is related to linguistic experience. Thus, differences in structural measures have been noted in auditory cortices in bilingual individuals (47) and also in simultaneous interpreters (48). As with the functional studies, however, such effects cannot be unambiguously attributed exclusively to training. Indeed, in the interpreters study, the difference observed was in the gyrification of auditory cortical regions, which is thought to mature early in development (49), raising the possibility that there may be some degree of predisposition involved.

To test specifically for the existence of anatomical predispositions, several studies have examined individual differences in learning novel speech-sound features. Anatomical MRI scans obtained before training show that white-matter features in left temporoparietal regions (50) and in left auditory cortex (51) are associated with faster learning (Fig. 3). These relationships were specific to speech learning, as they were not predictive of learning nonspeech sounds in control conditions. Related findings were provided in two studies examining how well individual listeners

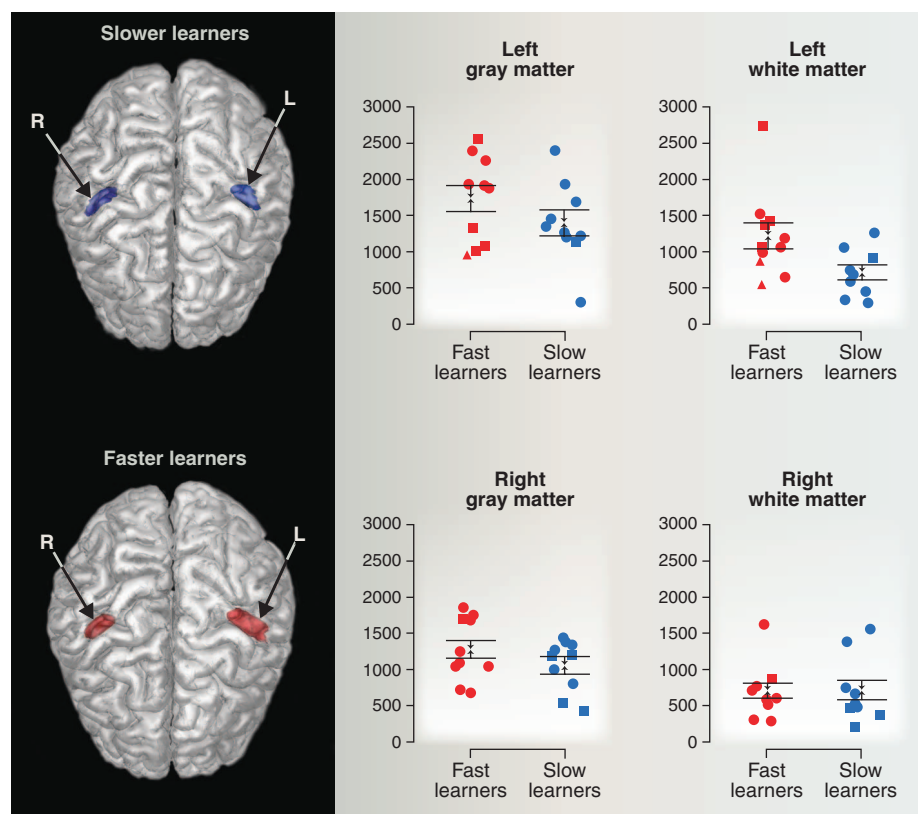


Fig. 3. Auditory cortex volume and its relation to speech perception learning ability. (Left panel) Renderings (view of brain from the top) of mean Heschl's gyrus volumes among individuals whose speed of learning to discriminate a foreign speech sound was relatively faster (red) or slower (blue). Note the relative size difference in the left Heschl's gyrus. **(Right panel)** Mean volume measures of segmented white and gray matter of Heschl's gyrus for faster and slower learners showing that the difference emerges primarily from the white matter on the left side. [Adapted with permission from (51)]

The Heavily Connected Brain

could learn to assign meaning to pseudowords that differed on the basis of acoustical features resembling those of a tone language. Those individuals who subsequently were better able to learn the words had larger volume of left auditory cortex (52), as well as enhanced white-matter organization in the left temporoparietal area (53). White-matter organization in left inferior frontal regions is also predictive of the ability to articulate speech sounds from a foreign language (54) and is associated with enhanced performance in an artificial grammar task (55).

Evidence is also mounting that the anatomical connectivity between specific cortical regions is a determinant of performance. Individual variability

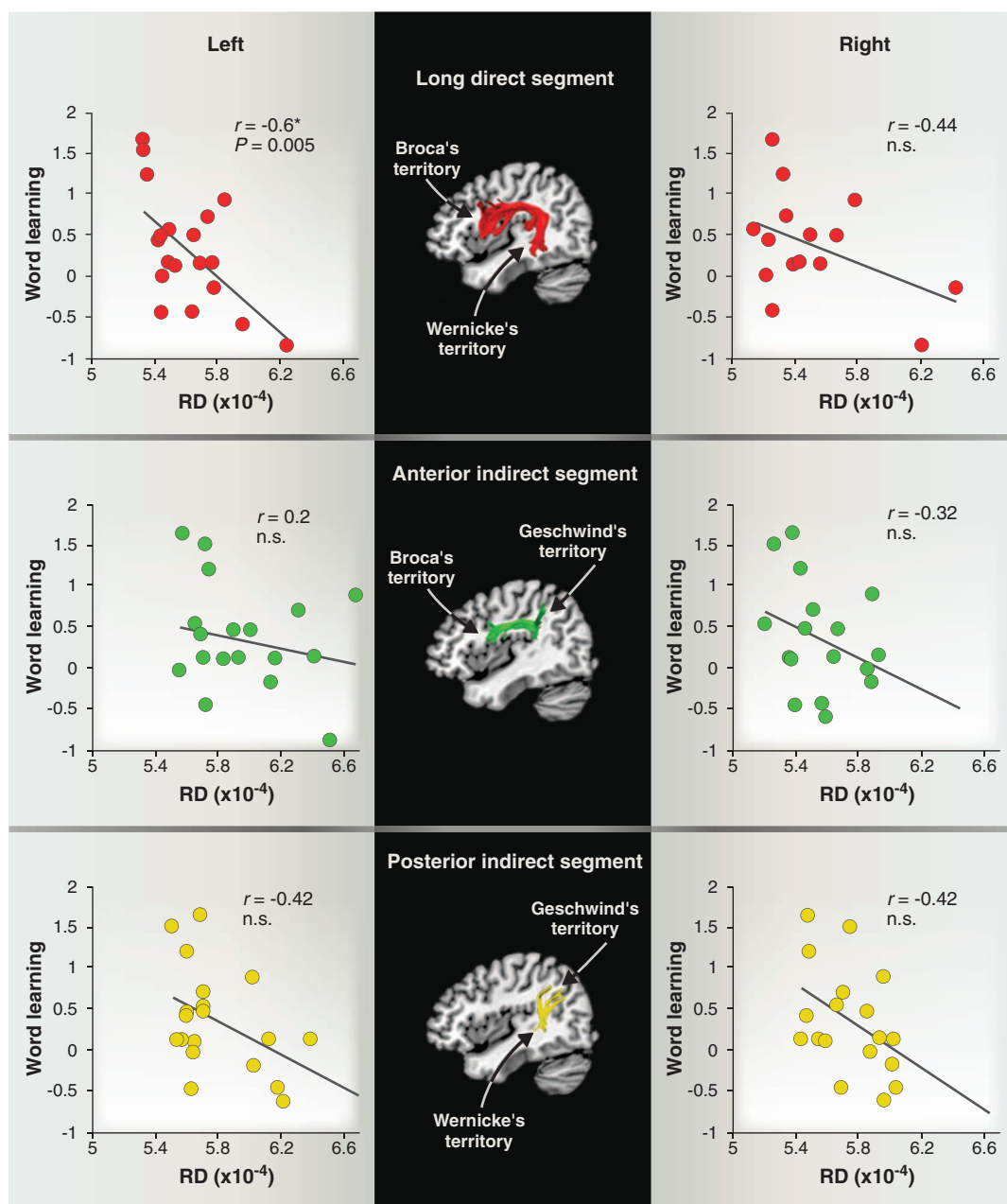
in white-matter organization of fiber tracts connecting frontal and temporal areas of the left hemisphere is associated with better learning of phoneme segmentation in an artificial language speech stream (56) (Fig. 4). This relationship is behaviorally specific, such that when rehearsal is blocked, a more ventral anatomical pathway correlates with learning, presumably reflecting access to an alternate route when the dorsal one is not accessible (57). The studies discussed in this section thus converge in demonstrating that interindividual variability in the distribution of various anatomical features is specifically predictive of subsequent performance or learning success. These relationships are relatively specific in that different

components of the language network are dissociable in terms of their contributions to speech perception versus production, for instance.

Questions, Future Directions, and Implications

Variation is an essential feature of all biological populations; as Darwin observed, without it, selection and hence evolution would not be possible. In cognitive neuroscience, the nature and meaning of individual variability have begun to receive more attention (58, 59). The related idea of neural predispositions for learning now appears to have sufficient empirical support to warrant concerted attention. The parallels that exist in the literature between structure and function, and

Fig. 4. Relation between individual ability to learn to segment new words from a speech stream and microstructure of the arcuate fasciculus. The latter is a fiber tract linking temporal cortex (Wernicke's territory) and inferior frontal cortex (Broca's territory), as well as premotor cortex. Each scatterplot represents individual word learning scores, expressed by d-prime measures, and the radial diffusivity (RD), a measure of white-matter structure. This anatomical feature is significantly predictive of word learning for the direct segment of the arcuate fasciculus (shown in red in top panel) in the left hemisphere. Indirect connections (middle and bottom panels) do not show a significant relationship. [Adapted with permission from (56)]



across domains, serve to motivate this question further. This brief review has provided a glimpse of how the concept may play out in two related domains, speech and music, which can serve as excellent model systems and which could profitably be studied in parallel to a greater extent. Many important questions remain that apply more generally beyond these domains. One obvious one is to identify the source of the individual differences, which in turn leads us to consider the interactions between genetic and epigenetic mechanisms with environmental factors, including the social environment. How these interactions play out with respect to ongoing maturational changes in the nervous system make the question all the more interesting, especially as sensitive periods have been described for both linguistic (60) and musical (61) functions. Another pertinent question is the extent to which individual differences are dissociable from one another; that is, do predispositions that favor one type of learning come at the expense of other abilities, or do they tend to be correlated? The evidence to date tends to indicate dissociations, but if we can identify the many separate predisposing factors that no doubt exist, we may also find that some of them cluster together. It also remains unclear whether predispositions for learning pertain to ultimate attainment potential, or merely speed of learning; the experimental evidence reviewed above suggests that both situations arise, and it is therefore important to not lump them together. An additional question is the extent to which the kinds of predispositions we have discussed represent traits or states; that is, are they stable over time, or do they reflect transient properties of a dynamically changing nervous system? Although much of the evidence seems to deal with the findings in terms of stable traits, given the evidence for experience dependency, it is also reasonable to assume that predispositions may themselves be affected by, or even be the consequence of, ongoing functional and structural changes.

The evidence reviewed here indicates that functional and structural properties of auditory and motor systems, and their interactions, can be construed as predictors of behavioral skill and learning in speech and music. But we do not yet fully understand the relationship between the functional and anatomical effects that are discussed above; nor is it clear how cortical and subcortical systems interact. Continued advances in neuroimaging will help us to understand what neural mechanisms underlie the phenomena under discussion. For example, variance in brain activity (62) may be a relevant indicator of the degree to which an individual nervous system can adapt to new circumstances and hence could help to explain individual proclivities. Similarly, pattern-analysis techniques are increasingly being applied to understand variability in neural activity (63) and could help to identify individual differences as well. Increasingly, both brain structure and

function are being modeled as complex networks (64), and the organization of these networks will no doubt also shed light on the kinds of effects we are discussing here. The human connectome project (www.humanconnectomeproject.org/) will be of importance in this respect, particularly as genomic, phenomic, and cognitive information is added in to help understand variation.

Ultimately, the implications and applications of this knowledge will certainly lead to beneficial outcomes, but may also raise ethical questions. It may seem far-fetched to suppose that some neural measure could in the future be used to decide if someone should benefit from a certain learning opportunity, but we should prepare to ward off inappropriate uses of knowledge with appropriate discussion. On an optimistic note, I would hope that any kind of knowledge that could make predictions about outcomes would be immensely useful—in a rehabilitation or a pedagogical setting, for instance—in identifying the optimal type of training regime that might be most beneficial to a given individual. To the extent that different individuals have different perceptual, motor, or cognitive strengths and weaknesses, our ability to identify them and their neural bases should help to provide the right kind of training or remediation. Sensory-motor skills are essential for communication, so knowing more about how these skills vary across a population will be important clinically. Even knowing something about the speed with which one should expect learning to proceed could be helpful in this regard. We each have a unique brain, without which the world would be a very boring place indeed. It will be up to us to use our increasing knowledge of this uniqueness in productive ways.

References and Notes

1. A. D. Patel, *Music, Language, and the Brain* (Oxford Univ. Press, New York, 2008).
2. J. E. Warren, R. J. Wise, J. D. Warren, *Trends Neurosci.* **28**, 636–643 (2005).
3. J. P. Rauschecker, S. K. Scott, *Nat. Neurosci.* **12**, 718–724 (2009).
4. G. Hickok, D. Poeppel, *Nat. Rev. Neurosci.* **8**, 393–402 (2007).
5. R. J. Zatorre, J. L. Chen, V. B. Penhune, *Nat. Rev. Neurosci.* **8**, 547–558 (2007).
6. S. C. Herholz, R. J. Zatorre, *Neuron* **76**, 486–502 (2012).
7. C. Y. Wan, G. Schlaug, *Neuroscientist* **16**, 566–577 (2010).
8. A. M. C. Kelly, H. Garavan, *Cereb. Cortex* **15**, 1089–1102 (2005).
9. F. W. Ohl, H. Scheich, *Curr. Opin. Neurobiol.* **15**, 470–477 (2005).
10. C. Pantev et al., *Nature* **392**, 811–814 (1998).
11. A. Shahin, D. J. Bosnyak, L. J. Trainor, L. E. Roberts, *J. Neurosci.* **23**, 5545–5552 (2003).
12. P. Schneider et al., *Nat. Neurosci.* **5**, 688–694 (2002).
13. P. C. Wong, E. Skoe, N. M. Russo, T. Dees, N. Kraus, *Nat. Neurosci.* **10**, 420–422 (2007).
14. G. Musacchia, M. Sams, E. Skoe, N. Kraus, *Proc. Natl. Acad. Sci. U.S.A.* **104**, 15894–15898 (2007).
15. G. M. Bidelman, J. T. Gandour, A. Krishnan, *J. Cogn. Neurosci.* **23**, 425–434 (2011).
16. T. Fujioka, B. Ross, R. Kakigi, C. Pantev, L. J. Trainor, *Brain* **129**, 2593–2608 (2006).
17. C. Lappe, S. C. Herholz, L. J. Trainor, C. Pantev, *J. Neurosci.* **28**, 9632–9639 (2008).
18. J. H. Song, E. Skoe, K. Banai, N. Kraus, *Cereb. Cortex* **22**, 1180–1190 (2012).
19. S. Koelsch, T. Fritz, K. Schulze, D. Alsop, G. Schlaug, *Neuroimage* **25**, 1068–1076 (2005).
20. E. H. Margulis, L. M. Mlsna, A. K. Uppunda, T. B. Parrish, P. C. M. Wong, *Hum. Brain Mapp.* **30**, 267–275 (2009).
21. J. M. Zarate, R. J. Zatorre, *Neuroimage* **40**, 1871–1887 (2008).
22. J. L. Chen, V. B. Penhune, R. J. Zatorre, *J. Cogn. Neurosci.* **20**, 226–239 (2008).
23. R. J. Ellis et al., *Neuroimage* **60**, 1902–1912 (2012).
24. N. Gaab, C. Gaser, G. Schlaug, *Neuroimage* **31**, 255–263 (2006).
25. L. Jäncke, N. Gaab, T. Wüstenberg, H. Scheich, H.-J. Heinze, *Brain Res. Cogn. Brain Res.* **12**, 479–485 (2001).
26. R. J. Zatorre, K. Delhommeau, J. M. Zarate, *Front. Psychol.* **3**, 544 (2012).
27. K. L. Hyde, I. Peretz, R. J. Zatorre, *Neuropsychologia* **46**, 632–639 (2008).
28. Y. Yotsumoto, T. Watanabe, Y. Sasaki, *Neuron* **57**, 827–833 (2008).
29. J. S. Pruitt, J. J. Jenkins, W. Strange, *J. Acoust. Soc. Am.* **119**, 1684–1696 (2006).
30. N. Golestani, R. J. Zatorre, *Brain Lang.* **109**, 55–67 (2009).
31. H. Menning, S. Imaizumi, P. Zwitserlood, C. Pantev, *Learn. Mem.* **9**, 253–267 (2002).
32. C. Alain, J. S. Snyder, Y. He, K. S. Reinke, *Cereb. Cortex* **17**, 1074–1084 (2007).
33. B. Opitz, A. D. Friederici, *Neuroimage* **19**, 1730–1737 (2003).
34. D. E. Callan et al., *Neuroimage* **19**, 113–124 (2003).
35. N. Golestani, R. J. Zatorre, *Neuroimage* **21**, 494–506 (2004).
36. P. C. M. Wong, T. K. Perrachione, T. B. Parrish, *Hum. Brain Mapp.* **28**, 995–1006 (2007).
37. N. Ventura-Campos et al., *J. Neurosci.* **33**, 9295–9305 (2013).
38. J. S. Damoiseaux et al., *Proc. Natl. Acad. Sci. U.S.A.* **103**, 13848–13853 (2006).
39. A. Baldassarre et al., *Proc. Natl. Acad. Sci. U.S.A.* **109**, 3516–3521 (2012).
40. R. J. Zatorre, R. D. Fields, H. Johansen-Berg, *Nat. Neurosci.* **15**, 528–536 (2012).
41. C. Gaser, G. Schlaug, *J. Neurosci.* **23**, 9240–9245 (2003).
42. P. Bermudez, J. P. Lerch, A. C. Evans, R. J. Zatorre, *Cereb. Cortex* **19**, 1583–1596 (2009).
43. S. L. Bengtsson et al., *Nat. Neurosci.* **8**, 1148–1150 (2005).
44. C. J. Steele, J. A. Bailey, R. J. Zatorre, V. B. Penhune, *J. Neurosci.* **33**, 1282–1290 (2013).
45. N. E. V. Foster, R. J. Zatorre, *Neuroimage* **53**, 26–36 (2010).
46. K. L. Hyde et al., *J. Neurosci.* **29**, 3019–3025 (2009).
47. V. Ressel et al., *J. Neurosci.* **32**, 16597–16601 (2012).
48. N. Golestani, C. J. Price, S. K. Scott, *J. Neurosci.* **31**, 4213–4220 (2011).
49. J. G. Chi, E. C. Dooling, F. H. Gilles, *Ann. Neurol.* **1**, 86–93 (1977).
50. N. Golestani, T. Paus, R. J. Zatorre, *Neuron* **35**, 997–1010 (2002).
51. N. Golestani, N. Molko, S. Dehaene, D. LeBihan, C. Pallier, *Cereb. Cortex* **17**, 575–582 (2007).
52. P. C. M. Wong et al., *Cereb. Cortex* **18**, 828–836 (2008).
53. F. K. Wong, B. Chandrasekaran, K. Garibaldi, P. C. M. Wong, *J. Neurosci.* **31**, 8780–8785 (2011).
54. N. Golestani, C. Pallier, *Cereb. Cortex* **17**, 929–934 (2007).
55. A. Flöel, M. H. de Vries, J. Scholz, C. Breitenstein, H. Johansen-Berg, *Neuroimage* **47**, 1974–1981 (2009).
56. D. López-Barroso et al., *Proc. Natl. Acad. Sci. U.S.A.* **110**, 13168–13173 (2013).
57. D. López-Barroso et al., *Cereb. Cortex* **21**, 2742–2750 (2011).
58. R. Kanai, G. Rees, *Nat. Rev. Neurosci.* **12**, 231–242 (2011).
59. H. Johansen-Berg, *Curr. Opin. Neurol.* **23**, 351–358 (2010).
60. P. K. Kuhl, *Neuron* **67**, 713–727 (2010).
61. V. B. Penhune, *Cortex* **47**, 1126–1137 (2011).
62. D. D. Garrett, N. Kovacevic, A. R. McIntosh, C. L. Grady, *Cereb. Cortex* **23**, 684–693 (2013).
63. J. D. Haynes, G. Rees, *Nat. Rev. Neurosci.* **7**, 523–534 (2006).
64. E. Bullmore, O. Sporns, *Nat. Rev. Neurosci.* **10**, 186–198 (2009).

Acknowledgments: I thank all the authors who shared their materials for figures. I acknowledge support from the Canadian Institutes of Health Research, the Natural Sciences and Engineering Research Council of Canada, the Canada Fund for Innovation, and the Fonds de Recherche Nature et Technologies/Société et Culture via its funding of the Centre for Research in Brain, Language and Music.

10.1126/science.1238414

On and Off Retinal Circuit Assembly by Divergent Molecular Mechanisms

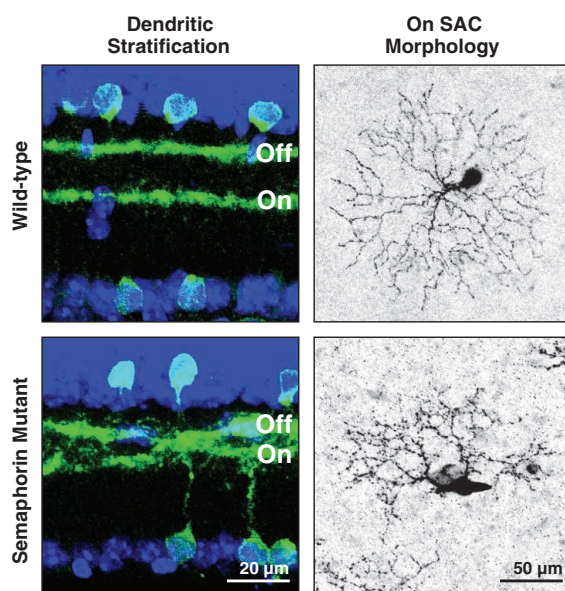
Lu O. Sun, Zheng Jiang, Michal Rivlin-Etzion, Randal Hand, Colleen M. Brady, Ryota L. Matsuoka, King-Wai Yau, Marla B. Feller, Alex L. Kolodkin*

Introduction: Direction-selective responses to visual cues depend upon precise connectivity between inhibitory starburst amacrine cells (SACs) and direction-selective ganglion cells (DSGCs). Motion is detected by SAC responses to illumination onset (On) or cessation (Off). On and Off SACs costratify in the inner plexiform layer of the vertebrate retina with distinct DSGC dendritic arborizations that mediate On or Off directional responses. Here, we study the molecular mechanisms that specify On versus Off SACs and the signaling pathways governing the functional assembly of murine retinal direction-selective circuitry. We show that signaling between the transmembrane guidance cue semaphorin 6A (Sema6A) and its receptor plexinA2 (PlexA2) regulates dendritic morphology of On but not Off SACs, thereby controlling direction-selective responses to visual stimuli.

Methods: We analyzed SAC stratification in the inner plexiform layer, and dendritic morphology of individual On and Off SACs, throughout retinal development in *Sema6A* and *PlexA2* mutant mice. We used dissociated retinal cultures to determine how neurites from genetically labeled SACs respond to exogenous Sema6A. We determined the light-evoked excitatory and inhibitory responses of *Sema6A*^{−/−} On SACs. Finally, we analyzed direction-selective responses in isolated retinas by On-Off direction-selective ganglion cells.

Results: Sema6A is expressed in On, but not Off, SACs, whereas PlexA2 is expressed in all SACs. In vitro, exogenous Sema6A repels neurites only from PlexA2⁺, Sema6A[−] SACs, the in vivo expression profile of Off SACs. In *PlexA2*^{−/−} or *Sema6A*^{−/−} retinas, SAC dendritic stratifications fail to completely segregate from each other; therefore, in vitro and in vivo observations suggest that repulsive interactions between Sema6A and PlexA2 mediate SAC dendritic stratification. Analysis of dendritic morphology in individual SACs in the x-y plane reveals that On SACs in *PlexA2*^{−/−} and *Sema6A*^{−/−} mutants are missing extensive portions of their dendritic fields, have asymmetric dendritic arbors, and exhibit self-avoidance defects; Off SACs in these mutants have normal x-y plane dendritic arbors. Specific On-Off bistratified direction-selective ganglion cells in *Sema6A*^{−/−} mutant retinas exhibit decreased tuning of On-directional motion responses, whereas Off responses in these same cells are unaffected, correlating the elaboration of symmetric SAC dendritic morphology and asymmetric responses to motion.

Discussion: Our findings show that, in addition to contributing to the separation between On and Off SAC dendritic stratifications into distinct inner plexiform layer laminae, Sema6A-PlexA2 signaling selectively regulates the elaboration of symmetric On SAC dendritic fields. Disruption of Sema6A-PlexA2 signaling ultimately results in compromised On, but not Off, directional tuning in a subclass of On-Off direction-selective ganglion cells. Our elucidation of molecular events critical for functional assembly of retinal direction-selective circuitry may have general implications for understanding the establishment of circuitry in which individual neurons participate in multiple distinct pathways.



READ THE FULL ARTICLE ONLINE

<http://dx.doi.org/10.1126/science.1241974>



Cite this article as L. O. Sun *et al.*, *Science* 342, 1241974 (2013). DOI: 10.1126/science.1241974

FIGURES IN THE FULL ARTICLE

Fig. 1. Sema6A is expressed in On, but not Off, SACs in vivo, and SACs lacking Sema6A avoid exogenous Sema6A in vitro.

Fig. 2. Sema6A-PlexA2 signaling segregates On and Off SAC dendritic stratifications in vivo.

Fig. 3. Sema6A-PlexA2 signaling regulates dendritic arborization and symmetric organization in On SACs.

Fig. 4. Sema6A-PlexA2 signaling is dispensable for Off SAC dendritic arborization and ChAT⁺ plexus organization.

Fig. 5. On direction-selective tuning of bistratified TRHR-GFP⁺ direction-selective ganglion cells is compromised in *Sema6A*^{−/−} mutants.

Fig. 6. Sema6A-PlexA2 signaling in the development of SACs and the functional assembly of direction-selective retinal circuits.

SUPPLEMENTARY MATERIALS

Materials and Methods

Figs. S1 to S17

Movies S1 to S6

References

Development of direction-selective circuitry. On and Off mouse SACs normally stratify in discrete layers (**top left**) and exhibit radial dendrite morphology (**top right**). Sema6A and its PlexA2 receptor are expressed in On SACs, but only PlexA2 is expressed in Off SACs. In *Sema6A* mutants, SACs fail to stratify (**bottom left**) and On SACs are misshapen (**bottom right**), compromising responses to "light on" directional cues.

The list of author affiliations is available in the full article online.

*Corresponding author. E-mail: kolodkin@jhmi.edu

On and Off Retinal Circuit Assembly by Divergent Molecular Mechanisms

Lu O. Sun,^{1,2} Zheng Jiang,^{1*} Michal Rivlin-Etzion,^{3*†} Randal Hand,^{1,2} Colleen M. Brady,^{1,2} Ryota L. Matsuoka,^{1,2‡} King-Wai Yau,¹ Marla B. Feller,³ Alex L. Kolodkin^{1,2§}

Direction-selective responses to motion can be to the onset (On) or cessation (Off) of illumination. Here, we show that the transmembrane protein semaphorin 6A and its receptor plexin A2 are critical for achieving radially symmetric arborization of On starburst amacrine cell (SAC) dendrites and normal SAC stratification in the mouse retina. Plexin A2 is expressed in both On and Off SACs; however, semaphorin 6A is expressed in On SACs. Specific On-Off bistratified direction-selective ganglion cells in *semaphorin 6A*^{-/-} mutants exhibit decreased tuning of On directional motion responses. These results correlate the elaboration of symmetric SAC dendritic morphology and asymmetric responses to motion, shedding light on the development of visual pathways that use the same cell types for divergent outputs.

The detection of object motion is a critical visual function. Direction-selective responses to visual cues by the vertebrate retina depend on the precise wiring of inhibitory starburst amacrine cells (SACs) onto direction-selective ganglion cells (DSGCs) (1–4). SACs are divided into onset (On) and cessation (Off) subtypes based on their function, which correlates with localization of their cell bodies and dendritic processes (5). On and Off SACs co-stratify with distinct DSGC dendritic arborizations that have the capacity to mediate On or Off directional responses (6–8), and SACs play a fundamental role in regulating DSGC output (9–12). Protocadherins mediate the self-avoidance of SAC dendrite processes and regulate the morphogenesis of both On and Off SACs (13). However, the molecular mechanisms that specify On versus Off SACs, and the signaling pathways governing the functional assembly of retinal direction-selective circuitry, remain unclear.

Class A plexin receptors (PlexAs) in the developing mouse retina are expressed largely in the inner plexiform layer (14, 15). To identify cell types expressing PlexA2, we performed double immunohistochemistry analyses and observed colocalization of PlexA2 and choline acetyltransferase (ChAT), which is expressed by SACs (Fig. 1, A to C). This observation was confirmed by in situ hybridization analysis (fig. S1, A and C) and by labeling in a *PlexA2-LacZ* reporter mouse (fig. S2, F to I). The protein distributions in the inner

plexiform layer of PlexA2 and semaphorin 6A (Sema6A), a transmembrane semaphorin that is a functional PlexA2 ligand in the mammalian nervous system (16, 17), are complementary with respect to PlexA2 expression in the Off region of the inner plexiform layer, but they exhibit selective overlap in the On region of the inner plexiform layer (Fig. 1, D to F, and fig. S1, E to H"). Sema6A immunoreactivity accumulates along the inner of the two PlexA2-immunopositive (PlexA2⁺) sublaminae, is observed in On but not Off inner plexiform layer neurites, and is found in the cell bodies of all PlexA2⁺ cells in the ganglion cell layer but not the inner nuclear layer (Fig. 1, G to I). Thus, Sema6A and PlexA2 are coexpressed in On, but not Off, SACs.

To investigate the functional importance of this selective PlexA2 and Sema6A protein localization, we isolated SACs from a mouse line, *ChAT::cre;ROSA^{LSL-TdTomato}*, in which both On and Off SACs are genetically labeled with TdTomato (fig. S3, A to C), and cultured them in vitro on stripes coated with recombinant Sema6A-Fc protein. As we observed in vivo, there are two populations of SACs in culture: Sema6A-positive (Sema6A⁺) and Sema6A⁻ SACs (fig. S1, I to K"). Neurites from wild-type Sema6A⁻ SACs avoid Sema6A-Fc stripes, whereas wild-type Sema6A⁺ SACs show no preference and extend their processes freely over Sema6A-Fc and control stripes (Fig. 1, J to K' and N). In contrast, both Sema6A⁻ and Sema6A⁺ SACs derived from *PlexA2*^{-/-} mutant retinas extend neurites equally over Sema6A-Fc and control stripes (Fig. 1, L to N), showing that in vitro exogenous Sema6A repels processes only from SACs that express PlexA2 but not Sema6A—the expression profile of Off SACs in vivo.

To address PlexA2 function in retinal development in vivo, we first characterized SAC sublamina neurite stratification and SAC cell body mosaic patterning in *PlexA2*^{-/-} retinas. SACs normally stratify in two discrete inner plexiform layer laminae: S2 and S4 (Fig. 2A). In *PlexA2*^{-/-} retinas,

however, these two stratifications fail, with full penetrance, to completely segregate from each other (Fig. 2B, and fig. S4, A and A'; *n* = 6 *PlexA2*^{-/-} mutants). This is in contrast to calretinin⁺ amacrine cells and retinal ganglion cells, TH⁺ and vGlut3⁺ amacrine cells, and NK3R⁺, Syt2⁺, and PKCα⁺ bipolar cells, all of which show normal axonal targeting and dendritic stratifications in the *PlexA2*^{-/-} retina (fig. S4, B to G'). In addition, *PlexA2*^{-/-} On and Off SACs exhibit indistinguishable density recovery profiles, and several additional cell body mosaic spacing parameters, compared with control SACs (fig. S5), showing that PlexA2 is dispensable for regulating SAC cell body mosaic spacing.

The in vivo protein distribution of PlexA2 and Sema6A in the inner plexiform layer, and the responses to Sema6A protein by SAC neurites in vitro (Fig. 1), suggest that Sema6A is involved in PlexA2-dependent SAC dendritic stratification. We tested this idea by analyzing *Sema6A*^{-/-} mutant retinas and found that *PlexA2*^{-/-} SAC dendritic stratification defect is phenocopied, with full penetrance and expressivity, in *Sema6A*^{-/-} retinas (Fig. 2C; *n* = 6 *Sema6A*^{-/-} mutants) and is not further enhanced in *PlexA2*^{-/-};*Sema6A*^{-/-} double mutant retinas (*dKO*) (Fig. 2, D and H; *n* = 4 *PlexA2*^{-/-};*Sema6A*^{-/-} mutants). This suggests that *PlexA2* and *Sema6A* are involved in the same signaling pathway that regulates SAC dendritic stratification in the inner plexiform layer (Fig. 2G). To determine whether the segregation of On and Off SAC processes is cell-type-autonomous, we generated a *ChAT::cre;PlexA2^{fl/fl}* mouse line in which PlexA2 is selectively ablated in all SACs (fig. S2, J to M). We observed in these mutant retinas the same stratification defects we found in *PlexA2*^{-/-} mice (Fig. 2, E, F, and H, and fig. S2, J' to M'). SAC dendritic stratification defects were not observed in other *PlexA* null mutant mice (*PlexA1*^{-/-}, *PlexA3*^{-/-}, and *PlexA4*^{-/-}) (fig. S6, A to C) or *neuropilin-1* and -2 deficient mice (fig. S6, D to F), suggesting that most secreted semaphorins do not mediate SAC stratification. The same is true for mutants in the genes encoding the remaining class 6 semaphorin proteins (*Sema6B*, *6C*, and *6D*) (18).

In early postnatal development, wild-type On and Off SAC processes are initially entangled at P0 and P2 but segregate into two distinct stratifications by P4 (Fig. 2I to K') (6, 19). We found that On and Off SAC dendrites in *ChAT::cre;ROSA^{LSL-TdTomato} PlexA2*^{-/-} mice failed to completely segregate by P4 (Fig. 2, O and O'). To further investigate these SAC dendritic process stratification defects, in which On and Off SAC processes apparently cross over between inner plexiform layers 2 and 4, we analyzed sparsely labeled SACs in *ChAT::cre^{ER};ROSA^{LSL-TdTomato};PlexA2*^{-/-} mutant retinas. We observed that dendrites of both On and Off SACs stratify normally in control retinas (*PlexA2*^{+/+}) but that both SAC types can stratify inappropriately in the

¹Solomon H. Snyder Department of Neuroscience, The Johns Hopkins University School of Medicine, Baltimore, MD 21205, USA. ²Howard Hughes Medical Institute, Baltimore, MD 21205, USA. ³Department of Molecular and Cell Biology and the Helen Wills Neuroscience Institute, University of California, Berkeley, Berkeley, CA 94720, USA.

*These authors contributed equally to this work

†Present address: Department of Neurobiology, Weizmann Institute of Science, Rehovot 76100, Israel.

‡Present address: Department of Developmental Genetics, Max Planck Institute for Heart and Lung Research, 61231 Bad Nauheim, Germany.

§Corresponding author. E-mail: kolodkin@jhmi.edu

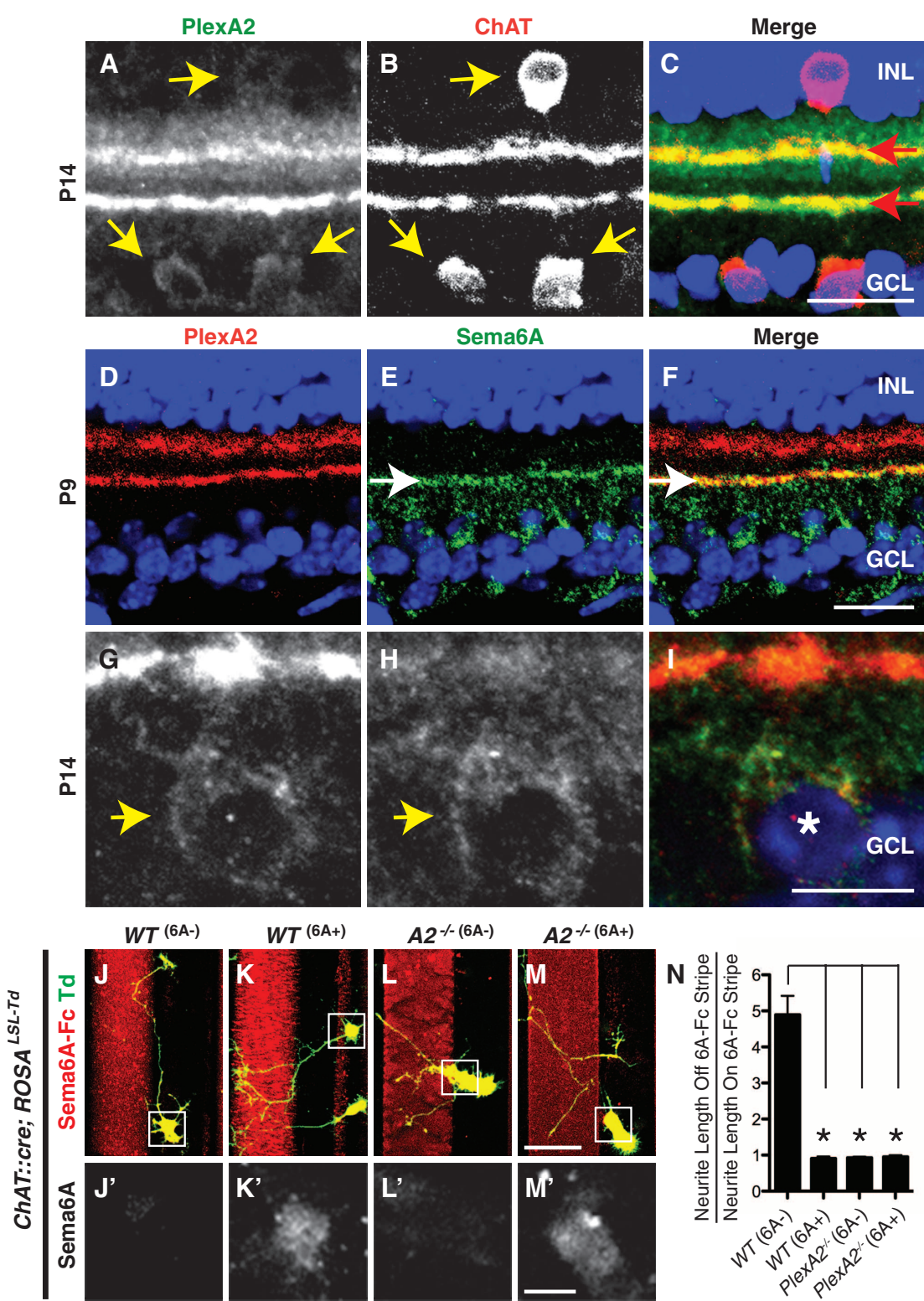
PlexA2^{-/-} mutants (fig. S3). We examined 35 *PlexA2*^{-/-} SAC processes that crossed between the On and Off ChAT bands and traced 17 of these to Off SACs and 18 to On SACs (fig. S3, D to L). Therefore, both in vitro and in vivo observations support the idea that *Sema6A*-*PlexA2* repulsive interactions are a critical component of the mo-

lecular mechanisms that underlie stratification of On and Off SAC dendritic processes.

The formation of distinct On and Off SAC sublamina dendritic process stratifications during early retinal development differentiates these two motion-detection circuits. Because *Sema6A* is expressed selectively and continuously in On,

but not Off, SACs (Fig. 1 and fig. S1), we next asked if *Sema6A*-*PlexA2* signaling functions later in retinal development to refine direction-selective circuitry by regulating On SAC dendritic morphology. To visualize On SAC dendritic morphology, we filled individual adult On SACs with Alexa-555 dye and confirmed their identity by

Fig. 1. *Sema6A* is expressed in On, but not Off, SACs in vivo, and SACs lacking *Sema6A* avoid exogenous *Sema6A* in vitro. (A to C) Mouse P14 retina sections immunostained with antibodies directed against *PlexA2* (green) and ChAT (red) reveal colocalization of *PlexA2* and ChAT immunoreactivity in cell bodies (yellow arrows) and in dendritic processes (red arrows). **(D to I)** Postnatal retina sections immunostained with antibodies to *PlexA2* (red) and antibodies to *Sema6A* (green) show that *PlexA2* and *Sema6A* exhibit mostly complementary protein distributions in the inner plexiform layer [white arrows in (E) and (F)] but that they are coexpressed in On SACs [yellow arrow heads in (G) and (H), white asterisk in (I)]. **(J to N)** Genetically labeled, dissociated SACs from wild-type (WT) retinas are divided into two populations in vitro: *Sema6A*⁻ (J and J') and *Sema6A*⁺ (K and K'). Neurites extending from WT *Sema6A*⁻ SACs avoid exogenous *Sema6A*-Fc stripes (J), whereas WT *Sema6A*⁺ SACs do not (K). *PlexA2*^{-/-} SACs, both *Sema6A*⁺ and *Sema6A*⁻, extend freely over *Sema6A*-Fc stripes [(L) and (M)]. The ratio of SAC neurite length off of *Sema6A*-Fc stripes to neurite length on *Sema6A*-Fc stripes is shown in (N) (*n* ≥ 15 SACs per genotype). Error bars, mean ± SEM. **P* < 0.01. Scale bars, 20 μm in (C) for (A) to (C), 20 μm in (F) for (D) to (F), 10 μm in (I) for (G) to (I), 40 μm in (M) for (J) to (M), and 10 μm in (M') for (J') to (M').



anti-ChAT immunostaining (fig. S7, A to C). Wild-type On SACs exhibited characteristic radially symmetric morphology (Fig. 3A), whereas *PlexA2*^{-/-} On SACs were missing extensive portions of their dendritic fields (Fig. 3B). Also,

normal SAC dendritic self-avoidance was compromised in *PlexA2*^{-/-} On SACs (Fig. 3, A' and B', and fig. S7, D to G). Unlike SAC self-avoidance defects previously described in protocadherin mutants (13), the *PlexA2*^{-/-} defects were con-

fined to the distal-most third of SAC dendritic processes. These same defects were found in *Sema6A*^{-/-} and *PlexA2*^{-/-}; *Sema6A*^{-/-} mutants (Fig. 3, C to D'). Quantification of total dendritic length (Fig. 3E), dendritic field area (Fig. 3F),

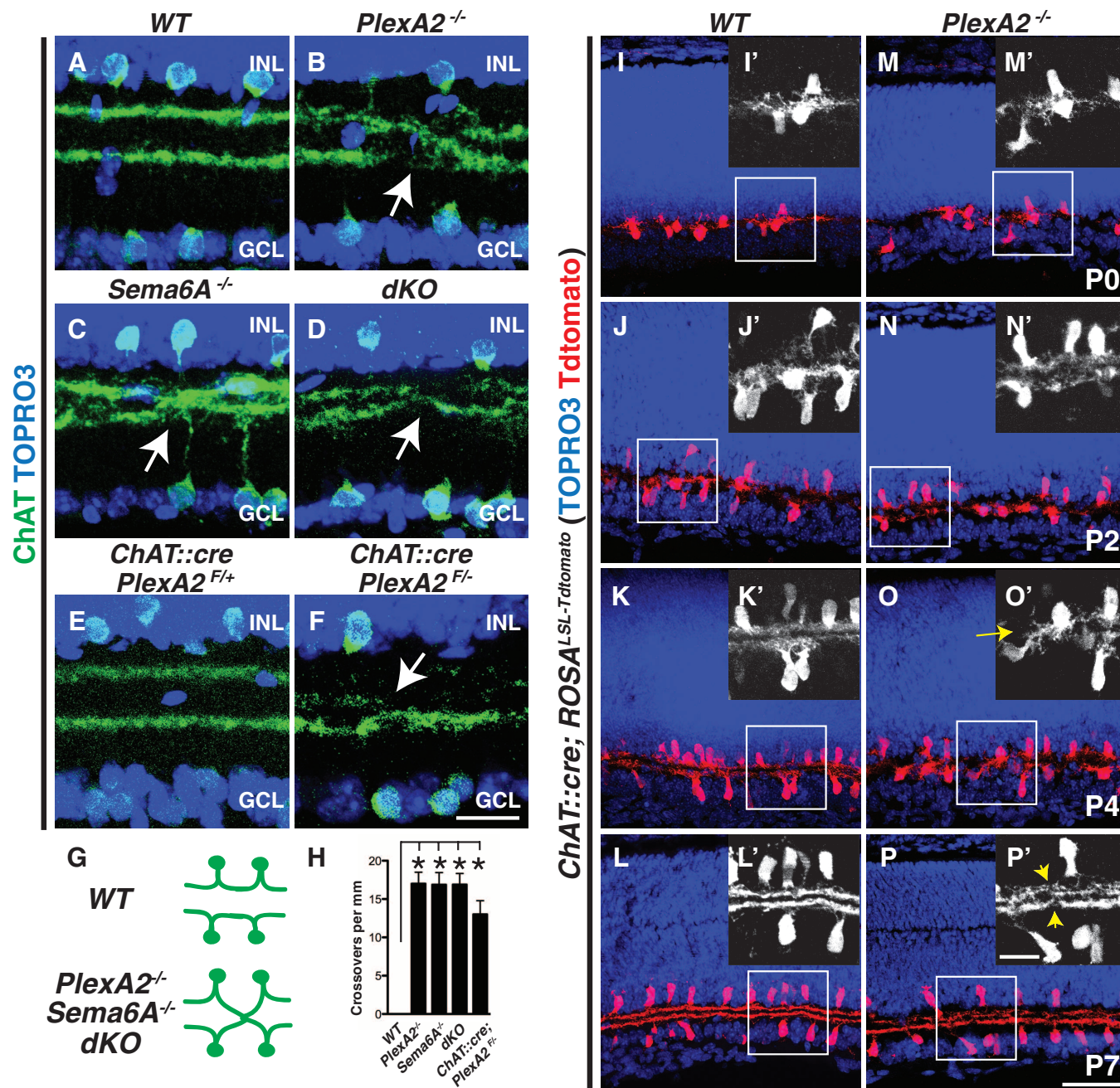


Fig. 2. Sema6A-PlexA2 signaling segregates On and Off SAC dendritic stratifications in vivo. (A to D) Wild-type (A), *PlexA2*^{-/-} (B), *Sema6A*^{-/-} (C), and *PlexA2*^{-/-}; *Sema6A*^{-/-} (D) adult retina sections immunostained with antibodies to ChAT. On and Off SAC processes fail, with full penetrance, to completely segregate in *PlexA2*^{-/-} (B), *Sema6A*^{-/-} (C), and *PlexA2*^{-/-}; *Sema6A*^{-/-} (D) retinas (stratification crossovers indicated by white arrows, $n \geq 4$ mice for each genotype). (E and F) Conditional removal of PlexA2 protein in SACs recapitulates *PlexA2*^{-/-} stratification defects ($n = 3$ mice). (G) Schematics of SAC dendritic stratification in WT, *PlexA2*^{-/-}, *Sema6A*^{-/-}, and *PlexA2*^{-/-}; *Sema6A*^{-/-} mutants. (H) Quantification of SAC stratification crossovers in (A) to (D) and in (F) ($n \geq 6$ retinas per genotype). Error bars, mean \pm SD * $P <$

0.001. (I to P') Characterization of SAC dendritic stratification in WT [(I) to (L')] and *PlexA2*^{-/-} [(M) to (P')] retinas using the SAC TdTomato genetic reporter. In WT retinas, On and Off SAC dendrites are intermingled at P0 [(I) and (I')]. They then segregate during early postnatal retinal development [(J) and (J')] and become completely separate stratifications by P4 [(K) and (K')]. SAC dendritic stratifications in *PlexA2*^{-/-} mutants [(M) and (M')], [(N) and (N')], and [(O) and (O')] are indistinguishable from WT [(I), (I'), (J), and (J')] at P0 and at P2. However, the stratification phenotype is observed by P4 in *PlexA2*^{-/-} retinas [(O) and (O')], yellow arrow] and persists through P7 [(P) and (P')], yellow arrowheads]. $n = 3$ mice for each genotype at each different developmental stage. Scale bars, 20 μ m in (F) for (A) to (F), 50 μ m in (P) for (I) to (P), and 20 μ m in (P') for (I') to (P').

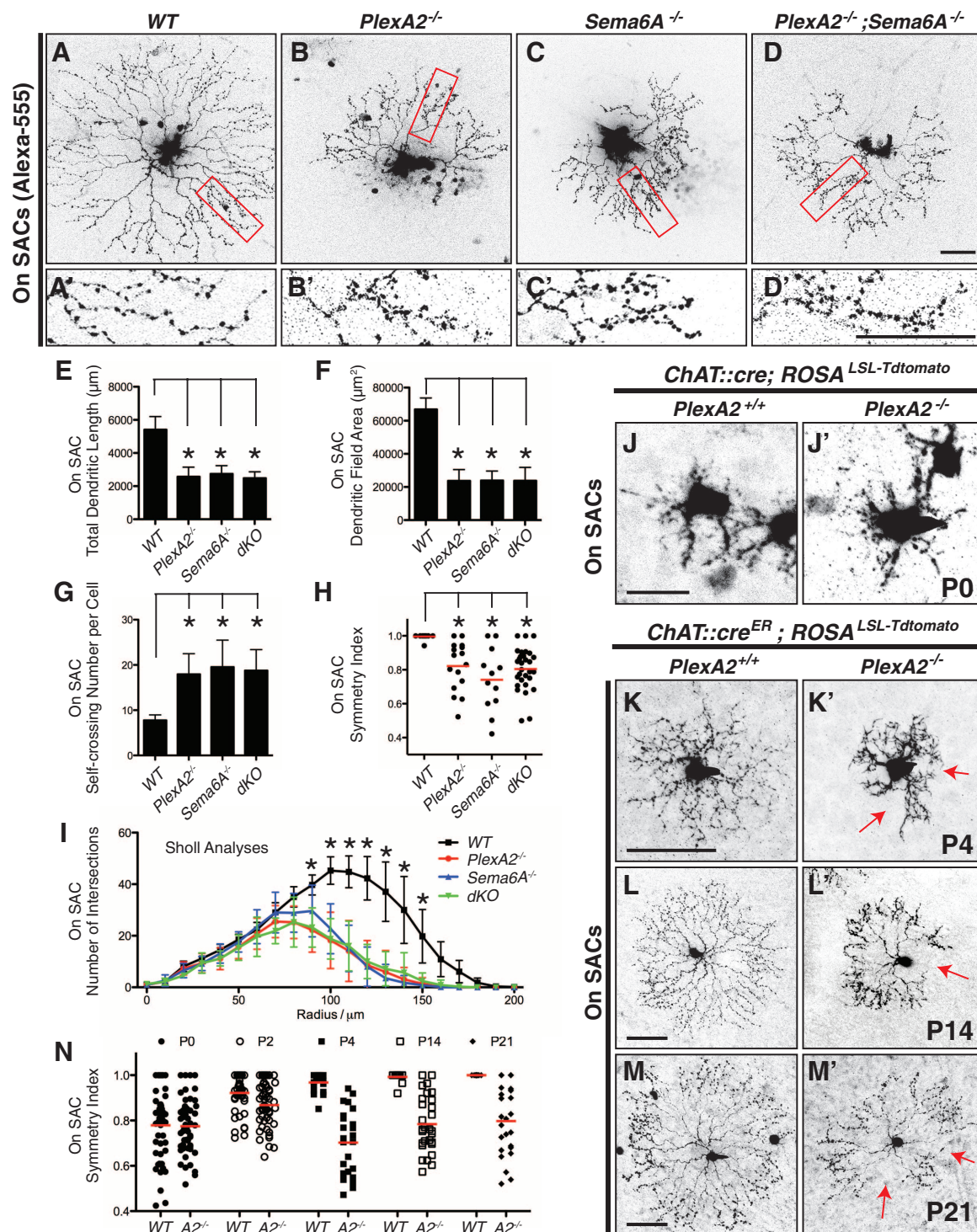


Fig. 3. Sema6A-PlexA2 signaling regulates dendritic arborization and symmetric organization in On SACs. (A to D) Single On SACs labeled with Alexa-555 in WT (A), *PlexA2*^{-/-} (B), *Sema6A*^{-/-} (C), and *PlexA2*^{-/-};*Sema6A*^{-/-} (D) adult retinas. (A' to D') Single-plane confocal images of magnified fields in (A) to (D) (red rectangles) show that higher-order distal dendrites in *PlexA2*^{-/-} (B'), *Sema6A*^{-/-} (C'), and *PlexA2*^{-/-};*Sema6A*^{-/-} (D') retinas exhibit self-avoidance defects in comparison with WT (A'). (E to I) Quantification of total dendritic length (E), dendritic field area (F), self-crossing number per cell (G), symmetry index (H), and dendritic complexity (I, measured by Sholl analyses) shows that overall dendritic morphology is disrupted in *PlexA2*^{-/-}, *Sema6A*^{-/-}, and *PlexA2*^{-/-};*Sema6A*^{-/-} retinas ($n \geq 12$ SACs per genotype). Error bars, mean \pm SD.

* $P < 0.01$. (J to M') Sparse genetic labeling of On SACs in WT retinas [(J) to (M)] shows that dendritic morphology of On SACs is not symmetric at P0 (J) but becomes symmetric during the course of early postnatal retinal development [(K) to (M)]. *PlexA2*^{-/-} On SACs (J') are indistinguishable from WT (J) at P0; however, they fail to establish dendritic process symmetry by P4 [red arrows in (K')] and throughout retinal development [red arrows in (L') and (M')]. (N) Quantification of the symmetry index in WT and *PlexA2*^{-/-} retinas through early postnatal retinal development. Red bars in (H) and (N) represent the mean value for each genotype. Scale bars, 50 μ m in (D) for (A) to (D), 50 μ m in (D') for (A') to (D'), 20 μ m in (J) for (J) and (J'), 50 μ m in (K) for (K) and (K'), 50 μ m in (L) for (L) and (L'), and 50 μ m in (M) for (M) and (M').

self-crossing number per SAC (Fig. 3G), symmetry index (Fig. 3H; defined in fig. S7I), and dendritic complexity (Sholl analysis, Fig. 3I) reveals that the overall dendritic arborization characteristics and symmetric dendritic organization are compromised in *PlexA2*^{-/-}, *Sema6A*^{-/-}, and *PlexA2*^{-/-}; *Sema6A*^{-/-} mutants.

In the developing rabbit retina, On SAC dendritic processes achieve symmetry by postnatal day 0 (P0) (20). In addition to our Alexa-555 injection experiments in adult mice, we used genetic sparse labeling to delineate On SAC morphology throughout postnatal murine retinal development. Wild-type On SACs exhibit asymmetric dendritic morphology at P0 and P2 (Fig. 3J and fig. S8A, top left panels) and display extensive dendritic

process motility early postnatally (movie S1). As early as P4, however, symmetric radial dendritic process organization was achieved (Fig. 3K and fig. S8A, bottom left panels) and then maintained throughout retinal development (Fig. 3, L to N). At P0, *PlexA2*^{-/-} On SAC dendrites resemble wild-type with respect to dendritic asymmetry and other dendritic organization parameters (Fig. 3, J' and N, $P = 0.9884$; and fig. S8, A and B); they also exhibit similar dendritic process motility (movie S2). Nonetheless, they still retain asymmetric dendritic morphology at P4 (Fig. 3, K' and N, $P < 0.001$; and fig. S8A, bottom right panels) or even later (P14 and P21) (Fig. 3, L', M', and N, $P < 0.001$; and fig. S8C). These same defects apply to *Sema6A*^{-/-} mutant retinas (fig. S9). We

did not observe any correlation between SAC dendritic asymmetry phenotypes and the overall location of On SAC cell bodies in *PlexA2*^{-/-} retinas; *PlexA2*^{-/-} On SACs in all four retinal quadrants exhibit the full range of dendritic process symmetry defects (fig. S10). Thus, in addition to contributing to the separation between On and Off SAC dendritic stratifications into distinct inner plexiform layer laminae, *Sema6A*-*PlexA2* signaling regulates the elaboration of symmetric On SAC dendritic fields during postnatal retina development.

To investigate whether *PlexA2*^{-/-} On SAC inner plexiform layer dendritic arborization phenotypes in the *x-y* plane (Fig. 3) are correlated with SAC dendritic stratification defects in the *z* plane

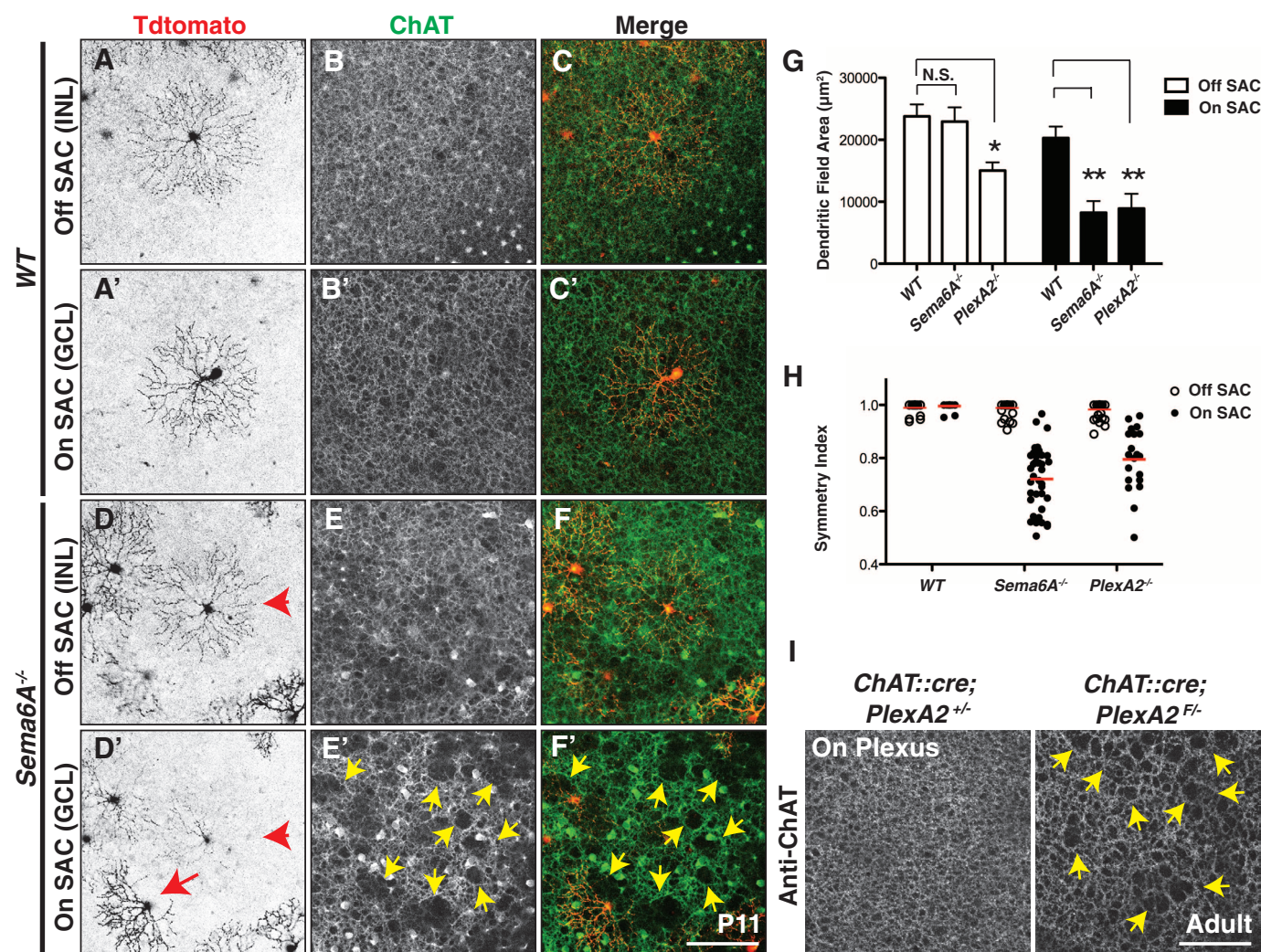


Fig. 4. *Sema6A*-*PlexA2* signaling is dispensable for Off SAC dendritic arborization and ChAT⁺ plexus organization. (A to F') Sparse genetic labeling of On [(A') and (D')] and Off [(A) and (D)] SACs coupled with anti-ChAT immunostaining of On [(B') and (E')] and Off [(B) and (E)] SAC dendritic plexuses in the same WT [(A) to (C')] and *Sema6A*^{-/-} [(D) to (F')] retinas. (D) to (F) and (D') to (F') are different focal planes from the same field. On and Off SACs in WT retinas exhibit stereotypic symmetrical morphology [(A) and (A')]. In contrast, overall dendritic organization of *Sema6A*^{-/-} On SACs [(D)], red arrow, but not Off SACs [(D) and (D'), red arrowhead], is disrupted. Similarly, SAC plexus organization revealed by anti-ChAT immunostaining

shows that only the *Sema6A*^{-/-} On SAC plexus is compromised, as indicated by large gaps and holes [yellow arrowheads in (E') and (F')]. (G and H) Quantification of dendritic field area (G) and symmetry index (H) of WT, *Sema6A*^{-/-}, and *PlexA2*^{-/-} On and Off SACs at P11. Red bars in (H) represent mean value for each genotype. Error bars, mean \pm SD. * $P < 0.01$; ** $P < 0.001$. (I) Dendritic plexus organization of On SACs in control (left) and *ChAT::cre*; *PlexA2*^{F/F} (right) retinas. Conditional removal of *PlexA2* protein in all SACs disrupts On, but not Off (see fig. S14, A and B), SAC plexus (yellow arrowheads in right panel). Scale bars, 100 μ m in (F') for (A) to (F'), 100 μ m in (I) for left and right panels.

of the inner plexiform layer (Fig. 2, A to D), we analyzed both the *x-y* projection images and *z*-stacked images of individual, genetically labeled, *PlexA2*^{-/-} On SACs. We found two classes of *PlexA2*^{-/-} On SACs: (i) those that stratify normally within the ChAT⁺ On sublaminae (11 out of 29 On SACs) (fig. S11, B and B'), and (ii) those that misstratify within the ChAT⁺ Off sublaminae (18 out of 29 On SACs) (fig. S11, C and C'). However, whether these *PlexA2*^{-/-} mutant SACs exhibit normal or aberrant dendritic stratification

within the ChAT⁺ sublaminae, they show the same dendritic field symmetry defects (fig. S11, D to G, and movie S3). Thus, *PlexA2*^{-/-} On SAC dendritic arborization phenotypes in the *x-y* plane are distinct from SAC dendritic stratification defects in the *z* plane.

The restricted expression of *Sema6A* in On SACs raises the possibility that *Sema6A* regulates only On, but not Off, SAC dendritic arborization in the *x-y* plane. In contrast, protocadherins expressed in both On and Off SACs (27) dictate

dendritic self-avoidance in both cell types (13). We investigated this issue by examining genetically labeled Off SACs. Indeed, *Sema6A*^{-/-} Off SACs (Fig. 4D) exhibit the normal, radially symmetric, dendritic morphology found in wild-type SACs (Fig. 4, A and A', quantified in Fig. 4H, and movie S4). *Sema6A*^{-/-} Off SACs also have normal dendritic field area, but *Sema6A*^{-/-} On SACs are abnormal (Fig. 4, D' and G). *PlexA2*^{-/-} Off SACs (figs. S12 and S13 and Fig. 4H) exhibit symmetric dendritic fields, both within and

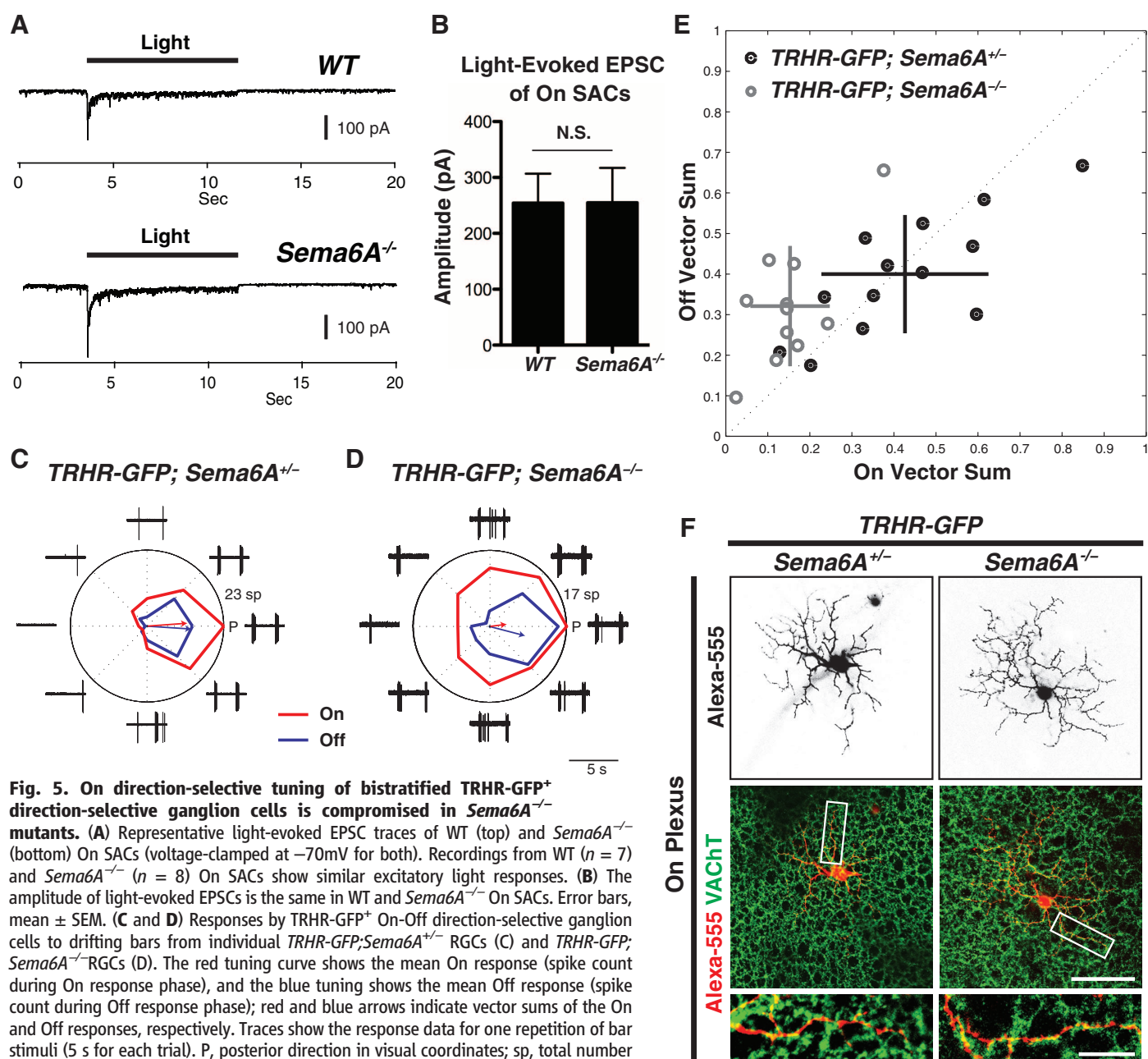


Fig. 5. On direction-selective tuning of bistratified *TRHR-GFP*⁺ direction-selective ganglion cells is compromised in *Sema6A*^{-/-} mutants. (A) Representative light-evoked EPSC traces of WT (top) and *Sema6A*^{-/-} (bottom) On SACs (voltage-clamped at -70mV for both). Recordings from WT (*n* = 7) and *Sema6A*^{-/-} (*n* = 8) On SACs show similar excitatory light responses. (B) The amplitude of light-evoked EPSCs is the same in WT and *Sema6A*^{-/-} On SACs. Error bars, mean ± SEM. (C and D) Responses by *TRHR-GFP*⁺ On-Off direction-selective ganglion cells to drifting bars from individual *TRHR-GFP*⁺; *Sema6A*^{+/-} RGCs (C) and *TRHR-GFP*⁺; *Sema6A*^{-/-} RGCs (D). The red tuning curve shows the mean On response (spike count during On response phase), and the blue tuning curve shows the mean Off response (spike count during Off response phase); red and blue arrows indicate vector sums of the On and Off responses, respectively. Traces show the response data for one repetition of bar stimuli (5 s for each trial). P, posterior direction in visual coordinates; sp, total number of spikes. (E) On vector sum values versus Off vector sum values for *TRHR-GFP*⁺; *Sema6A*^{+/-} cells (black filled circles) and *TRHR-GFP*⁺; *Sema6A*^{-/-} cells (gray rings). Horizontal and vertical lines represent SD values. (F) Alexa-555 dye-fills of individual *TRHR-GFP*⁺ On-Off direction-selective ganglion cells and immunostaining with antibody to VACHT in P30 *Sema6A*^{+/-} (left column) and *Sema6A*^{-/-} mutants (right column) reveal that *TRHR-GFP*⁺; *Sema6A*^{-/-} On-Off direction-selective ganglion cells still cofasciculate with On SAC dendritic processes and display normal dendritic arbor morphology in the On plexus (also see fig. S16). Scale bars, 100 μm in the middle right panel of (F) for top and middle panels, 25 μm in the bottom right panel of (F) for the bottom two panels.

outside of regions where On and Off SAC dendrites fail to separate from one another (fig. S11H). Reconstruction of individual *PlexA2*^{+/+} and *PlexA2*^{-/-} Off SAC dendritic arbors further illustrates that a fraction of mutant Off SAC dendritic processes from an individual SAC can stratify within the ChAT⁺ On sublamina without affecting the symmetric morphology of the entire Off SAC dendritic arbor (movies S5 and S6). We observed that *PlexA2*^{-/-} On SACs show a modest reduction in dendritic field area (Fig. 4G and fig. S13H), suggesting that PlexA2 may promote dendritic-process outgrowth in Off SACs.

The dendritic arborization defects observed in individual *Sema6A*^{-/-} and *PlexA2*^{-/-} mutant SACs can be generalized to the overall On SAC dendritic plexus organization. Using anti-ChAT immunostaining to label all On and Off SAC

dendritic processes, we observed that only On SAC dendritic plexuses are defective in *Sema6A*^{-/-} retinas (compare Fig. 4E' with Fig. 4, B, B', and E; quantification in fig. S12G). Large gaps and holes in the ChAT⁺ plexuses were found in areas where *Sema6A*^{-/-} On SACs failed to elaborate their dendrites (compare Fig. 4F' with Fig. 4, C, C', and F). The organization of the On SAC dendritic plexus is not likely mediated by the other Sema6 proteins because *Sema6B*^{-/-} and *Sema6C*^{-/-}; *Sema6D*^{-/-} double mutants exhibit normal On and Off SAC plexus organization (fig. S14C; quantification in fig. S14D). Defects in the *PlexA2*^{-/-} ChAT⁺ On plexus phenocopy those observed in *Sema6A*^{-/-} mutants (fig. S12, B to F'; quantification in S12G), and conditional removal of *PlexA2* in all SACs disrupts On, but not Off, ChAT⁺ dendritic plexus organization (Fig. 4I

and fig. S14, A and B). These results show that PlexA2 is cell-type-autonomously required for On, but not Off, SAC plexus organization.

To investigate the correlation between SAC morphological defects and function (22), we performed patch-clamp recordings from labeled On SACs in flat-mount retinas of *ChAT::cre; ROSA^{LSL-TdTomato}* mice in wild-type or *Sema6A*^{-/-} genetic backgrounds. Although *Sema6A*^{-/-} On SACs exhibit reduced dendritic length, coverage area, complexity, and symmetric organization (Fig. 3), the average amplitude of the light-evoked excitatory postsynaptic current (EPSC) is not different from wild-type (Fig. 5, A and B), showing that *Sema6A*^{-/-} On SACs retain normal light-evoked excitatory responses. However, *Sema6A*^{-/-} On SACs showed excess and aberrant light-evoked inhibitory postsynaptic currents (IPSCs) (fig. S15, A to C)

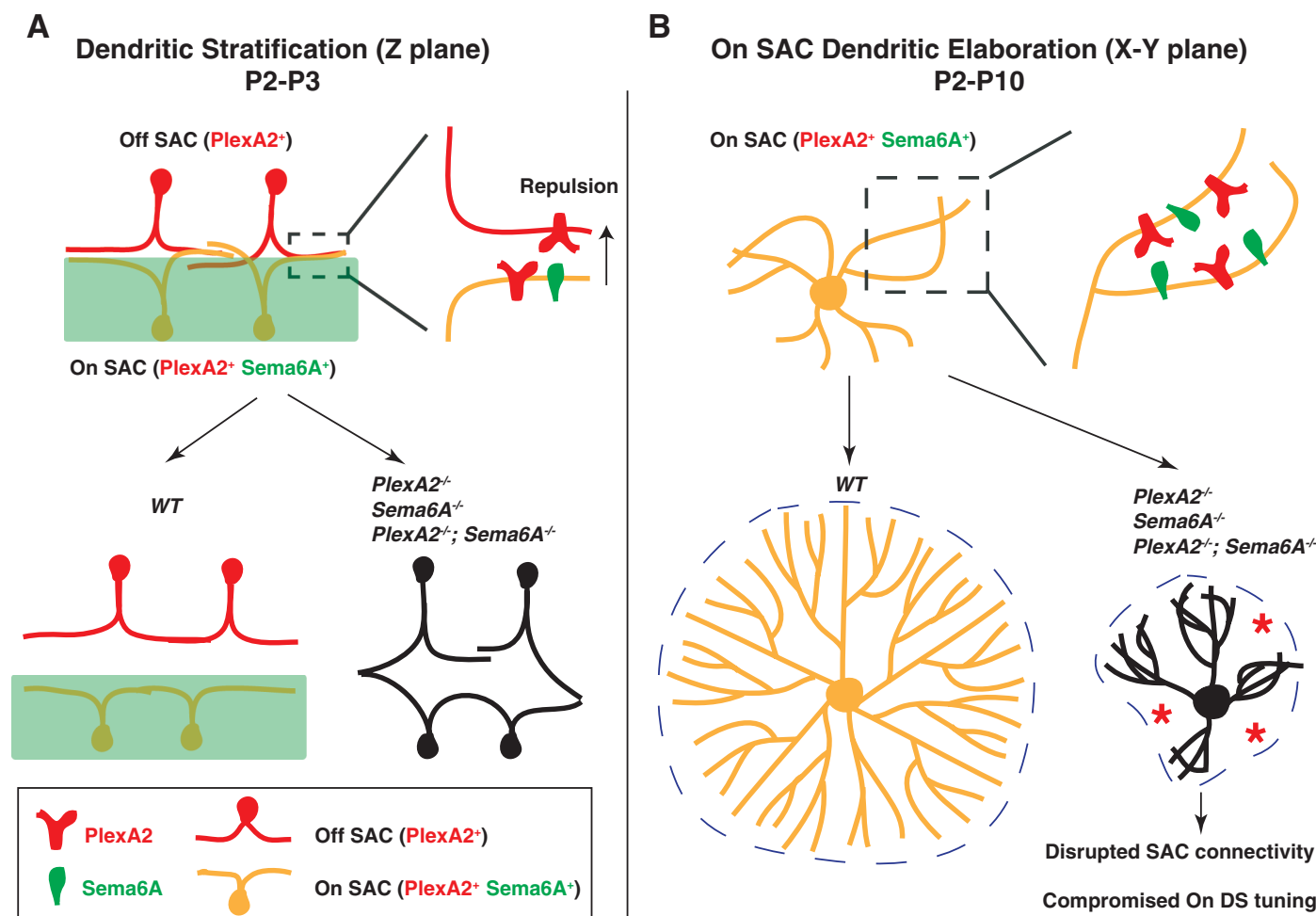


Fig. 6. Sema6A-PlexA2 signaling in the development of SACs and the functional assembly of direction-selective retinal circuits. Sema6A-PlexA2 signaling participates in two aspects of SAC development in the early postnatal mammalian retina. **(A)** In the z plane, PlexA2 is expressed in both On and Off SACs, whereas Sema6A is expressed only in the lower half of the inner plexiform layer and in On, but not Off, SACs. Repulsive Sema6A-PlexA2 signaling in trans segregates initially entangled On and Off SAC processes between P2 and P3. **(B)** In the x-y plane, continuous expression of both Sema6A and PlexA2 in On SACs functions to separate rapidly extending dendritic processes throughout early retinal development (P2 to P10). In WT

retinas, On SACs are not symmetrically organized at P0. In the presence of intact Sema6A and PlexA2 signaling, On SAC dendrites avoid each other during this early phase of SAC dendritic development, leading to elaboration of symmetric SAC dendritic fields by the end of postnatal retinal development. In the absence of Sema6A, PlexA2, or both, many On SAC dendrites fail to fully separate from one another. This affects dendritic process dynamics and eventually causes dendritic field area and symmetry defects in *Sema6A*^{-/-}, *PlexA2*^{-/-}, and *Sema6A*^{-/-}; *PlexA2*^{-/-} mutants. The disruption of On SAC dendritic plexuses affects GABA-mediated connectivity among On SACs and compromises directional tuning of On direction-selective responses.

mediated by γ -aminobutyric acid (GABA) receptors (fig. S15D). The mechanism underlying this change is presently unclear, although increased GABA-mediated lateral inhibition among *Sema6A*^{+/−} On SACs is one likely possibility.

SACs are essential for retina direction-selectivity (23). Their radial symmetric dendritic morphology is likely to be essential for generating direction-selective responses from direction-selective ganglion cells (3). To assess any perturbations in direction-selective output due to SAC morphological defects, we performed cell-patch recordings, using two-photon microscopy to target neurons for electrophysiological analysis, in *TRHR-GFP;Sema6A*^{+/−} and *TRHR-GFP;Sema6A*^{−/−} mouse lines. In these mice On-Off direction-selective ganglion cells with posterior motion detection preference are genetically labeled by green fluorescent protein (GFP) (24). *TRHR-GFP;Sema6A*^{+/−} direction-selective ganglion cells presented with drifting-bar motion stimulation displayed normal posterior-preferred directional tuning for both On and Off responses (Fig. 5C) (24). *TRHR-GFP;Sema6A*^{−/−} direction-selective ganglion cells, in contrast, showed compromised On direction-selective tuning (Fig. 5D, red line), although Off direction-selective tuning is preserved (Fig. 5D, blue line). Pooled data show that On responses in *TRHR-GFP;Sema6A*^{+/−} direction-selective ganglion cells have abnormal, broader, directional tuning, with the magnitudes of the On response vector sums being significantly lower than in the control group (Fig. 5E, 0.15 ± 0.09 for *TRHR-GFP;Sema6A*^{+/−} cells and 0.43 ± 0.20 for *TRHR-GFP;Sema6A*^{+/+} cells, mean \pm SD; $P < 0.01$, Mann-Whitney test). In contrast, *TRHR-GFP;Sema6A*^{−/−} Off direction-selective responses were not significantly broader than those observed in the control group (magnitude values of Off response vector sums: 0.32 ± 0.15 for *TRHR-GFP;Sema6A*^{+/−} cells and 0.40 ± 0.15 for *TRHR-GFP;Sema6A*^{+/+} cells; $P = 0.18$, Mann-Whitney test). Dye-fills of individual *TRHR-GFP*⁺ SACs. *Sema6A*-PlexA2 repulsive signaling may be constrained to early postnatal SACs when overlap with adjacent SAC dendritic processes is minimal, or it may be restricted to emerging dendritic branch points during the course of dendritic arbor growth. Therefore, it is critical to determine the spatial and temporal dynamics of plexin receptor activation during SAC development. In addition, protocadherin signaling (13), and likely additional mechanisms, also mediate SAC dendritic process self-avoidance and allow for inter-cellular SAC dendritic process overlap. Horizontal cells in the mouse retina express both *Sema6A* and another of its receptors, *PlexA4*, and horizontal cell dendrites in *PlexA4*^{−/−} mutants show self-avoidance defects (15). Taken together, our data show that semaphorin ligands and their cognate receptors expressed in the same neuron facilitate the elaboration of dendritic arbors during postnatal retinal development.

Disruption of *Sema6A*-PlexA2 signaling leads to morphological deficits in On SACs and ultimately results in severely compromised On directional tuning in a subclass of direction-selective ganglion cells. Our elucidation of molecular events critical for functional assembly of retinal direction-selective circuitry may have general implications for understanding the establishment of circuitry in which individual neurons participate in multiple, distinct pathways.

Despite our observation of SAC inner plexiform layer stratification defects in all *Sema6A*^{+/−} and *PlexA2*^{+/−} mutant retinas examined, there remain normally stratified SAC processes in these mutants such that most SAC dendrites are still confined to their normal ChAT⁺ sublaminae, suggesting that additional dendritic stratification mechanisms function in parallel to *Sema6A*-PlexA2 signaling to ensure proper SAC dendrite stratification. Our in vitro observation that exogenous *Sema6A* protein repels SAC neurites expressing *PlexA2* but not *Sema6A* (corresponding to Off SACs), but does not affect SAC neurites expressing both *PlexA2* and *Sema6A* (corresponding to On SACs), suggests that *Sema6A* and *PlexA2* use in trans repulsion to facilitate correct SAC stratification. The lack of a repulsive response to exogenous *Sema6A* by SACs that express both *Sema6A* and *PlexA2* likely reflects the silencing of *PlexA2* by ligand expressed in cis, as has been observed in murine sensory neurons that express both *Sema6A* and *PlexA4* and do not respond to exogenous *Sema6A* in vitro (25). Our data suggest that On SAC dendritic processes in vivo are not repelled by exogenous *Sema6A*, so defects in their laminar stratification in the inner plexiform layer may occur as a secondary consequence of Off SAC stratification defects or as a result of distinct *Sema6A*-PlexA2 signaling interactions.

During later postnatal retinal development, select and continuous expression of *Sema6A* in On SACs signals through *PlexA2* to elaborate dendritic morphology, including symmetric organization of dendritic processes (Fig. 6B); apparently, Off SACs use molecular mechanisms distinct from those used by On SACs to achieve symmetric dendritic arbors. *Sema6A*-PlexA2 repulsion likely serves to separate rapidly growing On SAC dendritic processes from one another within the same SAC; however, these repulsive interactions must not occur among neighboring *Sema6A*-PlexA2 repulsive signaling may be constrained to early postnatal SACs when overlap with adjacent SAC dendritic processes is minimal, or it may be restricted to emerging dendritic branch points during the course of dendritic arbor growth. Therefore, it is critical to determine the spatial and temporal dynamics of plexin receptor activation during SAC development. In addition, protocadherin signaling (13), and likely additional mechanisms, also mediate SAC dendritic process self-avoidance and allow for inter-cellular SAC dendritic process overlap. Horizontal cells in the mouse retina express both *Sema6A* and another of its receptors, *PlexA4*, and horizontal cell dendrites in *PlexA4*^{−/−} mutants show self-avoidance defects (15). Taken together, our data show that semaphorin ligands and their cognate receptors expressed in the same neuron facilitate the elaboration of dendritic arbors during postnatal retinal development.

Disruption of *Sema6A*-PlexA2 signaling leads to morphological deficits in On SACs and ultimately results in severely compromised On directional tuning in a subclass of direction-selective ganglion

on cells. Our elucidation of molecular events critical for functional assembly of retinal direction-selective circuitry may have general implications for understanding the establishment of circuitry in which individual neurons participate in multiple, distinct pathways.

References and Notes

1. J. B. Demb, Cellular mechanisms for direction selectivity in the retina. *Neuron* **55**, 179–186 (2007). doi: [10.1016/j.neuron.2007.07.001](https://doi.org/10.1016/j.neuron.2007.07.001); pmid: [17640521](https://pubmed.ncbi.nlm.nih.gov/17640521/)
2. W. Wei, M. B. Feller, Organization and development of direction-selective circuits in the retina. *Trends Neurosci.* **34**, 638–645 (2011). doi: [10.1016/j.tins.2011.08.002](https://doi.org/10.1016/j.tins.2011.08.002); pmid: [21872944](https://pubmed.ncbi.nlm.nih.gov/21872944/)
3. D. I. Vaney, B. Sivy, W. R. Taylor, Direction selectivity in the retina: Symmetry and asymmetry in structure and function. *Nat. Rev. Neurosci.* **13**, 194–208 (2012). pmid: [22314444](https://pubmed.ncbi.nlm.nih.gov/22314444/)
4. R. H. Masland, The neuronal organization of the retina. *Neuron* **76**, 266–280 (2012). doi: [10.1016/j.neuron.2012.10.002](https://doi.org/10.1016/j.neuron.2012.10.002); pmid: [23083731](https://pubmed.ncbi.nlm.nih.gov/23083731/)
5. L. M. Chalupa, E. Günhan, Development of On and Off retinal pathways and retinogeniculate projections. *Prog. Retin. Eye Res.* **23**, 31–51 (2004). doi: [10.1016/j.preteyeres.2003.10.001](https://doi.org/10.1016/j.preteyeres.2003.10.001); pmid: [14766316](https://pubmed.ncbi.nlm.nih.gov/14766316/)
6. R. C. Stacy, R. O. L. Wong, Developmental relationship between cholinergic amacrine cell processes and ganglion cell dendrites of the mouse retina. *J. Comp. Neurol.* **456**, 154–166 (2003). doi: [10.1002/cne.10509](https://doi.org/10.1002/cne.10509); pmid: [12509872](https://pubmed.ncbi.nlm.nih.gov/12509872/)
7. A. D. Huberman *et al.*, Genetic identification of an On-Off direction-selective retinal ganglion cell subtype reveals a layer-specific subcortical map of posterior motion. *Neuron* **62**, 327–334 (2009). doi: [10.1016/j.neuron.2009.04.014](https://doi.org/10.1016/j.neuron.2009.04.014); pmid: [19447089](https://pubmed.ncbi.nlm.nih.gov/19447089/)
8. J. N. Kay *et al.*, Retinal ganglion cells with distinct directional preferences differ in molecular identity, structure, and central projections. *J. Neurosci.* **31**, 7753–7762 (2011). doi: [10.1523/JNEUROSCI.0907-11.2011](https://doi.org/10.1523/JNEUROSCI.0907-11.2011); pmid: [21613488](https://pubmed.ncbi.nlm.nih.gov/21613488/)
9. T. Euler, P. B. Detwiler, W. Denk, Directionally selective calcium signals in dendrites of starburst amacrine cells. *Nature* **418**, 845–852 (2002). doi: [10.1038/nature00931](https://doi.org/10.1038/nature00931); pmid: [12192402](https://pubmed.ncbi.nlm.nih.gov/12192402/)
10. K. L. Briggman, M. Helmstaedter, W. Denk, Wiring specificity in the direction-selectivity circuit of the retina. *Nature* **471**, 183–188 (2011). doi: [10.1038/nature09818](https://doi.org/10.1038/nature09818); pmid: [21390125](https://pubmed.ncbi.nlm.nih.gov/21390125/)
11. W. Wei, A. M. Hamby, K. Zhou, M. B. Feller, Development of asymmetric inhibition underlying direction selectivity in the retina. *Nature* **469**, 402–406 (2011). doi: [10.1038/nature09600](https://doi.org/10.1038/nature09600); pmid: [21131947](https://pubmed.ncbi.nlm.nih.gov/21131947/)
12. K. Yonehara *et al.*, Spatially asymmetric reorganization of inhibition establishes a motion-sensitive circuit. *Nature* **469**, 407–410 (2011). doi: [10.1038/nature09711](https://doi.org/10.1038/nature09711); pmid: [21170022](https://pubmed.ncbi.nlm.nih.gov/21170022/)
13. J. L. Lefebvre, D. Kostadinov, W. V. Chen, T. Maniatis, J. R. Sanes, Protocadherins mediate dendritic self-avoidance in the mammalian nervous system. *Nature* **488**, 517–521 (2012). doi: [10.1038/nature11305](https://doi.org/10.1038/nature11305); pmid: [22842903](https://pubmed.ncbi.nlm.nih.gov/22842903/)
14. R. L. Matsuoka *et al.*, Class 5 transmembrane semaphorins control selective mammalian retinal lamination and function. *Neuron* **71**, 460–473 (2011). doi: [10.1016/j.neuron.2011.06.009](https://doi.org/10.1016/j.neuron.2011.06.009); pmid: [21835343](https://pubmed.ncbi.nlm.nih.gov/21835343/)
15. R. L. Matsuoka *et al.*, Guidance-cue control of horizontal cell morphology, lamination, and synapse formation in the mammalian outer retina. *J. Neurosci.* **32**, 6859–6868 (2012). doi: [10.1523/JNEUROSCI.0267-12.2012](https://doi.org/10.1523/JNEUROSCI.0267-12.2012); pmid: [22593055](https://pubmed.ncbi.nlm.nih.gov/22593055/)
16. F. Suto *et al.*, Interactions between plexin-A2, plexin-A4, and semaphorin 6A control lamina-restricted projection of hippocampal mossy fibers. *Neuron* **53**, 535–547 (2007). doi: [10.1016/j.neuron.2007.01.028](https://doi.org/10.1016/j.neuron.2007.01.028); pmid: [17296555](https://pubmed.ncbi.nlm.nih.gov/17296555/)
17. J. Renaud *et al.*, Plexin-A2 and its ligand, *Sema6A*, control nucleus-centrosome coupling in migrating granule cells. *Nat. Neurosci.* **11**, 440–449 (2008). doi: [10.1038/nn2064](https://doi.org/10.1038/nn2064); pmid: [18327254](https://pubmed.ncbi.nlm.nih.gov/18327254/)

18. R. L. Matsuoka, L. O. Sun, K. Katayama, Y. Yoshida, A. L. Kolodkin, *Sema6B*, *Sema6C*, and *Sema6D* expression and function during mammalian retinal development. *PLoS ONE* **8**, e63207 (2013). doi: [10.1371/journal.pone.0063207](https://doi.org/10.1371/journal.pone.0063207); pmid: [23646199](https://pubmed.ncbi.nlm.nih.gov/23646199/)
 19. K. J. Ford, M. B. Feller, Assembly and disassembly of a retinal cholinergic network. *Vis. Neurosci.* **29**, 61–71 (2012). doi: [10.1017/S0952523811000216](https://doi.org/10.1017/S0952523811000216); pmid: [21787461](https://pubmed.ncbi.nlm.nih.gov/21787461/)
 20. R. O. Wong, S. P. Collin, Dendritic maturation of displaced putative cholinergic amacrine cells in the rabbit retina. *J. Comp. Neurol.* **287**, 164–178 (1989). doi: [10.1002/cne.902870203](https://doi.org/10.1002/cne.902870203); pmid: [2477402](https://pubmed.ncbi.nlm.nih.gov/2477402/)
 21. J. L. Lefebvre, Y. Zhang, M. Meister, X. Wang, J. R. Sanes, Gamma-Protocadherins regulate neuronal survival but are dispensable for circuit formation in retina. *Development* **135**, 4141–4151 (2008). doi: [10.1242/dev.027912](https://doi.org/10.1242/dev.027912); pmid: [19029044](https://pubmed.ncbi.nlm.nih.gov/19029044/)
 22. B. N. Peters, R. H. Masland, Responses to light of starburst amacrine cells. *J. Neurophysiol.* **75**, 469–480 (1996). pmid: [8822571](https://pubmed.ncbi.nlm.nih.gov/8822571/)
 23. K. Yoshida *et al.*, A key role of starburst amacrine cells in originating retinal directional selectivity and optokinetic eye movement. *Neuron* **30**, 771–780 (2001). doi: [10.1016/S0896-6273\(01\)00316-6](https://doi.org/10.1016/S0896-6273(01)00316-6); pmid: [11430810](https://pubmed.ncbi.nlm.nih.gov/11430810/)
 24. M. Rivlin-Etzion *et al.*, Transgenic mice reveal unexpected diversity of on-off direction-selective retinal ganglion cell subtypes and brain structures involved in motion processing. *J. Neurosci.* **31**, 8760–8769 (2011). doi: [10.1523/JNEUROSCI.0564-11.2011](https://doi.org/10.1523/JNEUROSCI.0564-11.2011); pmid: [21677160](https://pubmed.ncbi.nlm.nih.gov/21677160/)
 25. L. Haklai-Topper, G. Mlechkovich, D. Savariego, I. Gokhman, A. Yaron, *Cis* interaction between Semaphorin6A and Plexin-A4 modulates the repulsive response to Sema6A. *EMBO J.* **29**, 2635–2645 (2010). doi: [10.1038/emboj.2010.147](https://doi.org/10.1038/emboj.2010.147); pmid: [20606624](https://pubmed.ncbi.nlm.nih.gov/20606624/)
- Acknowledgments:** We thank D. Ginty for the *ROSA^{LSL-Tdtomato}* mice, J. Nathans for *Six3-cre*, *ChAT::cre*, *ChAT::cre^{ER}*, and *ROSA^{iAP}* mice, and Y. Yoshida for the *Sema6B^{-/-}* and *Sema6C^{-/-};6D^{-/-}* eyes. We also thank S. Hattar, M. Riccomagno,

and Q. Wang for comments on the manuscript and all Kolodkin laboratory members for assistance and discussions throughout the course of this project. This work was supported by NS35165 (A.L.K.); EY06837 (K.-W.Y.); EY019498 and EY013528 (M.B.F.); and the Human Frontier Science Program Organization, the National Postdoctoral Award Program for Advancing Women in Science, and the Edmond and Lily Safra (ELSC) Fellowship for postdoctoral training in Brain Science (M.R.-E.). A.L.K. is an investigator of the Howard Hughes Medical Institute.

Supplementary Materials

www.sciencemag.org/content/342/6158/1241974/suppl/DC1
Materials and Methods
Figs. S1 to S17
Movies S1 to S6
References (26–35)

17 June 2013; accepted 25 September 2013
[10.1126/science.1241974](https://doi.org/10.1126/science.1241974)

Circadian Clock NAD⁺ Cycle Drives Mitochondrial Oxidative Metabolism in Mice

Clara Bien Peek,* Alison H. Affinati,* Kathryn Moynihan Ramsey, Hsin-Yu Kuo, Wei Yu, Laura A. Sena, Olga Ilkayeva, Biliana Marcheva, Yumiko Kobayashi, Chiaki Omura, Daniel C. Levine, David J. Bacsik, David Gius, Christopher B. Newgard, Eric Goetzman, Navdeep S. Chandel, John M. Denu, Milan Mrksich, Joseph Bass†

Introduction: The circadian clock is a transcriptional oscillator that is thought to couple internal energetic processes with the solar cycle. Circadian oscillation in activity of nicotinamide phosphoribosyltransferase (NAMPT), the rate-limiting enzyme in nicotinamide adenine dinucleotide (NAD⁺) biosynthesis, feeds back to regulate activity of the deacetylase SIRT1 and transcription of genes encoding core clock components. Despite evidence that NAD⁺-dependent enzymes are important in fasting and oxidative metabolism, it is not known how the circadian cycle might affect this process. We investigated the role of clock control of NAD⁺ in mitochondrial dynamics and energy production.

Methods: We monitored the response to fasting in liver of wild-type and circadian mutant mice. Quantitative analyses of NAD⁺ biosynthesis, lipid and glucose oxidation, and acetylation of mitochondrial proteins were performed across the circadian cycle in circadian mutant mice and in cell-based systems. Proteins displaying increased acetylation in *Bmal1* mutant liver were identified by mass spectrometry, and SIRT3 activity was evaluated using label-free self-assembled monolayer and matrix desorption ionization (SAMDI) mass spectrometry in liver lysate from *Bmal1* and *Sirt3* knockout mice. The role of NAD⁺ deficiency in SIRT3 activity, mitochondrial protein acetylation, lipid oxidation, and oxygen consumption was evaluated after intraperitoneal administration of the NAD⁺ precursor NMN to raise NAD⁺ levels in *Bmal1* mutant and wild-type mice.

Results: Lipid oxidation and mitochondrial protein acetylation exhibited circadian oscillations that corresponded with the clock-driven NAD⁺ cycle in mouse liver. Rhythmic NAD⁺ and oxidative cycles were self-sustained in fasted mice and in C2C12 myotubes, demonstrating clock control of mitochondrial function even when nutrient state remained constant. Transcription of glycolytic genes was antiphasic to lipid oxidation rhythms, and glycolytic gene expression and lactate production were increased in *Bmal1*^{-/-} fibroblasts, whereas the converse occurred in *Cry1*^{-/-}; *Cry2*^{-/-} mutants. Lack of *Bmal1* in liver led to decreased SIRT3 activity and increased mitochondrial protein acetylation, resulting in reduced function of oxidative enzymes. Finally, NAD⁺ supplementation with NMN restored protein deacetylation of SIRT3 targets and enhanced mitochondrial function in circadian mutant mice.

Discussion: Mitochondria are central to energy homeostasis in eukaryotes, and our results show that the circadian clock generates oscillations in mitochondrial oxidative capacity through rhythmic regulation of NAD⁺ biosynthesis. The clock thereby facilitates oxidative rhythms that correspond with the fasting-feeding cycle to maximize energy production during rest. Use of NAD⁺ as a central node in coupling circadian and metabolic cycles provides a rapid and reversible mechanism to augment mitochondrial oxidative function at the appropriate time in the light-dark cycle.

Circadian regulation of NAD⁺ biosynthesis synchronizes mitochondrial bioenergetics with the light-dark cycle. The core molecular clock is a transcription-translation oscillator composed of activators (CLOCK/BMAL1) that induce transcription of their own repressors (PER/CRY). Clock control of expression of the NAD⁺ biosynthetic enzyme NAMPT generates 24-hour variation of activity of the mitochondrial deacetylase SIRT3 and oxygen consumption. Rhythmic NAD⁺ oscillation couples mitochondrial bioenergetics with the light-dark cycle.

READ THE FULL ARTICLE ONLINE

<http://dx.doi.org/10.1126/science.1243417>



Cite this article as C. B. Peek *et al.*, *Science* 342, 1243417 (2013). DOI: 10.1126/science.1243417

FIGURES IN THE FULL ARTICLE

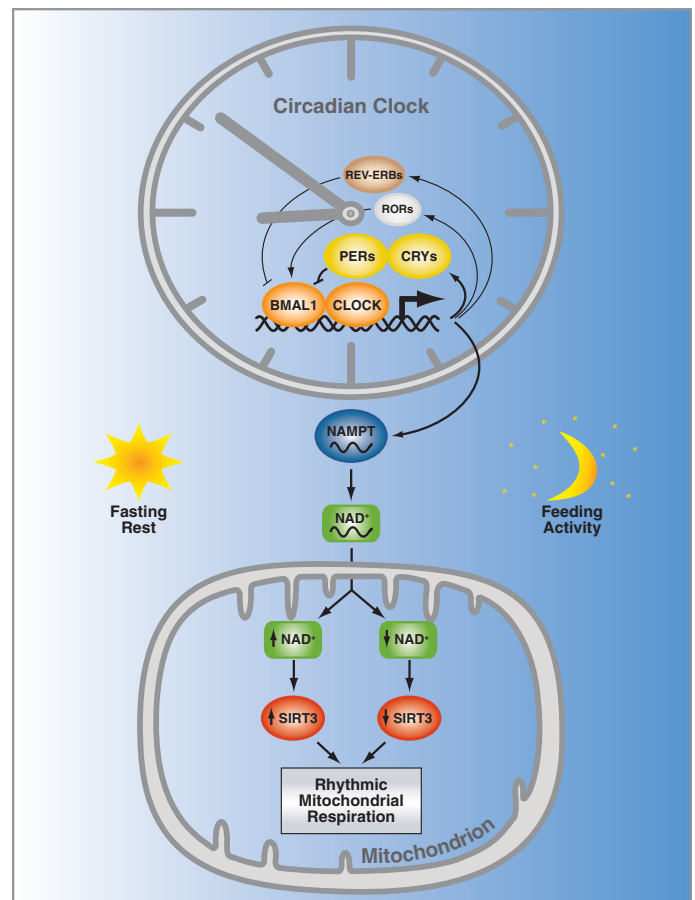
Fig. 1. Circadian clock control of mitochondrial oxidative function.

Fig. 2. Clock control of NAD⁺-dependent mitochondrial metabolism and protein acetylation.

Fig. 3. Circadian regulation of SIRT3 activity.

SUPPLEMENTARY MATERIALS

Supplementary Text
Figs. S1 to S9



Lists of authors and affiliations are available in the full article online.

*These authors contributed equally to this work.

†Corresponding author. E-mail: j-bass@northwestern.edu

Circadian Clock NAD⁺ Cycle Drives Mitochondrial Oxidative Metabolism in Mice

Clara Bien Peek,^{1,2*} Alison H. Affinati,^{1,2*} Kathryn Moynihan Ramsey,^{1,2} Hsin-Yu Kuo,^{3,4} Wei Yu,⁵ Laura A. Sena,^{6,7} Olga Ilkayeva,⁸ Biliana Marcheva,^{1,2} Yumiko Kobayashi,^{1,2} Chiaki Omura,^{1,2} Daniel C. Levine,^{1,2} David J. Bacsik,^{1,2} David Gius,⁹ Christopher B. Newgard,⁸ Eric Goetzman,¹⁰ Navdeep S. Chandel,^{6,7} John M. Denu,⁵ Milan Mrksich,^{3,4} Joseph Bass^{1,2†}

Circadian clocks are self-sustained cellular oscillators that synchronize oxidative and reductive cycles in anticipation of the solar cycle. We found that the clock transcription feedback loop produces cycles of nicotinamide adenine dinucleotide (NAD⁺) biosynthesis, adenosine triphosphate production, and mitochondrial respiration through modulation of mitochondrial protein acetylation to synchronize oxidative metabolic pathways with the 24-hour fasting and feeding cycle. Circadian control of the activity of the NAD⁺-dependent deacetylase sirtuin 3 (SIRT3) generated rhythms in the acetylation and activity of oxidative enzymes and respiration in isolated mitochondria, and NAD⁺ supplementation restored protein deacetylation and enhanced oxygen consumption in circadian mutant mice. Thus, circadian control of NAD⁺ bioavailability modulates mitochondrial oxidative function and organismal metabolism across the daily cycles of fasting and feeding.

The circadian clock is a molecular oscillator that enables light-sensitive organisms to coordinate nutrient storage and use in anticipation of daily periods of activity and rest. Circadian disruption in eubacteria and plants impairs metabolic efficiency and alters growth and reproduction (1, 2). Circadian and metabolic cycles are also closely coupled processes in animals, and at least 10% of all mRNAs exhibit daily oscillations in abundance in mammalian liver, including those from many genes involved in metabolic processes (3–9). Although mouse genetic studies have revealed that clock transcription factors modulate insulin secretion and maintain glucose homeostasis when animals are awake and feeding (10–13), whether the circadian system might also help to maintain energy homeostasis during fasting is less well understood.

Integration of circadian and metabolic cycles is suggested by studies showing that cellular redox status influences the activity of clock transcription factors (14). The abundance of the oxidoreductase factor nicotinamide adenine dinucleotide (NAD⁺) displays circadian rhythmicity due to direct clock transcriptional control of the rate-limiting enzyme in NAD⁺ biosynthesis, NAMPT (nicotinamide phosphoribosyltransferase) (15, 16). In turn, NAD⁺ salvage completes a short feedback loop by driving the activity of the deacetylase SIRT1, which regulates the activity of the CLOCK- and BMAL1-mediated forward limb of the clock (15, 16). In mitochondria, NAD⁺ also regulates SIRT3, a mitochondrial deacetylase important in fatty acid oxidation during fasting (17, 18). Thus, we hypothesized that the circadian clock may control mitochondrial function through rhythmic control of NAD⁺ biosynthesis and posttranslational protein deacetylation to facilitate lipid oxidation during fasting.

Circadian Clock Regulates Mitochondrial Oxidative Metabolism

We examined the role of the circadian clock in 24-hour oxidative cycles by determining whether fatty acid oxidation (FAO), measured by the rate of oxidation of [¹⁴C]oleate to [¹⁴C]CO₂, displayed an endogenous circadian rhythm. We monitored FAO and NAD⁺ in liver homogenates every 4 hours over the course of 48 hours from fasted wild-type mice maintained in constant darkness (Fig. 1A and supplementary text). We observed ~24-hour oscillations of FAO (Fig. 1A, blue line), with peaks occurring near the end of the rest period [circadian time (CT) 8 to 12; CT 32 to 36] that coincided with the rhythms of total cellular NAD⁺ (Fig. 1A, dashed yellow line) and mitochondrial

NAD⁺ (fig. S3A). Although an ultradian oscillation of NAD⁺ abundance occurred in ad libitum-fed mice (15), in fasted mice a single peak of NAD⁺ occurred during the rest period (Fig. 1A), suggesting that the 12-hour harmonic observed in the ad libitum state may be driven by behavioral feeding rhythms.

To determine whether the circadian clock regulates mitochondrial respiration cycles in addition to FAO, we monitored rhythms of oxygen consumption in live cell cultures of mouse C2C12 myoblasts, which when maintained as myotubes display robust PER2 rhythms after synchronization by exposure to a high concentration of serum (Fig. 1A). The C2C12 cycles of NAD⁺ accumulation and oxygen consumption were self-sustained across two complete circadian cycles and in phase with PER2 oscillation, indicating that they were not an acute response to serum exposure (Fig. 1A, green line, and fig. S4A). We further observed a 24-hour variation in glucose oxidation that was offset by 4 hours in phase from the rhythm of FAO (fig. S4B). Together, these data indicate the presence of intrinsic cycles of mitochondrial oxidative metabolism across the 24-hour day, independent of the feeding cycle.

To determine whether expression of the core molecular clock transcription factors has an impact on mitochondrial oxidative metabolism, we next analyzed respiration in mouse embryonic fibroblasts (MEFs) isolated from mice deficient in either the clock transcriptional activators (CLOCK and BMAL1) or repressors (CRY1 and CRY2) (Fig. 1B). MEFs lacking the clock activator gene *Bmal1* displayed decreased FAO and NAD⁺ concentrations, whereas MEFs lacking the clock repressors *Cry1* and *Cry2* showed increased FAO and amounts of NAD⁺ (Fig. 1D and fig. S1), indicating opposing effects of the forward (CLOCK- and BMAL1-mediated) and reverse (CRY- and PER-mediated) limbs of the clock on both NAD⁺ biosynthesis and oxidative metabolism, independent of cellular nutrient availability.

Consistent with impaired mitochondrial energy production from FAO, MEFs lacking the clock activator *Bmal1* produced ~30% less adenosine triphosphate (ATP) when maintained in medium containing galactose, which shifts ATP production from glycolysis to mitochondrial oxidative metabolism (19). In parallel, *Bmal1*^{−/−} MEFs produced ~3 times as much lactate when maintained in glucose-containing medium (Fig. 1B and fig. S1), demonstrating a dependence in these cells on ATP production through glycolysis. Conversely, clock repressor mutant MEFs displayed increased mitochondrial ATP production by ~30% in galactose and decreased lactate production in glucose-containing medium (Fig. 1B and fig. S1), consistent with increased mitochondrial oxidative metabolism.

In support of altered glycolytic metabolism in *Bmal1*^{−/−} mutants, we observed increased expression of key glycolytic genes at multiple time

¹Department of Medicine, Division of Endocrinology, Metabolism and Molecular Medicine, Northwestern University Feinberg School of Medicine, Chicago, IL 60611, USA. ²Department of Neurobiology, Northwestern University, Evanston, IL 60208, USA. ³Department of Chemistry, Northwestern University, Evanston, IL 60208, USA. ⁴Howard Hughes Medical Institute, Northwestern University, Evanston, IL 60208, USA. ⁵Department of Biomolecular Chemistry and Wisconsin Institute for Discovery, University of Wisconsin, Madison, WI 53715, USA. ⁶Department of Medicine, Division of Pulmonary and Critical Care Medicine, Northwestern University Feinberg School of Medicine, Chicago, IL 60611, USA. ⁷Department of Cell and Molecular Biology, Northwestern University Feinberg School of Medicine, Chicago, IL 60611, USA. ⁸Sarah W. Stedman Nutrition and Metabolism Center, Departments of Pharmacology and Cancer Biology and Medicine, Duke University Medical Center, Durham, NC 27705, USA. ⁹Department of Radiation Oncology, Northwestern University Feinberg School of Medicine, Chicago, IL 60611, USA. ¹⁰Department of Pediatrics, Children's Hospital of Pittsburgh, University of Pittsburgh School of Medicine, Pittsburgh, PA 15224, USA.

*These authors contributed equally to this work.

†Corresponding author. E-mail: j-bass@northwestern.edu

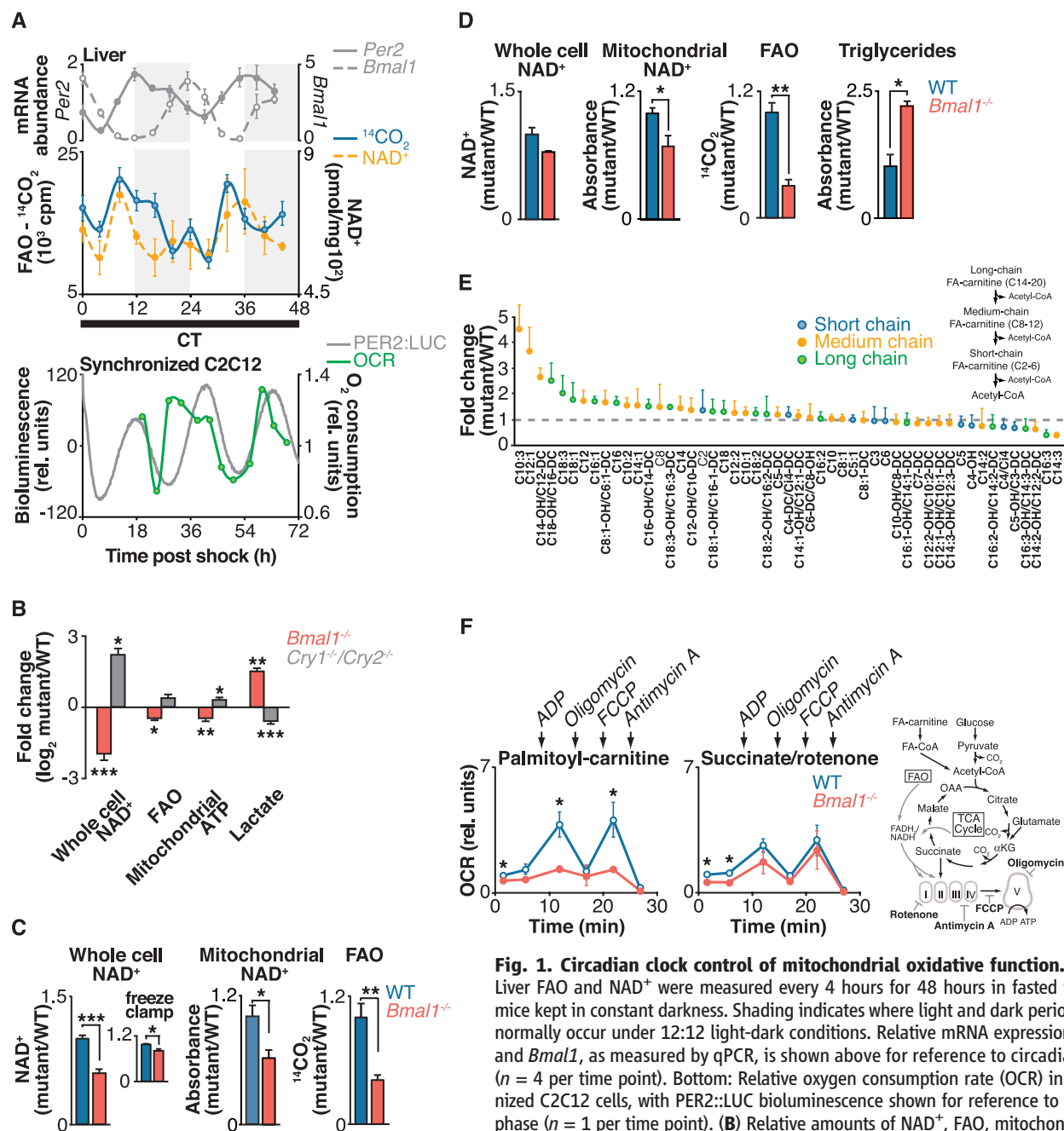


Fig. 1. Circadian clock control of mitochondrial oxidative function. (A) Top: Liver FAO and NAD⁺ were measured every 4 hours for 48 hours in fasted wild-type mice kept in constant darkness. Shading indicates where light and dark periods would normally occur under 12:12 light-dark conditions. Relative mRNA expression of *Per2* and *Bmal1*, as measured by qPCR, is shown above for reference to circadian phase ($n = 4$ per time point). Bottom: Relative oxygen consumption rate (OCR) in synchronized C2C12 cells, with PER2::LUC bioluminescence shown for reference to circadian phase ($n = 1$ per time point). (B) Relative amounts of NAD⁺, FAO, mitochondrial ATP (in galactose-containing media), and lactate (in glucose-containing media) in *Bmal1*^{-/-} and *Cry1*^{-/-}; *Cry2*^{-/-} MEFs compared to wild-type (WT) controls ($n = 6$). (C and D) Relative whole-cell and mitochondrial NAD⁺, FAO, and triglycerides in liver from fasted *Bmal1*^{-/-} liver compared to littermate controls at (C) ZT0 ($n = 4$ to 9) and (D) ZT12 ($n = 3$ or 4). Inset in (C): Relative NAD⁺ from freeze-clamped liver tissue ($n = 5$). (E) Acyl-carnitine profile in liver of *Bmal1*^{-/-} mice compared to WT ($n = 3$). (F) OCR in mitochondria isolated from liver of fasted WT and *Bmal1*^{-/-} mice in the presence of palmitoyl-carnitine or succinate plus rotenone treated sequentially with ADP, oligomycin, FCCP, and antimycin A at ZT0 ($n = 3$ or 4). Schematic shows FAO and TCA cycle pathways, and indicates both OCR substrates and metabolic inhibitors used to evaluate mitochondrial function in circadian mutants. * $P < 0.05$, ** $P < 0.01$, *** $P < 0.001$ for Student's two-tailed t test comparing single time points between WT and mutant averages. Data are represented as average \pm SEM.

points, not only in MEFs but also in liver, including liver pyruvate kinase (*L-Pk*), a catalyst of the final ATP-generating step in glycolysis and an established clock gene target that oscillates during fasting (fig. S5A) (20), as well as phosphofructokinase 1 (*Pfk1*), a rate-limiting glycolytic enzyme (fig. S5, B and C). In contrast, we observed decreased expression of these genes

in *Cry1*^{-/-}; *Cry2*^{-/-} MEFs (fig. S5B). The increased glycolysis in *Bmal1* mutants is unlikely to be an adaptive response to decreased NAD⁺, because glycolytic gene expression was normal in mice with liver-specific *Nampt* ablation (fig. S5D), although these animals exhibited decreased NAD⁺, FAO, and mitochondrial oxygen consumption (Fig. 2C). Likewise, MEFs treated with *n*-[4-(1-

benzoyl-4-piperidinyl)butyl]-3-(3-pyridinyl)-2E-propenamide (FK866), a specific inhibitor of nicotinamide phosphoribosyltransferase (NAMPT), displayed normal lactate production despite having low amounts of NAD⁺ (fig. S5E). Thus, circadian clock transcription factors appear to influence oxidative metabolism through modulation of lipid and glucose oxidation in addition to glycolysis.

We examined mitochondrial function in liver of mice lacking the clock activator gene *Bmal1*. Liver tissue of fasted mice at zeitgeber time (ZT) 0 and ZT12 [corresponding with the trough and peak of NAD^+ in animals maintained on a 12:12 light-dark cycle (15)] showed reduced FAO and decreased amounts of NAD^+ in whole cells and mitochondria (Fig. 1, C and D); *Bmal1*^{-/-} MEFs. We used freeze-clamp isolation of liver to evaluate the potential for post mortem decline in amounts of NAD^+ . Freeze-clamping increased the absolute amount of liver NAD^+ by ~17%, but we still observed a significant NAD^+ deficit in *Bmal1*^{-/-} liver relative to that in control liver (Fig. 1C, inset) (21). Amounts of hepatic FAO and NAD^+ were decreased in liver-specific *Bmal1*^{-/-} mutant mice, which suggested a tissue-specific role for the liver clock in regulation of NAD^+ biosynthesis and mitochondrial oxidative function (fig. S2A). Consistent with defective FAO, hepatic triglyceride levels were increased by a factor of 2.2 in *Bmal1*^{-/-} mutants at ZT12, corresponding with peak FAO in wild-type mice (Fig. 1D). Mass spectrometry analysis demonstrated an accumulation of long- and medium-chain fatty acyl-carnitines with normal amounts of the short-chain species in fasted *Bmal1*^{-/-} liver, indicating a physiologic role for the clock in energy homeostasis during fasting (Fig. 1E).

Impaired Oxidative Capacity in Isolated Mitochondria After Circadian Disruption

To address the impact of the circadian clock on intrinsic mitochondrial biochemical pathways, we isolated intact mitochondria from liver of wild-type and *Bmal1*^{-/-} mice at both ZT0 and ZT12 and monitored their oxygen consumption rate (OCR) in response to lipid and tricarboxylic acid (TCA) cycle intermediates (22). OCR measurements in isolated mitochondria were made in the presence of (i) adenosine diphosphate (ADP) to induce coupled respiration, (ii) the ATP synthase inhibitor oligomycin to measure OCR due to proton leak (uncoupled respiration), (iii) the drug FCCP [carbonyl cyanide 4-(trifluoromethoxy)phenylhydrazone] to uncouple electron transport from the proton gradient generated by ATP synthase and thereby measure maximal flux through the electron transport chain, and (iv) the complex III inhibitor antimycin A to completely halt electron flow and thereby measure nonrespiratory OCR (Fig. 1F, fig. S3, B and C, and supplementary text). Consistent with an intrinsic defect in mitochondrial FAO, *Bmal1*^{-/-} mitochondria had reduced OCR in the presence of long-chain fatty acids (palmitoyl-carnitine) as substrate (Fig. 1F and fig. S3, B and C). This defect was apparent during both coupled (in the presence of ADP) and uncoupled (in the presence of FCCP) respiration, indicating that the mutant mitochondria possess defects in the delivery of electrons from oxidative pathways to the electron transport chain (ETC). In contrast, OCR was normal in circadian mutant mitochondria in response to succinate plus rotenone, which trans-

fers electrons directly to complex II of the ETC, indicating that the ETC remains intact in the clock mutants (Fig. 1F). OCR in the presence of FCCP was also measured in circadian mutant mitochondria treated with other mitochondrial substrates, including medium-chain acyl-carnitine (octanoyl-carnitine), glutamate plus malate, and pyruvate plus malate (fig. S3, B and C). In addition to impaired OCR in circadian mutants in the presence of acyl-carnitines, we observed decreased OCR in the presence of pyruvate plus malate, but not in the presence of glutamate plus malate. Together, these data indicate defects at the level of the β -oxidation pathway in addition to pyruvate entry into the TCA cycle (Fig. 1F and fig. S3, B and C).

All OCR measurements were normalized to mitochondrial protein content in wild-type and mutant animals. Thus, the defects in OCR were not caused by differences in mitochondrial biogenesis. Further, *Bmal1*^{-/-} mutant livers contained normal numbers of mitochondria and displayed normal expression of enzymes that function in mitochondrial biogenesis and FAO, including targets of peroxisome proliferator-activated receptor γ coactivator 1 α (PGC-1 α), a central regulator of mitochondrial biogenesis (fig. S6). Together with the experiments using isolated mitochondria, these data suggest intrinsic defects in liver mitochondrial oxidative pathways in circadian mutants.

Low NAD^+ Contributes to Impaired Mitochondrial Function in Clock Mutants

To test whether NAD^+ deficiency causes mitochondrial oxidative defects in circadian mutant mice, we sought to restore NAD^+ levels in circadian mutant animals through administration of nicotinamide mononucleotide (NMN), a pro-drug that is the product of the NAMPT reaction (23, 24) (Fig. 2A). Injection of animals with NMN increased total cellular NAD^+ in *Bmal1*^{-/-} mouse liver to wild-type levels (Fig. 2A) and increased mitochondrial NAD^+ in the mutants from 53% to 73% of that in wild-type livers (fig. S3D). NMN treatment increased FAO in *Bmal1* mutant mice by a factor of ~2, from 41% to 84% of that in wild-type livers (Fig. 2A). Likewise, NMN significantly increased oxygen consumption during uncoupled (FCCP) respiration in isolated *Bmal1*^{-/-} mitochondria to that of wild-type mitochondria in the presence of palmitoyl-carnitine (Fig. 2B and supplementary text), indicating that NMN supplementation restores intrinsic mitochondrial lipid oxidation in circadian mutants and that circadian mutants lack critical amounts of NAD^+ that can be restored in vivo to improve mitochondrial oxidative capacity. Together with the observation that tissue-specific loss of *Nampt* in liver results in decreased NAD^+ , FAO, and OCR in the presence of palmitoyl-carnitine (Fig. 2C), these results indicate that the circadian clock controls mitochondrial oxidative metabolism through a posttranscriptional process involving NAD^+ biosynthesis.

Clock Regulates Acetylation and Activity of Mitochondrial Oxidative Enzymes

NAD^+ is an important cofactor in oxidative metabolism, and NAD^+ -dependent deacetylase activity affects protein acetylation in mitochondria (17, 25, 26). We therefore sought to identify differences in mitochondrial protein acetylation from livers of wild-type and *Bmal1*^{-/-} mice. Proteins were separated by two-dimensional gel electrophoresis and subjected to immunoblotting using antibody to acetyl-lysine (Fig. 2D). Subsequent mass spectrometry revealed a cluster of proteins with increased acetylation in *Bmal1*^{-/-} mitochondria, including several established SIRT3 targets [ornithine transcarbamylase (OTC), long-chain acyl dehydrogenase (LCAD), and 3-hydroxy-3-methylglutaryl-coenzyme A (CoA) synthase 2 (HMGCS2)] (17, 25, 27) as well as proteins that function in lipid metabolism [e.g., FAO enzymes such as LCAD, medium-chain acyl dehydrogenase (MCAD), electron-transferring flavoprotein (ETF), and enoyl-CoA hydratase short chain 2 (ECHS2)]. *Bmal1*^{-/-} liver mitochondria also displayed decreased enzymatic activity of the medium- and long-chain acyl-CoA dehydrogenases MCAD and LCAD at saturating substrate concentrations (Fig. 2E and fig. S7A), which suggests that circadian control of protein acetylation affects function. Consistent with clock control of mitochondrial enzyme acetylation, we observed ~24-hour oscillation in acetylation of MCAD across the light-dark cycle, with a nadir during the light period and a zenith during the dark period (Fig. 2F). This rhythm is consistent with increased deacetylase activity and FAO during the light or fasting period (mice being nocturnal) because increased amounts of NAD^+ increase deacetylase activity (24, 26, 28). Further, NMN supplementation restored MCAD activity in the *Bmal1* mutants to that of wild-type animals (Fig. 2G). Together, these data are consistent with clock regulation of acetylation and activity of mitochondrial oxidative enzymes that is mediated through circadian control of NAD^+ .

Clock-Driven NAD^+ Oscillations Regulate SIRT3 Activity

We observed increased acetylation of several targets of the NAD^+ -dependent deacetylase SIRT3, an important regulator of intrinsic mitochondrial function including FAO (29) (fig. S7C). To directly evaluate whether circadian disruption impaired SIRT3 activity, we analyzed the acetylation status of SIRT3 targets, including OTC, a urea-cycle protein identified in our proteomic screen (25); manganese superoxide dismutase (MnSOD) (30); and isocitrate dehydrogenase 2 (IDH2) (31, 32). Increased acetylation of OTC correlated with decreased enzymatic activity in circadian mutant liver, indicating that deficiency of SIRT3-mediated deacetylation of OTC reduced its activity (25) (Fig. 3A and fig. S7B). In *Bmal1*^{-/-} mutant liver, we also observed increased acetylation at specific lysine residues within MnSOD (Lys¹²²) (30) and IDH2 (Lys⁴¹³) (31) that are

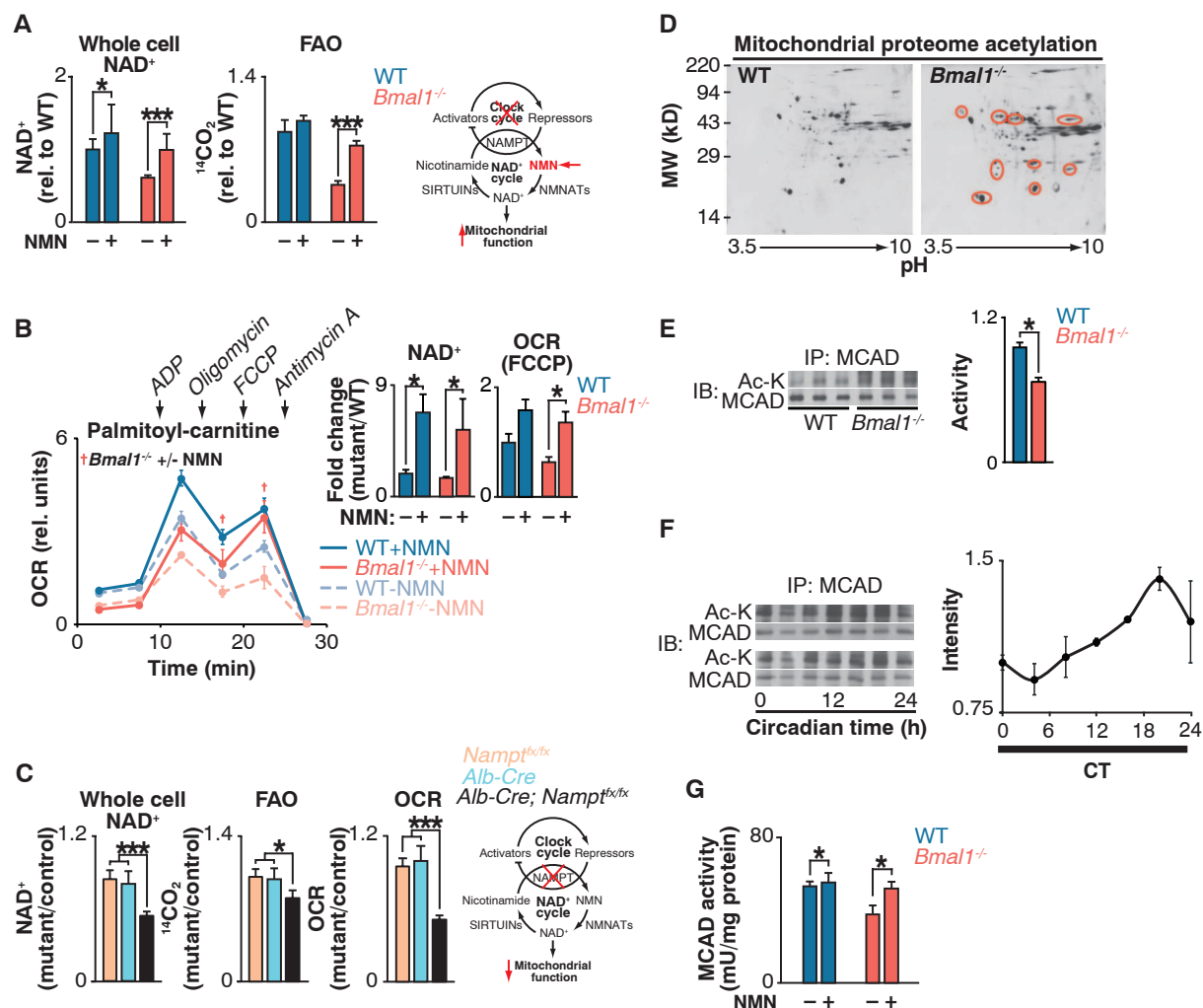


Fig. 2. Clock control of NAD^+ -dependent mitochondrial metabolism and protein acetylation. (A) NAD^+ and FAO in liver of WT and *Bmal1*^{-/-} mice injected with either saline or NMN (250 mg/kg) 12 hours before killing at ZT0 ($n = 6$). Schematic shows interaction of clock with NAD^+ salvage pathway, where the intermediate NMN bypasses the *Nampt* defect in circadian mutants. (B) OCR with palmitoyl-carnitine as substrate in mitochondria isolated from liver of fasted WT and *Bmal1*^{-/-} mice that had been injected once a day for 10 days with either saline or NMN (500 mg/kg) before killing at ZT0 ($n = 3$). Inset: Whole-cell NAD^+ after 10 days of NMN injections and quantification of uncoupled (FCCP) OCR. $\dagger P < 0.05$ indicates Student's two-tailed t test comparison between *Bmal1*^{-/-} mitochondria with and without NMN treatment. (C)

Relative NAD^+ , FAO, and palmitoyl-carnitine OCR in livers of liver-specific *Nampt*^{f/fx} animals ($n = 3$ to 6). (D) Two-dimensional gel electrophoresis of liver mitochondrial proteome from WT and *Bmal1*^{-/-} mice at ZT0. Red circles represent acetylated proteins. (E) Relative MCAD acetylation and activity in WT and *Bmal1*^{-/-} fasted liver mitochondrial extracts at ZT0 ($n = 6$). (F) Relative MCAD acetylation measured every 4 hours for 24 hours in fasted wild-type mice kept in constant darkness ($n = 4$). (G) Relative MCAD activity in liver of WT and *Bmal1*^{-/-} mice injected with either saline or NMN (250 mg/kg) 12 hours before killing at ZT0 ($n = 6$). $*P < 0.05$, $***P < 0.001$ for Student's two-tailed t test comparing single time points between WT and mutant averages. Data are represented as average \pm SEM.

established SIRT3 target sites (Fig. 3A). Further, MnSOD displayed ~24-hour rhythms of acetylation in wild-type mouse liver mitochondria (Fig. 3B), demonstrating that SIRT3 activity is under the control of the circadian clock. The abundance of SIRT3 remained unchanged in circadian mutant liver and across the circadian cycle in wild-type mice, which suggests that SIRT3 activity per se was altered, rather than the amount of the enzyme (fig. S8, A and B).

We examined the impact of NAD^+ deficiency on SIRT3 activity with the use of self-assembled monolayer and matrix desorption ionization (SAMDI), a mass spectrometry-based assay in which acetylated hexapeptide substrates

are assembled as a monolayer through thiol-maleimide binding to gold, avoiding the use of fluorescent labels (33). Using this assay, we established the NAD^+ concentration dependence for deacetylation of a SIRT3-selective peptide substrate (Fig. 3C, left). Amounts of endogenous wild-type and *Bmal1*^{-/-} liver NAD^+ [0.7 mM and 0.4 mM, respectively, as measured by high-performance liquid chromatography (HPLC)] corresponded to changes in SIRT3 activity (Fig. 3C, left) and were consistent with the hypothesis that SIRT3 activity was impaired in the circadian mutants due to reduced amounts of NAD^+ . Further, supplementation of circadian mutant liver extracts with saturating amounts of NAD^+

was sufficient to restore in vitro deacetylation of the SIRT3-selective peptide substrate, whereas SIRT3-deficient mice did not exhibit catalytic activity at the same concentration of NAD^+ (Fig. 3C, right).

To determine whether changes in the ratio of NAD^+ to its reduced form (NADH) contribute to the metabolic and acetylation changes observed in circadian mutants, we measured the amount of NAD^+ and NADH in *Bmal1*^{-/-} and control MEFs. Although amounts of both NAD^+ and NADH were significantly decreased in circadian mutant MEFs, the NAD^+/NADH ratio remained unchanged (fig. S9A). To determine whether a change in the amount of NADH was sufficient to

Materials and Methods

Animals

All animal care and use procedures were in accordance with guidelines of the Institutional Animal Care and Use Committee. For the constant darkness (DD) experiments, male C57BL/6J mice at 12 weeks of age were purchased from the Jackson Laboratory and maintained for 2 weeks on a 12:12 light dark (LD) cycle at the Northwestern University Center for Comparative Medicine before placement in DD. Starting 30 hours after mice were placed in DD, groups of mice ($n = 4$ per group) were subjected to an 18-hour fast before tissue collection, which occurred every 4 hours over a period of 44 hours (i.e., two complete LD cycles). For acute NMN treatment, 3- to 4-month-old *Bmal1*^{-/-} mutant and littermate control mice were intraperitoneally injected with either NMN (250 mg/kg) or saline 12 hours before tissue collection, and all mice were fasted 18 hours before killing. For longer-term NMN treatment, wild-type and *Bmal1*^{-/-} mice were intraperitoneally injected at ZT12 for 10 consecutive days with either NMN (500 mg/kg) or saline, and tissues were collected at ZT0 the day after the final injection. Blood glucose levels were measured by Precision Xtra glucometer at the time of killing. For freeze-clamp studies, 5-month-old wild-type and *Bmal1*^{-/-} mice were anesthetized with 100 μ l of Nembutal before tissue collection. Livers were freeze-clamped in situ with forceps precooled in liquid nitrogen and stored at -80°C (21).

Nucleotide Measurements

For measurement of whole-cell NAD^+ , frozen tissue or cells were extracted in 10% perchloric acid and neutralized in 0.75 M K_2CO_3 as described (15). NAD^+ and ATP were measured by HPLC with Shimadzu LC-20A pump and UV-VIS detector with a Supelco LC-18-T column (15 cm \times 4.6 cm). The HPLC was run at a flow rate of 1 ml/min with 100% buffer A (0.5 M KH_2PO_4 , 0.5 M K_2HPO_4) from 0 to 5 min, a linear gradient to 95% buffer A/5% buffer B (100% methanol) from 5 to 6 min, 95% buffer A/5% buffer B from 6 to 11 min, a linear gradient to 85% buffer A/15% buffer B from 11 to 13 min, 85% buffer A/15% buffer B from 13 to 23 min, and a linear gradient to 100% buffer A from 23 to 30 min. NAD^+ eluted as a sharp peak at 14 min and was normalized to tissue weight of frozen liver tissue or protein content of cultured cells. NAD^+ and nicotinamide were further analyzed and confirmed with liquid chromatography-mass spectrometry (LC-MS/MS) by the Washington University Metabolomics Facility. Mitochondrial NAD^+ , whole-cell NAD^+ , and NADH were also measured using a cycling enzymatic assay (Bioassay Systems).

Acyl-carnitine and Acetyl-CoA Measurements

Snap-frozen liver sections were homogenized in 50% aqueous HPLC grade acetonitrile containing 0.3% formic acid, frozen in liquid nitrogen and stored at -80°C until further preparation for

tandem mass spectrometry. After hepatic protein precipitation with methanol, supernatants were dried, esterified with hot, acidic methanol (for the acyl-carnitine extraction) and then analyzed by tandem mass spectrometry (Quattro Micro, Waters Corp., Milford, MA). Acyl-carnitines and acetyl-CoA were assayed by adapting described methods for analysis of amino acids in dried blood spots (38).

[¹⁴C]Oleate and [¹⁴C]Glucose Oxidation Assays

Whole liver tissue (200 mg) was excised and immediately placed in ice-cold buffer containing 250 mM sucrose, 1 mM EDTA, and 10 mM tris-Cl (pH 7.4). Tissue was homogenized using a Dounce homogenizer and incubated for 1 hour at 37°C in reaction buffer containing 100 mM sucrose, 10 mM tris-Cl (pH 7.4), 5 mM K_2PO_4 , 80 mM KCl, 1 mM MgCl_2 , 2 mM L-carnitine, 0.1 mM malate, 2 mM ATP, 0.05 mM coenzyme A, 1 mM dithiothreitol (DTT), 0.2 mM EDTA, 0.3% bovine serum albumin (BSA), 0.5% fatty acid-free BSA, and 1 μCi (0.125 mM) [¹⁴C]oleic acid-BSA (Perkin Elmer). CO_2 was released from the medium by addition of 35% perchloric acid and captured by Whatman filter paper saturated with 100% phenylethylamine. [¹⁴C] CO_2 counts were determined by scintillation counting. MEFs and C2C12 cells were incubated overnight in Dulbecco's modified Eagle medium (DMEM) containing either 0.5% fetal bovine serum (FBS) or no FBS, respectively, and 0.5% fatty acid-free BSA coupled to 100 μM oleic acid. [¹⁴C]Oleic acid (1.5 μCi) or U-[¹⁴C]glucose (2 μCi) was added to each well and cells were incubated for 2 hours at 37°C . [¹⁴C] CO_2 was captured and measured as described above.

Mouse Embryonic Fibroblast (MEF) Isolation

Pregnant mice were killed at embryonic day 14 or 15, and embryos were dissected away from the uterus and placed in $1\times$ phosphate-buffered saline (PBS). Heads and internal organs were removed and heads were subsequently used for genotyping. Blood was washed away from the remaining carcasses with $1\times$ PBS, and tissue was minced in trypsin-EDTA, followed by incubation with stirring for 30 min. Trypsin was neutralized with heat-inactivated FBS, and cells were pelleted by centrifugation at 270g for 5 min. After centrifugation, cells were resuspended in DMEM containing 15% FBS and plated at 10^6 cells per 100-mm dish. Media was changed 24 hours after plating. Cells were maintained in DMEM containing 15% FBS.

Mitochondrial ATP Production

MEFs were plated in 10-cm dishes and grown to 80% confluence. Media was changed to DMEM containing galactose (4.5 g/liter) and incubated for 24 hours. ATP levels were measured using HPLC as described above and normalized to protein content.

Lactate Production

The rate of lactate production was determined using a Lactate Reagent Kit (Biovision). *Bmal1*^{-/-},

Cry1^{-/-}; *Cry2*^{-/-}, and control MEFs were seeded onto a 6-well culture plate and incubated with fresh culture medium for 8 hours. An aliquot of medium was transferred to a 96-well plate and mixed with lactate reagent. Absorbance at 540 nm was measured using a V5 Spectromax spectrophotometer. Lactate values were normalized to cell number and divided by the length of incubation time. For FK866 treatments, MEFs were incubated with 100 μM FK866 for 24 hours before the media change.

C2C12 Synchronization

C2C12 myoblast cells were infected with *Period 2-luciferase* (*Per2-luc*) expressing lentivirus (gift of A. Liu, University of Memphis) (39) and maintained in DMEM that included 10% FBS and blastocidin (2.5 $\mu\text{g}/\text{ml}$) to select for stable *Per2-luc* integration. Two days before cell synchronization, confluent dishes were differentiated with 2% horse serum. Cells were then synchronized by serum shock every 4 hours for 44 hours with 50% horse serum as described (40). Twenty-four hours after the final shock, cells were collected and analyzed for NAD^+ , OCR, FAO, and glucose oxidation as described. In parallel, *Per2-luc* rhythms were simultaneously monitored in synchronized cells cultured in DMEM containing 0.1 mM luciferin using a LumiCycle apparatus (Actimetrics).

Liver Triglyceride Measurement

Frozen liver tissue was heated in alcoholic KOH at 60°C for 5 hours and precipitated with MgCl_2 . Samples were centrifuged for 30 min at 14,000 rpm and triglycerides were assayed with the Triglyceride Assay Kit (Stanbio).

Mitochondrial and Nuclear Isolation

For isolation of mitochondria for protein, fresh liver samples were dounce-homogenized in isolation buffer containing 0.25 M sucrose, 0.1 mM EDTA, 1 μM Trichostatin A (Sigma), and 20 mM nicotinamide, followed by centrifugation at 800g for 10 min at 4°C . Supernatants were centrifuged again at 800g for 10 min at 4°C to pellet mitochondria. To isolate liver mitochondria for OCR experiments (see below), mitochondria were prepared as recommended by Seahorse Biosciences. Briefly, mitochondria were isolated by dounce homogenization in buffer containing 70 mM sucrose, 210 mM mannitol, 5 mM HEPES, 1 mM EGTA, and 0.5% (w/v) fatty acid-free BSA (pH 7.2). After homogenization, extracts were centrifuged at 800g for 10 min at 4°C . The lipid layer was aspirated, supernatants were centrifuged again at 8000g for 10 min at 4°C , and pellets were resuspended in $1\times$ MAS buffer [70 mM sucrose, 220 mM mannitol, 10 mM KH_2PO_4 , 5 mM MgCl_2 , 2 mM HEPES, 1.0 mM EGTA, and 0.2% (w/v) fatty acid-free BSA (pH 7.2)]. For isolation of liver nuclei, fresh liver samples were first minced in hypotonic buffer containing 10 mM KCl, 1.5 mM MgCl_2 , 1 μM Trichostatin A, and 20 mM nicotinamide and incubated on ice for 20 min.

Samples were centrifuged at 3000g for 3 min to pellet the nuclei.

Oxygen Consumption Rate (OCR) Measurements

OCR was measured in isolated liver mitochondria and C2C12 cells as described (22, 41). Mitochondria (isolated as described above) were plated on Seahorse Biosciences 24-well culture plates (50 µg of protein per well) and centrifuged for 20 min at 2000g at 4°C to adhere mitochondria to base of wells. Respiratory substrates (80 µM palmitoyl- or octanoyl-carnitine plus 0.5 mM malate, 10 mM glutamate plus 10 mM malate, 10 mM pyruvate plus 10 mM malate, or 10 mM succinate plus 2 µM rotenone) were diluted in 1× MAS buffer, added to mitochondria at 37°C, and incubated for 10 min. Plates were placed in Seahorse XF24 Bioanalyzer, and mitochondrial OCR was measured before and after sequential addition of 4 mM ADP, 10 µM Oligomycin, 10 µM FCCP, and 10 µM Antimycin A.

Mitochondrial Number

To estimate mitochondrial number, we extracted total DNA from frozen liver tissue by phenol-chloroform extraction; DNA was subjected to quantitative polymerase chain reaction (qPCR) using primers designed against *Nd1* for mitochondrial DNA and *Gapdh* for nuclear DNA.

Protein Gel Electrophoresis and Immunoblotting

Protein from liver whole tissue, mitochondria, and nuclei was diluted in CellLytic MT Mammalian Tissue Lysis Reagent (Sigma) supplemented with protease inhibitors, 1 µM Trichostatin A, and 20 mM nicotinamide. Protein levels were quantified using DC Protein Assay (Biorad). Protein extracts were subject to SDS-polyacrylamide gel electrophoresis (PAGE) and transferred to nitrocellulose membranes (GE Healthcare). We used primary antibodies to acetylated lysine (Cell Signaling), MCAD (Santa Cruz Biotechnology), SIRT3 (Cell Signaling and generated in J. Denu laboratory), OTC (Abcam), COX4 (Cell Signaling), PGC1 (Santa Cruz Biotechnology), Ac-122-MnSOD [generated in D. Gius laboratory (30)], MnSOD (Millipore), Ac-413-IDH2 (Genetel Laboratories), and IDH2 (Santa Cruz). Mitochondrial protein extracts were subjected to 2D gel electrophoresis and probed with antibody to acetyl-lysine (Cell Signaling) by Kendrick Laboratories in Madison, WI. The 10 most hyperacetylated proteins were identified using SameSpots software; spots were excised from the gel and subjected to mass spectrometry.

Immunoprecipitation

MCAD was immunoprecipitated from 1.5 mg of mitochondrial lysates using 2 µg of mouse antibody to MCAD (Abcam) and Protein A/G-sepharose beads (GE healthcare) in CellLytic MT Mammalian Tissue Lysis Reagent (Sigma) sup-

plemented with protease inhibitors, 1 µM Trichostatin A, and 20 mM nicotinamide. MCAD was eluted by boiling in 1× SDS-PAGE loading buffer followed by immunoblotting for MCAD (Santa Cruz) and acetylated lysine (Cell Signaling). OTC immunoprecipitation and immunoblotting was performed as described (25). Briefly, mitochondrial lysate was incubated with antibody to OTC (Abcam; 1:500) at 4°C overnight. Protein A/G beads (Cell Signaling) were added and samples were incubated for another 3 hours. Beads were washed three times with lysis buffer (50 mM Tris-HCl, pH 7.5, 150 mM NaCl, 1 mM EDTA, 0.1% Nonidet P-40, 50 mM NaF, 1.5 mM Na₃VO₄ containing protease inhibitors, 1 mM DTT, and 1 mM phenylmethylsulfonyl fluoride). OTC was eluted by boiling in 1× SDS-PAGE loading buffer followed by immunoblotting for OTC (Abcam) and acetylated lysine [generated in J. Denu laboratory (25)].

Enzymatic Activity Assays

MCAD and LCAD activity was measured as previously described (17, 42). Briefly, mitochondrial extracts were diluted 1:10 in 50 mM Tris, pH 8.0, with 0.25% lubrol detergent to assist in solubilization. The samples were placed in a sonicating ice water bath for 30 s and then used directly in the anaerobic electron transfer flavoprotein (ETF) reduction assay. Activity was measured in 0.7 ml total volume of 50 mM Tris, pH 8.0, with 1 µM porcine ETF and 20 µM acyl-CoA substrate (either 2,6-dimethylheptanoyl-CoA or octanoyl-CoA for measurement of LCAD or MCAD activity, respectively). After addition of substrate, ETF fluorescence was followed for 1 min (excitation 340 nm, emission 490 nm). Activity measurements are expressed as milli-unit (mU) per milligram of total mitochondrial protein, with 1 mU defined as the amount of enzyme required to fully reduce 1 nmol of ETF in 1 min. OTC enzymatic activity was measured as described (25). Briefly, 10 µl of diluted mitochondrial fraction was added to a solution containing ornithine and triethanolamine to a final volume of 675 µl. OTC reactions were started by adding 75 µl of 150 mM carbamoyl phosphate. Final concentrations in assay of each reagent were 5 mM ornithine, 15 mM carbamoyl phosphate, and 270 mM triethanolamine, pH 7.7. After 30 min of incubation at 37°C, reactions were stopped by adding 375 µl of phosphoric acid/sulfuric acid (3:1, v/v). Citrulline production was determined by adding 47 µl of 3% 2,3-butanedionemonoxime, boiling in the dark for 15 min, and reading absorbance at 490 nm. Relative OTC activities were normalized with OTC levels through Western blotting.

Sirtuin Activity Assays

Liver tissue was flash-frozen in Buffer D (20 mM HEPES, pH 7.9, 100 mM KCl, 0.2 mM EDTA and protease inhibitors), thawed on ice, and homogenized in a Dounce homogenizer. Homogenates were centrifuged at 4000 rpm for 3 min,

and supernatant was removed to a separate tube. The pellets were resuspended in Buffer D and centrifuged at 14,000 rpm for 10 min. The supernatant was combined with the first supernatant and flash frozen. Lysates were thawed on ice and spun twice at 14,000 rpm to clear the lysate. Specific sirtuin activity was then measured from liver extracts using the SAMDI mass spectrometry assay. Liver extracts were diluted in KDAC buffer (25 mM Tris, pH 8.0, 137 mM NaCl, 2.7 mM KCl, 1 mM MgCl₂) to a final protein concentration of 1 mg/ml. TSA (Santa Cruz) was added to the diluted liver extracts to give a final concentration of 50 µM, and 5 µl of the resulting mixtures were distributed into separate wells of a 384-well plate. A protease inhibitor cocktail (1 µl, Roche) and NAD⁺ (1 µl, 4 mM final) were added to each reaction well. To initiate the reaction, 1 µl of the SIRT3-selective peptide substrate (Ac-GRK^AHYC-NH₂) was added at a final concentration of 4 µM, and the reaction plate was incubated at 37°C for 4 hours. Small volumes of each reaction (2 µl) were then transferred onto the maleimide-presenting monolayers to allow immobilization of the peptide substrate and product. The monolayers were then rinsed with distilled water and ethanol, dried under nitrogen, and treated with matrix (2,4,6-trihydroxyacetophenone, 20 mg/ml in acetone). The monolayers were analyzed by matrix-assisted laser desorption/ionization-time-of-flight (MALDI-TOF) MS to obtain a mass spectrum for each circular region, and activities were calculated from each spectrum as described (33).

Quantitative Real-Time PCR

Total RNA was extracted from frozen tissue with Tri Reagent (Molecular Research Center Inc.). cDNA was synthesized using the High Capacity cDNA Reverse Transcription kit (Applied Biosystems). Real-time PCR was performed and analyzed using an Applied Biosystems 7900HT Fast Real-Time PCR System (Applied Biosystems). PCR conditions were: one cycle of 10 min at 95°C, then 35 cycles of 10 s at 95°C, 15 s at 60°C. Relative expression levels (normalized to *Gapdh*) were determined using the comparative CT method.

Primer sequences

Primer	Sequence
Nd1 F	CCCATTGCGTTATTCTT
Nd1 R	AAGTTGATCGTAACGGAAGC
Gapdh F	CAAGGAGTAAGAAACCTGGACC
Gapdh R	CGAGTTGGGATAGGGCCCTCT
L-Pk F	AATATCACCCAGGTCGTGTC
L-Pk R	AAGAAACCACCGTGTCCAC
Ldha F	TCTCGGATGTTGTGAAGGTG
Ldha R	CTGCAGCTCCTCTGGATTTC
Pfk1 F	GCATCACCAACCTGTGTGTC
Pfk1 R	CGATGGTCAAGTGTGCGTAG
Pdk1 F	TGGTATGAGAACGCTAGGC
Pdk1 R	TGTCTGTCCTGGTGATTTCG
Pgk F	ATCAAGGCTGCTGTCCAAAG

References and Notes

- Y. Ouyang, C. R. Andersson, T. Kondo, S. S. Golden, C. H. Johnson, Resonating circadian clocks enhance fitness in cyanobacteria. *Proc. Natl. Acad. Sci. U.S.A.* **95**, 8660–8664 (1998). doi: [10.1073/pnas.95.15.8660](#); pmid: [9671734](#)
- A. N. Dodd *et al.*, Plant circadian clocks increase photosynthesis, growth, survival, and competitive advantage. *Science* **309**, 630–633 (2005). doi: [10.1126/science.1115581](#); pmid: [16040710](#)
- A. Balsalobre, F. Damiola, U. Schibler, A serum shock induces circadian gene expression in mammalian tissue culture cells. *Cell* **93**, 929–937 (1998). doi: [10.1016/S0092-8674\(00\)81199-X](#); pmid: [9635423](#)
- S. Panda *et al.*, Coordinated transcription of key pathways in the mouse by the circadian clock. *Cell* **109**, 307–320 (2002). doi: [10.1016/S0092-8674\(02\)00722-5](#); pmid: [12015981](#)
- J. J. McCarthy *et al.*, Identification of the circadian transcriptome in adult mouse skeletal muscle. *Physiol. Genomics* **31**, 86–95 (2007). doi: [10.1152/physiolgenomics.00066.2007](#); pmid: [17550994](#)
- X. Yang *et al.*, Nuclear receptor expression links the circadian clock to metabolism. *Cell* **126**, 801–810 (2006). doi: [10.1016/j.cell.2006.06.050](#); pmid: [16923398](#)
- K.-F. Storch *et al.*, Extensive and divergent circadian gene expression in liver and heart. *Nature* **417**, 78–83 (2002). doi: [10.1038/nature744](#); pmid: [11967526](#)
- T. Alenqhat *et al.*, Nuclear receptor corepressor and histone deacetylase 3 govern circadian metabolic physiology. *Nature* **456**, 997–1000 (2008). doi: [10.1038/nature07541](#); pmid: [19037247](#)
- D. Feng, M. A. Lazar, Clocks, metabolism, and the epigenome. *Mol. Cell* **47**, 158–167 (2012). doi: [10.1016/j.molcel.2012.06.026](#); pmid: [22841001](#)
- F. W. Turek *et al.*, Obesity and metabolic syndrome in circadian Clock mutant mice. *Science* **308**, 1043–1045 (2005). doi: [10.1126/science.1108750](#); pmid: [15845877](#)
- R. D. Rudic *et al.*, BMAL1 and CLOCK, two essential components of the circadian clock, are involved in glucose homeostasis. *PLoS Biol.* **2**, e377 (2004). doi: [10.1371/journal.pbio.0020377](#); pmid: [15523558](#)
- B. Marcheva *et al.*, Disruption of the clock components CLOCK and BMAL1 leads to hypoinsulinaemia and diabetes. *Nature* **466**, 627–631 (2010). doi: [10.1038/nature09253](#); pmid: [20562852](#)
- K. A. Lamia, K.-F. Storch, C. J. Weitz, Physiological significance of a peripheral tissue circadian clock. *Proc. Natl. Acad. Sci. U.S.A.* **105**, 15172–15177 (2008). doi: [10.1073/pnas.0806717105](#); pmid: [18779586](#)
- J. Rutter, M. Reick, L. C. Wu, S. L. McKnight, Regulation of clock and NPAS2 DNA binding by the redox state of NAD cofactors. *Science* **293**, 510–514 (2001). doi: [10.1126/science.1060698](#); pmid: [11441146](#)
- K. M. Ramsey *et al.*, Circadian clock feedback cycle through NAMPT-mediated NAD⁺ biosynthesis. *Science* **324**, 651–654 (2009). doi: [10.1126/science.1171641](#); pmid: [19299583](#)
- Y. Nakahata, S. Sahar, G. Astarita, M. Kaluzova, P. Sassone-Corsi, Circadian control of the NAD⁺ salvage pathway by CLOCK-SIRT1. *Science* **324**, 654–657 (2009). doi: [10.1126/science.1170803](#); pmid: [19286518](#)
- M. D. Hirschey *et al.*, SIRT3 regulates mitochondrial fatty-acid oxidation by reversible enzyme deacetylation. *Nature* **464**, 121–125 (2010). doi: [10.1038/nature08778](#); pmid: [20203611](#)
- S. C. Kim *et al.*, Substrate and functional diversity of lysine acetylation revealed by a proteomics survey. *Mol. Cell* **23**, 607–618 (2006). doi: [10.1016/j.molcel.2006.06.026](#); pmid: [16916647](#)
- L. D. Marroquin, J. Hynes, J. A. Dykens, J. D. Jamieson, Y. Will, Circumventing the Crabtree effect: Replacing media glucose with galactose increases susceptibility of HepG2 cells to mitochondrial toxicants. *Toxicol. Sci.* **97**, 539–547 (2007). doi: [10.1093/toxsci/kfm052](#); pmid: [17361016](#)
- A. Pizarro, K. Hayer, N. F. Lahens, J. B. Hogenesch, CircDB: A database of mammalian circadian gene expression profiles. *Nucleic Acids Res.* **41**, D1009–D1013 (2013). doi: [10.1093/nar/gks1161](#); pmid: [23180795](#)
- S. P. Davies, D. Carling, M. R. Munday, D. G. Hardie, Diurnal rhythm of phosphorylation of rat liver acetyl-CoA carboxylase by the AMP-activated protein kinase, demonstrated using freeze-clamping. Effects of high fat diets. *Eur. J. Biochem.* **203**, 615–623 (1992). doi: [10.1111/j.1432-1033.1992.tb16591.x](#); pmid: [1346520](#)
- G. W. Rogers *et al.*, High throughput microplate respiratory measurements using minimal quantities of isolated mitochondria. *PLOS ONE* **6**, e21746 (2011). doi: [10.1371/journal.pone.0021746](#); pmid: [21799747](#)
- S.-I. Imai, A possibility of nutraceuticals as an anti-aging intervention: Activation of sirtuins by promoting mammalian NAD biosynthesis. *Pharmacol. Res.* **62**, 42–47 (2010). doi: [10.1016/j.phrs.2010.01.006](#); pmid: [20085812](#)
- J. Yoshino, K. F. Mills, M. J. Yoon, S.-I. Imai, Nicotinamide mononucleotide, a key NAD⁺ intermediate, treats the pathophysiology of diet- and age-induced diabetes in mice. *Cell Metab.* **14**, 528–536 (2011). doi: [10.1016/j.cmet.2011.08.014](#); pmid: [21982712](#)
- W. C. Hallows *et al.*, Sirt3 promotes the urea cycle and fatty acid oxidation during dietary restriction. *Mol. Cell* **41**, 139–149 (2011). doi: [10.1016/j.molcel.2011.01.002](#); pmid: [21255725](#)
- C. Cantó *et al.*, The NAD⁺ precursor nicotinamide riboside enhances oxidative metabolism and protects against high-fat diet-induced obesity. *Cell Metab.* **15**, 838–847 (2012). doi: [10.1016/j.cmet.2012.04.022](#); pmid: [22682224](#)
- T. Shimazu *et al.*, SIRT3 deacetylates mitochondrial 3-hydroxy-3-methylglutaryl CoA synthase 2 and regulates ketone body production. *Cell Metab.* **12**, 654–661 (2010). doi: [10.1016/j.cmet.2010.11.003](#); pmid: [21109197](#)
- P. Belenky *et al.*, Nicotinamide riboside promotes Sir2 silencing and extends lifespan via Nrk and Urh1/Pnp1/Meu1 pathways to NAD⁺. *Cell* **129**, 473–484 (2007). doi: [10.1016/j.cell.2007.03.024](#); pmid: [17482543](#)
- M. D. Hirschey, T. Shimazu, J.-Y. Huang, B. Schwer, E. Verdin, SIRT3 regulates mitochondrial protein acetylation and intermediary metabolism. *Cold Spring Harb. Symp. Quant. Biol.* **76**, 267–277 (2011). doi: [10.1101/sqb.2011.76.010850](#); pmid: [22114326](#)
- R. Tao *et al.*, Sirt3-mediated deacetylation of evolutionarily conserved lysine 122 regulates MnSOD activity in response to stress. *Mol. Cell* **40**, 893–904 (2010). doi: [10.1016/j.molcel.2010.12.013](#); pmid: [21172655](#)
- W. Yu, K. E. Dittenhafer-Reed, J. M. Denu, SIRT3 protein deacetylates isocitrate dehydrogenase 2 (IDH2) and regulates mitochondrial redox status. *J. Biol. Chem.* **287**, 14078–14086 (2012). doi: [10.1074/jbc.M112.355206](#); pmid: [22416140](#)
- S. Someya *et al.*, Sirt3 mediates reduction of oxidative damage and prevention of age-related hearing loss under caloric restriction. *Cell* **143**, 802–812 (2010). doi: [10.1016/j.cell.2010.10.002](#); pmid: [21094524](#)
- Z. A. Gurard-Levin, K. A. Kilian, J. Kim, K. Bähr, M. Mrksich, Peptide arrays identify isoform-selective substrates for profiling endogenous lysine deacetylase activity. *ACS Chem. Biol.* **5**, 863–873 (2010). doi: [10.1021/cb100088g](#); pmid: [20849068](#)
- K. J. Bitterman, R. M. Anderson, H. Y. Cohen, M. Latorre-Esteves, D. A. Sinclair, Inhibition of silencing and accelerated aging by nicotinamide, a putative negative regulator of yeast sir2 and human SIRT1. *J. Biol. Chem.* **277**, 45099–45107 (2002). doi: [10.1074/jbc.M205670200](#); pmid: [12297502](#)
- W. K. Paik, D. Pearson, H. W. Lee, S. Kim, Nonenzymatic acetylation of histones with acetyl-CoA. *Biochim. Biophys. Acta* **213**, 513–522 (1970). doi: [10.1016/0005-2787\(70\)90058-4](#); pmid: [5534125](#)
- A. Nikiforov, C. Dölle, M. Niere, M. Ziegler, Pathways and subcellular compartmentation of NAD biosynthesis in human cells: From entry of extracellular precursors to mitochondrial NAD generation. *J. Biol. Chem.* **286**, 21767–21778 (2011). doi: [10.1074/jbc.M110.213298](#); pmid: [21504897](#)
- J. S. O'Neill, A. B. Reddy, Circadian clocks in human red blood cells. *Nature* **469**, 498–503 (2011). doi: [10.1038/nature09702](#); pmid: [21270888](#)
- J.-Y. Wu *et al.*,ENU mutagenesis identifies mice with mitochondrial branched-chain aminotransferase deficiency resembling human maple syrup urine disease. *J. Clin. Invest.* **113**, 434–440 (2004). pmid: [14755340](#)
- A. C. Liu *et al.*, Redundant function of REV-ERB α and β and non-essential role for Bmal1 cycling in transcriptional regulation of intracellular circadian rhythms. *PLOS Genet.* **4**, e1000023 (2008). doi: [10.1371/journal.pgen.1000023](#); pmid: [18454201](#)
- X. Zhang *et al.*, A non-canonical E-box within the MyoD core enhancer is necessary for circadian expression in skeletal muscle. *Nucleic Acids Res.* **40**, 3419–3430 (2012). doi: [10.1093/nar/gkr1297](#); pmid: [22210883](#)
- D. G. Nicholls *et al.*, Bioenergetic profile experiment using C2C12 myoblast cells. *J. Vis. Exp.* **46**, 2511 (2010). doi: [10.3791/2511](#); pmid: [21189469](#)
- E. S. Goetzman, The regulation of acyl-CoA dehydrogenases in adipose tissue by rosiglitazone. *Obesity* **17**, 196–198 (2009). doi: [10.1038/oby.2008.467](#); pmid: [18948967](#)

Acknowledgments: We thank P. Schumacker, R. Allada, S. Imai, G. Barish, members of the Bass lab for discussion and comments on the manuscript; K. Lamia and P. Schumacker for *Cry1^{-/-}*; *Cry2^{-/-}* MEFs and *Sirt3^{-/-}* mice, respectively; the Washington University Metabolomics Facility for nicotinamide measurements; the Northwestern University Skin Disease Research Center (NIH/NIAMS grant 5P30AR057216-05), and W. Song for technical assistance. Supported by National Institute of Diabetes and Digestive and Kidney Diseases grants F32 DK092034 (C.B.P.), F30 DK085936 (A.H.A.), and T32 DK007169 (B.M.); the Endocrine Society (D.J.B.); and NIH grants R01DK090242-03 (E.G.); P01DK58398 (C.B.N.); R01 AG038679 (J.M.D.); R01 CA152601-01, R01 CA152799-01A1, R01 CA168292-01A1, and R01 CA16383801A1 (D.G.); 5P01HL071643-10 (N.S.C.); and P01AG011412-16, R01HL097817-01, and R01DK090625-01A1 (J.B.). J.B. has financial interest in and serves as advisor to Reset Therapeutics, and has been a paid consultant for Merck, Janssen Pharmaceuticals, Vanda Pharmaceuticals, Gerson Lehrman Group, and Matsutani America. J.D. is a paid consultant for Sirtris, a GSK company. A provisional patent has been applied for by Northwestern University related to the role of the clock-NAD pathway in the mitochondrial control of cell growth, inflammation, and metabolism.

Supplementary Materials

www.sciencemag.org/content/342/6158/1243417/suppl/DC1
Materials and Methods
Supplementary Text
Figs. S1 to S9

18 July 2013; accepted 29 August 2013
Published online 19 September 2013;
[10.1126/science.1243417](#)

Structure-Based Design of a Fusion Glycoprotein Vaccine for Respiratory Syncytial Virus

Jason S. McLellan,¹ Man Chen,^{1*} M. Gordon Joyce,^{1*} Mallika Sastry,^{1*} Guillaume B. E. Stewart-Jones,^{1*} Yongping Yang,^{1*} Baoshan Zhang,^{1*} Lei Chen,¹ Sanjay Srivatsan,¹ Anqi Zheng,¹ Tongqing Zhou,¹ Kevin W. Graepel,¹ Azad Kumar,¹ Syed Moin,¹ Jeffrey C. Boyington,¹ Gwo-Yu Chuang,¹ Cinque Soto,¹ Ulrich Baxa,² Arjen Q. Bakker,³ Hergen Spits,³ Tim Beaumont,³ Zizheng Zheng,⁴ Ningshao Xia,⁴ Sung-Youl Ko,¹ John-Paul Todd,¹ Srinivas Rao,¹ Barney S. Graham,^{1†‡} Peter D. Kwong^{1†‡}

Respiratory syncytial virus (RSV) is the leading cause of hospitalization for children under 5 years of age. We sought to engineer a viral antigen that provides greater protection than currently available vaccines and focused on antigenic site Ø, a metastable site specific to the prefusion state of the RSV fusion (F) glycoprotein, as this site is targeted by extremely potent RSV-neutralizing antibodies. Structure-based design yielded stabilized versions of RSV F that maintained antigenic site Ø when exposed to extremes of pH, osmolality, and temperature. Six RSV F crystal structures provided atomic-level data on how introduced cysteine residues and filled hydrophobic cavities improved stability. Immunization with site Ø–stabilized variants of RSV F in mice and macaques elicited levels of RSV-specific neutralizing activity many times the protective threshold.

Respiratory syncytial virus (RSV) is one of the last remaining highly prevalent childhood pathogens without an approved vaccine. It is estimated to be responsible for 6.7% of deaths in children 1 month to 1 year of age and causes excess mortality in the elderly at levels comparable to influenza virus (1). Although RSV infection does not induce fully protective immunity, antibodies against the RSV fusion (F) glycoprotein can prevent severe disease in humans as demonstrated by passive prophylaxis with the F-directed antibody, palivizumab (Synagis) (2).

The proven success of palivizumab (3) has spurred vaccine efforts aimed at eliciting protective RSV F–directed antibodies. These efforts have been complicated by the conformational diversity of RSV F (4–8), a type I fusion glycoprotein that merges virus and host-cell membranes by using the difference in folding energy between two substantially different states: a metastable state adopted before virus-cell interaction (prefusion) and a stable state that occurs after merging of virus and cell membranes (postfusion). Both states exhibit epitopes targeted by neutralizing antibodies, and postfusion RSV F is being developed

as a vaccine candidate (6, 9). Recently, however, the major target of RSV-neutralizing antibodies elicited by natural infection was found to reside primarily on the prefusion conformation of RSV F (10). Antibodies such as 5C4 (7), AM22, and D25 (11, 12) are substantially more potent than palivizumab and target antigenic site Ø (zero), a metastable site located at the membrane-distal apex of the prefusion RSV F trimer (7).

To enhance elicitation of similarly potent antibodies, we engineered soluble variants of RSV F with stably exposed antigenic site Ø. These variants were characterized antigenically and crystallographically and tested for immunogenicity in mice and nonhuman primates (rhesus macaques).

Structure-Based Vaccine Strategy

We and others have engineered antigenicity (13–17) through structure-based design of the epitopes recognized by template neutralizing antibodies. For example, the crystal structure of motavizumab (a variant of palivizumab) bound to its F glycoprotein epitope (18) allowed us to create epitope scaffolds, which stably presented the motavizumab epitope on heterologous proteins (19). Although motavizumab-epitope scaffolds could elicit immune responses that recognized F, substantial neutralizing activity was not induced (19). We hypothesized that instead of a single epitope recognized by a single template antibody, it would be advantageous to present a “supersite” (20), comprising a collection of overlapping epitopes recognized by multiple antibodies. Even more preferable would be for such a site to be ultrasensitive to neutralization. These considerations led to a “neutralization-sensitive site” strategy: (i) to

identify a viral site targeted by multiple antibodies with extremely potent neutralizing activity, (ii) to determine the structure of the site in complex with a representative antibody, (iii) to engineer the stable presentation of the site in the absence of recognizing antibody, and (iv) to elicit high-titer protective responses through immunization with engineered antigens that stably present the neutralization-sensitive site (fig. S1).

Engineering of RSV F Antigens

Antigenic site Ø was chosen as the target site because of its recognition by RSV-neutralizing antibodies that are 10- to 100-fold more potent than palivizumab (7, 11, 12). We previously determined the structure of antigenic site Ø in complex with the D25 antibody (7). Structure determination involved appending the T4-phage fibrin trimerization domain (“foldon”) (21, 22) to the C terminus of the RSV F ectodomain (5) and binding of the prefusion-specific D25 antibody. Although these approaches stabilized antigenic site Ø, D25 binding sterically occluded the target site. To stably present antigenic site Ø in the absence of D25, we retained the C-terminal trimerization domain and combined it with other means of stabilization, including the introduction of cysteine pairs or cavity-filling hydrophobic substitutions.

The β -carbons of serine residues 155 and 290 are 4.4 Å apart in the D25-bound RSV F structure (7) and 124.2 Å apart in the postfusion structure (5) (Fig. 1 and fig. S2). A S155C-S290C double mutant (DS) [in which cysteine replaced serine at positions 155 and 290 (23)] formed stable RSV F trimers, expressed at 1.4 mg/liter, retained antigenic site Ø, and was homogeneous as judged by negative-stain electron microscopy (Table 1 and fig. S3) (24, 25). Other intrachain cysteine modifications, such as those between regions of RSV F that do not rearrange between pre- and postfusion states (e.g., S403C and T420C), did not stabilize antigenic site Ø (Table 1). We also tested potential interchain double-cysteine modifications, but none expressed at levels sufficient for enzyme-linked immunosorbent assay (ELISA) detection (table S1) (26).

We analyzed the D25-bound RSV F structure for hydrophobic cavities unique to the D25-bound conformation of RSV F that abutted regions that differed in the prefusion and postfusion states (27). Several such cavities were identified in the membrane-distal “head” of the prefusion structure, close to the binding site of D25, and we engineered hydrophobic substitutions to fill these cavities. S190F and V207L substitutions were predicted to adopt prevalent side-chain conformations with minimal clashes, whereas K87F, V90L, V220L, and V296F showed less steric compatibility. We assessed the impact of filling these cavities with pairs of changed residues. A S190F-V207L pair (Cav1) (Fig. 1), formed stable RSV F trimers, expressed at 2.2 mg/liter, and retained antigenic site Ø (Table 1). Moreover, K87F-V90L, S190F-

¹Vaccine Research Center, National Institute of Allergy and Infectious Diseases, National Institutes of Health, Bethesda, MD 20892, USA. ²Electron Microscopy Laboratory, Advanced Technology Program, SAIC-Frederick, Inc., Frederick National Laboratory for Cancer Research, Frederick, MD 21702, USA. ³AIMM Therapeutics, Academic Medical Center, 1105 BA Amsterdam, Netherlands. ⁴National Institute of Diagnostics and Vaccine Development in Infectious Diseases, Xiamen University, Xiamen, 361005, China.

*These authors contributed equally to this work.

†These authors contributed equally to this work.

‡Corresponding author. E-mail: bgraham@nih.gov (B.S.G.); pdkwong@nih.gov (P.D.K.)

V296F, and V207L-V220L variants showed enhanced retention of D25 recognition but expressed at less than 0.1 mg/liter (Table 1).

Other cavities we identified toward the center of prefusion RSV F were close to the fusion peptide, the trimer axis, and an acidic patch comprising residues Asp⁴⁸⁶, Glu⁴⁸⁷, and Asp⁴⁸⁹. We modeled several cavity-filling substitutions, including F137W, F140W, and F488W, and analyzed these substitutions in combination with D486H, E487Q, and D489H (table S1). Of the six combinations tested, only two (F488W and D486H-E487Q-F488W-D489H) expressed levels of purified RSV F trimer at greater than 0.1 mg/liter and retained D25 recognition. The D486H-E487Q-F488W-D489H variant (TriC) formed stable RSV F trimers, expressed at 0.8 mg/liter, and retained antigenic site Ø (Fig. 1 and Table 1).

We also tested the impact of destabilizing the postfusion conformation on the preservation of antigenic site Ø. The substitution V178N, which is predicted to introduce an *N*-linked glycan compatible with the prefusion but not the postfusion conformation of F, did not appear to stabilize antigenic site Ø, nor did V185E or I506K, which were predicted to place a glutamic acid or a lysine into the interior of the postfusion six-helix bundle (Table 1). In all, more than 100 RSV F variants were constructed (table S1), expressed in a 96-well transfection format (28) (fig. S4), and tested by ELISA of the culture supernatants for binding to D25 and motavizumab (figs. S5 and S6). Fifteen constructs were compatible with D25 binding, four of which retained D25 recognition for at least 7 days at 4°C, and three of these could be purified as homogeneous trimers that retained antigenic site Ø (table S1 and fig. S7). Overall, we observed a strong correlation between retention of D25 binding for at least 7 days at 4°C in 96-well supernatants and yield of purified trimers after large-scale expression and purification (fig. S5).

Combinatorial Optimization of Site Ø Stability

DS, Cav1, and TriC variants displayed a variety of physical and antigenic properties. The DS variant was the least stable to pH and temperature variation but was more permanently stabilized in the trimeric state, whereas a low level of continual conversion from trimer to aggregate was observed for Cav1 and TriC on size-exclusion chromatography. Combinations of the three variants improved retention of D25 reactivity to physical extremes, a characteristic helpful to manufacturing. Overall, the DS-Cav1 combination appeared optimal in terms of trimer yield and physical stability to extremes of temperature, pH, osmolality, and freeze-thaw (Table 1), and was homogeneous as judged by negative-stain electron microscopy (fig. S2).

Crystallographic Analysis

To provide atomic-level information, we determined crystal structures of site Ø-stabilized variants of RSV F (Fig. 2). The DS, Cav1, DS-Cav1, and

DS-Cav1-TriC variants all crystallized in similar 1.5 M tartrate (pH 9.5) conditions, and these cubic crystals diffracted x-rays to resolutions of 3.2 Å, 3.1 Å, 3.1 Å, and 2.8 Å, respectively (table S2). Molecular replacement solutions were obtained by using the D25-bound RSV F structure as a search model, and these revealed a single RSV F protomer in the asymmetric unit, with the trimeric F axis aligned along the crystallographic three-fold axis. Tetragonal crystals of Cav1 and cubic crystals of DS-Cav1 were also obtained from 1.7 M ammonium sulfate (pH 5.5) conditions, and these diffracted to resolutions of 2.4 Å and 3.0 Å, respectively (table S2). Molecular replacement revealed the tetragonal lattice to have a full RSV F trimer in the asymmetric unit and to be highly related to the tartrate cubic lattices. Overall, these structures revealed the engineered RSV F variants to be substantially in the D25-bound conformation (29).

Although the structure of the DS variant (Fig. 2, left column) revealed that the cysteine-substituted residues at 155 and 290 formed a disulfide bond that prevented triggering to the postfusion state, much of the membrane-distal portion of the RSV F trimer, including antigenic site Ø, was either disordered (residues 63 to 72 and 169 to 216) or in a different conformation. Thus, for example,

residues 160 to 168 in the DS structure extended the α2 helix instead of forming a turn and initiating the α3 helix, as in the D25-bound F structure (Fig. 2C, left). One possible explanation for the differences between the DS structure and the D25-bound RSV F structure is that antigenic site Ø in DS is flexible and crystallized in a conformation that does not bind D25 (30). Overall, the DS variant retained many of the features of the prefusion state of RSV F, including the fusion peptide in the interior of the trimeric cavity; however, it failed to fix antigenic site Ø in its D25-bound conformation (fig. S8).

In comparison with DS, the Cav1 structure (Fig. 2, second and third columns) was more ordered at its membrane-distal apex, with α3 helix, β3/β4 hairpin, and α4 helix clearly defined. Residues 137 to 202, which contain the S190F substitution, had a *C_α* root mean square deviation of 0.6 Å when compared with the D25-bound F structure. The higher degree of structural order was likely due to the S190F mutation that filled a cavity observed in the D25-bound F structure and increased van der Waals contacts with residues Ile⁵⁷, Lys¹⁷⁶, Val¹⁹², Glu²⁵⁶, Ser²⁵⁹, and Leu²⁶⁰. The other cavity-filling mutation in Cav1, V207L, was shifted by 5.5 Å compared with the D25-bound F structure, with the C-terminal portion of the

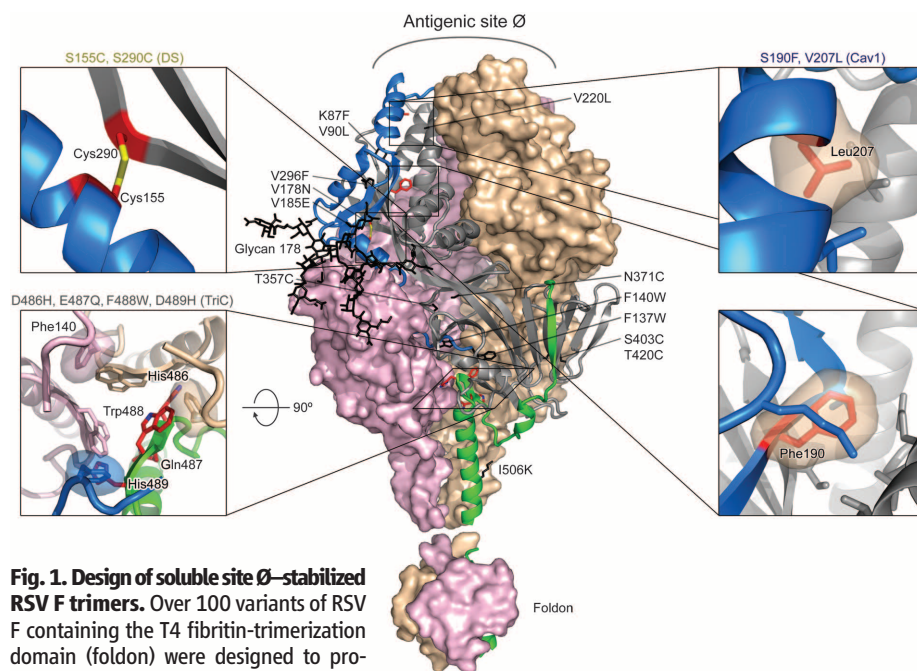


Fig. 1. Design of soluble site Ø-stabilized RSV F trimers. Over 100 variants of RSV F containing the T4 fibrin-trimerization domain (foldon) were designed to provide greater stability to antigenic site Ø (table S1). Shown here is the structure of the RSV F trimer in its D25-bound conformation with modeled C-terminal foldon. The trimer is displayed with two of the three F₁F₂ protomers in molecular surface representation (colored tan and pink), and the third F₁F₂ protomer in ribbon representation. The ribbon is colored gray in regions where it is relatively fixed between pre- and postfusion, and the N- and C-terminal residues that move more than 5 Å between pre- and postfusion conformations are colored blue and green, respectively. Mutations compatible with RSV F expression and initial D25 recognition (table S1), but insufficiently stable to allow purification of RSV F as a homogenous trimer (Table 1), are labeled and shown in stick representation (colored black). Insets show enlargements of stabilizing mutations in stick representation (colored red) for DS, Cav1, and TriC variants, all of which sufficiently stabilize antigenic site Ø to allow purification as a homogeneous trimer (Table 1).

residues 160 to 168 in the DS structure extended the α2 helix instead of forming a turn and initiating the α3 helix, as in the D25-bound F structure (Fig. 2C, left). One possible explanation for the differences between the DS structure and the D25-bound RSV F structure is that antigenic site Ø in DS is flexible and crystallized in a conformation that does not bind D25 (30). Overall, the DS variant retained many of the features of the prefusion state of RSV F, including the fusion peptide in the interior of the trimeric cavity; however, it failed to fix antigenic site Ø in its D25-bound conformation (fig. S8).

In comparison with DS, the Cav1 structure (Fig. 2, second and third columns) was more ordered at its membrane-distal apex, with α3 helix, β3/β4 hairpin, and α4 helix clearly defined. Residues 137 to 202, which contain the S190F substitution, had a *C_α* root mean square deviation of 0.6 Å when compared with the D25-bound F structure. The higher degree of structural order was likely due to the S190F mutation that filled a cavity observed in the D25-bound F structure and increased van der Waals contacts with residues Ile⁵⁷, Lys¹⁷⁶, Val¹⁹², Glu²⁵⁶, Ser²⁵⁹, and Leu²⁶⁰. The other cavity-filling mutation in Cav1, V207L, was shifted by 5.5 Å compared with the D25-bound F structure, with the C-terminal portion of the

α 4 helix kinking near Pro²⁰⁵ and adopting distinct conformations in the two crystallization conditions (Fig. 2, second and third columns), which suggested that the V207L mutation is unable to stabilize the α 4 helix in the D25-bound conformation.

A striking feature of the Cav1 structure in the tetragonal crystal lattice was the C terminus of F₂, which is disordered in the D25-bound F structure, but in Cav1, tunnels into the trimeric cavity alongside the fusion peptide. We also observed the C terminus to end with Ala¹⁰⁷, and not Arg¹⁰⁹, as expected after cleavage of the furin site (Arg¹⁰⁶-Ala¹⁰⁷-Arg¹⁰⁸-Arg¹⁰⁹) (31). In the Cav1 structure, the positive charge of Arg¹⁰⁶ was offset by an ordered sulfate ion (Fig. 2C). Biologically, the interior position of the F₂ C terminus may play a role in triggering structural rearrangements of F.

Comparison of the DS-Cav1 structures from the two cubic crystal forms (Fig. 2, second and third columns from right) to those of Cav1 revealed only minor differences (32). The largest differences occurred at the RSV F apex, including antigenic site Ø and specifically at residues 64 to 73 and 203 to 216. Notably, the atomic mobility (B-factor) was highest in this apex region for all of the site Ø-stabilized variants, perhaps indicative of intrinsic site Ø flexibility. However, site Ø has low atomic mobility when bound by D25, which reveals the ability of D25 to stabilize both overall and local RSV F conformations.

The structure of the DS-Cav1-TriC triple combination (Fig. 2, far right column) was also highly similar to other Cav1-containing RSV F variant structures. One difference in the electron density corresponded to an expanse of weak density at the membrane-proximal region, which approximated the dimensions of the T4-fibritin trimerization domain (33) but was not visible in other crystallized RSV F structures containing this domain, including the D25-bound structure (7). Small structural differences in packing likely allowed for the partial ordering of this domain (and may also have accounted for the increased diffraction limit of the DS-Cav1-TriC crystals relative to the other cubic variants), rather than differences in the interaction between the DS-Cav1-TriC stabilized RSV F and the trimerization domain.

The critical F488W substitution in the TriC alteration of residues 486 to 489 packed directly against the F488W substitutions in neighboring protomers of the RSV F trimer. The indole side chain of Trp⁴⁸⁸ pointed toward the trimer apex and also formed ring-stacking interactions with the side chain of Phe¹⁴⁰ of the fusion peptide (Fig. 2C, far right). This fusion peptide interaction, which is not observed in any of the Phe⁴⁸⁸-containing structures, likely inhibits the extraction of the fusion peptide from the prefusion trimer cavity and thus provides a structural rationale for

the ability of the F488W substitution to stabilize the prefusion state of RSV F (Table 1).

Immunogenicity of Antigenic Site Ø–Stabilized RSV F

To assess the effect of site Ø stabilization on the elicitation of RSV-protective humoral responses, we immunized CB6F1/J mice with various forms of RSV F, injecting each mouse with 10 µg RSV F combined with 50 µg polyinosinic-polycytidylic acid stabilized with polylysine carboxymethylcellulose (poly-ICLC) adjuvant at weeks 0 and 3, and measured the ability of week 5 sera to prevent RSV infection of HEP-2 cells. DS, Cav1, and TriC each elicited high titers of neutralizing activity [geometric mean 50% effective concentrations (EC₅₀ values) of 1826 to 2422]. This level was ~4 times that elicited by postfusion F (504 EC₅₀), and ~20 times the protective threshold (34). By comparison, DS-Cav1 elicited neutralizing activity of 3937 EC₅₀, roughly 8 times that of postfusion F and 40 times the protective threshold (34) (Fig. 3A).

To quantify antibody responses to different sites on prefusion RSV F, we used antigenic site Ø-occluded forms of RSV F. CB6F1/J mice immunized with 20 µg RSV F bound by antigenic site Ø-directed antibodies (comprising ~10 µg of RSV F and ~10 µg of the antigen-binding fragment of antibody) developed at week 5 geometric

Table 1. Antigenic and physical properties of engineered RSV F glycoprotein variants. Variants were often observed to exist in a mixture of oligomeric states on size-exclusion chromatography. If a measureable trimeric fraction was observed, then this is indicated by the label “Trimer,” and the various properties of the trimer fraction are listed. If no trimeric fraction was observed, then the oligomeric state of the dominant oligomeric species is provided. If the total yield before size-exclusion chromatography was

<0.1 mg/liter, then oligomeric state is listed as not determined (N.D.). Yield shown is for the specified oligomeric state. When no binding was observed for 1 µM Fab, the K_D is shown as >1000 nM; when total yield was <0.1 mg/liter, then the value for K_D is not applicable (N/A). For site II, palivizumab (Paliv); motavizumab (Mota). Physical stability refers to D25 reactivity retained after exposure to various physical extremes. There were 10 cycles of freeze-thaw. N/A, not applicable.

Mechanism of stabilization	RSV F variant	Oligomeric state	Yield (mg/liter)	Antibody K _D value (nM)							Physical stability (fractional D25 reactivity)								
				Site Ø			Site I		Site II		Site IV		Temp (°C)		pH		Osmolality (mM)		Freeze-thaw
				D25	AM22	5C4	131-2a	Paliv	Mota	101F	50	70	3.5	10.0	10	3000			
Cavity filling	K87F-V90L	Aggregate	0.3	>1000	>1000	>1000	7.6	1.7	0.17	1.6	N/A	N/A	N/A	N/A	N/A	N/A	N/A		
	F137W-F140W	N.D.	<0.1	N/A	N/A	N/A	N/A	N/A	N/A	N/A	N/A	N/A	N/A	N/A	N/A	N/A	N/A		
	F137W-F140W-F488W	N.D.	<0.1	N/A	N/A	N/A	N/A	N/A	N/A	N/A	N/A	N/A	N/A	N/A	N/A	N/A	N/A		
	S190F-V207L (Cav1)	Trimer	2.2	0.23	<0.10	9.3	>1000	43	<0.01	2.9	0.8	0.1	0.7	0.8	1.0	0.7	0.6		
	S190F-V296F	Aggregate	0.4	>1000	>1000	>1000	4.2	1.7	<0.01	1.6	N/A	N/A	N/A	N/A	N/A	N/A	N/A		
	V207L-V220L	Aggregate	0.4	>1000	>1000	>1000	2.8	0.99	0.014	0.69	N/A	N/A	N/A	N/A	N/A	N/A	N/A		
	D486H-E487Q-F488W-D489H (TriC)	Trimer	0.8	0.012	1.0	34	>1000	31	0.48	4.0	0.8	0.1	0.1	0.8	1.3	0.6	0.1		
	F488W	Trimer	1.7	0.087	0.25	27	>1000	32	0.1	4.7	0.9	0.1	0.1	0.7	1.1	0.5	0		
Disulfide formation	S155C-S290C (DS)	Trimer	1.4	0.29	<0.01	35	3.4	2.8	0.043	2.2	0.3	0	0.1	0.8	1.3	0.8	0.3		
	T357C-N371C	N.D.	<0.1	N/A	N/A	N/A	N/A	N/A	N/A	N/A	N/A	N/A	N/A	N/A	N/A	N/A	N/A		
	S403C-T420C	Aggregate	0.3	>1000	>1000	>1000	3.05	3.3	0.05	1.85	N/A	N/A	N/A	N/A	N/A	N/A	N/A		
N-Glycan addition	V178N	Aggregate	<0.1	>1000	>1000	>1000	7.2	3.1	0.11	1.64	N/A	N/A	N/A	N/A	N/A	N/A	N/A		
Postfusion destabilization	V185E	Aggregate	<0.1	>1000	>1000	>1000	3.5	1.7	0.11	1.64	N/A	N/A	N/A	N/A	N/A	N/A	N/A		
	I506K	Aggregate	<0.1	>1000	>1000	>1000	4.6	1.7	0.054	1.39	N/A	N/A	N/A	N/A	N/A	N/A	N/A		
Acid patch neutralization	D486H-E487Q-D489H	Aggregate	0.1	>1000	>1000	>1000	>1000	9.5	0.57	12.7	N/A	N/A	N/A	N/A	N/A	N/A	N/A		
Double combinations	DS-Cav1	Trimer	1.9	0.15	<0.01	13	>1000	23	0.041	3.2	0.9	0	0.8	0.9	1.0	0.8	0.7		
	DS-TriC	Trimer	0.6	0.17	<0.01	33	2.0	4.8	0.055	3.1	0.9	0	0.3	0.9	0.5	0.9	0.5		
	Cav1-TriC	Trimer	0.2	0.99	0.086	5.1	>1000	33	0.17	3.1	0.9	0.1	0.3	0.8	0.6	0.5	0		
Triple combinations	DS-Cav1-TriC	Trimer	1.3	0.17	0.02	18	>1000	20	0.10	3.2	0.9	0.1	0.6	0.9	0.6	0.6	0		

mean neutralizing titers of 911 and 1274 EC_{50} for AM22 and D25 complexes, respectively, roughly double that of postfusion at 10 $\mu\text{g}/\text{ml}$ and comparable to those elicited by postfusion at 20 $\mu\text{g}/\text{ml}$ (Fig. 3A). These findings suggested that the very high titers elicited by immunization with RSV F variants stabilized in the prefusion state, especially DS-Cav1, were a result of antibodies targeting antigenic site \emptyset .

To examine the generality of site \emptyset elicitation, we immunized rhesus macaques with DS-Cav1, DS, and postfusion forms of RSV F, injecting each macaque with 50 μg RSV F mixed with 500 μg poly-ICLC adjuvant at weeks 0 and 4 and mea-

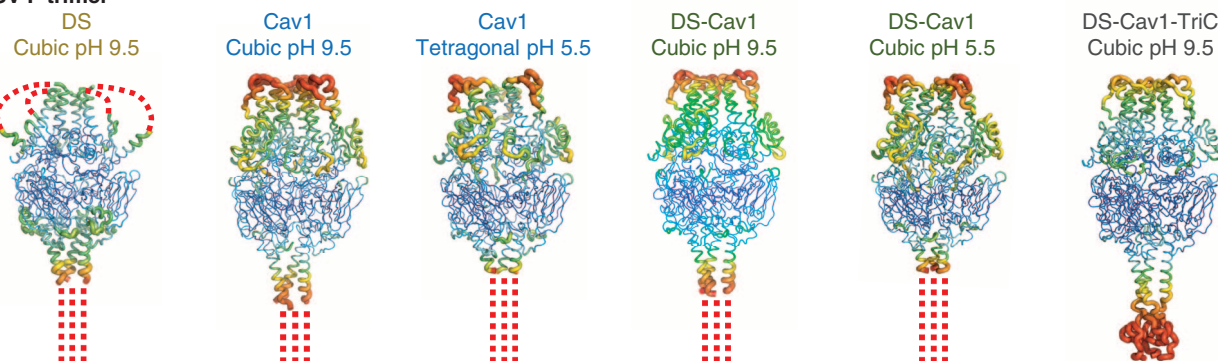
sured the ability of week 2, 4, 6, 8, 10, and 14 sera to inhibit RSV infection. Formulated proteins retained their expected antigenic profiles as measured by D25 binding to material from the injectate (fig. S9). At week 6, DS and DS-Cav1 elicited geometric mean titers of 1222 and 2578 EC_{50} , respectively, roughly 5 and 10 times those of postfusion F (287 EC_{50}) (Fig. 3B). By week 8, geometric mean titers of DS-Cav1 were roughly 70 times those elicited by postfusion F against the homologous RSV subtype A and more than 80 times titers against RSV subtype B (fig. S10 and table S4). Overall, these results demonstrate a conservation of the relative immunogenicity for

the different forms of RSV F immunogen between mice and primates, with DS-Cav1 eliciting RSV-protective titers many times the protective threshold in a primate immune system against both major RSV subtypes.

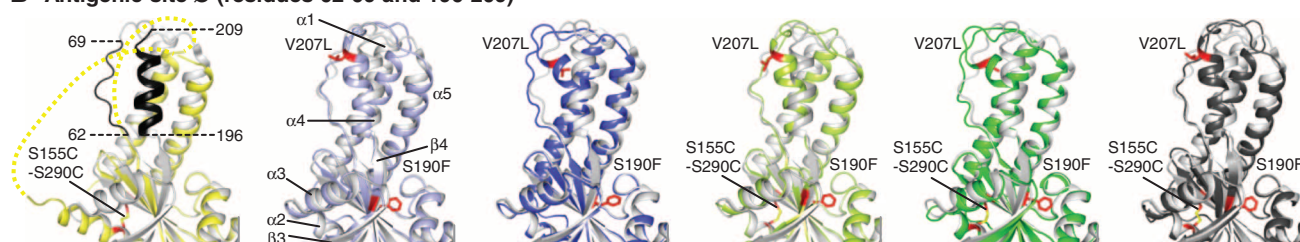
Optimization of RSV F Protective Responses

The interplay among design, physical and antigenic properties, atomic-level structure, and immunogenicity provides a basis for further optimization of RSV vaccine candidates (35). For example, to obtain insight into the relation between various antigenic and physical properties of engineered RSV Fs and the elicitation of RSV-protective

A RSV F trimer



B Antigenic site \emptyset (residues 62-69 and 196-209)



C Atomic-level details

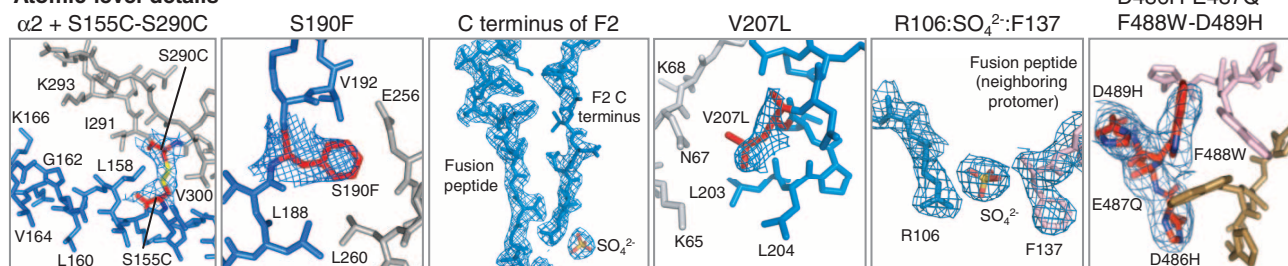


Fig. 2. Crystal structures of RSV F trimers, engineered to preserve antigenic site \emptyset . (A to C) Six structures for RSV F variants are shown, labeled by stabilizing mutation (DS, Cav1, DS-Cav1, and DS-Cav1-TriC) and the crystal lattice (cubic or tetragonal). (A) RSV F trimers are displayed in α -worm representation, colored according to atomic mobility factor, with regions of higher flexibility in warmer colors (red) and regions of lower flexibility in cooler colors (blue). Missing regions are shown as dotted lines. These occur at the C-terminal membrane-proximal region, where the foldon motif is not seen, except in the DS-Cav1-TriC structure (far right). In the DS structure, two loops in the head region are also disordered. (B) Antigenic site \emptyset of a RSV F protomer is displayed in ribbon diagram, with the structure of D25-bound RSV F in gray and different variants colored yellow (DS), light and dark blue (Cav1), light and dark green (DS-Cav1), and black (DS-Cav1-TriC). Residues

corresponding to antigenic site \emptyset are highlighted in black on the image at far left, and secondary structural elements are shown on the second image from left. Stabilizing mutations are labeled and shown in stick representation (colored red). Perpendicular view presented in figure S8. (C) Atomic-level details are shown in stick representation, colored the same as in Fig. 2, with regions of RSV F that change conformation between prefusion and postfusion conformation in red and blue, and those that remain constant in gray. Carbon atoms for stabilizing mutations are colored red. In Cav1 (pH 5.5) and in DS-Cav1 (pH 5.5) novel features were observed involving the interaction of the C terminus of the F₂ peptide with a sulfate ion and the fusion peptide. In the DS-Cav1-TriC structure, the D486H-E487Q-F488W-D489H mutations interact with the two neighboring protomers (colored tan and pink) around the trimer axis.

responses, one can correlate antigenic and physical properties (Table 1) with immunogenicity (Fig. 3). Such correlations indicate that increasing site Ø stability to physical extremes should increase protective titers elicited upon immunization (Fig. 4A) (36). Similarly, correlations between various conformational states or regions of RSV F (Fig. 2) and immunogenicity (Fig. 3) provide design insight into the conformation and regions of RSV F that provide the most protective responses. Specifically, enhancing structural mimicry of antigenic site Ø in its D25-bound conformation appears to be a promising strategy for improving protective antibody responses (Fig. 4B).

We should also be able to estimate the degree to which improvement can be obtained relative to a particular parameter. For example, once a correlation has been established between physical stability or structural mimicry and protective responses, physical stability can be maximized (e.g., to 100% retention of D25 binding) or structural mimicry idealized (e.g., to exact mimicry of the D25-bound conformation) to gain an estimate of the maximal improvement of the elicited protective response relative to that particular parameter. The results (Fig. 4, A and B) suggest that increased structural mimicry would likely not have much effect on immunogenicity but that additional physical stabilization of antigenic site Ø might improve the protective titers by up to four-fold. Independent parameters such as adjuvant, multimerization, delivery vehicle, or immunization regimen offer further avenues for improvement of the elicited response (37).

To quantify elicited binding responses, we coupled different variants of RSV F to an Octet biosensor tip and measured their reactivity with elicited sera (Fig. 4C). “Self-reactive” binding responses (with DS-Cav1, DS, or postfusion F on the biosensor tip and sera from animals immunized with DS-Cav1, DS, or postfusion F, respectively) were comparable for DS-Cav1, DS, and postfusion F. To provide insight into the binding responses relative to surfaces that were either shared or unique to DS-Cav1, DS, and postfusion F, we measured “cross-reactive” binding responses, for example, with DS-Cav1 on the biosensor tip and sera from animals immunized with DS or postfusion F, as well as binding responses with “preabsorbed” sera, to which different forms of RSV F had been added (Fig. 4C). We calculated the shared and unique surface areas, computed from crystal structures of DS-Cav1, DS, and postfusion F (fig. S11 and table S3), and analyzed these relative to the 36 measured binding responses in Fig. 4C. Strong correlation was observed between binding responses and calculated surface areas (Fig. 4D). Several outliers involved surfaces unique to DS-Cav1, surfaces that likely comprise antigenic site Ø. Together the results indicate that the quantity of elicited binding antibody was, to a first approximation, proportional to the surface area of the immunogen, independent of whether that immunogen was DS-Cav1,

DS, or postfusion F; within this overall similarity, antigenic site Ø elicited ~2 times the titer of binding antibody relative to its surface area. Overall, elicited EC₅₀ titers did not correlate with antigenic responses measured against either prefusion or postfusion forms of RSV F but did correlate with the level of prefusion-specific responses, either measured as a difference or as a ratio ($P = 0.005$) between prefusion-specific and postfusion-specific RSV F-directed responses (Fig. 4E) (38); the steep slope of this correlation likely reflects the substantially higher neutralization potency observed for prefusion-specific antibodies that target antigenic site Ø (7, 39).

Structural Vaccinology

Structural biology can be used in vaccine development to identify key sites by which to disable a pathogen, to pinpoint residue substitutions that inactivate toxoids, to stabilize select conformations of a subunit antigen, and to determine antibody-antigen complexes, which serve as the basis for epitope-specific strategies of elicitation. Notably, atomic-level control of antigenicity increasingly appears to be within the reach of structure-based design (16, 40, 41). With complex pathogens like malaria or meningococcus, antibody-mediated neutralizing activity can be directed against many potential antigens, and vaccine discovery has focused on identifying the best target antigen by methods including genomic analysis or “reverse vaccinology” (42–45). However, for pathogens such as HIV-1, influenza, or RSV, where neutralizing antibodies act almost exclusively through one or two envelope glycoproteins, a site- or supersite-specific strategy might have advantages. Specifi-

cally, a viral site of vulnerability to neutralizing antibody may be more amenable to structure-based design than a viral subunit, while also retaining a higher level of immunogenicity than an epitope-specific scaffold (46).

With site-specific vaccine strategies, selection of an appropriate target site is of crucial importance. Elicitation frequency, breadth, and potency are key considerations. Antigenic sites that comprise multiple overlapping epitopes of frequently elicited antibodies may be good targets, because of their expected capacity to elicit high levels of reactive antibodies in the general population. In terms of breadth, site Ø is among the most divergent of the antigenic sites on RSV; however, site Ø-directed antibodies such as D25 are capable of neutralizing most human RSVs, likely because of the relatively low genetic diversity of F among circulating human RSV strains, and both subtype A and B neutralizing activity was potentially induced by the stabilized RSV F glycoproteins reported here (table S4). Potency played a key role in our selection of site Ø as a vaccine target, and antigenic analysis of the elicited response (Fig. 4E) indicated potency of elicited antibodies to be crucial to the success of our site Ø-focused approach (47). Whether the “neutralization-sensitive site” strategy employed here will have success in other contexts thus depends on virus-specific factors such as circulating viral diversity and required level of neutralizing activity to achieve protection. Nonetheless, many of the lessons learned from our efforts with RSV, such as the importance of examining natural human immune responses and of selecting an appropriate target site, are generally applicable.

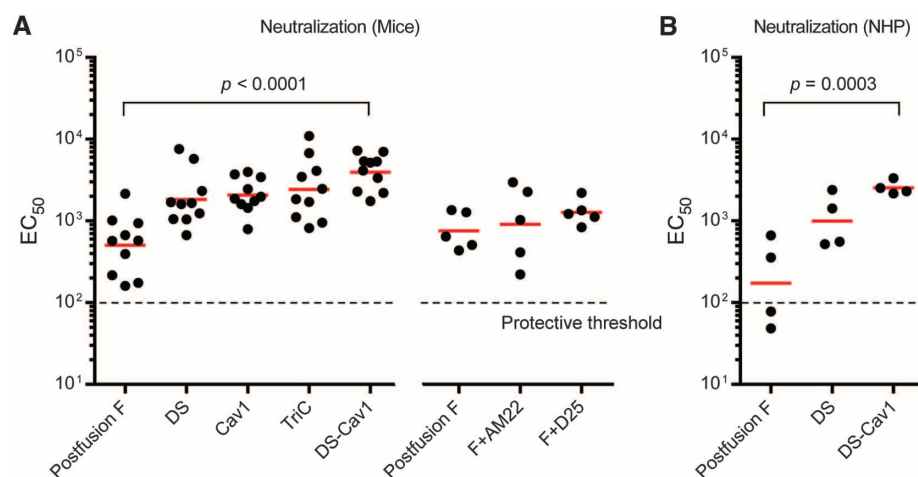


Fig. 3. Immunogenicity of engineered RSV F trimers. RSV F glycoproteins engineered to display antigenic site Ø elicit neutralizing titers significantly higher than those elicited by postfusion F. (A) Neutralization titers of sera from mice immunized with 10 µg of RSV F (left). Postfusion F, as well as RSV F bound by antibodies AM22 or D25, were administered at 20 µg of the RSV F–antibody complex per mouse (right). Titers from each mouse are shown as individual black dots, and geometric means are indicated by red horizontal lines. (B) Neutralization titers of sera from rhesus macaques (nonhuman primates, NHP) immunized with 50 µg of RSV F glycoprotein variants. Titers from each macaque are shown as individual black dots, and geometric means are indicated by red horizontal lines. Protective threshold (34) is indicated by a dotted line, and P values are provided for postfusion versus DS-Cav1 as assessed by two-tailed t test.

References and Notes

1. R. Lozano *et al.*, *Lancet* **380**, 2095–2128 (2012).
2. S. Johnson *et al.*, *J. Infect. Dis.* **176**, 1215–1224 (1997).
3. The IMPact-RSV Study Group, *Pediatrics* **102**, 531–537 (1998).
4. L. J. Earp, S. E. Delos, H. E. Park, J. M. White, *Curr. Top. Microbiol. Immunol.* **285**, 25–66 (2005).
5. J. S. McLellan, Y. Yang, B. S. Graham, P. D. Kwong, *J. Virol.* **85**, 7788–7796 (2011).
6. K. A. Swanson *et al.*, *Proc. Natl. Acad. Sci. U.S.A.* **108**, 9619–9624 (2011).
7. J. S. McLellan *et al.*, *Science* **340**, 1113–1117 (2013).
8. L. Liljeroos, M. A. Krzyzaniak, A. Helenius, S. J. Butcher, *Proc. Natl. Acad. Sci. U.S.A.* **110**, 11133–11138 (2013).
9. L. J. Anderson *et al.*, *Vaccine* **31** (suppl. 2), B209–B215 (2013).
10. M. Magro *et al.*, *Proc. Natl. Acad. Sci. U.S.A.* **109**, 3089–3094 (2012).
11. H. Spits, T. Beaumont, RSV-specific binding molecules and means for producing them. Patent Application 12/600,950 (2010).
12. T. Beaumont, A. Q. Bakker, E. Yasuda, RSV specific binding molecule. Patent Application 12/898,325 (2012).
13. D. R. Burton, *Nat. Rev. Immunol.* **2**, 706–713 (2002).
14. T. Zhou *et al.*, *Nature* **445**, 732–737 (2007).
15. G. Ofek *et al.*, *Proc. Natl. Acad. Sci. U.S.A.* **107**, 17880–17887 (2010).
16. J. Jardine *et al.*, *Science* **340**, 711–716 (2013).
17. A. T. McGuire *et al.*, *J. Exp. Med.* **210**, 655–663 (2013).
18. J. S. McLellan *et al.*, *Nat. Struct. Mol. Biol.* **17**, 248–250 (2010).
19. J. S. McLellan *et al.*, *J. Mol. Biol.* **409**, 853–866 (2011).
20. L. Kong *et al.*, *Nat. Struct. Mol. Biol.* **20**, 796–803 (2013).
21. V. P. Efimov *et al.*, *J. Mol. Biol.* **242**, 470–486 (1994).
22. K. A. Miroshnikov *et al.*, *Protein Eng.* **11**, 329–332 (1998).
23. Single-letter abbreviations for the amino acid residues are as follows: A, Ala; C, Cys; D, Asp; E, Glu; F, Phe; G, Gly; H, His; I, Ile; K, Lys; L, Leu; M, Met; N, Asn; P, Pro; Q, Gln; R, Arg; S, Ser; T, Thr; V, Val; W, Trp; and Y, Tyr.
24. Information on materials and methods is available on Science Online.
25. RSV F variants were assessed by transient expression in 96-well format (fig. S4). If supernatants retained reactivity with antibodies motavizumab and D25 after 1 week at 4°C, they were expressed by transient transfection of 1 liter of Expi293F cells, purified by use of appended His-tag and Streptaggl, and analyzed by size-exclusion chromatography (fig. S7).
26. The inability to express potential interchain double-cysteine substitutions, despite reasonable modeling in the mature prefusion F₁F₂ structure, may indicate that RSV F₀ protomers, before cleavage and removal of peptide 27, adopt substantially different interprotomer conformations.
27. Cavities in the D25-bound RSV F structure were visualized with PyMol using the “Cavities & Pockets Only” option for Surface settings. Amino acid substitutions designed to fill the resulting cavities were identified using the Mutagenesis wizard.
28. M. Pancera *et al.*, *PLOS ONE* **8**, e55701 (2013).
29. The engineered RSV F variants had α -root mean square deviations from the D25-bound conformation of 0.7 to 1.5 Å and from the postfusion conformation of approximately 30 Å.
30. Crystallized DS retained ~20% of its D25 recognition relative to crystallized Cav1 (normalized to motavizumab recognition) after 4 months at 20°C, thereby indicating that the crystallized DS was both capable of recognizing D25 as well as converting to a conformation incompatible with D25 binding. By contrast, soluble DS lost all recognition of D25 after 2 months of incubation at 4°C in PBS. We were unable to crystallize DS, which had been heat triggered at 50°C, despite the heat-triggered DS retaining a trimeric state on size exclusion chromatography.

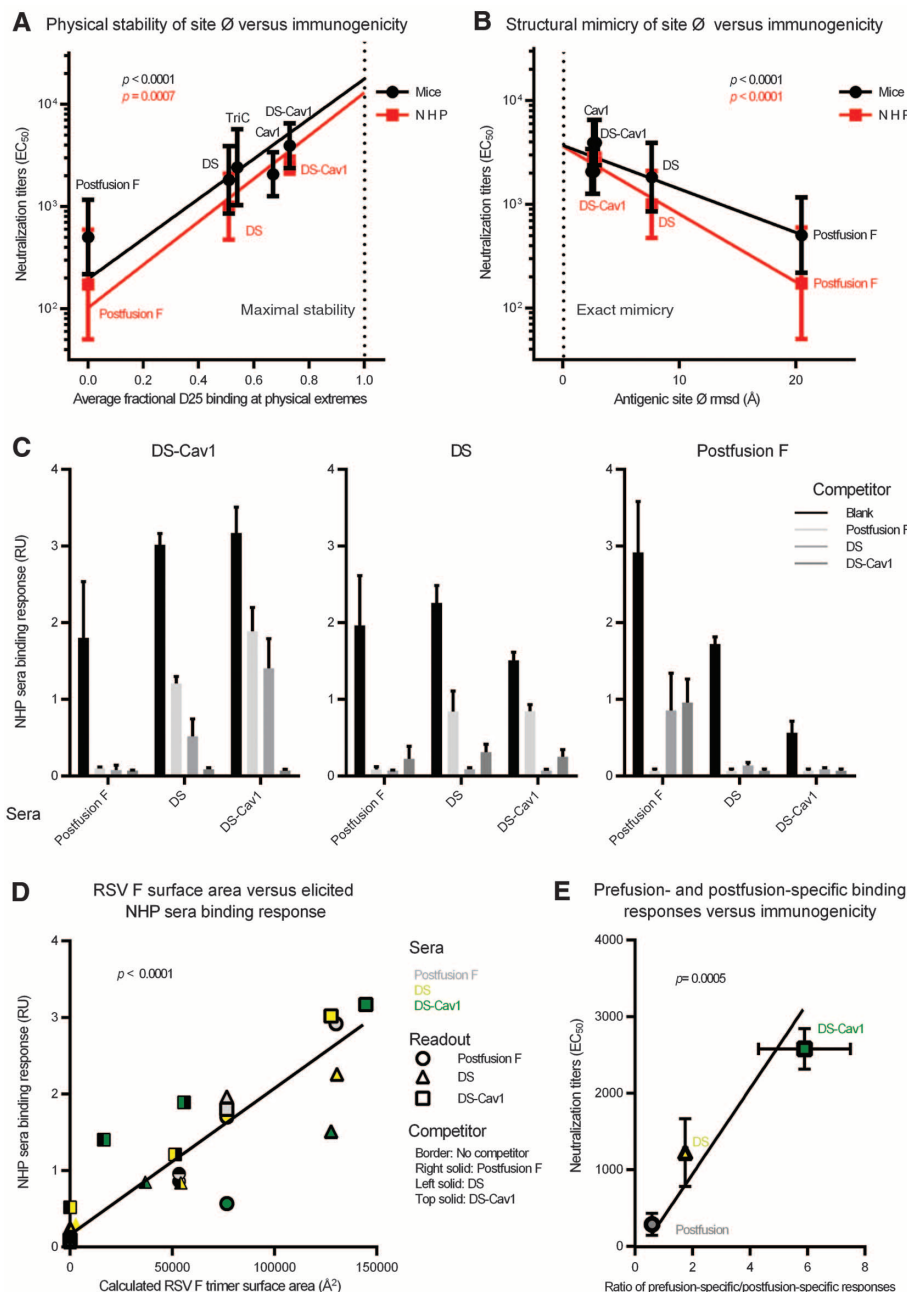


Fig. 4. Informatics of site Ø-stabilized RSV F immunogens. (A) Physical stability of site Ø versus immunogenicity. Physical stability (horizontal axis), as determined by the average of seven measurements of D25-retained activity in Table 1, is compared with elicited RSV-protective titers from Fig. 3 (vertical axis). (B) Structural mimicry of site Ø versus immunogenicity. Structural mimicry (horizontal axis) is the root-mean-square deviation of atom distances between different unbound RSV F structures (Fig. 2) and the D25-bound RSV F structure for all atoms within 10 Å of D25. This is compared with elicited RSV-neutralizing titers from Fig. 3 (vertical axis). (C) Antigenic analysis of sera from immunized macaques. Binding of sera to sensor-tip immobilized DS-Cav1 (left), DS (middle), or postfusion F (right) was measured directly (black bars) or after incubation with excess postfusion F (light gray bars), DS (gray bars), or DS-Cav1 (dark gray bars). The mean responses of four macaque sera are shown, with standard deviations as error bars. Additional analysis of immunized sera is shown in fig. S12. (D) Elicited binding responses relative to surface areas for shared or unique portions of immunogens. Surface areas were calculated (fig. S11 and table S3) and compared with binding responses for the 36 response measurements in (C). (E) Correlation of immunogenicity and antigenic specificity of immunized macaque sera. The mean EC_{50} neutralization titers (week 6) of the four macaque sera in each group are plotted against the ratio of prefusion-specific/postfusion-specific F binding responses in (C) (38).

31. Observing Ala107 rather than Arg109 at the C terminus of F₂ is not totally unexpected: Garten and Klenk (48) found that an arginine at the cleavage site of influenza hemagglutinin was trimmed by a cellular carboxypeptidase activity.
32. Ca-root mean square deviations of 0.86 Å for 447 residues between Cav1 and DS-Cav1 crystal structures obtained from ammonium sulfate; Ca-root mean square deviations of 0.47 Å for 447 residues of DS-Cav1 in cubic lattices.
33. J. Stetefeld *et al.*, *Structure* **11**, 339–346 (2003).
34. When palivizumab (Synagis) is dosed at a concentration of 15 mg/kg, serum levels at trough are ~40 µg/ml, which provides protection in infants from severe disease and protection in cotton rats from RSV infection. In our neutralization assay, ~40 µg/ml of palivizumab yields an EC₅₀ of 100.
35. G. J. Nabel, *Science* **326**, 53–54 (2009).
36. By contrast, affinity of RSV F variants for D25 antibody did not show correlation with elicitation of protective titers. Yield of RSV F trimers also did not correlate with protective titers.
37. Flexibility of an antigenic site may increase its immunogenicity by allowing the site to conform to a wider diversity of antibodies. We note in this context that the atomic-mobility factors of antigenic site Ø were among the highest in the RSV F ectodomain.
38. For the “prefusion” form of RSV F, we used the DS-Cav1 stabilized variant of RSV F.
39. It should be possible to deconvolute the elicited response, by using structurally defined probes, as shown with D25 and motavizumab-bound RSV F in fig. S12.
40. P. R. Dormitzer, G. Grandi, R. Rappuoli, *Nat. Rev. Microbiol.* **10**, 807–813 (2012).
41. M. L. Azoitei *et al.*, *Science* **334**, 373–376 (2011).
42. I. Delany, R. Rappuoli, K. L. Seib, *Cold Spring Harb. Perspect. Med.* **3**, a012476 (2013).
43. A. Sette, R. Rappuoli, *Immunity* **33**, 530–541 (2010).
44. D. G. Moriel *et al.*, *Proc. Natl. Acad. Sci. U.S.A.* **107**, 9072–9077 (2010).
45. M. Mora, C. Donati, D. Medini, A. Covacci, R. Rappuoli, *Curr. Opin. Microbiol.* **9**, 532–536 (2006).
46. Although an epitope-scaffold strategy may not elicit titers as high as a neutralization-sensitive site strategy, for specific antibodies—such as antibody MPE8 (49), which is capable of neutralizing not only RSV but other paramyxoviruses including human metapneumovirus—an epitope-specific strategy may suffice.
47. The magnitude of antibody activity is a crucial determinant of how well an individual will be protected following vaccination and how long protective responses will be maintained in infants who have passively acquired antibody from their mothers.
48. W. Garten, H. D. Klenk, *J. Gen. Virol.* **64**, 2127–2137 (1983).
49. D. Corti *et al.*, *Nature* **501**, 439–443 (2013).

Acknowledgments: We thank A. M. Salazar for poly-ICLC; J. Stuckey for assistance with figures; I. S. Georgiev and M. Pancera for assistance with immunogen design; G. J. Nabel, R. A. Seder, L. Shapiro, and members of the Structural Biology Section; Structural Bioinformatics Core Section; and Viral Pathogenesis Laboratory at the Vaccine Research Center for helpful comments; and J. Chrzas, J. Gonczy, U. Chinte, and staff at SER-CAT (Southeast Regional Collaborative Access Team) for help with x-ray diffraction data collection. The data presented in this manuscript are tabulated in the main paper and supplementary materials. Atomic coordinates and structure factors of the reported crystal structures have been deposited in the Protein Data Bank under accession codes 4MMQ to

4MMV. Support for this work was provided by the Intramural Research Program (National Institute of Allergy and Infectious Diseases) and the National Natural Science Foundation of China (81161120419 and 812111615). Use of insertion device 22 (SER-CAT) at the Advanced Photon Source was supported by the U.S. Department of Energy, Basic Energy Sciences, Office of Science, under contract W-31-109-Eng-38. H.S. and T.B. are inventors on an international patent application describing the technology used to isolate D25 and AM22 (Means and methods for influencing the stability of antibody producing cells, WO2007067046A1). A.Q.B. and T.B. are inventors on international patent applications for antibody D25 (RSV-specific binding molecules and means for producing them, WO2008147196A2) and antibody AM22 (RSV-specific binding molecule, WO2011043643A1). J.S.M., M.G.J., B.Z., B.S.G., and P.D.K. are inventors on U.S. patent applications describing the use of prefusion-stabilized RSV F glycoproteins as vaccine antigens (Prefusion RSV F proteins and their use, 61/798,389 and 61/863,909). J.S.M., M.C., Z.Z., N.X., and B.S.G. are inventors on a Chinese patent application for antibody 5C4 and its epitope (Anti-RSV high neutralization antibody and the peptide can be used for prevention of RSV infection and related disease, 201310082338.1). Reagents from the NIH are subject to nonrestrictive materials transfer agreements.

Supplementary Materials

www.sciencemag.org/content/342/6158/592/suppl/DC1
Materials and Methods
Figs. S1 to S12
Tables S1 to S4
References (50–61)

16 July 2013; accepted 25 September 2013
10.1126/science.1243283

REPORTS

Evolution of the Magnetic Field Structure of the Crab Pulsar

Andrew Lyne,^{1*} Francis Graham-Smith,¹ Patrick Weltevrede,¹ Christine Jordan,¹ Ben Stappers,¹ Cees Bassa,¹ Michael Kramer^{1,2}

Pulsars are highly magnetized rotating neutron stars and are well known for the stability of their signature pulse shapes, allowing high-precision studies of their rotation. However, during the past 22 years, the radio pulse profile of the Crab pulsar has shown a steady increase in the separation of the main pulse and interpulse components at $0.62^\circ \pm 0.03^\circ$ per century. There are also secular changes in the relative strengths of several components of the profile. The changing component separation indicates that the axis of the dipolar magnetic field, embedded in the neutron star, is moving toward the stellar equator. This evolution of the magnetic field could explain why the pulsar does not spin down as expected from simple braking by a rotating dipolar magnetic field.

The Crab pulsar (1) originated in the collapse of the core of a massive star in CE 1054, an event that was visible on Earth through the subsequent supernova explosion. Presently rotating at 30 times a second (2), intense

beams of electromagnetic radiation from the magnetic poles of the neutron star sweep across the Earth (3), resulting in a pulsed emission that has been observed since 1969 at radio wavelengths and subsequently at optical, x-ray, and gamma-ray wavelengths. The pulse profile is related to the shape of the beams, which are determined by the magnetic field structure of the underlying star as it rotates (3). We have therefore sought changes in the radio pulse profile in order to investigate any evolution in the structure of the stellar magnetic field.

High-quality daily observations of the Crab pulsar (PSR B0531+21, J0534+2200) have been made since 1991 with the 13-m radio telescope at Jodrell Bank Observatory at a frequency of 610 MHz. These measurements are supplemented by less-frequent observations using the 76-m Lovell Telescope at the higher frequency of 1400 MHz, designed to monitor dispersion measure. These data comprise part of a consistent set of pulse timing observations at Jodrell Bank (4, 5) that have provided a complete record of the rotation of the pulsar since 1984 and are available as an ephemeris to other observers (6). The radio pulse profile (Fig. 1) consists of a pair of components, the main pulse (MP) at 0° and the interpulse (IP) at 145° , which are closely associated with the components of the profiles observed in the high-energy regimes from optical to TeV gamma rays (7). At the comparatively low radio frequency of 610 MHz, there is also a steep-spectrum third component known as the precursor (PC) at -18° . This component is not detectable at 1400 MHz, although another, previously identified component, the low-frequency component (LFC) at -37° (8), is seen at both frequencies. The components HFC1 (at 200°) and HFC2 (at 260°) reported before (8) also appear in the 1400-MHz profile but are too weak to be addressed in this study.

The temporal evolution of the separation between the MP and other components (9) can be seen in Fig. 2 (IP) and Fig. 3 (LFC and PC), and

¹Jodrell Bank Centre for Astrophysics, School of Physics and Astronomy, University of Manchester, Manchester, M13 9PL, UK. ²Max Planck Institut für Radioastronomie, Auf dem Hügel 69, 53121 Bonn, Germany.

*Corresponding author. E-mail: andrew.lyne@manchester.ac.uk

variations in the relative integrated flux densities of the pulse components are shown in Fig. 4. Secular changes are observed in all three diagrams. The component separations and relative flux densities, together with their rates of change measured over the 22 years, are presented in Table 1. In summary, the most notable features are that (i) the separation of the IP from the MP at 610 MHz has increased by 0.14° , corresponding to $13 \pm 1 \mu\text{s}$ (Fig. 2), together with a consistent change at 1400 MHz; (ii) the separation of the LFC from the MP at 1400 MHz has increased by 2.4° , corresponding to $220 \pm 40 \mu\text{s}$ (Fig. 3A); (iii) the flux density of the IP has decreased relative to that of the MP by $\sim 6\%$ at 610 MHz and by $\sim 13\%$ at 1400 MHz (Fig. 4, A and B); and (iv) the flux density of the PC at 610 MHz has decreased relative to that of the MP by $\sim 13\%$ (Fig. 4C).

The origins of the pulse components are within a corotating magnetosphere that is embedded in the neutron star and extends almost to the light cylinder, the cylindrical surface at which the corotation velocity would reach the velocity of light. The source of the PC is believed to be located over a magnetic pole, at a small fraction of the distance to the light cylinder. The MP and IP components of the high-energy (optical, x-ray, and gamma-ray) profile originate in two high-altitude gaps in the magnetosphere, at the boundary between magnetic field lines that close within the light cylinder and the open field lines that are closer to the magnetic poles. This emission

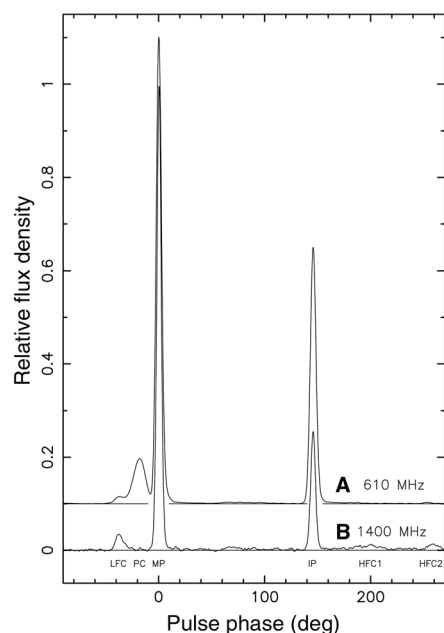


Fig. 1. The average pulse profiles of the Crab pulsar. (A) 610 MHz and (B) 1400 MHz. The locations of the features discussed in the text are indicated below the profiles: The MP and IP lie at rotational phases 0° and 145° , whereas the PC and LFC lie at -18° and -37° , respectively.

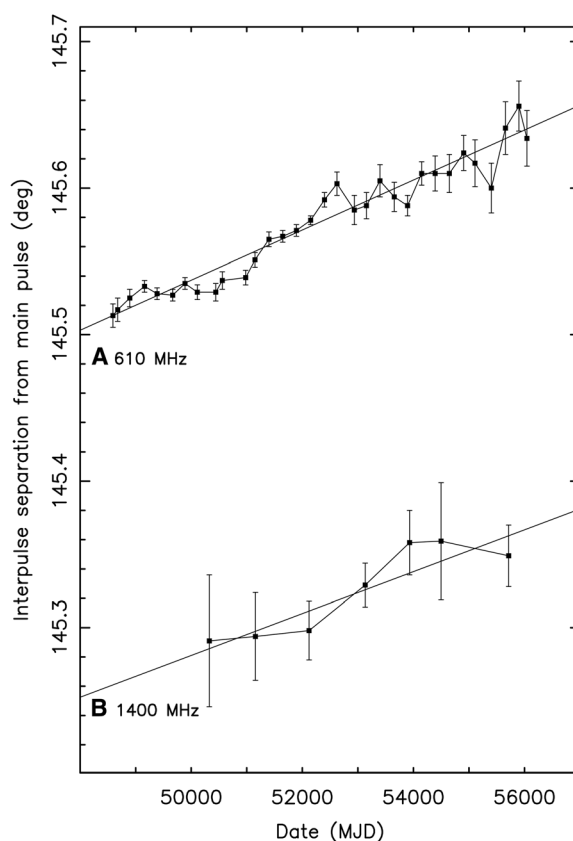


Fig. 2. The rotational separation of the IP from the MP. (A) 610 MHz and (B) 1400 MHz. Data at 610 MHz are displayed as mean values averaged over 500 days, calculated at 250-day intervals, whereas data at 1400 MHz are mean values averaged over 2000 days, calculated at 1000-day intervals.

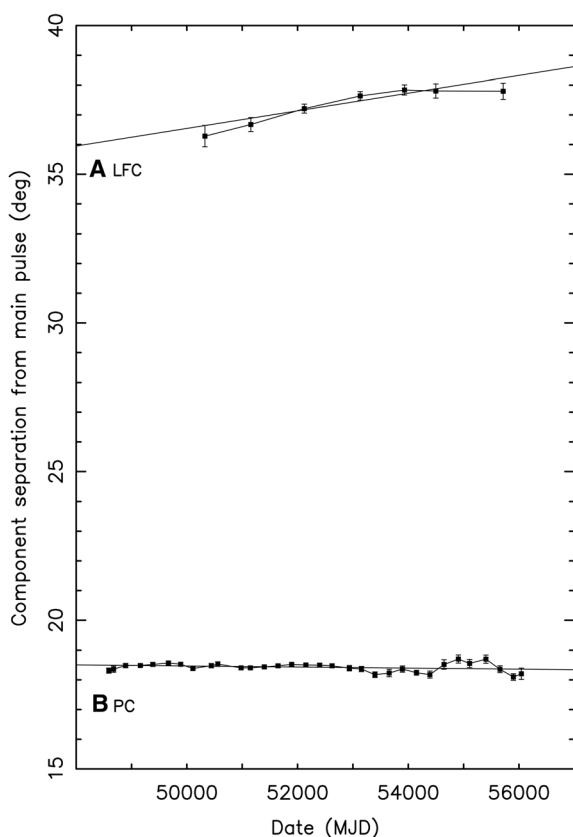


Fig. 3. The rotational separation of components of the Crab pulse profile from the MP. (A) The LFC at 1400 MHz and (B) the PC at 610 MHz. Data at 610 MHz are displayed as mean values averaged over 500 days, calculated at 250-day intervals, whereas data at 1400 MHz are mean values averaged over 2000 days, calculated at 1000-day intervals.

occurs in an extended region along each gap, whereas the combined effect of propagation time along the gap and relativistic effects concentrates the observed source into a caustic (10). Although this broadly describes the emission, the exact distribution depends on the specific emission model [e.g., (11–15)]. In the following, we construct a geometrical interpretation for the secular increase in the separation of the MP and IP radio emission. This is possible because the radio components are closely associated with the high-energy emission, thereby suggesting that high-energy models can be used to interpret the observed evolution of this separation.

The observed high-energy profile is a cut across a hollow conical surface of emission over one or both magnetic poles. The shape of the cone is determined by the inclination α of the magnetic axis to the rotation axis, and the position of the

cut depends on the viewing angle ζ , which is measured from the rotation axis. There is good evidence from the geometry of the x-ray torus in the pulsar wind nebula seen around the pulsar (16) that the viewing angle ζ is close to 63° . The observed secular increase of the separation between the IP and MP might be due to a change in viewing geometry due to precession (17) (on a time scale much larger than the 2.3% of the 960-year lifetime of the pulsar that our observations cover), or in α (i.e., alignment or counter alignment of the magnetic and rotation axes) or in the location within the magnetosphere of the source of emission. Although a long-period free precession of the neutron star might provide an appropriate change in the beam geometry, not only are there theoretical arguments why it should not occur (18, 19) but no pulsar has been shown to display the phenomenon [e.g., (20)]. Here, we dem-

onstrate that a change in α will result in a self-consistent interpretation.

The shape of the beam of the Crab pulsar has been modeled by several authors [e.g., (14, 21–23)], resulting in a range of estimates of α between 45° and 70° . Nevertheless, a common feature of these models is a prediction that an increasing α will result in an increasing peak separation [e.g., figures 5 and 2 in (22)], from which it can be deduced that the peak separation is expected to change at a rate of about 1° per degree change in α , although the exact relationship is somewhat model-dependent. The observed secular increase of the separation therefore indicates that the dipole axis is moving toward orthogonality. The observed component separation is increasing from 145.5° toward the symmetrical value of 180° at a rate of 0.62° per century (Fig. 2). We therefore interpret our observation as an increase of α at a comparable rate, at which rate the total change would have been about 6° during the lifetime of the pulsar so far.

It is difficult to relate the rapid apparent motion of the LFC, whose origin is not understood, to this geometric evolution in any detail. The changes in relative flux densities of the components are easier to understand because all the sources are highly coherent and are probably narrow beamed (24), so that small structural magnetospheric changes might cause large effects on the component flux densities.

The dipole magnetic field is embedded in the superconducting interior of the neutron star, either in the inner crust or in the core, and only a slow evolution can be expected. An evolution toward alignment rather than orthogonality is expected for a simple magnetic dipole. However, it has been pointed out that an evolution toward orthogonality may be expected because of the torque developed by the return current in the neutron star surface [e.g., (25)]. We also note that the increasing slowdown torque due to increasing α could at least in part explain the observed braking index value of 2.50 (5), rather than the 3.0 expected for classic magnetic dipole braking (26), or may be related to the occurrence of glitches seen in the pulsar (27, 28). If the sole departure from such classic slowdown, in which the rate of change of rotation rate $\dot{\nu} \propto \nu^3 \sin^2(\alpha)$, is a secular change in α at a rate $\dot{\alpha}$, the observed braking index n is given by $n = 3 + 2\nu/\dot{\nu} \times \dot{\alpha}/\tan(\alpha)$. Within the limitations of our model, the observed braking index can be explained if α increases at 0.6° per century, which is remarkably close to the rate of change in α required to explain the secular change in the pulse separation.

These observations provide evidence for a progressive change in the magnetic inclination of an isolated pulsar. The precise measurement of the small change in pulse profile, which leads to this conclusion, has depended on a long and consistent series of observations of one of the youngest pulsars. It is unlikely that comparable measurements can be made on any other pulsar in the near future.

Fig. 4. Relative flux densities of Crab pulse profile components.

Flux densities are given relative to that of the MP at the same frequency. (A) IP at 610 MHz, (B) IP at 1400 MHz, (C) PC at 610 MHz, and (D) LFC at 1400 MHz. Data at 610 MHz are displayed as mean values averaged over 500 days, calculated at 250-day intervals, whereas data at 1400 MHz are mean values averaged over 2000 days, calculated at 1000-day intervals.

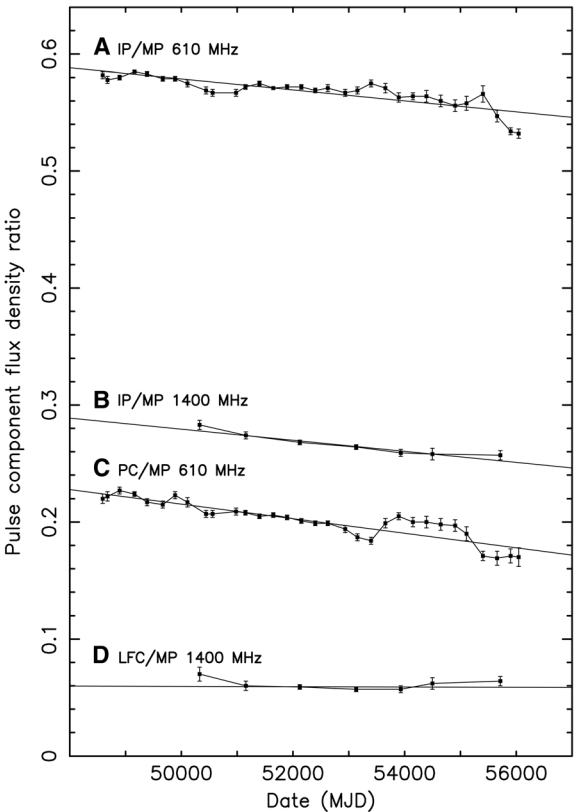


Table 1. The rotational positions and integrated flux densities of the IP, PC, and LFC of the radio profile of the Crab pulsar. Values are given in columns 2 and 4 relative to the MP at epoch modified Julian date = 53,000 at 610 MHz and 1400 MHz. Columns 3 and 5 contain the rates of change of these two quantities, respectively. Standard (1σ) errors are given in parentheses after the values and are in units of the least significant quoted digit.

	Position (°)	Rate of change (°/century)	Flux ratio	Rate of change (per century)
IP (610 MHz)	145.588 (2)	+0.62 (3)	0.5648 (6)	−0.172 (8)
IP (1400 MHz)	145.324 (9)	+0.5 (2)	0.265 (1)	−0.17 (3)
PC (610 MHz)	−18.415 (17)	−0.6 (3)	0.1967 (6)	−0.226 (11)
LFC (1400 MHz)	−37.43 (7)	+11 (2)	0.059 (1)	−0.005 (33)

References and Notes

1. D. H. Staelin, E. C. Reifstein 3rd, *Science* **162**, 1481–1483 (1968).
2. J. M. Comella, H. D. Craft, R. V. E. Lovelace, J. M. Sutton, G. L. Tyler, *Nature* **221**, 453–454 (1969).
3. T. Gold, *Nature* **218**, 731–732 (1968).
4. A. G. Lyne, R. S. Pritchard, F. G. Smith, *Mon. Not. R. Astron. Soc.* **233**, 667–676 (1988).
5. A. G. Lyne, R. S. Pritchard, F. G. Smith, *Mon. Not. R. Astron. Soc.* **265**, 1003–1012 (1993); <http://adsabs.harvard.edu/full/1993MNRAS.265.1003L>.
6. A. G. Lyne, C. A. Jordan, M. E. Roberts, *The Jodrell Bank Crab Pulsar Ephemeris* (University of Manchester, Manchester, 2013). (<http://www.jb.man.ac.uk/pulsar/crab.html>).
7. A. A. Abdo *et al.*, *Astrophys. J.* **708**, 1254–1267 (2010).
8. D. A. Moffett, T. H. Hankins, *Astrophys. J.* **468**, 779–783 (1996).
9. Materials and methods are available as supplementary material on Science Online.
10. M. Morini, *Mon. Not. R. Astron. Soc.* **202**, 495–510 (1983).
11. K. S. Cheng, C. Ho, M. Ruderman, *Astrophys. J.* **300**, 500–539 (1986).
12. R. W. Romani, I.-A. Yadigaroglu, *Astrophys. J.* **438**, 314–321 (1995).
13. A. G. Muslimov, A. K. Harding, *Astrophys. J.* **606**, 1143–1153 (2004).
14. J. Dyks, B. Rudak, *Astrophys. J.* **598**, 1201–1206 (2003).
15. R. W. Romani, K. P. Watters, *Astrophys. J.* **714**, 810–824 (2010).
16. C.-Y. Ng, R. W. Romani, *Astrophys. J.* **673**, 411–417 (2008).
17. D. I. Jones, N. Andersson, *Mon. Not. R. Astron. Soc.* **324**, 811–824 (2001).
18. J. Shaham, *Astrophys. J.* **214**, 251–260 (1977).
19. A. Sedrakian, I. Wasserman, J. M. Cordes, *Astrophys. J.* **524**, 341–360 (1999).
20. A. Lyne, G. Hobbs, M. Kramer, I. Stairs, B. Stappers, *Science* **329**, 408–412 (2010).
21. A. K. Harding, J. V. Stern, J. Dyks, M. Frackowiak, *Astrophys. J.* **680**, 1378–1393 (2008).
22. K. P. Watters, R. W. Romani, P. Weltevredre, S. Johnston, *Astrophys. J.* **695**, 1289–1301 (2009).
23. Y. J. Du, G. J. Qiao, W. Wang, *Astrophys. J.* **748**, 84 (2012).
24. A. G. Lyne, F. Graham-Smith, *Pulsar Astronomy*, 4th ed. (Cambridge Univ. Press, Cambridge, 2012).
25. V. S. Beskin, E. E. Nokhrina, *Astrophys. Space Sci.* **308**, 569–573 (2007).
26. W. W. Macy Jr., *Astrophys. J.* **190**, 153–164 (1974).
27. B. Link, R. I. Epstein, *Astrophys. J.* **478**, L91 (1997).
28. M. P. Allen, J. E. Horvath, *Astrophys. J.* **488**, 409–412 (1997).

Acknowledgments: Pulsar research at Jodrell Bank Centre for Astrophysics is supported by a Consolidated Grant from the U.K. Science and Technology Facilities Council.

Supplementary Materials

www.sciencemag.org/content/342/6158/598/suppl/DC1
Materials and Methods
References (29, 30)

15 July 2013; accepted 1 October 2013
10.1126/science.1243254

Quantum Limit of Heat Flow Across a Single Electronic Channel

S. Jezouin,^{1*} F. D. Parmentier,^{1*} A. Anthore,^{1,2†} U. Gennser,¹ A. Cavanna,¹ Y. Jin,¹ F. Pierre^{1†}

Quantum physics predicts that there is a fundamental maximum heat conductance across a single transport channel and that this thermal conductance quantum, G_Q , is universal, independent of the type of particles carrying the heat. Such universality, combined with the relationship between heat and information, signals a general limit on information transfer. We report on the quantitative measurement of the quantum-limited heat flow for Fermi particles across a single electronic channel, using noise thermometry. The demonstrated agreement with the predicted G_Q establishes experimentally this basic building block of quantum thermal transport. The achieved accuracy of below 10% opens access to many experiments involving the quantum manipulation of heat.

The transport of electricity and heat in reduced dimensions and at low temperatures is subject to the laws of quantum physics. The Landauer formulation of this problem (1–3) introduces the concept of transport channels: A quantum conductor is described as a particle waveguide, and the channels can be viewed as the quantized transverse modes. Quantum physics sets a fundamental limit to the maximum electrical conduction across a single electronic channel. The electrical conductance quantum $G_e = e^2/h$, where e is the unit charge and h is the Planck constant, was initially revealed in ballistic one-dimensional (1D) constrictions (4, 5). However, different values of the maximum electrical conductance are observed for different types of charge-carrying particles. In contrast, for heat conduction the equivalent thermal conductance quantum $G_Q = \pi^2 k_B^2 T / 3h \approx (1 \text{ pW/K}^2) T$ (which sets the

maximum thermal conduction across a single transport channel, k_B being the Boltzmann constant and T the temperature) is predicted to be independent of the heat carrier statistics, from bosons to fermions, including the intermediate “anyons” (6–16). In electronic channels, which carry both an electrical and thermal current, the predicted ratio $(\pi^2 k_B^2 / 3e^2) T$ between G_Q and G_e verifies and extends the Wiedemann-Franz relation down to a single channel (8, 9). In general, the universality of G_Q , together with the deep relationship between heat, entropy, and information (17), points to a quantum limit on the flow of information through any individual channel (6, 15).

The thermal conductance quantum has been measured for bosons, in systems with as few as 16 phonon channels (18, 19), and probed at the single-photon channel level (20, 21). For fermions, heat conduction was shown to be proportional to the number of ballistic electrical channels (22, 23). In (22), the data were found compatible, within an order of magnitude estimate, to the predicted thermal conductance quantum, whereas (23) demonstrated more clearly the quantization of thermal transport, but G_Q was not accessible by construction of the experiment.

We have measured the quantum-limited heat flow across a single electronic channel using the conceptually simple approach depicted in Fig. 1A. A micrometer-sized metal plate is electrically connected by an adjustable number n of ballistic quantum channels to a cold bath at temperature T_0 . Electrons in the small plate are heated up with a well-known Joule power (J_Q in Fig. 1A), and the resulting increased electronic temperature T_Ω is measured by direct thermometry based on noise measurements. Heat balance implies that the injected Joule power is compensated by the overall outgoing heat current

$$J_Q = nJ_Q^e(T_\Omega, T_0) + J_Q^{e-ph}(T_\Omega, T_0) \quad (1)$$

where $nJ_Q^e(T_\Omega, T)$ is the electronic heat flow across the n ballistic quantum channels. The flow $J_Q^{e-ph}(T_\Omega, T_0)$ is an additional contribution, here attributed to the transfer of heat from the hot electrons toward the cold phonon bath in the plate (and thus independent of n). The heat flow across a single ballistic electronic channel is then directly given by how much J_Q is increased to keep T_Ω constant when one additional electronic channel is opened. The quantum-limited heat flow for a single electronic channel connecting two heat baths at T_Ω and T_0 reads (8, 9)

$$J_Q^e(T_\Omega, T_0) = \frac{\pi^2 k_B^2}{6h} (T_\Omega^2 - T_0^2) \quad (2)$$

The quadratic temperature dependence reflects the fact that the temperature sets both the average energy of electronic excitations, as well as their number, the latter being proportional to the energy bandwidth.

The actual sample, displayed in Fig. 1B, was cooled down to $T_0 \approx 20 \text{ mK}$ in our experiment. The noise thermometry was performed with ultra-sensitive cryogenic electronics based on a home-grown high-electron-mobility transistor (24).

The ballistic quantum channels are formed in a high-mobility Ga(Al)As 2D electron gas by the field-effect tuning of two quantum point contacts

¹CNRS, Laboratoire de Photonique et de Nanostructures, UPR20, route de Nozay, 91460 Marcoussis, France. ²Univ Paris Diderot, Sorbonne Paris Cité, Département de Physique, 4 rue Elsa Morante, 75013 Paris, France

*These authors contributed equally to this work.

†Corresponding author. E-mail: anne.anthore@lpn.cnrs.fr (A.A.); frederic.pierre@lpn.cnrs.fr (F.P.)

(QPCs), labeled QPC₁ and QPC₂ in Fig. 1B. The potentials applied to the metal split gates (colored yellow in Fig. 1B) are set to fully transmit n electronic channels, in which case the QPC electrical conductances display clear plateaus [see fig. S5 in (25)]. The measured conductances $n_1 e^2/h$ and $n_2 e^2/h$ of QPC₁ and QPC₂, respectively, correspond to $n = n_1 + n_2$. For fully transmitted channels, the electron-photon coupling observed in the same sample for the case of partially transmitted channels (26) vanishes.

The heated-up metal plate, colored brown in Fig. 1B, is a micrometer-sized ohmic contact (25), which is electrically connected to cold electrodes located further away exclusively through the two QPCs. To approach the quantum limit of heat flow per channel, the electrical connection between the plate and the 2D electron gas located 94 nm below the surface must have a negligibly low resistance compared to h/e^2 . Moreover, the heated-up electrons must dwell in the plate for a time longer than the electron-electron energy exchange time, in order to relax toward a quasi-equilibrium situation characterized by a hot Fermi distribution at T_Ω . These two conditions set the minimum size of the ohmic contact (25); however, the ohmic contact must be small enough to minimize the heat transfer toward phonons, which is proportional to volume. The sample was optimized to fulfill these antagonistic requirements, achieving a negligibly small contact resistance, a typical dwell time in the 10 μ s range, and a dominating electronic heat flow for $T_\Omega \lesssim 70$ mK.

The sample was subjected to a strong perpendicular magnetic field in order to enter the integer quantum Hall effect (QHE) regime, at filling factors $\nu = 3$ or $\nu = 4$. In this regime, the current flows along the sample edges in so-called edge channels with a unique propagation direction (continuous red lines with arrows in Fig. 1B). One motivation for performing the experiment in this regime is the spatial separation between incoming and outgoing edge channels away from the QPC, which enables use of the large metal electrodes located further away as ideal cold reservoirs. Furthermore, it is easier to tune the QPCs to a discrete set of fully open channels (25), and the spin degeneracy is broken so that the electronic channels can be opened one at a time. Finally, the QHE regime allows for a simple implementation of the noise thermometry.

The injected Joule power J_Q was generated with an applied DC current (Fig. 1B) partly transmitted across the n_1 ballistic channels of QPC₁ into the plate (25).

The resulting increase $T_\Omega - T_0$ of the electronic temperature in the plate was determined from the increase ΔS_I in the measured spectral density of the current noise along the outgoing edge channels (25, 27, 28)

$$\Delta S_I = 2k_B(T_\Omega - T_0) \frac{G_e}{1/n_1 + 1/n_2} \quad (3)$$

The raw measurements of excess current noise ΔS_I versus applied DC current for $n \in \{2, 3, 4\}$

Fig. 1. Experimental principle and practical implementation.

(A) Principle of the experiment: Electrons in a small metal plate (brown disk) are heated up to T_Ω by the injected Joule power J_Q . The large arrows symbolize injected power (J_Q) and outgoing heat flows (nJ_Q^e, J_Q^{e-ph}). (B) False-colors scanning electron micrograph of the measured sample. The Ga(Al)As 2D electron gas is highlighted in light blue, the QPC metal gates in yellow and the micrometer-sized metallic ohmic contact in brown. The light gray metal gates are polarized with a strong negative gate voltage and are not used in the experiment. The propagation direction of two co-propagating edge channels (shown out of $\nu = 3$ or $\nu = 4$) is indicated by red arrows. QPC₁ is here set to fully transmit a single channel ($n_1 = 1$) and QPC₂ two channels ($n_2 = 2$), corresponding to a total number of open electronic channels $n = n_1 + n_2 = 3$. The experimental apparatus is shown as a simplified diagram. It includes two $L - C$ tanks used to perform the noise thermometry measurements around 700 kHz. The Joule power J_Q is injected on the micrometer-sized metallic electrode from the DC polarization current partly transmitted through QPC₁.

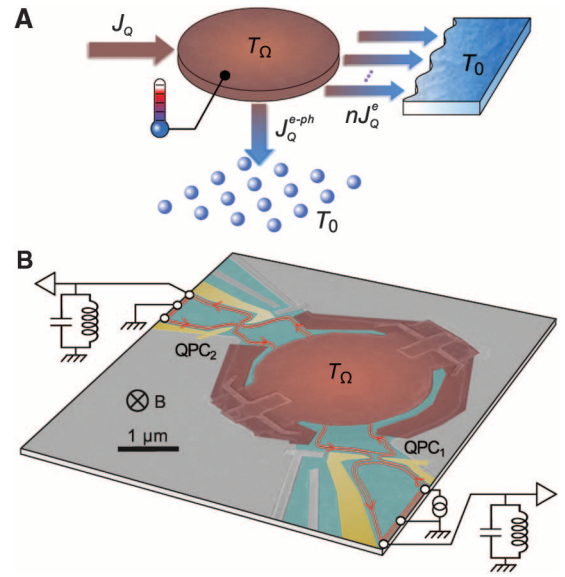
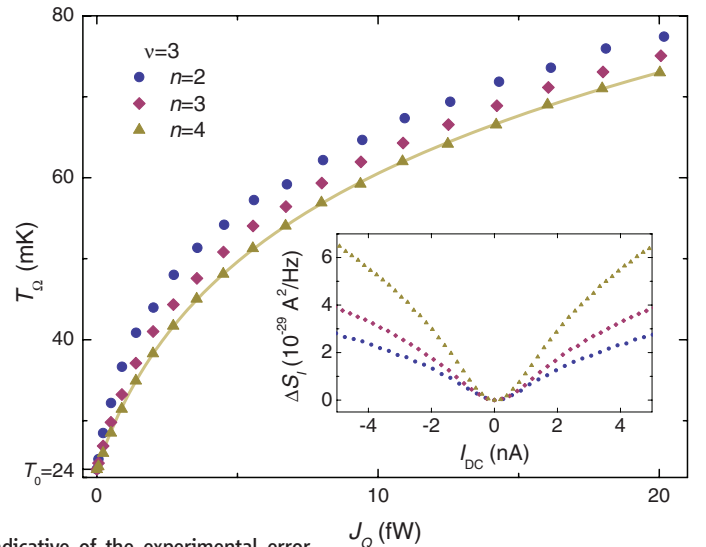


Fig. 2. Noise thermometry measurements versus injected power.

The electronic temperature T_Ω in the micrometer-sized ohmic contact is plotted as a function of the injected power J_Q at $\nu = 3$ and for a base electronic temperature $T_0 = 24$ mK. The symbols \bullet , \blacklozenge , and \blacktriangle correspond, respectively, to $n = 2, 3$, and 4 open electronic channels. The continuous line is a fit of the data for $n = 4$ open channels, including the heat transfer to phonons (see text). The size of the symbols is indicative of the experimental error bars. (Inset) Measured excess noise spectral density versus applied DC current. In the main panel, data at opposite DC currents, which are equal at our experimental accuracy, are averaged to improve the signal-to-noise ratio.



open electronic channels at $\nu = 3$ are shown as symbols in the inset of Fig. 2. Here $n = 2$ corresponds to $(n_1, n_2) = (1, 1)$, $n = 3$ is the average over the two equivalent configurations (1, 2) and (2, 1) [see fig. S6 in (25)], and $n = 4$ corresponds to (2, 2). The displayed data are measured on the top left electrode, behind QPC₂; the same excess noise, within 2%, was measured with another amplification chain on the bottom right electrode, behind QPC₁ (25).

The main panel of Fig. 2 shows these data recast as the measured electronic temperature in

the micrometer-sized plate T_Ω versus the injected Joule power J_Q . The base temperature $T_0 = 24$ mK was obtained separately, from a noise thermometry performed at $\nu = 3$ during the same experimental run (25). At fixed T_Ω , the distinct increase in J_Q as the number n of ballistic electronic channels is incremented by one directly corresponds to the heat flow across an individual electronic channel. We focus here on the low injected power regime $J_Q \lesssim 20$ fW, where the electronic heat flow nJ_Q^e is the most important contribution at $n = 4$ (25).

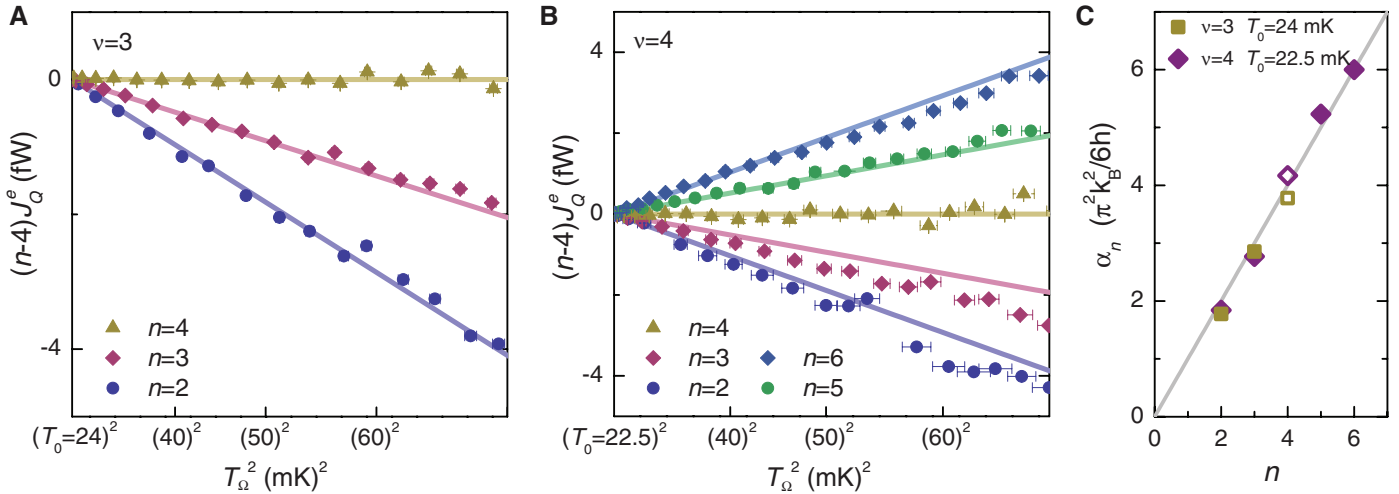


Fig. 3. Heat flow across ballistic electronic channels. (A and B) The symbols display the heat current across $|n - 4|$ electronic channels, with a positive (negative) sign for $n > 4$ ($n < 4$), as a function of the squared temperature T_Ω^2 of the micrometer-sized ohmic contact. The data in (A) [(B)] were measured at $\nu = 3$ ($\nu = 4$) at a base temperature $T_0 = 24$ mK ($T_0 = 22.5$ mK) for $n = 2, 3$, and 4 ($n = 2, 3, 4, 5, 6$), respectively from bottom to top. The continuous lines are the theoretical predictions for the quantum-limited heat

flow. (C) Extracted electronic heat current factor $\alpha_n \equiv nJ_Q^e / (T_\Omega^2 - T_0^2)$ in units of $\pi^2 k_B^2 / 6h$ (symbols) versus the number n of electronic channels. It is obtained from the fitted slopes α'_{n-4} of the data in (A) and (B) added to the separately extracted value of α_4 (see text and Fig. 2): $\alpha_n = \alpha'_{n-4} + \alpha_4$, with $\alpha_4 = 3.8$ ($\alpha_4 = 4.2$) at $\nu = 3$ ($\nu = 4$) shown distinctly as open symbols. The predictions for the quantum limit of heat flow fall on the continuous line $y = x$.

We now separate the electronic heat flow nJ_Q^e from the additional, a priori unidentified, contribution J_Q^{e-ph} , which is independent of the number n of open electronic channels. For this purpose, we use as a reference the $n = 4$ data corresponding to the most robust QPC plateaus $n_1 = n_2 = 2$.

First, we show that important information can already be extracted at $n = 4$ within a model-dependent approach. The $n = 4$ reference data $J_Q = J_Q^{e-ph} + 4J_Q^e$ are fitted with the standard expression for electron-phonon cooling in diffusive metals (29–31) $J_Q^{e-ph}(T_\Omega, T) = \Sigma\Omega(T_\Omega^5 - T_0^5)$ with $\Sigma\Omega$ a free parameter; for $4J_Q^e$ we used the predicted power law (see Eq. 2), $4J_Q^e = \alpha_4(T_\Omega^2 - T_0^2)$ with α_4 a free parameter. The fit is shown as a continuous yellow line in Fig. 2. The electron-phonon coupling parameter $\Sigma\Omega = 5.5$ nW/K⁵ extracted from the fit is a very typical value for similar metals (29–31) given the micrometer-sized ohmic contact volume $\Omega \sim 2 \mu\text{m}^3$. The extracted electronic heat flow $4J_Q^e$ is found to be $3.8(\pi^2 k_B^2 / 6h)(T_\Omega^2 - T_0^2)$, which is within 5% of the theoretically predicted value given by Eq. 2. The same $\Sigma\Omega$ and electronic heat current are obtained by repeating this analysis on the $n = 4$ data at the higher temperature $T_0 = 40$ mK, whereas a relatively small difference of about 20% is seen at filling factor $\nu = 4$ [see figs. S8 and S9 in (25)].

Second, following the model-free approach described earlier, we extract the amount of heat $(n - 4)J_Q^e(T_\Omega, T_0)$ flowing across the additional $(n - 4)$ ballistic electronic channels by subtracting from the measured J_Q with n open channels the $n = 4$ reference signal. At $n > 4$ ($n < 4$), $|n - 4|$ channels are opened (closed) with respect to the reference configuration. Given the extreme-

ly accurate fit described above, within experimental error bars, we choose to subtract the fit function, instead of using an arbitrary interpolation function between the measured $n = 4$ data points. The extracted variations of the electronic heat currents $(n - 4)J_Q^e$ are plotted as symbols in Fig. 3A as a function of the squared temperature T_Ω^2 , for the data at $\nu = 3$ and $T_0 = 24$ mK. Similar data obtained for $T_0 = 22.5$ mK at the different filling factor $\nu = 4$ and for up to $n = 6$ ballistic electronic channels (Fig. 3B) show larger scatter simply because of a lower experimental accuracy, due to the less favorable current-voltage conversion at this filling factor and a smaller acquisition time per point. We find that $(n - 4)J_Q^e$ is proportional to T_Ω^2 , as expected from theory (Eq. 2).

We now compare the extracted electronic heat currents with the quantitative prediction Eq. 2 for the quantum-limited heat flow. The experimentally extracted $(n - 4)J_Q^e(T_\Omega, T_0)$ are in good agreement with the theoretical predictions shown as continuous lines in Fig. 3, A and B. We then extract a quantitative experimental value for the quantum-limited heat flow by fitting the data $(n - 4)J_Q^e(T_\Omega, T_0)$ using the predicted and observed functional $\alpha'_{n-4}(T_\Omega^2 - T_0^2)$, with α'_{n-4} the only free parameter. Taking altogether the set of normalized slopes $\{\alpha'_{n-4}(n - 4)\}$ obtained within the model-free approach at $\nu = 3$ and $\nu = 4$, we find

$$\frac{J_Q^e(T_\Omega, T_0)}{T_\Omega^2 - T_0^2} = (1.06 \pm 0.07) \times \frac{\pi^2 k_B^2}{6h} \quad (4)$$

in agreement, at our experimental accuracy, with the theoretical prediction for the quantum-limited heat flow across a single channel, and therefore

with the predicted value given by the thermal conductance quantum. The displayed 7% uncertainty is the standard error on the mean value obtained from the six values $\{\alpha'_{n-4} / (n - 4)\}$, each weighted by the corresponding number $|n - 4|$ of electronic channels (25). This uncertainty ignores systematic sources of error, e.g., on the calibrated gain of the amplification chain (25). The accuracy can be improved by including the values of α_4 obtained at $\nu = 3$ and $\nu = 4$ within the model-dependent approach detailed earlier. Figure 3C displays as symbols the full electronic heat current factors $\{\alpha_n \equiv \alpha'_{n-4} + \alpha_4\}$ versus n , with the corresponding theoretical predictions $n \times \pi^2 k_B^2 / 6h$ falling on the continuous line. The same statistical analysis on the eight values of $\{\alpha_n / n\}$ yields $J_Q^e(T_\Omega, T_0) / (T_\Omega^2 - T_0^2) = (0.98 \pm 0.02) \times \pi^2 k_B^2 / 6h$ (25).

The present experiment demonstrates that the quantum-limited heat flow across a single electronic channel, which sets the scale of quantum interference effects, is now attainable at a few percent accuracy level. This opens access to many studies in the emergent field of quantum heat transport (32, 33), such as quantum phase manipulation of heat currents.

References and Notes

1. R. Landauer, *Z. Phys. B* **21**, 247–254 (1975).
2. P. W. Anderson, D. J. Thouless, E. Abrahams, D. S. Fisher, *Phys. Rev. B* **22**, 3519–3526 (1980).
3. M. Büttiker, *Phys. Rev. Lett.* **57**, 1761–1764 (1986).
4. B. J. van Wees et al., *Phys. Rev. Lett.* **60**, 848–850 (1988).
5. D. A. Wharam et al., *J. Phys. C* **21**, L209 (1988).
6. J. B. Pendry, *J. Phys. A* **16**, 2161–2171 (1983).
7. R. Maynard, E. Akkermans, *Phys. Rev. B Condens. Matter* **32**, 5440–5442 (1985).
8. U. Sivan, Y. Imry, *Phys. Rev. B Condens. Matter* **33**, 551–558 (1986).

9. P. N. Butcher, *J. Phys. Condens. Matter* **2**, 4869–4878 (1990).
10. C. L. Kane, M. P. A. Fisher, *Phys. Rev. Lett.* **76**, 3192–3195 (1996).
11. C. L. Kane, M. P. A. Fisher, *Phys. Rev. B* **55**, 15832–15837 (1997).
12. A. Greiner, L. Reggiani, T. Kuhn, L. Varani, *Phys. Rev. Lett.* **78**, 1114–1117 (1997).
13. L. G. C. Rego, G. Kirczenow, *Phys. Rev. B* **59**, 13080–13086 (1999).
14. I. V. Krive, E. R. Mucciolo, *Phys. Rev. B* **60**, 1429–1432 (1999).
15. M. P. Blencowe, V. Vitelli, *Phys. Rev. A* **62**, 052104 (2000).
16. D. R. Schmidt, R. J. Schoelkopf, A. N. Cleland, *Phys. Rev. Lett.* **93**, 045901 (2004).
17. C. Shannon, *Bell Syst. Tech. J.* **27**, 379–423 (1948).
18. K. Schwab, E. A. Henriksen, J. M. Worlock, M. L. Roukes, *Nature* **404**, 974–977 (2000).
19. C. S. Yung, D. R. Schmidt, A. N. Cleland, *Appl. Phys. Lett.* **81**, 31 (2002).
20. M. Meschke, W. Guichard, J. P. Pekola, *Nature* **444**, 187–190 (2006).
21. A. V. Timofeev, M. Helle, M. Meschke, M. Möttönen, J. P. Pekola, *Phys. Rev. Lett.* **102**, 200801 (2009).
22. L. W. Molenkamp, Th. Gravier, H. van Houten, O. J. A. Buijk, M. A. A. Mabesoone, C. T. Foxon, *Phys. Rev. Lett.* **68**, 3765–3768 (1992).
23. O. Chiatti *et al.*, *Phys. Rev. Lett.* **97**, 056601 (2006).
24. Y. X. Liang, Q. Dong, U. Gennser, A. Cavanna, Y. Jin, *J. Low Temp. Phys.* **167**, 632–637 (2012).
25. Materials and methods are available as supplementary materials on Science Online.
26. S. Jezouin *et al.*, *Nat. Commun.* **4**, 1802 (2013).
27. M. Büttiker, *Phys. Rev. Lett.* **65**, 2901–2904 (1990).
28. Y. M. Blanter, E. V. Sukhorukov, *Phys. Rev. Lett.* **84**, 1280–1283 (2000).
29. F. C. Wellstood, C. Urbina, J. Clarke, *Phys. Rev. B Condens. Matter* **49**, 5942–5955 (1994).
30. F. Pierre *et al.*, *Phys. Rev. B* **68**, 085413 (2003).
31. F. Giazotto, T. T. Heikkilä, A. Luukanen, A. M. Savin, J. P. Pekola, *Rev. Mod. Phys.* **78**, 217–274 (2006).
32. Y. Dubi, M. Di Ventra, *Rev. Mod. Phys.* **83**, 131–155 (2011).
33. F. Giazotto, M. J. Martínez-Pérez, *Nature* **492**, 401–405 (2012).

Acknowledgments: We gratefully acknowledge the contribution of V. Andreani to the noise measurement setup. This work was supported by the European Research Council (ERC-2010-StG-20091028, no. 259033).

Supplementary Materials

www.sciencemag.org/content/342/6158/601/suppl/DC1
Materials and Methods
Figs. S1 to S9
Table S1
References (34–42)

13 June 2013; accepted 16 September 2013
Published online 3 October 2013;
10.1126/science.1241912

Parameter Space Compression Underlies Emergent Theories and Predictive Models

Benjamin B. Machta,^{1,2} Ricky Chachra,¹ Mark K. Transtrum,^{1,3} James P. Sethna^{1*}

The microscopically complicated real world exhibits behavior that often yields to simple yet quantitatively accurate descriptions. Predictions are possible despite large uncertainties in microscopic parameters, both in physics and in multiparameter models in other areas of science. We connect the two by analyzing parameter sensitivities in a prototypical continuum theory (diffusion) and at a self-similar critical point (the Ising model). We trace the emergence of an effective theory for long-scale observables to a compression of the parameter space quantified by the eigenvalues of the Fisher Information Matrix. A similar compression appears ubiquitously in models taken from diverse areas of science, suggesting that the parameter space structure underlying effective continuum and universal theories in physics also permits predictive modeling more generally.

Physics owes its success (1) in large part to the hierarchical character of scientific theories (2). These theories of our physical world model natural phenomena as if physics at macroscopic length scales were almost independent of the underlying, shorter-length-scale details. For example, understanding string theory or the electroweak interaction is not necessary for quantitatively modeling the behavior of solids or superconductors active on longer length and time scales. The fact that many lower-level theories in physics can be systematically coarsened (renormalized) into macroscopic effective models establishes and quantifies their hierarchical character.

A similar emergent simplicity also appears in other areas of science (3–9). In many cases,

important predictions largely depend only on a few “stiff” combinations of parameters, followed by a sequence of geometrically less important “sloppy” ones (Fig. 1) (10–12). This recurring characteristic, termed “sloppiness,” naturally arises (13, 14) in models describing collective data (not chosen to probe individual system components) and has implications similar to those of the renormalization group (RG) and continuum limit methods of statistical physics. Both physics and sloppy models show weak dependence of macroscopic observables on microscopic details and allow effective descriptions with reduced dimensionality. To clarify this connection, we developed and applied an information theory–based generalization of sloppy model analysis to two well-understood physics models—a discrete model of diffusion and an Ising model of the ferromagnetic phase transition. For both models, we show that when observations are confined to long time or length scales, there is a similar compression of the microscopic parameter space, with sensitive or stiff directions corresponding to the relevant

macroscopic parameters (such as the diffusion constant). These results suggest that the hierarchy of theories in physics relies on the same parameter space compression that is ubiquitous in general multiparameter models.

The sensitivity of model predictions to changes in parameters is quantified by the Fisher Information Matrix (FIM). The FIM forms a metric on parameter space that measures the distinguishability between a model with parameters θ^μ and a nearby model with parameters $\theta^\mu + \delta\theta^\mu$ (15–18). This divergence is given by $ds^2 = g_{\mu\nu}\delta\theta^\mu\delta\theta^\nu$, where $g_{\mu\nu}$ is the FIM defined by

$$g_{\mu\nu} = -\sum_{\vec{x}} P_{\theta}(\vec{x}) \frac{\partial^2 \log P_{\theta}(\vec{x})}{\partial \theta^\mu \partial \theta^\nu} \quad (1)$$

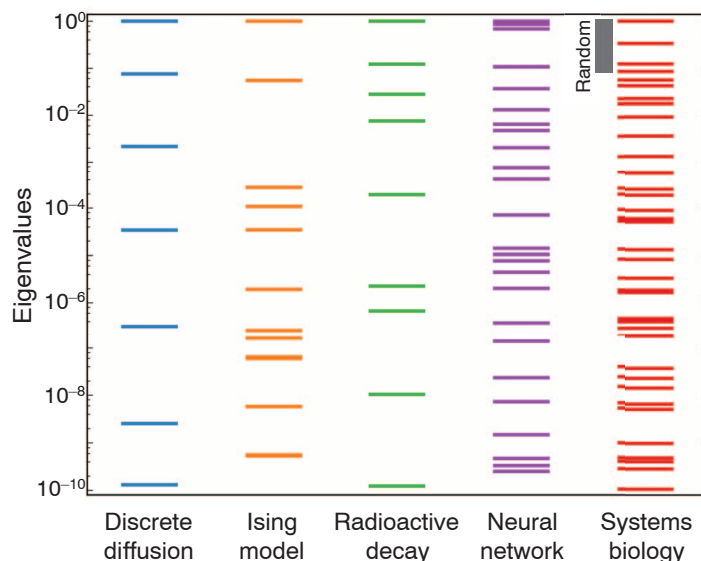
Here, $P_{\theta}(\vec{x})$ is the probability that a (stochastic) model with parameters θ^μ would produce observables \vec{x} . In the context of nonlinear least squares, g is the Hessian of χ^2 , the sum of squares of residuals of the data fit (15). Distance in this metric space is a fundamental measure of distinguishability in stochastic systems. Sorted by decreasing eigenvalues, eigenvectors of g describe progressively less important linear combinations of parameters that govern system behavior. Previously, it was shown that in nonlinear least squares models describing collective data, this metric’s eigenvalues have logarithms that are roughly uniformly distributed over many decades and reach extremely small values (Fig. 1). These eigenvalues quantify parameter space compression: A few stiff eigenvectors in each model point along directions where observables are sensitive to changes in parameters, whereas progressively sloppier directions make little difference. These sloppy parameter combinations cannot be inferred from collective data, and conversely, their exact values do not need to be known to quantitatively understand system behavior (12). Do physics models share this structure?

The diffusion equation is the canonical example of a continuum limit in physics. It governs behavior whenever small particles undergo

¹Laboratory of Atomic and Solid State Physics, Cornell University, Ithaca, NY 14853, USA. ²Lewis-Sigler Institute for Integrative Genomics, Princeton University, Princeton, NJ 08854, USA. ³Department of Physics and Astronomy, Brigham Young University, Provo, UT 84602, USA.

*Corresponding author. E-mail: sethna@lassp.cornell.edu

Fig. 1. Normalized eigenvalues of the FIM of various models. The diffusion and Ising models are explored here. A radioactive decay model and a neural network are taken from (14). The systems biology model is a differential equation model of a mitogen-activated protein kinase (MAPK) cascade taken from (10), and the adjoining band marked as “Random” shows a typical eigenvalue spread from a Wishart random matrix of the same size. (Additional examples are available in fig. S1.) In all models, the eigenvalues of the FIM are roughly geometrically distributed, with each successive direction substantially less important for system behavior (only the first 10 decades are shown). This means that inferring the parameter combination whose eigenvalue is smallest shown would require $\sim 10^{10}$ times more data than would the stiffest parameter combination. Conversely, the least important parameter combination is $\sqrt{10^{10}}$ times less important for understanding system behavior.



stochastic motion. The complex microscopic collisions are described by a general linear dynamical equation for the particle density, $\rho(r, \tau)$:

$$\partial_t \rho(r, \tau) = R\rho - V\partial_x \rho + D\partial_x^2 \rho + \sum_{n=3}^{\infty} C_n \partial_x^n \rho \quad (2)$$

Here, D is the diffusion constant, V is the net drift, R is the particle creation rate, coefficients C_n couple to higher-order gradient terms and scale as $C_n \propto \alpha^n$, where α is some microscopic length. As time τ proceeds, ρ smoothens over a length $\sim \sqrt{D\tau}$. The contribution of higher-gradient terms thus scales as $C_n/(D\tau)^{n/2} \sim (D\tau/\alpha^2)^{-n/2}$ and can be dropped to yield the three-term diffusion equation as the emergent continuum limit. Microscopic parameters describing the particles and their environment enter into this continuum description only through their effects on D , V , and R . We considered a microscopic model of stochastic motion and particle creation on a discrete one-dimensional (1D) lattice of sites. Parameters θ^μ give the probabilities that a particle will be at site $j + \mu$ after one time step given a starting particle at site j , for $-N \leq \mu \leq N$ (Fig. 2, inset). At the initial time, all particles are at the origin, $\rho_0(j) = \delta_{j,0}$. The observables, $\vec{x} \equiv \rho_\tau(j)$, are the densities of particles at some later time τ .

After a single time step, the distribution of particles is given by $\rho_1(j) = \theta^j$. This distribution depends independently on all of its parameters; thus, the FIM is the identity, $g_{\mu\nu} = \delta_{\mu\nu}$ (15). Because each parameter is independently measurable, there is no parameter space compression. When particles take several time steps before their positions are observed, some parameter combinations affect observable behavior much more sensitively than do others: The n th FIM eigenvalue scales as $\lambda_n \sim \tau^2(D\tau/a^2)^{-n/2}$ (Fig. 2) (15), where $a = N$ is the maximum hopping distance,

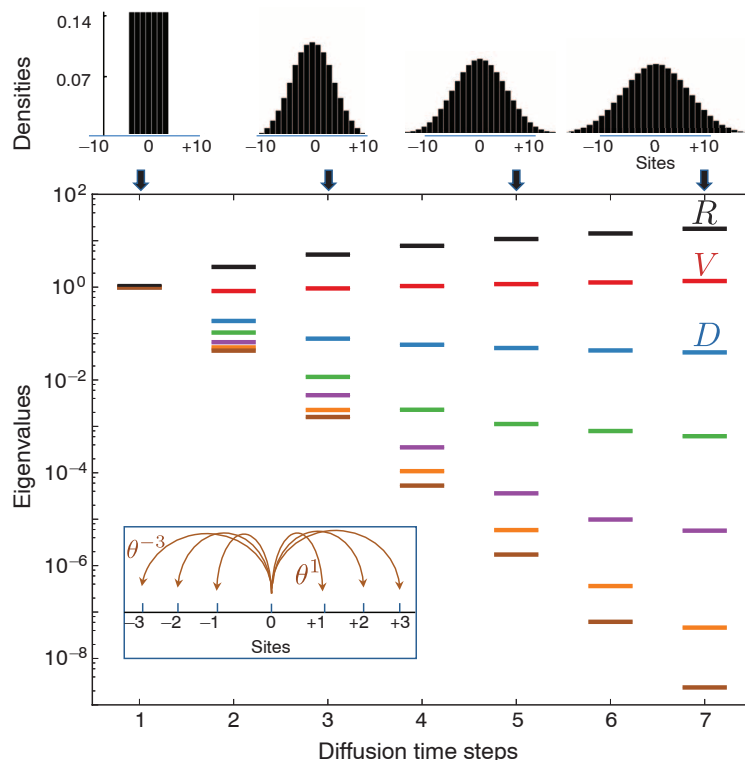


Fig. 2. FIM eigenvalues of a model of stochastic motion on a 1D lattice. The seven parameters describe probabilities of transitioning to nearby sites (bottom, inset). Observations are taken after a given number of time steps for the case in which all parameters take the value $\theta^\mu = 1/7$. The top row shows the resulting densities plotted at times $\tau = 1, 3, 5$, and 7 . The bottom plot shows the eigenvalues of the FIM versus number of steps. After a single time step, the FIM is the identity, but as time progresses, the spectrum of the FIM spreads over many orders of magnitude. The first eigenvector measures deviations in the net particle creation rate R from 0, the second measures a net drift V in the density, and the third corresponds to parameter combinations that do not affect these macroscopic parameters but instead measure the skew (green), kurtosis (purple), and higher moments of the resulting density (orange and brown).

our microscopic length scale. The information theory approach has automatically recapitulated the physics underlying the continuum limit; successive eigenvalues are separated by

the square of the factor $\sqrt{D\tau/a^2}$ governing the strength of successive terms in the gradient expansion (Eq. 2). The three stiffest eigenvalues can be shown to correspond precisely to R , V ,

and D ; further eigenvectors control the skew, kurtosis, and higher moments of the final distribution of particles through coefficients C_n that do not appear in continuum descriptions (Fig. 2) (15). This gives an information theoretic explanation for the wide applicability of the diffusion equation and quantifies a widely held intuition: One cannot infer microscopic parameters such as the bond angle of a water molecule from a diffusion measurement. Conversely, microscopic details are unnecessary for understanding the long-scale behavior.

Continuum models such as the diffusion equation arise when fluctuations are large only on the microscale. These models are valid when the observables are slow and large when compared with the natural scale of fluctuations. RG methods clarify that system behavior can be quantitatively modeled even when fluctuations are large on all scales, such as near critical points and for quantum field theories. The Ising model is the prototypical system exhibiting these self-similar fluctuations. Near its critical point, the Ising model predicts fractal domains whose statistics are universal; it not only describes magnetic fluctuations in ferromagnets, but also the density fluctuations near a liquid-gas transition and composition fluctuations near a liquid-liquid miscibility transition (19, 20). In the 2D square lattice Ising model, a “spin” at every site takes a value of $s_{ij} = \pm 1$, and observables are spin configurations $\vec{x} = \{s_{ij}\}$ or subsets \vec{x}^n , as defined below. Our generalized Ising model assigns to each spin configuration a probability given by its Boltzmann weight, $P_\theta(\vec{x}) = e^{-\mathcal{H}_\theta(\vec{x})}/Z$ and is parametrized through its Hamiltonian $\mathcal{H}_\theta(\vec{x}) = \theta^\mu \Phi_\mu(\vec{x})$. Parameters $\theta^{\alpha\beta}$ describe the coupling between spins and their neighbors at coordinates (α, β) away, so that $\Phi_{\alpha\beta}(\vec{x}) = \sum_{i,j} s_{ij} s_{i+\alpha, j+\beta}$, whereas θ^0 is the external field multiplying $\Phi_0(\vec{x}) = \sum_{i,j} s_{i,j}$ (Fig. 3, inset) (15). The usual nearest-neighbor Ising model has $\theta^{01} = \theta^{10} = -1/T$, $\theta^0 = h$, and $\theta = 0$ otherwise. We examined our generalized model near the critical point $T = T_c$, $h = 0$ of the usual model.

At the microscopic level, observables are entire spin configurations, and the Ising FIM is a sum of two- and four-spin correlation functions that can be readily calculated by use of Monte Carlo techniques (15, 21). The Ising model viewed at its microscopic scale has two-parameter combinations with large eigenvalues (Fig. 3, first column) (15). These two stiff eigenvectors control the so-called “relevant” variables of the RG, h and $t = (T - T_c)/T_c$, which affect long-distance behavior and have no analogy in the diffusion equation (22, 23). The remaining eigenvalues all cluster around a scale given by the system size and do not yet show parameter space compression. Their distribution is reminiscent of the spectrum seen in the diffusion equation when viewed at its microscopic scale, at which parameters could be independently measured from particular observables. Their corresponding eigenvectors are nonstiff parameter combinations that only affect

short-distance behavior (“irrelevant” RG variables). Nonetheless, the clustering of FIM eigenvalues (Fig. 3, first column) demonstrates that none of these parameter combinations are redundant for the description of microscopic data; a real “multiparameter” ferromagnet is not microscopically well-described by the two-parameter Ising model.

To understand how the Ising model provides a universal description for coarsened behavior, we restricted observables to spin configurations of a subset of lattice sites chosen via a checkerboard decimation procedure (Fig. 3, top row, insets). The FIM of Eq. 1 is now measured using as observables only those sites in a sublattice decimated by a factor 2^n , $\vec{x}^n = \{s_{ij}\}_{\{i,j\} \in n}$. For example, one level of decimation corresponds to the black sites on the checkerboard, whereas after two steps, only sites $\{i, j\}$ with even i and j remain. The distribution is still drawn from the ensemble defined by the original Hamiltonian defined on the full lattice. The calculation was implemented by using Compatible Monte Carlo (15, 24). The results from Monte Carlo are presented for a 64×64 lattice at its critical point in Fig. 3. From an information theory perspective, the results shown in Fig. 3 and analysis detailed

in (15) demonstrate that relevant variables are exactly those for which spatial coarsening preserves measurement precision. Crucially, the other eigenvectors of the metric become progressively less important under coarsening, just as for diffusion. As coarsening proceeds, the FIM eigenvalues shrink according to the corresponding irrelevant RG exponent (Fig. 3) (15). The presence of just two stiff FIM eigenvalues provides an alternative explanation of why the two-parameter Ising model can capture the universal behavior of a wide variety of physical systems near their critical points.

We have seen that neither the diffusion model nor the Ising model are sloppy at their microscopic scales. It is only upon coarsening the observables—either by allowing several time steps to pass or by only observing a subset of lattice sites—that a typical sloppy spectrum of parameter combinations emerges. Correspondingly, multiparameter models such as in systems biology and other areas of science are sloppy only when fit to experiments that probe collective behavior; if experiments are designed to measure one parameter at a time, no model compression can be expected (25, 26). In the models

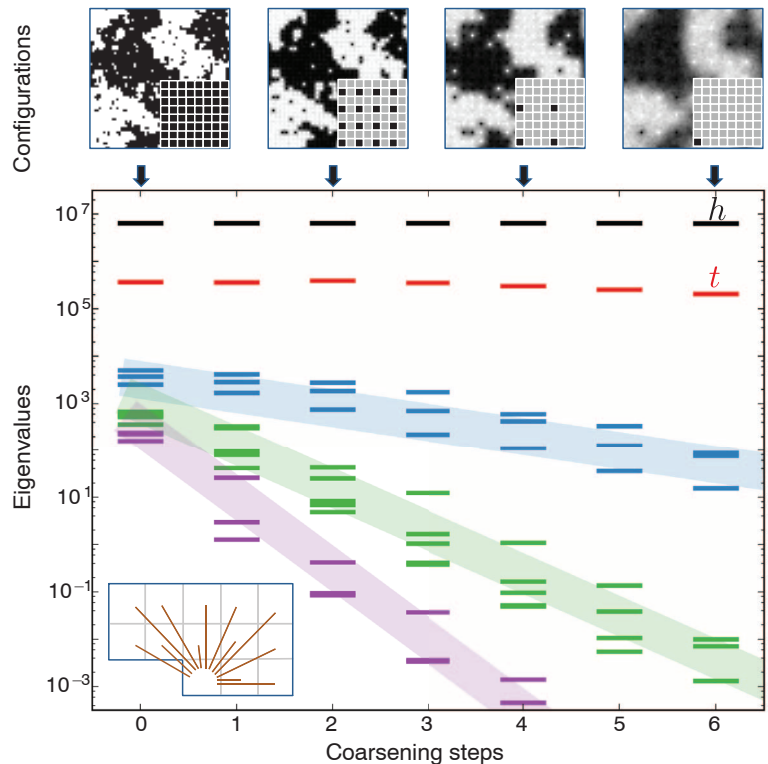


Fig. 3. FIM eigenvalues of an Ising model of ferromagnetism. Parameters describe nearest and nearby neighbor couplings (bottom, inset) and a magnetic field. Observables are spin configurations of all spins on a sublattice (dark sites in top, insets). (Top) One particular spin configuration generated by the model, suitably blurred for step > 0 to the average spin conditioned on the observed sublattice values. Some information about the configuration, such as the typical size of fluctuations, is preserved under this procedure, whereas other information such as the nearest-neighbor correlation amplitude is lost. The two largest eigenvalues, whose eigenvectors measure reduced temperature t and the applied field h do not decay substantially under coarsening. Further FIM eigenvalues shrink by a factor of $\sqrt{2}^{-2-2y_i}$, where y_i is the i th RG exponent (15). This shrinkage quantifies the information lost in each coarsening step.

examined here, there is a clear distinction between the short time or length scale of the microscopic theory and the long time or length scale of observables. As we show in (15), sloppiness in physics can be precisely traced to the ratio of these two scales—an important small variable. In the broad class of models in which such distinction of scales cannot be made, our explanation for sloppiness (27) is not yet unified with the RG and continuum methods of physics. Nonetheless, the striking similarity of their sloppy sensitivities lends perspective to the surprising power of mathematical modeling despite microscopic uncertainty.

References and Notes

- E. P. Wigner, *Commun. Pure Appl. Math.* **13**, 1–14 (1960).
- P. W. Anderson, *Science* **177**, 393–396 (1972).
- U. Alon, *Nature* **446**, 497 (2007).
- G. J. Stephens, B. Johnson-Kerner, W. Bialek, W. S. Ryu, *PLOS Comput. Biol.* **4**, e1000028 (2008).
- G. J. Stephens, L. C. Osborne, W. Bialek, *Proc. Natl. Acad. Sci. U.S.A.* **108**, 15565–15571 (2011).
- T. D. Sanger, *J. Neurosci.* **20**, 1066–1072 (2000).
- F. Corson, E. D. Siggia, *Proc. Natl. Acad. Sci. U.S.A.* **109**, 5568–5575 (2012).
- M. Schmidt, H. Lipson, *Science* **324**, 81–85 (2009).
- T. Mora, W. Bialek, *J. Stat. Phys.* **144**, 268–302 (2011).
- K. S. Brown *et al.*, *Phys. Biol.* **1**, 184–195 (2004).
- R. N. Gutenkunst *et al.*, *PLOS Comput. Biol.* **3**, 1871–1878 (2007).
- J. J. Waterfall *et al.*, *Phys. Rev. Lett.* **97**, 150601 (2006).
- M. K. Transtrum, B. B. Machta, J. P. Sethna, *Phys. Rev. Lett.* **104**, 060201 (2010).
- M. K. Transtrum, B. B. Machta, J. P. Sethna, *Phys. Rev. E Stat. Nonlin. Soft Matter Phys.* **83**, 036701 (2011).
- Materials and methods are available as supplementary materials on Science Online.
- S. Amari, H. Nagaoka, *Methods of Information Geometry* (American Mathematical Society, Providence, RI, 2000).
- I. J. Myung, V. Balasubramanian, M. A. Pitt, *Proc. Natl. Acad. Sci. U.S.A.* **97**, 11170–11175 (2000).
- V. Balasubramanian, *Neural Comput.* **9**, 349–368 (1997).
- P. M. Chaikin, T. C. Lubensky, *Principles of Condensed Matter Physics* (Cambridge Univ. Press, Cambridge, 1995).
- S. L. Veatch, O. Soubias, S. L. Keller, K. Gawrisch, *Proc. Natl. Acad. Sci. U.S.A.* **104**, 17650–17655 (2007).
- G. E. Crooks, *Phys. Rev. Lett.* **99**, 100602 (2007).
- J. Cardy, *Scaling and Renormalization in Statistical Physics* (Cambridge Univ. Press, Cambridge, 1996).
- G. Ruppeiner, *Rev. Mod. Phys.* **67**, 605–659 (1995).
- D. Ron, R. H. Swendsen, A. Brandt, *Phys. Rev. Lett.* **89**, 275701 (2002).
- F. P. Casey *et al.*, *IET Syst. Biol.* **1**, 190–202 (2007).
- J. F. Aggar, D. K. Witmer, F. M. White, B. Tidor, *Mol. Biosyst.* **6**, 1890–1900 (2010).
- In (13, 14), we used interpolation theorems and information geometry to show that multiparameter models fit to collective data have model manifolds that form hyper-ribbons in data space with geometrically spaced widths.

Acknowledgements: We thank S. Kuehn and S. Papanikolaou for helpful comments and discussions. This work was supported by NSF grants DMR 1005479 and DMR 1312160 and a Lewis-Sigler Fellowship (B.B.M.). Raw data and analysis code are available on request from the authors or via the Internet: www.lasp.cornell.edu/sethna/Sloppy/EmergentParameterCompression.

Supplementary Materials

www.sciencemag.org/content/342/6158/604/suppl/DC1

Supplementary Text

Figs. S1 and S2

References (28–42)

4 April 2013; accepted 24 September 2013

10.1126/science.1238723

Deterministically Encoding Quantum Information Using 100-Photon Schrödinger Cat States

Brian Vlastakis,^{1*} Gerhard Kirchmair,^{1†} Zaki Leghtas,^{1,2} Simon E. Nigg,^{1‡} Luigi Frunzio,¹ S. M. Girvin,¹ Mazyar Mirrahimi,^{1,2} M. H. Devoret,¹ R. J. Schoelkopf¹

In contrast to a single quantum bit, an oscillator can store multiple excitations and coherences provided one has the ability to generate and manipulate complex multiphoton states. We demonstrate multiphoton control by using a superconducting transmon qubit coupled to a waveguide cavity resonator with a highly ideal off-resonant coupling. This dispersive interaction is much greater than decoherence rates and higher-order nonlinearities to allow simultaneous manipulation of hundreds of photons. With a tool set of conditional qubit-photon logic, we mapped an arbitrary qubit state to a superposition of coherent states, known as a “cat state.” We created cat states as large as 111 photons and extended this protocol to create superpositions of up to four coherent states. This control creates a powerful interface between discrete and continuous variable quantum computation and could enable applications in metrology and quantum information processing.

Cavity quantum electrodynamics is a test-bed system for quantum optics, allowing the observation of strong interactions between photons and (artificial) atoms (1–3). Techniques using these systems allow the pro-

duction of nonclassical states of light, which have important uses for quantum communication, quantum computation, and investigations of fundamental quantum theory. For superconducting quantum circuits, cavity resonators have proven a valuable resource serving several roles: a quantum bus to generate entanglement between qubits (4), a quantum nondemolition probe allowing efficient quantum measurements (5, 6), a generator of single microwave photons (7, 8), and a quantum memory to store and shuttle information (9, 10). With its large Hilbert space, a cavity resonator also has the potential to store multiple quantum bits or redundantly encode information as necessary for quantum error correction. With the proper controls, a single cavity

could be made equivalent to a multiqubit register, allowing for simplifications of hardware design (11, 12). Although there have been some investigations of complex, multiphoton superpositions in superconducting cavity resonators, most techniques developed so far require fast qubit frequency tunability and are based on controlling individual photons one by one (13, 14). These implementations become increasingly burdensome for complex states or large photon numbers, making it desirable to develop a more natural method for controlling the large cavity Hilbert space.

We demonstrated a set of multiphoton operations by using a fixed-frequency superconducting transmon qubit coupled to a waveguide cavity resonator. We realized a highly ideal strong-dispersive coupling, where the strengths of the off-resonant qubit-cavity interactions were several orders of magnitude greater than the cavity decay rate and higher-order nonlinearities. This created a set of qubit-cavity entangling operations, allowing for control over the large cavity phase space. We implemented two of these operations: the qubit-state conditional cavity phase shift (15) and the photon-number conditional qubit rotation (14, 16). We combined these with unconditional qubit and cavity operations to perform direct measurements of the cavity Wigner function (17) and to efficiently generate large superposition states. By using these tools, we realized a recently proposed protocol (18) to deterministically encode quantum information in a cat state by creating an arbitrary superposition of quasi-orthogonal coherent states conditioned on an initial qubit state. We concatenated these entangling operations to encode quantum information into multiple phases of the cavity state, thereby creating multicomponent cat states and producing example states

¹Department of Physics and Department of Applied Physics, Yale University, New Haven, CT 06511, USA. ²Inria Paris-Rocquencourt, 78153 Le Chesnay Cedex, France.

*Corresponding author. E-mail: brian.vlastakis@yale.edu

†Present address: Institut für Quantenoptik und Quanteninformation, Österreichische Akademie der Wissenschaften, Otto-Hittmair-Platz 1, A-6020 Innsbruck, Austria, and Institut für Experimentalphysik, Universität Innsbruck, Technikerstrasse 25, A-6020 Innsbruck, Austria.

‡Present address: Department of Physics, University of Basel, CH-4056 Basel, Switzerland.

proposed for high-precision measurements surpassing the quantum-noise limit (19, 20). Unlike previous demonstrations of cat states (16, 21, 22), the procedures realized here allow for the deterministic generation of superimposed coherent states with arbitrary phase and amplitude. The set of operations demonstrated provides an efficient method to manipulate coherent states and could enable a variety of powerful methods for using cavity states in quantum information processing.

We realized qubit-photon quantum logic by using a strong off-resonant coupling of a qubit and cavity that can be described by the dispersive Hamiltonian (omitting higher-order nonlinear terms)

$$H/\hbar = \omega_q |e\rangle\langle e| + \omega_s a^\dagger a - \chi_{qs} a^\dagger a |e\rangle\langle e| \quad (1)$$

where $|e\rangle$ is the excited state of the qubit, $a^\dagger(a)$ are the raising (lowering) ladder operators of the cavity resonator, ω_{qs} are qubit and cavity transition frequencies, and χ_{qs} is the dispersive interaction between these modes. This interaction produces a state-dependent shift in either the qubit or cavity transition frequency. We exploited this conditional frequency shift to produce qubit-photon entanglement with two operations: conditional cavity phase shifts and conditional qubit rotations. The conditional cavity phase shift can be described as

$$C_\Phi = e^{i\Phi a^\dagger a |e\rangle\langle e|} \\ = \mathbb{1} \otimes |g\rangle\langle g| + e^{i\Phi a^\dagger a} \otimes |e\rangle\langle e| \quad (2)$$

where $|g\rangle$ is the ground state of the qubit and Φ is the conditional phase shift induced on the cavity state. This conditional phase appears from the free evolution of the dispersive Hamiltonian for a time τ where $\Phi = \chi_{qs}\tau$. For example, acting a conditional cavity phase shift on a coherent state while the qubit is in a superposition state produces an entangled qubit/cavity state, $C_\Phi\{|\alpha\rangle \otimes (|g\rangle + |e\rangle)\} = |\alpha, g\rangle + |\alpha e^{i\Phi}, e\rangle$ (disregarding normalization) (15).

Because a coherent state $|\alpha\rangle = e^{-\frac{|\alpha|^2}{2}} \sum_{n=0}^{\infty} \frac{\alpha^n}{\sqrt{n!}} |n\rangle$

is a superposition of Fock states $|n\rangle$ represented by a complex value α , this operation enables us to encode the qubit state information into the cavity phase and entangle the qubit with many photons simultaneously. For a special case, $C_{\Phi=\pi}$, the cavity state attains a conditional π shift per photon. This, in turn, causes the qubit state to acquire a phase shift conditional on there being exactly an odd number of photons in the cavity, resulting in a mapping of the cavity photon number parity to the qubit state. By using Ramsey interferometry, we used this gate to measure the cavity photon parity and ultimately the cavity Wigner function (17, 23, 24). The Wigner function is a representation of a quantum state in a continuous variable basis and can be expressed as $W(\alpha) = \frac{2}{\pi} \text{Tr}[D_\alpha^\dagger \rho D_\alpha P]$, where $D_\alpha = e^{a\alpha^\dagger - \alpha a}$ is the cavity displacement operator, $P = e^{i\pi a^\dagger a}$ is the photon number parity operator, and ρ is the cavity state density matrix. A direct Wigner measurement is produced by measuring the mean photon parity $\langle P \rangle$ at many points in the cavity phase space, which we used to completely determine the quantum state of the cavity.

The second operation, the conditional qubit rotation, is a rotation on the qubit state conditional on the photon number of the cavity state. Because the qubit transition frequency is strongly photon number dependent, we can drive a particular transition selective on a cavity Fock state (14, 16). A rotation on the qubit state conditioned on the m th photon Fock state can ideally be described as

$$R_{n,0}^m = |m\rangle\langle m| \otimes R_{n,0} + \sum_{n \neq m} |n\rangle\langle n| \otimes \mathbb{1} \quad (3)$$

where $R_{n,0}$ is a qubit rotation about a vector \hat{n} with rotation angle θ . In practice, this operation will result in residual photon-dependent phase shifts because of the ac Stark effect, which we corrected for the purposes of this experiment (24). In order to realize these two entangling operations, we had to achieve dispersive shifts much greater than the qubit and cavity decoherence rates, $\chi_{qs} \gg \gamma, n_{\max} \kappa_s$,

where γ is the qubit decay rate, κ_s is the storage cavity decay rate, and n_{\max} is the maximum occupied photon number. This dispersive approximation (Eq. 1) is valid in a low photon number regime where the dispersive interaction $\chi_{qs} a^\dagger a |e\rangle\langle e|$ is much greater than higher-order nonlinear terms, such as the cavity self-Kerr $K_s a^{\dagger 2} a^2$, and the nonlinearity of the dispersive shift $\chi'_{qs} a^{\dagger 2} a^2 |e\rangle\langle e|$ (25). Combined with unconditional qubit and cavity manipulations, these two entangling operations give us a powerful tool set for controlling the joint qubit-cavity system (12, 18, 24).

Our experiment consists of two waveguide cavity resonators (16, 26) coupled to a transmon qubit (Fig. 1A). Cavity 1 was used for photon-state manipulation, preparation, and storage with transition frequency $\frac{\omega_s}{2\pi} = 8.18$ GHz and decay rate $\frac{\kappa_s}{2\pi} = 7.2$ kHz $= \frac{1}{2\pi \times 22.1 \mu s}$ (limited by internal losses). Cavity 2 was used for qubit-state detection with transition frequency $\frac{\omega_q}{2\pi} = 9.36$ GHz and decay rate $\frac{\gamma}{2\pi} = 330$ kHz $= \frac{1}{2\pi \times 480 ns}$ (limited by output coupling for increased readout fidelity). Both cavities were coupled to a “vertical” transmon qubit (16, 24) with transition frequency $\frac{\omega_q}{2\pi} = 7.46$ GHz and decay rate $\frac{\gamma}{2\pi} = 36$ kHz $= \frac{1}{2\pi \times 4.4 \mu s}$ (limited by internal losses). This system creates a dispersive interaction between the qubit and storage cavity mode, resulting in a state-dependent frequency shift $\frac{\chi_{qs}}{2\pi} = 2.4$ MHz. We independently measured (24) higher-order nonlinear terms K_s and χ'_{qs} , allowing us to put a limit on the maximum accessible photon number for this experiment: $n \ll n_{\max} = \min[\chi_{qs}/\chi'_{qs} = 560, \chi_{qs}/K_s = 650, \chi_{qs}/\kappa_s = 330]$. By combining a conditional cavity phase shift with a conditional qubit rotation, we sequentially entangled then disentangled the qubit and cavity to map a qubit state to a superposition of quasi-orthogonal coherent states (18). Following the sequence outlined in Fig. 1B, we started with an unentangled qubit-cavity state $|\psi_0\rangle = |\beta\rangle \otimes (|g\rangle + |e\rangle)$ (disregarding normalization), where $|\beta\rangle$ is a coherent state. Performing a conditional cavity π phase shift on the initialized state created an entangled qubit-cavity state $|\psi_1\rangle = C_\pi |\psi_0\rangle = |\beta, g\rangle + |-\beta, e\rangle$. This state, where the qubit state is entangled with the phases of the superimposed coherent states, is often referred

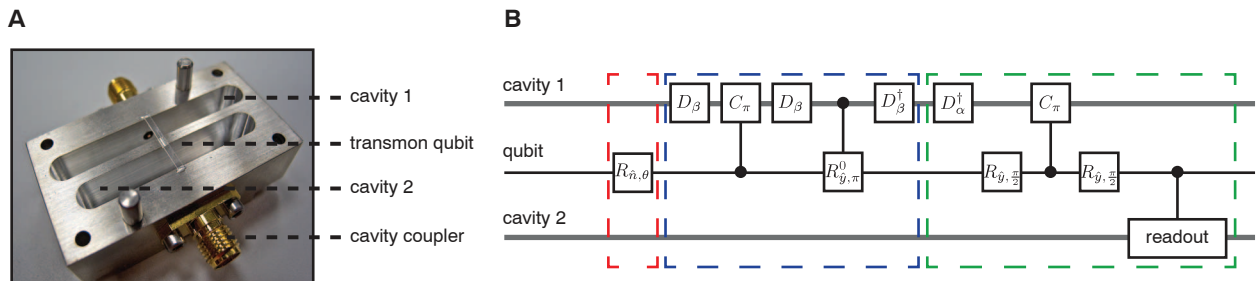


Fig. 1. Experimental device and protocol. (A) A cross section shows the device, machined from two halves of aluminum alloy, which contains two cavity resonators and holds a sapphire chip with a lithographically patterned transmon qubit. (B) The protocol for mapping and measuring a qubit state into a superposition of coherent states is performed in three

steps: qubit-state preparation (red) using a single qubit rotation $R_{\hat{n},\theta}$; qubit to cavity-state mapping (blue) using conditional operations C_π and $R_{y,\pi}^0$ with cavity displacements D_β ; and cavity-state Wigner tomography (green) using Ramsey interferometry with unconditional qubit rotations $R_{y,\pi/2}$.

to as a Schrödinger cat, which has been studied in other quantum systems (15, 27). We can unconditionally displace this state to obtain $|\psi_2\rangle = D_\beta|\psi_1\rangle = |2\beta, g\rangle + |0, e\rangle$. At this point, we can apply a qubit π rotation conditional on the cavity vacuum state $|0\rangle$, which produces the unentangled cat state $|\psi_3\rangle \approx R_{\pi, \pi}^0|\psi_2\rangle = (|2\beta\rangle + |0\rangle) \otimes |g\rangle$. Because of the nonorthogonality of coherent states, this operation will leave some remaining entanglement, which rapidly decreases with cat state size and can be neglected compared with other experimental imperfections. An additional displacement results in the final state $|\psi_4\rangle = D_{-\beta}|\psi_3\rangle = (|\beta\rangle + |-\beta\rangle) \otimes |g\rangle$. As an example, we created the target cavity state $|\psi_{\text{target}}\rangle = \mathcal{N}(|\beta\rangle + |-\beta\rangle)$, where $\mathcal{N} \approx \frac{1}{\sqrt{2}}$ with $|\beta| = \sqrt{7}$, resulting in a fidelity $F = \langle\psi_{\text{target}}|\psi_{\text{target}}\rangle = 0.81$, which we confirmed by direct Wigner tomography (Fig. 2A). This procedure can be generalized to any arbitrary qubit state and cavity phase that maps as

$$|0\rangle \otimes \left\{ \cos\left(\frac{\theta}{2}\right)|g\rangle + \sin\left(\frac{\theta}{2}\right)e^{i\phi}|e\rangle \right\} \rightarrow \left\{ \cos\left(\frac{\theta}{2}\right)|\beta\rangle + \sin\left(\frac{\theta}{2}\right)e^{i\phi}|\beta e^{i\phi}\rangle \right\} \otimes |g\rangle \quad (4)$$

where θ and ϕ are parameters of the initial qubit state and when the superimposed coherent states are sufficiently orthogonal $|\langle\beta|\beta e^{i\phi}\rangle|^2 \ll 1$. Figure 2B shows the creation of cat states conditioned by qubit states prepared at the six cardinal points of the Bloch sphere.

Two special forms of cat states result in complete destructive interference of either odd or even Fock state amplitudes. Known as the even (or odd) cat states $|\beta\rangle \pm |-\beta\rangle$, these states

produce superpositions of only even (or odd) photon numbers. This interference can be showcased in the dispersive regime by performing qubit spectroscopy after the creation of one of these cavity states. Because of the strong-dispersive interaction, each spectral peak reveals a photon number probability of the prepared cavity state (28). For a coherent state $|\beta\rangle$, the qubit spectrum will represent a Poissonian photon number distribution $P_n(|\beta\rangle) = |\langle n|\beta\rangle|^2 = \frac{e^{-|\beta|^2}|\beta|^{2n}}{n!}$. An even and odd cat state of equivalent amplitude follows this same envelope but with destructive interference for the odd and even photon number states, respectively, $P_n(|\beta\rangle \pm |-\beta\rangle) \approx (1 \pm e^{i\pi n}) \frac{e^{-|\beta|^2}|\beta|^{2n}}{n!}$. We perform spectroscopy on the qubit with three prepared states: $|\beta, g\rangle$, $|\beta\rangle + |-\beta\rangle \otimes |g\rangle$, and $|\beta\rangle - |-\beta\rangle \otimes |g\rangle$ for $|\beta| = 2.3$, illustrating the discreteness of the electromagnetic signals in the cavity and revealing the nonclassical nature of the generated cat states (Fig. 3A).

Unlike building photon superpositions one by one (13, 14), this mapping protocol can scale to cavity states with larger quantum superpositions by merely increasing the displacement amplitude. The size of a quantum superposition in a cat state $S = |\beta_1 - \beta_2|^2$ is determined by its square distance in phase space between the two superimposed coherent states, $|\beta_1\rangle$ and $|\beta_2\rangle$ (21). To characterize S without performing full state tomography, we measured cuts of the Wigner function along the axis perpendicular to its quantum interference, $W[\text{Re}(\alpha) = 0, \text{Im}(\alpha)]$. The interference fringes in these cuts appear as $W[0, \text{Im}(\alpha)] = Ae^{-2|\text{Im}(\alpha)|^2} \cos[2\sqrt{S} \text{Im}(\alpha) + \delta]$, where A and δ are the fringe amplitude and phase (29). By using this method, we created and confirmed cat states

with sizes from 18 to 111 photons (Fig. 3B). The increased oscillation rate of these fringes with S shows the increased sensitivity to small displacements in cavity field because of larger quantum superpositions [see (24) for proof-of-principle Heisenberg-limited phase estimation]. Reduced fringe visibility with larger sizes is due to the increased sensitivity to cavity decay. Other factors also contribute, namely, infidelity in Wigner tomography and qubit decoherence during preparation.

Because the methods outlined here are deterministic, entangling operations can be combined to create complex nonclassical cavity states. By using a conditional cavity phase shift for various phases Φ , we can encode quantum information to a particular phase of a coherent state. With this operation, we can create superpositions of multiple coherent states, multicomponent cat states. We used gates $C_{2\pi/3}$ and $C_{\pi/2}$ to create three- and four-component cat states (Fig. 4, A to C) with fidelity $F_A = 0.60$, $F_B = 0.58$, and $F_C = 0.52$ (24). The skewing of these states is caused by the inherited cavity self-Kerr. Additional factors contributing to infidelity include photon decay during preparation and measurement as well as tomography pulse errors. The state in Fig. 4C, also known as the compass state, contains overlapping interference fringes revealing increased sensitivity to cavity displacements in both quadratures simultaneously (19).

We have demonstrated the efficient generation and detection of coherent state superpositions using off-resonant interactions inherent in the cavity QED architecture. The tools and techniques described here require only a fixed-frequency, strong-dispersive interaction and realize an inter-

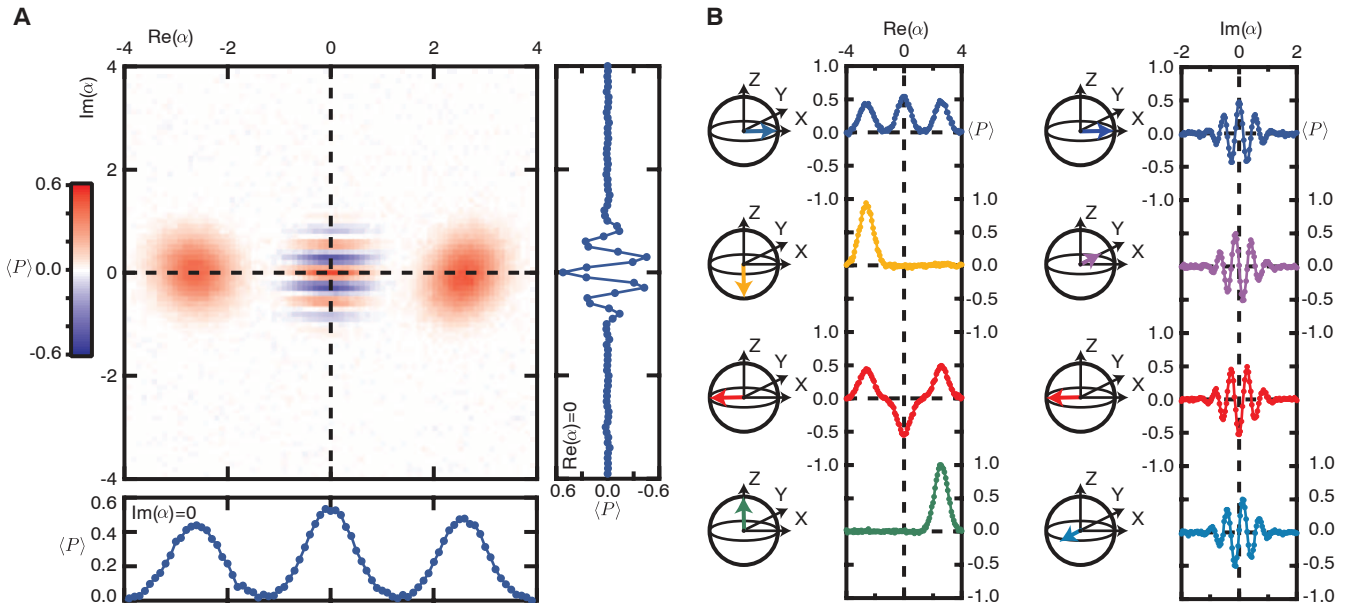


Fig. 2. Wigner tomography of coherent state superpositions. (A) Wigner tomography of the cavity state $|\psi\rangle = \mathcal{N}(|\beta\rangle + |-\beta\rangle)$ with $|\beta| = \sqrt{7}$ and $\mathcal{N} \approx \frac{1}{\sqrt{2}}$ using an 81-by-81 grid of tomography displacements showcases the interference fringes characteristic of a quantum superposition. Cuts along the real and imaginary axes reveal the relative population and quantum inter-

ference of the superimposed coherent states. The visibility of these interference fringes is reduced because of cavity decay during preparation and measurement (a perfect superposition would achieve unity mean photon parity). (B) By using qubit states initially prepared in the six cardinal points of the Bloch sphere, we mapped populations and phases in a resulting cat state.

face between discrete and continuous variable quantum computation (30). This can lead to simplified methods for individual storage and re-

trieval of multiqubit states in a cavity resonator and creates ways to perform multiqubit stabilizer measurements (31) or to redundantly encode infor-

mation for quantum error correction (12) using minimal hardware. Additional applications include Heisenberg-limited measurement (19, 20, 24) and quantum information storage in thermally excited resonator states (32).

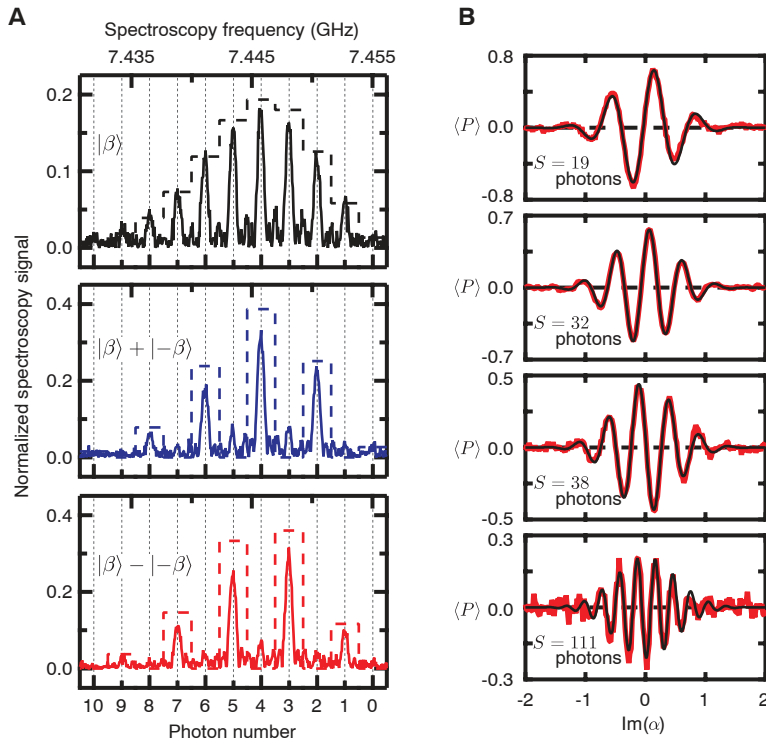
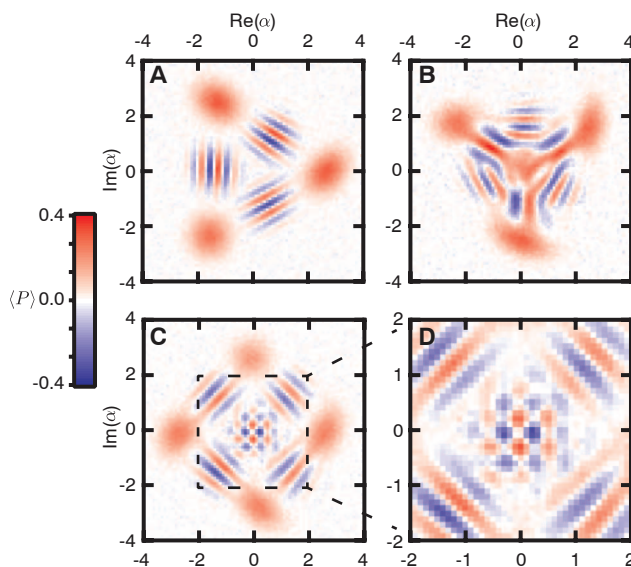


Fig. 3. Qubit spectroscopy and scaling to large photon superpositions. (A) Photon number splitting is observed when performing spectroscopy of a qubit dispersively coupled to the storage cavity with three different prepared states: a coherent state $|\beta\rangle$, even cat state $|\beta\rangle + |-\beta\rangle$, and odd cat state $|\beta\rangle - |-\beta\rangle$ with amplitude $|\beta| = 2.3$. Each spectral peak corresponds to the probability for a photon number state following a Poissonian distribution. Dashed bar plots show the expected photon probabilities for each of these states. Notice that even and odd cat states show destructive interference for the odd and even photon numbers. These spectra are acquired by deconvolving the measured signal with the Fourier spectrum of the finite-width spectroscopy pulse. (B) Cuts along the imaginary axis of the measured Wigner function for each prepared cat state reveal quantum superpositions with up to 111 photons in size. Cat state size S is determined by these measured interference fringes following the relation $Ae^{-2|\text{Im}(\alpha)|^2} \cos[2\sqrt{S} \text{Im}(\alpha) + \delta]$, where S , A , and δ are fit parameters.

Fig. 4. Multicomponent cat states. By using conditional cavity phase shifts $C_{2\pi/3}$ and $C_{\pi/2}$, we created superpositions of three and four coherent states. Shown here is Wigner tomography of cavity states: (A) $|\beta\rangle + e^{i\lambda_1}|\beta e^{i2\pi/3}\rangle + e^{i\lambda_2}|\beta e^{i4\pi/3}\rangle$, where $|\beta| = \sqrt{7}$, $\lambda_1 = 0.6\pi$, and $\lambda_2 = -0.3\pi$; (B) $|0\rangle + e^{i\mu_1}|-\beta\rangle + e^{i\mu_2}|\beta e^{i\pi/3}\rangle + e^{i\mu_3}|\beta e^{i2\pi/3}\rangle$, where $|\beta| = \sqrt{7}$, $\mu_1 = 0.5\pi$, $\mu_2 = -0.4\pi$, and $\mu_3 = -0.2\pi$; and (C) $|\beta\rangle + e^{i\nu_1}|\beta\rangle + |-\beta\rangle + e^{i\nu_2}|-\beta\rangle$, where $|\beta| = \sqrt{7}$, $\nu_1 = \pi$, and $\nu_2 = -0.2\pi$. (D) A closer inspection of the quantum interference in (C) reveals increased sensitivity to cavity displacements in both quadratures simultaneously.



References and Notes

1. J. M. Raimond *et al.*, *J. Phys. B* **38**, S535–S550 (2005).
2. R. Miller *et al.*, *J. Phys. B* **38**, S551–S565 (2005).
3. A. Wallraff *et al.*, *Nature* **431**, 162–167 (2004).
4. L. DiCarlo *et al.*, *Nature* **460**, 240–244 (2009).
5. R. Vijay, D. H. Slichter, I. Siddiqi, *Phys. Rev. Lett.* **106**, 110502 (2011).
6. M. Hatridge *et al.*, *Science* **339**, 178–181 (2013).
7. A. A. Houck *et al.*, *Nature* **449**, 328–331 (2007).
8. C. Eichler *et al.*, *Phys. Rev. Lett.* **109**, 240501 (2012).
9. P. J. Leek *et al.*, *Phys. Rev. Lett.* **104**, 100504 (2010).
10. M. Mariantoni *et al.*, *Nat. Phys.* **7**, 287–293 (2011).
11. D. Gottesman, A. Kitaev, J. Preskill, *Phys. Rev. A* **64**, 012310 (2001).
12. Z. Leghtas *et al.*, *Phys. Rev. Lett.* **111**, 120501 (2013).
13. M. Hofheinz *et al.*, *Nature* **459**, 546–549 (2009).
14. B. R. Johnson *et al.*, *Nat. Phys.* **6**, 663–667 (2010).
15. M. Brune *et al.*, *Phys. Rev. Lett.* **77**, 4887–4890 (1996).
16. G. Kirchmair *et al.*, *Nature* **495**, 205–209 (2013).
17. L. Lutterbach, L. Davidovich, *Phys. Rev. Lett.* **78**, 2547–2550 (1997).
18. Z. Leghtas *et al.*, *Phys. Rev. A* **87**, 042315 (2013).
19. W. H. Zurek, *Nature* **412**, 712–717 (2001).
20. C. M. Caves, A. Shaji, *Opt. Commun.* **283**, 695–712 (2010).
21. S. Deléglise *et al.*, *Nature* **455**, 510–514 (2008).
22. A. Ourjoumtsev, H. Jeong, R. Tualle-Brouiri, P. Grangier, *Nature* **448**, 784–786 (2007).
23. P. Bertet *et al.*, *Phys. Rev. Lett.* **89**, 200402 (2002).
24. See accompanying supplementary materials for details.
25. M. Boissonneault, J. M. Gambetta, A. Blais, *Phys. Rev. A* **79**, 013819 (2009).
26. H. Paik *et al.*, *Phys. Rev. Lett.* **107**, 240501 (2011).
27. C. Monroe, D. M. Meekhof, B. E. King, D. J. Wineland, *Science* **272**, 1131–1136 (1996).
28. D. I. Schuster *et al.*, *Nature* **445**, 515–518 (2007).
29. S. Haroche, J. M. Raimond, *Exploring the Quantum: Atoms, Cavities, and Photons* (Oxford Univ. Press, Oxford, 2006).
30. S. L. Braunstein, P. van Loock, *Rev. Mod. Phys.* **77**, 513–577 (2005).
31. S. E. Nigg, S. M. Girvin, *Phys. Rev. Lett.* **110**, 243604 (2013).
32. H. Jeong, T. Ralph, *Phys. Rev. A* **76**, 042103 (2007).

Acknowledgments: We thank M. D. Reed, M. Hatridge, and T. L. Brecht for discussions. This research was supported by NSF (grant PHY-0969725), the Office of the Director of National Intelligence (ODNI), the Intelligence Advanced Research Projects Activity (IARPA) through the Army Research Office (W911NF-09-1-0369), and the U.S. Army Research Office (W911NF-09-1-0514). Facilities use was supported by the Yale Institute for Nanoscience and Quantum Engineering (YINQE) and NSF (MRSEC DMR 1119826). S.M.G. and Z.L. acknowledge support from NSF (DMR-1004406). M.M. and Z.L. acknowledge support from French Agence Nationale de la Recherche under the project EPOQ2 (ANR-09-JCJC-0070).

Supplementary Materials

www.sciencemag.org/content/342/6158/607/suppl/DC1
Materials and Methods
Supplementary Text
Figs. S1 to S10
Tables S1 and S2
References (33–37)

16 July 2013; accepted 18 September 2013
Published online 26 September 2013;
10.1126/science.1243289

Real-Space Identification of Intermolecular Bonding with Atomic Force Microscopy

Jun Zhang,^{1*} Pengcheng Chen,^{1*} Bingkai Yuan,¹ Wei Ji,^{2†} Zhihai Cheng,^{1†} Xiaohui Qiu^{1†}

We report a real-space visualization of the formation of hydrogen bonding in 8-hydroxyquinoline (8-hq) molecular assemblies on a Cu(111) substrate, using noncontact atomic force microscopy (NC-AFM). The atomically resolved molecular structures enable a precise determination of the characteristics of hydrogen bonding networks, including the bonding sites, orientations, and lengths. The observation of bond contrast was interpreted by *ab initio* density functional calculations, which indicated the electron density contribution from the hybridized electronic state of the hydrogen bond. Intermolecular coordination between the dehydrogenated 8-hq and Cu adatoms was also revealed by the submolecular resolution AFM characterization. The direct identification of local bonding configurations by NC-AFM would facilitate detailed investigations of intermolecular interactions in complex molecules with multiple active sites.

Intermolecular bonding has been experimentally characterized mainly through crystallography via x-ray and electron diffractions, as well as through infrared, Raman, nuclear magnetic resonance, and near-edge extended absorption fine-structure spectroscopy (1, 2). At the single-molecule level, state-of-the-art scanning tunneling microscopy (STM) is a technique widely used to elucidate the molecular structure and chemical specificity of surface-immobilized species (3–5). The bonding interactions between molecules in self-assemblies were also evidenced in scanning tunneling hydrogen microscopy (6). Nevertheless, most of the characterization techniques are, thus far, more sensitive to the covalent structures of the molecules, and in many cases, theoretical calculations of intermolecular interaction are also not as precise as those for covalently bound species.

Recently, noncontact atomic force microscopy (NC-AFM) has achieved superior resolution in real-space that has enabled the identification of the chemical structure, adsorption configurations, and chemical transformation of individual molecules (7–10). For example, the difference in bond order in aromatic molecules was distinguished via electron-density-dependent Pauli repulsion with CO-functionalized NC-AFM tips (11), and AFM tomography revealed the angular symmetry of a chemical bond on surface (12). Herein, we used NC-AFM to investigate the intermolecular interactions in 8-hydroxyquinoline (8-hq) (Fig. 1A) molecular assemblies formed on Cu(111) at liquid helium (LHe) and room temperatures (RTs). The hydrogen bonds (H bonds) formed between 8-hq molecules were characterized by

high-resolution AFM images, and the local bonding configuration was determined with the atomic precision. We also observe the coordination complex composed of dehydrogenated 8-hq and Cu adatoms. The observations were validated with *ab initio* density functional theory (DFT) calculations.

The 8-hq molecules deposited on Cu(111) at LHe temperature appeared as individual molecules or randomly assembled aggregates (fig. S1) (13). For the single 8-hq molecules, DFT calculations suggest that the molecular plane is slightly tilted with respect to the substrate because of the weak interactions between the OH group and the N atom of 8-hq and Cu(111) surface. Compared with the calculated total electron density of the molecule shown in Fig. 1B, the STM

image (Fig. 1C) exhibits no internal features of the heterocycle because the tunneling current is primarily sensitive to the local density of states near the Fermi level. In contrast, the AFM images with a CO-functionalized tip revealed the submolecular structure of 8-hq through the short-range Pauli repulsive force (Fig. 1, D to F). The calculated electron density map (Fig. 1B) qualitatively reproduces the observed contrast in frequency shift (Δf) in the AFM image. Here, the AFM sensor measured the total force of three components (7, 14): (i) the long-range attractive electrostatic forces, responsible for the overall negative Δf background in the images; (ii) the attractive van der Waals force, which contributed to the dark halo surrounding the molecule without atomic corrugation; and (iii) the short-range Pauli repulsion, which contributed to the atomic contrast of molecular structure with respect to the metal substrate. When the tip height was decreased (Fig. 1, D to F), the increasing proportion of Pauli repulsion in the total force enhanced contrast in the AFM images. Although a quantitative understanding of the AFM imaging mechanism is nontrivial, a direct correlation between the AFM images and the chemical structure of a molecule can still be rationalized. In our case, the heterocyclic skeleton and the hydroxyl group of 8-hq were readily distinguished. The pyridine ring in the heterocycle is slightly pronounced, which may be caused by tilting of the molecular plane on the substrate. A further interpretation of the topography need also take into account the difference in electron density of the phenol ring and the pyridine ring.

The AFM images of the 8-hq molecular aggregates (Fig. 2, A and B) reveal bonding-like

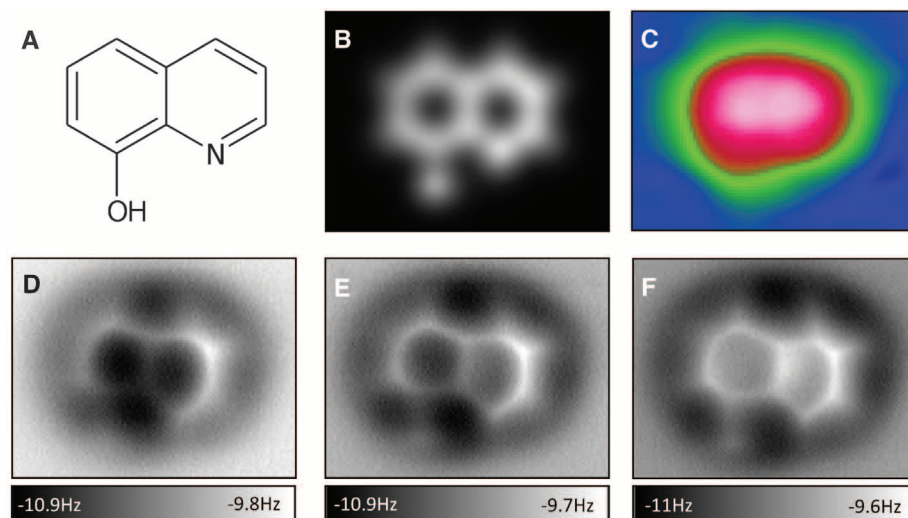


Fig. 1. STM and AFM measurements and DFT calculations of single 8-hq on Cu(111). (A) Chemical structure of 8-hq. (B) DFT-calculated molecular electron density maps at a distance of 150 pm above the molecule. (C) Constant-current STM topography image (voltage $V = -100$ mV, current $I = 100$ pA) with a CO-functionalized tip. (D to F) Constant-height AFM frequency shift images ($V = 0$ V, amplitude $A = 100$ pm) at different tip heights. The tip height Δz was set with respect to a reference height given by the STM set point above (~ 100 mV, 100 pA) the bare Cu(111) substrate in the vicinity of the molecule. The plus (or minus) sign denotes the increase (or decrease) of tip height. (D) $\Delta z = +30$ pm; (E) $\Delta z = +10$ pm; (F) $\Delta z = 0$ pm. The size of all images is 1.3 by 1.0 nm.

¹Key Laboratory of Standardization and Measurement for Nanotechnology, Chinese Academy of Sciences, National Center for Nanoscience and Technology, Beijing 100190, China. ²Department of Physics, Renmin University of China, Beijing 100872, China.

*These authors contributed equally to this work.

†Corresponding author. E-mail: xhqi@nanoctr.cn (X.Q.); chengzh@nanoctr.cn (Z.C.); wji@ruc.edu.cn (W.J.)

features between adjacent molecules in the assemblies that were reproduced in all of the observations, whereas these features were not observed in the corresponding STM images at the same regions [see fig. S3 and (13)]. A close examination of the position and orientation of the bonding-like structures indicated that they coincide very well with the expected locations of H bonds formed between 8-hq molecules (Fig. 2, C and D). The results from recent theoretical and experimental investigations suggest that the H bond has both an electrostatic origin and a partly covalent character (15, 16). Despite extensive studies of H bonding in supramolecular and biological systems using various techniques, direct identification of the bonding configuration of the H bond in real-space is elusive (17).

The formation of covalent bonds in unimolecular reactions has recently been reported (10). The bond contrast in the AFM images has been qualitatively compared with the bond order, where the higher local electron density leads to stronger Pauli repulsion exerted on the tip (10, 11). In our observations, the Δf contrast of these intermolecular bonds is comparable to that of intramolecular covalent bonds in the constant-height images, as also evident in the force spectroscopy measurements (fig. S4) (13). Given the clearly identified bonding sites, we could perform a detailed analysis of the H bond configurations (18). The apparent bond lengths of the intermolecular H bonds were measured, as summarized in fig. S5 (13), and can be used as a reference for data acquired through other characterization methods to understand the effect of the substrate on H bonding (19).

Our study also revealed differences in the H bond configurations in the 8-hq self-assemblies on surface and those in the bulk crystal. In addition to the conventional H bond, which involves only the OH group and N atom of 8-hq, we also observed H bond formation between the aromatic rings and the OH group or N atom. These results provide direct evidence for the influence of substrate on the intermolecular bonding characteristics (1, 20).

We performed DFT calculations on two types of molecular clusters to further understand the origin of the contrast of intermolecular H bonds in our observation. In Fig. 3A, the paired 8-hq molecules were bonded by two H bonds of O-H \cdots N, as illustrated by the black dotted lines in Fig. 3B (21). The calculated total electron density plotted in Fig. 3C shows a bright spot at the position of the O atom and a protrusion toward the adjacent molecule around the position of the N atom. The in-plane plot of the differential charge density (Fig. 3D), which is defined as $\rho_{\text{DCD}} = \rho_{\text{Total}} - \rho_{\text{Substrate}} - \sum \rho_{\text{Molecule}}$ (where ρ_{Total} is the electron density of 8-hq adsorbed on the Cu substrate, $\rho_{\text{Substrate}}$ is the electron density of the Cu substrate, and ρ_{Molecule} is the electron density of 8-hq), reflects the charge redistribution after the bond forms between two 8-hq molecules and indicates that covalent-like characteristics developed from

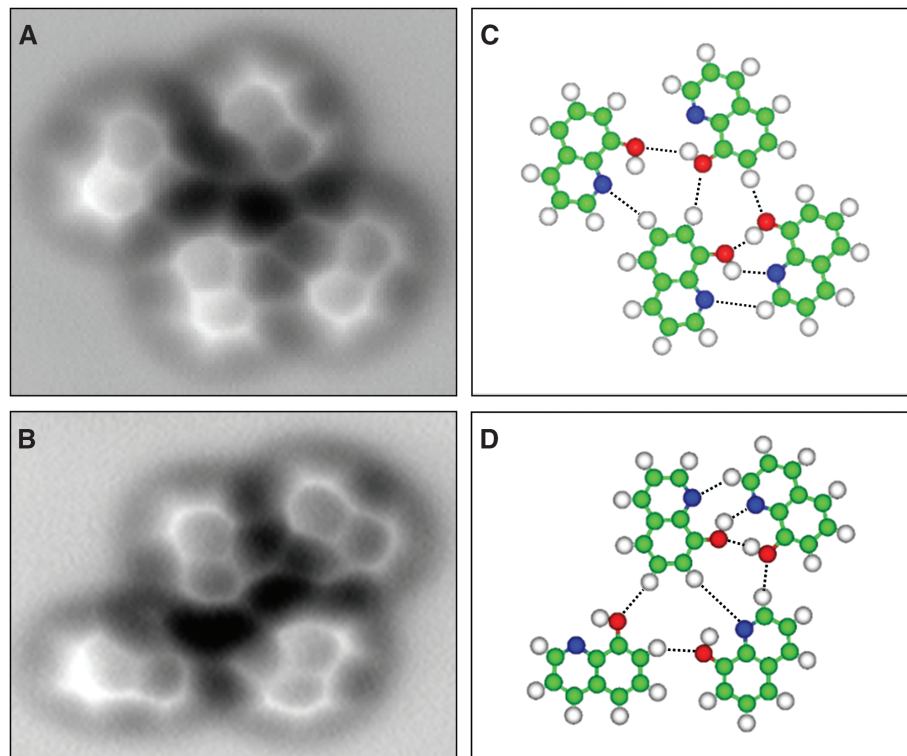


Fig. 2. AFM measurements of 8-hq assembled clusters on Cu(111). (A and B) Constant-height frequency shift images of typical molecule-assembled clusters and their corresponding structure models (C and D). Imaging parameters: $V = 0$ V, $A = 100$ pm, $\Delta z = +10$ pm. Image size: (A) 2.3 by 2.0 nm; (B) 2.5 by 1.8 nm. The dashed lines in (C) and (D) indicate likely H bonds between 8-hq molecules. Green, carbon; blue, nitrogen; red, oxygen; white, hydrogen.

charge reductions near the H and N atoms that led to charge accumulation between them. As expected, the enhanced charge density at N and O is consistent with the charge transfer from H to N and O atoms, whereas the charge accumulation offers an additional repulsive force to the tip at the region along the H bonding direction. Thus, the observed line feature between the two 8-hq molecules in the AFM image is attributed to a joint effect that results from both the covalent charge in H \cdots N and the charge transferred from H to N and O. The above interpretation is primarily based on the simplified mechanism of tip-to-sample Pauli repulsion (22). A quantitative understanding of the image contrast of an H bond may require further consideration of the relaxation of the CO molecule attached on the tip apex (11). In another configuration (Fig. 3, E to H), DFT calculations also concluded electron density redistribution in the proximity of the newly formed bond. In this unconventional C-H \cdots N hydrogen bond, the effect of charge accumulation between N and H atoms is much weaker compared with that in the O-H \cdots N hydrogen bond (1, 15).

When 8-hq was deposited onto Cu(111) at RT, the molecules formed highly ordered dimers and trimers, which are distinct from the H-bonded aggregates formed at the LHe temperature. No internal structures of these dimers and trimers could be resolved in the high-resolution STM images (fig. S8). The size of these molecular

aggregates did not correspond to those of the H-bonded clusters from DFT calculations. The AFM images of the dimers and trimers (Fig. 4, A and B) allowed the identification of the outer edge of the molecules corresponding to the positions of H or C atoms, but the inner edge was blurred.

The dehydrogenation of the hydroxyl group on Cu(111) at RT has been widely reported (23). Our experimental and theoretical calculation results also suggest that the individual 8-hq molecules exist as radical species that are weakly bound to the substrate by O and N atoms in a tilted orientation (fig. S7). Alternatively, the highly mobile 8-hq radicals coordinate with Cu adatoms on surface to form an organometallic complex (24). The proposed chemical structures of a dimer and trimer, respectively, in which the dehydrogenated 8-hq is assembled via an O(N)-Cu bond, are shown in Fig. 4, C and D. The calculated geometric sizes of these 8-hq complexes agree well with the AFM observations.

When the AFM is operated in the Pauli repulsion regime, the repulsive force from the outermost-shell valence electrons is also relevant to $\nabla^2 \varphi_n(r)$, which is in the form of kinetic energy. Here, $\varphi_n(r)$ is the electron wave function of the n th eigenstate of the sample. The kinetic energy reflects the localization property of electrons, which can be estimated by the electron localization function (ELF) (25). The ELF of the dimer

Fig. 3. AFM measurements and DFT calculations of 8-hq dimers on Cu(111). Constant-height frequency shift image of the O-H...N dimer (A) and the N...H-Ph dimer (Ph, phenyl) (E) and their corresponding DFT-calculated structure models (B and F), electron density maps (C and G), and charge difference maps (D and H). Imaging parameters: $V = 0$ V, $A = 100$ pm, $\Delta z = +50$ pm (A), $\Delta z = +10$ pm (E). Image size: (A) 1.6 by 1.6 nm; (E) 1.5 by 2.0 nm. The dashed frames in (B) and (F) indicate the calculation regions in (D) and (H).

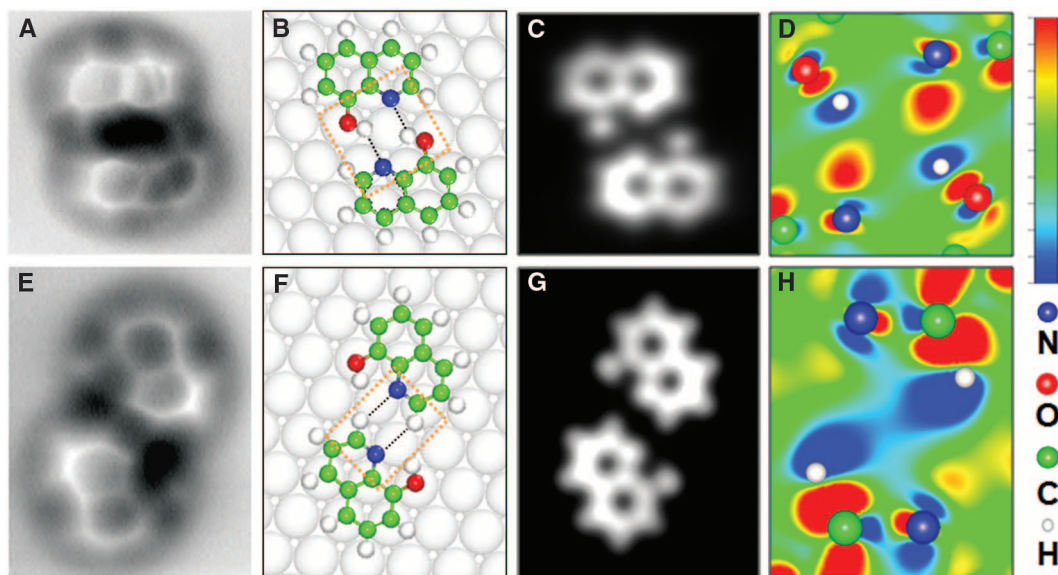
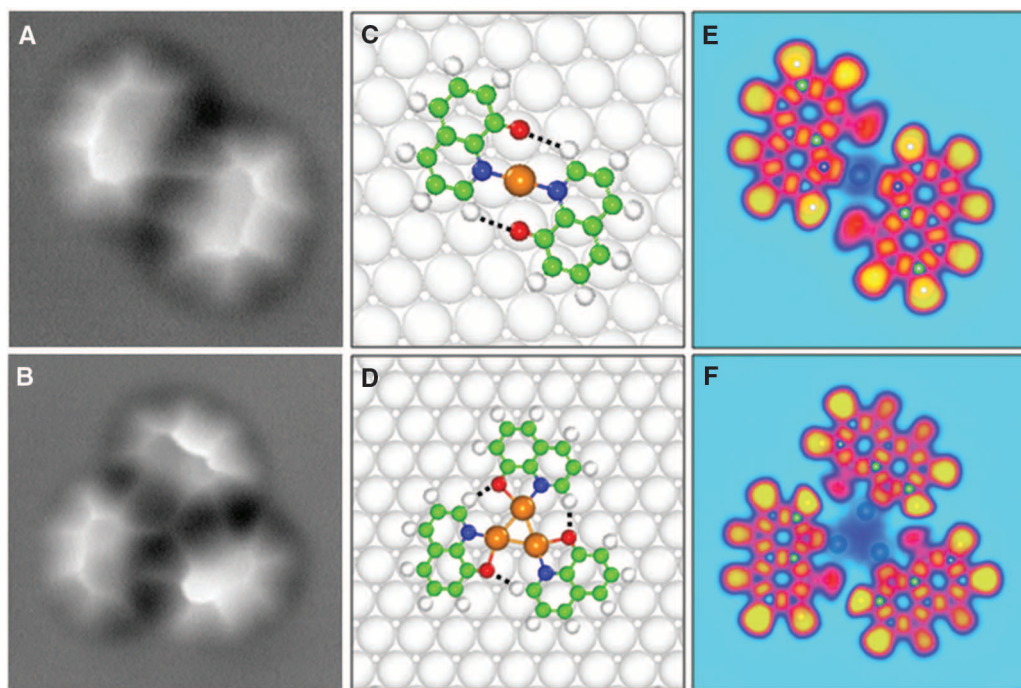


Fig. 4. AFM measurements and DFT calculations of coordination complexes (dehydrogenated 8-hq and copper adatoms) on Cu(111). Constant-height AFM frequency shift images (A and B), the corresponding DFT-calculated structure models (C and D), and electron localization function maps (E and F) of dimer (Cu_2q_2) and trimer (Cu_3q_3) complexes (q, dehydrogenated 8-hq). Imaging parameters: (A) $V = 0$ V, $A = 100$ pm, $\Delta z = +100$ pm, 2.0 by 2.0 nm; (B) $V = 0$ V, $A = 100$ pm, $\Delta z = +80$ pm, 2.4 by 2.4 nm. The tip height Δz was set with respect to a reference height given by the STM set point (-30 mV, 100 pA) above the bare Cu(111) substrate. The dashed lines in (C) and (D) refer to the H bonds formed in the complexes. The complexes were formed by depositing 8-hq on Cu(111) at RT. Orange spheres represent Cu adatoms.



and trimer exhibited strongly localized electron density donation from N to Cu, whereas the electrons between the Cu-Cu bonding are rather delocalized (Fig. 4, E and F). We attributed the bonding features in the central regions of the dimer and trimer to N-Cu coordination bonding, similar to the observed formation of the metal-organic coordinate bond excited by inelastic electrons (9, 26). According to the ELF, the O-Cu bond is strongly polarized, and the most shared electrons of the bond are localized around O; thus, the AFM signal is negligible. The C-H...O hydrogen bonds formed in the dimer and trimer were detectable in AFM because of the localized electrons around O and H.

Structural details—including the molecular conformation, the bond configuration, and the interacting sites on the functional groups—acquired from high-resolution noncontact AFM images provided useful insights into the mechanisms of molecular assembly and recognition. Because the H bond is ubiquitous in nature and central to biological functions, the present technique may provide an important and complementary characterization method for unraveling the fundamental aspects of molecular interactions at the single-molecule level. The observation of H bonding in real-space may also stimulate theoretical discussion about the nature of this intermolecular interaction.

References and Notes

1. K. Müller-Dethlefs, P. Hobza, *Chem. Rev.* **100**, 143–168 (2000).
2. C. A. Hunter, *Angew. Chem. Int. Ed.* **43**, 5310–5324 (2004).
3. H. J. Lee, W. Ho, *Science* **286**, 1719–1722 (1999).
4. R. Temirov, S. Soubatch, A. Luican, F. S. Tautz, *Nature* **444**, 350–353 (2006).
5. P. Liljeroth, J. Repp, G. Meyer, *Science* **317**, 1203–1206 (2007).
6. C. Weiss, C. Wagner, R. Temirov, F. S. Tautz, *J. Am. Chem. Soc.* **132**, 11864–11865 (2010).
7. L. Gross, F. Mohn, N. Moll, P. Liljeroth, G. Meyer, *Science* **325**, 1110–1114 (2009).
8. L. Gross *et al.*, *Nat. Chem.* **2**, 821–825 (2010).
9. F. Albrecht, M. Neu, C. Quest, I. Swart, J. Repp, *J. Am. Chem. Soc.* **135**, 9200–9203 (2013).
10. D. G. de Oteyza *et al.*, *Science* **340**, 1434–1437 (2013).
11. L. Gross *et al.*, *Science* **337**, 1326–1329 (2012).

12. J. Welker, F. J. Giessibl, *Science* **336**, 444–449 (2012).
13. Supplementary materials are available on *Science* Online.
14. L. Gross, *Nat. Chem.* **3**, 273–278 (2011).
15. T. Steiner, *Angew. Chem. Int. Ed.* **41**, 48–76 (2002).
16. G. R. Desiraju, *Angew. Chem.* **123**, 52–60 (2011).
17. The observation of an intramolecular hydrogen bond was tentatively proposed by Gross *et al.* in the study of the organic compound cephalandole A (8).
18. The measured bond length may involve the amplification effect of CO on the tip apex, as discussed in (11). It should also be noted that the expected bending of $X-H \cdots Y$ was not resolved in all of the hydrogen bonds shown in Fig. 2, A and B. The exact mechanism was not understood.
19. G. Jones, S. J. Jenkins, D. A. King, *Surf. Sci.* **600**, 224–228 (2006).
20. J. Carrasco, A. Hodgson, A. Michaelides, *Nat. Mater.* **11**, 667–674 (2012).
21. We found that it is difficult to obtain a high-resolution AFM image on this specific type of 8-hq dimer compared with single molecules or other molecular aggregates.

- These dimers often accidentally dislocate during AFM imaging, indicating a weaker interactions between the molecules and the substrate. We suggested that the formation of two hydrogen bonds in the dimer weaken the binding interaction of -OH and N of 8-hq to the metal substrate. Note that the optimal imaging parameters for this dimer (see the Fig. 3A legend) are different from those used for other molecular clusters.
22. We conducted a further calculation (13) following the method proposed in (27).
 23. X. C. Guo, R. J. Madix, *Surf. Sci.* **341**, L1065–L1071 (1995).
 24. J. V. Barth, G. Costantini, K. Kern, *Nature* **437**, 671–679 (2005).
 25. B. Silvi, A. Savin, *Nature* **371**, 683–686 (1994).
 26. F. Mohn *et al.*, *Phys. Rev. Lett.* **105**, 266102 (2010).
 27. N. Moll, L. Gross, F. Mohn, A. Curioni, G. Meyer, *New J. Phys.* **14**, 083023 (2012).

Acknowledgments: This project is partially supported by the Ministry of Science and Technology of China (grants 2012CB933001 and 2012CB932704), the Natural Science

Foundation of China (grants 21173058, 21203038, 11274308, and 11004244), the Beijing Natural Science Foundation (grant 2112019), and the Basic Research Funds in Renmin University of China from the Central Government (grant no. 12XNLJ03). W.J. was supported by the Program for New Century Excellent Talents in Universities. Calculations were performed at the Physics Lab for High-Performance Computing of Renmin University of China and Shanghai Supercomputer Center. We thank W. Ho, P. Grutter, and L. Gross for valuable discussion and technical advice.

Supplementary Materials

www.sciencemag.org/content/342/6158/611/suppl/DC1
Materials and Methods
Figs. S1 to S9
References (28–32)

1 July 2013; accepted 9 September 2013
Published online 26 September 2013;
10.1126/science.1242603

One-Dimensional Electrical Contact to a Two-Dimensional Material

L. Wang,^{1,2*} I. Meric,^{1*} P. Y. Huang,³ Q. Gao,⁴ Y. Gao,² H. Tran,⁵ T. Taniguchi,⁶ K. Watanabe,⁶ L. M. Campos,⁵ D. A. Muller,³ J. Guo,⁴ P. Kim,⁷ J. Hone,⁷ K. L. Shepard,^{1†} C. R. Dean^{1,2,8†}

Heterostructures based on layering of two-dimensional (2D) materials such as graphene and hexagonal boron nitride represent a new class of electronic devices. Realizing this potential, however, depends critically on the ability to make high-quality electrical contact. Here, we report a contact geometry in which we metalize only the 1D edge of a 2D graphene layer. In addition to outperforming conventional surface contacts, the edge-contact geometry allows a complete separation of the layer assembly and contact metallization processes. In graphene heterostructures, this enables high electronic performance, including low-temperature ballistic transport over distances longer than 15 micrometers, and room-temperature mobility comparable to the theoretical phonon-scattering limit. The edge-contact geometry provides new design possibilities for multilayered structures of complimentary 2D materials.

Atomically thin two-dimensional (2D) materials (1, 2)—such as graphene, hexagonal boron nitride (BN), and the transition metal dichalcogenides (TMDCs)—offer a variety of outstanding properties for fundamental studies and applications. More recently, the capability to assemble multiple 2D materials with complementary properties into layered heterogeneous structures presents an exciting new opportunity in materials design (2–11), but several fundamental challenges remain, including making good electrical contact to the encapsulated 2D layers. Electrically interfacing 3D metal electrodes to 2D

materials is inherently problematic. For graphene devices, the customary approach is to metalize the 2D surface. However, graphene lacks surface bonding sites, so the lack of chemical bonding and strong orbital hybridization leads to large contact resistance (12–19). In multilayer structures, the requirement to expose the surface for metallization presents additional restrictive demands on the fabrication process. For example, encapsulated BN/graphene/BN heterostructures (BN-G-BN) need to be assembled sequentially so as to leave the graphene surface accessible during metallization, because no process to selectively remove the BN layers has been identified. Moreover, polymers used during both the layer assembly and lithography steps are difficult to remove (20). Their presence can degrade the electrical contact (21, 22) and channel mobility (23) and contaminate the layer interfaces, causing bubbles and wrinkles that multiply with the addition of each successive layer, limiting typical device size to $\sim 1 \mu\text{m}$ (2, 4, 24).

We demonstrate a new device topology where 3D metal electrodes are connected to a 2D graphene layer along the 1D graphene edge (14, 19, 25–27). We first encapsulate the graphene

layer in BN. The entire multilevel stack is then etched to expose only the edge of the graphene layer, which is in turn metalized. This contact geometry is similar to that in conventional semiconductor field-effect transistors (FETs), where doped 3D bulk regions make lateral contact to a 2D electron gas. Although carrier injection is limited only to the 1D atomic edge of the graphene sheet, the contact resistance is remarkably low (as low as 100 ohm- μm in some devices). The edge-contact process also allows a complete separation of the layer assembly and contact metallization processes, which permits implementation of a polymer-free layer assembly method. Combining these two techniques, we fabricated graphene devices with unprecedented performance exhibiting room-temperature mobility up to 140,000 cm^2/Vs and sheet resistivity below 40 ohms per square at $n > 4 \times 10^{12} \text{ cm}^{-2}$, comparable to the theoretical limit imposed by acoustic phonon scattering. At temperatures below 40 K, we observed ballistic transport over length scales longer than 15 μm .

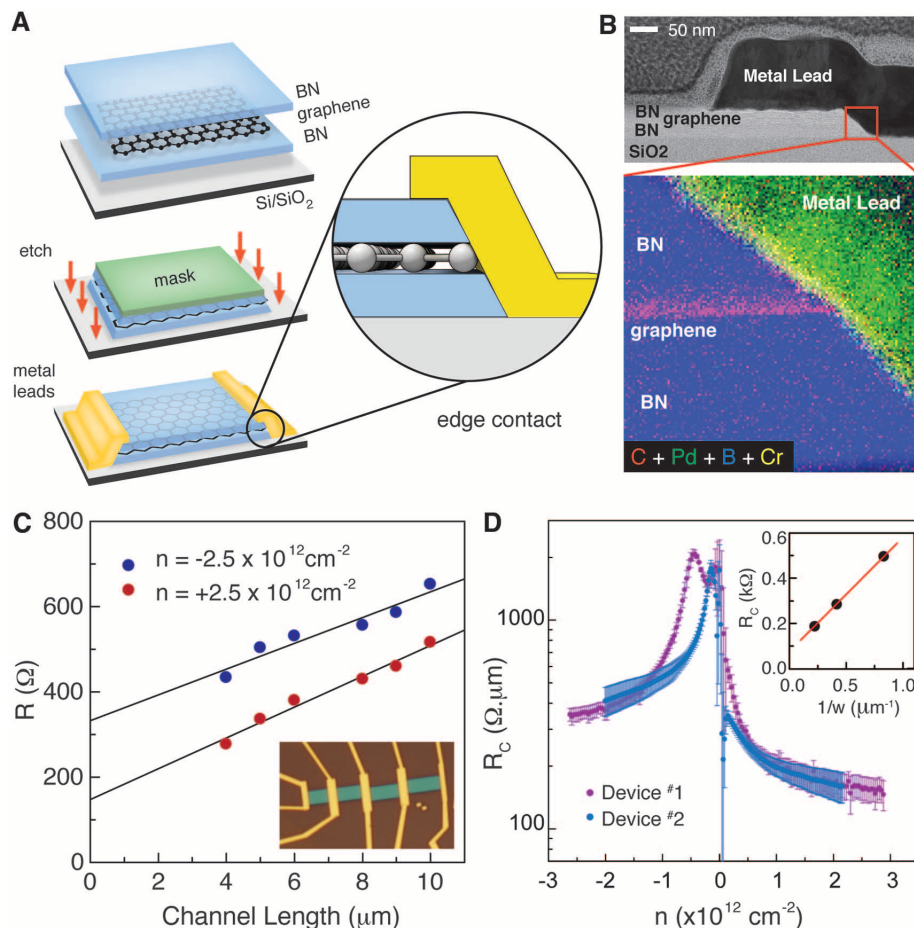
The edge-contact fabrication process is illustrated in Fig. 1A. Beginning with a BN-G-BN heterostructure, a hard mask is defined on the top BN surface by electron-beam lithography (EBL) of a hydrogen-silsesquioxane (HSQ) resist. The regions of the heterostructure outside of the mask are then plasma-etched (see supplementary materials section 1.2) to expose the graphene edge. Finally, metal leads (1 nm Cr/15 nm Pd/60 nm Au) are deposited by electron beam evaporation to make electrical contact along this edge (other metal combinations showed inferior performance) (table S1). In Fig. 1B, a cross section scanning transmission electron microscope (STEM) image of a representative device shows the resulting geometry of the edge-contact. In the magnified region, electron energy-loss spectroscopy (EELS) mapping confirms that the graphene and metal overlap at a well-defined interface. From the angle of the etch profile ($\sim 45^\circ$), we expect that the graphene terrace is exposed only 1 to 2 atoms deep. Within the resolution of the STEM image, there is no evidence of metal diffusion into the graphene/BN interface, confirming the truly edge

¹Department of Electrical Engineering, Columbia University, New York, NY 10027, USA. ²Department of Mechanical Engineering, Columbia University, New York, NY 10027, USA. ³School of Applied and Engineering Physics, Cornell University, Ithaca, NY 14853, USA. ⁴Department of Electrical and Computer Engineering, University of Florida, Gainesville, FL 32611, USA. ⁵Department of Chemistry, Columbia University, New York, NY 10027, USA. ⁶National Institute for Materials Science, 1-1 Namiki, Tsukuba 305-0044, Japan. ⁷Department of Physics, Columbia University, New York, NY 10027, USA. ⁸Department of Physics, The City College of New York, New York, NY 10031, USA.

*These authors contributed equally to this work.

†Corresponding author. E-mail: cdean@ccny.cuny.edu (C.R.D.); shepard@ee.columbia.edu (K.L.S.)

Fig. 1. Edge-contact. (A) Schematic of the edge-contact fabrication process. (B) High-resolution bright-field STEM image showing details of the edge-contact geometry. The expanded region shows a magnified false-color EELS map (fig. S6) of the interface between the graphene edge and metal lead. (C) Two-terminal resistance versus channel length at fixed density, measured from a single graphene device in the TLM geometry. Solid line is a linear fit to the data. Inset shows an optical image of a TLM device with edge-contacts. (D) Contact resistance calculated from the linear fit at multiple carrier densities for two separate devices. Error bars represent uncertainty in the fitting. Inset shows resistance scaling with contact width measured from a separate device.



nature of the contact. The EELS map additionally indicates that contact was made predominantly to the Cr adhesion layer.

To characterize the quality of the edge-contact, we used the transfer-length method (TLM). Multiple two-terminal graphene devices consisting of a uniform 2- μm channel width but with varying channel lengths were fabricated, and their resistances were measured as a function of carrier density n induced by a voltage applied to a silicon back gate. Figure 1C shows the resistance versus channel length, measured at two different carrier densities. In the diffusive regime, where the channel length remains several times longer than the mean free path, the total resistance in a two-terminal measurement can be written as $R = 2R_C(W) + \rho L/W$, where R_C is the contact resistance, L is the device length, W is the device width, and ρ is the 2D channel resistivity; R_C and ρ were extracted as the intercept and slope of a linear fit to the data shown here for two separate devices (Fig. 1D). R_C was remarkably low, reaching $\sim 150 \text{ ohm}\cdot\mu\text{m}$ for n-type carriers at high density. This value is $\sim 25\%$ lower than the best reported surface contacts without additional engineering such as chemical (18) or electrostatic (17) doping.

Because this value is obtained in a two-terminal geometry, it includes the intrinsic limit set by the quantum resistance of the channel, which can be subtracted to yield an extrinsic contact resistance

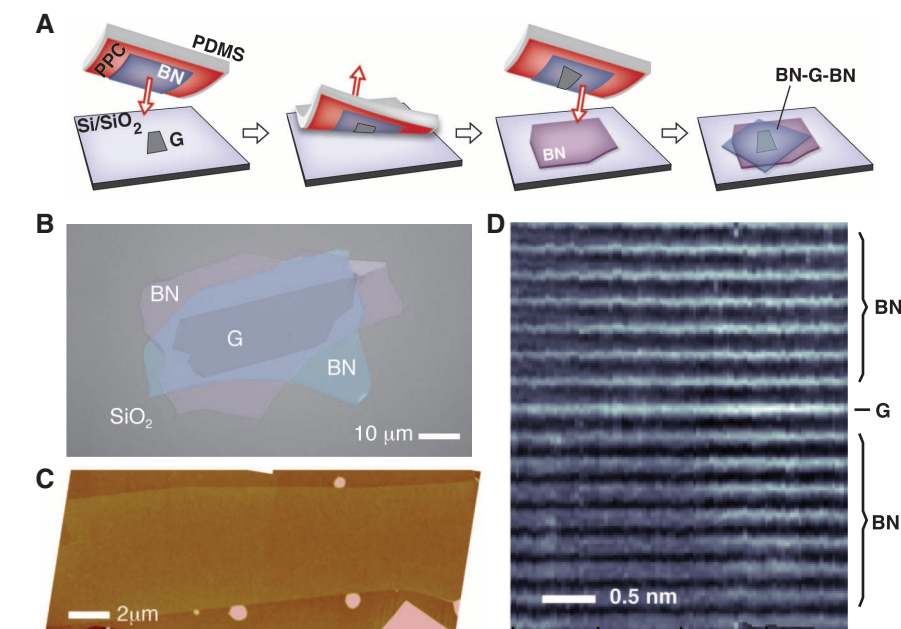


Fig. 2. Polymer-free layer assembly. (A) Schematic of the van der Waals technique for polymer-free assembly of layered materials. (B) Optical image of a multilayered heterostructure using the process illustrated in (A). (C) AFM image of a large-area encapsulated graphene layer showing that it is pristine and completely free of wrinkles or bubbles except at its boundary. (D) High-resolution cross-section ADF-STEM image of the device in (C). The BN-G-BN interface is found to be pristine and free of any impurities down to the atomic scale.

nearly 100 ohm- μm (fig. S4). In both devices, the contact resistance is asymmetric, being lower by a factor of 2 to 3 when the device is gated to be n-type versus p-type. This asymmetry is consistent with electrical contact being made primarily to the Cr adhesion layer, as suggested by the cross-section EELS map (Fig. 1B), because the Cr work function is ~ 0.16 eV lower than that of graphene (12). The contact resistance scales inversely with the contact width (inset in Fig. 1D), as expected for the edge-contact geometry. Finally, we find that the contact resistance is largely independent of temperature (fig. S9), in contrast with the linear temperature scaling that has been reported for surface contacts (15).

To better understand why edge-contacts can lead to low contact resistance, we investigated the structure and behavior of the interface using a first-principle atomistic model. Ab initio simulation assuming a Cr metal electrode indicates that edge-contacts lead to shorter bonding distance with larger orbital overlap than surface contacts,

consistent with previous calculations for other common metals in the same contact geometry (25). We also used density functional theory (DFT) combined with the nonequilibrium Green's function (NEGF) to calculate the transmission efficiency of the contact. Incorporation of some additional interfacial species, such as oxygen, which might result from the etch process, can actually help to improve bonding and increase the transmission. Results from the simulation (supplementary materials section 2.5) are in good agreement with the experimental data, predicting a contact resistance as low as 118 ohm- μm at $E - E_{\text{CNP}} = 0.16$ eV ($n = 2.2 \times 10^{12} \text{ cm}^{-2}$) for a Cr(110)-O-graphene interface, where $E - E_{\text{CNP}}$ represents the fermi energy of graphene relative to the energy corresponding to the charge neutrality point. In both our data and the model, the contact resistance diverged near the charge neutrality point, which could be expected given a decrease of density of states in the 2D graphene layer. Experimentally, we observed an additional local peak

in the contact resistance at finite negative density. We have observed that exposure of the graphene edge to a weak O_2 plasma immediately before metallization can cause this satellite peak position to vary (fig. S10), indicating that the origin of the second peak may relate to the specific chemistry of the edge termination.

The edge-contact geometry described here enables a new fabrication process that allows us to construct encapsulated BN-G-BN heterostructures before introduction of metal contacts. In this technique, strong van der Waals (vdW) interaction between 2D materials was used to assemble the layered structure directly. Figure 2A shows a schematic of the process where an isolated few-layer BN flake is used as a stamp to successively pick up alternating layers of monolayer graphene and few-layer BN (a detailed description of the vdW assembly process can be found in supplementary materials section 1.1). A critical feature of this technique compared with previous methods to mechanically layer 2D materials is that the active

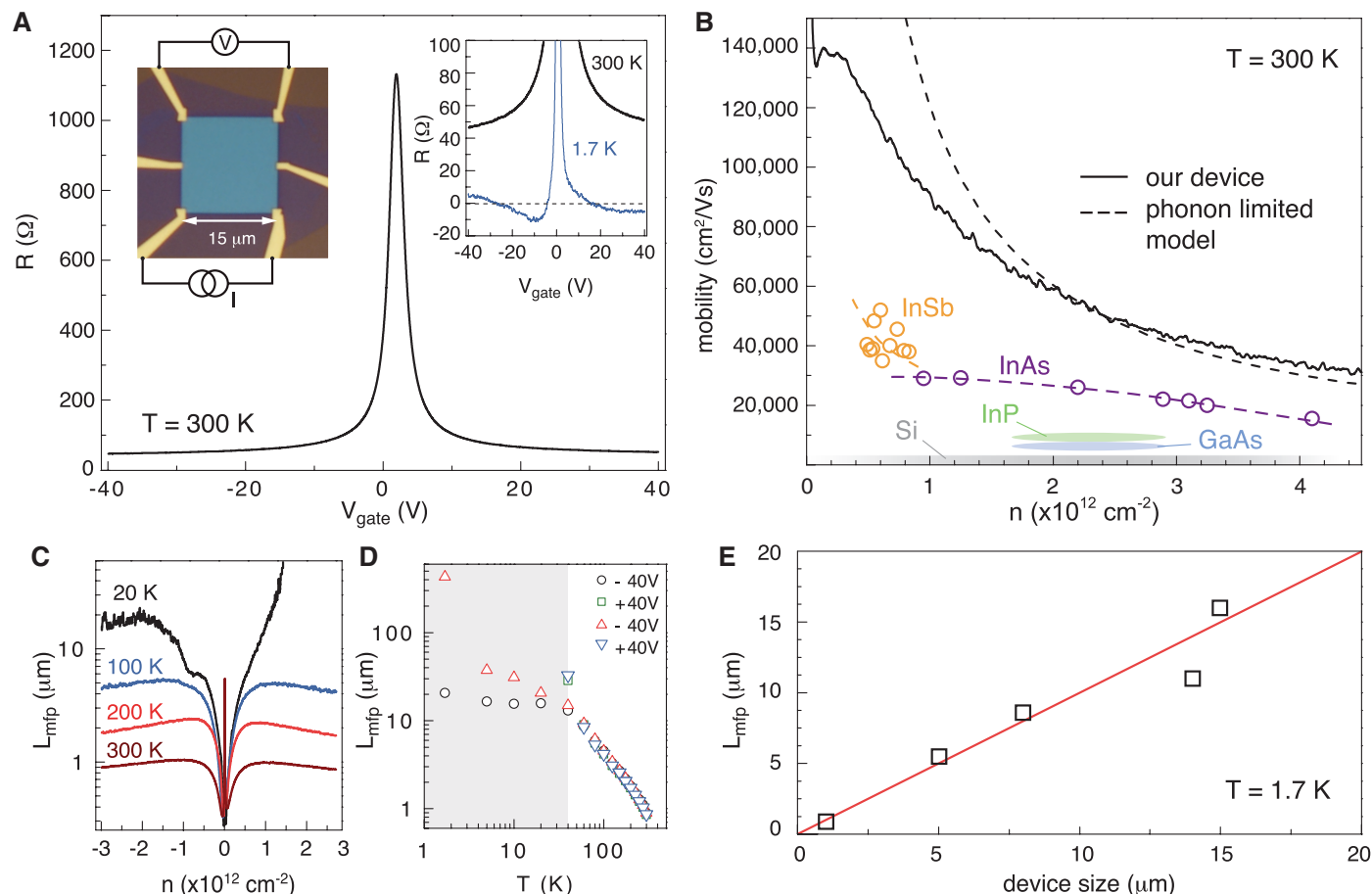


Fig. 3. Large-area, high-performance, BN-G-BN devices. (A) Four-terminal resistivity measured from a $15 \mu\text{m} \times 15 \mu\text{m}$ device fabricated by the van der Waals assembly technique with edge-contacts. The left inset shows an optical image of the device. Low-temperature response is shown in the right inset. A negative resistance is observed, indicating ballistic transport. (B) Room-temperature mobility versus density (solid black curve). Dashed black curve indicates the theoretical mobility limit due to acoustic-phonon scattering (28, 29). Remaining data points label the range of mobilities

reported in the literature for high-performance 2D semiconductor FETs (30, 31). (C and D) Calculated mean free path versus density and temperature for the device shown in (A). Shaded region in (D) indicates the temperature below which the mean free path exceeds the device size. Circle and squares correspond to the "a" configuration and triangles correspond to the "b" configuration of the van der Pauw measurement (supplementary materials section 1.5). (E) Lower bound mean free path at $T = 1.7$ K for devices with size varying from 1 to $15 \mu\text{m}$.

interfaces do not contact any polymer throughout the process, reducing impurities trapped between the layers. Figure 2C shows an atomic force microscope (AFM) image of a BN-G-BN heterostructure made by vdW assembly. The graphene appears clean and free of macroscopic contamination over the entire device area, $\sim 200 \mu\text{m}^2$. In Fig. 2D, a high-resolution cross section STEM image shows that the resulting interface is pristine down to the atomic scale, with the graphene layer nearly indistinguishable from the adjacent BN lattice planes.

Figure 3A shows electrical transport from a large-area, $15 \mu\text{m} \times 15 \mu\text{m}$, BN-G-BN device fabricated by combining vdW assembly with edge-contacts. The transport characteristics indicate the graphene device to be remarkably pristine, reaching a room-temperature mobility in excess of $140,000 \text{ cm}^2/\text{Vs}$. At carrier density $|n| = 4.5 \times 10^{12} \text{ cm}^{-2}$, the sheet resistivity is less than ~ 40 ohms per square (fig. S13), corresponding to an equivalent 3D resistivity below $1.5 \mu\Omega\text{m}\cdot\text{cm}$, smaller than the resistivity of any metal at room temperature. Indeed, the remarkable feature of this device response is the simultaneous realization of both high mobility and large carrier density. Using the simple Drude model of conductivity, $\sigma = ne\mu$, where μ is the electron mobility, we calculate a mobility of $\sim 40,000 \text{ cm}^2/\text{Vs}$ at densities as large as $n \sim 4.5 \times 10^{12} \text{ cm}^{-2}$. In this high-density regime, the measured mobility is comparable to the acoustic-phonon-limited mobility theoretically predicted for intrinsic graphene (28, 29). The room-temperature response of the graphene device reported here outperforms all other 2D materials, including the highest mobility 2D heterostructures fabricated from III-V (groups III and V in the periodic table) semiconductors (30, 31) (Fig. 3B) by at least a factor of 2 over the entire range of technologically relevant carrier densities.

At low temperatures, four-terminal measurement yields a negative resistance (inset in Fig. 3A), indicating quasiballistic transport (4) over at least $15 \mu\text{m}$. In the diffusive regime, the mean free path, L_{mfp} , can be calculated from the conductivity, σ , according to $L_{\text{mfp}} = \sigma h/2e^2 k_F$ where $k_F = \sqrt{\pi n}$ is the Fermi wave vector. In Fig. 3C, L_{mfp} versus applied gate voltage is shown for selected temperatures from 300 K down to 20 K. The mean free path increases with gate voltage until it saturates at a temperature-dependent value at high density. This maximum L_{mfp} increases monotonically with decreasing temperature until the mean free path approaches the device size at $T \sim 40$ K (Fig. 3D). In the low-temperature ballistic regime, four-terminal measurement is dominated by mesoscopic effects (32) and the calculated mean free path exhibits large variation, depending on the measurement geometry. The temperature dependence therefore provides only a lower bound of the mean free path.

The negative resistance observed at base temperature indicates that electrons travel ballistically across the diagonal of the square, corresponding to a mean free path as large as $21 \mu\text{m}$ in this

device. This value corresponds to an electron mobility of $\sim 1,000,000 \text{ cm}^2/\text{Vs}$ at a carrier density of $\sim 3 \times 10^{12} \text{ cm}^{-2}$. We repeated this measurement for devices varying in size from 1 to $15 \mu\text{m}$. As seen in Fig. 3E, the maximum mean free path scales linearly with device size. This result indicates that in our devices the low-temperature mobility is limited by the available crystal size, and we have not reached the intrinsic impurity-limited scattering length. Even higher mobility could be expected for larger-area devices, which may be realized by combining recent progress in scalable growth techniques (33, 34) together with the edge-contact geometry described here.

References and Notes

1. M. Xu, T. Liang, M. Shi, H. Chen, *Chem. Rev.* **113**, 3766–3798 (2013).
2. A. K. Geim, I. V. Grigorieva, *Nature* **499**, 419–425 (2013).
3. C. R. Dean *et al.*, *Nat. Nanotechnol.* **5**, 722–726 (2010).
4. A. S. Mayorov *et al.*, *Nano Lett.* **11**, 2396–2399 (2011).
5. L. Wang *et al.*, *ACS Nano* **6**, 9314–9319 (2012).
6. C. R. Dean *et al.*, *Nature* **497**, 598–602 (2013).
7. L. A. Ponomarenko *et al.*, *Nature* **497**, 594–597 (2013).
8. B. Hunt *et al.*, *Science* **340**, 1427–1430 (2013).
9. L. Britnell *et al.*, *Science* **335**, 947–950 (2012).
10. T. Georgiou *et al.*, *Nat. Nanotechnol.* **8**, 100–103 (2013).
11. L. Britnell *et al.*, *Science* **340**, 1311–1314 (2013).
12. G. Giovannetti *et al.*, *Phys. Rev. Lett.* **101**, 026803 (2008).
13. C. Gong *et al.*, *J. Appl. Phys.* **108**, 123711 (2010).
14. F. Léonard, A. A. Talin, *Nat. Nanotechnol.* **6**, 773–783 (2011).
15. F. Xia, V. Perebeinos, Y. M. Lin, Y. Wu, P. Avouris, *Nat. Nanotechnol.* **6**, 179–184 (2011).
16. M. S. Choi, S. H. Lee, W. J. Yoo, *J. Appl. Phys.* **110**, 073305 (2011).
17. D. Berdebes, T. Low, Y. Sui, J. Appenzeller, M. S. Lundstrom, *IEEE Trans. Electron. Dev.* **58**, 3925–3932 (2011).
18. J. S. Moon *et al.*, *Appl. Phys. Lett.* **100**, 203512 (2012).
19. J. T. Smith, A. D. Franklin, D. B. Farmer, C. D. Dimitrakopoulos, *ACS Nano* **7**, 3661–3667 (2013).

20. M. Ishigami, J. H. Chen, W. G. Cullen, M. S. Fuhrer, E. D. Williams, *Nano Lett.* **7**, 1643–1648 (2007).
21. J. A. Robinson *et al.*, *Appl. Phys. Lett.* **98**, 053103 (2011).
22. J. Yamaguchi, K. Hayashi, S. Sato, N. Yokoyama, *Appl. Phys. Lett.* **102**, 143505 (2013).
23. N. Lindvall, A. Kalabukhov, A. Yurgens, *J. Appl. Phys.* **111**, 064904 (2012).
24. S. J. Haigh *et al.*, *Nat. Mater.* **11**, 764–767 (2012).
25. Y. Matsuda, W.-Q. Deng, W. A. Goddard III, *J. Phys. Chem. C* **114**, 17845–17850 (2010).
26. K. Cho *et al.*, *MRS Proc.* **1259**, S14–S35 (2010).
27. Y. Wu *et al.*, *AIP Adv.* **2**, 012132 (2012).
28. E. Hwang, S. Das Sarma, *Phys. Rev. B* **77**, 115449 (2008).
29. J. H. Chen, C. Jang, S. Xiao, M. Ishigami, M. S. Fuhrer, *Nat. Nanotechnol.* **3**, 206–209 (2008).
30. B. R. Bennett, R. Magno, J. B. Boos, W. Kruppa, M. G. Ancona, *Sol. Stat. Elec.* **49**, 1875–1895 (2005).
31. J. Orr *et al.*, *Phys. Rev. B* **77**, 165334 (2008).
32. S. Datta, *Electronic Transport in Mesoscopic Systems* (Cambridge Univ. Press, London, 1995).
33. W. Yang *et al.*, *Nat. Mater.* **12**, 792–797 (2013).
34. Z. Liu *et al.*, *Nano Lett.* **11**, 2032–2037 (2011).

Acknowledgments: This work is supported by the Department of Defense through the National Defense Science and Engineering Graduate Fellowship Program, the National Science Foundation (DMR-1124894), the Air Force Office of Scientific Research (FA9550-09-1-0705), the Office of Naval Research (ONR) (N000141310662 and N000141110633), the Defense Advanced Research Projects Agency (under ONR Grant N000141210814), and the Nano Material Technology Development Program through the National Research Foundation of Korea (2012M3A7B4049966). We thank E. H. Hwang and S. Das Sarma for helpful discussion.

Supplementary Materials

www.sciencemag.org/content/342/6158/614/suppl/DC1
Materials and Methods
Supplementary Text
Figs. S1 to S14
Tables S1 to S2
References (35–46)

7 August 2013; accepted 26 September 2013
10.1126/science.1244358

Pacific Ocean Heat Content During the Past 10,000 Years

Yair Rosenthal,^{1*} Braddock K. Linsley,² Delia W. Oppo³

Observed increases in ocean heat content (OHC) and temperature are robust indicators of global warming during the past several decades. We used high-resolution proxy records from sediment cores to extend these observations in the Pacific 10,000 years beyond the instrumental record. We show that water masses linked to North Pacific and Antarctic intermediate waters were warmer by $2.1 \pm 0.4^\circ\text{C}$ and $1.5 \pm 0.4^\circ\text{C}$, respectively, during the middle Holocene Thermal Maximum than over the past century. Both water masses were $\sim 0.9^\circ\text{C}$ warmer during the Medieval Warm period than during the Little Ice Age and $\sim 0.65^\circ$ warmer than in recent decades. Although documented changes in global surface temperatures during the Holocene and Common era are relatively small, the concomitant changes in OHC are large.

Small, yet persistent perturbations in the balance of incoming solar radiation (insolation) reaching Earth's surface and outgoing long-wave radiation can lead to substantial climate change. Nevertheless, relating climate variations to radiative perturbations is not straightforward due to the inherent noise of the system

caused by large temporal (seasonal to decadal) and spatial variability of the climatic response. A long-term perspective of climate variability relative to known radiative perturbations can place the recent trends in the broader framework of natural variability. The comparison with paleoclimate reconstructions of surface temperatures

is, however, complicated because of the limited number of proxy records, their uneven geographical distribution, and the seasonal ecological biases of the proxies (1, 2).

Globally averaged instrumental surface temperatures have registered little increase in recent decades, despite a considerable imbalance in the planetary energy budget (3). The apparent discrepancy is attributed to the warming of the ocean’s interior over the same period. Instrumental records show that the increase in ocean heat content (OHC) accounts for ~90% of the expected warming of Earth, thereby demonstrating that OHC more reliably represents the response of Earth’s energy budget to radiative perturbations than do surface temperatures (4–6). Furthermore, subsurface water masses are directly ventilated in the high-latitude oceans, where they average the highly variable surface conditions, thereby providing an integrated measure of long-term trends. Here, we place the recent observations of OHC in the framework of long-term changes during the Holocene and the Common era.

We use a suite of sediment cores along bathymetric transects in the Makassar Strait and Flores Sea in Indonesia (figs. S1 and S2) to document changes in the temperature of western equatorial Pacific subsurface and intermediate water masses throughout the Holocene [0 to 10 thousand years before the present (ky B.P.)] (Table 1). This region is well suited to reconstruct Pacific OHC, as thermocline and intermediate water masses found here form in the mid- and high-latitudes of both the northern and southern Pacific Ocean and can be traced by their distinctive salinity and density as they flow toward the equator (7) (fig. S3). The Makassar Strait between Borneo and Sulawesi, the Lifamatola Passage east of Sulawesi on the northern side of the Indonesian archipelago, and the Ombai and Timor Passages to the south serve as major conduits for exchange of water between the Pacific and Indian Oceans; water flow through

these passages is collectively referred to as the Indonesian Throughflow (ITF) (8). The upper thermocline component of the ITF (~0 to 200 m) is dominated by contributions from North Pacific and, to a lesser extent, South Pacific subtropical waters, marked by a subsurface salinity maximum (figs. S3 and S4). Within the lower thermocline (~200 to 500 m) the inflow of low-salinity North Pacific Intermediate Water (NPIW) dominates the ITF flow (fig. S4). The higher- and relatively uniform-salinity water below the main thermocline (~450 to 1000 m) is referred to as Indonesian Intermediate Water, which is formed in the Banda Sea by strong vertical mixing between shallow, warm, relatively fresh waters and deep, cold, relatively salty waters (8, 9). At intermediate depths, the Banda Sea gets contributions from the South Pacific through the northwestward-flowing New Guinea Coastal Undercurrent (NGCUC). Studies suggest that the NGCUC carries a substantial contribution from the Antarctic Intermediate Water, spreading into the Banda Sea through the Lifamatola and Makassar passages (10). The main subthermocline outflows through the Timor and Ombai passages reverse intermittently, thereby allowing inflow of Indian Ocean water into the Indonesian seas (8, 11, 12). Thus, the hydrography of intermediate water in this region is linked to and influenced by surface conditions in the high latitudes of the Pacific Ocean, as is also suggested from the distribution of anthropogenically produced chlorofluorocarbon along these isopycnal layers (7).

We studied well-dated sediment cores (table S1) in the Makassar Strait. Shallow cores (450 to 600 m) are used to reconstruct the hydrographic history of the lower thermocline, which currently is strongly influenced by NPIW. Deeper cores (650 to 900 m) from the Bali Basin on the western edge of the Flores Sea are arguably under greater influence of Southern Hemisphere (SH) water masses.

We use Mg/Ca measurements in the benthic foraminifer *Hyalinea balthica* for reconstructing intermediate water temperatures (IWTs). This species is ideally suited to track small temperature changes due to its high Mg/Ca-temperature sensitivity [Mg/Ca = (0.488 ± 0.03)·IWT] (13, 14). The error on IWT estimates is ±0.7°C for raw

data and ±0.35°C [one standard error of the estimate (SEE)] for composite records. The oxygen isotopic composition of seawater (δ¹⁸O_{sw}), used here as an analog for salinity, is estimated from the paired benthic foraminiferal oxygen isotopic composition (δ¹⁸O_c) and Mg/Ca data (15). Our reconstructions show that IWTs at all depths were substantially warmer in the early and middle Holocene than during the late Holocene (Fig. 1). Specifically, IWT at 500 m was ~10°C between 10.5 and 9 thousand years ago (ka), increased to a maximum of ~10.7°C between 8 to 6 ka, and began decreasing after 6 ka, reaching ~7.8°C at the core top (~100 years B.P.). In the 600-, 650-, and 900-m cores, a maximum IWT of ~8.2°C occurred between 10.5 and 9 ka and started decreasing after 9 ka, earlier than at the shallower site, reaching ~5.8°C at the core top (~100 to 300 years B.P.) (Table 1). The deepest site at 900 m shows an identical temperature trend with the 600- and 650-m sites. After correcting for sea-level rise from the early to mid-Holocene (15), we calculate Holocene cooling trends of ~2.2 ± 0.4°C and ~1.5 ± 0.3°C at 500 m and 600 to 900 m, respectively. Benthic foraminiferal δ¹⁸O_c records at 600 and 650 m show a ~0.15 per mil increase from the middle to late Holocene and no major change at 500 m (fig. S5). These small changes cannot fully account for the cooling, thereby suggesting concomitant changes in salinity.

In contrast with the substantial IWT cooling, reconstructions of sea surface temperature (SST), based on Mg/Ca ratios in the mixed-layer foraminifer *Globigerinoides ruber* from multiple sites in the Indo-Pacific Warm Pool (IPWP), show only ~0.5°C cooling from ~9 ka to the 20th century (16) (Fig. 1). Mg/Ca records of the subsurface planktonic foraminifer *Pulleniatina obliquiculata* that calcify at about 75- to 100-m depth (17, 18) suggest ~1.0°C cooling of the upper IPWP thermocline from the middle to the late Holocene (18–20). Thus, it seems that the Holocene subsurface cooling affected the water column below the mixed-layer and down to 900 m.

The early Holocene warmth and subsequent IWT cooling in Indonesia is likely related to temperature variability in the higher-latitude source waters. To assess the mechanisms that caused these hydrographic variations, we estimate down-core

¹Institute for Marine and Coastal Sciences and Department of Earth and Planetary Sciences, Rutgers University, 71 Dudley Road, New Brunswick, NJ 08901, USA. ²Lamont-Doherty Earth Observatory of Columbia University, Palisades, NY 10964, USA. ³Department of Geology and Geophysics, Woods Hole Oceanographic Institution, Woods Hole, MA 02543, USA.

*Corresponding author. E-mail: rosenantha@imcs.rutgers.edu

Table 1. Core location and bottom water temperature and salinity at each site. Also given are the interval covered by each of the records, the average sedimentation rate, and the estimated core top ages. The “Period” column indicates maximum length. HL, Holocene length. psu, practical salinity units.

Site	Lat.	Long.	Depth (m)	Temp. (°C)	Salinity (psu)	Period	Avg. sed. rate (cm/ky)	Estimated core top age (year CE)
<i>Makassar Strait</i>								
31MC/32GGC	3° 53.00'S	119° 27.24'E	455	8.1	34.481	CE	180	1990/1950
70GGC	3° 24.40'S	119° 23.41'E	482	7.8	34.500	HL	40	1900
34GGC	3° 53.16'S	119° 26.47'E	503	7.5	34.512	CE	180	1930/1600
47MC/48GGC	3° 53.30'S	119° 25.66"E	605	6.7	34.539	CE	150	1940/1640
<i>Flores Sea</i>								
13GGC	7° 22.04'S	115° 12.72'E	594	6.5	34.547	HL	60	1830
10GGC	3° 24.54'S	115° 15.56'E	649	6.1	34.553	HL	50	1650
6MC/7GGC	7° 28.24'S	115° 21.53'E	920	5.2	34.583	HL/CE	75	1980/1600

salinities and densities for the 500- and 600- to 650-m depths. A temperature-salinity-density plot suggests that although the water masses were significantly warmer during the early middle Holocene than the late Holocene, their densities remained relatively constant throughout the Holocene (fig. S6). Thus, Holocene IWT cooling must have been largely compensated by freshening at the high-latitude source regions.

Intermediate water temperature records exhibit a Holocene thermal maximum (HTM) and Neoglacial cooling known from various terrestrial and marine records of the Northern Hemisphere (NH) and the SH [e.g., (1, 21–23)]. We compare our IWT anomalies with a recently published compilation of surface temperature records (23, 24). The anomalies are calculated relative to the reference period of 1850 to 1880 CE, as determined from the companion multicore records at each site (Fig. 2). Between 9 and 6 ka, the 500-m IWT trends resemble the NH surface high-latitude reconstruction (24), suggesting that the

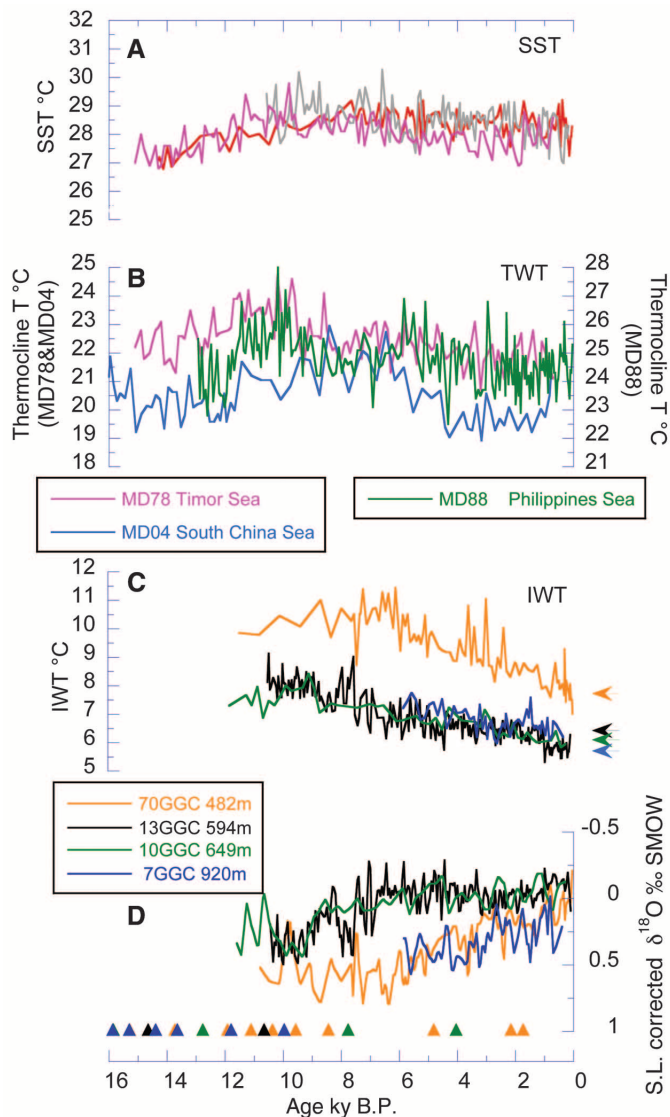
HTM was $2.5 \pm 0.4^\circ\text{C}$ warmer than in the late 20th century. This is consistent with the surface estimate of $2.1 \pm 0.2^\circ\text{C}$ for the 30°N to 90°N latitudinal belt and is more than double the global $\sim 0.7^\circ\text{C}$ trend (24). The records from the deeper (600- to 900-m) sites, which arguably receive greater contributions from the SH, indicate that the IWT was $1.5 \pm 0.4^\circ\text{C}$ warmer during the HTM than the late 20th century. In contrast, the recent surface temperature reconstruction for the 30°S to 90°S band does not show a discernible trend throughout the Holocene (24). The discrepancy between our deep IWT record and the SH reconstruction might be due to the limited number of records used in the SH reconstruction and the uncertainty associated with estimating temperatures from ice-core records (24). Due to the strong vertical mixing in the Banda Sea, we cannot rule out the possibility that our 600- to 900-m IWT records were also primarily affected by North Pacific waters; however, we note the consistency with records showing Holocene cooling of $\sim 1^\circ\text{C}$

to 2°C of SST north and south of the South Pacific Subtropical Convergence (23). The similarity between these SSTs and our IWT trends supports the proposed link to SH climate. The similar IWT trends observed between 480 and 900 m suggest that on orbital time scales, changes in Pacific OHC are largely determined by climate changes in the high latitudes that possibly respond to changes in the tilt of Earth's axis since the early Holocene (24). Changes in the seasonal cycle of the high latitudes, driven by Earth's precession, might be expected to affect the formation and heat-exchange rate of intermediate water masses. However, the similar cooling at intermediate depths influenced by both northern- and southern-sourced water masses, despite the antisymmetry in the precessional forcing, suggests that on these time scales, Earth's obliquity exerts the dominant influence on high-latitude temperatures and that OHC is highly sensitive to the changes at these latitudes. Although the exact mechanism is still unresolved, based on our density reconstructions we suggest that small perturbations in high-latitude climate are efficiently transferred to the ocean's interior along isopycnal surfaces, largely by density-compensated temperature changes, a mechanism proposed to explain modern observations (25). Over a long time, the ocean's interior acts like a capacitor and builds up large (positive and negative) heat anomalies that reflect and, more importantly, affect the global climate. We posit that the cooling of the thermocline and, to a lesser extent, the surface water in the IPWP (16), which is apparently at odds with model simulations forced by changes in insolation and atmospheric CO_2 throughout the Holocene, might have been caused by upward mixing of intermediate water in the Indonesian seas.

Multi- and gravity cores provide a record of IWT variability during the past two millennia. Because there is no major difference between the records at ~ 500 , 600, and 900 m (fig. S7), we averaged these three records (Fig. 3). During the Common era, centennial IWT variability (500 to 900 m) is coherent with and closely follows changes in the overlying SST (26) and the NH (27, 28). IPWP SSTs are within error of modern (~ 1950 CE) values between 900 and 1200 CE during the Medieval Warm Period (MWP) and are colder by $0.75 \pm 0.35^\circ\text{C}$ between 1550 and 1850 CE during the Little Ice Age (LIA), followed by nonmonotonic warming in the past 150 years (26). Concomitantly, Pacific IWT was $0.9 \pm 0.35^\circ\text{C}$ (1 SEE) warmer during the MWP than during the LIA. Within age-model errors, the cooling trend from the MWP to LIA is of the same magnitude as, but possibly lags, the cooling of the overlying surface water and the NH. However, whereas the NH reconstructions (27, 28) show general nonmonotonic warming of $\sim 0.5 \pm 0.15^\circ\text{C}$ for the period of 1850 to 1950 CE, which is consistent with the instrumental record for the NH (24°N to 90°N) during the same period (29), we see no significant change in IWT ($\Delta\text{IWT} = 0.15 \pm 0.35^\circ\text{C}$) between 1850 and 1950 CE (Fig. 3).

Fig. 1. Down-core records from sites in the IPWP.

(A) Mg/Ca-derived SST from the Makassar Strait (70GGC, red), Flores Sea (13GGC, gray), and Timor Sea (MD78, magenta) (16, 18). (B) Mg/Ca-derived thermocline water temperature (TWT) from sites in the Timor Sea (18), Philippines Sea (20), and northern South China Sea (19) (see fig. S2 for map of sites). (C) Intermediate water temperatures from the Indonesian bathymetric transect. (D) Bottom water $\delta^{18}\text{O}_{\text{sw-iv}}$ corrected for ice volume (iv) effect. Age models for the records are based on accelerator mass spectrometry ^{14}C dating (table S1) and marked with triangles at the bottom. ^{14}C date color coding is as shown in the bottom key. S.L., sea level; SMOW, standard mean ocean water; ‰, per mil.



The difference between the IWT and SST estimates in the same core and elsewhere likely reflects the fact that it takes several decades for the intermediate water masses to reach the western equatorial Pacific from their high-latitude origins (7). To the extent that our reconstruction reflects high-latitude climate conditions in both hemispheres, it differs considerably from the recent

surface compilations, which suggest $\sim 2^\circ\text{C}$ MWP-to-LIA cooling in the 30°N to 90°N zone, whereas the 30°S to 90°S zone warmed by $\sim 0.6^\circ\text{C}$ during the same interval (24). In contrast, our composite IWT records of water masses linked to NH and SH water masses imply similar patterns of MWP-to-LIA cooling at the source regions. The inferred similarity in temperature anomalies at both hemi-

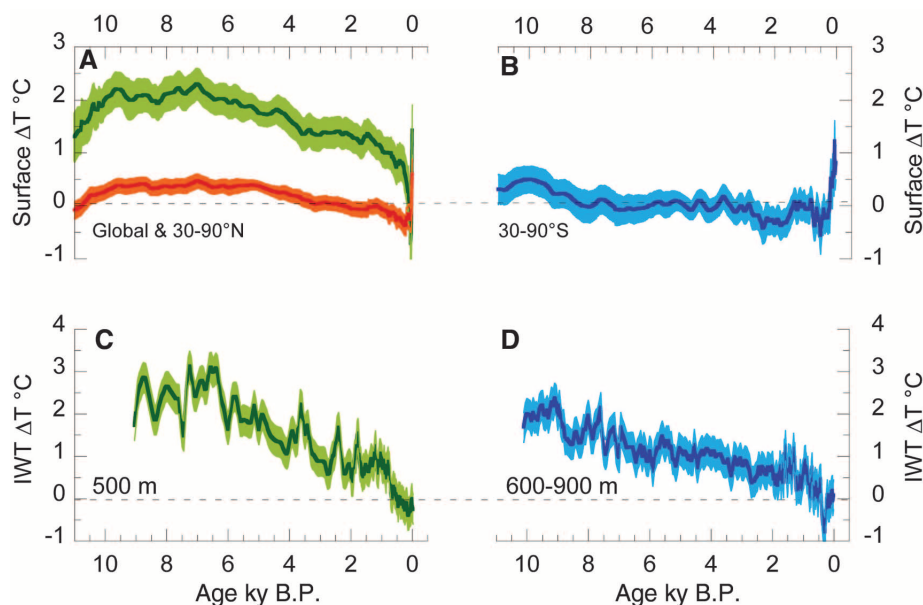
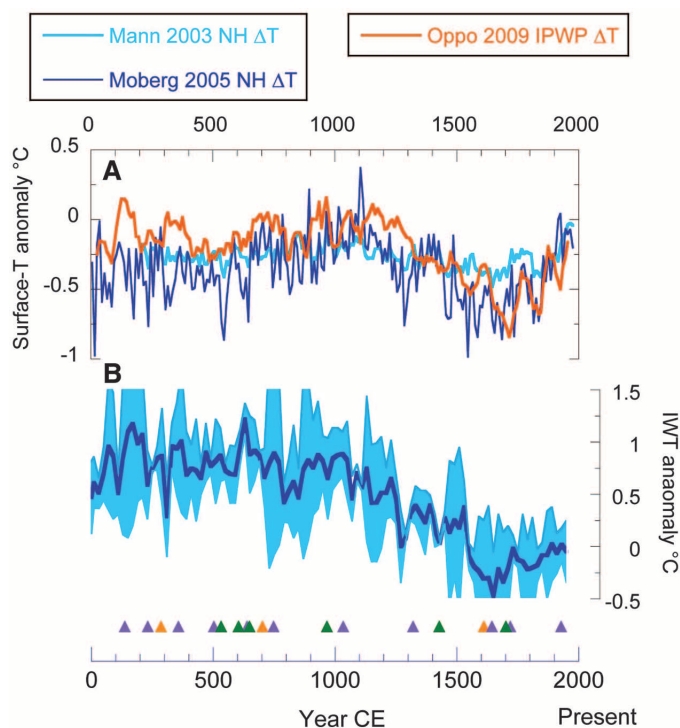


Fig. 2. Comparison between Holocene reconstructions of surface and intermediate-water temperatures. (A) Global (red) and 30°N to 90°N (green) surface temperatures anomalies, (B) 30°S to 90°S surface temperature anomalies (24), (C) changes in IWT at 500 m, and (D) changes in IWT at 600 to 900 m. All anomalies are calculated relative to the temperature at 1850 to 1880 CE. Shaded bands represent ± 1 SD. Note the different temperature scales.

Fig. 3. Temperature anomaly reconstructions for the Common era relative to the modern data (note that the age scale is in Common era years with the present on the right). (A) Change in SST from the Makassar Straits [orange, based on (26) compared with NH temperature anomalies (27, 28)]. (B) Compiled IWT anomalies based on Indonesian records spanning the ~ 500 - to 900 -m water depth (for individual records, see fig. S7). The shaded band represents ± 1 SD.



spheres is consistent with recent evidence from Antarctica (30), thereby supporting the idea that the HTM, MWP, and LIA were global events. Furthermore, the similar expressions in both hemispheres indicate a strong link to global radiative perturbations rather than a regional response to changes in ocean circulation.

With no additional IWT records, it is difficult to assess the global extent of the trends we have reconstructed. Instead, we evaluate the possible implications for Pacific OHC at four discrete periods during the Holocene. We consider three sensitivity cases, whereby the observed IWT trends in Indonesia are applied to 25, 50, and 75% of the Pacific volume between 0 and 700 m (15) (Fig. 4). The reconstructed OHC is compared with modern observations for the whole Pacific at the same depth range (5). The comparison suggests that Pacific OHC was substantially higher during most of the Holocene than in the past decade (2000 to 2010), with the exception of the LIA. The difference is statistically significant, even if the OHC changes apply only to

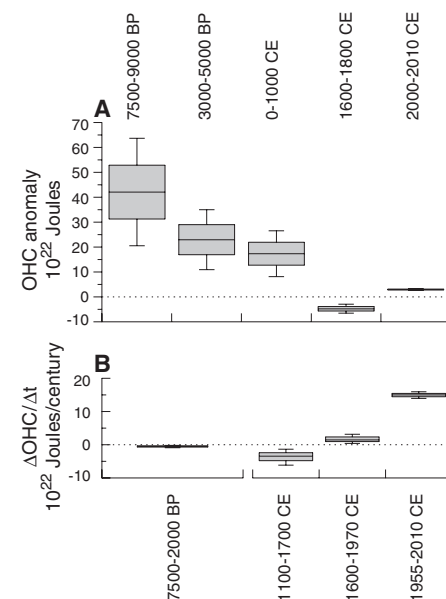


Fig. 4. Holocene changes in Pacific Ocean heat content. (A) Reconstructed anomalies in Pacific OHC in the 0- to 700-m depth interval for the early Holocene, mid-Holocene, MWP, and LIA periods. Reconstructed anomalies are calculated relative to the reference period of 1965 to 1970 CE (15). (B) Reconstructed rates of OHC change during the main transition periods. Reconstructed anomalies and rates are compared with modern observations for the 2000 to 2010 and 1955 to 2010 CE periods, respectively (5). The middle line at each box represents an average estimate for 50% of the Pacific volume between 0 and 700 m, whereas the top and bottom quartiles of the box represent 62.5 and 37.5% of the total volume in this depth interval, respectively. The bottom whiskers represent 25% of the volume; the top whisker denotes 75%. The modern value is based on the entire Pacific volume for 0 to 700 m.

the western Pacific (~25% Pacific volume), although there are indications that similar trends extended farther east (15). The modern rate of Pacific OHC change is, however, the highest in the past 10,000 years (Fig. 4 and table S3).

The current response of surface temperatures to the ongoing radiative perturbation is substantially higher than the response of the ocean's interior, due to the long whole-ocean equilibration time. However, on longer time scales the oceanic response is likely different, as seen in our records where past changes in IWT were much larger than variations in global surface temperatures. The large variations in IWT and inferred OHC during the Holocene and Common era, when global temperature anomalies were relatively small, imply elevated sensitivity to climate conditions in the high latitudes, which, on a multidecadal scale, likely enables the ocean to mediate perturbations in Earth's energy budget.

References and Notes

- H. Wanner *et al.*, *Quat. Sci. Rev.* **27**, 1791–1828 (2008).
- L. Leduc, R. Schneider, J.-H. Kim, G. Lohmann, *Quat. Sci. Rev.* **29**, 989–1004 (2010).
- D. R. Easterling, M. F. Wehner, *Geophys. Res. Lett.* **36**, L08706 (2009).
- S. Levitus, J. Antonov, T. P. Boyer, C. Stephens, *Science* **287**, 2225–2229 (2000).
- S. Levitus *et al.*, *Geophys. Res. Lett.* **39**, L10603 (2012).
- J. Hansen *et al.*, *Science* **308**, 1431–1435 (2005).
- R. A. Fine, R. Lukas, F. M. Bingham, M. J. Warner, R. H. Gammon, *J. Geophys. Res.* **99**, 25063–25080 (1994).
- A. Gordon, *Oceanography* **18**, 14–27 (2005).
- L. D. Talley, J. Sprintall, *J. Geophys. Res.* **110**, C10009 (2005).
- W. Zenk *et al.*, *Prog. Oceanogr.* **67**, 245–281 (2005).
- S. Wijffels, J. Sprintall, M. Fieux, N. Bray, *Deep Sea Res. Part II Top. Stud. Oceanogr.* **49**, 1341–1362 (2002).
- J. Sprintall, S. E. Wijffels, R. Molcard, I. Jaya, *J. Geophys. Res.* **114**, C07001 (2009).
- Y. Rosenthal *et al.*, *Geophys. Geochem. Geosys.* **12**, 1–17 (2011).
- A. Morley *et al.*, *Earth Planet. Sci. Lett.* **308**, 161–171 (2011).
- Supplementary materials are available on Science Online.
- B. K. Linsley, Y. Rosenthal, D. W. Oppo, *Nat. Geosci.* **3**, 578–583 (2010).
- M. Mohtadi *et al.*, *Paleoceanography* **26**, PA3219 (2011).
- J. Xu, A. Holbourn, W. Kuhnt, Z. Jian, H. Kawamura, *Earth Planet. Sci. Lett.* **273**, 152–162 (2008).
- S. Steinke *et al.*, *Global Planet. Change* **78**, 170–177 (2011).
- H. Dang, Z. Jian, F. Bassinot, P. Qiao, X. Cheng, *Geophys. Res. Lett.* **39**, 1–5 (2011).
- V. Masson *et al.*, *Quat. Res.* **54**, 348–358 (2000).
- P. A. Mayewski *et al.*, *Quat. Res.* **62**, 243–255 (2004).
- H. C. Bostock *et al.*, *Quat. Sci. Rev.* **74**, 35–57 (2013).
- S. A. Marcott, J. D. Shakun, P. U. Clark, A. C. Mix, *Science* **339**, 1198–1201 (2013).
- C. Mauritzen, A. Melsom, R. T. Sutton, *Nat. Geosci.* **5**, 905–910 (2012).
- D. W. Oppo, Y. Rosenthal, B. K. Linsley, *Nature* **460**, 1113–1116 (2009).
- M. E. Mann *et al.*, *Proc. Natl. Acad. Sci. U.S.A.* **105**, 13252–13257 (2008).
- A. Moberg *et al.*, *Nature* **433**, 613–617 (2005).
- T. M. Smith, R. W. Reynolds, T. C. Peterson, J. Lawrimore, *J. Clim.* **21**, 2283–2296 (2008).
- A. J. Orsi, B. D. Cornuelle, J. P. Severinghaus, *Geophys. Res. Lett.* **39**, 1–7 (2012).

Acknowledgments: We are indebted to Y. S. Djajadihardja, F. Syamsudin, the captain and crew of our 2003 *RV Baruna Jaya VIII* cruise, the Indonesian Agency for Assessment and Application of Technology (BPPT), and the Center of Research and Development for Oceanography (LIPI) of Indonesia for their support of this project. This work was also supported by the NSF. We thank M. Chong, K. Esswein, A. Morely, S. Woodard, and S. Howe for technical assistance; A. L. Gordon for helpful discussions; and the National Ocean Sciences Accelerator Mass Spectrometry and Radio analytical facilities at Woods Hole Oceanographic Institution. Helpful comments from reviewers are highly appreciated.

Supplementary Materials

www.sciencemag.org/content/342/6158/617/suppl/DC1

Supplementary Text

Figs. S1 to S8

Tables S1 to S3

References

21 May 2013; accepted 30 September 2013

10.1126/science.1240837

Reconstructing the Microbial Diversity and Function of Pre-Agricultural Tallgrass Prairie Soils in the United States

Noah Fierer,^{1,2*} Joshua Ladau,³ Jose C. Clemente,⁴ Jonathan W. Leff,^{1,2} Sarah M. Owens,^{5,6} Katherine S. Pollard,^{3,7} Rob Knight,^{8,9} Jack A. Gilbert,^{5,10} Rebecca L. McCulley¹¹

Native tallgrass prairie once dominated much of the midwestern United States, but this biome and the soil microbial diversity that once sustained this highly productive system have been almost completely eradicated by decades of agricultural practices. We reconstructed the soil microbial diversity that once existed in this biome by analyzing relict prairie soils and found that the biogeographical patterns were largely driven by changes in the relative abundance of Verrucomicrobia, a poorly studied bacterial phylum that appears to dominate many prairie soils. Shotgun metagenomic data suggested that these spatial patterns were associated with strong shifts in carbon dynamics. We show that metagenomic approaches can be used to reconstruct below-ground biogeochemical and diversity gradients in endangered ecosystems; such information could be used to improve restoration efforts, given that even small changes in below-ground microbial diversity can have important impacts on ecosystem processes.

After the European settlement of the midwestern United States in the mid-19th century, the tallgrass prairie ecosystem was profoundly altered by the removal of key animal taxa (including bison), fire suppression, and the plowing under of native grasses. Together these land-use changes contributed to the most substantial decline of any major ecosystem in North America (1, 2). This ecosystem, which once covered nearly 10% of the contiguous United States (>65 million ha), has been reduced to a small fraction of its historical extent (3). Cultivation and row crop agriculture, now practiced across

most of the tallgrass prairie biome, not only replaced species-rich plant communities with monoculture croplands, but also drastically altered the physicochemical and biological characteristics of prairie soils. Except for a few prairie relicts that have never been tilled, the soils currently found throughout the region bear little resemblance to their pre-agricultural state (4–7). We confirmed the effect of cultivation on soil microbial communities by directly comparing bacterial communities in cultivated soils with paired uncultivated soils collected from throughout the native tallgrass prairie range (table S1), and found that the

cultivated soils harbored bacterial communities that were significantly distinct in composition from those found in the corresponding native prairie soils (fig. S1).

Owing to the historical and biological importance of the native tallgrass prairie, there have been various attempts to predict the historical distributions of plants and animals across this ecosystem [e.g., (8)]. However, comparable reconstructions of below-ground microbial diversity have, to our knowledge, never been attempted, hindering our understanding of how soil microbes may have once influenced plant production, nutrient retention, and soil carbon dynamics in this ecosystem. By coupling metagenomic sequence data, which capture the phylogenetic and functional diversity of existing soil microbial communities (9, 10) found in tallgrass prairie remnants, to spatially explicit models (11), which predict the structure

¹Department of Ecology and Evolutionary Biology, University of Colorado, Boulder, CO 80309, USA. ²Cooperative Institute for Research in Environmental Sciences, University of Colorado, Boulder, CO 80309, USA. ³The Gladstone Institutes, University of California, San Francisco, CA 94158, USA. ⁴Department of Genetics and Genomic Sciences and Department of Medicine, Mount Sinai School of Medicine, New York, NY 10029, USA. ⁵Institute of Genomic and Systems Biology, Argonne National Laboratory, Argonne, IL 60439, USA. ⁶Computation Institute, University of Chicago, Chicago, IL 60637, USA. ⁷Institute for Human Genetics and Division of Biostatistics, University of California, San Francisco, CA 94143, USA. ⁸Department of Chemistry and Biochemistry, University of Colorado, Boulder, CO 80309, USA. ⁹Howard Hughes Medical Institute, Boulder, CO 80309, USA. ¹⁰Department of Ecology and Evolution, University of Chicago, Chicago, IL 60637, USA. ¹¹Department of Plant and Soil Sciences, University of Kentucky, Lexington, KY 40546, USA.

*Corresponding author. E-mail: noah.fierer@colorado.edu

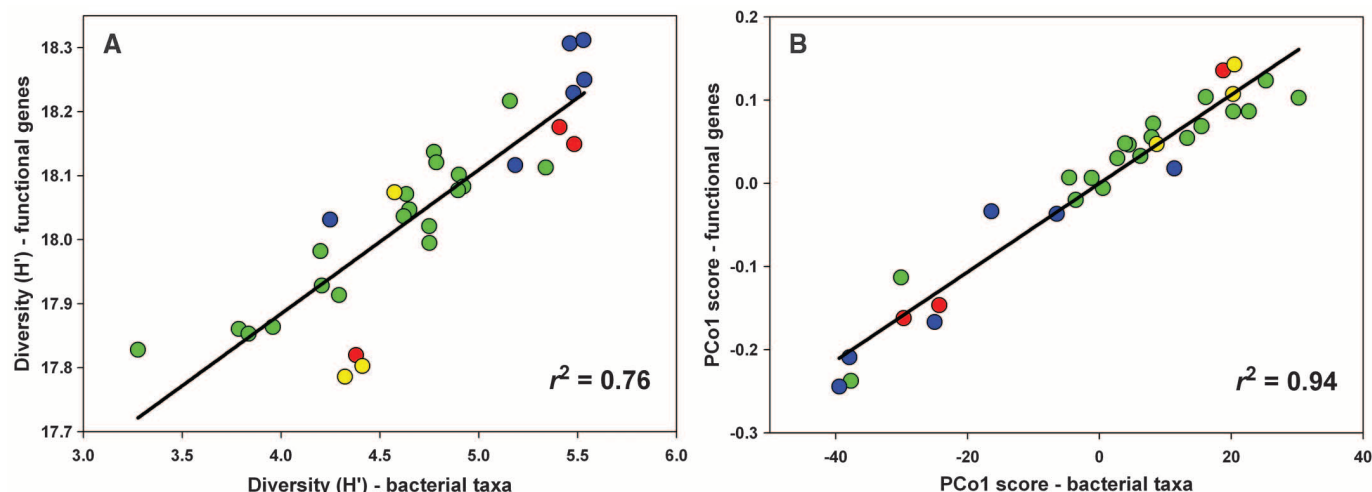


Fig. 1. Relationships between taxonomic and functional diversity (A) and community similarity patterns (B) across the 31 sites, with x axes showing taxonomic comparisons and y axes showing comparisons based on functional genes. Points are colored according to latitude (red, $<35^{\circ}\text{N}$; yellow, 35° to 40°N ; green, 40° to 45°N ; blue, $>45^{\circ}\text{N}$). The Shannon

index (H') and the Bray-Curtis index of community similarity were used as measures of α diversity and β diversity, respectively. The general β diversity patterns are shown here using the principal coordinates score for the first axis; Mantel tests conducted directly from the distance matrices confirm the significance of the correlation shown in (B) (Mantel $r = 0.95$, $P < 0.001$).

of soil microbial communities across environmental gradients, we can reconstruct these communities across the historical extent of the tallgrass prairie ecosystem.

We collected surface soils (top 10 cm) from 31 remnant native prairie sites (found primarily in cemeteries or nature preserves) that were carefully selected to span the range of climate conditions found throughout the tallgrass prairie ecosystem (fig. S2 and table S1). To the best of our knowledge, none of the sampled sites were ever tilled and all were dominated by native tallgrass prairie plant species (e.g., *Andropogon*, *Panicum*, and *Sorghastrum*) when soil samples were collected at the height of the growing season. To characterize the bacterial and archaeal communities, we pyrosequenced a polymerase chain reaction (PCR)-amplified region of the 16S rRNA gene (12) and compared relative diversity levels across the samples by standardizing sequencing depth to 940 reads per sample (13). Microbial α diversity (measured using the Shannon index, H') was not uniformly distributed across the tallgrass prairie (Fig. 1A and table S2). However, none of the measured edaphic variables were significantly correlated with taxonomic diversity ($P > 0.1$ in all cases). Instead, taxonomic diversity was most strongly correlated with precipitation levels (table S3), just as moisture availability is often a strong predictor of plant and animal diversity at comparable spatial scales (14).

To complement the taxonomic analyses and to characterize microbial functional diversity, we used shotgun metagenomics to determine the diversity of known protein-coding genes in each community (10, 12). All samples were compared at an equivalent survey depth of 1.8 million randomly selected annotated reads per sample. Although these annotations are based only on previously described genes and much of the

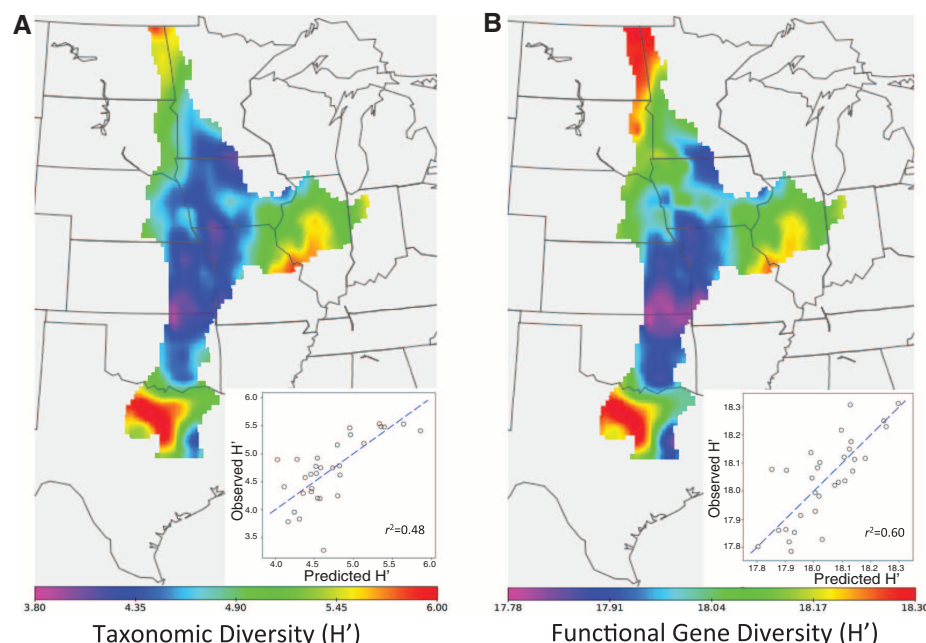


Fig. 2. Predicted diversity patterns (calculated using the Shannon index, H') of bacterial taxa (A) and functional genes (B). Inset plots show the cross-validation results, comparing observed and predicted diversity values for the 31 sampled locations.

functional diversity contained within soil [or other environments where the majority of taxa have not been well characterized (15)] is therefore missed, we did find that the functional diversity that could be annotated within the microbial communities correlated well with taxonomic diversity (Fig. 1A). There has been considerable debate in the field of ecology as to how the taxonomic diversity of communities relates to the observed functional, or trait-level, diversity (16); we found a strong positive correlation between the functional and taxonomic diversity

of soil microbial communities (Fig. 1A). This pattern is also commonly observed in plant and animal communities (17, 18). Therefore, the abundant soil microbial taxa do not appear to exhibit a high degree of functional redundancy (or equivalence), as is often assumed (19); reductions in taxonomic diversity were associated with decreases in the breadth of functional traits contained within these soil communities.

To extend our results beyond the 31 soils directly assayed, we constructed spatially explicit models of the taxonomic and functional diversity

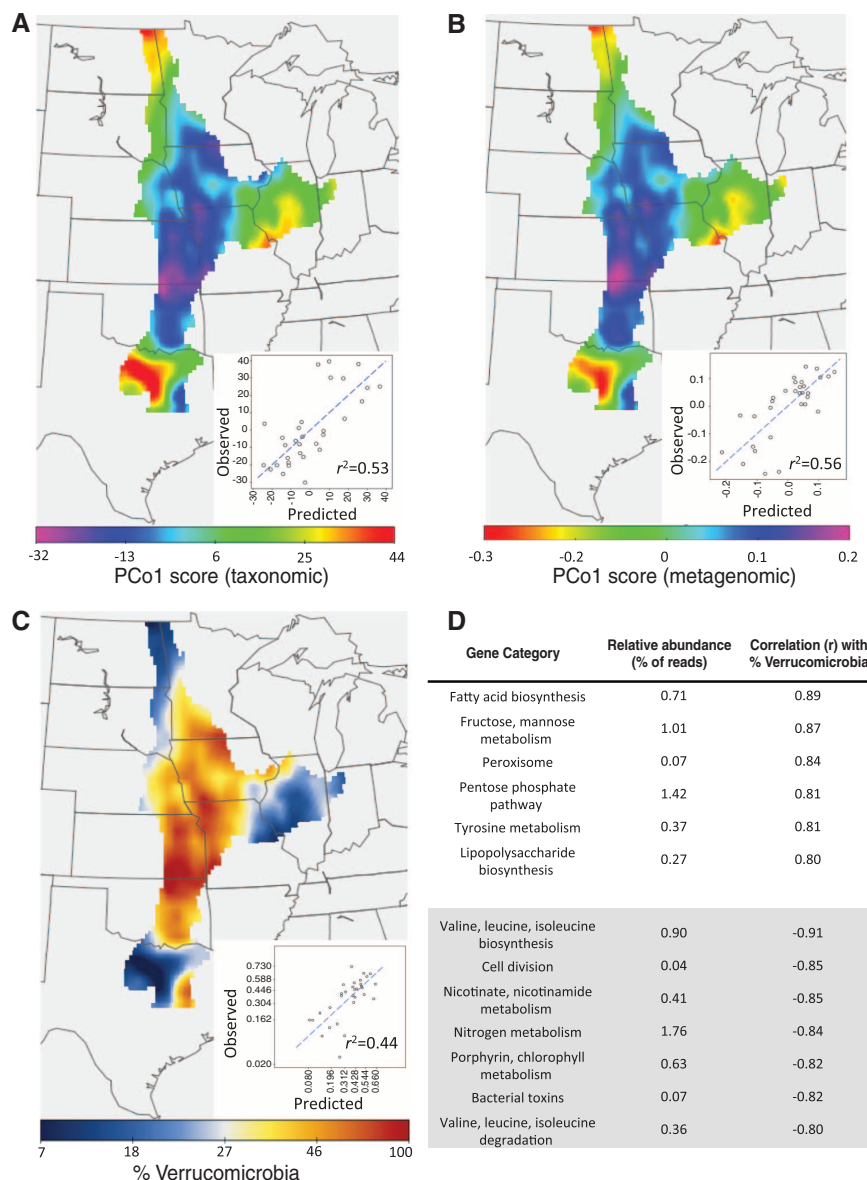


Fig. 3. Maps showing bacterial community types based on their taxonomic composition (A) or functional gene composition (B). Locations similar in hue indicate those communities that are more similar in composition. (C and D) The patterns shown in (A) and (B) appear to be largely driven by variation in verrucomicrobial abundances (% of reads) (C). Shown in (D) are functional gene categories strongly correlated with verrucomicrobial abundances, only including those gene categories represented by >0.001% of the shotgun metagenomic reads with r values greater than 0.8 or less than -0.8.

of soil bacterial communities throughout the historical extent of the native tallgrass prairie using a species distribution modeling approach (20, 21). These models were based solely on climatic variables (tables S3 and S4), not soil characteristics, because we do not know what soil characteristics would have been found across the biome >150 years ago when the native tallgrass prairie ecosystem was still intact (current soil maps are not likely to reflect historical soil properties that have been profoundly altered by decades of cultivation). The best-fit models of Shannon diversity were able to predict >50% of the variance in bacterial taxonomic and functional diversity across the sampled sites (table S3), a predictive power similar to

comparable models of regional plant or animal diversity (20), with soils from the middle latitudes having less taxonomic and functional diversity than those in the northernmost and southernmost portions of the range (Fig. 2). This pattern contrasts with the biogeographical patterns observed in many plant and animal communities where diversity often peaks in the middle of biomes, which suggests that the “mid-domain effect” (22), or related explanations for such diversity gradients, may not be broadly applicable across the tree of life.

The taxonomic composition of the microbial communities and their functional attributes varied considerably across the 31 sampled tallgrass prairie sites. Communities that were taxonomi-

cally similar were also similar with respect to their functional characteristics as these two distinct measures were well correlated (i.e., communities that shared many taxa in common also shared many functional attributes) (Fig. 1B). Model predictions of the patterns in community similarity show that the soils in the central portion of the tallgrass prairie range harbored communities that were taxonomically (Fig. 3A) and functionally (Fig. 3B) distinct from those found on the edges of the range. The relative abundances of many taxa changed across the sampled soils (table S2), but the α diversity patterns (Fig. 2) and the patterns in community similarity (Fig. 3) were both closely tied to changes in the relative abundance of Verrucomicrobia (Fig. 3C and table S2), the dominant bacterial phylum across the collected soils (fig. S2 and table S2). Although often underestimated (23), Verrucomicrobia represented >50% of the bacterial 16S rRNA sequences in the prairie soils from the mid-latitudes but only <15% of the sequences on the edges of the range (Fig. 3C and table S2). These patterns in verrucomicrobial abundances were nearly identical whether abundances were determined by the PCR-based 16S rRNA gene analyses or by analyzing the 16S rRNA genes recovered from the shotgun metagenomic data (fig. S3); this finding provides independent evidence for the high relative abundances of Verrucomicrobia in many of these soils.

Verrucomicrobia are clearly dominant in the tallgrass prairie soils, but their ecology remains poorly understood because members of this group are difficult to culture and study in the laboratory (23, 24). The Verrucomicrobia identified from the prairie soils were not diverse; only five phylogenotypes accounted for >75% of the verrucomicrobial sequences from this data set (fig. S4). All of the more abundant verrucomicrobial taxa were classified as belonging to the *Spartobacteria* class, but the taxa were not closely related to previously cultivated verrucomicrobial isolates (fig. S4), making it difficult to determine the ecological attributes of these taxa. Our understanding of soil microbial communities in prairie soils will clearly benefit from efforts to directly determine the phenotypes of the Verrucomicrobia that dominated the majority of the native tallgrass prairie soils.

Although the ecological attributes of these verrucomicrobial taxa cannot be directly assessed with these data, we used a niche-modeling approach in combination with the shotgun metagenomic data to gain some insight into the ecology of the Verrucomicrobia and to try to explain the distribution patterns shown in Fig. 3C. We found that spatial variability in the abundance of Verrucomicrobia could be predicted from climatic conditions (table S3) and that this group was most abundant in soils exposed to intermediate temperature and precipitation conditions (Fig. 3C and fig. S2). However, this correlation with climatic conditions may represent only a distal control on their distribution patterns. The shotgun metagenomic data lend support to the hypothesis that Verrucomicrobia are relatively slow-growing taxa

that thrive under conditions of limited nutrient availability (25, 26). Specifically, verrucomicrobial abundances were positively correlated with a variety of genes associated with carbohydrate metabolism but were negatively correlated with genes associated with nitrogen metabolism and cell division (Fig. 3D). Verrucomicrobia may thus represent a large component of below-ground communities in regions where changes in the quantity or quality of plant organic matter inputs constrain the growth of more copiotrophic taxa. This hypothesis is congruent with results indicating consistent declines in the relative abundances of Verrucomicrobia when soils from across North America were amended with nutrients (27). Likewise, this hypothesis is consistent with recent genomic information obtained from *Spartobacteria aquaticum*, an aquatic Verrucomicrobia that is within the same class as the dominant soil Verrucomicrobia observed here, that appears to specialize on the degradation of more recalcitrant carbon compounds (28).

Our reconstructions of microbial diversity and functional capabilities across the tallgrass prairie ecosystem could be used to guide and monitor the hundreds of prairie restoration efforts currently underway throughout the midwestern United States (29). Maps of the soil microbial communities that once existed in this ecosystem may provide targets to help improve the long-term success of prairie restoration efforts, as restoration efforts are often more successful when they also try to restore below-ground communities (30). Such information may be particularly important if the goal is to restore key ecosystem functions, such as soil carbon sequestration, that are strongly controlled by the below-ground communities. Likewise, deviation in soil microbial communities from the predicted pre-agricultural state could be used to quantify the extent of degradation experienced by soils throughout the native prairie range. More generally, this work demonstrates that we can use recent advances in high-throughput microbial community characterization to reconstruct the biogeographical patterns in the diversity and functional capabilities of microbes across a nearly extinct ecosystem. This approach could be extended more broadly to quantify how historical changes in environmental conditions may have altered the diversity and function of below-ground communities in other systems or to determine how human-induced climate change may alter ecosystem properties in the future.

References and Notes

- P. Sims, P. Risser, in *North American Terrestrial Vegetation*, M. Barbour, W. Billings, Eds. (Cambridge Univ. Press, New York, 2000), pp. 325–356.
- F. Samson, F. Knopf, W. Ostlie, *Wildl. Soc. Bull.* **32**, 6–15 (2004).
- F. Samson, F. Knopf, *Bioscience* **44**, 418–421 (1994).
- V. J. Allison, Z. Yermakov, R. M. Miller, J. D. Jastrow, R. Matamala, *Soil Biol. Biochem.* **39**, 505–516 (2007).
- D. R. Huggins et al., *Soil Tillage Res.* **47**, 219–234 (1998).
- K. Jangid et al., *Soil Biol. Biochem.* **42**, 302–312 (2010).
- S. G. Baer, D. J. Kitchen, J. M. Blair, C. W. Rice, *Ecol. Appl.* **12**, 1688–1701 (2002).
- E. J. Martinson et al., *Phys. Geogr.* **32**, 583–602 (2011).
- S. G. Tringe, E. M. Rubin, *Nat. Rev. Genet.* **6**, 805–814 (2005).
- N. Fierer et al., *Proc. Natl. Acad. Sci. U.S.A.* **109**, 21390–21395 (2012).
- N. Fierer, J. Ladau, *Nat. Methods* **9**, 549–551 (2012).
- N. Fierer et al., *ISME J.* **6**, 1007–1017 (2012).
- See supplementary materials on Science Online.
- B. A. Hawkins et al., *Ecology* **84**, 3105–3117 (2003).
- J. A. Gilbert, R. O'Dor, N. King, T. M. Vogel, *Microb. Inform. Exp.* **1**, 5 (2011).
- H. Hillebrand, B. Matthiessen, *Ecol. Lett.* **12**, 1405–1419 (2009).
- O. L. Petchey, K. J. Gaston, *Ecol. Lett.* **5**, 402–411 (2002).
- S. Diaz, M. Cabido, *Trends Ecol. Evol.* **16**, 646–655 (2001).
- M. Bradford, N. Fierer, in *Soil Ecology and Ecosystem Services*, D. Wall, Ed. (Oxford Univ. Press, Oxford, 2012), pp. 189–198.
- J. Franklin, J. Miller, *Mapping Species Distributions: Spatial Inference and Prediction* (Cambridge Univ. Press, New York, 2010).
- J. Ladau et al., *ISME J.* **7**, 1669–1677 (2013).
- R. K. Colwell, D. C. Lees, *Trends Ecol. Evol.* **15**, 70–76 (2000).
- G. T. Bergmann et al., *Soil Biol. Biochem.* **43**, 1450–1455 (2011).
- S. J. Joseph, P. Hugenholtz, P. Sangwan, C. A. Osborne, P. H. Janssen, *Appl. Environ. Microbiol.* **69**, 7210–7215 (2003).
- U. N. da Rocha, F. D. Andreote, J. L. Azevedo, J. D. van Elsas, L. van Overbeek, *J. Soils Sed.* **10**, 326–339 (2010).
- P. H. Janssen, P. S. Yates, B. E. Grinton, P. M. Taylor, M. Sait, *Appl. Environ. Microbiol.* **68**, 2391–2396 (2002).
- K. S. Ramirez, J. M. Craine, N. Fierer, *Glob. Change Biol.* **18**, 1918–1927 (2012).
- D. P. Herlemann et al., *mBio* **4**, e00569-12 (2013).
- J. Harris, *Science* **325**, 573–574 (2009).
- P. Kardol, D. A. Wardle, *Trends Ecol. Evol.* **25**, 670–679 (2010).

Acknowledgments: We thank K. McLauchlan and three anonymous reviewers for their critical feedback on earlier versions of the manuscript; R. Jackson for his help with soil collection and analyses; and J. Henley for her help with the laboratory analyses. Supported by NSF grants DEB-0953331 (N.F.) and DMS-1069303 (K.S.P.), the Howard Hughes Medical Institute (R.K.), Gordon and Betty Moore Foundation grant 3300 (K.S.P.), U.S. Department of Energy contract DE-AC02-06CH11357 (J.A.G.), and USDA National Research Initiative 2005-35101-15335/17371 (R.L.M.). All amplicon data have been deposited in the European Nucleotide Archive under accession number ERP003610; the accession number for the shotgun metagenomic data is ERP003954. Data have also been made available through the Dryad data depository.

Supplementary Materials

www.sciencemag.org/content/342/6158/621/suppl/DC1
Materials and Methods
Figs. S1 to S4
Tables S1 to S4
References (31–50)

25 July 2013; accepted 2 October 2013
10.1126/science.1243768

Structural Basis for flg22-Induced Activation of the *Arabidopsis* FLS2-BAK1 Immune Complex

Yadong Sun,^{1*} Lei Li,^{2*} Alberto P. Macho,³ Zhifu Han,^{1†} Zehan Hu,¹ Cyril Zipfel,³ Jian-Min Zhou,^{2†} Jijie Chai^{1†}

Flagellin perception in *Arabidopsis* is through recognition of its highly conserved N-terminal epitope (flg22) by flagellin-sensitive 2 (FLS2). Flg22 binding induces FLS2 heteromerization with BRASSINOSTEROID INSENSITIVE 1-associated kinase 1 (BAK1) and their reciprocal activation followed by plant immunity. Here, we report the crystal structure of FLS2 and BAK1 ectodomains complexed with flg22 at 3.06 angstroms. A conserved and a nonconserved site from the inner surface of the FLS2 solenoid recognize the C- and N-terminal segment of flg22, respectively, without oligomerization or conformational changes in the FLS2 ectodomain. Besides directly interacting with FLS2, BAK1 acts as a co-receptor by recognizing the C terminus of the FLS2-bound flg22. Our data reveal the molecular mechanisms underlying FLS2-BAK1 complex recognition of flg22 and provide insight into the immune receptor complex activation.

Innate immunity in higher eukaryotes relies on the perception of conserved signature components of pathogens, termed pathogen-associated molecular patterns (PAMPs), by plasma membrane-localized pattern recognition receptors (PRRs). In

plants, PRRs are mainly receptor kinases (RKs) or receptor-like proteins, and several of them carry leucine-rich repeats (LRRs) in their ectodomains for PAMP recognition. Upon recognition of PAMPs, PRRs initiate an array of shared immune responses, leading to PAMP-triggered immunity (1).

Present in most higher plant species and critical for antibacterial immunity (1), flagellin-sensitive 2 (FLS2) is an LRR-RK and acts as the PRR for bacterial flagellin by recognizing the epitope flg22 (2–6). Direct recognition of flg22 by FLS2 is sufficient for inducing immune responses, establishing FLS2 as a flagellin receptor (7). Flg22 binding nearly instantly triggers FLS2 association with the LRR-RK BRI1-associated kinase 1 (BAK1) (8, 9). BAK1 also interacts with the LRR-RK

¹School of Life Sciences, Tsinghua University, Beijing 100084, China, and Tsinghua-Peking Center for Life Sciences, Beijing 100084, China. ²State Key Laboratory of Plant Genomics and National Center for Plant Gene Research, Institute of Genetics and Developmental Biology, Chinese Academy of Sciences, Beijing 100101, China. ³The Sainsbury Laboratory, Norwich Research Park, Norwich NR4 7UH, UK.

*These authors contributed equally to this work.

†Corresponding author. E-mail: chajijie@mails.tsinghua.edu.cn (J.C.); jmjzhou@genetics.ac.cn (J.-M.Z.); hanzhifu@mails.tsinghua.edu.cn (Z.Han)

Fig. 1. Ectodomains mediate the flg22-induced heterodimerization of FLS2 and BAK1. (A) Overall structure of FLS2LRR-flg22-BAK1LRR. The positions of LRR3 and LRR16 are indicated by blue numbers. "N" and "C" represent the N and C terminus, respectively. Color codes are indicated. (B) Flg22 binds to a shallow groove at the inner surface of the FLS2LRR solenoid. FLS2LRR is shown in electrostatic surface (in transparency). The FLS2LRR-interacting residues in flg22 are shown stick. I, Ile; Q, Gln. White, blue, and red indicate neutral, positive, and negative surfaces, respectively. Detailed interactions of the left and right highlighted regions are shown in Fig. 2, A and B, respectively. (C) Structural comparison of the ligand-bound FLS2LRR with the free FLS2 Δ LRR2-6. For clarity, the N- and C-terminal sides of the flg22-bound FLS2LRR are not shown. Numbers in blue indicate the positions of LRRs.

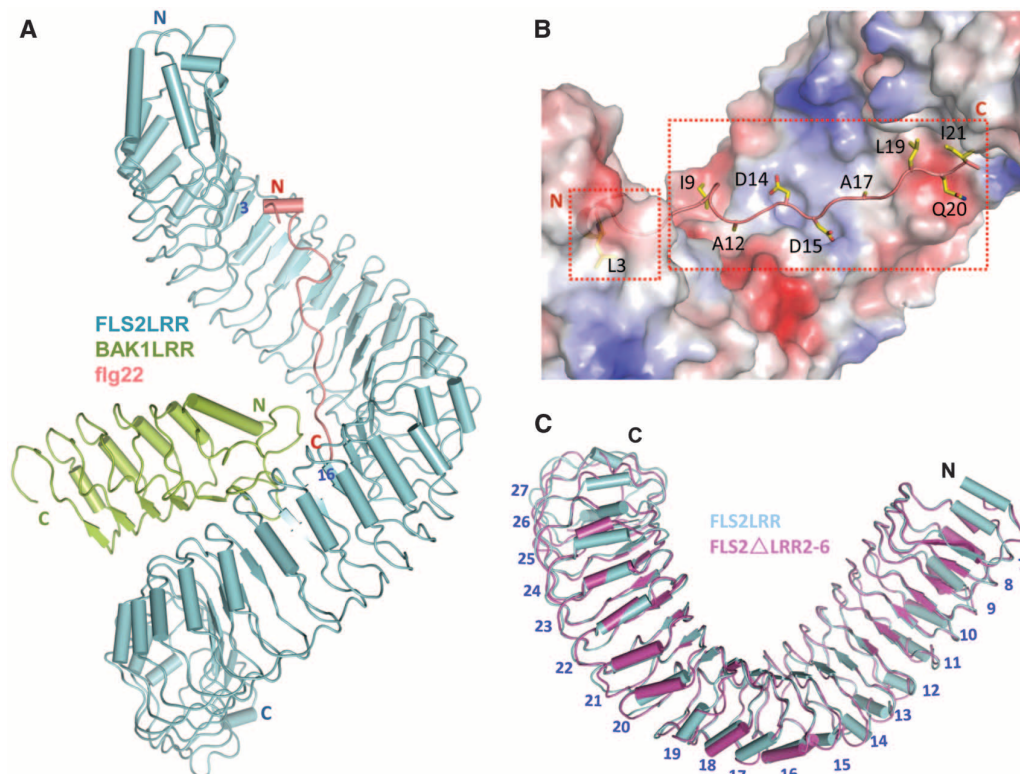
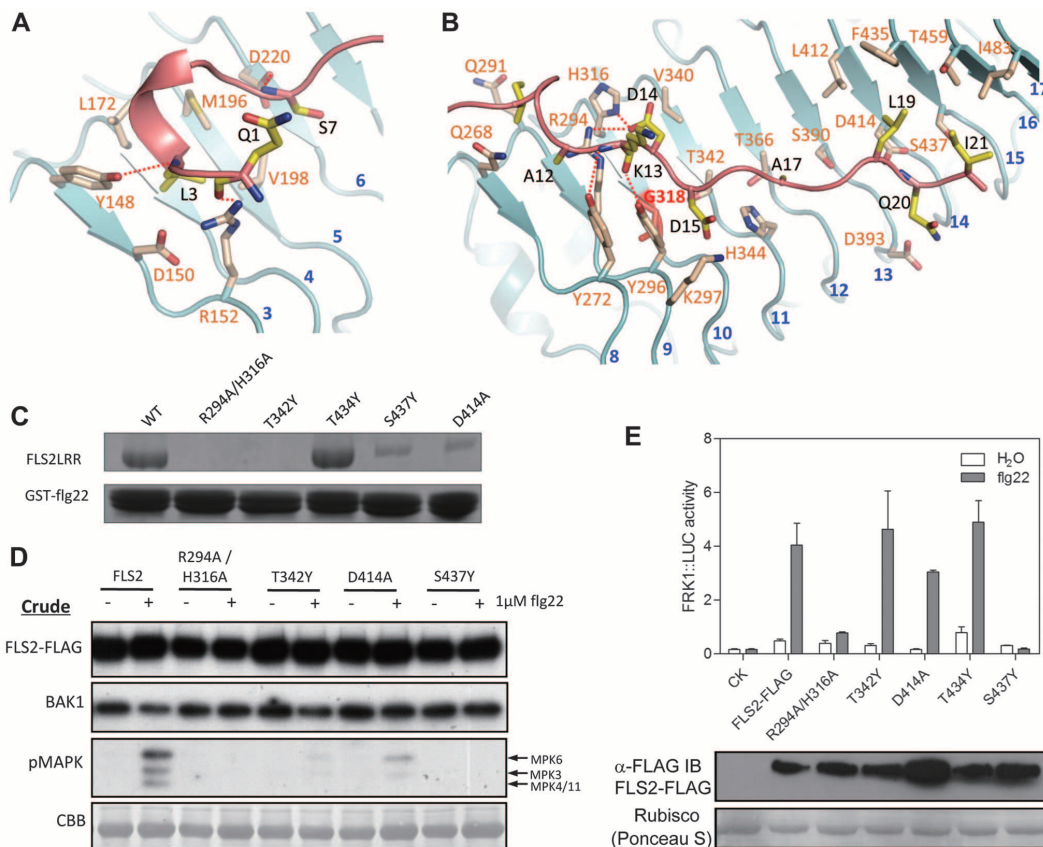


Fig. 2. Mechanism of flg22 recognition by FLS2. (A) Interaction of the N-terminal portion (residues 1 to 7) of flg22 with FLS2LRR. The side chains FLS2LRR and flg22 are labeled in cream white and yellow, respectively. (B) Interaction of the C-terminal side (residues 8 to 21) of flg22 with FLS2LRR. FLS2 Gly³¹⁸ is indicated in red. K, Lys; S, Ser; T, Thr. (C) FLS2LRR mutations reduce interaction with GST-flg22. GST-flg22 bound to GS4B agarose was used to precipitate various FLS2LRR wild-type (WT) and mutant proteins. The bound proteins were visualized by SDS-polyacrylamide gel electrophoresis (PAGE) with Coomassie blue staining. The assay was repeated three times. (D) FLS2 mutations compromise MPK phosphorylation. Null *fls2* mutant mesophyll protoplasts were transfected with plasmids as indicated. The samples were separated into two and treated with water (-) or 1 μ M flg22 (+). Immunoblots were analyzed by using antibodies against FLAG, BAK1, or pMPK. CBB, Coomassie brilliant blue. (E) FLS2 mutations attenuate flg22-induced *FRK1::LUC* expression. Null *fls2* mutant *Arabidopsis* mesophyll protoplasts were transfected with plasmids as indicated along with *35S::R-LUC* and *FRK1::LUC*. The *FRK1::LUC* activity was determined after protoplasts were treated with 1.0 μ M flg22 for 10 min. IB, immunoblot.



BR INSENSITIVE 1 (BRI1) to positively regulate brassinosteroid (BR) signaling (10, 11). BAK1 is also called SERK3, a member of the subfamily of SERK LRR-RKs (12).

BAK1 also forms heteromers with several other PRRs and is a major component of plant immunity (13, 14). The flg22-induced FLS2-BAK1 heteromerization results in their trans-phosphorylation (8, 9, 15). Flg22 also induces FLS2- and BAK1-dependent phosphorylation of BIK1 (BOTRYTIS-INDUCED KINASE 1, a receptor-like cytoplasmic kinase) and dissociation of BIK1 from FLS2 for plant immunity (16, 17).

To confirm that the ectodomains of FLS2 and BAK1 are sufficient to form an flg22-induced complex, we used glutathione *S*-transferase (GST) precipitation, gel filtration, and coimmunoprecipitation (Co-IP) to assay their interaction. Collectively, the data from these assays (fig. S1) showed that the extracellular LRR domains of *Arabidopsis* FLS2 (residues 25 to 800, FLS2LRR) and BAK1 (residues 1 to 220, BAK1LRR) formed a monomeric heterodimer induced by flg22. But it remains possible that full-length FLS2 forms homo-oligomers (18).

To understand the molecular mechanism underlying FLS2 recognition of flg22, we solved the crystal structure of the FLS2LRR-flg22-BAK1LRR

complex at 3.06 Å (Fig. 1A and table S1). None of the dimeric packing related by crystallographic symmetry can be biologically relevant (fig. S2), further supporting the gel filtration data (fig. S1B). This is in contrast with flagellin-induced Toll-like receptor 5 (TLR5) homodimerization (19). The structure of FLS2LRR is superhelical (fig. S3) and resembles that of BRI1LRR (20, 21). Flg22, which is well defined by electron density but the last residue (fig. S4), binds to the concave surface of FLS2LRR by running across 14 LRRs (LRR3 to LRR16) (Fig. 1, A and B), confirming previous hypotheses (22, 23). The flg22 binding groove is largely conserved in tomato FLS2 (fig. S5). The FLS2LRR-BAK1LRR heterodimerization is both flg22- and receptor-mediated. The C terminus of flg22 is sandwiched between FLS2LRR and BAK1LRR, whereas direct FLS2LRR-BAK1LRR interactions stem from anchoring of BAK1LRR to the C-terminal portion of FLS2LRR (Fig. 1A). The structural organization of FLS2LRR-BAK1LRR differs from the m-shaped homo- or heterodimeric TLRs (24). Nonetheless, the C-termini of BAK1LRR and FLS2LRR are similarly oriented, presumably pointing to the membrane surface.

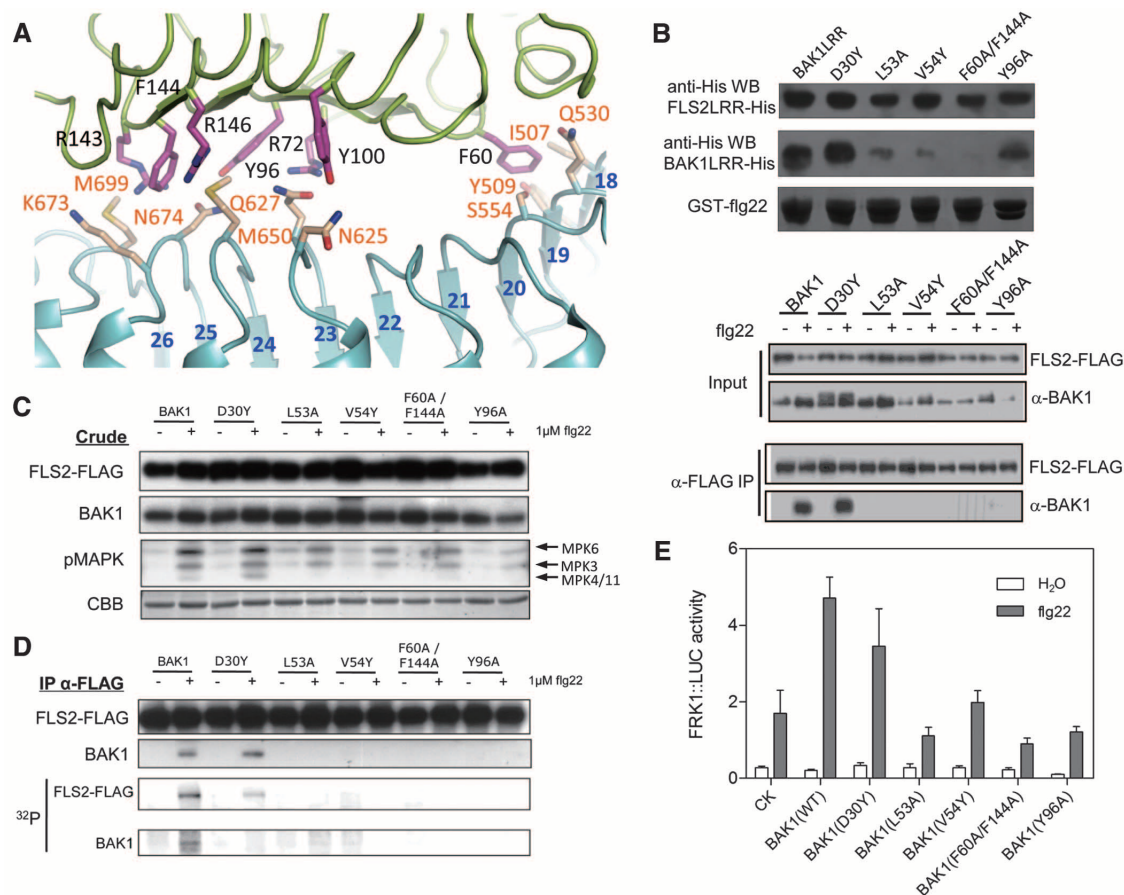
Interactions of flg22 with FLS2LRR can be divided into two parts separated by a kink (flg22

Asn¹⁰ and Ser¹¹) in the central region of the peptide (Fig. 1B). Before the kink, the N-terminal seven residues bind to FLS2 LRR2 to LRR6 (FLS2LRR2-6) (Fig. 2A). Thus, deletion of these four LRRs would negate FLS2 interaction with the N- but not the C-terminal segment of flg22, phenocopying an flg22 variant with the N-terminal seven residues deleted (flg15) (4). Indeed, an FLS2LRR mutant with five LRRs deleted, FLS2ΔLRR2-6, still formed an flg22-induced complex with BAK1LRR (fig. S6). Structural superposition of the FLS2ΔLRR2-6 mutant with FLS2LRR bound by flg22 and BAK1LRR showed that the two structures are nearly identical (Fig. 1C), with a root mean square deviation = 0.43 Å over 543 Cα-aligned atoms, suggesting that, in the cellular milieu as well, conformational changes in FLS2LRR may not be necessary for flg22 binding and heterodimerization with BAK1LRR.

Both hydrogen bonds and hydrophobic contacts mediate flg22 interaction with FLS2LRR. Flg22 Leu³ inserts into a hydrophobic pocket of FLS2 (Fig. 2A). In addition to hydrophobic contacts, FLS2 Arg¹⁵² and FLS2 Tyr¹⁴⁸ also engage hydrogen bonds with flg22 Gln¹ and flg22 Leu³, respectively. The two residues are highly varied in tomato FLS2 (fig. S5), which can adversely

Fig. 3. Direct FLS2LRR-BAK1LRR interactions.

(A) The C-terminal side of FLS2LRR mediates its interaction with BAK1. M, Met; N, Asn. (B) Direct contacts of FLS2 and BAK1 are required for their interaction. (Top) The assays were performed as described in Fig. 2C except that FLS2LRR and BAK1LRR were analyzed by antibodies against His (anti-His). The assay was repeated for three times. (Bottom) Mutagenesis assays for BAK1 mutants in null *bak1-4* mutant mesophyll protoplasts. FLAG- and hemagglutinin (HA)-tagged FLS2 and BAK1 constructs were coexpressed in WT *Arabidopsis* protoplasts. Co-IP assay was performed to detect FLS2-BAK1 interaction after treatment with (+) or without (-) 1.0 μM flg22. (C) Mutations of the FLS2-interacting residues in BAK1 compromise MPK phosphorylation. The assays were performed as described in Fig. 2D. (D) Mutations of the FLS2-interacting residues in BAK1 compromise FLS2 and BAK1 phosphorylation. Immunoprecipitated FLS2-FLAG was incubated in the presence of radioactive [³²P]γ-ATP (adenosine triphosphate). Immunoblots were analyzed by using antibodies against FLAG or BAK1. In vitro phosphorylation is



revealed by autoradiography (i.e., ³²P). (E) FLS2-BAK1 interactions are important for flg22-induced FRK1 expression. The assays were performed as described in Fig. 2E. Error bars indicate SEM.

affect recognition of the N-terminal part of flg22 by the latter. This may explain the fact that flg15 displays a low activity in *Arabidopsis* but is fully active in tomato cells (23). The C-terminal 14 amino acids, particularly those after the kink, form denser interactions with FLS2LRR, burying a surface area of 1817 Å² compared with 373 Å² by the N-terminal seven amino acids. Consistently, flg15 still bound FLS2LRR (fig. S7A), agreeing with previous cell-based assays (3). Flg22 Asp¹⁴ and Asp¹⁵, important for FLS2 interacting (fig. S7A) and immunogenic activities (3), bind to two positively charged pockets (Figs. 1B and 2B). The hydrogen bonds formed between FLS2 Tyr²⁷² and Tyr²⁹⁶ and flg22 Lys¹³ also contribute to the interactions around this interface. In contrast, flg22 Asn¹⁰ and flg22 Lys¹³ (whose side chain is not involved in interaction with FLS2LRR) are solvent-exposed (fig. S4), and their mutations generated little effect on the flg22 activity (3). Flg22 Leu¹⁹ and Ile²¹ bind to two neighboring hydrophobic pockets. Mutation of flg22 Ala¹⁷ that contacts FLS2 Thr³⁶⁶ underneath to tyrosine (Fig. 2B) reduced flg22 interaction with FLS2LRR (fig. S7A). All the amino acids critical for flg22 binding to FLS2LRR are conserved among FLS2-activating bacteria (fig. S8).

Further supporting our structural observations, a precipitation assay showed that FLS2 with two mutations, Arg²⁹⁴ and His³¹⁶ to Ala (24), R294A/H316A, resulted in no FLS2LRR-flg22

interaction (Fig. 2C), phenocopying flg22 D14A (D, Asp) (3). FLS2 Thr³⁴² is located immediately underneath the peptide (Fig. 2B). Mutation of this residue, but not the unrelated FLS2 Thr⁴³⁴, to the bulkier tyrosine abolished the interaction with GST-flg22. Consistently, FLS2 G318R (G, Gly) (Fig. 2B) caused by ethyl methanesulfonate-induced mutation *fls2-24* does not bind flg22 (4). Mutations of other FLS2 residues from the interface also compromised interaction with GST-flg22 (Fig. 2C). The mutations affecting FLS2LRR recognition of flg22 disrupted flg22-induced FLS2-BAK1 interaction in *Arabidopsis* protoplasts (fig. S9). Furthermore, flg22-induced FLS2 and BAK1 phosphorylation (fig. S9), mitogen-activated protein kinase (MPK) activation (Fig. 2D) and expression of *FRK1::LUC* (Fig. 2E), a reporter gene induced by multiple PAMPs, were also attenuated when the FLS2 mutants were transiently expressed in null *fls2* mesophyll protoplasts. Together, these results indicate that these residues are functionally important in the plant cell.

A cluster of bulky BAK1 amino acids, including Arg⁷², Tyr⁹⁶, Tyr¹⁰⁰, Arg¹⁴³, Phe¹⁴⁴, and Arg¹⁴⁶, directly contacts with those from FLS2LRR23-26 (Fig. 3A), whereas BAK1Phe⁶⁰ interacts with residues from FLS2LRR18-20. These FLS2-interacting residues are conserved between *Arabidopsis* BAK1 and tomato SERK3 (fig. S10). Supporting the structural observations,

BAK1 F60A/F144A (F, Phe) and BAK1 Y96A (Y, Tyr), but not the negative control BAK1 D30Y, attenuated flg22-induced FLS2-BAK1 heterodimerization in the precipitation assay and in null mutant *bak1-4* mesophyll protoplasts (Fig. 3B). These critical BAK1 amino acids were also important for flg22-induced FLS2 and BAK1 phosphorylation (Fig. 3, C and D). The activation of MPKs by flg22 seems differently affected by the BAK1 mutations, because the activation of MPK3 and MPK6 was slightly diminished 10 min after treatment with the peptide, whereas MPK4/MPK11 was not activated to a detectable level at the same time point (Fig. 3C). Moreover, unlike wild-type BAK1, these critical BAK1 mutants (Fig. 3E) only partially restored the expression of *FRK1::LUC* to null mutant *bak1-4* mesophyll protoplasts. Consistently, the BAK1 L53A, V54Y, and Y96A (L, Leu; V, Val) transgenic lines were abolished or severely compromised in production of reactive oxygen species (fig. S11).

The C-terminal segment of flg22 bridges FLS2LRR and BAK1LRR (Fig. 1A), reminiscent of auxin that act as a molecular “glue” to connect its receptor with a signaling partner (25). Flg22 Gly¹⁸, conserved among the FLS2-activating bacterial flagellins but not in non-FLS2-eliciting bacteria (fig. S8), fits in the inner-curved loop (residues 52 to 54) of BAK1 but makes no contact with FLS2LRR (Fig. 4A). Flg22-BAK1LRR

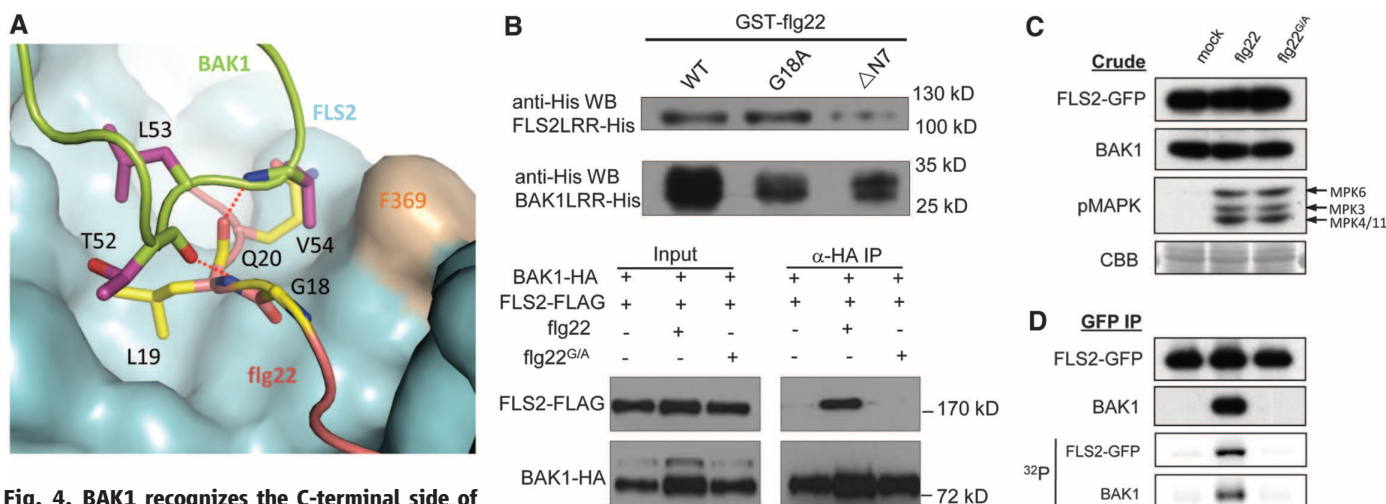
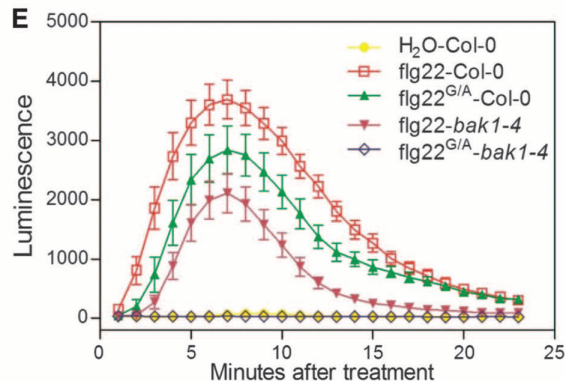


Fig. 4. BAK1 recognizes the C-terminal side of the FLS2-bound flg22. (A) A selective role of flg22 Gly¹⁸ in interaction with BAK1. FLS2LRR is shown in surface (blue), with flg22 (salmon) and BAK1LRR (green). The side chains from BAK1LRR and flg22 are shown in purple and yellow, respectively. (B) Gly¹⁸ is required for the flg22-induced FLS2LRR-BAK1LRR interaction but not for FLS2 binding in vitro and in null *fls2* mutant mesophyll protoplasts. The assays were performed as described in Fig. 3B. (C) The Flg22 G18A mutation has little effect on MPK phosphorylation in mesophyll protoplasts. The assays were performed as described in Fig. 2D. (D) Gly¹⁸ is required for flg22-induced FLS2-BAK1 interaction and the complex activation in seedlings. The assays were performed as described in Fig. 3D. GFP, green fluorescent protein. (E) The flg22 G18A mutation modestly affects generation of ROS in planta. WT *Arabidopsis* leaves were treated with water, 100 nM flg22, or 100 nM flg22 G18A.

WT *Arabidopsis* leaves were treated with water, 100 nM flg22, or 100 nM flg22 G18A.



interaction is further stabilized by two hydrogen bonds formed between Flg22 Leu¹⁹ and BAK1 Thr⁵² and Val⁵⁴. Limited by space, any other amino acids at flg22 Gly¹⁸ would generate steric clashes with the BAK1 loop and consequently attenuate their interaction. Supporting this hypothesis, the mutant peptides flg22 G18A and flg22 G18Y, although they had a comparable FLS2LRR binding activity with the wild-type peptide, exhibited a compromised and no activity of inducing FLS2LRR-BAK1LRR interaction, respectively, in the GST precipitation and Co-IP assay in protoplasts (Fig. 4B and fig. S7B). The mutant peptide flg22 G18A seemed to activate MPKs as efficiently as the wild-type flg22 (Fig. 4C), although it failed to induce an interaction and activation between FLS2 and BAK1 (Fig. 4D). Nevertheless, the generation of reactive oxygen species (ROS) in *Arabidopsis* wild-type Col-0 leaves induced by flg22 G18A and flg22 G18Y was modestly and strongly reduced, respectively (Fig. 4E and fig. S12). The phenotypes generated by the mutations of flg22G¹⁸ are reminiscent of the *bik1* mutant that is substantially compromised in PAMP-induced resistance but not the flg22-induced MPK activation (26), indicating that downstream signaling is differentially affected by perturbations to the receptor complex. An flg22 mutant lacking the C-terminal two residues acts antagonistically with the wild-type peptide (3, 23). This deletion, although not disrupting interaction with FLS2LRR (Fig. 4B and fig. S7), exposes a free carboxylic acid that may perturb the flg22 Gly¹⁸-mediated FLS2LRR-BAK1LRR interaction.

As observed for the TLR heterodimers (24), the flg22-induced FLS2-BAK1 complex does not seem to be homo-oligomeric for its activation. Ligand-induced homodimerization has been demonstrated in chitin elicitor receptor kinase 1 activation (27). Thus, ligand-induced homo- or heterodimerization appears to be a common mechanism of plant receptor kinases and TLRs (24) for signaling. TLR4 and its co-receptor, MD-2, homodimerize after lipopolysaccharide binding (28), presumably because of the lack of an intracellular signaling domain in MD-2. Similarly, homodimerization or oligomerization could be important for activation of those receptor kinases that form ligand-induced heteromers with receptor-like proteins lacking an intracellular kinase domain.

The sequential recognition of flg22 by FLS2 and BAK1 is required to form a signaling-active complex (Figs. 2 to 4), indicating that BAK1 acts as a co-receptor with FLS2. One feature of the mammalian co-receptors is their promiscuity in ligand binding (29). This may also hold true for BAK1 as a co-receptor, because it forms ligand-dependent heteromers with several RKs (13, 14). Indeed, a recent study showed that SERK1 and most likely BAK1 are co-receptors with BRI1 (30). The two interfaces between FLS2LRR and BAK1LRR seems collaborative, because mutations in either of them led to a great reduction or loss of FLS2-BAK1 interaction (Figs. 3

and 4). The direct FLS2LRR-BAK1LRR interface could be responsible for formation of the flg22-independent FLS2-BAK1 complex detected in some studies (9, 13, 15), but it remains possible that the interface is induced by BAK1 recognition of the FLS2-bound flg22. Future studies differentiating the two possibilities will help unravel the mechanism of flg22-induced FLS2-BAK1 activation.

References and Notes

1. T. Boller, G. Felix, *Annu. Rev. Plant Biol.* **60**, 379–406 (2009).
2. C. Zipfel *et al.*, *Nature* **428**, 764–767 (2004).
3. G. Felix, J. D. Duran, S. Volko, T. Boller, *Plant J.* **18**, 265–276 (1999).
4. L. Gómez-Gómez, T. Boller, *Mol. Cell* **5**, 1003–1011 (2000).
5. T. Meindl, T. Boller, G. Felix, *Plant Cell* **12**, 1783–1794 (2000).
6. Z. Bauer, L. Gómez-Gómez, T. Boller, G. Felix, *J. Biol. Chem.* **276**, 45669–45676 (2001).
7. D. Chinchilla, Z. Bauer, M. Regenass, T. Boller, G. Felix, *Plant Cell* **18**, 465–476 (2006).
8. D. Chinchilla *et al.*, *Nature* **448**, 497–500 (2007).
9. B. Schulze *et al.*, *J. Biol. Chem.* **285**, 9444–9451 (2010).
10. K. H. Nam, J. Li, *Cell* **110**, 203–212 (2002).
11. J. Li *et al.*, *Cell* **110**, 213–222 (2002).
12. V. Hecht *et al.*, *Plant Physiol.* **127**, 803–816 (2001).
13. M. Roux *et al.*, *Plant Cell* **23**, 2440–2455 (2011).
14. A. Heese *et al.*, *Proc. Natl. Acad. Sci. U.S.A.* **104**, 12217–12222 (2007).
15. B. Schwessinger *et al.*, *PLOS Genet.* **7**, e1002046 (2011).
16. D. Lu *et al.*, *Proc. Natl. Acad. Sci. U.S.A.* **107**, 496–501 (2010).
17. J. Zhang *et al.*, *Cell Host Microbe* **7**, 290–301 (2010).
18. W. Sun *et al.*, *Plant Cell* **24**, 1096–1113 (2012).
19. S. I. Yoon *et al.*, *Science* **335**, 859–864 (2012).

20. J. She *et al.*, *Nature* **474**, 472–476 (2011).
21. M. Hothorn *et al.*, *Nature* **474**, 467–471 (2011).
22. F. M. Dunning, W. Sun, K. L. Jansen, L. Helft, A. F. Bent, *Plant Cell* **19**, 3297–3313 (2007).
23. K. Mueller *et al.*, *Plant Cell* **24**, 2213–2224 (2012).
24. D. H. Song, J. O. Lee, *Immunol. Rev.* **250**, 216–229 (2012).
25. X. Tan *et al.*, *Nature* **446**, 640–645 (2007).
26. F. Feng *et al.*, *Nature* **485**, 114–118 (2012).
27. T. Liu *et al.*, *Science* **336**, 1160–1164 (2012).
28. B. S. Park *et al.*, *Nature* **458**, 1191–1195 (2009).
29. K. Myhre, G. C. Globe, *Cell. Signal.* **21**, 1548–1558 (2009).
30. J. Santiago, C. Hensler, M. Hothorn, *Science* **341**, 889–892 (2013); 10.1126/science.1242468.

Acknowledgments: We thank S. Huang and J. He at Shanghai Synchrotron Radiation Facility (SSRF) for assistance with data collection. This research was funded by State Key Program of National Natural Science of China (31130063) and the National Outstanding Young Scholar Science Foundation of China (31025008) to J.C.; Chinese Natural Science Foundation (31230007) and Chinese Ministry of Science and Technology (2011CB100700) to J.-M.Z.; and the Gatsby Charitable Foundation and the European Research Council to C.Z. A.P.M. is supported by a postdoctoral fellowship from the Federation of European Biochemical Societies. The coordinates and structural factors for FLS2LRR-flg22-BAK1LRR and FLS2 Δ LRR-6 have been deposited in Protein Data Bank with accession codes 4MN8 and 4MNA, respectively.

Supplementary Materials

www.sciencemag.org/content/342/6158/624/suppl/DC1
Materials and Methods
Figs. S1 to S12
Table S1
References (31–38)

26 July 2013; accepted 30 September 2013
Published online 10 October 2013;
10.1126/science.1243825

Regulation of Temperature-Responsive Flowering by MADS-Box Transcription Factor Repressors

Jeong Hwan Lee,¹ Hak-Seung Ryu,¹ Kyung Sook Chung,¹ David Posé,^{2*} Soonkap Kim,¹ Markus Schmid,² Ji Hoon Ahn^{1†}

Changes in ambient temperature affect flowering time in plants; understanding this phenomenon will be crucial for buffering agricultural systems from the effects of climate change. Here, we show that levels of *FLM- β* , an alternatively spliced form of the flowering repressor *FLOWERING LOCUS M*, increase at lower temperatures, repressing flowering. *FLM- β* interacts with SHORT VEGETATIVE PHASE (SVP); SVP is degraded at high temperatures, reducing the abundance of the SVP–*FLM- β* repressor complex and, thus, allowing the plant to flower. The *svp* and *flm* mutants show temperature-insensitive flowering in different temperature ranges. Control of SVP–*FLM- β* repressor complex abundance via transcriptional and splicing regulation of *FLM* and posttranslational regulation of SVP protein stability provides an efficient, rapid mechanism for plants to respond to ambient temperature changes.

For plants, successful reproduction requires careful timing of flowering to match pollinator availability and growing-season temperature restrictions. Multiple environmental factors, including day length and temperature, affect this crucial change from vegetative to reproductive growth (1–3). Various components regulate flower-

ing in response to extremes in temperature such as cold (vernalization) or heat stress (4, 5). Small changes in ambient temperature also affect flowering time (6–8), with colder temperatures generally delaying flowering. However, our understanding of ambient temperature-responsive flowering remains limited. Because day length and temperature

vary with latitude, flowering responses condition the global distribution of plant species. Therefore, identifying the key components in the regulation of ambient temperature responses and examining their interactions will help limit the effects of climate change on agricultural productivity (9, 10).

To identify the component(s) functioning in ambient temperature-responsive flowering, we first identified different wild *Arabidopsis* isolates from specific geographic locations, or accessions, that do not respond to ambient temperature. To do this, we screened the flowering time, as measured by leaf number at flowering, of 57 *Arabidopsis thaliana* accessions at different ambient temperatures (23° and 16°C) under long-day (LD) conditions (see supplementary materials and methods and table S1). The sample set included 55 rapid-cycling accessions, which have nonfunctional *FRIGIDA* (*FRI*) and *FLOWERING LOCUS C* (*FLC*) alleles (11–13). We mainly used accessions with nonfunctional *FRI* and *FLC* alleles because *FLC* has a large effect on flowering at low temperature (14). Nd-0, a high-temperature-insensitive accession under short-day (SD) conditions (15) in which *FLOWERING LOCUS M* (*FLM*) is deleted (16), flowered with similar leaf numbers at 23° and 16°C (fig. S1), confirming that a loss of *FLM* activity leads to flowering that is not affected by high or low ambient temperatures in rapid-cycling accessions (15).

To investigate whether ambient temperature regulates *FLM*, we used a *gFLM::GUS* reporter to examine *FLM* expression. *FLM* was expressed in the leaf and shoot apical region at 23° and 16°C, and its expression increased in the leaf vasculature at 16°C (fig. S2). *FLM* transcript is alternatively spliced and expression of the *FLM-β* transcript, which encodes the functional *FLM-β* (17), increased in both leaves and the shoot apex at 16°C. By contrast, *FLM-α* and *FLM-δ*, which may encode non-canonical proteins, were down-regulated at the apex at 16°C (fig. S2). Thus, temperature-dependent alternative splicing may regulate *FLM* activity in ambient temperature-responsive flowering (18). Similar results were observed in 13 accessions, irrespective of whether they were temperature-sensitive, and causative polymorphisms that may affect *FLM* alternative splicing were not identified (fig. S3). Mutations in the photoperiod and autonomous pathway genes and vernalization and gibberellic acid treatments did not affect *FLM* expression (fig. S4). These data suggest that ambient temperature regulates *FLM* expression (15).

FLOWERING LOCUS M is a MADS-box protein that can assemble into multimeric protein com-

plexes (19, 20). We used yeast two-hybrid screens to identify *FLM*-interacting proteins, screening $\sim 1.8 \times 10^7$ yeast transformants with an *Arabidopsis* seedling cDNA library, using *FLM-β* as bait. This screen identified SHORT VEGETATIVE PHASE (*SVP*) (table S2 and fig. S5), a regulator of ambient temperature-responsive flowering (21), suggesting that a *SVP-FLM-β* complex might regulate flowering in response to ambient temperature. Unlike *svp* (see below), mutants of the other interactors identified in this screen did not show ambient temperature-insensitive flowering (fig. S6); therefore, we concentrated our subsequent analysis on *SVP*.

To investigate the temperature range of *FLM* function, we examined the temperature responses of *flm*, *flc*, and *svp* mutants (15, 21) between 27° and 5°C, the typical daily temperature range experienced by wild *Arabidopsis* plants (22). Lower temperatures delayed flowering of wild-type (WT)

plants (Fig. 1A). By contrast, *svp-32* mutants flowered early at all temperatures tested (Fig. 1A; Table 1, experiments 1 to 5; and fig. S7). *flm-3* mutants also flowered early, except at <10°C, indicating that temperature sensitivity was restored below 10°C. Flowering of *flc-3* mutants was delayed below 16°C, demonstrating that temperature sensitivity was restored below 16°C. These findings suggest that *SVP* functions at a wide range of temperatures (5° to 27°C). Consistent with this notion, in double mutants, *svp* suppressed the temperature responses of *flm-3* and *flc-3* at 5° to 27°C (Fig. 1A; fig. S7; and table S3, experiments 1 to 5). These findings suggest that these three MADS-box proteins act at different temperatures and that *SVP* exerts the strongest effect.

To examine the effect of *SVP*, we measured expression of genes that promote flowering. Expression of *FLOWERING LOCUS T* (*FT*), *TWIN*

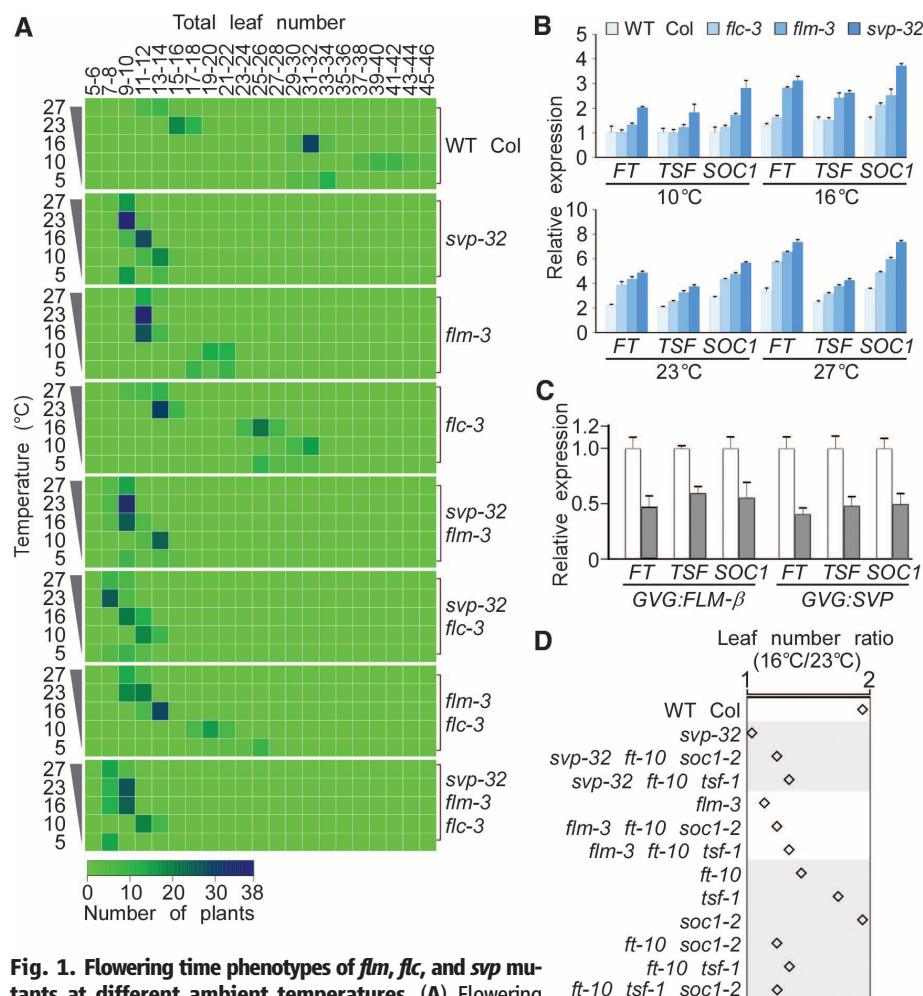


Fig. 1. Flowering time phenotypes of *flm*, *flc*, and *svp* mutants at different ambient temperatures. (A) Flowering time of various mutant combinations of *svp-32*, *flm-3*, and *flc-3* at 27°, 23°, 16°, 10°, and 5°C under LD conditions. Distribution of flowering time is presented as a heat map. (B) Expression of *FT*, *TSF*, and *SOC1* in *svp-32*, *flm-3*, and *flc-3* mutants at different temperatures under LD conditions. Samples were harvested at zeitgeber time (ZT) 16. The expression level of each gene in WT Col plants at 10°C was set to 1. Error bars indicate SEM of three biological replicates. (C) Expression of *FT*, *TSF*, and *SOC1* in *GVG:FLM-β* and *GVG:SVP* plants with (gray) or without (white) dexamethasone (DEX) treatment. The expression levels were measured 8 hours after 30 μM DEX treatment. Error bars indicate SEM of two biological replicates. (D) Leaf number ratio (16° and 23°C) of various single, double, and triple mutants of *svp-32*, *flm-3*, and *flc-3*.

¹Creative Research Initiatives, Department of Life Sciences, Korea University, Seoul 136-701, South Korea. ²Max Planck Institute for Developmental Biology, Department of Molecular Biology, Spemannstrasse 35, 72076 Tübingen, Germany.

*Present address: Instituto de Hortofruticultura Subtropical y Mediterránea, Universidad de Málaga—Consejo Superior de Investigaciones Científicas, Departamento de Biología Molecular y Bioquímica, Facultad de Ciencias, Universidad de Málaga, 29071 Málaga, Spain.

†Corresponding author. E-mail: jahn@korea.ac.kr

SISTER OF FT (TSF), and *SUPPRESSOR OF OVEREXPRESSION OF CONSTANS 1 (SOC1)* increased at all temperatures (27° to 10°C) in *svp-32* mutants (Fig. 1B). We excluded 5°C, as flowering of WT plants was not further delayed at 5°C (Fig. 1A), and expression of cold- and vernalization-responsive genes (23) increased at 5°C (fig. S8). *FT*, *TSF*, and *SOC1* expression was higher in *flm-3* mutants at 16° to 27°C and in *flc-3* mutants at 23° to 27°C, the functional temperature ranges of *FLM* and *FLC*. The effect of *SVP* on the expression of *FT*, *TSF*, and *SOC1* was also observed in double and triple mutants (fig. S9). Moreover, *FT*, *TSF*, and *SOC1* expression was reduced in plants carrying the inducible constructs *GVG:FLM-β* and *GVG:SVP* after induction with dexamethasone (Fig. 1C and fig. S10). Thus, the different temperature insensitivity of *svp-32*, *flm-3*, and *flc-3* mutants can be explained by differential expression of *FT*, *TSF*, and *SOC1* at different temperatures. Consistent with this finding, *ft-10 soc1-2* or *ft-10 tsf-1* double mutations suppressed the early flowering of *svp-32* and *flm-3* mutants at different temperatures (Table 1, experiments 6 and 7, and table S3, experiments 6 and 7). Also, *svp-32 ft-10 soc1-2* and *flm-3 ft-10 soc1-2* triple mutants showed more pronounced insensitivity to temperature than *svp-32 ft-10 tsf-1* and *flm-3 ft-10 tsf-1* triple mutants, respectively (Fig. 1D). However, the expression levels of *SQUAMOSA PROMOTER BINDING PROTEIN-LIKE* genes and pri-microRNA 172a (24–26), known temperature-responsive genes, were not altered in *svp-32*, *flm-3*, and *flc-3* mutants (fig. S11). These findings suggest that *FT*, *TSF*, and *SOC1* are major downstream targets of *SVP*, *FLM*, and *FLC* in ambient temperature-responsive flowering.

We next investigated expression of *FLM* and *SVP* and interaction of their proteins. *FLM-β* was spatio-temporally coexpressed with *SVP* (fig. S12), and *FLM-β* and *SVP* colocalized in the nucleus of *Arabidopsis* cells (fig. S13). In vitro pull-down assays demonstrated that *FLM-β* interacts with *SVP* (Fig. 2A). Furthermore, bimolecular fluorescence complementation analysis showed a signal in the nucleus in onion cells coexpressing the yellow fluorescent protein (YFP) N terminus fused to *SVP* and the YFP C terminus fused to *FLM-β* at 23° and 16°C (Fig. 2B). Coimmunoprecipitation assays using tobacco leaves confirmed the interaction between *SVP* and *FLM-β* (Fig. 2C). Chromatin immunoprecipitation analysis revealed that *FLM* binds to the *FT*, *TSF*, and *SOC1* loci in WT plants, and *FLM* binding decreased in the *svp-32* background (Fig. 2D; fig. S14A; and table S3, experiment 8). Similarly, *SVP* binding to *FT*, *TSF*, and *SOC1* was also reduced in the *flm-3* background (fig. S14B and table S3, experiment 9). These findings suggest that *FLM-β* and *SVP* act together in the control of ambient temperature-responsive flowering.

We next asked how ambient temperature changes regulate *SVP*, *FLM*, and *FLC* activities. Analysis by reverse transcription quantitative polymerase chain reaction (qPCR) showed that, in contrast to *FLM-β* and *FLC*, *SVP* transcript levels increased with tem-

Table 1. Flowering time of mutants. RLN, rosette leaf number; CLN, cauline leaf number; TLN, total leaf number; StDev, standard deviation, *n*, number of individuals.

Genotype	RLN	CLN	TLN	TLN StDev	TLN range	<i>n</i>
<i>Experiment 1 (27°C, long days)</i>						
Col (wild type)	10.2	3.0	13.2	±1.9	11–17	15
<i>svp-32</i>	7.8	1.6	9.4	±0.7	8–10	18
<i>flm-3</i>	8.7	3.1	11.8	±0.8	11–13	16
<i>flc-3</i>	9.9	2.4	12.3	±1.6	10–14	20
<i>Experiment 2 (23°C, long days)</i>						
Col (wild type)	13.3	3.4	16.7	±0.9	15–19	30
<i>svp-32</i>	7.8	2.0	9.8	±0.5	9–10	42
<i>flm-3</i>	8.6	2.9	11.5	±0.5	11–12	38
<i>flc-3</i>	10.9	2.6	13.5	±1.1	12–16	37
<i>Experiment 3 (16°C, long days)</i>						
Col (wild type)	25.6	5.8	31.4	±1.0	30–34	35
<i>svp-32</i>	8.6	2.5	11.1	±0.7	10–12	34
<i>flm-3</i>	9.4	2.5	11.9	±0.9	11–14	33
<i>flc-3</i>	20.5	4.8	25.3	±1.4	23–28	35
<i>Experiment 4 (10°C, long days)</i>						
Col (wild type)	33.2	7.8	41.0	±2.6	38–46	26
<i>svp-32</i>	10.4	2.7	13.1	±0.9	12–15	27
<i>flm-3</i>	15.6	4.5	20.1	±1.2	17–22	27
<i>flc-3</i>	25.0	5.6	30.6	±1.5	28–32	26
<i>Experiment 5 (5°C, long days)</i>						
Col (wild type)	26.2	6.2	32.4	±1.5	30–34	18
<i>svp-32</i>	8.6	1.9	10.5	±2.2	9–14	22
<i>flm-3</i>	15.4	4.0	19.4	±1.8	17–21	21
<i>flc-3</i>	22.0	5.7	27.7	±2.1	26–31	19
<i>Experiment 6 (23°C, long days)</i>						
Col (wild type)	11.9	2.9	14.8	±0.9	13–16	26
<i>svp-32</i>	6.5	2.6	9.1	±0.9	8–10	25
<i>flm-3</i>	10.1	2.0	12.1	±0.9	11–13	26
<i>tsf-1</i>	12.0	5.0	17.0	±2.0	15–19	24
<i>soc1-2</i>	20.6	4.5	25.1	±1.2	23–27	26
<i>ft-10</i>	33.4	11.2	44.6	±3.4	41–48	25
<i>ft-10 soc1-2</i>	49.9	10.6	60.5	±3.6	56–65	25
<i>ft-10 tsf-1</i>	52.4	9.6	62.0	±2.5	59–65	26
<i>svp-32 ft-10 soc1-2</i>	47.6	10.6	58.2	±1.8	56–60	26
<i>flm-3 ft-10 soc1-2</i>	46.7	10.7	57.4	±2.0	55–60	27
<i>svp-32 ft-10 tsf-1</i>	28.1	7.9	36.0	±1.8	34–38	15
<i>flm-3 ft-10 tsf-1</i>	32.1	9.9	42.0	±2.7	39–45	17
<i>ft-10 soc1-2 tsf-1</i>	63.9	18.5	82.4	±6.8	75–90	8
<i>Experiment 7 (16°C, long days)</i>						
Col (wild type)	22.2	5.9	28.1	±2.4	25–31	16
<i>svp-32</i>	7.0	2.4	9.4	±1.0	8–11	15
<i>flm-3</i>	10.5	2.7	13.2	±0.6	12–14	17
<i>tsf-1</i>	24.0	5.7	29.7	±1.9	27–32	18
<i>soc1-2</i>	39.8	7.4	47.2	±2.7	44–50	19
<i>ft-10</i>	52.3	9.8	62.1	±2.2	59–65	13
<i>ft-10 soc1-2</i>	59.3	13.1	72.4	±4.7	67–78	12
<i>ft-10 tsf-1</i>	64.8	15.1	79.9	±4.6	75–85	13
<i>svp-32 ft-10 soc1-2</i>	59.1	11.3	70.4	±3.2	67–74	15
<i>flm-3 ft-10 soc1-2</i>	58.3	9.1	67.4	±3.7	63–72	14
<i>svp-32 ft-10 tsf-1</i>	35.0	10.7	45.7	±4.7	41–51	15
<i>flm-3 ft-10 tsf-1</i>	41.3	14.0	55.3	±4.6	50–60	16
<i>ft-10 soc1-2 tsf-1</i>	78.1	23.3	101.4	±4.1	97–106	9

perature (Fig. 3A). *SVP* protein was readily detectable at low temperatures, but it became less abundant at higher temperatures (Fig. 3B and fig. S15A). For example, the amount of *SVP* rapidly diminished within 12 hours in *pSVP:SVP:HA svp-32* plants transferred from 23° to 27°C. By contrast, a control protein

(*FT*) was stable at high temperature for 12 hours (fig. S15B). *SVP* degradation at high temperatures was inhibited by the proteasome inhibitor MG132 (Fig. 3B), suggesting that the 26S proteasome pathway mediates temperature-dependent degradation of *SVP*. In WT protoplasts transfected with

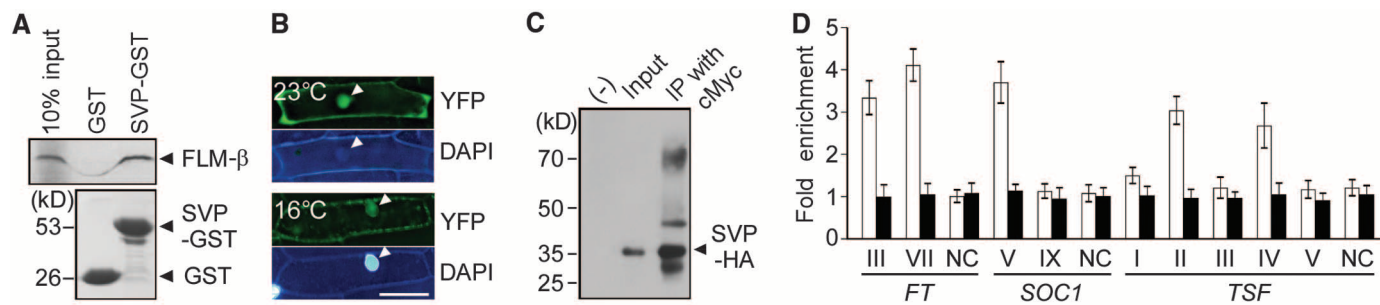


Fig. 2. Protein-protein interaction between FLM- β and SVP. (A) In vitro glutathione S-transferase (GST) pull-down assay. Coomassie-stained SVP-GST and GST proteins are shown below. Input, 10% of 35 S-labeled FLM- β . kD, kilodaltons. (B) Bimolecular fluorescence complementation using SVP-nYFP and FLM- β -cYFP (nYFP, N-terminal YFP fragment; cYFP, C-terminal YFP fragment) in onion epidermal cells at 23°C and 16°C. Arrowheads indicate nuclei. Scale bar, 200 μ m. DAPI, 4',6-diamidino-2-phenylindole. (C) Coimmunoprecipitation with anti-HA

antibody. (-) denotes protein extracts without DNA infiltration. Input, 10% of the protein extracts. (D) Chromatin immunoprecipitation analysis of FLM binding to the genomic regions of *FT*, *TSF*, and *SOC1* in *pFLM:gFLM::GFP flm-3* (white) and *pFLM:gFLM::GFP svp-32 flm-3* (black) mutants at 16°C under LD conditions. Samples were harvested at ZT 16. Relative enrichment was calculated by comparing samples immunoprecipitated with GFP and cMyc antibodies. Error bars indicate SEM of two biological replicates. NC, negative control.

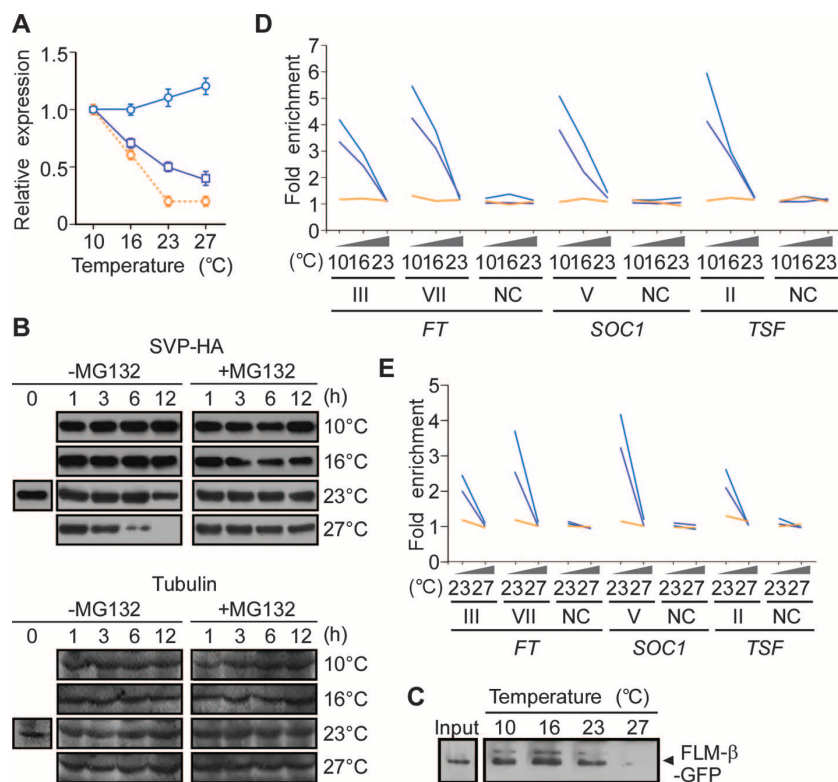


Fig. 3. Temperature-dependent destabilization of SVP protein and temperature-dependent binding of the SVP-FLM- β complex to downstream target genes. (A) Expression of SVP (blue), FLC (purple), and FLM- β (orange) in WT Col seedlings at different temperatures under LD. Samples were harvested at ZT 16. Error bars indicate SEM of three biological replicates. (B) Temperature-dependent destabilization of SVP (left) and the effect of MG132 on SVP protein quantities (right). *pSVP::SVP::HA svp-32* plants incubated at 23°C were transferred to different temperatures after cycloheximide treatment. Tubulin was used as a loading control. h, hours. (C) Coimmunoprecipitation assays showing the temperature-dependent abundance of the SVP-FLM- β complex at different temperatures. *Arabidopsis* mesophyll protoplasts transiently overexpressing SVP-HA and FLM- β -GFP at different temperatures were immunoprecipitated with anti-HA antibody and then immunoblotted for GFP. Input, the protein extracts used before coimmunoprecipitation assay. (D and E) Chromatin immunoprecipitation analysis of SVP binding to the genomic regions of *FT*, *TSF*, and *SOC1* in *pSVP::SVP::HA svp-32* (blue), *pSVP::SVP::HA svp-32 flc-3* (purple), and *pSVP::SVP::HA svp-32 flm-3* (orange) mutants under temperature-shift conditions under LD (D) and SD (E) conditions. Samples were harvested at ZT 16 (D) or ZT 8 (E). The amplified regions used for qPCR experiments are shown in fig. S14A. Relative enrichment was calculated by comparing samples immunoprecipitated with HA and cMyc antibodies. SEM of two or three biological replicates is presented in table S4.

35S::SVP::GFP (GFP, green fluorescent protein), we also observed consistent proteasome-dependent SVP degradation at higher temperatures (fig. S16). We then tested whether these changes in SVP levels affect the SVP-FLM- β complex at different temperatures. Using hemagglutinin (HA)-tagged SVP and GFP-tagged FLM- β proteins in a coimmunoprecipitation assay, we detected more SVP-FLM- β complex at low temperatures and a gradual decrease in complex abundance with increasing temperature (Fig. 3C and fig. S17). These findings suggest that the posttranslational regulation of SVP might modulate the abundance of the SVP-FLM- β repressor complex in the control of ambient temperature-responsive flowering.

To test whether the different MADS-box complexes bind to downstream targets in a temperature-dependent manner, we performed chromatin immunoprecipitation experiments using *pSVP::SVP::HA svp-32*, *pSVP::SVP::HA svp-32 flc-3*, and *pSVP::SVP::HA svp-32 flm-3* plants (fig. S18) grown at 23°C, 16°C, and 10°C. As expected, chromatin immunoprecipitation assays with anti-HA in *pSVP::SVP::HA svp-32* plants showed enrichment of *FT*, *TSF*, and *SOC1* genomic regions. Also, SVP binding to its target sequences increased at low ambient temperatures under LD conditions (Fig. 3D and table S4). For example, SVP binding to the *FT* locus VII region (21, 27) increased by 3.4- and 4.9-fold at 16°C and 10°C, respectively. The *flm* mutation abolished SVP binding to its target sequences, and the *flc* mutation reduced SVP binding (average: 24.7% decrease) at 10°C. We also observed increased SVP binding at low temperature under SD conditions (average: 3.0-fold) (Fig. 3E and table S4). Moreover, the loss of FLM activity inhibited SVP binding to target sequences, which suggests that a repressor complex of SVP and FLM- β acts as a major mediator of the ambient temperature signal within a temperature range of 10°C to 27°C. However, considering the restored temperature response of the *flm-3* mutant at 10°C, we cannot exclude the possibility that SVP may interact with itself, FLC, or other MADS-box protein(s) to mediate ambient temperature signals (19, 20).

A balance between inductive and repressive signals determines optimal flowering time for successful reproduction in seasonal environments (28, 29). Our data demonstrate the importance of the repressors SVP, FLM- β , and FLC, which affect flowering at different but partially overlapping temperature ranges (fig. S19). However, we cannot exclude the possibility that the importance of SVP and FLM- β may not extend to *Arabidopsis* winter annual accessions. At lower temperatures, increased SVP protein interacts with FLM- β to repress flowering by direct binding to downstream targets. At higher temperatures, SVP protein levels decline, allowing expression of the downstream target genes and enabling flowering at that temperature. We propose that repressive activity of SVP requires FLM- β in the same complex and that SVP protein stability modulates the abundance of the SVP-FLM- β repressor complex to regulate ambient temperature-responsive flowering. SVP-like proteins have conserved functions across plant species (30, 31); therefore, control of SVP-FLM- β repressor complex abundance could be a general strategy for plants to adjust the balance of inductive and repressive signals under fluctuating temperature conditions.

References and Notes

1. A. Srikanth, M. Schmid, *Cell. Mol. Life Sci.* **68**, 2013–2037 (2011).
2. S. Penfield, *New Phytol.* **179**, 615–628 (2008).

3. J. H. Lee, J. S. Lee, J. H. Ahn, *J. Plant Biol.* **51**, 321–326 (2008).
4. S. Sung, R. M. Amasino, *Annu. Rev. Plant Biol.* **56**, 491–508 (2005).
5. N. A. Delk, K. A. Johnson, N. I. Chowdhury, J. Braam, *Plant Physiol.* **139**, 240–253 (2005).
6. A. H. Fitter, R. S. Fitter, *Science* **296**, 1689–1691 (2002).
7. B. I. Cook, E. M. Wolkovich, C. Parmesan, *Proc. Natl. Acad. Sci. U.S.A.* **109**, 9000–9005 (2012).
8. P. Q. Craufurd, T. R. Wheeler, *J. Exp. Bot.* **60**, 2529–2539 (2009).
9. A. B. Nicotra *et al.*, *Trends Plant Sci.* **15**, 684–692 (2010).
10. J. T. Anderson, D. W. Inouye, A. M. McKinney, R. I. Colautti, T. Mitchell-Olds, *Proc. Biol. Sci.* **279**, 3843–3852 (2012).
11. U. Johanson *et al.*, *Science* **290**, 344–347 (2000).
12. S. D. Michaels, R. M. Amasino, *Plant Cell* **11**, 949–956 (1999).
13. C. C. Sheldon *et al.*, *Plant Cell* **11**, 445–458 (1999).
14. J. Lempe *et al.*, *PLOS Genet.* **1**, e6 (2005).
15. S. Balasubramanian, S. Sureshkumar, J. Lempe, D. Weigel, *PLOS Genet.* **2**, e106 (2006).
16. J. D. Werner *et al.*, *Proc. Natl. Acad. Sci. U.S.A.* **102**, 2460–2465 (2005).
17. K. C. Scortecchi, S. D. Michaels, R. M. Amasino, *Plant J.* **26**, 229–236 (2001).
18. S. Balasubramanian, D. Weigel, *Plant Signal. Behav.* **1**, 227–228 (2006).
19. S. de Folter *et al.*, *Plant Cell* **17**, 1424–1433 (2005).
20. X. Gu *et al.*, *Nat. Commun.* **4**, 1947 (2013).
21. J. H. Lee *et al.*, *Genes Dev.* **21**, 397–402 (2007).
22. A. M. Wilczek *et al.*, *Science* **323**, 930–934 (2009).
23. D. M. Bond, E. S. Dennis, E. J. Finnegan, *Plant Cell Environ.* **34**, 1737–1748 (2011).
24. J. J. Kim *et al.*, *Plant Physiol.* **159**, 461–478 (2012).
25. H. J. Cho *et al.*, *FEBS Lett.* **586**, 2332–2337 (2012).

26. J. W. Wang, B. Czech, D. Weigel, *Cell* **138**, 738–749 (2009).
27. C. A. Helliwell, C. C. Wood, M. Robertson, W. James Peacock, E. S. Dennis, *Plant J.* **46**, 183–192 (2006).
28. I. Bäurle, C. Dean, *Cell* **125**, 655–664 (2006).
29. Y. Kobayashi, D. Weigel, *Genes Dev.* **21**, 2371–2384 (2007).
30. J. H. Lee, S. H. Park, J. H. Ahn, *Plant Sci.* **185–186**, 97–104 (2012).
31. B. Trevaskis *et al.*, *Plant Physiol.* **143**, 225–235 (2007).

Acknowledgments: We thank R. Amasino, C. Dean, I. Lee, I. Hwang, C. M. Park, J. Puterill, D. Weigel, and P. Wigge for kindly providing research materials and D. H. Kim, B. R. Kim, H. J. Cho, S. H. Kim, S. M. Hong, H. S. Jung, and S. J. Yoo for their technical assistance. J.H.L. was supported by a Korea University Grant. D.P. and M.S. were supported by the ERA-NET Plant Genomics BLOOMNET project (SCHM1560/7-1). This work was supported by a National Research Foundation of Korea grant funded by the Korea government (Ministry of Science, ICT, and Future Planning) (2008-0061988) to J.H.A. The authors declare no conflicts of interest. GenBank accession numbers are KF496888 to KF496899 (FLM sequences of *Arabidopsis* WT accessions). Materials described here are available from J.H.A. The genomic FLM-GFP line will be distributed for noncommercial research under a standard materials transfer agreement by the Max Planck Institute for Developmental Biology.

Supplementary Materials

www.sciencemag.org/content/342/6158/628/suppl/DC1
Materials and Methods
Figs. S1 to S19
Tables S1 to S5
References (32–56)

28 May 2013; accepted 3 September 2013

Published online 12 September 2013;
10.1126/science.1241097

Mosaic Copy Number Variation in Human Neurons

Michael J. McConnell,^{1,2,7,8,9} Michael R. Lindberg,⁷ Kristen J. Brennan,^{1*} Julia C. Piper,^{1,2,†} Thierry Voet,^{3,4} Chris Cowing-Zitron,¹ Svetlana Shumilina,⁷ Roger S. Lasken,^{5,6} Joris R. Vermeesch,³ Ira M. Hall,^{7,9,‡} Fred H. Gage^{1,‡}

We used single-cell genomic approaches to map DNA copy number variation (CNV) in neurons obtained from human induced pluripotent stem cell (hiPSC) lines and postmortem human brains. We identified aneuploid neurons, as well as numerous subchromosomal CNVs in euploid neurons. Neurotypic hiPSC-derived neurons had larger CNVs than fibroblasts, and several large deletions were found in hiPSC-derived neurons but not in matched neural progenitor cells. Single-cell sequencing of endogenous human frontal cortex neurons revealed that 13 to 41% of neurons have at least one megabase-scale de novo CNV, that deletions are twice as common as duplications, and that a subset of neurons have highly aberrant genomes marked by multiple alterations. Our results show that mosaic CNV is abundant in human neurons.

Neuronal genomes exhibit elevated levels of aneuploidy (1–3) and retrotransposition (4–6) relative to other cell types; this finding has fueled speculation that somatic genome variation may contribute to functional diversity in the human brain (7–10). The prevalence of copy number variations (CNVs) has been difficult to assess, given the limited ability of conventional genome-wide methods to detect CNVs that are rare within a population of cells, as most somatic mutations are expected to be. Recently, two methods have been developed to map large-scale CNVs in single cells: microarray analysis of multiple displacement amplification (MDA) products (11) and single-cell

sequencing (12). Here, we applied both of these approaches to single human neurons.

We examined human neurons from two neurotypic sources (fig. S1A): (i) human induced pluripotent stem cells [i.e., hiPSC-derived neurons (fig. S2)] and (ii) human postmortem frontal cortex (FCTX) neurons (fig. S3). We employed fluorescence-activated cell sorting (FACS) to obtain neurons from neuronogenic hiPSC cultures using synapsin:green fluorescent protein (GFP) expression and from postmortem tissue using NeuN immunostaining (13). After multiple displacement amplification (MDA) (14), we hybridized single hiPSC-derived neuronal genomes to Affymetrix 250K single-

nucleotide polymorphism (SNP) arrays [as in (11)]. We subjected single neurons from postmortem tissue to Illumina DNA sequencing using a custom version of the single-cell sequencing protocol developed by Navin *et al.* (12), which combines the GenomePlex whole-genome amplification method with Nextera-based library preparation (15). We developed stringent quality-control measures to ensure that only the highest-quality amplification reactions and data sets were included in downstream analyses (see methods).

To detect CNVs, we first aggregated raw copy number measurements over very large genomic intervals. We then selected interval sizes that were 1 to 2 orders of magnitude larger than the local

¹Laboratory of Genetics, Salk Institute for Biological Studies, La Jolla, CA 92037, USA. ²Crick-Jacobs Center for Theoretical and Computational Biology, Salk Institute for Biological Studies, La Jolla, CA 92037, USA. ³Center for Human Genetics, KU Leuven, 3000 Leuven, Belgium. ⁴Single-Cell Genomics Centre, Wellcome Trust Sanger Institute, Hinxton, Cambridge CB10 1SA, UK. ⁵J. Craig Venter Institute, San Diego, CA 92121, USA. ⁶Skaggs School of Pharmacy and Pharmaceutical Sciences, University of California San Diego, La Jolla, CA 92093, USA. ⁷Department of Biochemistry and Molecular Genetics, University of Virginia School of Medicine, Charlottesville, VA 22908, USA. ⁸Center for Brain Immunology and Glia, University of Virginia, Charlottesville, VA 22908, USA. ⁹Center for Public Health Genomics, University of Virginia, Charlottesville, VA 22908, USA.

*Present address: Icahn School of Medicine at Mount Sinai, New York, NY 10029, USA.

†Present address: Department of Organismic and Evolutionary Biology, Harvard University, Cambridge, MA 02138, USA.

‡Corresponding author. E-mail: irahall@virginia.edu (I.M.H.) and gage@salk.edu (F.H.G.)

amplification biases reported for single-cell DNA amplification (16, 17). For SNP array data, we calculated the median copy number in 100-probe bins, which corresponds to a mean genomic interval of 666 kb; for sequencing data, we measured read-depth in bins composed of 500 kb of uniquely mappable sequence (mean size of 687 kb). CNVs were identified using circular binary segmentation (18) combined with strict filtering based on the number of consecutive bins identified by segmentation and the amplitude of CNV predictions relative to the noise (median absolute deviation) of each data set. These methods and filtering criteria resulted in a mean CNV size detection limit of 6.7 Mb for SNP array data and 3.4 Mb for sequencing data. A subset ($n = 7$) of the MDA-amplified hiPSC-derived neurons, analyzed by both SNP array and sequencing, showed high concordance (fig. S1B and fig. S4). Subchromosomal deletions (Fig. 1, A and C) and duplications (Fig. 1, B and D) were identified in both groups of neurons.

We examined neurons from three hiPSC lines, referred to as C, D, and E, that were generated from three different individuals as neurotypic controls for a hiPSC-based disease model (19). Analysis of bulk DNA from C and D line donor fibroblasts or hiPSC-derived neural progenitor

cells (NPCs) revealed no clonal genomic aberrations. Of 40 single neurons analyzed [for C, ($n = 21$); D, ($n = 6$); E, ($n = 13$)], 27 had copy number profiles consistent with bulk DNA, but 13 had unique genomes. In total, we identified seven whole-chromosome gains, four whole-chromosome losses, and 12 subchromosomal CNVs (range: 7 to 156 Mb) in 13 hiPSC-derived neurons (Fig. 2A, fig. S5, and table S1). Each CNV was identified in merely one neuron, which suggests that the CNVs are not early clonal events but rather are unique to single cells or distinct lineages.

The CNVs detected in C and D line hiPSC-derived neurons were distinct from those seen in either C or D line fibroblasts or NPCs (Fig. 2). Of 29 fibroblasts, 6 had single CNVs (range: 5.2 to 27.7 Mb) and one was aneuploid ($-22, -X$) (Fig. 2A). Among 19 hiPSC-derived NPCs, only 6 duplications were observed (Fig. 2A). Technical replicates of five fibroblasts and three hiPSC-derived neurons showed high concordance, and principal component analysis also showed that replicates from each individual neuron clustered distinctly from both the fibroblasts and the other two neurons (fig. S2E). Comparison of CNVs in the three cell types (Fig. 2B) showed that neurons have significantly larger CNVs than fibroblasts

(Kolmogorov-Smirnov test, $P < 0.001$). In addition, we found deletions only in hiPSC-derived neurons and not in hiPSC-derived NPCs.

We performed two additional experiments to confirm that low-level aneuploidy and CNVs occur in single fibroblasts. First, we obtained single-cell clones by limiting dilution. Each single fibroblast was expanded to ~20 sister cells over 7 days; then, we obtained individual sister fibroblasts from three different clonal expansions. In one of these clones, chromosome missegregation was observed as a gain of Chr2 in one cell and a loss of Chr2 in a sister cell (Fig. 3A). Non-clonal CNVs were also detected, so we performed a second experiment using fluorescence in situ hybridization (FISH) for a common hiPSC CNV on Chr20 (20) and for ChrX. Consistent with genomic analysis of bulk DNA, 20 metaphase spreads from this population karyotyped as euploid, but 13 out of 200 were aneuploid for ChrX (Fig. 3B) and 26 out of 200 nuclei had a Chr20 CNV (Fig. 3C). These data show that two distinct approaches (SNP array and FISH) detect large nonclonal CNVs that arise in single human cells in culture.

We next sought to determine whether mosaic CNVs were also present in FCTX neurons from postmortem human brains. For these experiments

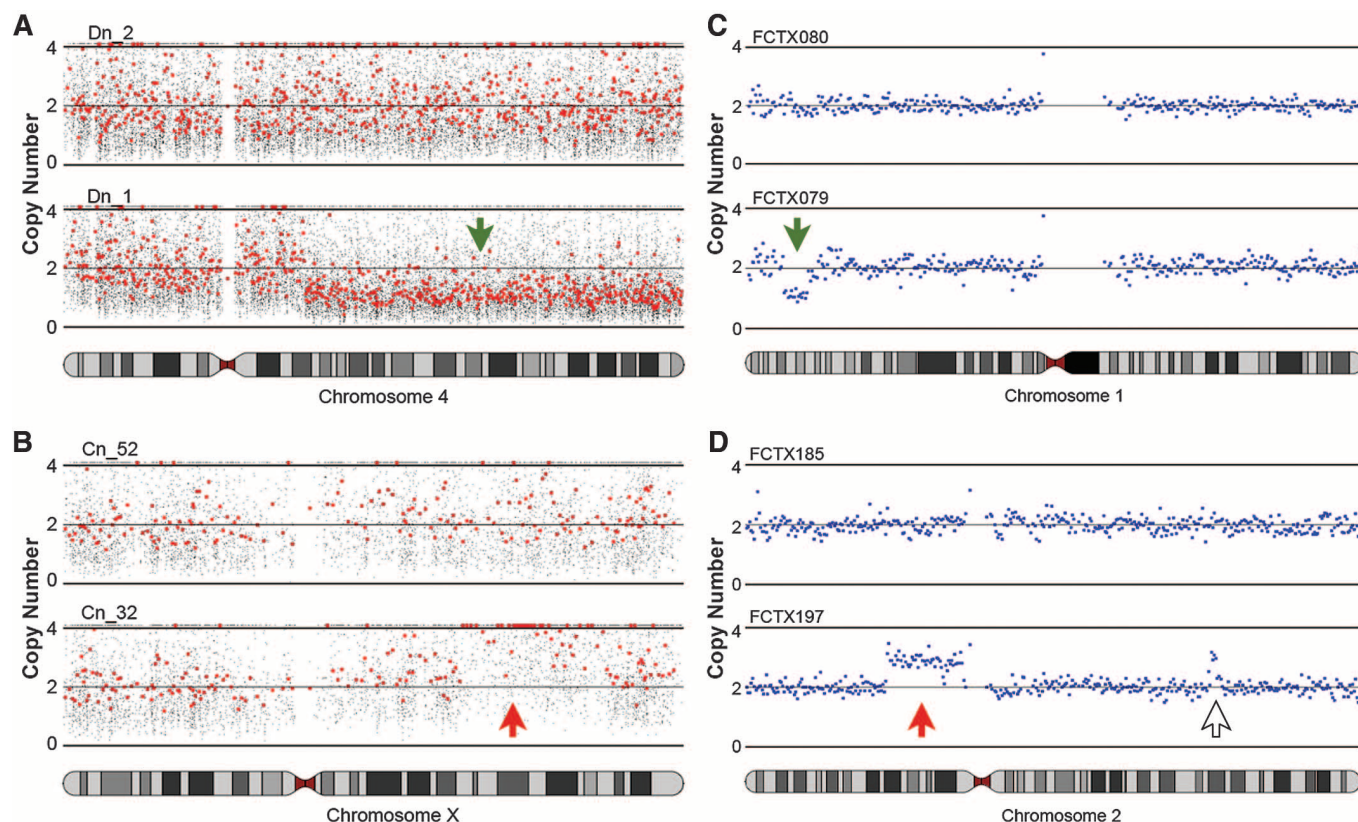


Fig. 1. Mosaic copy number variation (CNV) is detected in human neurons. (A and B) Subchromosomal deletions (green down arrow) and duplications (red up arrow) are observed in hiPSC-derived neurons. (A) Neuron Dn_1 has a deletion on chromosome (chr) 4q (bottom); neuron Dn_2 has no CNV on Chr4 (top). Small gray dots show the predicted copy number at individual SNPs; red dots show every 30th SNP. (B) Neuron Cn_32 has a duplication on ChrXq (bottom); neuron Cn_2 does not (top). (C and D) Single-cell sequencing reveals

subchromosomal deletions (green down arrow) and duplications (red up arrow) in FCTX neurons. (C) FCTX079 has a deletion on Chr1p (bottom); FCTX080 does not (top). Blue dots show raw copy number predictions obtained by read-depth analysis (mean window size ~687 kb; see methods). (D) Neuron FCTX197 has a duplication on Chr2p (bottom), whereas FCTX185 does not (top). Another likely duplication on Chr2q in FCTX197 (open arrow) comprised only four consecutive bins and therefore failed our five-bin confidence threshold.

we used the single-cell sequencing method (12), which offers superior sensitivity to microarray approaches because of the digital nature of DNA sequence data (12, 21). After benchmarking the sequencing approach with trisomic male fibroblasts in which we identified 100% trisomy 21 and monosomy X (Fig. 3D, fig. S6, and table S2), we sequenced 110 FCTX neurons from three different individuals [a 24-year-old female (NICHD Brain Bank ID no. 5125; $n = 19$), a 26-year-old male (ID no. 1583; $n = 41$), and a 20-year-old female (ID no. 1846; $n = 50$)] and used strict filtering criteria to identify high-confidence CNVs (see methods) composed of five or more consecutive bins. We identified 100% monosomy X and Y in the 41 male neurons (Fig. 4A, fig. S7, and table S3) as expected, and simulation experiments indicate that our methods detected CNVs at high sensitivity and specificity, with a predicted mean false-negative rate of 17% and a predicted mean false-discovery rate of 0.6% (fig. S8; see methods).

We identified one or more somatic CNVs in 45 of the 110 (41%) FCTX neurons analyzed (Fig. 4, fig. S7, and table S2). The vast majority of somatic CNVs were subchromosomal alterations ranging in size from 2.9 to 75 Mb, although we also identified one putative chromosome gain and two losses where CNV calls affected >50% of the chromosome (e.g., FCTX155) (Fig. 4A). Subchromosomal CNVs were distributed throughout the genome, and in only one case did two independent CNVs share the same breakpoints (a 3-Mb subtelomeric deletion on Chr16 in FCTX198 and FCTX224 (fig. S7 and table S2). However, a number of loci were affected by multiple

“small” CNVs less than 20 Mb in size ($N = 133$), and small CNVs were preferentially found at telomeres (Fig. 4B), with 23.3% extending to the chromosome end (2067-fold enrichment by Monte-Carlo simulation, see methods). Small CNVs are not enriched with features known to affect genome stability, such as transposons, segmental duplications, or fragile sites; neither are they enriched with germline CNVs or known genes (fig. S9). Subchromosomal deletions were prevalent in each of the three individuals and were twice as common as duplications, on average, which might be explained by a bias toward DNA loss in nondividing postmitotic neurons; however, the third individual (no. 1846) was unique in also showing abundant duplications (fig. S3, D to G). These results demonstrate that somatic CNVs are a common feature of neuronal genomes and suggest that the relative abundance of different CNV classes may vary among individuals.

The overall high mutational load that we report in neurons is predominantly due to a small number of cells with highly aberrant genomes. Whereas the majority of FCTX neurons exhibited 0 (59%) or 1 or 2 CNVs (25%), 17 cells (15%) accounted for 108 of the 148 CNV calls (73%), and 7 cells accounted for nearly half (49%) of all calls (Fig. 4C). Aberrant cells are marked by multiple copy number switches on distinct chromosomes, with interdigitated altered and unaltered segments that adhere well to the expectation of integer-like copy number states measured by digital DNA sequencing technology. Similar, if less dramatic, examples of this phenomenon were apparent in hiPSC neurons, where several

cells harbored multiple alterations. For example, hiPSC-derived neuron Cn_32 had five events: loss of Chr13, three duplications, and one deletion (fig. S10). Similarly, two FCTX neurons had more than 10 events. One of these, FCTX155, was aneuploid for most of Chr2 and had 18 deletions and one duplication (Fig. 4A). We did not observe similarly aberrant copy number profiles among the 16 control fibroblasts analyzed by sequencing (fig. S6) or among the 42 fibroblasts or 19 NPCs analyzed by SNP array (fig. S5). Taken together, these results suggest that a subset of neurons is especially prone to large-scale genome alterations.

Single-cell genome analysis is inherently challenging, because all existing approaches require amplification of the genome before measurement; thus, validation is impossible because one cannot know the state of a single-cell's genome before it was amplified. However, several lines of evidence argue that the vast majority of events we report are true CNVs. First, we used methods that were previously validated on clonally related cell populations, including tumors (12) and eight-cell embryos (11). Second, we report megabase-scale CNVs that are orders of magnitude larger than the amplicons generated by whole-genome amplification. Indeed, previous studies have noted that amplification artifacts tended to be small (<10 kb) and distributed relatively uniformly across the genome (16, 17); therefore, simple amplification effects cannot readily explain the large-scale deviations in copy number that we observe. It is also difficult to explain how such effects could cause both gains and losses of DNA that

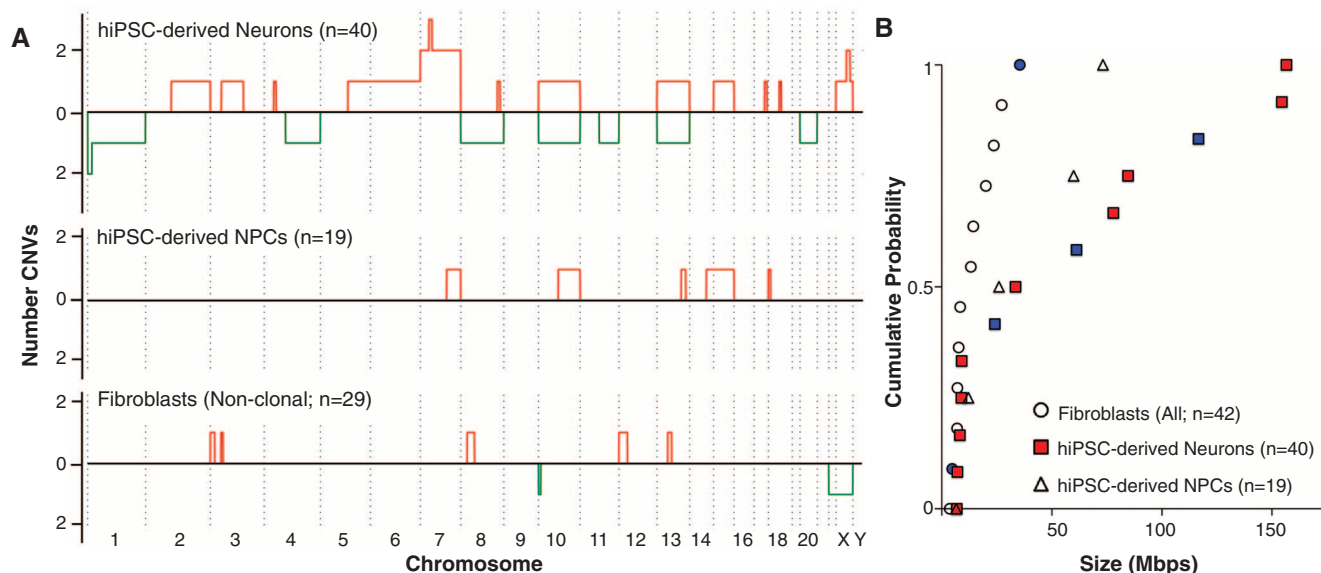


Fig. 2. Large CNVs are found in hiPSC-derived neurons. (A) Whole and subchromosomal duplications (red) and deletions (green) are summarized for 40 hiPSC-derived neurons (top). The y axis value represents the number of times each genomic interval was deleted (below in green) or duplicated (above in red). CNVs were detected in 9 out of 21 C neurons (Cn), 2 out of 6 D neurons (Dn), and 2 out of 13 E neurons (En). In donor hiPSC-derived NPC populations (middle), CNVs were detected in 1 out of 10 D NPCs (Dp) and 3 out of 9 C NPCs (Cp). In donor fibroblast populations (bottom), CNVs were detected in 7 out of

20 D fibroblasts (Df) and 0 out of 9 C fibroblasts (Cf). Note that chromosomes are not plotted to scale because data are summarized in 100-SNP bins. (B) Subchromosomal CNVs in fibroblasts were significantly smaller than in hiPSC-derived neurons (Kolmogorov-Smirnov test, $P < 0.001$). No deletions were observed in NPCs. Deletions are denoted with blue markers; all other markers indicate duplications. Aneuploidies are not included in this plot. For completeness, subchromosomal CNVs from clonal fibroblasts (Fig. 3) were included in this plot, bringing the total n to 42 fibroblasts.

produce integral copy number values by sequencing. Third, the postmortem interval is unlikely to contribute significantly to our results, because DNA degradation cannot generate duplications and because we observed large deletions in both FCTX and hiPSC-derived neurons. Fourth, Monte-Carlo simulation experiments showed that our CNV detection methods identify hemizygous gains and losses at high sensitivity and are not affected by random fluctuations in sequence coverage.

Fifth, we have employed strict quality-control measures to exclude data sets with uneven or noisy amplification or that (in the case of sequence data) do not exhibit expected integer-like copy number profiles (see methods). Finally, and perhaps most important, many of our CNV calls appear to be extremely high quality based on their size, amplitude, and integer-like properties (see Fig. 4A, fig. S6, and fig. S7), and a subset (30 to 56%) is robust to a series of increasingly strict CNV detection

parameters (fig. S11). At increased stringency, the overall number of CNVs diminishes but the core results do not change: CNVs are apparent in a significant fraction of neurons (13 to 24%), there is a predominance of deletions relative to duplications (fig. S11A), and we observe a subset of neurons with highly aberrant genomes marked by multiple copy number oscillations (fig. S11D). Therefore, although we cannot definitively exclude the possibility of as-yet-undescribed single-cell amplification

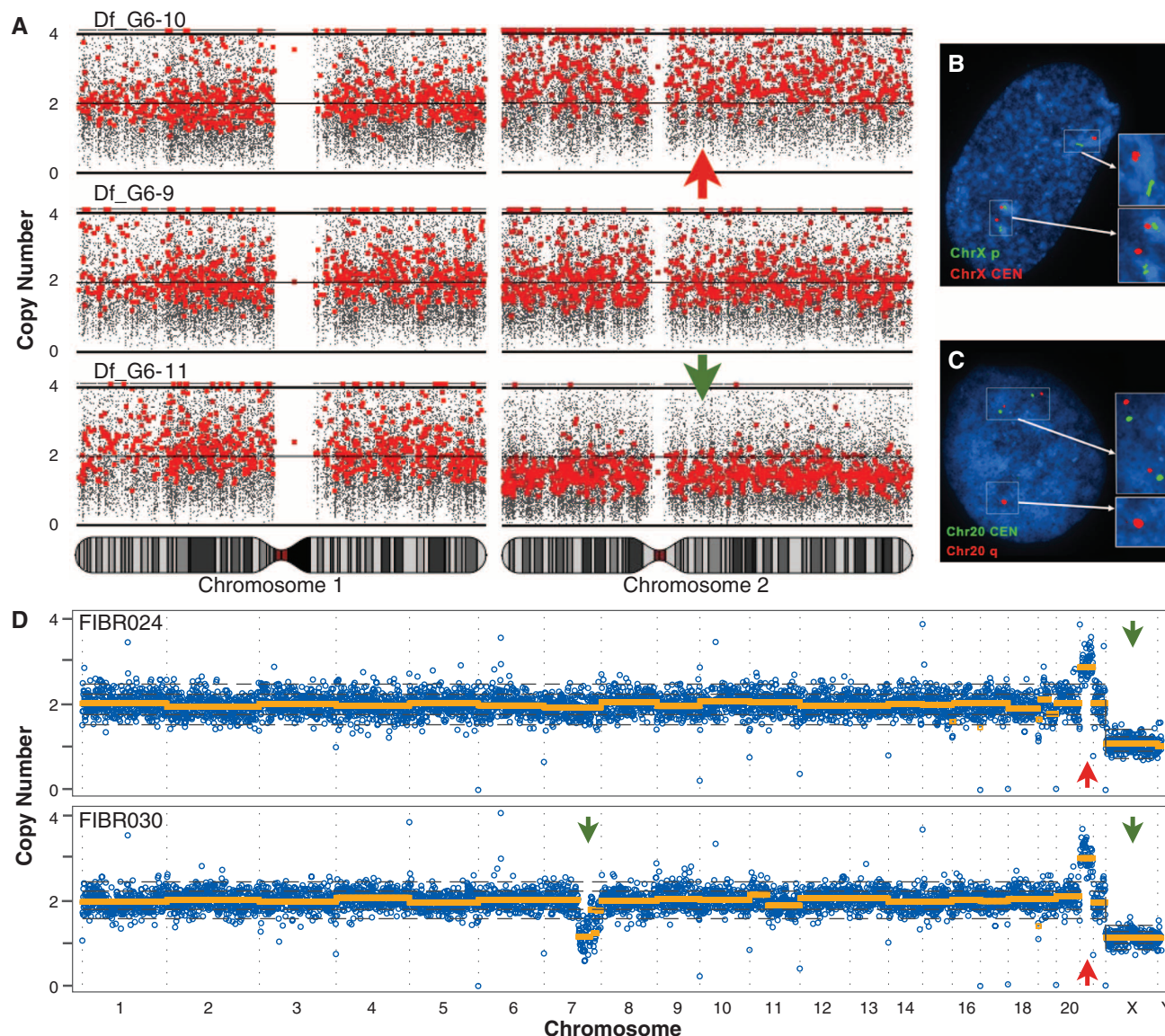


Fig. 3. Large CNVs are found in cultured fibroblasts. (A) Single fibroblasts obtained by limiting dilution were expanded to a population of ~20 clonal fibroblasts after 7 days in vitro (DIV). In one clonal population, a reciprocal chromosome missegregation event was detected. One fibroblast was trisomic for Chr2 (top) and a sister was monosomic for Chr2 (bottom). Chromosome 1 is shown along with the third euploid cell. (B and C) Two groups of Df (passages 7 and 8) were summarized in (Fig. 2A); a parallel culture of the p7 group was sent for karyotyping and FISH. Out of 20 metaphase chromosome spreads, 20 were euploid. (B) FISH was performed for a ChrX p arm telomere (green) and ChrX centromere (red). Out of 200 nuclei, 13 were aneuploid. (C) FISH was performed for the Chr20 centromere (green) and Chr20 CNV (red). Out of 200 nuclei, 26 had the CNV. (D) Single-cell sequencing of two male fibroblasts with

karyotypically defined trisomy 21. Genome-wide copy number profiles show that, in both cells, most of the genome is present at two copies, Chr21 is present at three copies, and ChrX is present at one copy. In addition, we identified a large deletion on Chr7q in FIBR030. DNA copy number (y axis) was calculated by read-depth analysis of variably sized genomic windows containing 500 kb of uniquely mappable sequence (blue), and CNVs were detected by circular binary segmentation (orange). Green (down) and red (up) arrows denote deletions and duplications, respectively, that were identified by segmentation and passed filtering criteria. Reported CNVs comprise five or more consecutive bins and exceed two median absolute deviations (MADs). Dotted gray lines show 1 and 2 MADs from the median copy number of each data set. See figs. S6 and S7 for plots of additional cells.

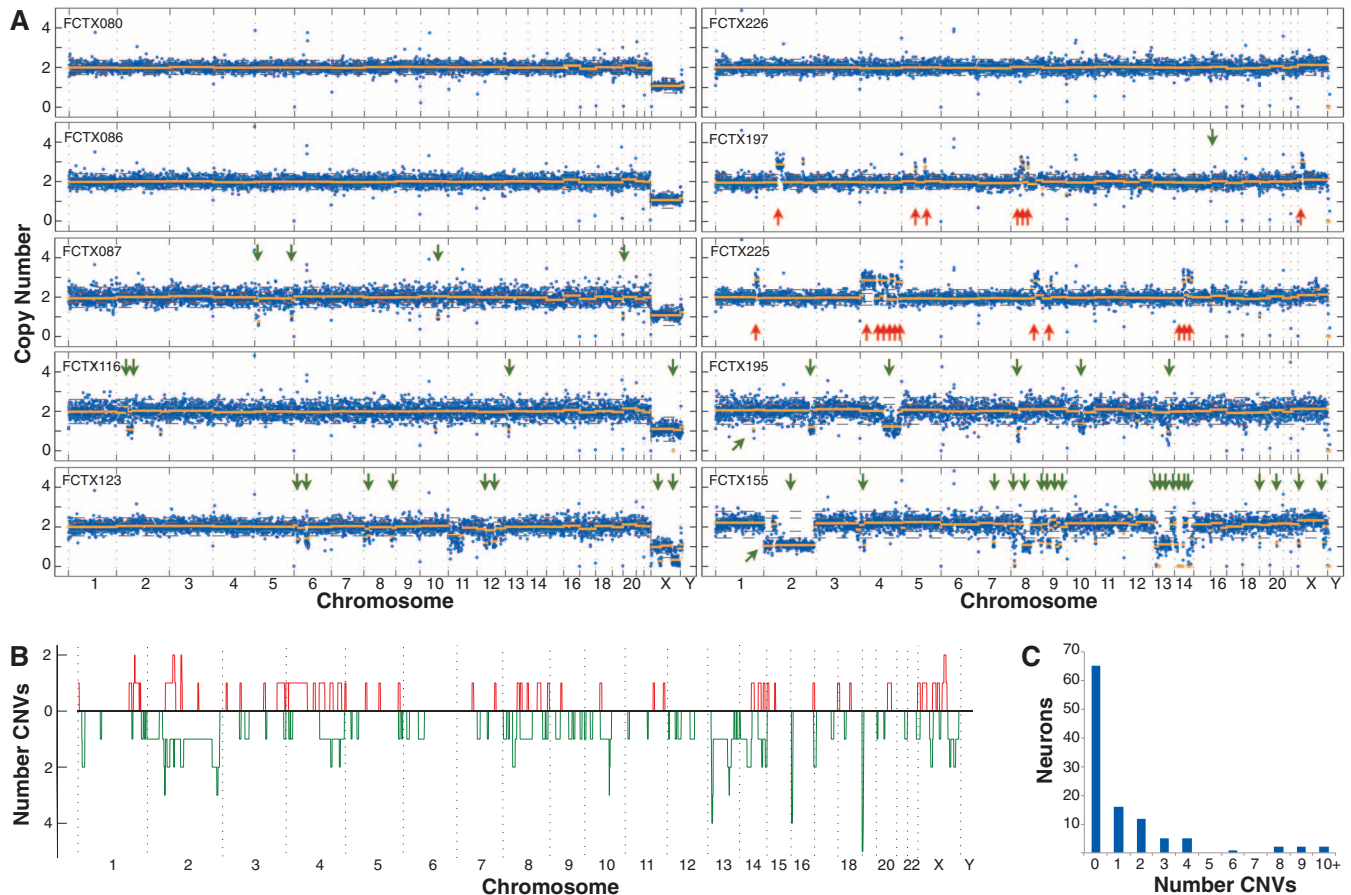


Fig. 4. Identification of CNVs in postmortem neurons using single-cell sequencing. (A) Genome-wide copy number profiles of five male (left) and five female (right) neurons from two individuals, no. 1583 and no. 1846, respectively. Data are plotted exactly as in Fig. 3D. Arrows denote deletions (green, down and at an angle in FCTX195 and 155) and duplications (red, up) that were identified by copy number segmentation and passed filtering criteria. Note that single-copy

"losses" of ChrX in cells from male individual no. 1583 are not indicated by arrows, but were identified in 100% of cells. See fig. S7 for plots of all cells. (B) Whole and subchromosomal duplications (red) and deletions (green) are summarized for the 110 FCTX neurons as in Fig. 2A. (C) The number of individual neurons (y axis) that exhibited a given number of CNVs (x axis). See fig. S11 for results at different CNV detection stringency thresholds.

artifacts, the above observations strongly argue that the central results and conclusions of our study are not attributable to technical factors.

Using three completely independent single-cell approaches (SNP array, sequencing, and FISH), we find that a subset of cultured fibroblasts has megabase-scale CNVs. Recently, small CNVs (<1 Mb) have been estimated to occur in skin fibroblasts at a frequency of perhaps 30%; however, no large CNVs were reported in this study (22). In order to study single somatic cells, Abyzov *et al.* (22) reprogrammed fibroblasts and performed deep whole-genome sequencing on the hiPSC cell lines that emerged. In contrast, we analyzed single cultured fibroblasts directly using lower-resolution methods that cannot resolve small CNVs (<1 Mb). Given that many large CNVs are expected to be deleterious and may adversely affect reprogramming or clonal expansion in culture, we believe that the two findings are not inconsistent.

Our single-cell genomic analysis of human neurons extends the observation of somatic mosaicism in the nervous system to the single-cell level. Several studies using bulk DNA from somatic tissues, including brain, have found CNVs among mono-

zygotic twins (23) and in different organs or brain regions from the same individual (24, 25). These studies were only able to detect CNVs present in >10% of the cells in the bulk sample and, thus, have only provided a coarse assessment of somatic mosaicism. We have shown that mosaic CNV is abundant in human neurons. Additional work will be required to address the full spectrum of somatic mutation in neurons and other cell lineages; however, it is possible that some neuronal lineages acquire genomic instability during development, which leads to subsequent diversification of neuronal genomes, or that individual neurons become prone to large-scale mutational events because of widespread DNA damage. A recent study has implicated electrophysiological activity as a source of double-strand DNA breaks in neurons (26), and small circular DNAs caused by excision have been reported in multiple somatic cell types, including neurons (27, 28). Additionally, retrotransposon activity is known to cause subchromosomal deletions and other rearrangements in human cells (29–32); thus, higher levels of retrotransposon activity during human neurogenesis (5, 33) may also contribute to the prevalence of CNVs in neuronal genomes.

The effect of somatic genome diversification on neuronal function remains unknown. One straightforward hypothesis is that neurons with different genomes will have distinct molecular phenotypes because of altered transcriptional or epigenetic landscapes. We expect that ongoing development of single-cell technologies will allow for this hypothesis to be tested by measuring multiple states of the same neuron (e.g., the genome and the epigenome, transcriptome, or proteome). We have shown that hiPSC-derived neurons recapitulate somatic variation, as observed in endogenous human neurons; thus, hiPSCs may offer a tractable system for applying single-cell approaches to understanding the consequences of somatic mosaicism. In the future, the ability to manipulate and measure genomic diversity in human neural circuits in vitro may help to reveal the consequences of somatic mosaicism in the brain.

References and Notes

1. S. K. Rehen *et al.*, *Proc. Natl. Acad. Sci. U.S.A.* **98**, 13361–13366 (2001).
2. S. K. Rehen *et al.*, *J. Neurosci.* **25**, 2176–2180 (2005).
3. Y. B. Yurov *et al.*, *PLOS ONE* **2**, e558 (2007).
4. A. R. Muotri *et al.*, *Nature* **435**, 903–910 (2005).

5. J. K. Baillie *et al.*, *Nature* **479**, 534–537 (2011).
6. G. D. Evrony *et al.*, *Cell* **151**, 483–496 (2012).
7. E. M. Ostertag, H. H. Kazanian, *Nature* **435**, 890–891 (2005).
8. T. Singer, M. J. McConnell, M. C. Marchetto, N. G. Coufal, F. H. Gage, *Trends Neurosci.* **33**, 345–354 (2010).
9. S. L. Martin, *Nature* **460**, 1087–1088 (2009).
10. D. M. Bushman, J. Chun, *Semin. Cell Dev. Biol.* **24**, 357–369 (2013).
11. E. Vanneste *et al.*, *Nat. Med.* **15**, 577–583 (2009).
12. N. Navin *et al.*, *Nature* **472**, 90–94 (2011).
13. K. L. Spalding, R. D. Bhardwaj, B. A. Buchholz, H. Druid, J. Frisén, *Cell* **122**, 133–143 (2005).
14. F. B. Dean *et al.*, *Proc. Natl. Acad. Sci. U.S.A.* **99**, 5261–5266 (2002).
15. A. Adey *et al.*, *Genome Biol.* **11**, R119 (2010).
16. R. S. Lasken, *Biochem. Soc. Trans.* **37**, 450–453 (2009).
17. R. S. Lasken, T. B. Stockwell, *BMC Biotechnol.* **7**, 19 (2007).
18. A. B. Olshen, E. S. Venkatraman, R. Lucito, M. Wigler, *Biostatistics* **5**, 557–572 (2004).
19. K. J. Brennand *et al.*, *Nature* **473**, 221–225 (2011).
20. L. C. Laurent *et al.*, *Cell Stem Cell* **8**, 106–118 (2011).
21. T. Baslan *et al.*, *Nat. Protoc.* **7**, 1024–1041 (2012).
22. A. Abyzov *et al.*, *Nature* **492**, 438–442 (2012).
23. C. E. Bruder *et al.*, *Am. J. Hum. Genet.* **82**, 763–771 (2008).
24. M. O'Huallachain, K. J. Karczewski, S. M. Weissman, A. E. Urban, M. P. Snyder, *Proc. Natl. Acad. Sci. U.S.A.* **109**, 18018–18023 (2012).
25. A. Piotrowski *et al.*, *Hum. Mutat.* **29**, 1118–1124 (2008).
26. E. Suberbielle *et al.*, *Nat. Neurosci.* **16**, 613–621 (2013).
27. T. Maeda *et al.*, *Biochem. Biophys. Res. Commun.* **319**, 1117–1123 (2004).
28. Y. Shibata *et al.*, *Science* **336**, 82–86 (2012).
29. N. Gilbert, S. Lutz-Prigge, J. V. Moran, *Cell* **110**, 315–325 (2002).
30. P. A. Callinan *et al.*, *J. Mol. Biol.* **348**, 791–800 (2005).
31. N. Gilbert, S. Lutz, T. A. Morrish, J. V. Moran, *Mol. Cell. Biol.* **25**, 7780–7795 (2005).
32. D. E. Symer *et al.*, *Cell* **110**, 327–338 (2002).
33. N. G. Coufal *et al.*, *Nature* **460**, 1127–1131 (2009).

Acknowledgments: We thank D. Husband (Salk), L. Moore (Salk), S. Jackmaert (KU Leuven), R. Layer (University of Virginia) and R. Clark (University of Virginia) for technical assistance; A. Prorock and Y. Bao (UVA Sequencing Core) for DNA sequencing; and all members of the Gage laboratory for critical feedback on the project. We thank M. L. Gage for editorial comments. F.H.G. thanks the Center for Academic Research and Training in Anthropogeny (CARTA) for support and perspective. This work was supported by a Crick-Jacobs

Junior Fellowship to M.J.M.; a University of Leuven (KU Leuven) SymbioSys grant (PFV/10/016) to J.R.V. and T.V.; a Mather's Family Foundation grant, a NIH TR01 (R01 MH095741), the J.P.B. Foundation, Annette Merle-Smith, and a Helmsley Foundation grant to F.H.G.; and an NIH New Innovator Award (DP20D006493-01) and Burroughs Wellcome Fund Career Award to I.M.H. Human tissue was obtained from the National Institute for Child Health and Human Development (NIH) Brain and Tissue Bank for Developmental Disorders at the University of Maryland, Baltimore, MD, contract HHSN2752009000011C, ref. no. N01-HD-9-011. The hiPSC lines used in this study are available from the Coriell Cell Repository. Microarray data have been deposited in the National Center for Biotechnology Information (NCBI) Gene Expression Omnibus (GSE51538), and DNA sequence data have been deposited in the NCBI Short-Read Archive (SRP030642).

Supplementary Materials

www.sciencemag.org/content/342/6158/632/suppl/DC1

Materials and Methods

Figs. S1 to S11

Tables S1 to S3

References (34–46)

19 July 2013; accepted 1 October 2013

10.1126/science.1243472

Resident Neural Stem Cells Restrict Tissue Damage and Neuronal Loss After Spinal Cord Injury in Mice

Hanna Sabelström,¹ Moa Stenudd,¹ Pedro Réu,^{1,2} David O. Dias,¹ Marta Elfineh,¹ Sofia Zdunek,¹ Peter Damberg,³ Christian Göritz,¹ Jonas Frisén^{1*}

Central nervous system injuries are accompanied by scar formation. It has been difficult to delineate the precise role of the scar, as it is made by several different cell types, which may limit the damage but also inhibit axonal regrowth. We show that scarring by neural stem cell–derived astrocytes is required to restrict secondary enlargement of the lesion and further axonal loss after spinal cord injury. Moreover, neural stem cell progeny exerts a neurotrophic effect required for survival of neurons adjacent to the lesion. One distinct component of the glial scar, deriving from resident neural stem cells, is required for maintaining the integrity of the injured spinal cord.

Scar formation in the injured spinal cord limits secondary damage by providing mechanical stability and restricting infiltration by inflammatory cells (1–3) but also contributes to the failure of severed axons to regrow (2, 4–6). Resident neural stem cells give rise to the majority of new astrocytes making the glial scar in the injured spinal cord (7, 8). Transplantation of stem cells, or stem cell–derived cells, to the injured spinal cord can improve functional recovery (9). The mechanisms underlying this effect are not fully understood, but trophic effects as well as remyelination of spared axons appear most important (9–13). Modulating the response of endogenous neural stem cells may offer an alternative to cell transplantation, but this requires an understanding of the function of these cells in response to spinal cord injury.

The neural stem cells in the adult mouse spinal cord constitute a small cell population, denoted ependymal cells, lining the central canal (8, 14–16). To address the role of ependymal cells in the spinal cord injury response, we selectively blocked their generation of progeny by deleting all *Ras* genes, which are required for cells to go through the G₁ phase of mitosis (17, 18). We established FoxJ1-CreER mice, which allow conditional genetic recombination specifically in ependymal cells in the adult spinal cord after administration of tamoxifen (8), homozygous for *H-Ras* and *N-Ras* null alleles and homozygous for floxed *K-Ras* alleles (17). The mice also carried a *R26R-YFP* (YFP, yellow fluorescent protein) reporter allele to allow visualization of recombination. Tamoxifen was administered to adult mice to delete *K-Ras* (we refer to these mice as FoxJ1-rasless), and matched mice with the same genotype receiving vehicle (referred to as FoxJ1 mice) were used as controls (fig. S1).

Ependymal cell proliferation was selectively reduced in the intact spinal cord (Fig. 1, A and B),

as well as after a dorsal funiculus incision in FoxJ1-rasless mice (Fig. 1, C to E, and fig. S2, A to E). Ependymal cell progeny starts migrating from the ependymal layer toward the injury site within 3 days after injury in control mice, where it almost exclusively differentiates to scar-forming astrocytes (7, 8, 14, 19). There was no migration of recombined cells from the ependymal layer in FoxJ1-rasless mice (Fig. 1F and fig. S2, F and G), establishing this as a suitable system for assessing the role of neural stem cell progeny after spinal cord injury.

We made transverse incisions by cutting the dorsal funiculus and dorsal horns at C4 in matched FoxJ1 and FoxJ1-rasless mice (*n* = 14 in each group), and we analyzed these animals 14 weeks later. All FoxJ1 control mice developed a dense glial scar at the site of the lesion (Fig. 1G). In contrast, only 3 out of 14 FoxJ1-rasless mice developed largely normal scars at the injury site. The majority of FoxJ1-rasless mice (79%) failed to form compact scar tissue and had varying degrees of tissue defects, ranging from small cavities (21%) and less compact scars with larger cavities (29%) to a single large cyst (29%) occupying the lesion area (Fig. 1, H to J).

Pericytes play a key role in spinal cord scar formation by giving rise to the fibrotic compartment of the scar (18). The fibrotic compartment was enlarged in FoxJ1-rasless mice compared with FoxJ1 control mice, suggesting that increased fibrosis may partly compensate for the absence of ependymal cell progeny (fig. S3A). Similarly, there appeared to be a compensatory increase in scarring by resident astrocytes, which were unrecombined and not deriving from ependymal cells (Fig. 1, G to J, and fig. S3B). Resident astrocytes are molecularly and, potentially, functionally distinct from astrocytes generated by ependymal cells, which are mostly negative for glial fibrillary acidic protein (8). In addition to resident astrocytes (20), oligodendrocyte lineage cells have also been suggested to generate scar-forming astrocytes in the

¹Department of Cell and Molecular Biology, Karolinska Institute, SE-171 77 Stockholm, Sweden. ²Center for Neuroscience and Cell Biology, University of Coimbra, 3004-517 Coimbra, Portugal. ³Department of Clinical Science, Intervention and Technology, Karolinska Institute, SE-171 77 Stockholm, Sweden.

*Corresponding author. E-mail: jonas.frisen@ki.se

injured forebrain (21), but this is not the case in the spinal cord (7, 16).

After the 14-week recovery period, remaining lesions in FoxJ1-rasless mice were considerably deeper, the area of damaged tissue was larger, and the spinal cord at the site of the lesion was thinner compared with FoxJ1 control animals (Fig. 2, A to C, and fig. S3, C and D). In contrast, mice with blocked pericyte response, which fail to seal the lesion and regain tissue integrity (18), did not have lesions extending deeper or increased atrophy compared with control animals (fig. S4).

To assess the consequence of enlarged lesions, we examined the integrity of the corticospinal tract, a major axonal tract located immediately ventral to the lesion in this paradigm. Scar tissue penetrated the corticospinal tract in 1 of 14 FoxJ1 control mice (Fig. 2D). In contrast, the scar tissue and tissue defects extended through and disrupted the corticospinal tract in 9 of 14 FoxJ1-rasless mice (Fig. 2, E and F) ($P = 0.002$, Fisher's exact test), suggesting that secondary enlargement of the lesion in the absence of scarring by ependymal cell progeny severed the corticospinal tract and, potentially, other axons.

To delineate the time course for the extension of the lesions in FoxJ1-rasless mice, we followed additional cohorts of FoxJ1-rasless ($n = 6$) and FoxJ1 control animals ($n = 10$) longitudinally by magnetic resonance imaging (MRI). The first scan

was made within 2 hours after injury, to establish the depth of the original lesion ($524 \pm 102 \mu\text{m}$ in FoxJ1-rasless and $584 \pm 63 \mu\text{m}$ in FoxJ1 control mice, mean \pm SEM, $P = 0.60$). Lesions in FoxJ1 control animals gradually contracted with 17% of their initial depth at 9 weeks after injury. Lesion depth was reduced in 6 of 10 FoxJ1 mice and unaltered ($\pm 5\%$ compared to initial lesion) in the remaining mice after 9 weeks. In contrast, there was a gradual extension of lesions by 29% at 9 weeks in FoxJ1-rasless mice. Lesion depth was extended in all FoxJ1-rasless mice (Fig. 2, G and H). The difference in the change in depth with time between FoxJ1 and FoxJ1-rasless animals was first statistically significant at the 3-week time point ($P = 0.003$ for week 3, Student's t test; $P = 0.002$ for all time points, analysis of covariance). Three-dimensional (3D) reconstruction of magnetic resonance images revealed that the lateral extension of the lesion was reduced over time in both FoxJ1 and FoxJ1-rasless animals, whereas lesions extended centrally to become deeper in only FoxJ1-rasless animals (Fig. 2, G to I, and movies S1 to S4).

The glial scar is normally compartmentalized with resident astrocytes forming the periphery of the scar and ependymal cell-derived astrocytes forming the central part (7). Reactive astrocytes are implicated in restricting the infiltration of inflammatory cells and protecting against the sec-

ondary damage they cause (2, 3). However, the secondary damage in FoxJ1-rasless mice was not preceded by increased infiltration of inflammatory cells. In contrast, fewer inflammatory cells were present in the injured spinal cord segment of FoxJ1-rasless mice compared with FoxJ1 mice ($P = 0.03$) (fig. S5). This finding suggests that restricting the secondary damage caused by inflammation may be a specific function for resident astrocytes, whereas ependymal cell-derived astrocytes may primarily be required to reinforce the injured spinal cord.

The atrophy of the spinal cord in FoxJ1-rasless mice extended two segments rostral and caudal to the lesion. More distant spinal cord segments were unaffected (Fig. 3A and fig. S6A). Analysis of the thickness of the spinal cord at the time of lesion and 9 weeks after injury in the same animals by MRI confirmed the increased atrophy in the absence of neural stem cell progeny (Fig. 3B). Quantification of the number of neurons revealed an $\sim 20\%$ increase in neuronal loss in FoxJ1-rasless mice compared with FoxJ1 control mice 14 weeks after injury (Fig. 3C), largely restricted to the dorsal horn (fig. S6B). Specific neuronal subpopulations in the dorsal horn were differentially affected: 64 to 66% of neurokinin-1 receptor-expressing projection neurons in lamina 1 and 32 to 46% of calbindin-expressing interneurons were lost, whereas the

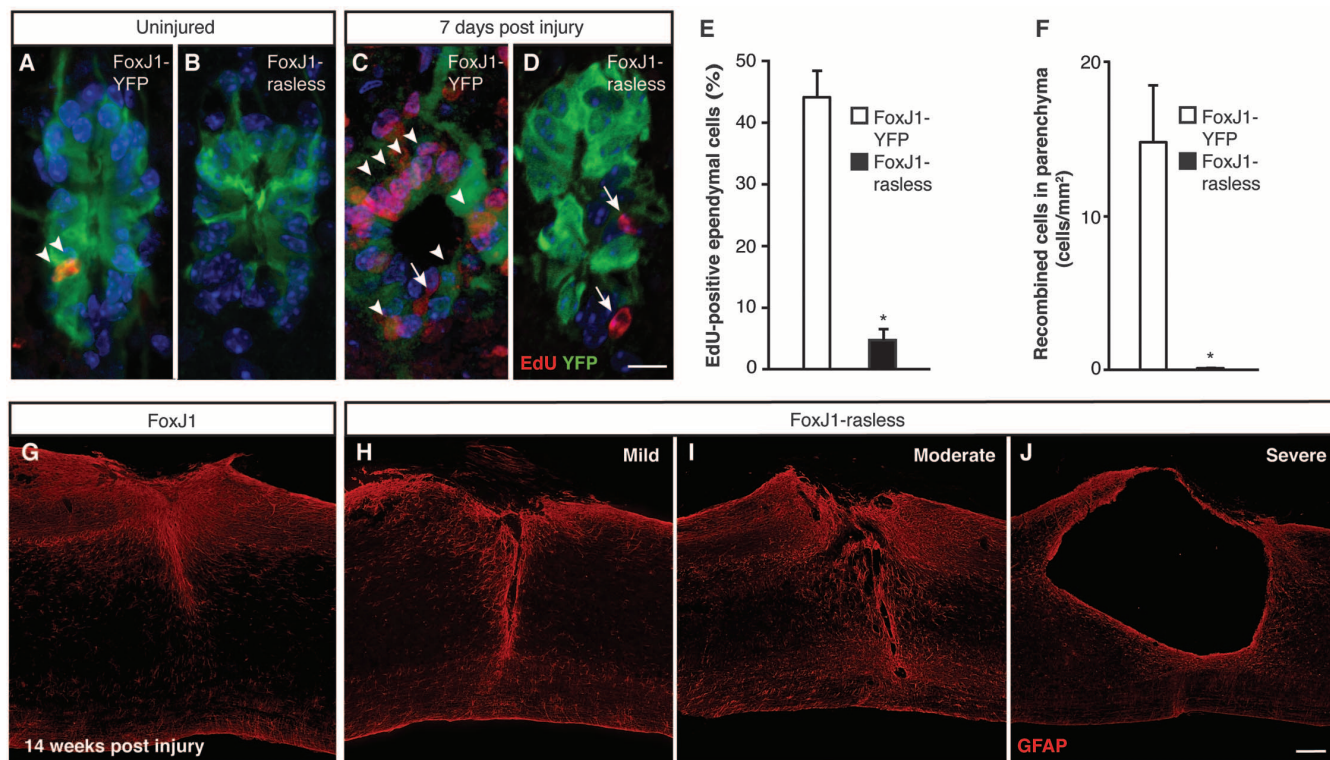


Fig. 1. Impaired scar formation in the absence of neural stem cell progeny. Ependymal cell incorporation of 5-ethynyl-2'-deoxyuridine is reduced in the absence of *Ras* genes in intact spinal cord (A and B) and 7 days after injury (C to E). Arrowheads and arrows point to proliferating recombined (A and C) and unrecombined (C and D) ependymal cells, respectively. Injury-induced migration is blocked in rasless ependymal cells

(F). Sagittal view of the lesion site 14 weeks after injury in a FoxJ1 control mouse (G) and FoxJ1-rasless mice (H to J). Recombined ependymal cells express YFP in (A) to (D), and cell nuclei are labeled with 4',6-diamidino-2-phenylindole (DAPI) and appear blue. * $P < 0.05$, ** $P < 0.01$; Student's t test. Error bars show SEM. Scale bars represent $10 \mu\text{m}$ in (A) to (D) and $200 \mu\text{m}$ in (G) to (J). GFAP, glial fibrillary acidic protein.

number of protein kinase C γ (PKC γ)-positive interneurons in lamina 2 was unaffected in FoxJ1-rasless mice compared with FoxJ1 mice (Fig. 3,

D to F). The degree of neuronal loss did not correlate to injury depth (coefficient of determination $r^2 = 0.013$ caudal and $r^2 = 0.016$ rostral to

the injury), suggesting that it may not be a direct consequence of the enlarged lesions in FoxJ1-rasless mice. Furthermore, mice in which we had

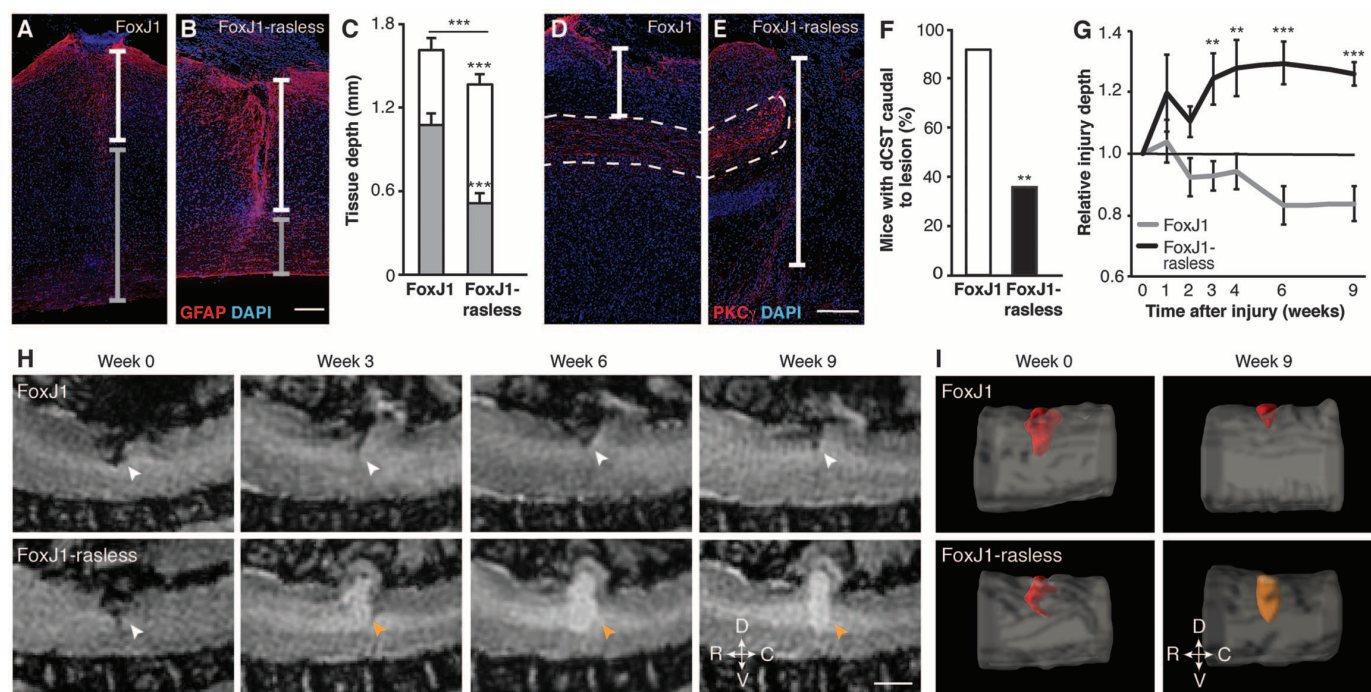
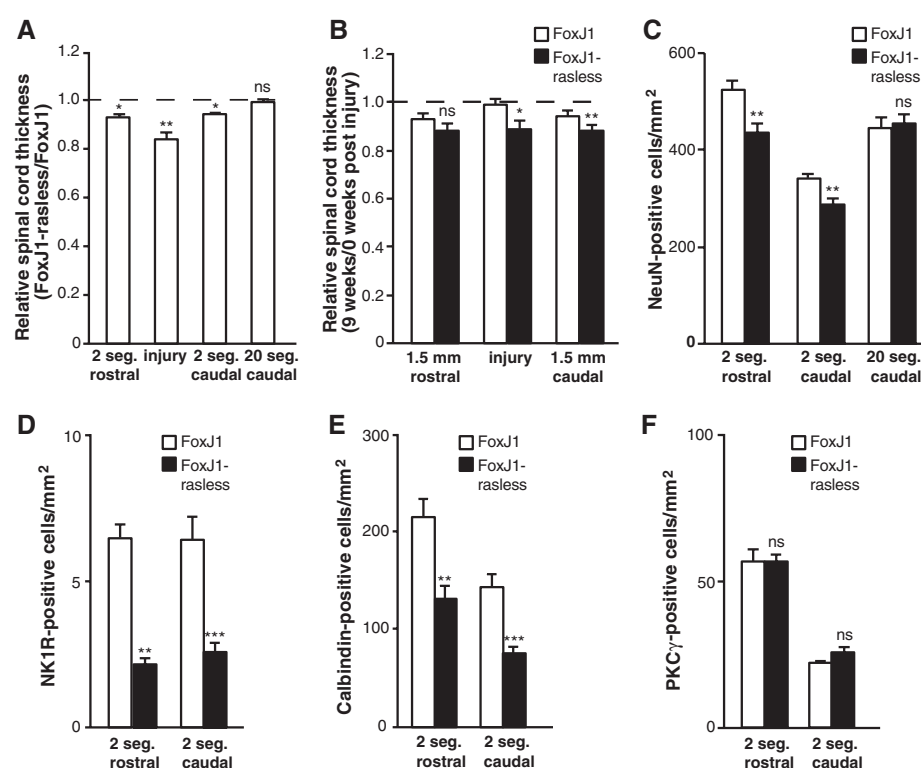


Fig. 2. Neural stem cell progeny reduces tissue damage after spinal cord injury. Glial scars (white markers) are deeper and less tissue is spared (gray markers) in the spinal cord 14 weeks after injury in FoxJ1-rasless mice (A to C). The dorsal corticospinal tract (dCST) marked by PKC γ (white dashed outline) is more frequently severed in FoxJ1-rasless mice compared with FoxJ1 control mice (D to F). Magnetic resonance images show increasing injury depth in FoxJ1-rasless mice and contraction of the lesion in FoxJ1 control mice

(G). Serial magnetic resonance images of a lesion (white arrowheads) in a FoxJ1 control mouse and a lesion developing a cyst (orange arrowheads) in a FoxJ1-rasless mouse (H). 3D reconstruction of magnetic resonance images in (H) show reduced lesion size (red) in a FoxJ1 mouse and a cyst (orange) in a FoxJ1-rasless mouse (I). D, dorsal; V, ventral; R, rostral; C, caudal. $^{*}P < 0.01$, $^{***}P < 0.001$; Student's t test (C and G), Fisher's exact test (F). Error bars show SEM. Scale bars represent 200 μ m in (A), (B), (D), and (E) and 1 mm in (H).

Fig. 3. Neuronal loss in the absence of neural stem cell-derived scar tissue. Increased spinal cord atrophy in segments adjacent to the lesion in FoxJ1-rasless mice 14 weeks after injury (A). Spinal cord thickness measured in magnetic resonance images 0 and 9 weeks after injury shows an increased atrophy in FoxJ1-rasless mice (B). The total number of neurons is reduced in segments adjacent to the lesion of FoxJ1-rasless mice 14 weeks after injury (C). NK1R-positive projection neurons (D) and calbindin-positive interneurons (E) are preferentially lost, whereas there is no reduction in the number of PKC γ -positive interneurons (F). seg, segments. $^{*}P < 0.05$, $^{**}P < 0.01$, $^{***}P < 0.001$; Student's t test. ns, not significant. Error bars show SEM.



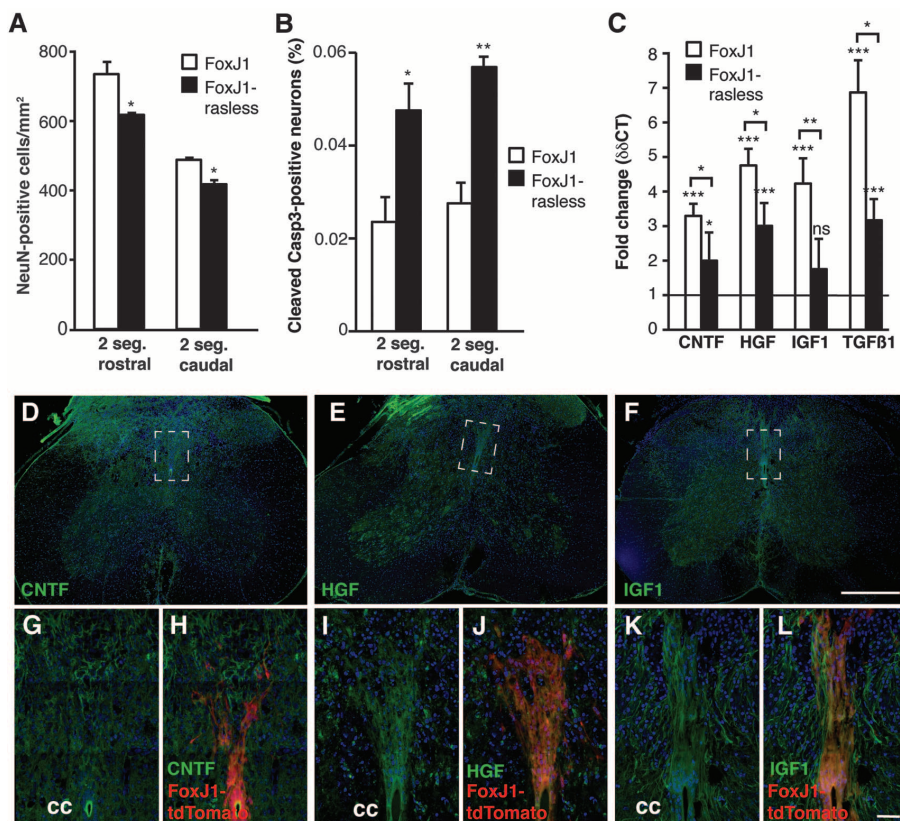


Fig. 4. Neural stem cell progeny is a major source of neurotrophic support after spinal cord injury. The number of neurons in segments adjacent to the lesion (A) and neurons undergoing apoptosis (B) 14 days after injury. mRNA levels of neurotrophic factors 14 days after injury compared with uninjured control mice (horizontal line) (C). FoxJ1-rasless mice have a reduced expression of neurotrophic factors 14 days after injury compared with FoxJ1 control mice (C). $\Delta\Delta\text{CT}$, delta delta cycle threshold. Ependymal progeny (red) expresses CNTF, HGF, and IGF-1 (D to L) 14 days after injury in control mice. Boxed areas in (D) to (F) are showed in higher magnification in (G) to (L). cc, central canal. * $P < 0.05$, ** $P < 0.01$, *** $P < 0.001$; Student's t test. Error bars show SD. Scale bars represent 500 μm in (D) to (F) and 50 μm in (G) to (L).

blocked scarring by pericyte-derived cells did not have increased neuronal loss or atrophy (fig. S6, C and D). Together, these findings suggest that the neuronal loss in FoxJ1-rasless mice may be independent from the deficient scarring and secondarily extended lesions and that ependymal cell progeny may have a trophic effect on nearby neurons.

We analyzed the number of neurons in FoxJ1 and FoxJ1-rasless mice at an earlier time point in an additional cohort of animals ($n = 3$ in each group). Approximately half the number of neurons that were lost at 14 weeks had already been lost 2 weeks after injury; neuronal death continued in subsequent weeks (Fig. 4A). Quantification of the number of cleaved caspase 3-positive apoptotic neurons demonstrated an increased number of dying neurons in the absence of ependymal cell progeny 2 weeks after injury (Fig. 4B), establishing this as a relevant time point to assess potential mechanisms for the increased neuronal loss in the absence of neural stem cell progeny.

Brain and spinal cord lesions trigger the production of neurotrophic factors (22, 23), although the importance of this has been unknown. We confirmed the previously reported increased expres-

sion of *CNTF*, *HGF*, *IGF-1*, and *TGFβ1* (CNTF, ciliary neurotrophic factor; HGF, hepatocyte growth factor; IGF, insulin-like growth factor; TGFβ, transforming growth factor-β) mRNA in the injured spinal cord (22, 24, 25) (Fig. 4C). Experimental administration of some of the corresponding proteins promotes neuronal survival after spinal cord injury (13, 24, 26), indicating that the endogenous levels are limiting. Immunohistochemistry in the injured spinal cord of control mice demonstrated that CNTF, HGF, and IGF-1 were synthesized by ependymal cell-derived astrocytes (Fig. 4, D to L, and fig. S7). FoxJ1-rasless mice had a statistically significant 47 to 77% attenuation of the up-regulation of mRNA for the neurotrophic factors (Fig. 4C). This finding establishes neural stem cell-derived cells as a major source of neurotrophic support after spinal cord injury and may explain the increased neuronal loss in the absence of ependymal cell progeny in FoxJ1-rasless mice.

Reducing scar formation has been a goal in many therapeutic strategies, but given our results, inhibiting scar formation by endogenous neural stem cells in the injured spinal cord does not appear attractive. Transplantation of spinal cord neu-

ral stem cells, which mainly give rise to astrocytes, promotes functional recovery (27). Steering the differentiation of these cells so that they also give rise to substantial numbers of remyelinating oligodendrocytes further improves the outcome (27). Thus, rather than suppressing scarring by resident neural stem cells, it is interesting to consider augmenting or modulating this response after spinal cord injury.

References and Notes

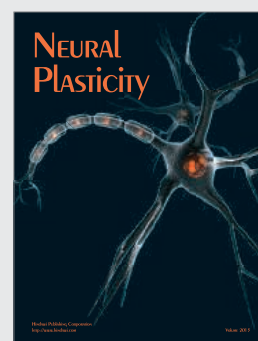
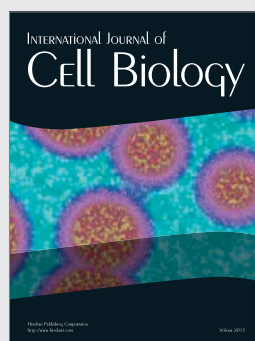
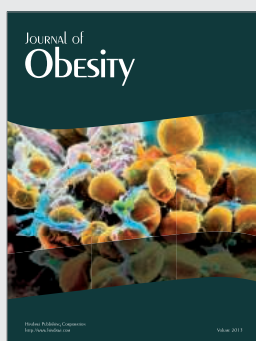
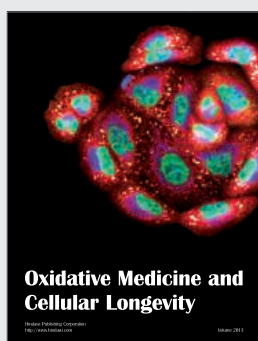
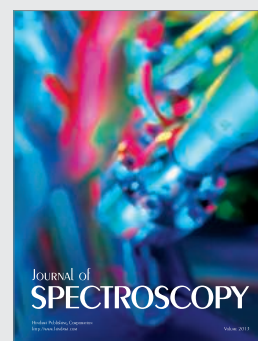
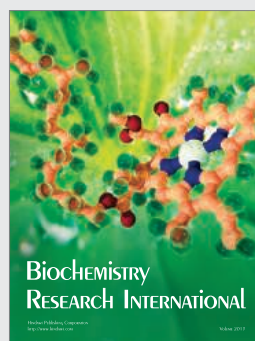
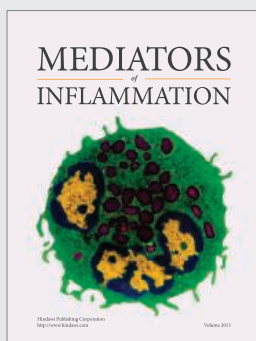
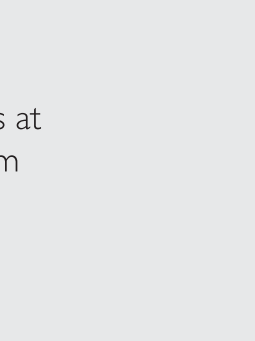
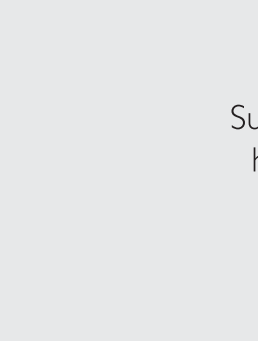
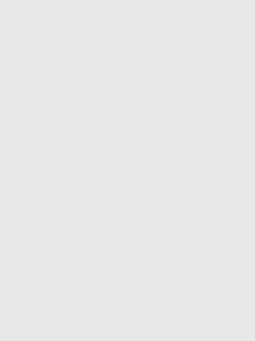
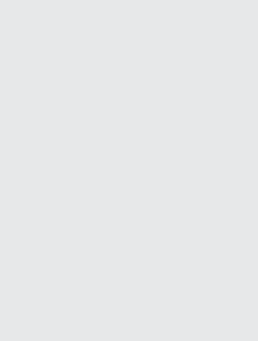
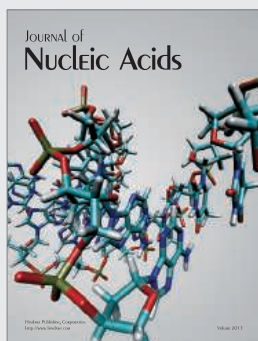
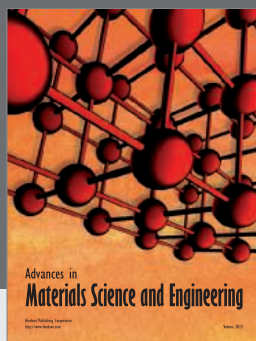
1. M. Pekny *et al.*, *J. Cell Biol.* **145**, 503–514 (1999).
2. S. Okada *et al.*, *Nat. Med.* **12**, 829–834 (2006).
3. J. E. Herrmann *et al.*, *J. Neurosci.* **28**, 7231–7243 (2008).
4. J. W. Fawcett, *J. Neurotrauma* **23**, 371–383 (2006).
5. J. Silver, J. H. Miller, *Nat. Rev. Neurosci.* **5**, 146–156 (2004).
6. M. V. Sofroniew, *Trends Neurosci.* **32**, 638–647 (2009).
7. F. Barnabé-Heider *et al.*, *Cell Stem Cell* **7**, 470–482 (2010).
8. K. Meletis *et al.*, *PLOS Biol.* **6**, e182 (2008).
9. F. Barnabé-Heider, J. Frisén, *Cell Stem Cell* **3**, 16–24 (2008).
10. J. Yan, A. M. Welsh, S. H. Bora, E. Y. Snyder, V. E. Koliatsos, *J. Comp. Neurol.* **480**, 101–114 (2004).
11. P. Lu, L. L. Jones, E. Y. Snyder, M. H. Tuszynski, *Exp. Neurol.* **181**, 115–129 (2003).
12. A. Yasuda *et al.*, *Stem Cells* **29**, 1983–1994 (2011).
13. K.-S. Hung *et al.*, *J. Neurosurg. Spine* **6**, 35–46 (2007).
14. C. B. Johansson *et al.*, *Cell* **96**, 25–34 (1999).
15. C. V. Pfenninger, C. Steinhoff, F. Hertwig, U. A. Nuber, *Glia* **59**, 68–81 (2011).
16. H. Sabelström, M. Stenudd, J. Frisén, *Exp. Neurol.* 10.1016/j.expneurol.2013.01.026 (2013).
17. M. Drosten *et al.*, *EMBO J.* **29**, 1091–1104 (2010).
18. C. Göritz *et al.*, *Science* **333**, 238–242 (2011).
19. A. J. Mothe, C. H. Tator, *Neuroscience* **131**, 177–187 (2005).
20. A. Buffo *et al.*, *Proc. Natl. Acad. Sci. U.S.A.* **105**, 3581–3586 (2008).
21. J. Kohyama *et al.*, *Proc. Natl. Acad. Sci. U.S.A.* **105**, 18012–18017 (2008).
22. G. W. J. Hawryluk *et al.*, *Stem Cells Dev.* **21**, 2222–2238 (2012).
23. M. Nieto-Sampedro *et al.*, *Science* **217**, 860–861 (1982).
24. K. Kitamura *et al.*, *J. Neurosci. Res.* **85**, 2332–2342 (2007).
25. R. B. Tripathi, D. M. McTigue, *J. Comp. Neurol.* **510**, 129–144 (2008).
26. J. Ye *et al.*, *Brain Res.* **997**, 30–39 (2004).
27. C. P. Hofstetter *et al.*, *Nat. Neurosci.* **8**, 346–353 (2005).

Acknowledgments: We thank F. Barnabé-Heider and O. Bergmann for discussions and M. Barbacid for providing *Ras* mutant mice through a materials transfer agreement with Centro Nacional de Investigaciones Oncológicas (Spanish National Cancer Institute, CNIO), Spain. Requests for mice should be directed to M. Barbacid (CNIO, Spain). This study was supported by the Swedish Research Council, the Swedish Cancer Society, the Karolinska Institute, Tobias Stiftelsen, AFA Försäkrings, StratRegen, and Knut och Alice Wallenbergs Stiftelse. D.O.D. and P.R. were supported by the Foundation for Science and Technology from the Portuguese government (SFRH/BD/63164/2009 and SFRH/BD/33465/2008).

Supplementary Materials

www.sciencemag.org/content/342/6158/637/suppl/DC1
Supplementary Text
Figs. S1 to S7
Movies S1 to S4

28 June 2013; accepted 23 September 2013
10.1126/science.1242576

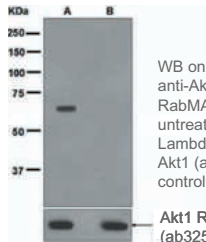


Submit your manuscripts at
<http://www.hindawi.com>

What can **RabMAbs[®]** do for you?

#1	Low background
#2	Post-Translational Modifications
#3	Excellent for IHC usage
#4	Multiple Applications

RabMAbs[®] offer high quality antibodies detecting post-translational modifications such as phosphorylation:



WB on NIH/3T3 using anti-Akt 1 Phospho (pT450) RabMAb (ab108266). (A) untreated or (B) treated with Lambda Phosphatase. Akt1 (ab32510) as a pan control

Akt1 RabMAb (ab32510)



Rabbit Monoclonal Antibodies (RabMAbs[®]) offer multiple advantages to bring you the highest quality antibody possible.

Discover more at abcam.com/RabMAbs



Better results — on any sequencing platform

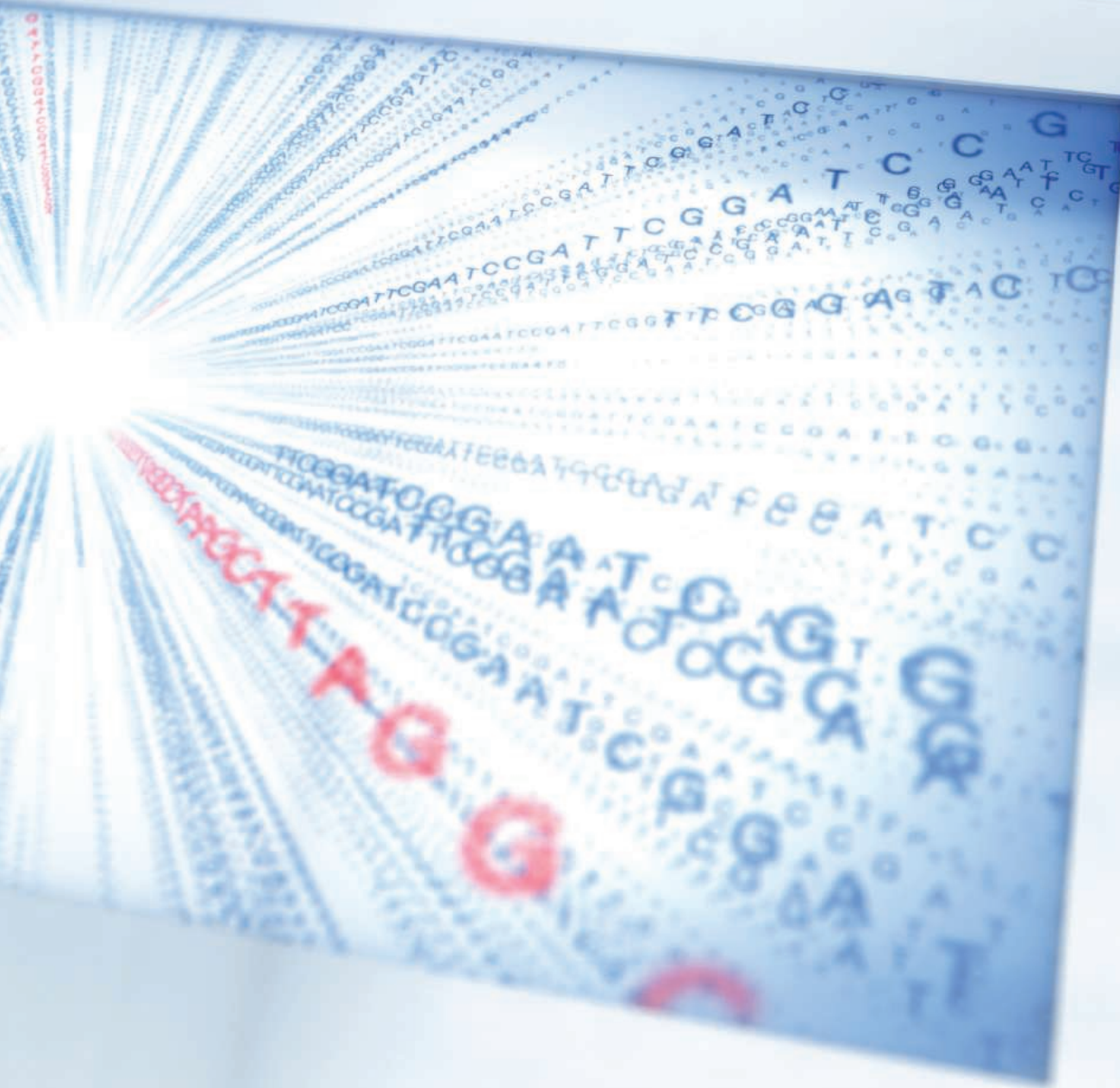
Get the most from your NGS

Discover new and innovative solutions,
dedicated for use with any NGS workflow

Streamline your next-generation sequencing (NGS) workflow and achieve high-quality results you can rely on.

- **Highly specific and selective nucleic acid purification and target enrichment**
- **Unbiased whole genome amplification from a single cell**
- **High DNA library yields using optimized workflows that allow ~50% time-savings**
- **Outstanding results on any sequencing platform**
- **Intuitive, knowledge-based data interpretation for deeper insight into NGS results**

Visit www.qiagen.com/goto/NGS to learn more!



Sample & Assay Technologies

Make ends meet.



Gibson Assembly[®] Cloning Kit

New England Biolabs has revolutionized your laboratory's standard cloning methodology. The Gibson Assembly Cloning Kit combines the power of the Gibson Assembly Master Mix with NEB 5-alpha Competent *E. coli*, enabling fragment assembly and transformation in just under two hours. Save time, without sacrificing efficiency.

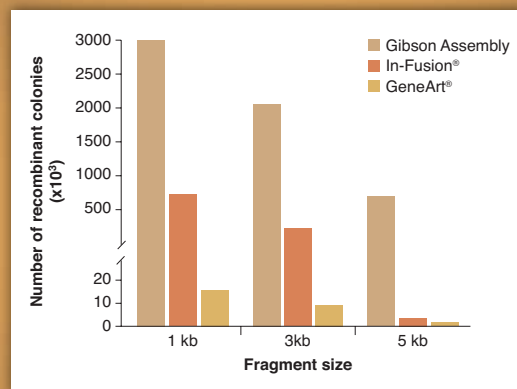
Making ends meet is now quicker and easier than ever before, with the Gibson Assembly Cloning Kit from NEB.

NEBuilder[™]
for Gibson Assembly

Visit NEBGibson.com to view the latest tutorials and to try our primer design tool.

IN-FUSION[®] is a registered trademark of Clontech Laboratories, Inc.
GENEART[®] is a registered trademark of Life Technologies, Inc.
GIBSON ASSEMBLY[®] is a registered trademark of Synthetic Genomics, Inc.

Gibson Assembly Cloning Kit provides robust transformation efficiencies



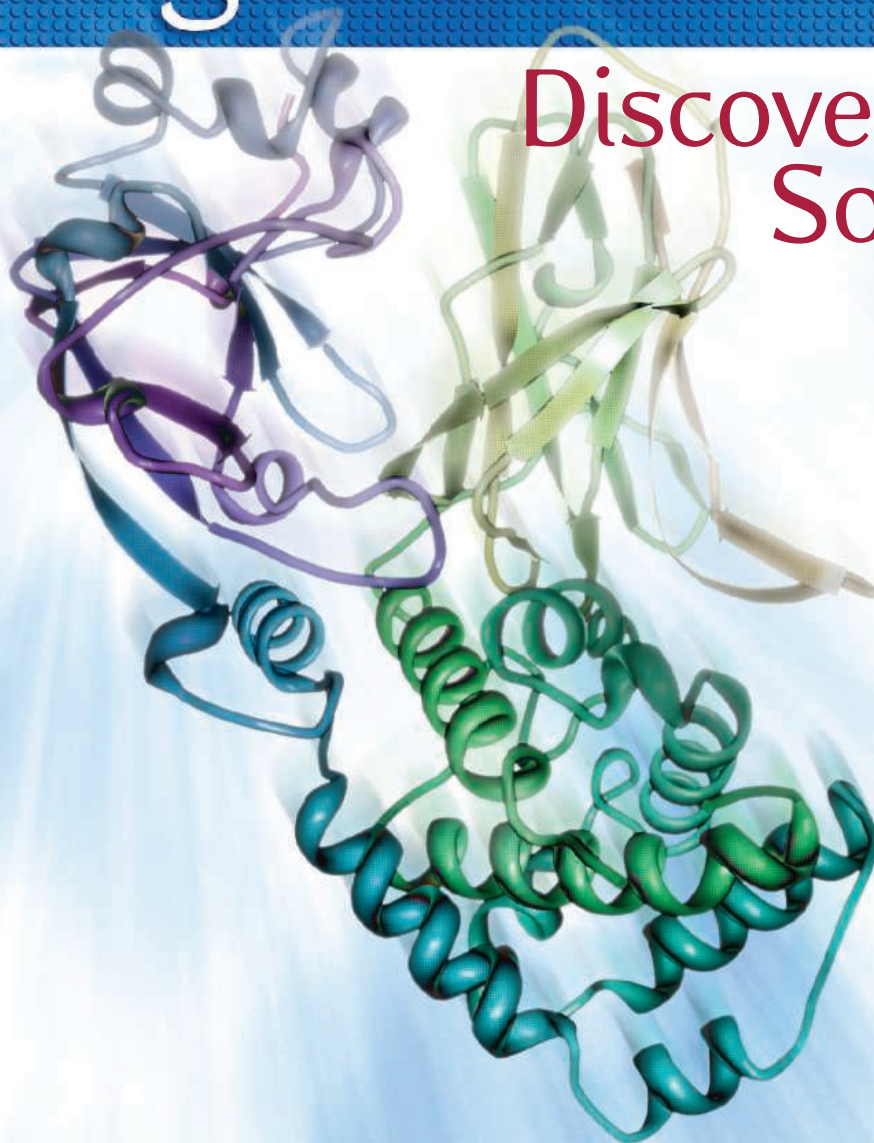
Assembly reactions containing 25 ng of linear pUC19 vector and 0.04 pmol of each fragment were performed following individual suppliers' recommended protocols and using the competent cells provided with the kit. The total number of recombinant colonies was calculated per 25 ng of linear pUC19 vector added to the assembly reaction.

SGIDNA

Some components of this product are manufactured by New England Biolabs, Inc. under license from Synthetic Genomics, Inc.

Reagent Proteins

Discover the
Source



Reagent Proteins is the source

With over 5,000 recombinant proteins available, *Reagent Proteins* provides seamless access to the highest quality reagent, pre-clinical and cGMP grade proteins for research purposes.



SimpleStep[™] ELISA kits – make your life easier



Mix → Wash → Read. It's that easy.

Discover our new single wash sandwich ELISA
assay offering improved performance.

Discover more at abcam.com/SimpleStep

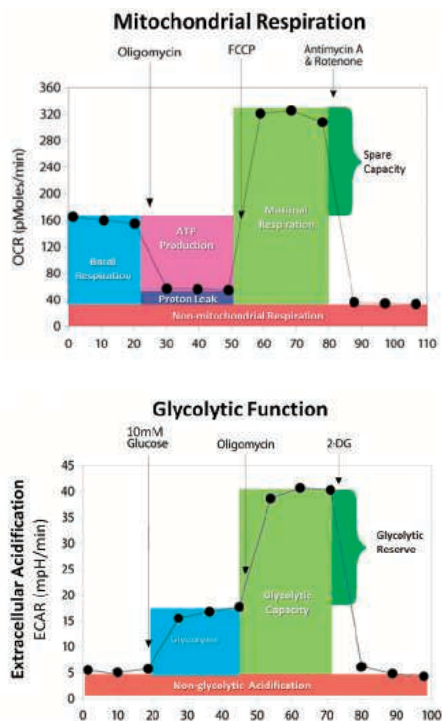
 **SimpleStep[™]**

“ WE’RE BRINGING A NEW PERSPECTIVE TO
cancer metabolism research

FIRST WE MADE IT POSSIBLE – NOW WE’VE MADE IT EASY.

XF technology provides the easiest and most comprehensive assessment of cancer cell metabolism, measuring glucose and glutamine metabolism, and fatty acid oxidation of cancer cells in a microplate, in real-time! ”

— David Ferrick, PhD,
CSO, Seahorse Bioscience



The Seahorse XF^e Extracellular Flux Analyzer

Measurements of cellular glycolysis are essential to understanding cancer, immune response, stem cell differentiation, aging, and cardiovascular and neurodegenerative diseases. The XF^e Analyzer and XF Glycolysis Stress Test Kit make it easy to measure the three key parameters of cellular glycolysis in a microplate: glycolysis, glycolytic capacity, and glycolytic reserve, revealing critical information not evident in mitochondrial respiration measurements alone.



See what's possible.

Scan this QR code to view videos and see what the XF Analyzer can achieve.
Visit www.seahorsebio.com/science for more information!

Seahorse Bioscience

BD Accuri™ C6 Systems

Perfectly suited to support demanding educational environments.



Learn. Teach. Master.

The BD Accuri C6 is a perfect fit for personal research, student mastery, and core lab use. It's easy to learn and operate, powerful enough for the majority of routine flow applications, and small enough for easy transport, making it perfect for the demands of the educational environment. Affordably priced, it may just be one of the best valued instrument in your lab.

The 4-color BD Accuri C6 allows for teaching and learning in a guided way, through templates, and factory pre-sets. The system also collects and stores 7.2 decades of data to empower novice users to make corrections if errors are made.



Helping all people
live healthy lives

Those new to flow cytometry will appreciate the simplicity of the BD Accuri C6, while experts will appreciate the extensive capabilities and workflow advantages. Core lab managers will be able to better allocate resources, offloading routine applications and reserving higher-end systems for more complex, multi-parameter duties. Researchers will find it empowering for personal research and affordable.

Find out how your teaching institution and lab could benefit from owning BD Accuri C6 systems by visiting bdbiosciences.com/go/learn.

BD flow cytometers are Class 1 Laser Products.
For Research Use Only. Not for use in diagnostic or therapeutic procedures.
BD, BD Logo and all other trademarks are property of Becton, Dickinson and Company. © 2013 BD
23-15581-00

BD Biosciences
2350 Qume Drive
San Jose, CA 95131
bdbiosciences.com

Suit(Ab)le.

We're selective. We're specific. We're scientists.
We create the antibodies that are most relevant
for today's research needs.

As a thoughtful producer, we take a selective approach to offering the best antibodies for each target. Our team of R&D scientists combs research and collaborates with leading institutions to identify only the most relevant antibodies for your research. Our expertise combines the pioneering work of Chemicon® and Upstate®, but our wisdom doesn't stop there. We constantly review, assess and determine which antibodies are the most suitable – those which provide the right level and type of data. It is our job to understand your needs so we can offer you the best of the best.

Put the most suitable
antibodies to work for you.
www.emdmillipore.com/Ab

(Ab)

EMD Millipore is a division of Merck KGaA, Darmstadt, Germany

EMD Millipore and the M logo are trademarks and Chemicon and Upstate are registered trademarks of Merck KGaA, Darmstadt, Germany. 04/2013 BS GEN-13-08111
© 2013 EMD Millipore Corporation, Billerica, MA USA. All rights reserved.



Science Translational
Medicine is pleased
to announce the

AAAS Martin and Rose Wachtel Cancer Research Award

This annual award honors early-career cancer researchers who have performed outstanding work in the field of cancer research. Nominees must have received their PhD or MD within the last 10 years. The award winner will be invited to deliver a public lecture on his or her research and will receive a cash award of \$25,000. The award winner's Perspective will be published in *Science Translational Medicine*.

Call for
Nominations
for 2014 Award
Due by March 1st, 2014

Nomination packages must include the following materials, written in English:

- A letter describing the nominee's significant contributions to cancer research, including supporting publications. The letter should explain how the candidate's research promises to make a lasting impact on the cancer field. (Applicants may nominate themselves.)
- A letter of support from another scientist who knows the applicant's work.
- The nominee's curriculum vitae.
- A Perspective (1500 words maximum, 1 figure) written by the nominee describing their research project and explaining how it advances our understanding of cancer. The research described in the Perspective must be in the field of cancer and the nominee must have performed or directed the work within the last 10 years.

Submit nominations to wachtelprize@aaas.org and put "Wachtel Award Nomination" in the subject line. For more information see: <http://www.aaas.org/aboutaaas/awards/wachtel/>.

This award is funded by an endowment established through a bequest from Martin Wachtel and is presented by Science Translational Medicine.

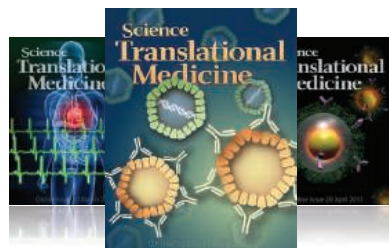
Science Translational Medicine

Integrating Science, Engineering, and Medicine

Publishing results that harness the
basic sciences to advance human
health in all areas of medicine

Submit your research
ScienceTranslationalMedicine.org

Recommend to your library
ScienceOnline.org/recommend



scitranslmededitors@aaas.org



LAMBDA VF-5 Tunable filter changer

NEW!



Introducing the world's first filter changer to use tunable thin-film optical filters. The Sutter **LAMBDA VF-5** allows you to quickly access any center bandpass from 330 to 800nm in nanometer increments. Building on the VersaChrome® filters from Semrock®, the **LAMBDA VF-5** maintains transmission over the tuning range of each filter.

Easy Wavelength Selection

Wavelength range as wide as 330-800nm
Keypad or computer interface (USB or serial)

Flexible

Suitable for excitation or emission
Easily switch between fluorophore combinations
Optional liquid light guide offers absolute vibration isolation
Images pass through filters

Thin filter advantage

High transmission
Steep spectral edges
High out-of-band blocking
Polarization independence
(s and p nearly identical)

SUTTER INSTRUMENT

PHONE: 415.883.0128 | FAX: 415.883.0572
EMAIL: INFO@SUTTER.COM | WWW.SUTTER.COM

**eppendorf
& Science**
**PRIZE FOR
NEURO
BIOLOGY**

Congratulations
to Dr. Michael Yartsev
CV Starr Research Fellow
Princeton Neuroscience
Institute



And the Winner is ...

Eppendorf & Science Prize for Neurobiology

Congratulations to Michael Yartsev on winning the 2013 Eppendorf & Science Prize. Dr. Yartsev used an unusual animal model, the bat, to study the underlying neural mechanisms of spatial memory and navigation in the mammalian brain. His approach allowed for both a comparative examination of current hypotheses as well as novel insight into long standing questions in the field. His work also underscores the potential benefits of using new animal models in neuroscience.

Learn more at: www.eppendorf.com/prize


The annual US\$25,000 Eppendorf & Science Prize for Neurobiology honors scientists, like Dr. Yartsev, for their outstanding contributions to neurobiology research. Dr. Yartsev is the twelfth recipient of this international award. He will be presented with the Prize at a ceremony held during the week of the 2013 Annual Meeting of the Society for Neuroscience in San Diego.

You Could Be Next.

If you are 35 years of age or younger and currently performing neurobiology research, you could be next to win the 2014 Prize. Deadline for entries is June 15, 2014.

eppendorf





NO ANTIBODY. NO PROBLEM.

Breakthrough multiplex RNA
in situ hybridization for any gene
with RNAscope® technology.

Be Amazed.

Because up to 76% of protein-coding genes have no reliable antibody for immunohistochemistry (IHC), your research often comes to a screeching halt while you wait for a new antibody to be developed. We say forget your antibody problems. Choose RNAscope technology. With rapid probe design and universal assay workflows for any gene, RNAscope frees you from the hassles of antibody screening, saving you precious time and effort, while delivering publication quality data.

Learn more about RNAscope now at
www.acdbio.com/no-antibody

For research use only, not intended for diagnostic procedures. RNAscope®, RNAscopeVS™, CTCscope™, DNAscope™, RNAflow™, No Antibody No Problem™, Why Wait?™, and Now You Can See Any RNA™ are registered trademarks or trademarks of Advanced Cell Diagnostics, Inc. in the United States or other countries. All rights reserved. ©2013 Advanced Cell Diagnostics, Inc.

SEE ACD@
SfN 2013
BOOTH 3104

Advanced Cell Diagnostics



AAAS Travels



AEGEAN ODYSSEY

April 21-May 5, 2014

Athens • Delphi • Mykonos
Santorini • Knossos • Crete

Explore the cultural heritage of ancient Greece and pay homage to the great Parthenon Temple on the Acropolis. Visit the Oracle at Delphi, against the backdrop of Mt. Parnassos. On Crete we'll unravel the mysteries of the Minoans. Sparkling museums and fascinating archaeological sites will enchant us! \$3,995 + air.

**For a detailed brochure,
please call (800) 252-4910**

All prices are per person twin share + air



BETCHART EXPEDITIONS Inc.

17050 Montebello Rd, Cupertino, CA 95014

Email: AAASInfo@betchartexpeditions.com

www.betchartexpeditions.com



Join the Conversation!

Twitter is a great way to connect with AAAS members and staff about the issues that matter to you most. Be a part of the discussion while staying up-to-date on the latest news and information about your personal member benefits.

**Follow us @AAASmember
and join the conversation
with #AAAS**



MemberCentral.aaas.org



NOW THAT'S ADVAAANCED

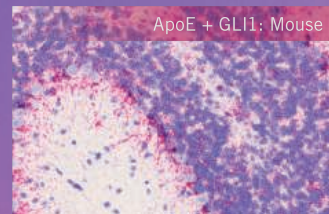
Atlas Antibodies Advanced Polyclonals, or AAA Polyclonals, are designed for antigen uniqueness and optimal epitope recognition. This together with affinity purification on the recombinant antigen and extensive quality control provides you with the most specific, reliable and versatile antibodies possible.



Atlas Antibodies Advanced Polyclonals.
Triple A rated.

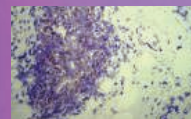


Learn more today at atlasantibodies.com

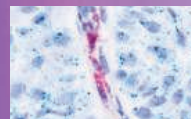


No Antibody. No Problem.

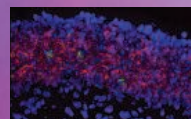
Get immediate results with
RNAscope® ISH Assays for
any gene in any species.



RNAscope Single-Plex ISH
FGFR1 mRNA
FFPE breast cancer tissue



RNAscope 2-Plex ISH
PECAM1 and EGFR mRNA
FFPE breast cancer tissue



RNAscope Multiplex ISH
OMP and OLF73 mRNA
Fresh-frozen olfactory bulb

Exquisite sensitivity
Custom probes in < 2 weeks
Over 27,000 predesigned probes
Complete the assay and see your
data in one day
Easy and guaranteed to work

www.acdbio.com/no-antibody

Be Amazed.



AAAS | 2014 ANNUAL MEETING

13-17 FEBRUARY • CHICAGO

MEETING GLOBAL CHALLENGES:
DISCOVERY AND INNOVATION

Advance your career at the 2014 AAAS Annual Meeting!

Attend career development workshops and network with thousands of scientists, engineers, educators, policymakers, communicators, and journalists in Chicago.

Career development workshops include:

- Knowing Your Worth: The Art (and Etiquette) of Negotiating a Job Offer
- Manage Your Online Profile, Maximize the Visibility of Your Work, and Make an Impact!
- Getting Started in Social Media
- Grant Skills Are Career Skills: Integrate to Accelerate
- Editing Your Own Papers and Proposals: How to Wow Reviewers and Aid Readers

The complete workshop list and full scientific program are available online.

Register today!

www.aaas.org/meetings



Auto XY Stage

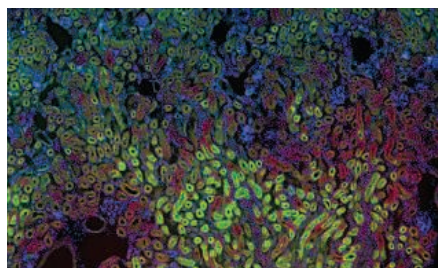
Auto Focus

Auto Cell Counting

Auto Image Capture



AutoEasy



High quality, automated imaging made simple.

With so many ways to automate cell counting and image analyses, the Cytation™3 Cell Imaging Multi-Mode Reader saves time and improves your workflow; all at a reasonable price. It can also be upgraded at any time to a Hybrid multi-mode microplate reader for enhanced flexibility and value.

To see all it can do for live cell applications, visit www.cytation3.com.

Think Possible

BioTek®



www.biotek.com

CLAMPING DEVICE

The DrySyn 3-Position Clamp has been designed to enable chemists performing parallel synthesis to secure up to three round-bottomed flasks or condensers to a standard boss head. Incorporating a novel fast grip/release mechanism, the DrySyn 3-position clamp minimizes reaction setup time and enables you to remove your reactions from the heat source quickly and safely should the need arise. Ruggedly constructed from aluminium and stainless steel, the compact and affordably priced DrySyn 3-position clamp is available in a range of sizes to securely hold condensers and flasks from 10 mL to 500 mL. The DrySyn 3-position clamps are fully compatible with Asynt's DrySyn MULTI, MULTI-M, and MULTI-S heating block systems.

Asynt

For info: +44-(0)-1638-781709 | www.asynt.com



PELTIER-COOLED INCUBATORS

Peltier-cooled incubators feature solid-state Peltier cooling and are designed for biological and genomics laboratory researchers engaged in fruit fly and biochemical oxygen demand (BOD) research. Operating within the temperature range (15°C to 40°C) to optimize the growth of drosophila (or fruit flies) for research studies, the Peltier-cooled incubators are available in two models, the 3915FL and 3915LT. The incubator is designed to create optimal conditions for the rearing of fruit flies used in a variety of biological, genetics, and physiology studies. With Peltier cooling technology, temperature variation due to coil corrosion caused by fly secretion is no longer a concern and the growth of flies is more consistent. Fully controllable LED lights mimic day and night conditions without impacting temperature performance, programmable temperature ranges, and uniform temperature throughout the chamber. A mechanical convection airflow system ensures even air distribution and excellent temperature uniformity throughout the units.

Thermo Fisher Scientific

For info: 866-984-3766 | www.thermoscientific.com/incubators

PROTEIN ANALYSIS

Over recent years, magnetic bead systems have become indispensable for protein analysis, with many companies adopting this technology to produce a variety of innovative assays. As an alternative to the enzyme-linked immunosorbent assay (ELISA) for specific protein quantification, Bio-Rad has enhanced its MAGPIX platform for multiplex magnetic bead-based immunoassays, with the new Bio-Plex Manager MP software. The MAGPIX supports Bio-Plex assays, which are based on Luminex xMAP technology. Essentially relying on the use of differentially detectable analyte capture beads and fluorescently labeled detection antibodies, the Bio-Plex system provides researchers with the ability to detect and quantify up to 50 analytes within a single reaction well. This upgraded interface ensures reliable performance that is intuitive even for the most inexperienced user. Bio-Plex Manager MP allows users to set up protocols, control the instrument, and effortlessly integrate with other Bio-Plex software packages such as Bio-Plex Data Pro.

Bio-Rad

For info: 800-424-6723 | www.biorad.com

REFRIGERATED OPEN TANK

A refrigerated open tank that delivers up to 400 watts of cooling at 20°C is now available. Designed to provide continuous cooling to 0°C (32°F), this 13 L bath is ideal for applications where bath temperatures at or below ambient are required. A heated thermostat, such as the PolyScience MX Immersion Circulator, is required for temperature control. The 13L Refrigerated Open Tank features a 0°C to 150°C (32°F to 302°F) working temperature, Cool Command refrigeration technology, and an insulated stainless steel reservoir with 22.9 x 29.8 x 19.7 cm (9 x 11.75 x 7.75 in.) working access. It is available for either 120V, 60Hz or 240V, 50Hz operation.

PolyScience

For info: 800-229-7569 | www.polyscience.com

HYPOXIA/ROS ASSAYS

The Cyto-ID Hypoxia/Oxidative Stress Detection Kit and Mito-ID O₂ and pH Sensor Probes provide unique and time-saving solutions to enable accurate profiling of hypoxia, reactive oxygen species (ROS), and mitochondrial dysfunction related to oxidative stress. The Cyto-ID Hypoxia/Oxidative Stress Detection Kit uses two membrane-permeable, fluorogenic probes to simultaneously detect hypoxia and ROS in live cells. The Hypoxia probe fluoresces red following its conversion by increased nitroreductase activity, while the Oxidative Stress Detection Reagent fluoresces green in the presence of a wide range of ROS. The kit is suitable for analysis of suspension or adherent cells by fluorescent microscopy or flow cytometry, using industry-standard filter/laser combinations. Mito-ID Extracellular O₂ Sensor Kits utilize an oxygen-sensitive phosphorescent probe that increases in signal intensity with O₂ consumption and can be multiplexed with the Mito-ID Extracellular pH Sensor Probe, a pH-sensitive phosphorescent probe that monitors cellular acid extrusion resulting from mitotoxicity-associated increases in glycolytic flux.

Enzo Life Sciences

For info: 800-942-0430 | www.enzolifesciences.com

Electronically submit your new product description or product literature information! Go to www.sciencemag.org/products/newproducts.dtl for more information. Newly offered instrumentation, apparatus, and laboratory materials of interest to researchers in all disciplines in academic, industrial, and governmental organizations are featured in this space. Emphasis is given to purpose, chief characteristics, and availability of products and materials. Endorsement by *Science* or AAAS of any products or materials mentioned is not implied. Additional information may be obtained from the manufacturer or supplier.

Science Signaling

The Leading Journal for Cell Signaling

Publishing key findings of broad
relevance in the multidisciplinary
field of cell signaling

Submit your research

ScienceSignaling.org

Recommend to your library

ScienceOnline.org/recommend

Join the ranks of high-profile papers
published in *Science Signaling*:

CANCER BIOLOGY

Vemurafenib Potently Induces Endoplasmic
Reticulum Stress–Mediated Apoptosis in
BRAFV600E Melanoma Cells

D. Beck *et al.* (F. Meier), *Sci. Signal.* **6**, ra7 (2013)

NEUROSCIENCE

Requirement for Nuclear Calcium Signaling in
Drosophila Long-Term Memory

J.-M. Weislogel *et al.* (H. Bading), *Sci. Signal.* **6**, ra33 (2013)

CELL AND MOLECULAR BIOLOGY

A Nontranscriptional Role for HIF-1 α as a Direct
Inhibitor of DNA Replication

M. E. Hubbi *et al.* (G. L. Semenza), *Sci. Signal.* **6**, ra10 (2013)

IMMUNOLOGY

Monovalent and Multivalent Ligation of the
B Cell Receptor Exhibit Differential Dependence
upon Syk and Src Family Kinases

S. Mukherjee *et al.* (A. Weiss), *Sci. Signal.* **6**, ra1 (2013)

COMPUTATIONAL AND SYSTEMS BIOLOGY

Cross-Species Protein Interactome Mapping
Reveals Species-Specific Wiring of Stress
Response Pathways

J. Das *et al.* (H. Yu), *Sci. Signal.* **6**, ra38 (2013)

Chief Scientific Editor

Michael B. Yaffe, M.D., Ph.D.

Massachusetts Institute of Technology

Editor

Nancy R. Gough, Ph.D.

AAAS, Washington, DC



sciencesignalingeditors@aaas.org

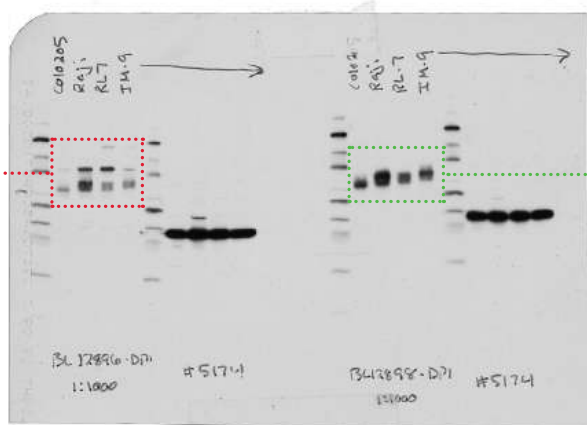
You've carefully
designed your
experiment.

Taylor Ngo started at CST 8
years ago and is currently in
the Molecular Biology group.

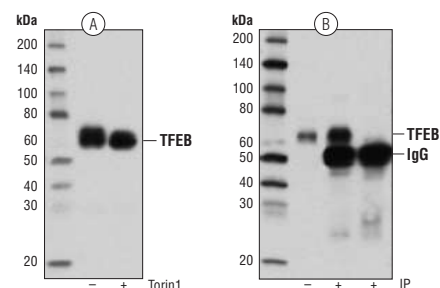
Does your antibody measure up?

We validate all our antibodies in-house. If it's not specific, it doesn't ship.

REJECTED
Extra Band
Weak Signal



**CST
APPROVED**
Clean Band
Strong Signal



TFEB Antibody #4240: (A) WB analysis of Raji cell extracts, untreated (-) or Torin1-treated, using #4240 (Torin1 treatment induces dephosphorylation). **(B)** IP of TFEB from COLO 205 cells using #4240 (lane 2) or Normal Rabbit IgG #2729 (lane 3). Lane 1 is 10% input.

WB analysis of various cell extracts using two development samples at 1:1000 dilution. GAPDH (D16H11) XP® Rabbit mAb #5174 was used as a loading control.

Please visit our website to request a copy of our new white paper – *A Guide to Successful Western Blotting*.

www.cellsignal.com/successfulWB

© 2013 Cell Signaling Technology, Inc. Cell Signaling Technology® and XP® are trademarks of Cell Signaling Technology, Inc.



Cell Signaling
TECHNOLOGY®

There's only one

Science



Science Careers Advertising

For full advertising details, go to ScienceCareers.org and click For Employers, or call one of our representatives.

Tracy Holmes
Worldwide Associate Director
Science Careers
Phone: +44 (0) 1223 326525

THE AMERICAS

E-mail: advertise@sciencecareers.org
Fax: 202-289-6742

Tina Burks
East Coast/West Coast/South America
Phone: 202-326-6577

Marci Gallun
Midwest/Canada
Phone: 202-326-6582

Candice Nulsen
Corporate
Phone: 202-256-1528

Online Job Posting Questions
Phone: 202-312-6375

EUROPE / INDIA / AUSTRALIA / NEW ZEALAND / REST OF WORLD

E-mail: ads@science-int.co.uk
Fax: +44 (0) 1223 326532

Axel Gesatzki
Phone: +44 (0)1223 326529

Sarah Lelarge
Phone: +44 (0) 1223 326527

Kelly Grace
Phone: +44 (0) 1223 326528

JAPAN

Yuri Kobayashi
Phone: +81-(0)90-9110-1719
E-mail: ykobayas@aaas.org

CHINA / KOREA / SINGAPORE / TAIWAN / THAILAND

Ruolei Wu
Phone: +86-1367-1015-294
E-mail: rwu@aaas.org

All ads submitted for publication must comply with applicable U.S. and non-U.S. laws. *Science* reserves the right to refuse any advertisement at its sole discretion for any reason, including without limitation for offensive language or inappropriate content, and all advertising is subject to publisher approval. *Science* encourages our readers to alert us to any ads that they feel may be discriminatory or offensive.

Science Careers

From the journal *Science*



ScienceCareers.org



AAAS is here – helping scientists achieve career success.

Every month, over 400,000 students and scientists visit ScienceCareers.org in search of the information, advice, and opportunities they need to take the next step in their careers.

A complete career resource, free to the public, *Science* Careers offers a suite of tools and services developed specifically for scientists. With hundreds of career development articles, webinars and downloadable booklets filled with practical advice, a community forum providing answers to career questions, and thousands of job listings in academia, government, and industry, *Science* Careers has helped countless individuals prepare themselves for successful careers.

As a AAAS member, your dues help AAAS make this service freely available to the scientific community. If you're not a member, join us. Together we can make a difference.

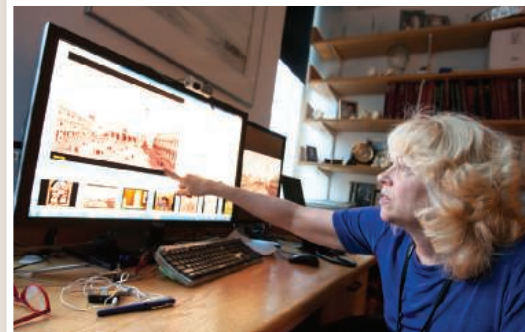
To learn more, visit
aaas.org/plusyou/sciencecareers



Making Sense of Our Senses



When people express their love of life, they often describe corporeal sensations—the taste of dark chocolate, the rapture of listening to Mozart’s complex symphonies, or the radiant vision of the sun rising above the sea. While the emotions our senses elicit have moved our souls for ages, sensory neuroscientists are only now beginning to understand how the brain encodes and processes the information inundating our bodies. Understanding the basic mechanisms underlying our perceptions is only one area of sensory science in which scientists are building their careers. Others are translating these research findings into innovations that improve how we experience life, from restoring hearing loss to dampening pain to enriching the scents and flavors of every day products. **By Amy Maxmen**



Margaret Livingstone

Technological advances in areas such as induced pluripotent stem (iPS) cell systems, DNA sequencing, and optogenetics have been accelerating every aspect of sensory science over the past decade. **Ruth McKernan**, the chief scientific officer of the pain and sensory disorder unit at Pfizer’s Neusentis, based in Cambridge, U.K., is well aware of the recent technological tidal wave. Having entered sensory science in the early 1980s as a graduate student studying neuroscience at the University of London, McKernan has seen the trends change from her studies of neurotransmitter release at single synapses in the rat brain to the ability to now analyze the activity of hundreds of neurons at once.

“This field has been revolutionized by technology,” McKernan says. “We can now answer questions using very large datasets,” drawn from the genetic analyses of hundreds of people and from electrophysiological experiments measuring the output from many neurons synchronously, in real time. Researchers are beginning to learn how the brain integrates thousands of scattered bits of information into recognizable smells, tastes, and objects. And industry scientists are markedly more focused on applying this knowledge and learning to manipulate receptors that respond to the external environment or transmit information.

At Pfizer, for example, McKernan’s team puts the bulk of their sensory science efforts into pain research. With a prescription painkiller market worth more than \$40 billion (according to the research report “Pain Management Review and Outlook 2011”), many major pharmaceutical companies are working to develop treatments that are superior to ones that currently exist. Smaller, yet significant efforts in industry also go toward developing treatments for hearing loss and vision problems. “Vision and hearing are more minor industry research areas compared to pain,” says McKernan, “but they will be growing in the future as we learn more about how these senses work, and develop ways to treat disorders with small

molecules, antibodies, and stem cells.”

In addition to designing treatments for sensory system malfunctions, jobs are available in the private sector for neuroscientists who want to enrich the lives of our sentient selves. Companies built around this goal serve a sustained need, says **Ahmet Baydar**, the vice president of global research and development at International Flavors & Fragrances, based in Union Beach, New Jersey. He says, “Our industry will be around as long as people eat and drink, and want to smell nice.”

DESIGNER TASTES AND SMELLS

Scientists moved closer to understanding the neurological mechanisms of olfactory perception after Richard Axel and Linda Buck’s 1991 Nobel-winning discovery of about 10,000 genes that encode odorant receptors. Each receptor detects a discrete number of odorous molecules in the air and sends signals to the brain for processing.

Researchers can grow their careers around expanding upon this basic knowledge or finding creative applications for this research. For example, there are about 60 scientists who focus exclusively on taste and smell at the Monell Chemical Senses Center in Philadelphia, Pennsylvania. There, sensory neurophysiologist **Johannes Reisert** seeks to understand fundamental questions about how smell works through recording the electrophysiological properties and analyzing the gene expression of olfactory cells while mice are exposed to a variety of scents. Other Monell researchers investigate questions geared toward real-world solutions since some **continued>**

“Our industry will be around as long as people eat and drink, and want to smell nice.”

—Ahmet Baydar



Ahmet Baydar

Upcoming Features

Regional Focus: China—November 15

Faculty—February 7

Postdoc—February 28





Johannes Reisert

○ “[Talking with industry representatives] puts us into a more translational mindset so that we seriously consider how our work could be applied in the real world.”
—Johannes Reisert

wine, shampoo, and other sundries based on taste and smell, scientists will find no shortage of opportunities in companies that cater to the senses. Baydar, at International Flavors & Fragrances, says the company’s sales continue to increase in both developed and emerging markets. The company employs a few hundred scientists with neuroscience, molecular biology, and chemistry backgrounds who focus on a variety of questions, such as how to reduce a food’s salt content without changing its taste. The company’s researchers must design creative, noninvasive ways to assess how people’s brains respond to taste and smell. For that reason, when interviewing job candidates Baydor looks for signs of creativity and the ability to design and run research projects. A good publication record or the ownership of patents often indicates these qualities, he says. Baydor does not assign projects, but asks scientists to come up with their own using the company’s resources. For example, the company’s impressively large database of color-odor associations can be used by researchers, he says, to “look for correlations ... to understand why certain fragrance mixtures relax people, energize them, or make them happy or sad.”

Not all taste and smell research is geared toward improving products for human consumption; some research is designed to help with disease interventions. At Rockefeller University in New York City, neuroscientist **Leslie Vosshall** has dedicated her career to studying how olfaction affects behavior in a variety of animal models. With funding from the Bill and Melinda Gates Foundation and the Howard Hughes Medical Institute, she has been investigating how mosquitoes seek out their hosts using olfaction. Learning

of their projects are funded by food, fragrance, and drug companies that are looking for advice. For example, a company may be interested in how to mask the bitter taste of a medicine. To address this, Monell researchers investigate how bitter taste receptors function or how bitterness interacts with other sensory information. Reisert enjoys talking about real-world problems with people who visit Monell from industry, because “it puts us into a more translational mindset so that we seriously consider how our work could be applied in the real world,” he explains.

With a world full of people buying food,



how to disrupt this ability could lead to interventions that end mosquito-transmitted diseases, such as malaria and dengue fever. In another project, Vosshall studies how hunger in *Drosophila melanogaster* intersects with their perception of smell. The Boston-based nonprofit organization, The Klarman Family Foundation, supports the project because such avenues of research could shed light on the biological basis of eating disorders.

The diverse portfolio of Vosshall’s funding stream is no accident. “Food intake and appetite are sensory issues,” Vosshall says. Although researchers should never pursue projects that do not interest them scientifically, she advises, scientists should think about how their interests might coincide with those of foundations willing to support basic sensory science. After all, grants from the National Institutes of Health (NIH) have become quite difficult to get as federal budgets tighten.

“The secret recipe for staying in the business is to diversify your funding portfolio,” Vosshall explains.

AMPLIFYING THE SOUNDS AROUND US

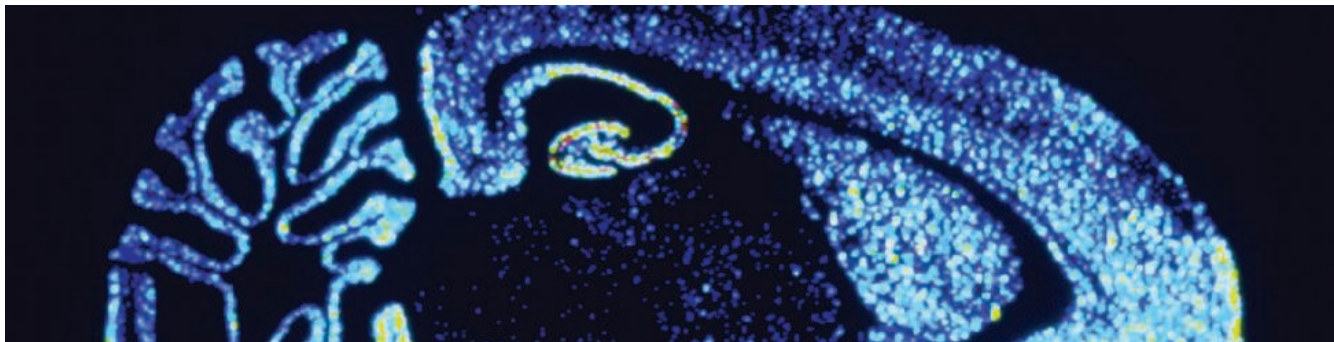
How slight vibrations within the eardrum communicate all of the qualities of sound continues to intrigue scientists, who are still working toward more fully understanding the inner workings of the auditory system. Much research is specifically focused on the causes and repair of inner ear hair cell damage, a common cause of deafness.

Jim Hudspeth, a neuroscientist at Rockefeller University studying hair cell development sees sound research moving in two directions: molecular and integrative. “One line of research focuses on how [hair] cells change sound into electrical signals and how they amplify inputs,” he says. The other direction asks questions such as “how are complex sounds analyzed and converted into language?” Or, “how do we lock in on a conversation and avoid the noises going on around it?” he explains. Neither research avenue is linked to a single technique, and both typically require specialized laboratory equipment to conduct hearing research.

Hudspeth uses a zebrafish model because the hair cells are more accessible than those found in mammals. His research uses gene expression analysis, mechanical and electrical recordings, and mathematical modeling of how vibrations are amplified through the auditory system. Hudspeth recommends that early career scientists who are interested in the field find laboratories equipped with soundproof rooms and tools for measuring sound, or look for positions that offer generous startup grants and access to a skilled technician since it may be necessary to build and equip a specialized space.

While hair cell regeneration remains a subject for basic research, technologies that improve hearing, such as cochlear implants, have been in use for decades. These implants replicate hair cell-induced auditory nerve transmission using stimulators and an electrode array. **Jim Patrick**, the chief scientist at Cochlear, a company for cochlear implant products based in New South Wales, Australia, was hooked on the technology from the moment his team placed the first cochlear implant in a deaf volunteer in 1978. With the implant, the patient was able to hear sounds, just well enough to make out what peoples’ lips were saying. “It’s the most amazing feeling to help change people’s lives,” Patrick says. Since then, the company has developed five generations of implants that have provided progressively better hearing.

Abhijit Kulkarni, the vice president of research and technology at Advanced Bionics, a cochlear implant company based in Valencia, California, says that scientists at the company benefit from skills in biomedical, electrical, or biomechanical engineering that **continued>**



Imagine a world without mental suffering...

At **Roche Neuroscience**, we develop medicines for conditions such as autism, schizophrenia, and Alzheimer's disease for which there are no effective treatments. Our strategy is based on understanding disease pathophysiology, genetics, and circuitry, along with identification of biomarkers to diagnose patients and assess disease progression, which results in tailored multimodal clinical programs to prove efficacy.

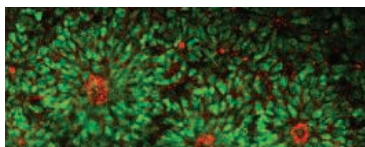
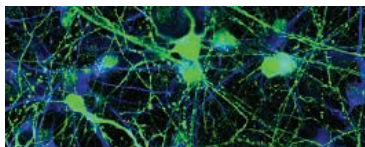
In **Neurodevelopmental Disorders**, we are harnessing the emerging understanding of autism genetics and its effects on synaptic circuits to develop new discovery platforms. These include modeling autism-related cellular phenotypes using patient-derived

iPS cells and generating and characterizing new animal models of autism. With our ongoing clinical trials we aim to expand our understanding of these disorders, identify points of therapeutic intervention, and improve core symptoms such as social behavior and cognitive deficits.

In **Psychiatry**, we are taking a neural circuits-based approach to understand neural pathways that underlie symptom domains such as cognitive function and motivational state, which are affected in psychiatric disorders. We are also identifying signaling pathways affected in psychiatric illness to identify novel drug targets. Several programs are in clinical development for next generation therapies for dis-

orders such as schizophrenia and depression, where we are targeting unmet needs such as negative symptoms or cognitive deficits.

We also have several active projects in the area of **Neurodegenerative Disorders**, such as Alzheimer's and Parkinson's Disease. In this area, our understanding of disease pathophysiology, together with the identification of biomarkers of disease progression which predate clinical symptoms, has led us to run trials in prodromal Alzheimer's patients, where we are attempting to alter the course of the disease before the onset of dementia.



Doing now what patients need next

We are a dynamic and innovative organization, committed to recruiting the best scientific talent to address some of the biggest challenges in modern medicine. If you would like to be part of an industry-leading Neuroscience team, please visit

<http://careers.roche.com>

Featured Participants

Advanced Bionics
www.advancedbionics.com

Cochlear
www.cochlear.com

Harvard Medical School
neuro.med.harvard.edu

International Flavors & Fragrances
www.iff.com

Monell Center
www.monell.org

Rockefeller University
www.rockefeller.edu

Neusentis, a Pfizer Research Unit
www.neusentis.com

University of New South Wales, School of Medical Sciences
medicalsciences.med.unsw.edu.au

ViSSee
www.vissee.ch



Richard Vickery

"It's the most amazing feeling to help change people's lives."

—Jim Patrick

help researchers translate basic findings into products that change lives. "Translational research is not something that people necessarily learn in graduate school," Kulkarni says, "We are always looking to bridge the science with technology."



CONSTRUCTING VISUAL REALITIES

To understand how the brain converts patterns of light into images, scientists often study individual components of the visual system. For example, to study object recognition, **Margaret Livingstone**, a neurobiologist at Harvard Medical School in Boston, measures the neuronal activity in the temporal lobe of monkeys as they look at different items. Livingstone figures out how that

information is processed into object recognition using specialized software programs. For this type of research, she explains, a background in computer programming is necessary since her team performs a lot of data analysis. She recommends that scientists who want to grow their career in vision science take programming classes or workshops, which are routinely held at various universities.

Beyond studying how the brain integrates visual information, some scientists in academia and industry are using visual neuroscience in ways that might not have been predicted 20 years ago. For instance, **Nicola Rohrseitz**, the founder of ViSSee, based in Zurich, Switzerland, and his team have developed a software platform that makes cameras function like a fly eye, which can measure speed and distance between obstacles while in motion. In graduate school, Rohrseitz modeled how the fly eye recognizes and assesses this information, and his team at ViSSee now uses these models to program software that will translate the data into action. The technology has been used to create "touchless screens" that can detect the hand gestures of surgeons, for instance, to control high-tech equipment, such as CT scanners.

TOUCHING UPON TREATMENTS

Touch may be the first sense that humans develop in the womb, although it might also be the least understood of the senses, says **Richard Vickery**, a neuroscientist at the University of New South Wales in Australia who studies how the cat brain responds to touch.

Perhaps the lack of information on touch might account for the dearth in

adequate pain medications in the United States. Even though over \$40 billion worth of prescription pain medications are sold each year in the United States, the drugs do not provide relief for more than half of the 100 million Americans living in chronic pain. These drugs also come with risks like addiction and liver damage. Recently, Congress requested that the NIH and the U.S. Food and Drug Administration increase their focus on pain research.

In order to discover more effective pain medications, **Clifford Woolf** at Harvard Medical School examines how the nervous system processes injuries to sensory fibers, and how the extent of that process-

ing differs among people with different genetic backgrounds. Using this information, he also hopes to create better animal models for pain research by inserting mutations underlying specific pain-inducing diseases in humans into the mouse genome. "There have been many failures in Phase 2b studies of pain medications that looked wonderful in rodent models," Woolf says, "which raises the worry that the mouse models we are currently using are not good predictors of human efficacy." Funders apparently agree with him. Recently his project to create better mouse models was supported by a neuroscience consortium funded by the Massachusetts Life Sciences Center that involves scientists from universities in Massachusetts and seven international pharmaceutical companies.

Many biopharmaceutical companies support research and development in the area of pain management. Pfizer's McKernan says the company focuses on the different ways in which pain works, and on genomic analyses of patients with genetic pain disorders like erythromelalgia—linked to mutations in a gene encoding a sodium channel, causing sufferers to feel as though their limbs are burning—so that they might develop more personalized treatments. While one person might benefit from a drug that blocks ion channels, for example, another might be better off with one that activates opioid receptors. When hiring, McKernan explains, "We are interested in people with expertise in bioinformatics, electrophysiology, genetics, and iPS cell technology." She adds that Pfizer often collaborates with scientists in academia, and students who are curious about drug discovery might consider a postdoctoral fellowship at the company. "Learning something that no one knows is a privilege, but to then turn that into something that helps people, that's just the best thing you could hope for out of your job," says McKernan.

Amy Maxmen is a freelance writer living in Brooklyn, New York.

DOI: 10.1126/science.opms.r1300138



The CNRM is a collaborative intramural federal research program involving the U.S. Department of Defense and the National Institutes of Health joining clinicians and scientists across disciplines to catalyze innovative approaches to traumatic brain injury (TBI) research. The Uniformed Services University heads the operations of the CNRM (www.usuhs.mil/cnrm).

Neuroscience/Neuroradiology Research

USU Department of Radiology and Radiological Sciences

Exceptional opportunity for a proven leader to serve as Principal Investigator of the CNRM Translational Imaging Facility. This state-of-the-art research facility includes a new Bruker Biospec 7T/20 MRI and a Siemens Inveon Multimodality PET/CT scanner with full-time physicists, technologists, and administrative personnel. Adjacent CNRM core facilities support development of TBI models and behavioral assessments. Candidates must have Ph.D., M.D., or equivalent with expertise in pre-clinical research applications of MRI and/or PET approaches and an interest in collaborative studies of assessment and repair using TBI models. In addition to CNRM funding of the facility, the Principal Investigator will develop an extramurally-funded independent research program and contribute to teaching of medical and/or graduate students.

Please apply online at www.hjf.org/careers, "Advanced Search"
Job Opening ID = 208698

Position is located in Bethesda, MD at the Uniformed Services University of the Health Sciences. Employment is with the Henry M. Jackson Foundation for the Advancement of Military Medicine, an equal opportunity employer.



Boston Children's Hospital



Harvard Medical School

Boston Children's Hospital Harvard Medical School Neuroscience and Developmental Neuroscience Assistant Professor

Applications are being considered for a full-time, tenure-track position in the Program in Neurobiology and in the Departments of Psychiatry and Neurology at Boston Children's Hospital and Harvard Medical School. The successful candidate will hold either a PhD or MD degree and will have research interests relevant to the development, function or pathology of the nervous system, broadly defined, including studies of the neurobiological basis of behavior, mood, and cognitive function and their disturbance in psychiatric conditions. The faculty position is within the vibrant and highly interactive research environment of the FM Kirby Neurobiology Center directed by Clifford J Woolf, MD, PhD. This multidisciplinary basic science research center, affiliated with Boston Children's Hospital's Departments of Psychiatry and Neurology resides within a very strong and collegial research community in neuroscience and related disciplines throughout Harvard Medical School and Harvard University. Modern laboratory space is available in the new Center for Life Sciences Building. Candidates with an interest in translational research can participate in the Hospital's Translational Neuroscience Research Center. We are seeking exceptional scientists to establish vigorous independent research programs, form productive collaborations and promote translation of their research. The investigators will hold both Boston Children's Hospital and Harvard Medical School faculty appointments.

Please submit a current CV, a 2- or 3- page description of research interests and future directions, and three to five reference letters. Materials should be sent by **January 20th, 2014** to: **Neuroscience Search Committee, c/o NeuroAPSearch@gmail.com**

Equal Opportunity/Affirmative Action Employer.



Louisiana State University Health Sciences Center – Shreveport Vice Chancellor for Research

The LSU Health Sciences Center in Shreveport, LA is seeking candidates for the role of Vice Chancellor for Research. The individual selected for this position will provide executive leadership for research administration and planning, and will work with fellow leaders to strengthen the campus research enterprise and infrastructure for an innovative and multi-disciplinary research program across North Louisiana.

The Vice Chancellor for Research will lead the institution in all areas of research. The Vice Chancellor will represent the campus in matters related to research including federal and state agencies, other research institutions and the local community. A priority for the incumbent will be to facilitate translational research opportunities. Additionally, the Vice Chancellor will be the designated Institutional Official responsible for research across the organization.

The institution's 436 bed University Hospital serves an urban and rural population of approximately 2.5 million, encompassing 25,000 square miles in Louisiana, East Texas, and Southwestern Arkansas. The resources for basic and clinical research are excellent. We have a long history of successful research collaboration between the basic science and clinical departments. The Virginia Shehee Biomedical Research Institute is ~160,000 total square feet and includes wet lab and staffed core facilities, such as for cellular imaging, DNA array analysis, and mass spectroscopy-proteomics. For more information on this opportunity at LSUHSC please visit us at <http://www.lsuhscrestshreveport.edu/VCRworkingProspectus>

Successful candidates must be an MD/PhD or MD with an outstanding record of scholarly achievement, including a history of independent federal research funding, serving as a principal investigator and having administrative experience relevant to clinical and basic research. Requirements include an understanding of the diverse forms of research and scholarship conducted at a comprehensive research university, and an informed perspective about federally sponsored programs, intellectual property, technology transfer and commercialization in the university setting.

The search is being led by Glenn Mills, MD, FACP, Professor of Medicine, Chief, Section of Hematology and Oncology and Director, Feist-Weiller Cancer Center. Interested candidates may submit curriculum vitae via email at ShvFacultyRecruiting@lsuhsc.edu. Materials that cannot be submitted electronically may be mailed to: Vice Chancellor for Research Recruitment, Human Resource Management, 1501 Kings Highway, Shreveport, LA 71103.

LSU Health Shreveport respects diversity in the workplace and is an Equal Opportunity Employer.

Two Tenure-track Positions in Neuroscience

The Department of Cell Biology and Neuroscience (<http://cbns.ucr.edu>) at the University of California, Riverside seeks to appoint highly qualified neuroscientists at the rank of **Assistant Professor** who wish to build active research programs in the following areas: **(1) Glial-Neuronal Interactions/Synaptic Plasticity.** Primary research interests would be directed toward, but not limited to, learning and memory, neuroendocrine regulation, reactive gliosis leading to altered brain function, and roles for glia in synapse formation and neurodegenerative disease. **(2) Neurogenesis/Neurodevelopment.** Primary research interests are directed toward understanding molecular and cellular mechanisms of development, including neurogenesis, synaptogenesis, neural migration, origins and developmental programs of progenitor cells, and mechanisms of circuit formation. We are particularly interested in candidates who employ modern interdisciplinary research approaches using either vertebrate or invertebrate models of neural-glia interactions, synaptic plasticity, and normal or aberrant neurodevelopment leading to disorders of the nervous system.

Curriculum vitae, statements of research and teaching approaches, and contact information for at least three letters of reference should be uploaded electronically through AP Recruit. For Glial-Neuronal Interactions/Synaptic Plasticity: <https://aprecruit.ucr.edu/apply/JPF00029>; For Neurogenesis/Neurodevelopment: <https://aprecruit.ucr.edu/apply/JPF00030>. Review of applications will begin **6 January 2014** and continue until the position is filled. Position will be available 1 July 2014.

*The University of California is an
Equal Opportunity/Affirmative Action Employer.*



Diversifying Neuroscience

Are you a postdoctoral scholar or assistant professor in a neuroscience-related field?

Do you identify as someone from a group underrepresented in neuroscience?

Are you interested in receiving in-depth career support and direction over a two-year period?

Join the BRAINS professional development program

Applications for the next cohort open in 2014

Visit brains.washington.edu

E-mail brains@uw.edu

In order to be eligible to participate in BRAINS, you must be a citizen or permanent resident of the United States and from a group or background recognized as underrepresented in neuroscience. Please visit our website for detailed eligibility information. Program Funded by NINDS Grant 1R25NS076416-01



**QUEENSLAND BRAIN INSTITUTE (QBI),
THE UNIVERSITY OF QUEENSLAND,
BRISBANE, AUSTRALIA**

SENIOR RESEARCH FELLOWSHIP IN LEARNING AND MEMORY

The role Establish a laboratory to lead QBI's research activity in the area of Learning and Memory. The laboratory will explore the fundamental processes regulating Learning and Memory and how these functions may be disrupted in disease processes like dementia.

Remuneration AUD\$100,275 – \$115,623 p.a. (Level C), AUD\$120,739 – \$133,018 p.a. (Level D), or AUD\$155,529 p.a. (Level E), plus up to 17% super. Level of appointment will be commensurate with qualifications, experience and academic achievements. Full-time, fixed-term appointment for an initial period of five years (renewal subject to funding and performance) at Research Academic Level C-E, with a competitive start-up package.

Applications close 1 December 2013
Job No. 495149

To apply: Go to www.uq.edu.au/uqjobs to obtain a copy of the position description and application process. UQ is an equal opportunity employer.



**Karolinska
Institutet**

Postdoctoral Fellowship in Systems Neuroscience

A postdoc position is available in the Mammalian Locomotor Laboratory, at the Department of Neuroscience, **Karolinska Institute**, in Stockholm, Sweden. The laboratory is offering a creative and international environment, focusing on functional operation and molecular logic of neural networks controlling movements. We are using an array of experimental approaches including molecular mouse genetics, imaging, optogenetics, electrophysiology and anatomy to decipher the function of the networks.

We are looking for an outstanding researcher that has extensive experience with electrophysiology/imaging either in vitro or in vivo. Candidates must have a PhD degree in systems neuroscience. It is an advantage to have insights in mouse genetics and molecular biology. The candidate must be able to work in an integrated team. Strong dedication to science is an absolute requirement. The candidate must be fluent in English. Go to ki.se/jobs to submit your application.

Karolinska Institute is one of the world's leading medical universities. Since 1901 the Nobel Assembly at Karolinska Institute has selected the Nobel laureates in Physiology or Medicine.



AAAS is here – promoting universal science literacy.

In 1985, AAAS founded Project 2061 with the goal of helping all Americans become literate in science, mathematics, and technology. With its landmark publications *Science for All Americans* and *Benchmarks for Science Literacy*, Project 2061 set out recommendations for what all students should know and be able to do in science, mathematics, and technology by the time they graduate from high school.

As a AAAS member, your dues help support Project 2061. If you are not yet a member, join us. Together we can make a difference.

To learn more, visit
aaas.org/plusyou/project2061





Working together to work wonders.™

Established in 1891 as the University of Texas Medical Department, the University of Texas Medical Branch (UTMB) is home to the oldest medical school in Texas. Since then, UTMB Health has grown from one building, 23 students and 13 faculty members to a modern health science center with more than 70 major buildings, more than 2,500 students and more than 1,000 faculty. The 84-acre campus includes four schools, three institutes for advanced study, a major medical library, a network of hospitals and clinics that provide a full range of primary and specialized medical care, an affiliated Shriners Burns Hospital, and numerous research facilities. UTMB Health is a component of the University of Texas System.

The city of Galveston is a popular tourist and cruise ship destination that includes beaches, museums, historical architecture, a vibrant arts community, and excellent restaurants; all located only 45 minutes away from Houston, the nation's fourth largest city.

UTMB Health is an Equal Opportunity, Affirmative Action Institution, which proudly values diversity. Candidates of all backgrounds, including persons with disabilities, are encouraged to apply.

VACCINOLOGY FACULTY POSITION SEALY CENTER FOR VACCINE DEVELOPMENT

The SCVD is recruiting a faculty member in vaccine technology (including vaccine platforms, novel adjuvants and improved delivery technologies) or chronic diseases. Our "Vaccines for Chronic Diseases" initiative led by the SCVD (www.utmb.edu/scvd) includes the UTMB's Cancer Center, Center for Addiction Research and Mitchell Center for Neurodegenerative Diseases. This initiative encompasses research at all stages of vaccine development, from basic science/discovery through clinical studies. The successful candidate will be a highly motivated researcher with an established record of extramural funding, or the potential to establish a robust research program, as well as the ability to work in a highly collaborative and interdisciplinary environment. We are recruiting individuals holding MD, PhD, and/or DVM degrees at the Assistant, Associate or Full Professor level, including tenure-track positions for suitably qualified individuals.

UTMB Health provides a rich environment for research, with a number of highly interactive centers of excellence and biomedical institutes all of which have interests in vaccine development. With this wealth of expertise and our state-of-the-art core facilities, UTMB offers outstanding opportunities for collaboration and multidisciplinary research.

Interested candidates should send their curriculum vitae, statement of research interests and names of three references electronically to:

Nigel Bourne, PhD
Professor, Pediatric Vaccinology
Sealy Center for Vaccine Development
University of Texas Medical Branch
301 University Blvd, Route 0436
Galveston, TX, 77555-0436
scvd@utmb.edu

DEPARTMENT OF NEUROLOGY DIRECTOR OF THE MITCHELL CENTER

AND VICE CHAIR FOR RESEARCH

The Department of Neurology at the University of Texas Medical Branch (UTMB) seeks an accomplished basic scientist or a clinician scientist to lead the Mitchell Center for Neurodegenerative Diseases. Established in 2006, the Mitchell Center is part of a robust research enterprise at UTMB, which includes \$148M in research expenditures and departments ranked among the National Institute of Health's top 10. The individual will also serve as Vice Chair for Research for the Department of Neurology and hold the Endowed Sealy Distinguished Chair. Applicants must have a PhD or MD, PhD and the qualifications to be appointed as Professor (tenure track). The successful candidate will possess a strong record of investigative extramural funding, mentoring junior scientists and clinician-scientists.

Interested candidates should submit their curriculum vitae and names of three references electronically to:

Anish Bhardwaj, M.D., M.B.A.
John Sealy Chairman and Professor
Department of Neurology
Assistant Dean for Faculty Affairs
University of Texas Medical Branch
301 University Blvd, Route 0539
Galveston, Texas 77555-0539
anbhardw@utmb.edu

VECTOR BIOLOGIST FACULTY POSITION DEPARTMENT OF PATHOLOGY

The Department of Pathology is recruiting a Vector Biologist faculty position at the Assistant, Associate or full Professor level. The department is interested in enhancing its successful program involving mosquito- and tick-borne pathogens. Applicants must have a Ph.D., M.D., D.V.M., or equivalent degree in an appropriate field, with a productive research record related to arthropod-pathogen-vertebrate host interactions. Preference will be given to applicants with experience, capability and success in vector-borne disease research demonstrated by an established independent research program. Responsibilities will include establishing an innovative, externally funded vector biology research program, collaborating with others studying vector-borne pathogens, participating in intra- and inter-departmental conferences and meetings, and other activities in the department, pursuing scholarly activities to include research, publications, and presentations at national and international meetings, and teaching of graduate and medical students. Salary and academic rank are commensurate with experience. An excellent benefits package is included.

UTMB has excellent infrastructure to conduct research in BSL-2, BSL-3 and BSL-4 laboratories. Arthropod rearing and containment facilities are available for pathogen-free and pathogen-infected mosquitoes, ticks and other vectors at Arthropod Containment levels (ACL) 2, 3, and 4.

Interested applicants should send curriculum vitae, a statement of personal and academic goals, and names of three references to:

David H. Walker, M.D., Chairman
Department of Pathology
University of Texas Medical Branch
301 University Boulevard, Rte 0609
Galveston, Texas 77555-0609
dwalker@utmb.edu



Medical School

Faculty Position in Virology

The Department of Microbiology at the University of Minnesota Medical School invites applications for a faculty position to be filled at the tenure-track Assistant Professor level. We seek an outstanding scientist who will establish a competitive research program in virology with the potential to complement the University's research programs studying herpesviruses, HIV-1, and viral immunology. The new position is part of the University's commitment to the study of infectious diseases, which includes a major capital investment in a new Microbiology Research Facility. This building will be the latest addition to the Biomedical Discovery District and research home to departmental faculty. The University of Minnesota offers exceptional startup support, a dynamic intellectual environment, and outstanding research and core facilities. Additional information about the Department of Microbiology, affiliated institutes and centers, and the graduate training program, can be found on the departmental web site: <http://www.microbiology.med.umn.edu>.

Minimum qualifications: Ph.D., M.D., or equivalent in a relevant field of study, plus applicable postdoctoral or faculty experience. To apply, please upload a curriculum vitae and concise summary of current and planned research in response to requisition number **187542** at <http://employment.umn.edu>. Please also arrange to have 3 letters of recommendation sent to microbiology@umn.edu or **Virology Search Committee, Department of Microbiology, University of Minnesota, MMC 196, 420 Delaware Street S.E., Minneapolis, MN 55455**.

The University of Minnesota shall provide equal access to and opportunity in its programs, facilities, and employment without regard to race, color, creed, religion, national origin, gender, age, marital status, disability, public assistance status, veteran status, sexual orientation, gender identity, or gender expression.

复旦大学脑科学研究院

The Institutes of Brain Science,
Fudan University

Principal Investigator & Postdoctoral Associate Positions

The Institutes of Brain Science, Fudan University, Shanghai, China is recruiting in the fields of neuroscience and neurological disorders.

Principal Investigator Positions: Applicants must have a Ph.D. or M.D. degree with more than 2-year postdoctoral experience, an impressive research record, and the capacity to develop a vigorous and independent research program.

Postdoctoral Fellow/Associate positions are available for recent Ph.D.s with good training in neuroscience or related fields.

We offer competitive salary & benefits and a dynamic, creative and supportive international research environment.



Please visit <http://iobs.fudan.edu.cn> for more info and send application to: Ms. Rong Chen (ibs@fudan.edu.cn).

THE UNIVERSITY OF HONG KONG



Tenure-Track Assistant Professor in Chemical Biology (Ref.: 201301014)

Applications are invited for tenure-track appointment as Assistant Professor in Chemical Biology in the Department of Chemistry. The position will be tenable from July 1, 2014 or as soon as possible thereafter, on a three-year term basis, with the possibility of renewal and with consideration for tenure during the second three-year contract.

Applicants should have a Ph.D. degree with a strong background and research record in the general area of chemical biology. The appointee is expected to develop original and independent research programs, and excel in both undergraduate and postgraduate teaching. A suitable start-up fund for research will be provided to the appointee. Information about the Department can be obtained at <http://www.chemistry.hku.hk>.

A globally competitive remuneration package commensurate with the appointee's qualifications and experience will be offered. At current rates, salaries tax does not exceed 15% of gross income. The appointment will attract a contract-end gratuity and University contribution to a retirement benefits scheme, totalling up to 15% of basic salary, as well as annual leave, and medical benefits. Housing benefits will be provided as applicable.

Applicants should send a completed application form, together with an up-to-date C.V., a research proposal, and a statement of teaching philosophy by e-mail to scchem@hku.hk. They should also arrange for submission, to the same e-mail address as stated above, three reference letters from senior academics. One of these senior academics should be asked to comment on the applicant's ability in teaching. Please indicate clearly the reference number in the subject of the e-mail. Application forms (341/1111) can be obtained at <http://www.hku.hk/apptunit/form-ext.doc>. Further particulars can be obtained at <http://jobs.hku.hk/>. **Closes December 15, 2013.**

The University thanks applicants for their interest, but advises that only shortlisted applicants will be notified of the application result.

The University is an equal opportunity employer and is committed to a No-Smoking Policy



The Mina Jo Powell Endowed Chair in Neuromuscular and Neurological Degenerative Disease at the Florida State University College of Medicine

The Florida State University College of Medicine invites applications to the **Mina Jo Powell Endowed Chair in Neuromuscular and Neurological Degenerative Disease** in the Department of Biomedical Sciences. Successful candidates will have an M.D. and/or a Ph.D. degree, international recognition as leader in neuromuscular or neurodegenerative disease research and a strong history of extramural research support. The candidate will be expected to participate in medical and graduate education. Opportunities to continue clinical practice may be available for qualified and eligible applicants.

Please submit a letter of application, curriculum vitae, a one-page overview of current and future research plans, and a list of at least three references in a single PDF file to biomedfacultysearch@med.fsu.edu. If interested please apply to Florida State University at <https://jobs.fsu.edu>, job ID #36247. We will begin to review the applications on **November 15, 2013**.

The mission of the College of Medicine is to prepare compassionate physicians who discover and advance knowledge and deliver the highest quality patient-centered medicine to communities with the greatest need. The Research and Discovery mission of the College is facilitated by more than 150,000 sq. ft. of state-of-the-art laboratory space, core labs in proteomics, genomics, confocal microscopy, flow cytometry, and cell culture. The department of Biomedical Sciences covers the entire spectrum of preclinical disciplines. The Department's research is broadly focused on understanding the molecular bases of human diseases (<http://med.fsu.edu/biomed>), with neurological and psychiatric disorders being the focus of research at the Center for Brain Repair (<http://www.med.fsu.edu/BrainRepair>). Many Departmental faculty participate in the FSU Interdisciplinary Graduate Program in Neuroscience (<http://neuro.fsu.edu/>). Other resources available locally include structural and functional MR imaging facilities at the FSU National High Magnetic Field Laboratory (<http://magnet.fsu.edu/>), and the FSU Clinical Research Network (CRN), a statewide, collaborative, research network of faculty, community-based healthcare professionals and researchers that supports clinical and translational research (<http://med.fsu.edu/research/crn/>).

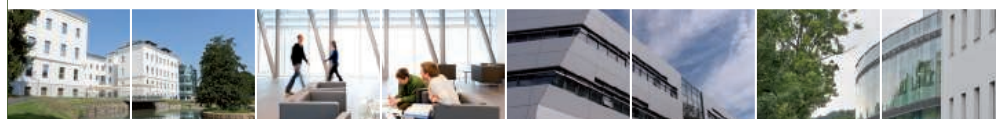
The Florida State University is an
Equal Opportunity/Affirmative Action Employer.

Are you

a graduate of Natural Sciences, Mathematics, or Computer Science?
Looking for a chance to start your scientific career as a PhD student?
Interested in crossing scientific boundaries?

Deadline for students wishing to enter the program in the fall of 2014 is **January 15, 2014**
 For further information, please consult www.ist.ac.at/gradschool

IST Austria is committed to equality and diversity.



FACULTY POSITION AVAILABLE Anatomy

Anatomy faculty at Des Moines University engage students in a dynamic evidence-based discipline that fosters a professional environment of scholarly activity and service. Offering instruction in courses and systems in gross anatomy, histology, embryology and neuroanatomy, the Anatomy Department provides the foundation for basic medical sciences and the keystone of physical diagnosis.

Qualifications include an earned doctorate from an accredited university in a relevant field required; postdoctoral experience preferred; record of teaching experience in anatomical sciences; demonstrated or potential for successful independent scholarly activity including ability to sustain an extramurally funded research program; excellent oral and written communication skills; basic PC knowledge and skills. Gross anatomy and histology experience highly desirable.

To be eligible for consideration, candidates are asked to provide (a) a complete CV; (b) detailed letter of interest addressed to the Anatomy Department Chair; (c) full contact information for 3 professional references –email, phone and cell phone; (d) detailed “statement of teaching philosophy and research interests.” All documents must be submitted online only at www.dmu.edu/employment.



DES MOINES UNIVERSITY

Candidates with questions specific to this position may call Dr. Donald Matz, Department Chair, 515-271-1653.

For more information on the immediate Des Moines, Iowa area, please visit www.desmoinesmetro.com.

Des Moines University is an equal opportunity/affirmative action employer. The University seeks excellence through diversity among its administrators, faculty, employees and students. The University prohibits discrimination on the basis of race, color, national origin, creed, religion, age, disability, sex, gender identity, sexual orientation, veteran status, genetic information or any other legally protected status. Applications by members of all underrepresented groups are encouraged.



The College of Science at the University of Notre Dame has begun a strategic hiring initiative, *Advancing Our Vision*, which will grow the faculty at all levels by about 18 positions over the next three years. Multiple searches are under way to fill these strategic positions.

Applied and Computational Mathematics and Statistics: The Department of Applied and Computational Mathematics and Statistics seeks to hire multiple junior and senior level faculty over the next three years including an assistant professor in multidisciplinary applied mathematics in any specialty that builds on existing activities. Exceptional candidates at the tenured level may also be considered. A statistician at the tenured level in any area of research that builds on our existing activities is also desired with preference for those with multidisciplinary collaborations. acms.nd.edu/job-opportunities/

Mathematics: The Department of Mathematics invites applications for an instructorship; candidates in any specialty compatible with the research interests of the department will be considered. Applications for a tenure-track assistant professor are also sought with priorities in algebra and partial differential equations. Applications are also sought for a full professor who will be an internationally recognized mathematician expected to play a crucial role in significantly augmenting the research group in topology and quantum field theory. math.nd.edu/job-opportunities/

Network and Nuclear Physics: The Department of Physics invites applications for one tenure track faculty position in network physics with preference towards biophysical and neuronal networks. Joint appointments will be explored. The Department also invites applications for two tenure-track positions in nuclear physics, in the areas of experimental and theoretical nuclear astrophysics to strengthen the existing program at the Nuclear Science Laboratory. physics.nd.edu/employment-opportunities/

Analytical Sciences and Engineering: Since 2006, Notre Dame has initiated the fastest growing analytical sciences program in the U.S. The positions range from junior level through tenured senior faculty to endowed chair appointments. Successful candidates may choose to establish their programs in the Department of Chemistry and Biochemistry or the Department of Chemical and Biomolecular Engineering, or both. chemistry.nd.edu/employment-opportunities/

Cancer: As part of a campus-wide initiative associated with the Harper Cancer Research Institute, multiple open-rank, tenure-track faculty positions are available in the broad area of cancer research. Individuals engaged in basic and translational cancer research using organotypic and/or animal models of cancer are especially encouraged to apply. A vigorous, externally supported research program is expected. biology.nd.edu/employment/

Disease Epidemiology: The Eck Institute for Global Health and multiple departments are seeking candidates for two tenure-track assistant/associate professors in disease epidemiology, particularly in investigating the epidemiology, population dynamics, and control of infectious diseases from a global perspective with a focus on low and middle income countries. We seek individuals interested in establishing a strong international research program. biology.nd.edu/employment/

Stem Cell Biology: The Adult Stem Cell Initiative invites applications for two tenured/tenure-track positions in stem cell biology with open rank (full, associate and assistant professor). We seek candidates with research expertise within one or more broad areas in adult stem cell and iPS cell biology, including, but not limited to developmental and regenerative biology, niche interactions, mechanisms underlying cell dedifferentiation/reprogramming, regulation of pluripotency, and disease models. biology.nd.edu/employment/

The University of Notre Dame is an Equal Opportunity Employer with a strong institutional commitment to diversity and endeavors to foster a vibrant learning community.

science.nd.edu



ICTP - RESEARCH SCIENTIST (Particle and Astroparticle Physics) ref. 11TSC0827TP

The Abdus Salam International Centre for Theoretical Physics (ICTP), is a world-class institution focused on research in basic sciences with responsibility for the promotion, dissemination and support of science, especially in developing countries. It operates under the aegis of UNESCO and IAEA, and it is located in Trieste (Italy). ICTP seeks applications for a position in Particle and Astroparticle Physics.

The incumbent will initiate, develop and coordinate competitive research and training programmes in the field of Particle and Astroparticle Physics, and is also expected to lecture in the High Energy Diploma Programme and other programmes and to participate in joint PhD programmes with Italian institutions

All candidates must possess:

- Advanced University degree (Ph.D. or equivalent) in High Energy Physics, Particle or Astroparticle Physics
- At least 4 years of relevant scientific research experience at the national and international levels
- Demonstrated professional experience in the field of Particle or Astroparticle Physics
- Experience in the design and implementation of research projects in the field of Particle or Astroparticle Physics
- Excellent analytical skills. Ability to collect, synthesise and analyse information from various sources
- Proven ability to lead, manage and motivate staff and teams and to work effectively in a multidisciplinary and multicultural environment
- Capacity to build and maintain partnerships with internal and external stakeholders
- Excellent knowledge of English

The annual remuneration, based on UNESCO P-3 level, will start at \$93,500, and is exempt from income tax. There is an attractive benefits package which includes 30 days of annual vacation, home travel, education grant for dependent children, pension plan and medical insurance.

More information and on line application at:

<https://unesco.taleo.net/careersection/2/joblist.ftl>

Deadline for receipt of applications: **7 December 2013.**

For further information please contact ICTP Personnel Office:

personnel_office@ictp.it

FOCUS ON NEUROSCIENCE



Department of Neuroscience

The Department of Neuroscience invites applications for a new tenure track faculty position at the rank of Assistant or Associate Professor. Fields of interest include mechanistic studies of ion channels, membrane transporters or receptors using biophysical techniques, and/or structural biological approaches. The position carries competitive salary and start-up funds. Successful candidates will be expected to develop and maintain an active research program within an exciting and vibrant academic environment. The University of Texas at Austin has strong and interactive research programs in Physics, Chemistry, Molecular Biology, Neuroscience, Computer and Computational Science, Statistics, Mathematics and Engineering with a culture of cross disciplinary collaboration. Successful candidates will have their laboratories in the new Norman Hackerman Building located within the heart of campus.

Austin is located in the Texas hill country and is widely recognized as one of America's most beautiful and livable cities. Please send curriculum vitae, summary of research interests, and names of five references to:

Dr. Richard Aldrich
Department of Neuroscience
The University of Texas at Austin
1 University Station, C7000
Austin, TX 78712-0132

Homepage: <http://www.biosci.utexas.edu/neuroscience>

The University of Texas at Austin is an Equal Opportunity Employer. Qualified women and minorities are encouraged to apply; a background check will be conducted on applicants selected

Faculty of Science

The Faculty of Science at the University of Zurich invites applications for an

Assistant Professorship Tenure Track in Molecular Approaches to Renewable Energies

in the context of the newly established research focus at the University of Zurich, Light to Chemical Energy Conversion (LightChEC www.lightchec.uzh.ch) with the ultimate goal to design concepts for artificial photosynthesis, the Department of Chemistry wishes to appoint an assistant professor (with tenure track). The LightChEC centre includes research groups from the UZH Chemistry and the Physics Departments as well as from the Swiss Federal Laboratories for Materials Science and Technology, EMPA. We seek an outstanding and innovative chemist with a strong background in photocatalysis or related areas such as photochemistry, electrochemistry, molecular solar cells, surface science or supramolecular chemistry from either a synthetic or a mechanistic point of view. The candidate is expected to teach a limited contingent at the undergraduate and graduate level in either English or German.

The University of Zurich provides generous research support, including earmarked funds for personnel running expenses and competitive start-up packages. The city of Zurich offers a stimulating scientific environment, with many opportunities for collaborations with research groups within the faculty and at neighbouring institutions. Application packages should include a cover letter, complete curriculum vitae, statement of current and future research plans, list of publications and the names and addresses of three potential referees. The documents should be addressed to Prof. Dr. Michael Hengartner, Dean of the Faculty of Science, University of Zurich, and submitted as a single PDF file at www.mnf.uzh.ch/mare at the latest by November 21, 2013. Further information can be obtained by contacting Prof. Dr. Roger Alberto, Department of Chemistry, at ariel@aci.uzh.ch, and by visiting the new Department website at www.chem.uzh.ch. The University of Zurich is an equal opportunities employer. Applications from women are particularly encouraged.

Applications are invited for:-

School of Life Sciences

The School invites applications for faculty posts at Associate Professor / Assistant Professor rank with prospect for substantiation.

(1) Associate Professor / Assistant Professor (Marine Biology) (Ref. 1314/052(665)/2)

Applicants should have a doctoral degree in a relevant biological science discipline. Applicants showing excellence in any area of marine biology will be considered, particularly those demonstrating experience using modern biological approaches to study marine ecology, biodiversity and/or conservation. The appointee will (a) teach courses in marine biology and related disciplines; (b) develop a competitive research programme with external grant support; and (c) collaborate with faculty members in marine biology and/or environmental science. He/she will be a member of the Simon F.S. Li Marine Science Laboratory, a facility in the School specifically equipped for laboratory and field studies of marine organisms.

(2) Associate Professor / Assistant Professor (Organelle Biogenesis and Function) (Ref. 1314/053(665)/2)

Applicants should (i) have a PhD degree in cell biology, biochemistry, molecular biology or a related field; (ii) specialize in cell biology and molecular biology; (iii) have strong interest in engaging in collaborative research in cell biology, particularly using TEM 3D tomography or in-vitro reconstitution methods to study organelle biogenesis and function in model organisms; (iv) have demonstrated potential for establishing a research programme of high quality and international impact; (v) have relevant postdoctoral training with a proven record of accomplishment; and preferably (vi) have teaching experience. Applicants with demonstrated research excellence, scholarships and a track record of extramural competitive funding are particularly encouraged to apply. The appointee will be a member of a newly established Centre for Organelle Biogenesis and Function funded by the Area of Excellence (AoE) funding scheme of the Research Grants Council of Hong Kong.

(3) Associate Professor / Assistant Professor (Food and Nutritional Sciences) (Ref. 1314/054(665)/2)

Applicants should have (i) a PhD degree in a relevant biological science discipline; and (ii) demonstrated potential for excellence in both teaching and research. Applicants with achievement in any aspect of food and nutritional sciences will be considered, particularly those with experience in applying modern biological approaches to the study of food biotechnology, molecular nutrition, and/or nutrigenomics. For those who are in the field of nutrition, registration as a dietician will be desirable but not essential. The appointee will (a) teach undergraduate and postgraduate courses in his/her field of expertise; (b) develop a significant research programme with external grant support; and (c) undertake administrative duties. Multidisciplinary research collaboration is encouraged within the School and with other units at the University.

For posts (1) to (3): Appointments will normally be made on contract basis for up to three years initially commencing August 2014, which, subject to mutual agreement, may lead to longer-term appointment or substantiation later. Review of applications will begin in mid-November 2013 and will continue until the posts are filled.

Salary and Fringe Benefits

Salary will be highly competitive, commensurate with qualifications and experience. The University offers a comprehensive fringe benefit package, including medical care, a contract-end gratuity for appointments of two years or longer, and housing benefits for eligible appointees. Further information about the University and the general terms of service for appointments is available at <http://www.per.cuhk.edu.hk>. The terms mentioned herein are for reference only and are subject to revision by the University.

Application Procedure

Application forms are obtainable (a) at <http://www.per.cuhk.edu.hk>, or (b) in person/by mail with a stamped, self-addressed envelope from the Personnel Office, The Chinese University of Hong Kong, Shatin, N.T., Hong Kong, or (c) by fax polling at (852) 3943 1461.

Please send the completed application form, full curriculum vitae, and a research plan (in .pdf format) by e-mail to laurenlee@cuhk.edu.hk (subject line: SEARCH2013MRN - <name of the applicant> [for post (1)]; SEARCH2013OBF - <name of the applicant> [for post (2)]; SEARCH2013FNS - <name of the applicant> [for post (3)]), preferably by November 15, 2013. Please also arrange three letters of recommendation to be forwarded by referees directly to laurenlee@cuhk.edu.hk. The Personal Information Collection Statement will be provided upon request. Please quote the reference number and mark 'Application – Confidential' on cover.

NINS National Institutes of Natural Sciences

We, the National Institutes of Natural Sciences (NINS), Japan, are pleased to announce the opening of the following positions for female researchers¹ in the fields of astronomy, fusion science, basic biology, physiological sciences or molecular science. We would like to request your assistance in identifying suitable applicants for these positions.

- Research fields, position titles and number of recruitments**
Astronomy: Assistant Professor (1 position)
Fusion science: Specially Appointed Associate Professor or Specially Appointed Assistant Professor (1 position)
Basic biology: Associate Professor (1 position)
Physiological sciences: Project Associate Professor (1 position)
Molecular science: Professor or Associate Professor (1 position)
- Application Deadline:** Tuesday - December 10, 2013
- Expected starting date:**
 As early as possible after being selected.
- For more information:**
 National Astronomical Observatory of Japan (NAOJ):
<http://www.nao.ac.jp/en/about-naoj/recruit.html>
 National Institute for Fusion Science (NIFS):
<http://www.nifs.ac.jp/en/jinji/index.html>
 National Institute for Basic Biology (NIBB):
<http://www.nibb.ac.jp/about/recruit/2013/09/associate25.html>
 National Institute for Physiological Sciences (NIPS):
<http://www.nips.ac.jp/eng/contents/recruit>
 Institute for Molecular Science (IMS):
<http://www.ims.ac.jp/english/whatsnew/2013/recruit1210.html>
- Miscellaneous:**
 NINS is promoting gender equality, observing the Equal Employment Opportunity Law.

¹ Under Article 8 of the Equal Employment Opportunity Law (Special Provisions of Measures Pertaining to Women Workers), NINS is recruiting female researchers in order to increase the proportion of female workers in our institutes.

MICHIGAN STATE UNIVERSITY

Departments of Biochemistry and Molecular Biology Microbiology and Molecular Genetics

The Departments of Biochemistry and Molecular Biology (www.bmb.msu.edu) and Microbiology and Molecular Genetics (www.mmgs.msu.edu) invite applications for a tenure-track faculty position at the Assistant or Associate Professor level whose research applies synthetic biology to bioenergy-related questions. We are particularly interested in candidates using innovative, systems-level approaches in yeast to investigate fundamental biological processes, although outstanding investigators using other microbial systems and synthetic approaches will also be considered. Successful candidates will join the highly collaborative interdisciplinary environment at MSU and interact with ongoing research efforts in the Great Lakes Bioenergy Research Center (glbrc.msu.edu).

Review of application materials will begin on **December 6, 2013** and continue until a suitable candidate is identified. Applicants should prepare a single PDF containing, in order, the following documents: cover letter, CV, description of research interests and future directions, and statement of teaching philosophy. The PDF should be uploaded to <https://jobs.msu.edu> (position #8599). Three or more letters of reference should be sent separately to BioenergyFacultySearch@cns.msu.edu. Questions regarding this position may be sent to the Chair of the Search Committee, Eric Hegg, at BioenergyFacultySearch@cns.msu.edu.

MSU is an Affirmative-Action, Equal-Opportunity Employer and is committed to achieving excellence through diversity. The University actively encourages applications of women, persons of color, veterans, and persons with disabilities, and we endeavor to facilitate employment assistance to spouses or partners of candidates for faculty and academic staff positions.

UC RIVERSIDE

VIROLOGY FACULTY POSITION INSTITUTE FOR INTEGRATIVE GENOME BIOLOGY

The Institute for Integrative Genome Biology at the University of California, Riverside invites applications for a new faculty member at the **ASSISTANT PROFESSOR** level to develop a state-of-the-art research program in the area of mammalian virology. The successful candidate will join an innovative and multidisciplinary Institute for Integrative Genome Biology (IIGB) that connects theoretical and experimental researchers from different departments in Life, Physical and Mathematical Sciences, Medicine, Engineering and various campus based Centers. The Institute has a vibrant faculty and excellent state-of-the-art facilities with advanced instrumentation and technical support in genomics, proteomics, microscopy and imaging, and bioinformatics. The individual will become a member of a major academic department in his/her area of expertise with opportunities for a secondary appointment in a variety of departments and colleges. Areas of interest could include the molecular biology of replication and gene expression of RNA viruses, virus-host interactions, innate and adaptive immunity and viral pathogenesis. Candidates working on state-of-the-art mammalian model systems are especially encouraged to apply.

Candidates who incorporate systems biology approaches, large-scale genomics, next generation sequencing, bioinformatics and/or visual microscopy to their research programs are preferred. The successful candidate will be expected to establish and maintain a vigorous, innovative and collaborative research program that is well funded, teach effectively at the undergraduate and graduate levels, and participate in departmental and interdepartmental graduate programs. Applicants must have a Ph.D. and postdoctoral experience. Review of applications will begin on **December 1, 2013**, and continue until the position is filled. Interested individuals should send: (1) a curriculum vitae, (2) a statement of research interests, and (3) three letters of reference. All information should be sent to <https://aprecruit.ucr.edu/apply/JPF00019>. For additional information, visit <http://www.genomics.ucr.edu/>, <http://cnas.ucr.edu/faculty/openings.html>

*The University of California is an
Equal Opportunity/Affirmative Action Employer.*

Assistant/Associate Professor Department of Cell & Developmental Biology SUNY Upstate Medical University • Syracuse, NY

The Department of Cell & Developmental Biology at SUNY Upstate Medical University in Syracuse, New York invites applications for two tenure-track positions at the Assistant/Associate Professor level. Candidates must have a PhD or equivalent degree and postdoctoral experience in cell biology or a related field. Applicants with interests in all areas of cellular function and differentiation are welcome; those with expertise in cardiovascular-related areas are particularly encouraged to apply. Applicants at the Associate Professor level should have an established track record of funding and research productivity. All candidates are expected to develop and maintain a vigorous extramurally funded research program and participate in the education of both medical and graduate students. Candidates with active NIH, NSF or equivalent funding are preferred.

The Department provides a strong, collaborative research community with interests in developmental model systems, signaling, cell motility and the cytoskeleton. We offer excellent resources to support new faculty including high-end imaging facilities, newly-renovated space, competitive salaries and startup packages, and active faculty mentoring. Syracuse provides a diverse, dynamic and affordable metropolitan environment with easy access to the outstanding recreational opportunities of the Adirondack Mountains and the Finger Lakes, while the proximity of SUNY Upstate to Syracuse University and SUNY ESF campuses fosters many productive scientific interactions. To learn more go to <http://www.upstate.edu/cdb/>.

Please submit a CV and a research statement describing past accomplishments and future plans, as a single PDF file, and arrange to have three letters of recommendation sent to: fontanek@upstate.edu.

Review of applications will begin Dec. 1 and continue until the position is filled.



At SUNY Upstate Medical University we strive to promote a professional environment that encourages varied perspectives from faculty members with diverse life experiences. A respect for diversity is one of our core values. We are committed to recruiting and supporting a rich community of outstanding faculty, staff and students. We actively seek applications from women and members of underrepresented groups to contribute to the diversity of our university community in support of our teaching, research and clinical missions.



THE DEPARTMENT OF CHEMICAL & BIOLOGICAL ENGINEERING, UNIVERSITY OF WISCONSIN-MADISON invites applications for two tenure-track/tenured faculty positions at the assistant, associate or full professor level. Candidates with truly outstanding accomplishments in any area of research of importance to chemical and biological engineering will be considered for either position, with preference given to the following fields:

- Inorganic materials synthesis and state-of-the-art characterization (PVL 77711).
- Statistical mechanics, atomistic simulations and thermodynamics (PVL 77712).

For more information, please visit ohr.wisc.edu and search by PVL number. Apply online at facsearch.cbe.wisc.edu.

Applications received by **December 31, 2013** will receive full consideration.

Women and candidates from groups traditionally under-represented in engineering are strongly encouraged to apply.



PEDIATRIC Infectious Diseases

Open Rank, Open Tenure. The Division of Infectious Diseases in the Department of Pediatrics is seeking applications from highly qualified M.D., M.D./Ph.D. or Ph.D., for faculty positions. The Division of Infectious Diseases has a long history of NIH supported laboratory and clinical research. The selected individuals will work collaboratively to expand current research programs as well as establish new areas of research in respiratory viruses and bacterial infections. These positions will be provided generous start-up packages as well as secondary appointment in basic science department and Centers of Excellence at UAB to further the capacity of research in infectious diseases at UAB.

QUALIFICATIONS

The successful candidates for these positions must have a successful record in research with current NIH funding. In addition, the ideal candidates should possess:

- Experience in the academic medical center setting
- A proven track record of research initiation
- Demonstrated research collaboration skills
- Strong communication skills and the highest of ethical standards

Interested applicants should contact:

William Britt, M.D.
Professor, Division of Ped Infectious Diseases
1600 7th Avenue South, CHB #107
Birmingham, AL 35233
Email: wbritt@peds.uab.edu

UAB is an Equal Opportunity/Affirmative Action Employer committed to fostering a diverse, equitable and family-friendly environment in which all faculty and staff can excel and achieve work/life balance irrespective of ethnicity, gender, faith, gender identity and expression as well as sexual orientation. A pre-employment background investigation is performed on candidates selected for employment. In addition, UAB Medicine maintains a drug-free and tobacco-free work environment. Physicians and other clinical faculty candidates, who will be employed by the University of Alabama Health Services Foundation (UAHSF) or other UAB Medicine entities, must successfully complete a pre-employment drug and nicotine screen to be hired. UAB also encourages applications from individuals with disabilities and veterans.



Open Rank Faculty Position University of Maryland College Park Department of Cell Biology and Molecular Genetics

The Department of Cell Biology and Molecular Genetics at the University of Maryland College Park is seeking to fill a tenure-track faculty position in the broad areas of cell biology and molecular genetics using animal, plant, or microbial systems. The appointment may be made at the Assistant, Associate, or Full Professor level, commensurate with qualifications and experience.

The successful candidate will be expected to maintain a cutting-edge externally funded research program that synergizes with existing core groups in the department including genomics and gene regulation, RNA structure and function, plant biology, microbial pathogenesis and immunology, and virology. The appointed candidate will also participate in undergraduate and graduate teaching. Applicants must have a doctorate degree, an outstanding publication record, and a commitment to excellence in teaching.

The University of Maryland, College Park is the flagship campus of the University System of Maryland. Close proximity to Washington DC, Baltimore, and the Maryland Biotechnology Corridor facilitates interactions with an extraordinary range of major research institutions such as NIH, NIST, FDA, USDA and JCVI, in addition to providing a rich cultural environment.

Applications should be submitted electronically to <https://ejobs.umd.edu/postings/22217> and addressed to Dr. Charles Delwiche, chair of the faculty search committee. Applications should consist of a single PDF file containing (1) a cover letter, (2) curriculum vitae, (3) summary of research plans (maximum two pages) and teaching philosophy (one page), and (4) contact information for at least three references. Complete applications should be received by **January 31, 2014**, but will be accepted until the position is filled.

The University of Maryland is an Affirmative Action/Equal Opportunity Employer. Women and members of underrepresented groups are especially encouraged to apply.



Faculty Positions in Regenerative and Aging Biology

The Mount Desert Island Biological Laboratory, located in Bar Harbor, Maine, is an independent biomedical research institution undergoing rapid growth and development. We are seeking outstanding scientists for recruitment at the Assistant, Associate and Full Professor levels. Successful applicants will have research programs focused broadly on regenerative and aging biology; will be addressing significant questions in these areas at an integrative level using state-of-the-art genomic, genetic and molecular approaches; will be utilizing non-mammalian model organisms including genetically tractable species such as *C. elegans* and zebrafish; and will have a strong interest in translating relevant discoveries into new tools and therapies. Candidates must possess a Ph.D. or M.D. degree, have a strong record of continuous research productivity, and have either active funding or clearly demonstrated potential for funding.

The MDI Biological Laboratory provides a uniquely collaborative and multidisciplinary research environment, outstanding scientific resources, and at least 80% protected time for development and maintenance of independent, externally funded faculty research programs. Start-up packages and salary are highly competitive and commensurate with current rank and experience. Successful candidates will have appointments in the Davis Center for Regenerative Biology and Medicine, an NIH-funded Center of Biomedical Research Excellence, and adjunct appointments at neighboring academic research institutions.

Please apply electronically at http://www.mdibl.org/job_opportunities.php. Include a cover letter, vitae, detailed research and career development plans, and the names and addresses of four references. Review of applications will continue until the positions are filled. Please direct any inquiries to asaucier@mdibl.org.

<http://www.mdibl.org>

MDI Biological Laboratory is an AA/EO Employer.

Science Careers is the forum that answers questions.



Science Careers is dedicated to opening new doors and answering questions on career topics that matter to you. With timely feedback and a community atmosphere, our careers forum allows you to connect with colleagues and experts to get the advice and guidance you seek as you pursue your career goals.

Science Careers Forum:

- » Relevant Career Topics
- » Timely Advice and Answers
- » Community, Connections, and More!

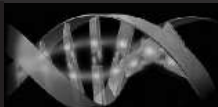
Visit the forum and join the conversation today!



Your Future Awaits.



Faculty Position in Functional Genomics



The Wistar Institute, an NCI-designated Cancer Center and independent research institute in Philadelphia, is seeking an outstanding candidate for a faculty position in the Center for Systems and Computational Biology (CSCB) and the Cancer Center Program in Gene Expression and Regulation. We are seeking candidates at the rank of Assistant or Associate Professor to develop or expand an extramurally-funded research program in functional genomic approaches to cancer biology and pathogenesis. Specific areas of interest include (but are not limited to) genetic and epigenetic changes in cancer, genomic responses to chemotherapy and drug-resistance, high-throughput functional genetic or chemical biology-based screens for defining the molecular pathogenesis of cancer. Of particular interest are candidates integrating innovative bioinformatics and NextGen sequencing based experimental approaches to problems in human cancer.

The Wistar Institute, an NCI-designated Cancer Center, offers highly competitive start-up support, salary and fringe benefits in addition to a superb and interactive research environment, including a newly constructed state-of-the-art research tower and outstanding core facilities in proteomics, genomics, microscopy, high-throughput molecular screening, bioinformatics, and flow cytometry. The Institute's location adjacent to the University of Pennsylvania campus provides for academic and clinical collaborations, and opportunities for training graduate students.

Applications will be reviewed as received and will be accepted until the position is filled. To ensure timely consideration, applicants should submit applications before **December 10, 2013**. The application should include: a curriculum vitae, a brief summary of past and future research interests, history of research funding support (if applicable), and three letters of reference. Applications should be sent by e-mail to: **Paul Lieberman, Search Committee Chair**, c/o Maria Colelli (colelli@wistar.org), The Wistar Institute, 3601 Spruce Street, Philadelphia, PA 19104. EOE/AA/M/F/D/V.



For more information about us, visit our web site at
www.wistar.org



Join the Conversation!

Twitter is a great way to connect with AAAS members and staff about the issues that matter to you most. Be a part of the discussion while staying up-to-date on the latest news and information about your personal member benefits.

**Follow us @AAASmember
and join the conversation
with #AAAS**



MemberCentral.aaas.org

WOMEN IN SCIENCE

forging
new pathways in
green
science



Read inspiring stories of women working in "Green Science" who are blending a unique combination of enthusiasm for science and concern for others to make the world a better place.

Download this
free booklet
[ScienceCareers.org/
L'OrealWiS](http://ScienceCareers.org/L'OrealWiS)



This booklet is brought to you by the
AAAS/Science Business Office
in partnership with the
L'Oreal Foundation



Genomics Faculty Positions

The Department of Biological Sciences at Clemson University invites applications for two full-time tenure-track faculty appointments to begin August 2014; one in Microbial Genomics and one in Eukaryotic Genomics. Clemson University is ranked 21st among national public universities by *U.S. News & World Report* and is located on Lake Hartwell near the Blue Ridge mountains in beautiful Upstate South Carolina. The department offers degrees in microbiology, biological sciences, and environmental toxicology.

Applicants must have a PhD, postdoctoral experience, and a strong publication record. The successful applicant is expected to establish a nationally recognized, externally funded research program, and to contribute to the Department's undergraduate and graduate teaching missions. We offer very competitive salaries and start-up packages. We anticipate making the appointments at the Assistant Professor level.

Microbial Genomics: We seek colleagues using cutting-edge genomic or metagenomic techniques to address important questions in virology, microbial-host interactions, microbial ecology, or pathogenesis.

Eukaryotic Genomics: We seek colleagues who are applying genomic tools to address important biological questions ranging from human health and disease to the origin and maintenance of organismal diversity and adaptation.

Applications must include a CV, three reprints, a research plan, a statement of teaching interests and contact information for three references. Review of applications will begin **December 1, 2013** and continue until the position is filled. Application materials should be sent by e-mail as one PDF file to: microsearch@clemson.edu for the Microbial position or to biosearch@clemson.edu for the Eukaryotic position. Further information about these positions and the department are available at: <http://www.clemson.edu/biosci> and <http://findjobs.clemson.edu>.

Clemson University is an Affirmative Action/Equal Opportunity Employer and does not discriminate against any individual or group of individuals on the basis of age, color, disability, gender, national origin, race, religion, sexual orientation, veteran status or genetic information.

SMART

SCIENCE, MATHEMATICS & RESEARCH FOR TRANSFORMATION

PART OF THE NATIONAL DEFENSE EDUCATION PROGRAM

SCHOLARSHIP FOR SERVICE PROGRAM

Undergraduate, graduate, and doctoral students pursuing degrees in Science, Technology, Engineering, & Mathematics (STEM) fields

SMART Scholars receive:

- + Full tuition and educational fees
- + Generous cash stipend
- + Employment with Department of Defense facilities after graduation
- + Summer internships, health insurance, & book allowance

For more information and to apply, visit

For more information and to apply, visit [HTTP://SMART.ASEE.ORG](http://SMART.ASEE.ORG)

In accordance with Federal statutes and regulations, no person on the grounds of race, color, age, sex, national origin or disability shall be excluded from participating in, denied the benefits of, or be subject to discrimination under any program activity receiving financial assistance from the Department of Defense.



POSITIONS OPEN

CARNEGIE
INSTITUTION FOR
SCIENCE

POSTDOCTORAL FELLOWSHIPS

The Geophysical Laboratory, Carnegie Institution of Washington, invites applications for postdoctoral fellowships. The Geophysical Laboratory emphasizes interdisciplinary experimental and theoretical research in fields spanning geoscience, microbiology, chemistry, and physics. The Laboratory supports world-class facilities in high-pressure research; organic, stable isotope and biogeochemistry; mineral physics and petrology; and astrophysics.

Please visit website: <https://jobs.carnegiescience.edu/jobs/carnegie-fellowships-for-the-geophysical-laboratory/> to view a list of required materials and application instructions. Also, see website: <http://www.gi.ciw.edu/> for a listing of personnel, current research interests, and major facilities.

Completed applications for Carnegie fellowships should be submitted by January 15, 2014.

The Geophysical Laboratory is an Equal Opportunity Employer.

CARL MOORE ENDOWED CHAIR in
Chemistry and Biochemistry
Loyola University Chicago

The Department of Chemistry and Biochemistry invites applications for the Carl Moore Endowed Chair beginning fall 2014. Preference is for an appointment at the rank of **PROFESSOR**, although advanced **ASSOCIATE PROFESSORS** will also be considered for the position. Applicants from all research areas of chemistry or biochemistry will be considered but analytical biochemistry is of particular interest for this position. A Ph.D. degree in chemistry, biochemistry, or in a closely related field is required. At the time of application, the successful candidate will be expected to have a tenured appointment and an externally funded research program as well as a notable number of highly cited publications. The incumbent will be expected to maintain an internationally recognized and a competitive externally funded research program, leading to continued publications and funding opportunities. This appointment will be accompanied by a reduced teaching load. The Department offers Ph.D., MS, and ACS approved B.S. degrees. For more details about the department, visit website: <http://www.luc.edu/chemistry>. Candidates should complete an online application at website: <http://www.careers.luc.edu>, with a cover letter, curriculum vitae, and a description of research and teaching interests. Applicants should provide the names and e-mail addresses of three individuals prepared to speak to their professional qualifications for this position. Review of applications will begin on December 15, 2013 and applications will be accepted until the position is filled. *Underepresented minorities and women are especially encouraged to apply.* Loyola University Chicago is an Equal Opportunity/Affirmative Action Employer.

ASSISTANT PROFESSOR OF BIOLOGY
Saint Anselm College
Manchester, NH

The Department of Biology invites applications for a tenure-track Assistant Professor position beginning August 2014. A Ph.D. and support of the College's mission are required. The successful candidate will teach Comparative Anatomy (with lab), Human Anatomy and Physiology (with lab), and a third course in their specific area of expertise. Continued research activities and mentoring of undergraduates are also integral to this position. Qualified individuals should submit a cover letter and curriculum vitae online at website: <http://www.anselm.edu/hr>. Three letters of recommendation should be submitted to Dr. Donald Rhodes, e-mail: drhodes@anselm.edu, no later than December 1, 2013.

Successful candidates will be able to assist the college to further its strategic goals for institution-wide diversity and inclusiveness.



Nontraditional
Careers:
Opportunities
Away From
the Bench
Webinar

Want to learn more about exciting and rewarding careers outside of academic/industrial research? View a roundtable discussion that looks at the various career options open to scientists and strategies you can use to pursue a nonresearch career.

Now Available
On Demand

www.sciencecareers.org/webinar

Produced by the
Science/AAAS Business Office.

Science Careers

From the journal Science AAAS

Your
career
is our
cause.

Get help
from the
experts.

www.sciencecareers.org

- Job Postings
- Job Alerts
- Resume/CV Database
- Career Advice
- Career Forum

Science Careers

From the journal Science AAAS

Help employers
find you. Post
your resume/cv.

Science Careers

From the journal Science AAAS

www.ScienceCareers.org

MARKET PLACE

immunodx@immunodx.com

Enhancing HIV, SIV, and human B/T cell and infectious disease state research and diagnostics for over 20 years. Recombinant proteins, antibodies and specialty biological products for Research, Diagnostics and Therapeutics applications. (800)-573-1700

ImmunoRllc Formerly ImmunoDiagnostics, Inc.
1 Presidential Way, Suite 104, Westbrook, ME 04090
781-938-6300 immunodx@immunodx.com